NASA CR-66855

ATTITUDE-REFERENCED RADIOMETER STUDY
VOLUME II
PRECISION RADIOMETRIC SYSTEM

August 1969

Prepared under Contract No. NAS 1-8801 by

HONEYWELL INC.
Aerospace Division
Minneapolis, Minnesota

for

NATIONAL AERONAUTICS AND SPACE ADMINISTRATION

FOREWORD

This report is Volume II of a five volume set documenting the results of an Attitude-Referenced Radiometer Study (ARRS), Part I, performed under National Aeronautics and Space Administration Contract No. NAS1-8801.

A previous analytical and design study under contract No. NAS 1-6010 indicated the feasibility of the measurement package and identified critical design and development problems. Having previously established the feasibility of the radiometric measurement package, this study provided advancement of techniques for the design and fabrication of precision radiometric and attitude determination systems for use in an earth-orbiting spacecraft. The effort was devoted to solving the critical design and development problems in Part I. Design requirements and conceptual design of the systems, based on analytical analyses, are established and reported within this study effort.

This volume documents the effort expended in radiometer system design and attitude reference radiometer system integration.

Honeywell Inc., Aerospace Division, performed this study program under the technical direction of Mr. J.C. Bates. The Part I effort was conducted from 1 January 1969 to 10 October 1969.

Acknowledgement is extended to Control Data Corporation for their contributions in attitude determination hardware considerations, to Lockheed Missiles and Space Corporation for their contributions in radiometry and inflight calibration, and to Carson Systems, Inc., for their contribution in experiment package system and interfacing.

Gratitude is extended to NASA Langley Research Center for their technical guidance, under the program technical direction of Messrs. A. Jalink and J.A. Dodgen, with direct assistance from Messrs. D. Hesketh, D. Hinton, W.C. Hodge, and H.J. Curfman Jr., as well as the many people within their organization.

CONTENTS

CONTENTS (CONCLUDED)

LIST OF ILLUSTRATIONS

LIST OF ILLUSTRATIONS (CONTINUED)

LIST OF ILLUSTRATIONS (CONTINUED)

LIST OF ILLUSTRATIONS (CONTINUED)

LIST OF ILLUSTRATIONS (CONTINUED)

LIST OF ILLUSTRATIONS (CONTINUED)

LIST OF ILLUSTRATIONS (CONTINUED)

LIST OF ILLUSTRATIONS (CONCLUDED)

LIST OF TABLES

LIST OF TABLES (CONTINUED)

LIST OF TABLES (CONCLUDED)

ATTITUDE REFERENCED RADIOMETER STUDY
VOLUME II: PRECISION RADIOMETRIC SYSTEM

By: John R. Thomas, William R. Williamson, Honeywell Inc.; Lester B. Florant, Herman P. Grienel, Allan D. Hoffman, Lockheed Missiles and Space Corp.; John C. Carson, Carson Systems, Inc.

SUMMARY

This volume documents those aspects of the Attitude-Referenced Radiometer Study devoted to advancing the techniques for the design, analysis, and fabrication of applicable radiometric systems and the overall ARRS system interface. Basic radiometric requirements, derived under contract NAS 1-6010, are radiometer accuracy of 0.03 W/m^2-sr, repeatability of 0.005 W/m^2-sr, and noise equivalent radiance of 0.005 W/m^2-sr in a spectral interval encompassing the atmospheric 15μ CO_2 absorption band, primary calibration accuracy of better than 1%, and inflight calibration stability of 0.1%. The study was organized into four major areas - system interface, radiometer, calibration (primary and inflight) and critical component testing.

In the system interface area a technique was developed for rapid and complete identification and determination of the effects on all ARRS subsystems of varying design or performance parameters in any one subsystem. The analysis tool developed for this function is the parameter variation checklist (PVCL).

A comprehensive generalized radiometer analytical model was developed to be used as a tool in the design, analysis, and evaluation of those radiometer configurations applicable to the ARRS radiometer performance goals. The analytical model describes propagation of external and internal signal, noise, and error through the radiometer and includes a description of the radiometer transfer function (spatial and temporal) signal processing, and ground data reduction.

An operational Primary Calibration System (PCS) concept was defined and the preliminary design of an engineering model completed. This PCS design includes a simulated extended radiance source and the capability of calibrating radiometers of up to 24-inch aperture diameters with up to a 2 mr x 2 mr field of view. A variable level flight model Inflight Calibration (IFC) concept was defined and the preliminary design of an engineering model completed.

In the critical component test area, a technique was developed to measure the 15μ reflectance of large diameter collimating reflectors with an accuracy of better than 0.1%. In separate mirror reflectance tests, several small gold-coated ULE quartz and Cervit mirrors were subjected to various simulated

space environments - including temperature, vacuum, and irradiation - and were found to exhibit an average reflectance degradation of 0.2%. Long-term vacuum aging tests of an IFC blackbody source and mirror reflectance were initiated and are continuing.

INTRODUCTION

The study goal was to advance techniques for the design, analysis, and fabrication of precision radiometric systems for use in earth-orbiting spacecraft. The study covered both analytical and experimental work on a selected attitude referenced radiometer for a rolling wheel satellite to be used for earth coverage horizon measurements, earth resources surveys, or synoptic meteorological measurements. Principal elements of the radiometric system include the spaceborne radiometer and Inflight Calibrator(IFC), and the ground based Primary Calibration System (PCS). Previous analytical and experimental work accomplished under contract NAS 1-6010 demonstrated that practical radiometric systems for accomplishing the previously cited missions are feasible. This effort was to examine and solve the critical design and development problems identified in the earlier studies.

Those studies showed that LWIR radiometer design and analysis techniques were lacking in the availability of a unified approach using standardized analysis models for the evaluation and tradeoff studies of different types of radiometer configurations. Consequently, in the area of radiometer design the study goal was the development of a generalized analytical model of LWIR radiometers encompassing those configurations applicable to ARRS-type missions. A requirement imposed on the analytical model was to predict performance characteristics of radiometers capable of the following performance:

- Accuracy: 0.03 W/m^2-sr
- Noise equivalent radiance: 0.005 W/m^2-sr
- Dynamic range: 2000 (peak input of 10 W/m^2-sr)
- Dynamic response: < 100 μsec
- Field-of-view: 0.2 x 1 mrad

Feasibility of practical ground-based and IFC concepts were demonstrated by analysis and experiment in NAS 1-6010. Primary calibration studies indicated that the optimum concept uses a continuous temperature variable blackbody source projected to infinity by collimating optics larger in aperture diameter than the radiometer being calibrated. That recommendation was reviewed and substantiated by the present study and a calibration system design was undertaken. Configuration of all system elements was specified including vacuum chamber, vacuum system, cooling system, blackbody source and temperature control, and collimating optics. The main problem associated

with the type of calibration system designed is in the reflectance of the collimating mirror used to project the calibration source to infinity. For better than 1% calibration, the total collimator reflectivity must be known to better than 1%. This accuracy is unattainable throughout industry, government, or university facilities. Consequently, effort was devoted to determining a method for measuring collimator reflectance to better than 1% including experimental verification of the chosen method.

Similar circumstances existed for IFC. The NAS 1-6010 recommendations for IFC concepts were reviewed and the optimum concept of a flight unit selected. Design of an engineering model IFC was undertaken and critical component deficiencies identified. The selected IFC concept is similar to that used for primary calibration - radiance from a small blackbody source is collimated into the radiometer optics by a removeable collimating reflector. Available flightworth blackbody sources were found to be lacking in required temperature stability. Modifications for increased stability were made to a commercially available source and extended time stability tests started.

In the IFC, as in the PCS, the collimator is a critical element; however, it is the reflectance stability rather than the actual reflectance that is critical. Any instability in the IFC mirror reflectance from the time of primary calibration through the mission life will propagate directly into calibration instability. The IFC stability goal is 0.1%; no information could be found in the literature indicating that mirror reflectance exhibited that degree of stability. Consequently, tests were run using simulated space environments to determine the reflectance stability that could be expected.

Other areas of critical components were examined and recommended tests were identified; tests in these areas were not, however, conducted. Tests were outlined for

- Detectors
- Choppers
- Spectral filter
- Detector/relay optics mount

SYSTEM AND INTERFACE

The ARRS study was directed at the development of technology and analytical tools with the broadest possible applicability. Interfaces between the radiometric and attitude determination functions and their interaction with the system and mission in which they reside will constrain this applicability. In the following paragraphs these constraints will be defined and their implications discussed.

System Baseline Design

This section defines the limits of applicability of the ARRS radiometric and attitude determination design, analysis, and technological development. The section is organized as a baseline design summary; however, instead of parameter values, ranges and the implications of exceeding them are discussed.

During the course of the study a running check was maintained against the effects of each defined quantity on other elements of the system, with particular emphasis on the loss of generality incurred by such definition. Performance of this activity was documented by the maintainence of the Parameter Variation Check List (PVCL); see Table 1. This device permitted the accounting for, without freezing, the effects of parameter variations on each other and on the type of system and mission constraint. In the table the circled numbers reference the explanatory notes developed as a part of the updating activity that continued throughout the study. These are presented in Appendix A and form the basis for subsequent paragraphs in this section.

Although initially used only as an accounting tool, the PVCL has become a useful device for future applications of the ARRS results. In general, each new mission or system application will in part conform to the ARRS conditions of applicability and in some other ways it will not. The PVCL with its associated notes will act as a reminder of which of these is which and, where extension or modification of the ARRS results is required, will indicate the method of solution.

Table 2 summarizes the results of studies in the major areas of concern to systems integration, the most significant of which is the alignment problem. It had been hoped at the outset of the study that a method could be found of monitoring the angular relations between starmapper and radiometer lines-of-sight independently of either of their internal configurations. Although no basic obstacle to this goal was uncovered, neither was any currently available device found capable of performing as required. Therefore, at such time as the results of the ARRS study are to be applied to the fabrication of a measurement system, an alignment monitor design tailored to that application will probably be required.

TABLE 1. - PARAMETER VARIATION CHECK MATRIX

Constraining element / Parameter	Mission	Spacecraft	Attitude determination	Radiometer	Data handling	Alignment monitor	Other
Radiometer							
1. Spectral band	1 2 3				4	5 6	
2. Scan rate	1	2	3		4		
3. Weight		1					
4. Volume and envelope		1 2	3 4				
5. Operating temperature	1 2	3 5	4				
6. Redundancy	1	2	3			4	
7. Power dissipation		1					
8. Cooling system	1	2 3	4				
9. Detector type	1				2		
10. Transfer function	1				2		3
11. Field of view	1	2				3	
12. Optics configuration		1	2			3	4
a) Aperture		1					
b) f/-number		1					
13. Chopper type	1		2		4		3
14. Chopper frequency					1		
15. Dynamic range	1				2		
16. Structural materials		1	2			3	
17. Internal alignment						1	
18. Stray radiation	1	2				3	
19. Inflight calibration system (number of levels)					1		
Attitude determination							
1. Torque models	1	2		3			
2. Scan rate		1			2		
3. Operating temperature				1			
4. Sensor type	1	2		3		4	
5. Volume		1		2			
6. Stray light baffling	1	2 4				3	
7. Viewing geometry	1	2		3			
8. Transfer function					1		2
9. Internal alignment						1	
10. Output bit rate					1		2
11. Redundancy	1	2		3			
12. Power dissipation		1		2			
13. Structural materials		1		2		3	
14. Field of view	1	2		3			
15. Scan type	1	2					

TABLE 2. - ATTITUDE REFERENCED RADIOMETRIC SYSTEM INTEGRATION

Interface	Integration problem	Study result
Radiometer/starmapper	Operating temperature: Can starmaper perform over range of possible radiometer temperatures? Alignment problem, if not?	Possible, in general, to find combination of materials such that starmapper can perform from 150 to 300°K
	Alignment: Can a monitoring approach be found which is independent of radiometer and starmapper configurations?	Yes, in principle, but not yet in practice; i.e., the devices appear feasible but do not exist
Radiometer/spacecraft	Volume available: How much assymetry can be tolerated?	Inconclusive; up to factor of 1.1 was shown compatible with attitude determination performance
	Thermal control: How warm can radiometer run?, effects of gradients, power dissiaption	Inconclusive; significant improvement at lower temperatures; IFC power marginal at 200K
Radiometer/data link/ground reconstruction	Chopper rate versus buffer size: How much to reduce aliasing error to tolerable levels?	Two times/dwell time (baseline approach) appears adequate
	Bandwidth constraints and distortion: Can signal spectrum be recovered to prescribed accuracy within Δf limits?	Inconclusive, but promising results
Radiometer/attitude determination	Optimum scan rate: Is NER achievable at scan rate that provides adequate control?	Yes, D^*'s can be obtained at levels that render this trade-off insignificant over scan rate range of 1 to 5 rpm
Attitude determination/ spacecraft	Volume available: Are baffles for daylight starmapping consistent with baseline spacecraft design?	No, not without alternation of radiometer interface (e. g. size) or spacecraft
Starmapper/data handling system	Storage required: On-board processing, false count rates versus storage constraints at maximum scan rate	60 000 bit maximum can be adhered to

Baseline Design Summary

The general ARRS functional requirement is to perform, from a space platform, precise, high-resolution, LWIR radiometric measurements accurately associable with a pointing direction in geocentric coordinates. The system functional elements involved in performing this overall function are related as shown in Figure 1.

Basic characteristics that define the class of systems to which the ARRS study applies and from which cannot be significantly deviated are as follows:

- Passive scan
- Spin stabilization
- Low to intermediate altitude (200 to 1000 n. mi.)
- Resolution/attitude reference range $\approx$ 0.01°
- Radiometric spectral region - LWIR (8 to 40μ)
- Accuracy/precision regime: $\approx$ 1% or 0.03 W/m^2 - sr

Additional elements defined to act as a context for performance of the study are as shown in Table 3.

The constraints of precision, altitude, resolution, and pointing are predominate in determining the range in the parameters describing these functions, as summarized in Table 4.

Mission constraints. -- Under the heading of mission are the following items:

- Data acquisition - types of measurements that must or can be performed, limits on rates, support data required
- Environments - launch, orbit, storage
- Spacecraft - volume, weight, power

Data acquisition: The types of measurements that can generally be performed by an LWIR sensing system are summarized in Table 5.

The predominant constraint on the type and quality of the measurement to be made is the bandwidth limitation. For the same amount of data in a given spectral increment, the bandwidth requirement is proportional to the number of such increments and the number of spatial resolution elements recorded. These quantities are tradeable against one another, and these data requirements tradeoffs will in general determine the character of the measurement system.

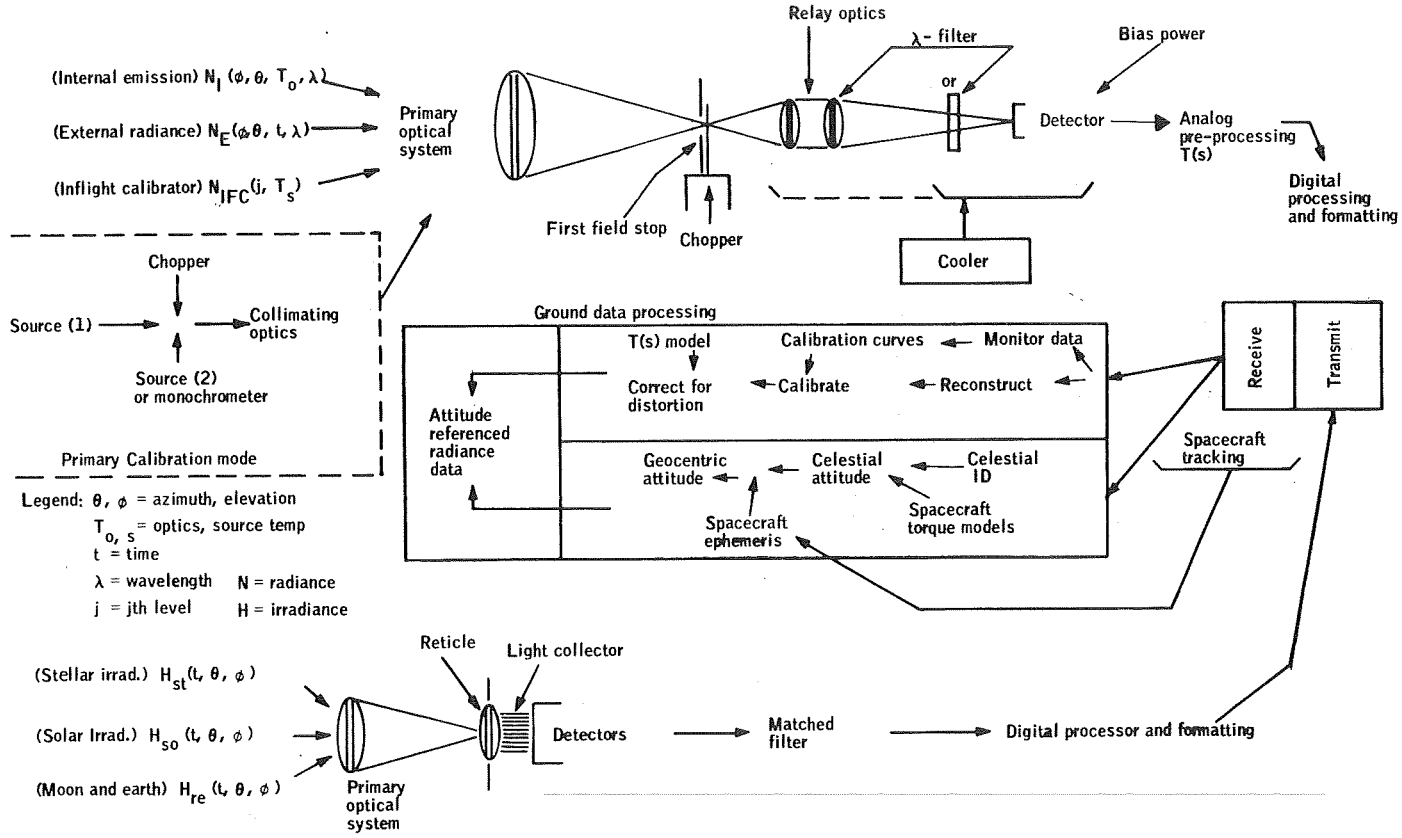

Figure 1. Attitude-Referenced Radiometric System Schematic Description

TABLE 3. - ARRS BASELINE SUMMARY

Item	Description	Item	Description
Satellite system		ARRS frozen characteristics	
Orbit	• 500 km altitude • 3 p.m. - 3 a.m sun synchronous (±2 hr)	Design "technology" constraints	• No moving parts except radiometer chopper and inflight calibration if absolutely necessary
Spacecraft	• Rolling wheel		• No active thermal control
Life	• one year	Minimum redundancy	• Celestial sensors (full) • IR detector • IR chopper • Inflight calibration • Serial electronics
Attitude control	• Intermittant magnetic torquing • V-head horizon sensor		
Spin rate	• 1 to 5 rpm • Spin axis _ orbit plane ±5°		
ARRS - satellite interface		Radiometer	• Cooled detector • Solid cryogen cooler • Optical chopping for d-c response
ARRS operating temperature	• 200 to 300°K nominal • predictable to ±20°K		• Variable temperature source plus collimator as primary standard
Mechanical	• Tight thermal and "loose" mechanical coupling to spacecraft baseplate		• Vacuum calibration and store
Radiation	• No solar illumination of radiometer aperture; shield also obscures solar paddles	Attitude determination	• Discrete discontinuous attitude sampling plus math model of spacecraft
Data handling	• 0 to 5 v output to sample, quantize and storage compatible with STADAN		

TABLE 4. - ARRS PARAMETER BOUNDS

System element:	Description/parameter	Value	Reason for bound
I. Radiometer			
A. System	1) Spectral band, $\Delta\lambda$, microns	14.0 to 16.3	Worst case, HDM application
	2) Scan rate, rpm	1 to 5	Low: data requirements, attitude control High: bandwidth, NER
	3) Ambient temperature, °K	150 to 300	Range achievable on-orbit passively
	4) Power dissipation, W (@ 200°K, if cooled)	< 2	To stay compatible with passive cooling to as low as 200°/c
B. Primary Optics	1) Configuration	Open	
	2) Aperture, in.	Open	Resolution, NER, envelope
	3) f/-number	Open	Low: practical limit High: NER, envelope
	4) Resolution (IFOV) mr. azimuth	0.2 to 10	Data requirements, size constraints
	elevation	0.1 to 1.0	
C. Relay Optics	1) Configuration	Open	
	2) Temperature, °K	65 to 300	Total practically achievable
D. Chopper	1) Frequency, KHz	0.5 to 10	Resolution
	2) Type	Open	
E. Spectral Filter	1) Location	Open	
	2) Temperature, °K	< 80	NER, emission effects on accuracy
F. Detector	1) Type	Open	
	2) Temperature, °K	10 to 80	Performance range of usable detectors
G. Cooler	1) Type	Solid cryogen	Life, power
	2) Temperature, °K	16, 65	Result of previous study
	3) Design load @ 1 year life, mw	25	Result of previous study
H. Inflight Calibrator	1) Source temperature, °K	Open	
	2) Number of levels	> 5	Sufficient to solve multilevel problem
I. On-board Electronics	1) Information bandwidth cycles/mr	1 to 5	Data requirements, representative applications
	2) Dynamic range (W/m^2-sr)	> 2000:1 (0.005-10)	Data requirement
J. Primary Calibration	1) Type source	Variable temperature	Advanced state of development
	2) Temperature range, °K	< 80 to > 250	Corresponds to dynamic range
	3) Extent (field angle) mr	> 3	Corresponds to nominal resolution element
II. Attitude determination sensors			
A. System	1) Scan rate, rpm	1 to 5	
	2) Operating temperature, °K	150 to 300	Interface with radiometer
	3) Power dissipation @ 200°K, w	< 1	Compatibility with passive thermal control
	4) Volume	Open	
	5) Daylight operation	Open	
B. Primary Optics	1) Configuration	Open	
	2) Field of view, degrees	10 to 30	Useful range for star sensing
	3) Viewing (cant) angle, degrees	Open	
	4) Baffle type	Open	
C. Electronic Processing	1) Output bit rate, bits/orbit	< 60,000	Storage constraint -- worst case
	2) Transfer function	Open	

TABLE 5.- MEASUREMENT APPLICATIONS

Type	Typical application	ARRS applicability
1) Single channel, single wavelength radiometry	Absolute thermal and radiance mapping (OSP, Nimbus, Tiros, ERTS)	Excellent
2) Multi-spectral radiometry	Atmospheric and constituent concentration measurement (Nimbus, (ERTS)	Excellent
3) Spectroscopy	Vertical temperature profile inversion (Nimbus)	Poor
4) Imagery	Relative thermal mapping (ERTS, TOSS)	Good in some areas, Poor in others

The ARRS study was aimed at that class of instrumentation suited for measurement types 1 and 2, and, although the study was conducted primarily for the 14 to 16μ interval, the results are quite generally applicable for any measurement integrated over a band (as opposed to a spectrometric measurement) when the band is located between 8 and 25 microns. The number of such channels is limited to of the order of five by cooler capacity and data rate constraints of the baseline configuration; but, the results of the study pertaining to radiometers are easily generalizable to systems with larger values for these constraints. A more serious, inherent limitation comes from the class of optical systems included in the study. These are basically simple, narrow-field instruments ideally suited for high-precision radiometry but different in kind from wide-field imagining systems.

The latter are characterized by more complexity - i.e., more elements and structures in the optical path - and are inherently more susceptible to stray radiation and self-emission effects than the simpler, narrow-field instruments. These considerations render those parts of the radiometer analytical model having to do with stray radiation and internal emission less readily usable for imaging-type applications. Analysis performed in areas such as detector response modeling, inflight calibrations, and transfer function modeling will, however, be useful in these applications.

Within the class of narrow-field, single-channel instruments, the constraint on data rate will still be a major limiting factor. This constraint derives chievely from the maximum on-board storage available. The storage required is given by the expression:

$$C_s \text{ (bits)} = m \left[n \frac{\dot{\phi}}{\Delta\phi} \delta_\phi \; f_{\Delta\phi} \, q \, \Delta t + k \right]$$

where

m = number of orbits for which data are stored prior to readout

n = number of detector channels

$\dot{\phi}$ = scan rate (rad/sec)

$\Delta\phi$ = resolution element dimension in scan direction (i.e., $\frac{\Delta\phi}{\dot{\phi}} = c_d$, dwell time)

δ_ϕ = portion of each scan stored

$f_{\Delta\phi}$ = samples (chop cycles) per resolution element

q = bits/sample

Δt = sec/orbit

k = attitude, inflight calibration, and housekeeping storage requirements per orbit

Considering the horizon definition case,

$\delta_\phi \simeq 3°/360° = 1/120$

$m = 1$

$n = 1$

$\Delta t = 5.4 \times 10^3$ sec

$k = 60 \times 10^3$ bits, attitude determination
50×10^3 bits, monitors
100×10^3 bits, inflight calibration

The number for inflight calibration would be decreased considerably if on-board averaging were used; i.e., it was assumed here that each sample of the 100/level would be stored. The monitors were computed individually; an example is a typical temperature monitor where a ±20° range would be covered with 0.05° resolution, resulting in a 10-bit word for each monitor. Assuming a readout rate of one/minute and 30 such sensors, a 27-kilo bit/orbit total is reached. Other monitors and time words make up the remainder of the 50-kilo bits/orbit allocated.

The quantity $f_{\Delta\phi}/\Delta\phi$ is a measure of the system resolving capability; one-half of this number is the maximum frequency in terms of number of cycles/rad permissible in the input signal for no aliasing, or sampling, error.

For a system with a dynamic range of 2000:1, the number of levels should exceed 4000, or 12 bits/word, to render this a negligible source of noise.

Figure 2 illustrates some of these relations. Note that for the set of parameters used in the HDMP feasibility design - $\dot{\phi} = \pi \times 10^{-1}$ (3 rpm), $\Delta\phi = 2 \times 10^{-4}$ rad, and $f_{\Delta\phi} = 2$ - the storage requirement per orbit is roughly 1.8 megabits. This is marginal in terms of a solid-state memory, probably limited in choice to MOS or plated-wire memories.

These problems are exaggerated by the stringent requirements on measurement accuracy. The usual approach for achieving high fidelity by means of excessive bandwidth cannot be used. Signal frequencies near the limit of system resolving capability will generally experience distortion. Care must be taken to avoid sampling error and other sources associated with limiting.

Environments: These are grouped into three areas in time - prelaunch, launch and on-orbit.

During the prelaunch period the prime areas of importance unique to ARRS type systems are radiometer cleanliness. and maintainence of the stored cryogen. After the last radiometer primary calibration, probably prior to shipment to the launch base, any contamination of optical surfaces could results in loss of calibration. This and the likelihood of cold internal surfaces will probably lead to the evacuation and sealing of the radiometer until the beginning of orbit operations. Again, owing to the cleanliness requirement, vacuum pumping for extended periods must be by means of vac-ion techniques or an equivalent.

Vacuum lines must also be supplied to the ullage tubes of the stored cryogen until launch. No other special care appears necessary after "topping off", which can occur several days prior to launch.

On-orbit, for those applications where the radiometer is cooled significantly (e.g., to less than 220°K), direct irradiation of the aperture by the sun cannot be permitted. This constraint will limit the combinations of time of launch, orbital inclination, and scan angles, all of which are preferably determined solely by the data requirements of coverage. For example, in a polar orbit, coverage of one of the poles will be excluded in a noon orbit. In a measurement of the earth's limb, however, this coverage would probably be lost because of stray radiation produced by the proximity of the sun to the line-of-sight.

Spacecraft: The study was addressed to measurements from spin-stabilized spacecraft with the spin vector approximately normal to the plane of the orbit. This permits totally passive (i.e., no moving parts) scan generator for the radiometer. For the attitude determination problem, this presents a configuration amenable to modeling, hence requiring no active star tracking or inertial platforms. Generalization of the results to a vertically-oriented, CMG-controlled spacecraft, for example, is subject to the following qualifications:

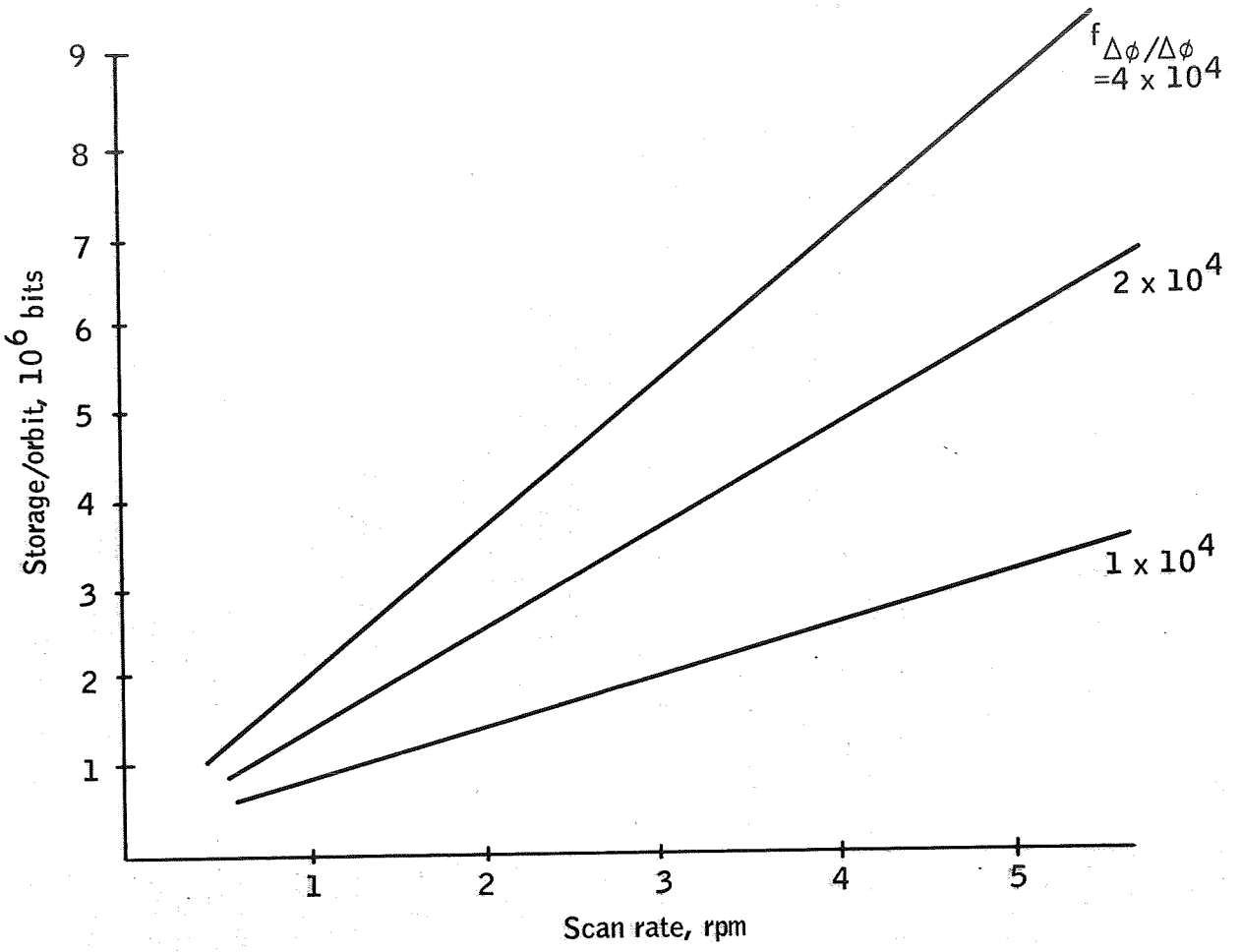

Figure 2. Output Bit Rate Relations

a) All of the torque models are invalid; however, portions of the basic attitude determination program may be usable in some cases where the control system operation is intermittent.

b) Scan generation would have to be accomplished mechanically for both the starmappers and the radiometer. Other than the additional alignment problems, this poses no great difficulty. The radiometer analytical model would require extension to cover the additional element, but this should not affect the validity of the current components of the model.

Payload integration. -- The subject of the paragraph is the integration of the celestial sensors with the radiometer. Four considerations are pertinent - choice of materials, thermal, alignment, and the geometrical relation of the sensors' and radiometer lines-of-sight. All of these primarily affect one performance parameter, determination of the direction of the radiometer line of sight to within 20 arc sec. A secondary factor in the thermal interface relates to the isolation required between the starmapper and radiometer to prevent undesirable gradients. This, however, has not proven significant in any of the designs considered in the study.

A typical allocation of line-of-sight errors is given in Table 6. These requirements are achievable, but in the area of alignment generally become major design determinants - structure considerations alone determine optical concept design, for example. To make the instrument design technology developed under ARRS free of this configuration dependence, it was decided to explore the possibility of separate, on-board alignment sensing.

The basic approach to alignment sensing is as depicted in Figure 3. A point source is positioned at the field stop of the radiometer and the resultant collimated light sensed by the alignment sensor. The latter is integrated with an autocollimator by which it maintains its own alignment with respect to a reference surface. A similar arrangement exists within the starmapper and is referenced to the same surface, whose orientation and stability is not critical. Also shown in the possibility for direct alignment between the radiometer and starmapper alignment sensors.

Figure 4 shows a typical sensor-autocollimator design concept. Proper choice of spectral interval for the light sources permits operation without interference with the radiometer or starmapper functions. Sensors of this type have been shown to be capable of 1 arc sec accuracy over at least a 60 arc sec range.

The major problem with such a device in an ARRS application is its effect on the production of stray radiation in both the starmappers and the radiometer.

TABLE 6. - LINE-OF-SIGHT DETERMINATION ERROR ALLOCATION

Item	Allocation, arc sec
Attitude determination relative to celestial coordinate system	±14
Orbit determination	±10
Spacecraft data processing	± 3
Time correlation	± 3
Ground data processing and star ephemean	± 3
Radiometer internal alignment	± 5
Celestial sensor internal alignment	+ 5
Radiometer - celestial sensor alignment	± 5
	RSS = ±20

It is possible, for the Classical Newtonian Configuration (or any with a central blockage), to place the sensor in the shadow of the secondary mirror, thus minimizing stray radiation problems. This arrangement is illustrated in Figure 5, along with the analogous approach for the off-axis parabola. In the latter case an extension of the primary mirror is required to keep the alignment sensor out of the main optical path. An extension of the type shown - toward the optical axis - should not produce any serious problems.

The problem is greatly simplified by the location of the limiting field stop at the primary focus, rendering detector and relay optics alignment noncritical. In some designs it is useful to make the detector itself the limiting stop, rendering the alignment and alignment sensing more difficult. Even though the detector is the limiting stop, there will also be a stop at the primary focus of sufficient size only to accommodate detector motion. Monitoring just to this field stop, however, would produce inadequate results.

Figure 6 depicts an approach to alignment sensing in such a configuration. A point source located in the plane of the primary focus is imaged onto a corner-reflecting surface (e. g., Porro roof prism) at the detector mount. This method would be sensitive to detector cross-axis translations and lens tilts. The spectral interval cannot be chosen on a noninterference basis as before if the spectral filter is located within the relay optics. In such cases, it will be necessary to operate the sensor intermittently.

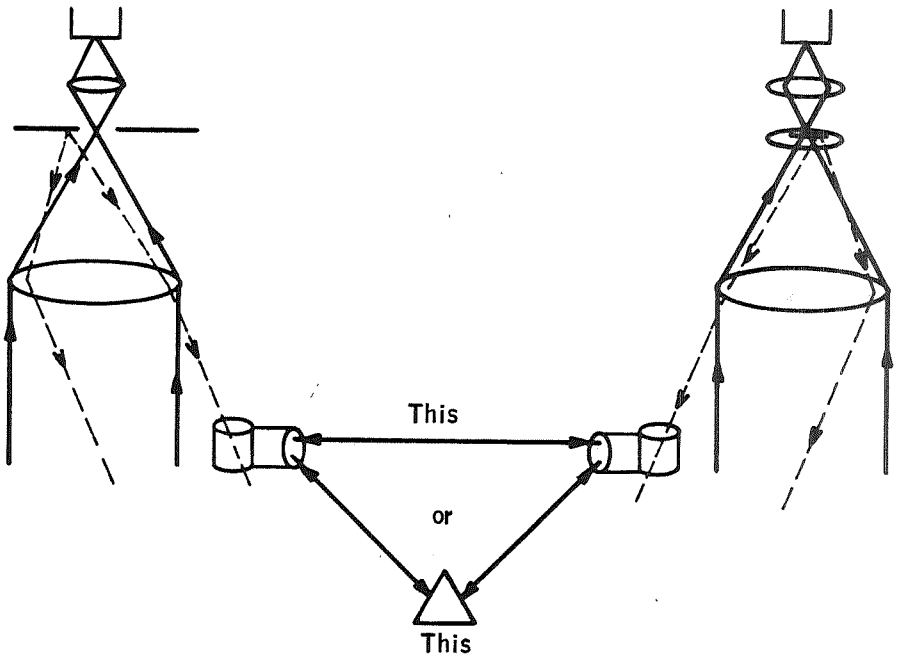

Figure 3. Alignment Monitor Schematic Description

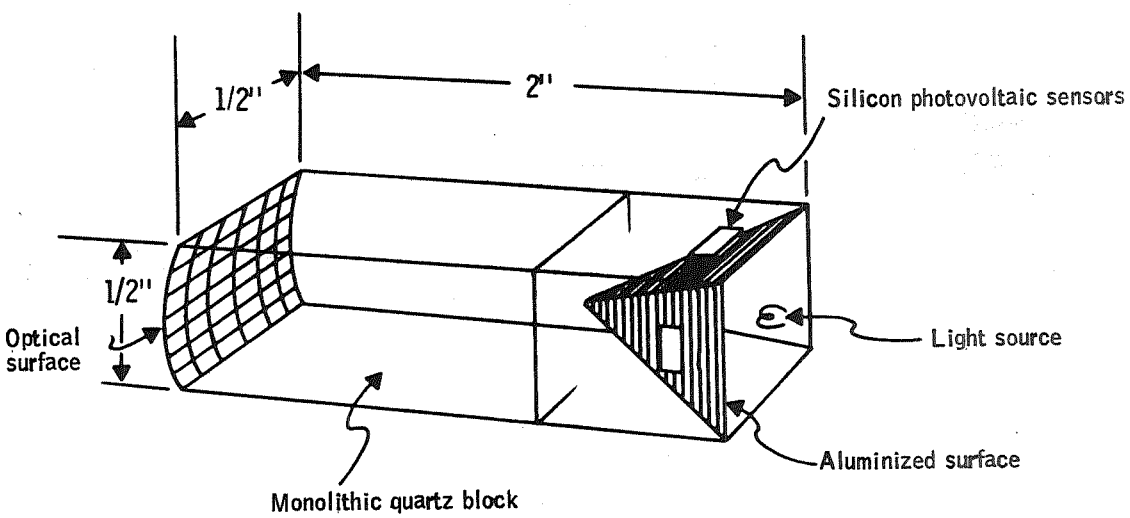

Figure 4. Basic Alignment Sensor Design

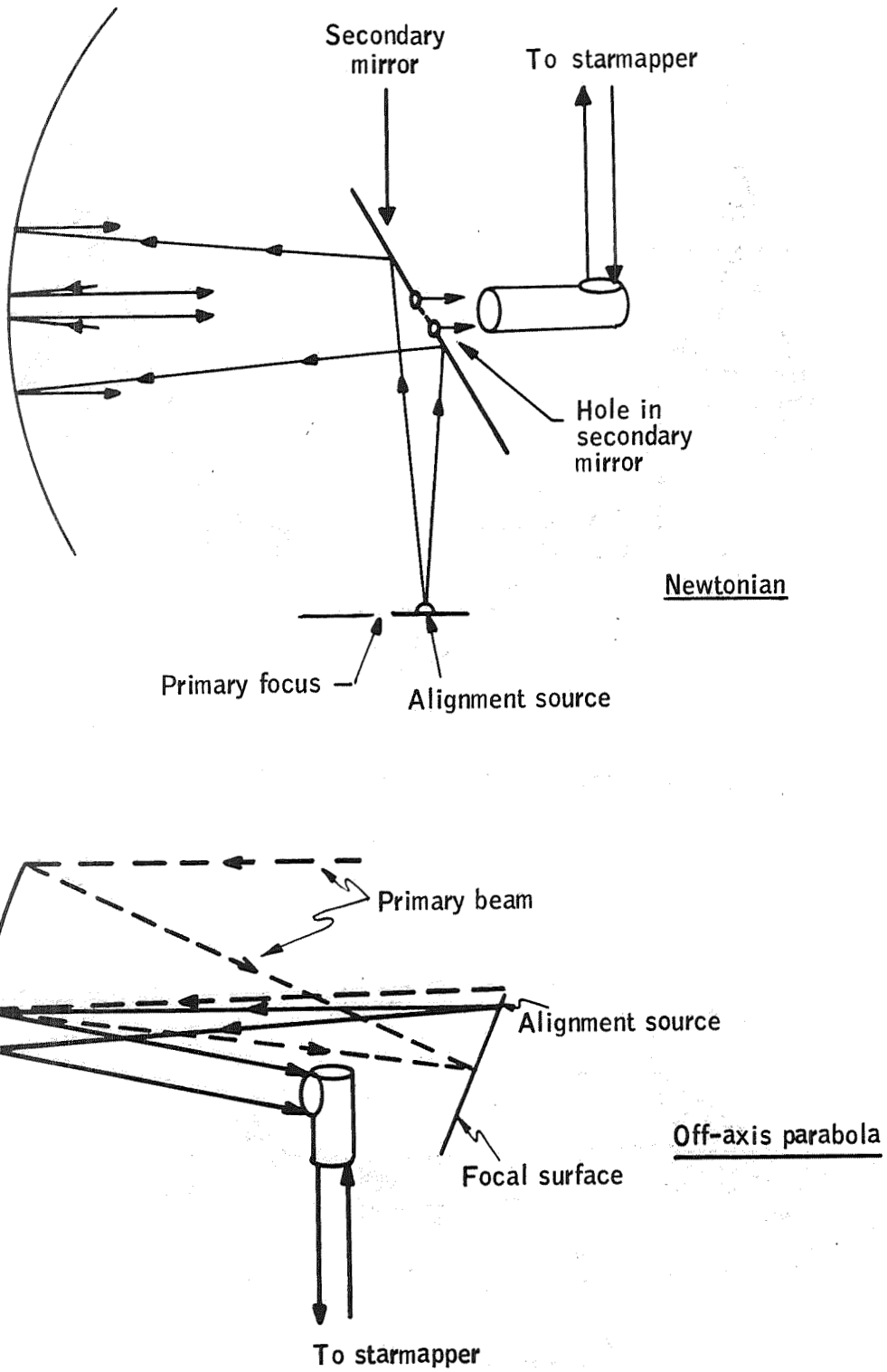

Figure 5. Method for Keeping Alignment Sensor Out of Main Beam

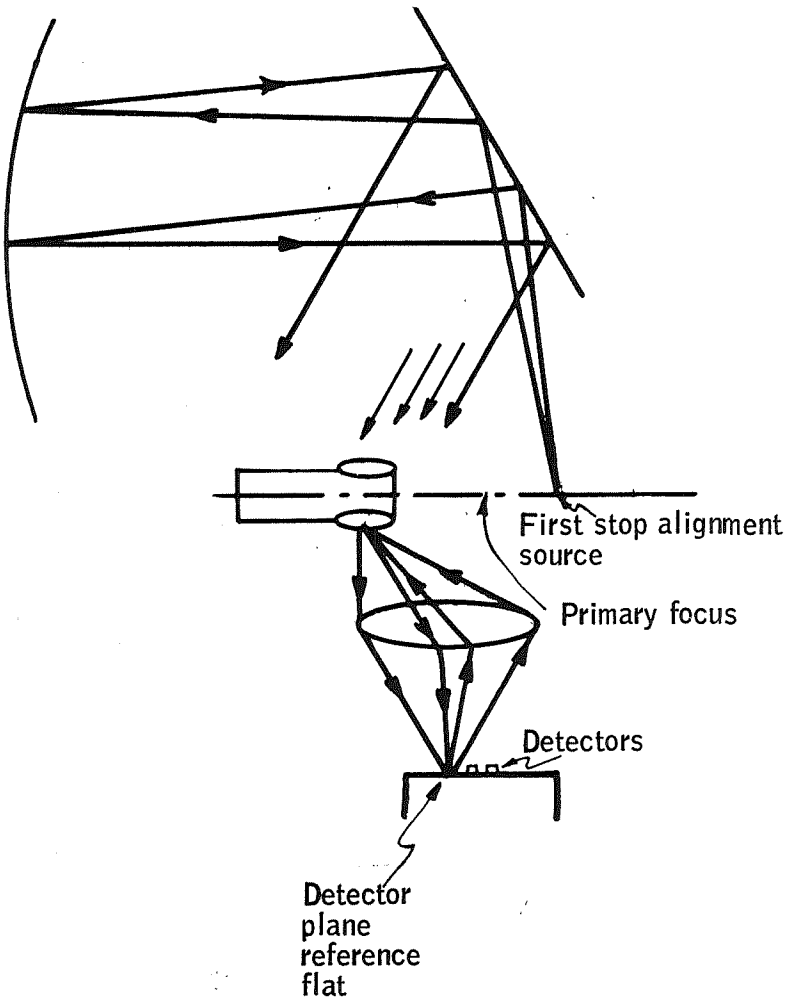

Figure 6. Alignment Sensor Concept for Detector as Limiting Field Stop

Thus far no distinction has been made between the axes to be monitored. If the starmapper and radiometer axes are parallel, it might seem that only angles in the scan direction need be sensed. However, the starmapper field of view may extend far enough off-axis to create a problem for a single-axis measurement. If the starmapper one/half field angle is 10°, then the coupling of rotational errors about the optical axis into pitch-errors is proportional to tan 10°, about 0.15. That is, a 20 arc/sec error in starmapping roll would convert to a 3 arc sec uncertainty in radiometer pitch. This coupling is probably sufficiently weak to account for structurally, rather than monitor. Canted starmappers are likely, however, and here the situation rapidly becomes such that this rotation must be measured. Moreover, it is not necessarily true that other applications will be concerned with single axis pointing accuracy only.

The problem of detecting rotation about the starmapper axis relative to the radiometer becomes that of measuring (or securing) the reticle rotation as there is no effect from rotation of the optical elements about their own axes This would seem straightforward, involving a reference surface -- e.g., on the edge of reticle -- converting rotation into tilt, which is readily detectable using the same technique as before.

A survey was made of vendors for such devices; no combination specifically meeting the ARRS requirement was found.* A major detailed design effort would only be justified for an application clearly demanding the use of such a set of devices.

*In fact, in most cases the devices had been designed for an order of magnitude more precision with a concomitant, and intolerable, size penalty.

GENERAL RADIOMETER MODELING AND ANALYSIS

RADIOMETRIC MEASUREMENT SYSTEM DESIGN AND ANALYSIS

The Radiometric System is defined as the combined radiometer, primary calibration and inflight calibration assembly. The purpose of the radiometric portion of the ARRS Study was to extend both the performance in terms of radiometric accuracy and repeatability and the means for predicting it for such systems to a new level. To do this required development and extension of analytical tools and generation of component data and new component measurement techniques. In this section the reasons why these were necessary will be explored and analytical modeling objectives and requirements will be defined.

Measurement System Requirements

The quality of a radiometric measurement is determined by the values on the following parameters:

- Total noise equivalent radiance (NER): The input or signal radiance level required to produce a system signal output equal to the rms (i.e., 1σ) noise level at the system output. This quantity has significance for a specified spectral interval and angular resolution. Therefore, this should be expressed as $NER_{\Delta\lambda, \Delta\Omega}$.

- Spectral interval ($\Delta\lambda$): In this study, spectral interval is understood as that interval outside of which all uncompensatable energy sources are to be treated as error sources, and inside of which the input signal energy is treated as though uniformly spaced across the interval.

- Dynamic range: Dynamic range is the ratio of maximum signal level, for which response is specified, to the 1σ noise level of the measurement.

- Resolution, with two types of definitions: (a) in terms of the inverse of the maximum spatial frequency to which the measurement is sensitive, or for which the output signal is reduced a fixed amount from that at the frequency of maximum response, or (b) in terms of the limiting field stop in the optical system, often the detector itself. These (a and b) are made the same by specifying resolution as the inverse of the lowest spatial frequency other than dc, at which the system response is zero.

- Accuracy: Accuracy is the degree to which the measurement is relatable to a physical standard; specification is in terms of error and is expressed as a percentage (scale uncertainty) and as an absolute quantity (bias or offset uncertainty). Either of these may be random or systematic.

- Precision: This is the repeatability of a given measurement, also expressed as scale and bias. The distinction between instrument-to-instrument repeatability for the same measurement and accuracy is often ignored and in ARRS applications is of little significance.

The set of values, or ranges of them, for these performance requirements deriving from the ARRS applications ultimately creates the need for new analytical tools, more component data, and new methods at both measurement of components and calibration of instruments. These requirements are summarized in Table 7.

TABLE 7.- ARRS PERFORMANCE REQUIREMENTS

Parameter	Requirement
1) NER	≤ 0.005 w/m^2 - sr
2) Spectral interval	14.0 to 16.3 μ
3) Dynamic range	0.005 to 10.0 w/m^2 - sr
4) Resolution (in scan direction)	Best: 1×10^{-4} rad Worst: 1×10^{-3} rad
5) Accuracy	Scale: $\leq 1\%$ Bias: ≤ 0.03 w/m^2 - sr (whichever is larger)
6) Single instrument precision	Scale: $\leq 1\%$ Bias: ≤ 0.005 w/m^2 - sr (whichever is larger)

Prediction of an instrument on system performance to these levels of precision was largely beyond the capacity of available analytical techniques and requires quality not usually found in existent component data. The problem is compounded by the number of contributions to each type of error, requiring maximum individual allotments $< 0.1\%$ and 0.003 w/m^2 - sr, respectively, for scale and bias contributions. This implies that virtually all computations and measurements must be good to three, and often four, places. "Good" here means precise (numerically accurate) and complete (including all factors that could produce a variation in the third decimal place).

Analytical, predictive modeling is needed for two kinds of activities -- performance prediction (e.g., error analyses) and design decision making (i.e., how to judge the difference in two approaches to this order of precision). The following paragraphs provide a discussion of these two types of problems in order to establish the objectives of the radiometric measurement analytical modeling.

Design Considerations

Many aspects of radiometer design and analysis would require considerable new information to agree with the ARRS precision requirement, regardless of spectral interval; the LWIR region has additional problems unique to that interval. The fact that the observable is thermal emission and that the observed object is often colder than the radiometer indicates the nature of the problem. Coupling of the measurement instrument to the measured quantity and amongst the instrument's components creates a large number of terms that must be accounted for each time a parameter value is computed or a tradeoff conducted. The following paragraphs explore these extensive modeling requirements; used to develop the modeling objectives, the following discussion will also indicate how and when they may be applied.

Design evolution. -- Figure 7 illustrates a typical sequence of decisions pursuant to defining a radiometer configuration. For a particular application, the starting point may vary; however, since the process invariably reiterates at least once, essentially the same area is always covered in basically the order shown.

The detector, optical, and transfer function parameters are related by the equation for radiometer NER:

$$NER = NER\left(f^{\#},\ D_c,\ \tau_D,\ D^{**}_{\lambda,f,1},\ \Delta\Omega,\ \delta_o,\ \delta_e\right)$$

where

$f^{\#}$ = optical system f-number (focal length / diameter)

D_c = optical system collecting aperture diameter

τ_D = resolution element dwell time

$D^{**}_{\lambda,f,1}$ = inverse of detector NER referenced to unity bandwidth, area, and solid angle

$\Delta\Omega$ = elemental resolution solid angle

δ_o, δ_e = optical and electronic transmissions

For a given NER, $\Delta\lambda$, and $\Delta\Omega$ the choice of detector usually dwindles to a small number; for the ARRS parameters there are only three, Ge:Cu, Ge:Cd,

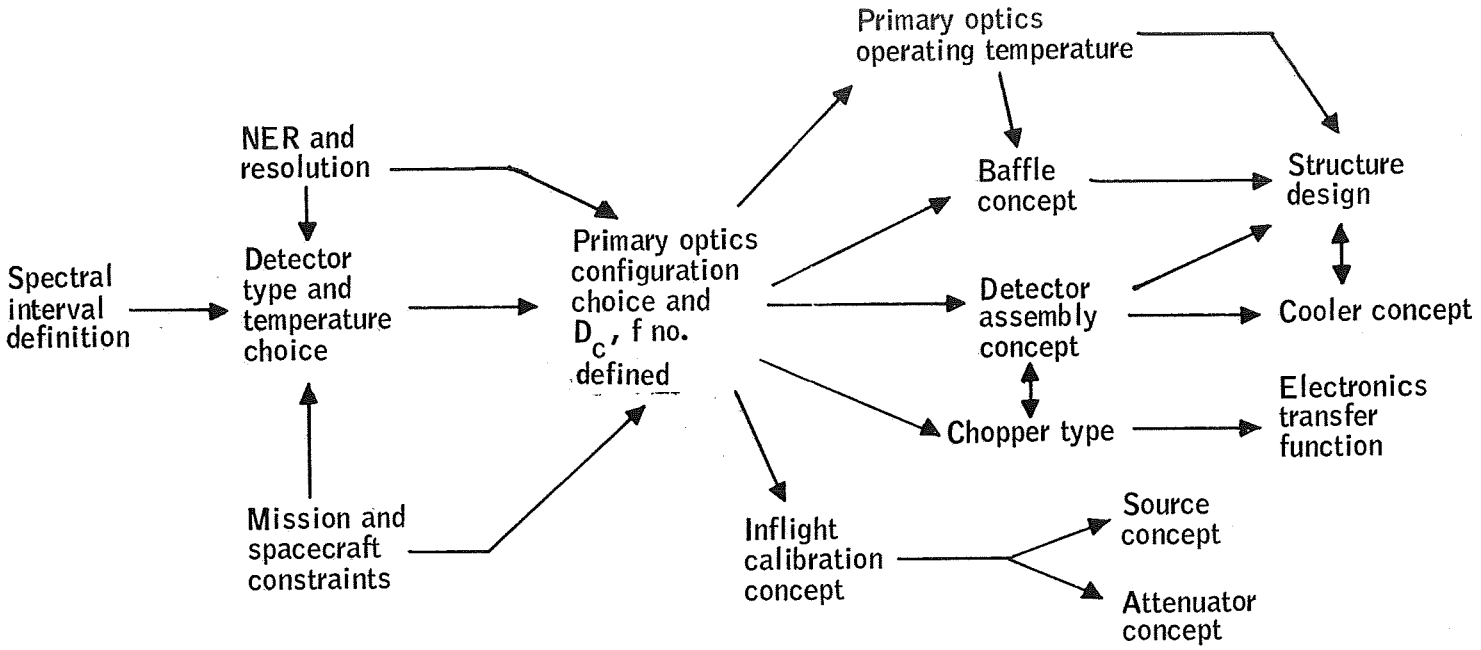

Figure 7. Typical Decision Flow for Radiometer Configuration Definition

and HgCdTe. The detectivities of each of these are sufficiently different as to be a determinant in choice and size of the optical system. With the focal length determined and the detector size and layout defined, the chopping method may be chosen and the rate-amplitude-stability tradeoffs may be determined.

Figure 8 shows the interrelations between performance parameters, shown in double circles, and the component characteristics that determine or affect the performance. The figure also shows how the choice of each component affects the choice of other components.

Choice of detector: When choosing the detector, its parameters need only be known approximately (e.g., to ±10 to 20%) because this choice is determined almost solely by the NER-cooling tradeoff; precision is not required for these quantities. However, as can be seen from Figure 8, this choice affects several other design parameters -- dynamic range, electrical transfer function, spectral response, and, through linearity, the inflight calibration design. These effects are in turn modified by emission related to the system ambient temperature and by radiation from the object plane.

Choice of primary optics configuration: In this case a tradeoff peculiar to thermal radiometry arises. The choice of optics from an NER basis always points to the fastest (lowest $f^{\#}$) configuration affording the desired resolution and with the detector well positioned for cooling purposes. This approach tends toward using complexity -- more elements, structure, etc. -- to achieve the desired performance; however, in an LWIR instrument more elements produce more internal emission and more ways for stray radiation to enter the system. To be able to conduct this tradeoff requires the ability to determine these effects quite precisely. For example, in an absolute radiometer using a chopper, theoretically only the input signal is chopped; hence, self emission is unimportant. However, when the self emission is 100 times greater than the input, can the spurious modulation be kept to less than 1:1000? And to what extent is this spurious effect dependent on structural members such as a secondary element support spider? The answers to these questions require a precise and detailed method for accounting for all of the sources of radiant flux on the detector.

Primary optics operating temperature: The allowable range of ambient temperature from the aspect of spacecraft capability defined for ARRS is 150 to 300°K, over which the 14 to 16 μ radiance varies a factor of 16. This can mean the difference between the self emission being at a level of three to 50 times the minimum signal for an emittance of 0.05. The affected quantities are D* and bias errors. The effect is well enough computable for the D* problem, but the error computation is only concerned with variations in the last place. Again, a model for the internally generated radiant flux onto the detector is required.

Inflight calibrator concept: The portion of the source, its temperature, how the radiation is introduced optically, and how multiple levels are achieved all require analysis of the interaction (radiative coupling) and scattering of these elements.

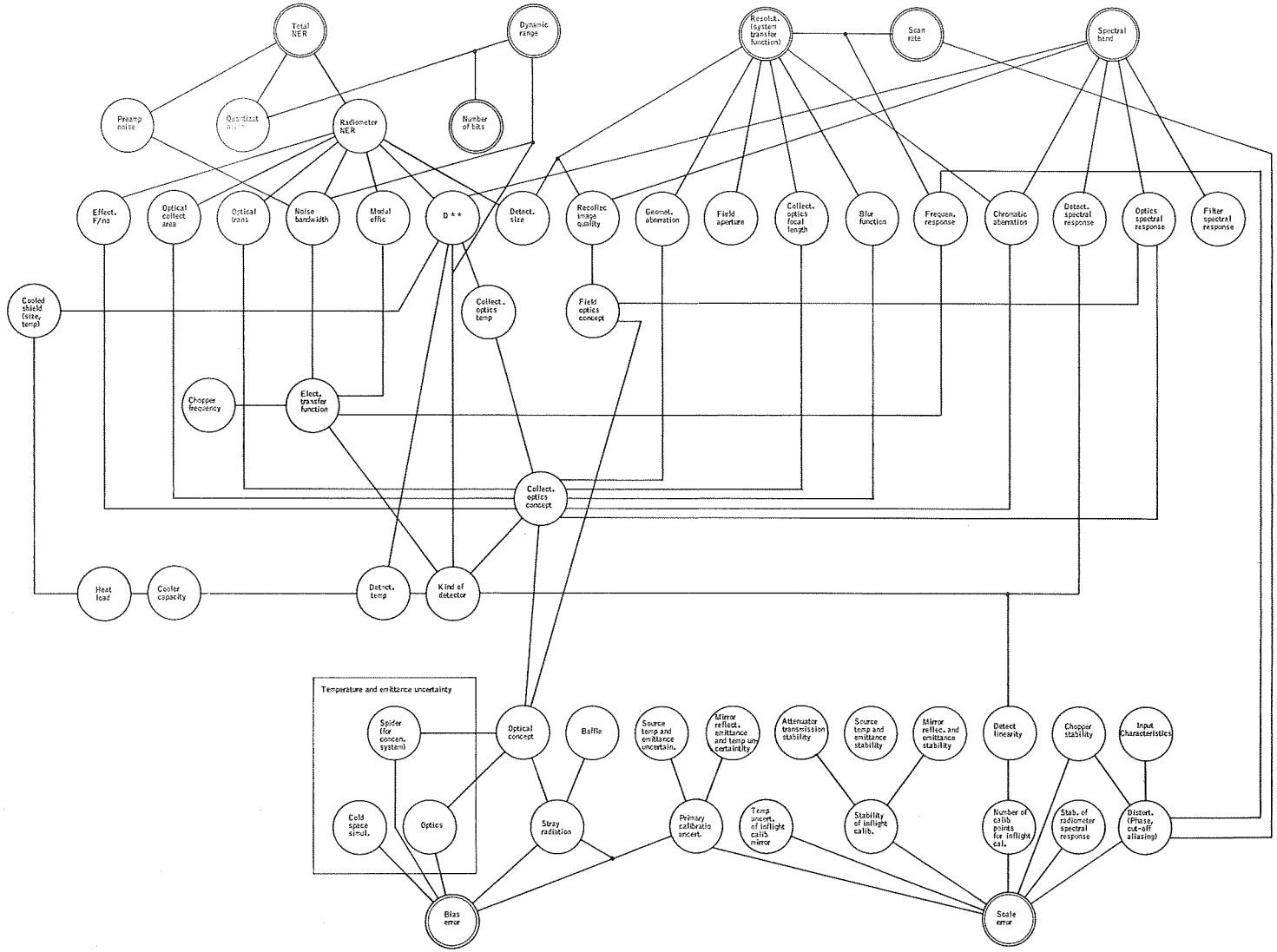

Figure 8. Radiometric Performance and Design Determinants Interrelations

Chopper type and design: From the point of view of signal recovery, it is desirable to chop at the maximum possible rate consistent with the detector time constant. Chopper design, however, places an additional constraint on this parameter. For space applications it is also desirable to use vibrational mechanisms as opposed to rotary types to generate the chopping motion. The ARRS requirements of 10 to 30 x 10^{-3} in. amplitude and 1 to 10KHz frequency are marginally achievable in the best available choppers.

Moreover, the data storage limitations coupled with the fact that the samples should be taken synchronously with the chopper tend to place an upper limit on chopper frequency. This latter constraint need not be as binding as the former, because filtering prior to storage can reduce the final from the original rate.

The limit on chopping rate will in turn limit the on-board electronic filter characteristics, producing distortion. Moreover, if there is any signal energy beyond one-half chop frequency, aliasing errors are produced. Evaluation of these effects when they are as small as 0.1 percent required an extension of existing analytical and computer techniques.

Error generation. -- The primary factors that determine scale and bias errors are shown at the bottom of the Figure 8. It will be noted that the same sources and system elements appear here as for the design determinants discussed above. That is, to compute these errors requires a model of the energy -- internal emissions and stray radiation -- that gets to the detector, a model of the detector's response to that energy, and a model of the electronic operations involved in transferral of that response into output data. The difference is that here the concern is with uncertainties and instabilities of the basic quantities rather than their absolute values. This makes the modelling requirement even more severe.

Modeling requirements summary. -- The dichotomy between design evolution and error generation in the preceding paragraphs is artificial. For a radiometer whose governing requirement is accuracy, error analyses and computations are an intrinsic part of the design evolution. The reason for treating them separately was to ensure the addition of those modelling requirements (and design coverage) that have only to do with design decisions. Table 8 summarizes the ARRS modeling requirements.

SIGNAL AND NOISE ANALYTICAL MODEL

Approach

Two independent approaches were taken in an attempt to arrive at a sufficiently general analytical model describing propagation of signal, noise, and error through radiometers applicable to the range of ARRS boundary parameters. The two approaches differed only in their starting point on a relative scale of generality, and both led to the same end product. One approach, described in Appendix B, involved deriving configuration independent general equations and applying them to specific radiometer configurations. The second approach, described here, involved deriving the equations describing a number of specific

TABLE 8. - MODELING REQUIREMENTS

Item	Source (design = D, error = E)	Requirement
Signal generation	D	Optical configuration Detector response Operating temperature Type of relay optics
	E	Temperature stability, emittance stability and uniformity Reflectance stability and uniformity
Detector response model	D	Inflight calibrator levels Transfer function System operating temperature
	E	Linearity Dependence on detection temperature Dependence on optics temperature
Transfer function model	D	Chopping frequency, system resolution, filter design Memory size Distortion correction technique
	E	Chopper stability effects Blur function change effects Electronics transfer function shift effects Aliasing

configurations and assembling these equations into a single expression applicable to configurations consisting of any combination of those radiometer components contained in the initial configurations studied. The nine configurations which formed the basis of the general model are listed in Table 9, and the specific radiance propagation models are presented in Appendix C.

Modeling of radiance propagation and error propagation was initially approached as two separate parallel tasks. It soon became apparent that a unified approach would achieve superior results by obtaining a single model capable of describing radiance, noise, and error propagation. This unified approach was then pursued.

The parallel error modeling task was concluded. The resultant specific error model is described in Appendix D. This model was used in a sensitivity analysis to obtain insight into error propagation and error values preparatory to applying the general analytical model in a similar sensitivity analysis; results are also presented in Appendix D.

TABLE 9. - SPECIFIC RADIOMETER CONFIGURATIONS CONSIDERED

Configuration number	Collector optics	Relay optics
1	Low pass filter supported Cassegrainian	Cassegrainian pair
2	Low pass filter supported Newtonian	Cassegrainian pair
3	Off-axis paraboloid	Off-axis paraboloidal pair
4	Single lens	Single-lens pair
5	Spike-window supported Cassegrainian	Single-lens pair
6	Spike-supported Newtonian	Single-lens pair
7	Off-axis paraboloid	Single-lens pair
8	Spoke supported Cassegrainian	Cassegrainian pair
9	Spoke supported Newtonian	Cassegrainian pair

A general model evolved by continuously updating and expanding previous models as additional terms were analyzed. Initially, only a direct radiance propagation chain was modelled. This direct chain considered only radiance propagation in one direction, from collecting aperture towards the detector.

Even the earliest model conceived revealed that at least the radiation reflected from the detector must be taken into consideration since the detector material can never be expected to be completely absorptive. Because of this, an indirect radiation-propagation chain is created that is comprised of transfer function coefficients. Additional radiance terms from all elements in the radiation path were also added.

In further investigating the model, it was discovered that primary reflections from elements in the direct and the indirect radiation-propagation chains affect the receivable signal at the detector. Secondary and higher-order reflections from the detector have not yet been taken into account specifically. The effects of back-forth reflections between succeeding elements or groups of elements in the propagation chains have not been considered to date.

The model was improved successively by incorporating systematic and random errors. Generally, systematic errors describe bias or offsets, short- and long-term drifts, frequency, phase and wavelength shifts, nonuniformities in reflectance, transmittance and emittance distributions, temperature gradients, and other uncertainties in fractions of the nominal or average quantities involved. Usually, these errors can be accounted for by careful measurements, subsequent computations, and especially by appropriate

calibration. Noise that is known to be correlated to every apparent radiance term and occurs in the electronic circuitry as well must be handled statistically (variance or rms value). Normally, it cannot be taken out by measurement or calibration, but can be reduced to a limited degree in the data-handling process, for example, by adequately filtering data electronically.

Model Description

General description. -- The model is presented here in two formats -- a compressed, or simplified, model shown in Figure 9 and an expanded model containing all terms as shown in Figure 10. In each format the model consists of the following groups in the direct radiation-propagation chain:

- Input
- Collector optics
- Modulator
- Relay optics
- Cold stop
- Detector
- Data processor

Each group may be a single element or a combination of single- or multiple-element subassemblies that have to perform specific functions within the entire radiometric system, as described in Table 10.

A quite similar sequence, using the same groups, can be described for the indirect radiation-propagation chain. The grouping is shown in Table 11. Groups denoted by (a) contain both transfer functions and radiance terms. A transfer function defined by the product of the blockage factor and the reflectivity of the inflight calibrator's attenuator* is I^b; the radiance term must be taken into account in the input block of the inflight calibrator. Groups II through IV contain only transfer functions of groups II' through IV' of the direct radiation-propagation chain.

Tables 10 and 11 show that a change in the configuration of a particular group in the direct chain must affect automatically the interrelated group in the indirect chain. For this reason, the generality of the compressed model can be demonstrated by considering specific configurations within separated particular groups. Such specific configurations have been investigated especially for the collector optics. The investigations resulted in an expanded signal and error flow model. This model reflects simultaneously all specific configurations considered to date. Thus, it can be applied to every particular radiometer concept by only assigning the corresponding transfer-function values and radiance terms. For simplification, the expanded model shown applies only

*Notice that the compressed model does not include the reflectivity of the IFC collimator optics; it is, however, included in the expanded general model.

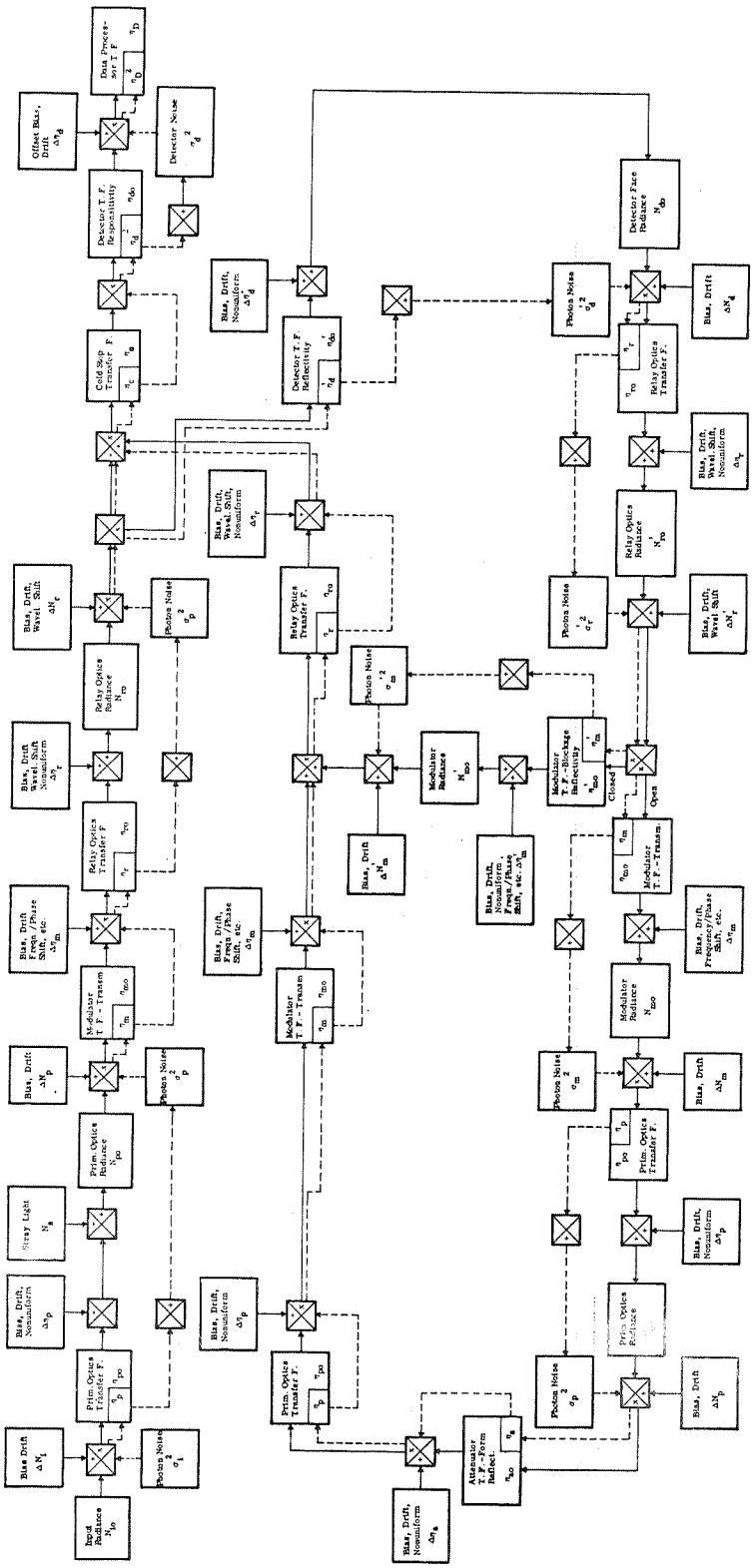

Figure 9. Generalized Compressed Signal and Error Model

TABLE 10.- GROUPING FOR DIRECT RADIATION-PROPAGATION CHAIN

Group	Denotation	Task
I	Input	Radiance of target scene or its simulation and calibration-unit radiances
II	Primary optics	Formation of scene image at the collector system's focal plane
III	Monitor	Initiating generation of a time-varying radiant flux at end of radiation-propagation chain by chopping primary optics output at the collector's focal plane
IV	Relay optics	1. Passing radiation from primary scene image through a convenient field stop for elimination of unwanted light 2. Collimating, bandpass filtering, and reimaging the receivable radiation 3. Passing radiation through a cavity for restriction of the acceptance cone for detectable radiation from all sources in front of the cavity
V	Cold-stop	Conversion of radiance into irradiance or photon-flux density
VI	Detector	Conversion of irradiance into radiant power or photon-flux and subsequently into a processible output voltage
VII	Data processor	1. Passing the signal through electrical filter of a preamplifier to reject noise for optimum signal-to-noise ratio and spatial resolution 2. Sampling preamplifier output voltage in discrete time intervals and amplifying it to become suitable for transmission to and computation by a ground station

TABLE 11. - GROUPING FOR INDIRECT RADIATION-PROPAGATION CHAIN

Modulator branch		Attenuator branch
		I Input
		II Primary optics
		III Modulator
	IV Relay optics	
	VI[a] Detector input	
	IV[a] Relay optics	
III[a] Modulator		III[a] Modulator
		II[a] Primary optics
		I[b] Attenuator
		II ' Primary optics
		III ' Modulator
	IV ' Relay optics	
	V Cold stop	
	VI Detector	
	VII Data processor	

[a]Contain both transfer functions and radiance terms

[b]Transfer function defined by product of blockage factor and reflectivity of inflight calibrator's attenuator

two-element optical components, i. e., collector and the relay-optics collimator and concentrator. However, it is easily applicable to single- and multiple-element components. The model is comprised of all refractive, all reflective, refracto-reflective, and reflecto-refractive configurations, including different support structures for secondary-collector optics elements.

The model is illustrated in Figure 10, where chains 1 and 3 describe radiance propagation towards the detector; chain 1 relating to direct propagation of input radiance and internally emmited radiance, and chain 3 relating to propagation of internally reflected and scattered radiation. Chains 2 and 4 describe propagation in the opposite direction, toward the entrance aperture. All chains inter-act. For example, radiance incident on the detector is absorbed and reflected. The reflected conponent propagates back through the radiometer elements which cause further reflection and scattering, some of which then propagates back to the detector. Chain 5 refers to higher order indirect propagation. It has not been detailed since it is identical to Chain 4 except that it would not contain terms describing radiation internally emitted toward the entrance aperture; those terms should be included only once and they are shown in Chain 4.

In subsequent subsections, analytical expressions of symbols used are explained, signal and noise propagations are described in detail, and recommendations for future improvements are given.

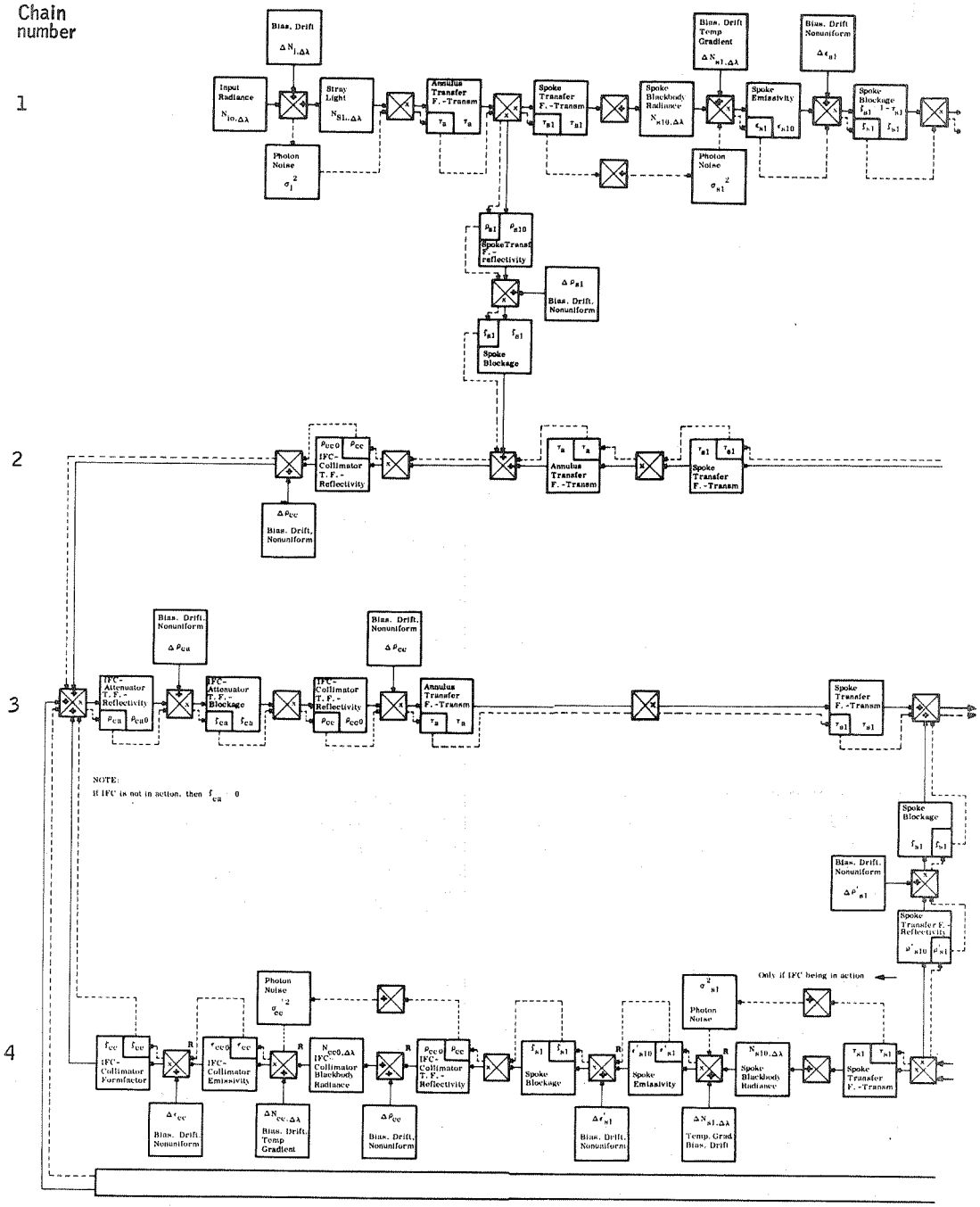

Figure 10. Generalized Expanded Signal and Error Model

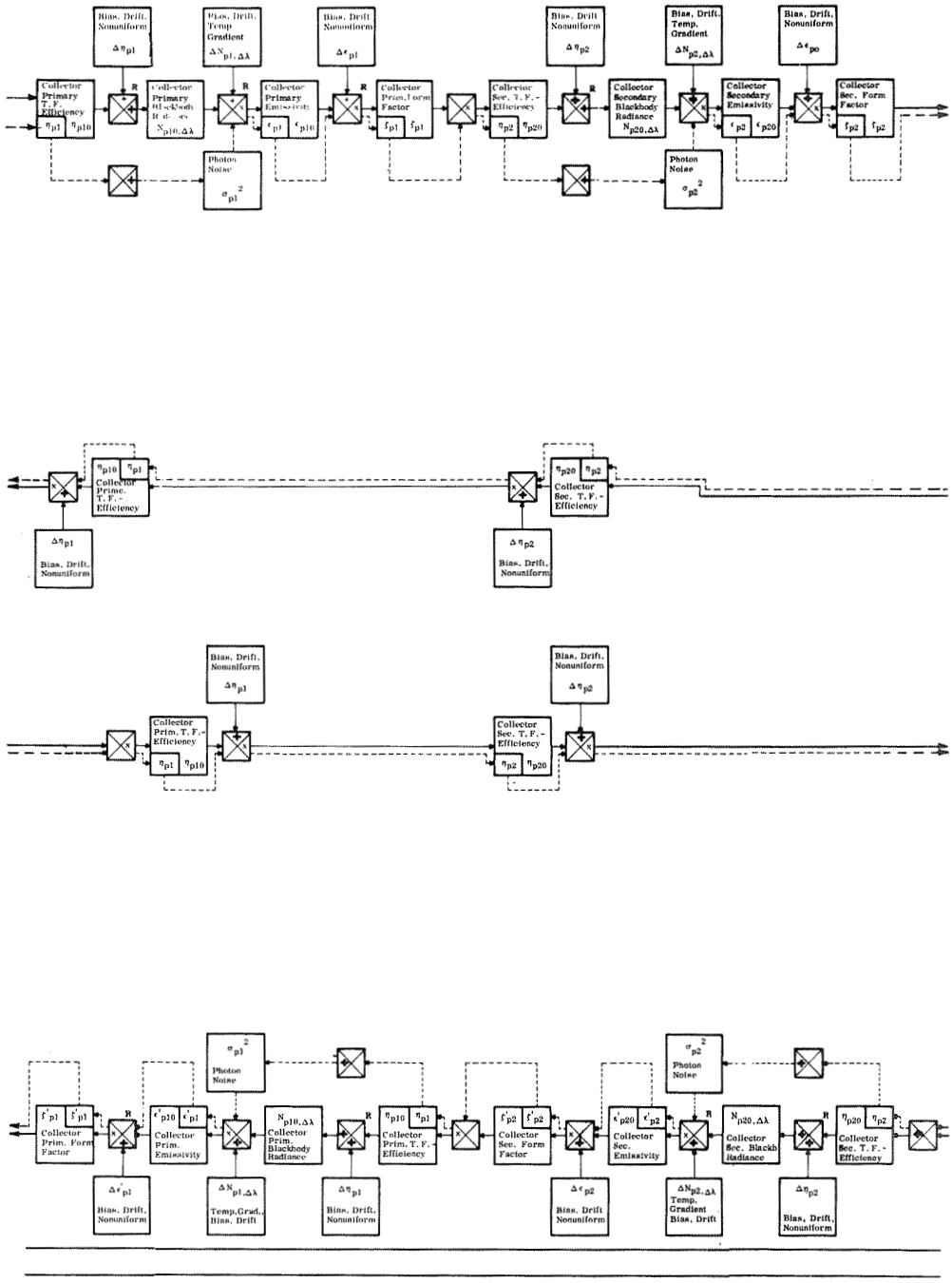

Figure 10. Generalized Expanded Signal and Error Model (Continued)

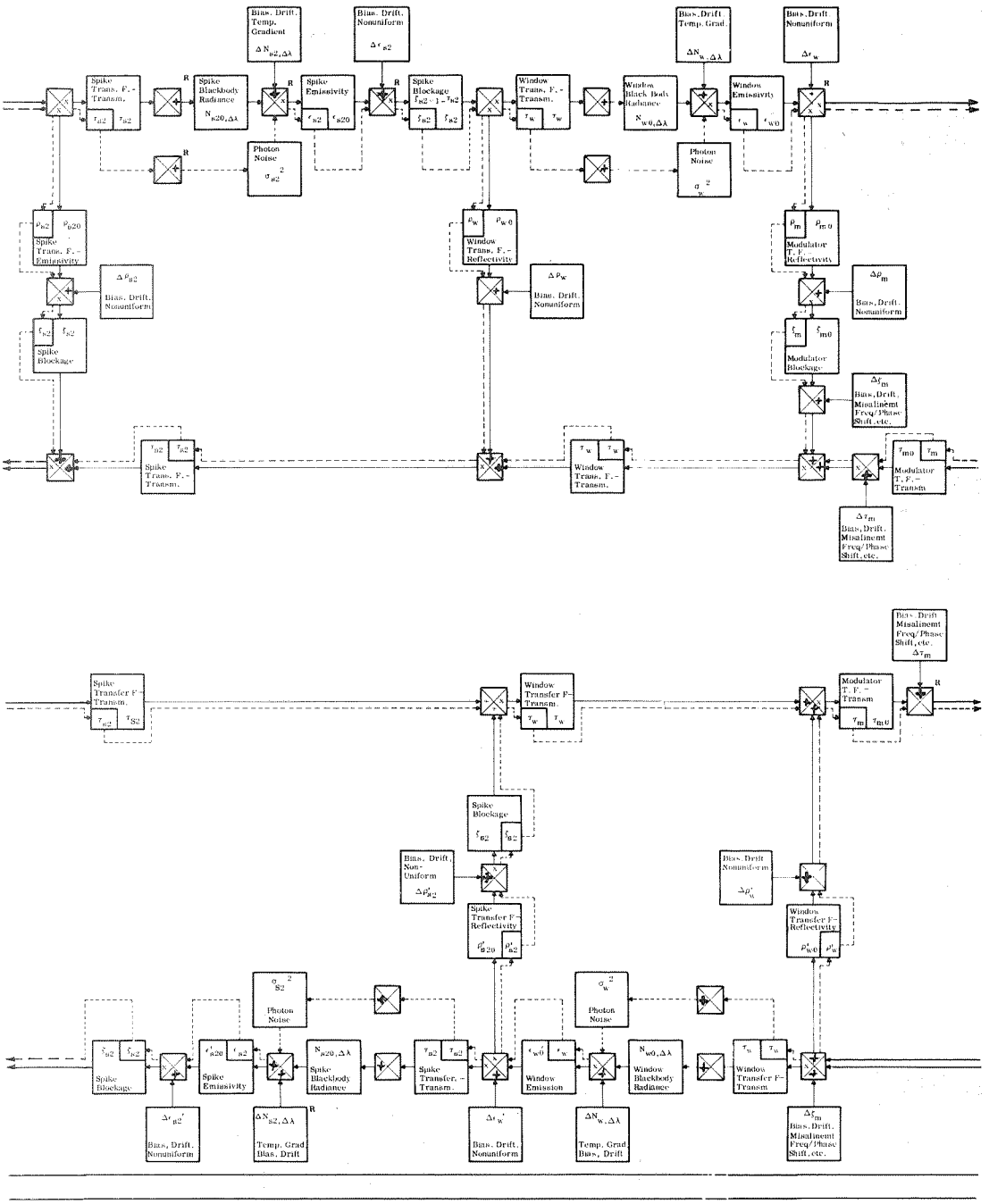

Figure 10. Generalized Expanded Signal and Error Model (Continued)

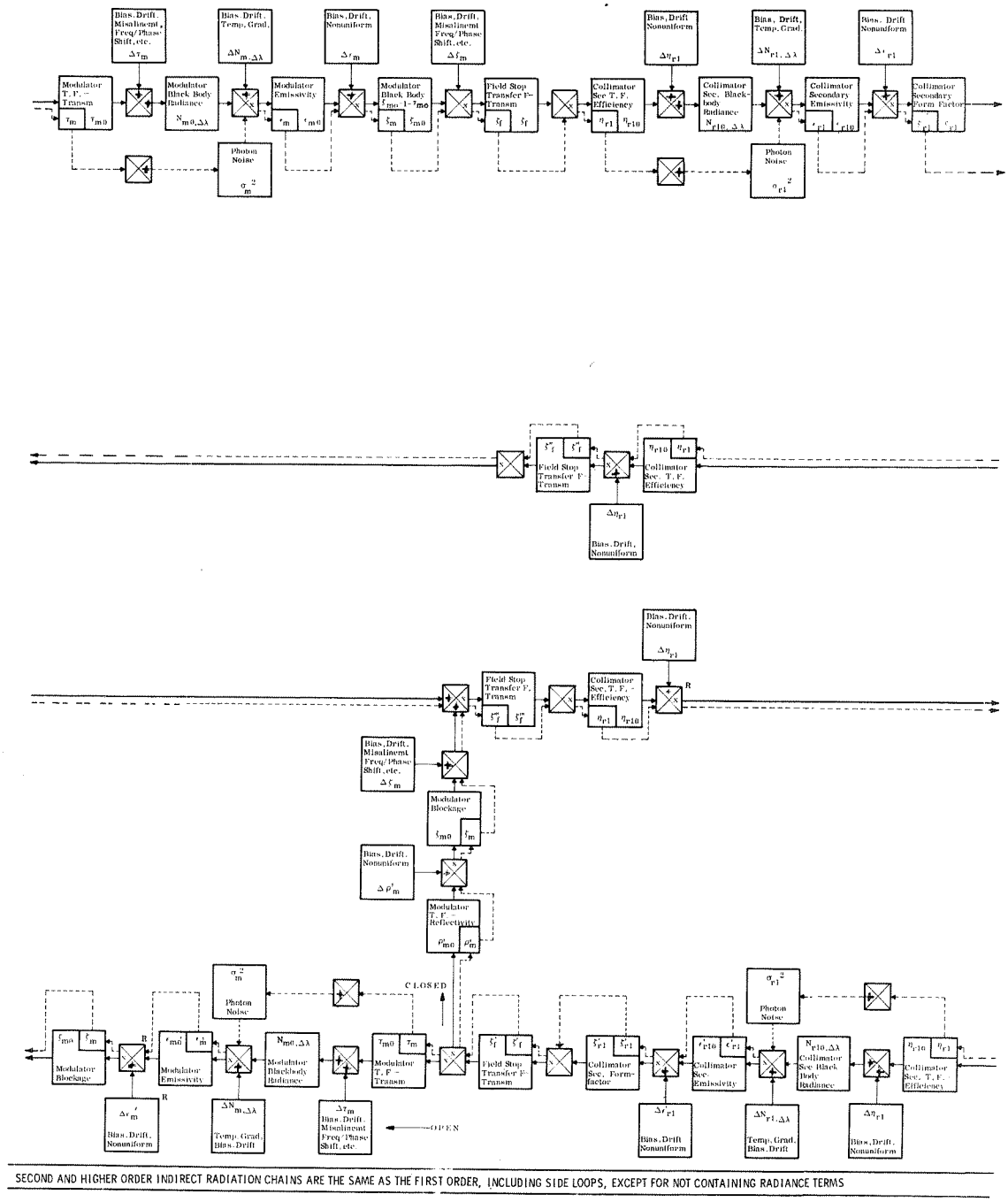

Figure 10. Generalized Expanded Signal and Error Model (Continued)

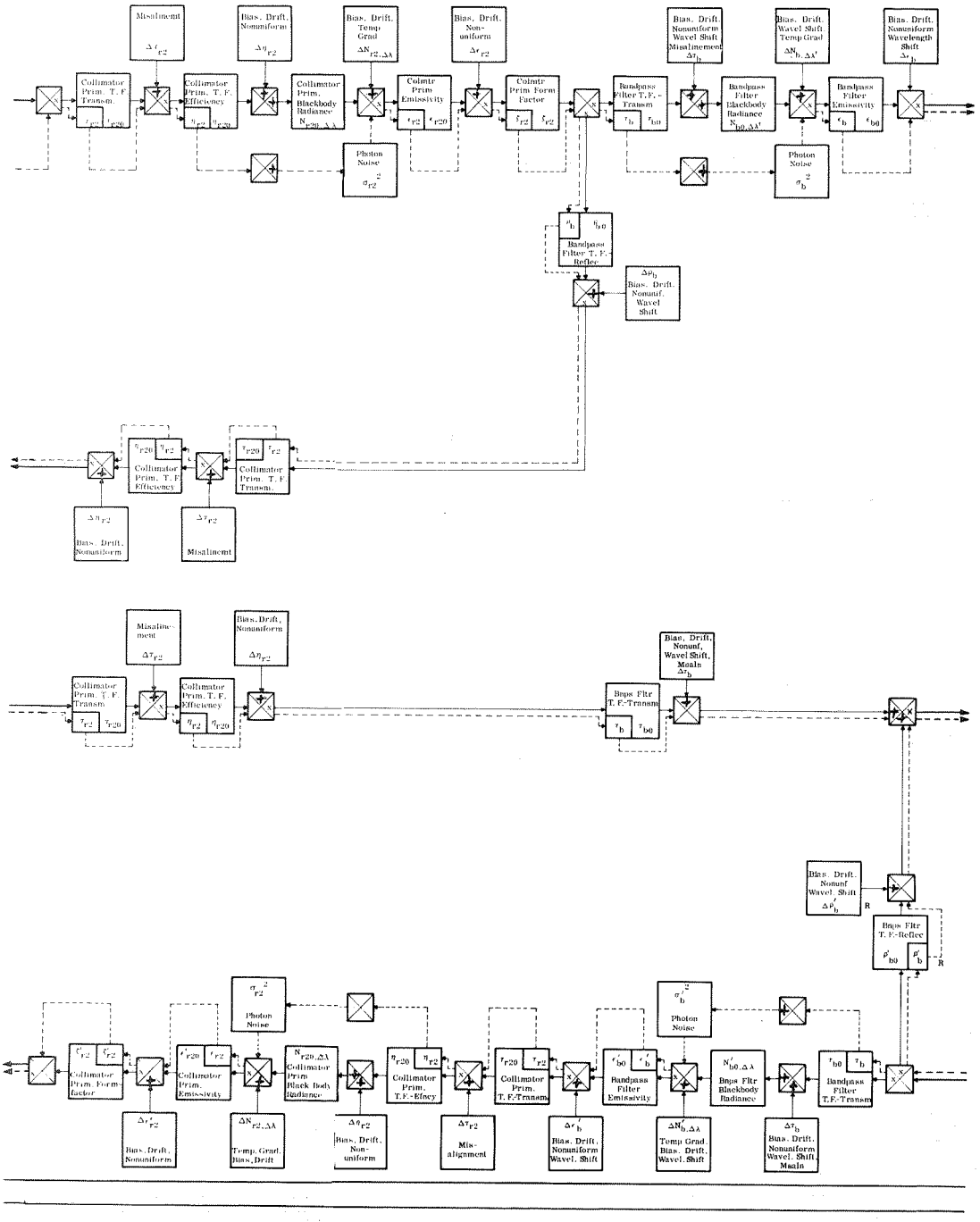

Figure 10. Generalized Expanded Signal and Error Model (Continued)

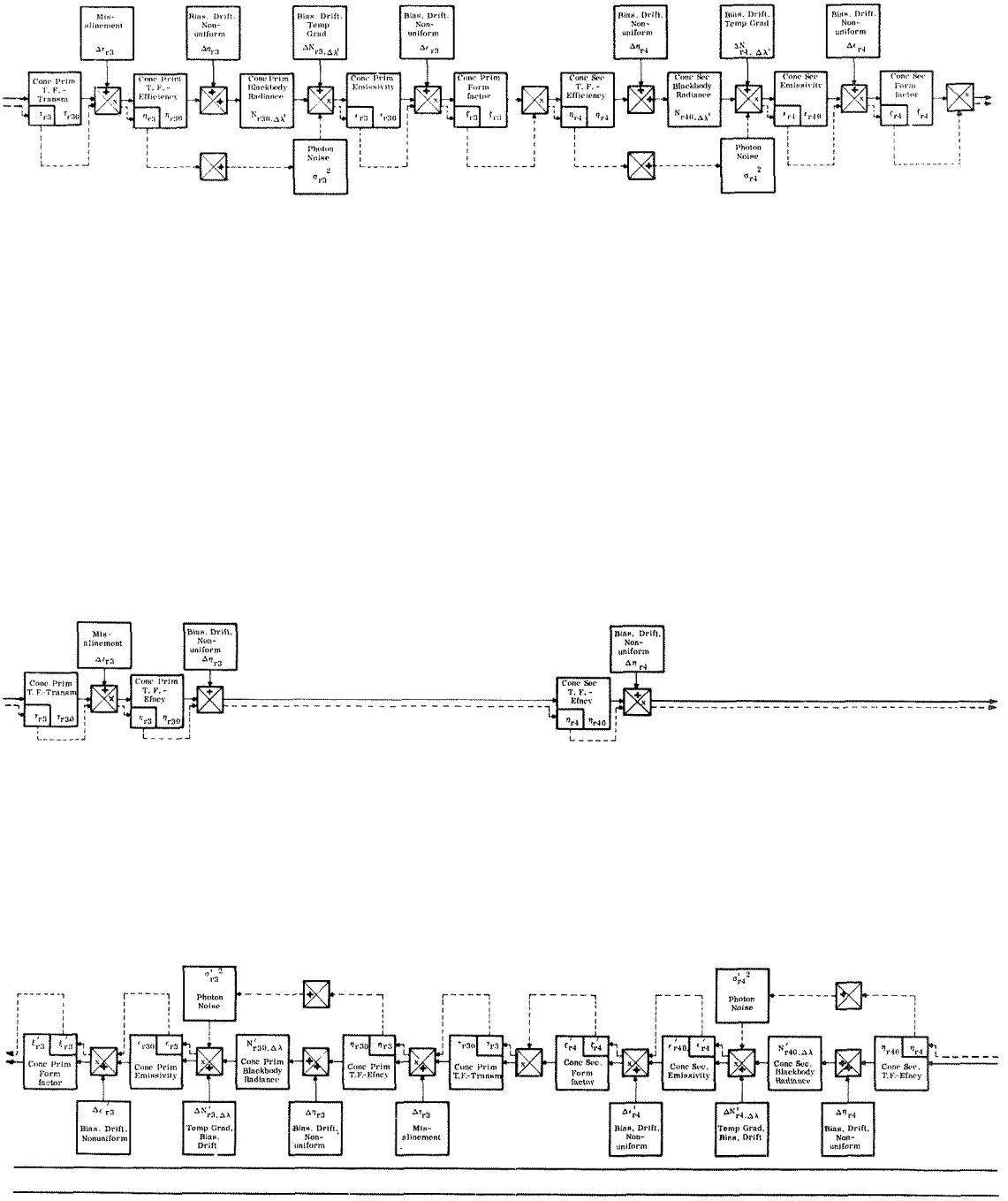

Figure 10. Generalized Expanded Signal and Error Model (Continued)

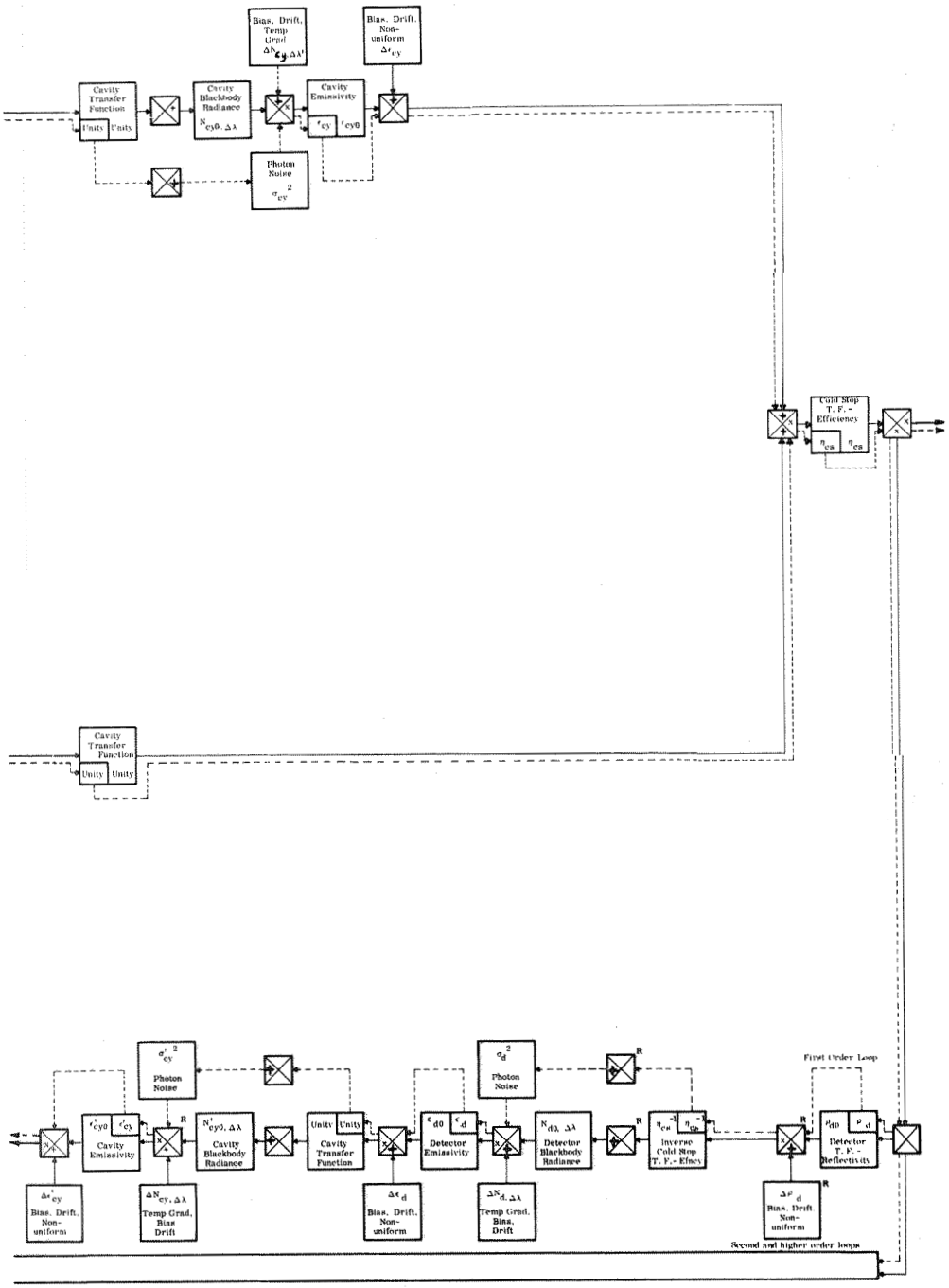

Figure 10. Generalized Expanded Signal and Error Model (Continued)

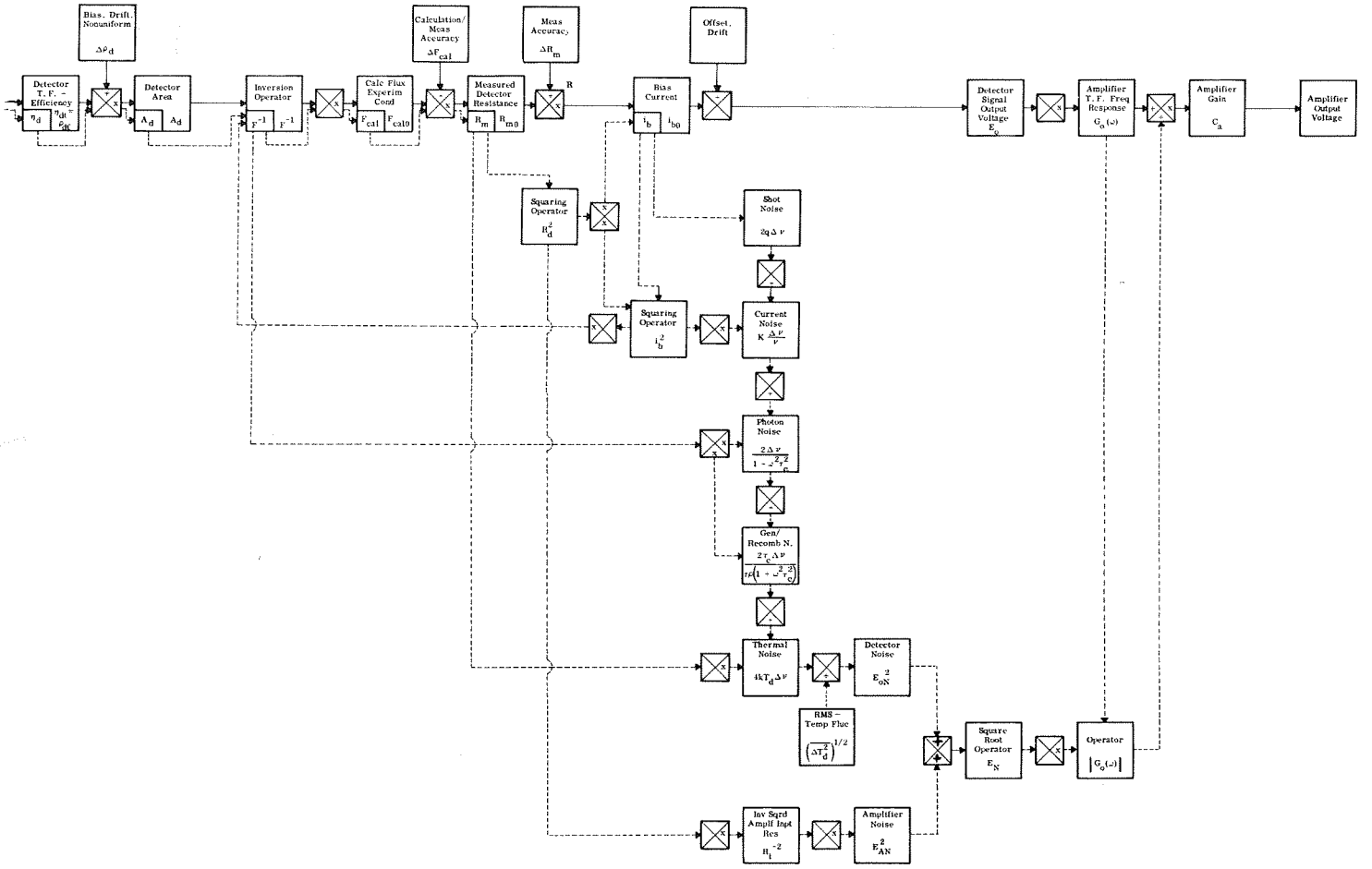

Figure 10. Generalized Expanded Signal and Error Model (Concluded)

Analytical expressions. -- Elements in both the direct-radiation propagation chains of the compressed and expanded signal and error flow models are described by

- A multiplicative transfer function or efficiency factor
- An additive radiance term

With regard to the m-th element, the general symbols used are designated by

- The expression η_m for the transfer function which may be either a single or a multiple efficiency factor, and which must be replaced in its single term by the reflectivity ρ_p of reflective or by the transmissivity τ_m of refractive ements
- The expression $N_m \epsilon_m \zeta_m$ for radiance of the surface involved

N_m is the blackbody radiance (w/m^2 - sr or photons/sec-m^2-sr), determined in the model either in the wavelength region of bandpass-filter transmission $\Delta\lambda = \lambda_2 - \lambda_1$, or in the sensitivity region of the detector, $\Delta\lambda' = \lambda_c - 0$, where λ_c = cutoff wavelength of the detector. The analytical expression for N_m is given by Planck's law

$$N_{m,\Delta\lambda} = \int_{\lambda_1}^{\lambda_2} 2c^2h\,\lambda^{-5}\left[\exp\left(\frac{ch}{\lambda kT}\right) - 1\right]^{-1} d\lambda$$

where

c = velocity of light = 3×10^8 m-sec^{-1}

h = Planck's constant = 6.63×10^{-34} w sec^2

k = Boltzmann's constant = 1.38×10^{-23} w sec deg^{-1}

T = temperature °K

The expression ϵ_m is the mean emissivity in the wavelength intervals $\Delta\lambda$ and $\Delta\lambda'$, respectively; ϵ_m is equal to $(1-\rho_m)$ for reflective, or to $\alpha_m = (1 - \rho_m - \tau_m)$ for refractive elements. Analytically ϵ_m is defined by

$$\epsilon_m = \langle \epsilon_m(\lambda) \rangle_{av} = \frac{1}{\Delta\lambda}\int_{\lambda_1}^{\lambda_2} \epsilon_m(\lambda)\, d\lambda$$

The expression ζ_m is a form factor equal to the ratio of the real surface area to its projection on a plane that passes through the real surface apex. A general analytical expression cannot be derived since ζ_m is a design dependent parameter; however, in some cases an analytical expression can be obtained easily by appropriate integration -- for example, in situations where spherical or on-axis paraboloidal surfaces are involved.

The expression used in the model to represent the actual radiance of an element constitutes an approximation applied to show readily the data flow. The exact expression for this radiance would read

$$N_{m,\Delta\lambda} = \int_{\lambda_1}^{\lambda_2} 2c^2h\,\lambda^{-5}\left[\exp\left(\frac{ch}{\lambda kT}\right) - 1\right]^{-1} \epsilon_m(\lambda)\,\zeta_m\,d\lambda$$

Note that, in some cases in the model, ζ_m denotes a blockage factor, i.e., a type of efficiency coefficient; in these cases, one has the relation

$$\zeta_m = 1 - \tau_m$$

Also, note that the blockage factor of the modulator is a function of time depending on the chopper frequency and the geometrical configuration.

Form factors are assumed to remain essentially constant. Emissivities, ϵ, are supposed to be functions of λ only. Efficiency factors and radiance terms are generally subject to systematic errors; e.g.,

$$\eta_m = \eta_{mo}\left(1 \pm \frac{\Delta\eta_m}{\eta_{mo}}\right)$$

$$N_{m,\Delta\lambda} = N_{mo,\Delta\lambda}\,\epsilon_{mo}\,\zeta_m\left(1 \pm \frac{\Delta N_{m,\Delta\lambda}}{N_{mo,\Delta\lambda}}\right)$$

The systematic errors may be dependent on time t, temperature T, environmental degradation, and other parameters. For example, one may define

$$\Delta\eta_m = \Delta\eta_m(t\,;\,T\,;\,r\,,\,\theta) \qquad \text{and} \qquad \Delta N_{m,\Delta\lambda} = \Delta N_{m,\Delta\lambda}(T)$$

where r, θ = conveniently chosen polar coordinates to describe possible nonuniformities

Table 12 contains symbols, meanings, and analytical expressions for each of the direct and indirect radiation chain elements; these are derived on the following pages.

Earth radiance: Radiation received at a point in space from the earth can be described in terms of basic physical-radiation characteristics combined with spatial distribution characteristics and in-path modification components.

From any part of the target area, the radiance can be described (ref. 1) as follows: If U is defined as radiant energy in Joules, then

$$F \text{ is defined as radiant power, } \frac{\partial U}{\partial t} \text{ in watts}$$

N_λ = spectral radiance

= radiant energy per unit time, per unit solid angle, per unit projected area, per unit wavelength interval

$$= \frac{\partial^4 U}{\cos\theta \, \partial t \, \partial A \, \partial \Omega \, \partial \lambda} \quad W/m^2\text{-sr-}m_\lambda$$

where

t is time in sec

A cos θ is the projected area

Ω is the solid angle (sr)

λ is the wavelength (m)

For spatial distribution, the function $N_\lambda(x, y)$ must be evaluated. The in-path modification components (scattering, absorption, radiation from molecules above the CO_2 band; hence, with different temperature distributions) also will be functions of x and y.

For radiometer error analysis, the block for earth is considered to represent an ideal input. Errors due to a nonideal real target are considered system errors. No consideration is given for such factors as possible nonuniformity of the earth within the field of view and in-path modification of the signal.

Earth levels are limited to the range 0.005-10.0 W/m^2-sr for radiance, N, within the band of 14.0 to 16.28 microns.

TABLE 12. - GENERAL RADIOMETER MODEL ANALYTICAL EXPRESSIONS

Symbol		Meaning	Analytical expression	Source or substantiation
Analytical	Computer			
$N_{io,\Delta\lambda}$	BO	Input radiance	$N_{io,\Delta\lambda} = N_{10,\Delta\lambda}(T)$	Empirical (except for calibration)
$N_{LN,\Delta\lambda}$	BSO	Stray light	a	Empirical
τ_a	CTO	Annulus transfer function, transmission	$\tau_a = \frac{A_o - A_1}{A_o} = \frac{r_o^2 - r_1^2}{r_o^2}$	Geometrical configuration
τ_{s1}	CT1	Spoke transfer function, transmission	$\tau_{s1} = \frac{(A_o - A_1) - A_{s1}}{A_o - A_1}$	Geometrical configuration
$N_{s10,\Delta\lambda}$	B1	Spoke blackbody radiance	$N_{s10,\Delta\lambda} = 2c^2h \int_{\lambda_1}^{\lambda_2} \lambda^{-5} [\exp(\frac{hc}{\lambda k T_{s10}}) - 1]^{-1} d\lambda$	Planck law
ϵ_{s10}	E1	Spoke emissivity	$\epsilon_{s10} = 1 - \rho_{s10}$	NASA SP-164 thermal radiation heat transfer
ξ_{s1}	Z1	Spoke blockage	$\xi_{s1} = \frac{A_{s1}}{A_o - A_1}$	Geometrical configuration
η_{P10}	CE2	Collector primary transfer function, efficiency	$\eta_{P10} = \begin{cases} \rho_{P10} \text{ for reflective systems} \\ \tau_{P10} \text{ for refractive systems} \end{cases}$	
$N_{P10,\Delta\lambda}$	B2	Collector primary blackbody radiance	$N_{P10,\Delta\lambda} = 2c^2h \int_{\lambda_1}^{\lambda_2} \lambda^{-5} [\exp(\frac{hc}{\lambda k T_{P_{10}}}) - 1]^{-1} d\lambda$	Planck law
ϵ_{P10}	E2	Collector primary emissivity	$\epsilon_{P10} = \begin{cases} 1 - \rho_{P10} & \text{reflective system} \\ 1 - \tau_{P10} - \rho_{P10} & \text{refractive system} \end{cases}$	NASA SP-164 thermal radiation heat transfer
ξ_{P1}	Z2	Collector primary formfactor	$\xi_{P1} = \frac{A_{P1}}{A_o - A_1}$	Geometrical configuration
η_{P20}	CE3	Collector secondary transfer function, efficiency	$\eta_{P20} = \begin{cases} \rho_{P20} & \text{reflective} \\ \tau_{P20} & \text{refractive} \end{cases}$	
$N_{P20,\Delta\lambda}$	B3	Collector secondary blackbody radiance	$N_{P20,\Delta\lambda} = 2c^2h \int_{\lambda_1}^{\lambda_2} \lambda^{-5} [\exp(\frac{hc}{\lambda k T_{P20}}) - 1]^{-1} d\lambda$	Planck law
ϵ_{P20}	E3	Collector secondary emissivity	$\epsilon_{P20} = \begin{cases} 1 - \rho_{P20} & \text{reflective} \\ 1 - \tau_{P20} - \rho_{P20} & \text{refractive} \end{cases}$	
ξ_{P2}	Z3	Collector secondary formfactor	$\xi_{P2} = \frac{A_{P2}}{A_1}$	Geometrical configuration
τ_{s2}	CT4	Spike transfer function, transmission	$\tau_{s2} = \frac{A_i - A_{s2}}{A_i}$	Geometrical configuration
$N_{s20,\Delta\lambda}$	B4	Spike blackbody radiance	$N_{s20,\Delta\lambda} = 2c^2h \int_{\lambda_1}^{\lambda_2} \lambda^{-5} [\exp(\frac{hc}{\lambda k T_{s20}}) - 1]^{-1} d\lambda$	Planck law
ϵ_{s20}	E4	Spike emissivity	$\epsilon_{s1} = 1 - \rho_{s1}$	NASA SP-164 thermal radiation heat transfer
ξ_{s2}	Z4	Spike blockage	$\xi_{s2} = 1 - \tau_{s2} = \frac{A_{s2}}{A_i}$	Geometrical configuration
ρ_{cso}	C28	IFC-attenuator transfer function, reflectivity	$\rho_{cso} = \rho_{cso}(\tau_{cso})$	Empirical
ξ_{ca}	Z28	IFC-attenuator blockage	ξ_{ca}	Empirical
ρ_{s10}	C1	Spoke transfer function, reflectivity	$\rho_{s10} = \rho_{s10}(\tau_{s10})$	Empirical
ρ_{s20}	C4	Spike transfer function, reflectivity	$\rho_{s20} = \rho_{s20}(\tau_{s20})$	Empirical
ρ_{wo}	C5	Window transfer function, reflectivity	$\rho_{wo} = \rho_{wo}(\tau_{20})$	Empirical
ρ_{mo}	C6	Modulator transfer function, reflectivity	$\rho_{mo} = \rho_{mo}(\tau_{mo})$	Empirical
ρ_{bo}	C10	Bandpass filter transfer function, reflectivity	$\rho_{bo} = \rho_{bo}$	Empirical
η_{cs}	CE30	Cold stop transfer function, efficiency	$\eta_{cs} = \begin{cases} \rho_{cs} & \text{reflective} \\ \tau_{cs} & \text{refractive} \end{cases}$	
ρ'_{bo}	C18	Bandpass filter transfer function, reflectivity	$\rho'_{bo} = \rho'_{bo}(\tau_{bo})$	Empirical
ρ'_{mo}	C22	Modulator transfer function, reflectivity	$\rho'_{mo} = \rho'_{mo}(\tau_{mo})$	Empirical
ρ'_{wo}	C23	Window transfer function, reflectivity	$\rho'_{wo} = \rho'_{wo}(\tau_{wo})$	Empirical
ρ'_{s20}	C24	Spike transfer function, reflectivity	$\rho'_{s20} = \rho'_{s20}(\tau_{s20})$	Empirical
ρ'_{s10}	C27	Spoke transfer function, reflectivity	$\rho'_{s10} = \rho'_{s10}(\tau_{s10})$	Empirical

[a] $N_{SL,\Delta\lambda} = \frac{16c^2h}{a^2b^2\pi^2} \int_{\lambda_1}^{\lambda_2} \epsilon(\lambda)\lambda^{-5} \left[\exp\left(\frac{hc}{\lambda kT}\right) - 1\right]^{-1} \int_0^{2\pi} \int_R^a \int_0^{\theta_o} \int_{r_1(\theta)}^{r_2(\theta)} \frac{J_1^2 \frac{D\pi\epsilon}{\lambda}}{r} dr d\theta dR d\beta d\lambda$

TABLE 12. - GENERAL RADIOMETER MODEL ANALYTICAL EXPRESSIONS (Continued)

Symbol		Meaning	Analytical expression	Source or substantiation
Analytical	Computer			
τ_w	CT5	Window transfer function, transmission	$\tau_w = \tau_w(\lambda, T; r_w, \theta_w)$	Empirical
$N_{wo,\Delta\lambda}$	B5	Window blackbody radiance	$N_{wo,\Delta\lambda} = 2c^2h\int_{\lambda_1}^{\lambda_2} \lambda^{-5}\left[\exp\left(\frac{hc}{\lambda kT_w}\right)-1\right]^{-1} d\lambda$	Planck law
ϵ_{wo}	E5	Window emissivity	$\epsilon_{wo} = 1-\tau_{wo}-\rho'_{wo}$	NASA SP-164 thermal radiation heat transfer
τ_{mo}	CT6	Modulator transfer function, transmission	$\tau_{mo} = 1 - \xi_{mo}$; $\xi_{mo} = \xi_{mo}(t)$	Analytical
$N_{mo,\Delta\lambda}$	B6	Modulator blackbody radiance	$N_{mo,\Delta\lambda} = 2c^2h\int_{\lambda_1}^{\lambda_2} \lambda^{-5}\left[\exp\left(\frac{hc}{\lambda kT_m}\right)-1\right]^{-1} d\lambda$	Planck law
ϵ_{mo}	E6	Modulator emissivity	$\epsilon_{mo} = 1 - \rho_{mo}$	NASA SP-164 thermal radiation heat transfer
ξ_{mo}	Z6	Modulator blockage	$\xi_{mo} = \xi_{mo}(t)$	ARRS monthly progress report no. 3, LMSC 682989, p. 63
ξ_f	CT7	Field stop transfer function, transmission	$\xi_f = \frac{A_f}{A_b}$	Geometrical configuration
η_{r10}	CE8	Collimator secondary transfer function, efficiency	$\eta_{r10} = \begin{cases}\rho_{r10} & \text{reflective}\\ \tau_{r10} & \text{refractive}\end{cases}$	
$N_{r10,\Delta\lambda}$	B8	Collimator secondary blackbody radiance	$N_{r10,\Delta\lambda} = 2c^2h\int_{\lambda_1}^{\lambda_2} \lambda^{-5}\left[\exp\left(\frac{hc}{\lambda kT_{r10}}\right)-1\right]^{-1} d\lambda$	Planck law
ϵ_{r10}	E8	Collimator secondary emissivity	$\epsilon_{r10} = 1 - \rho_{r10}$	NASA SP-164 thermal radiation heat transfer
ξ_{r1}	Z8	Collimator secondary formfactor	$\xi_{r1} = \frac{A_{r1}}{A'_i}$	Geometrical configuration
τ_{r20}	CT9	Collimator primary transfer function, transmission	τ_{r20} $\begin{cases}=1 \text{ well aligned system}\\ \neq 1 \text{ misaligned system}\end{cases}$	Geometrical configuration
η_{r20}	CE9	Collimator primary transfer function, efficiency	$\eta_{r20} = \begin{cases}\rho_{r20} & \text{reflective system}\\ \tau_{r20} & \text{refractive system}\end{cases}$	
$N_{r20,\Delta\lambda}$	B9	Collimator primary blackbody radiance	$N_{r20,\Delta\lambda} = 2c^2h\int_{\lambda_1}^{\lambda_2} \lambda^{-5}\left[\exp\left(\frac{hc}{\lambda kT_{r20}}\right)-1\right]^{-1} d\lambda$	Planck law
ϵ_{r20}	E9	Collimator primary emissivity	$\epsilon_{r20} = \begin{cases}1-\rho_{r20} & \text{reflective}\\ 1-\tau_{r20}-\rho_{r20} & \text{refractive}\end{cases}$	NASA SP-164 thermal radiation heat transfer
ξ_{r2}	Z9	Collimator primary formfactor	$\xi_{r2} = \frac{A_{r2}}{A_o-A_i} = 1 - \tau_{r2}$	Geometrical configuration
τ_{bo}	CT10	Bandpass filter transfer function, transmission	$\tau_{bo} = \tau_{bo}(\lambda; t; T; r, o)$	Empirical
$N_{bo,\Delta\lambda'}$	B10	Bandpass filter blackbody radiance	$N_{bo,\Delta\lambda'} = 2c^2h\int_{o}^{\lambda_c} \lambda^{-5}\left[\exp\left(\frac{hc}{\lambda kT_b}\right)-1\right]^{-1} d\lambda$	Planck law
ϵ_{bo}	E10	Bandpass filter emissivity	$\epsilon_{bo} = 1 - \tau_{bo} - \rho_{bo}$	NASA SP-164 thermal radiation heat transfer
$N'_{r30,\Delta\lambda}$	B17	Concentrator primary blackbody radiance	$N'_{r30,\Delta\lambda} = 2c^2h\int_{o}^{\lambda_c} \lambda^{-5}\left[\exp\left(\frac{hc}{\lambda kT_{r30}}\right)-1\right]^{-1} d\lambda$	Planck law
ϵ'_{r30}	E17	Concentrator primary emissivity	$\epsilon'_{r30} = \begin{cases}1-\rho'_{r30} & \text{reflective}\\ 1-\tau_{r30}-\rho'_{r30} & \text{refractive}\end{cases}$	Geometrical configuration
ξ'_{r3}	Z17	Concentrator primary formfactor	$\xi'_{r3} = \frac{A'_{r3}}{A'_o-A'_i}$	Geometrical configuration
$N'_{bo,\Delta\lambda}$	B18	Bandpass filter blackbody radiance	$N'_{bo,\Delta\lambda} = 2c^2h\int_{o}^{\lambda_c} \lambda^{-5}\left[\exp\left(\frac{hc}{\lambda kT_b}\right)-1\right]^{-1} d\lambda$	Planck law
ϵ'_{bo}	E18	Bandpass filter emissivity	$\epsilon'_{bo} = 1 - \tau_{bo} - \rho'_{bo}$	NASA SP-164 thermal radiation heat transfer
ϵ'_{r20}	E19	Collimator primary emissivity	$\epsilon'_{r20} = \begin{cases}1-\rho'_{r20} & \text{reflective}\\ 1-\tau_{r20}-\rho'_{r20} & \text{refractive}\end{cases}$	NASA SP-164 thermal radiation heat transfer
ξ'_{r2}	Z19	Collimator primary formfactor	$\xi'_{r2} = \frac{A'_{r2}}{A'_o-A'_i}$	Geometrical configuration
ϵ'_{r10}	E20	Collimator secondary emissivity	$\epsilon'_{r10} = 1 - \rho'_{r10}$	NASA SP-164 thermal radiation heat transfer
ξ'_{r1}	Z20	Collimator secondary formfactor	$\xi'_{r1} = \frac{A'_{r1}}{A'_i}$	Geometrical formfactor
ξ'_f	CT21	Field stop transfer function, transmission	$\xi'_f = \frac{A'_f}{A'_b}$	Geometrical configuration

TABLE 12. - GENERAL RADIOMETER MODEL ANALYTICAL EXPRESSIONS (Concluded)

Symbol		Meaning	Analytical expression	Source or substantiation
Analytical	Computer			
ε'_{mo}	E22	Modulator emissivity	$\varepsilon'_{mo} = 1 - \rho'_{mo}$	NASA SP-164 thermal radiation heat transfer
ε'_{wo}	E23	Window emissivity	$\varepsilon'_{wo} = 1 - \tau_w - \rho'_w$	NASA SP-164 thermal radiation heat transfer
ε'_{s20}	E24	Spike emissivity	$\varepsilon'_{s1} = 1 - \rho'_{s1}$	NASA SP-164 thermal radiation heat transfer
ε'_{P20}	E25	Collector secondary emissivity	$\varepsilon'_{P20} = \begin{cases} 1 - \rho'_{P20} & \text{reflective} \\ 1 - \tau_{P20} - \rho'_{P20} & \text{refractive} \end{cases}$	NASA SP-164 thermal radiation heat transfer
ξ'_{P2}	Z25	Collector secondary formfactor	$\xi'_{P2} = \frac{A'_{P2}}{A_i}$	Geometrical configuration
ε'_{P10}	E26	Collector primary emissivity	$\varepsilon'_{P10} = \begin{cases} 1 - \rho'_{P10} & \text{reflective} \\ 1 - \tau_{P10} - \rho'_{P10} & \text{refractive} \end{cases}$	NASA SP-164 thermal radiation heat transfer
ξ'_{P1}	Z26	Collector primary formfactor	$\xi'_{P1} = \frac{A'_{P1}}{A_o - A_i}$	Geometrical configuration
ε'_{s10}	E27	Spoke emissivity	$\varepsilon'_{s10} = 1 - \rho'_{s10}$	NASA SP-164 thermal radiation heat transfer
τ_{r30}	CT11	Concentrator primary transfer function, transmission	$\tau_{r30} \begin{cases} = 1 & \text{well aligned system} \\ \neq 1 & \text{misaligned system} \end{cases}$	Geometrical configuration
η_{r30}	CE11	Concentrator primary transfer function, efficiency	$\eta_{r30} = \begin{cases} \rho_{r30} & \text{reflective system} \\ \tau_{r30} & \text{refractive system} \end{cases}$	
ε_{r30}	E11	Concentrator primary emissivity	$\varepsilon_{r30} = \begin{cases} 1 - \rho_{r30} & \text{reflective} \\ 1 - \tau_{r30} - \rho_{r30} & \text{refractive} \end{cases}$	NASA SP-164 thermal radiation heat transfer
ξ_{r3}	Z11	Concentrator primary formfactor	$\xi_{r3} = \frac{A_{r3}}{A_o - A_i}$,	Geometrical configuration
η_{r40}	CE12	Concentrator secondary transfer function, efficiency	$\eta_{r40} = \begin{cases} \rho_{r40} & \text{reflective system} \\ \tau_{t40} & \text{refractive system} \end{cases}$	
$N_{r40, \Delta\lambda'}$	B12	Concentrator secondary blackbody radiance	$N_{r40, \Delta\lambda'} = 2c^2h \int_o^{\lambda_c} \lambda^{-5} \left[\exp\left(\frac{hc}{\lambda k T_{r40}}\right) - 1\right]^{-1} d\lambda$	Planck law
ε_{r40}	E12	Concentrator secondary emissivity	$\varepsilon_{r40} = \begin{cases} 1 - \rho_{r40} & \text{reflective} \\ 1 - \tau_{r40} - \rho_{r40} & \text{refractive} \end{cases}$	NASA SP-164 thermal radiation heat transfer
ξ_{r4}	Z12	Concentrator secondary formfactor	$\xi_{r4} = \frac{A_{r4}}{A_i}$	Geometrical configuration
τ_{cy}	CT13	Cavity transfer function, unity	$\tau_{cy} = 1$	
$N_{cyo, \Delta\lambda'}$	B13	Cavity blackbody radiance	$N_{cyo, \Delta\lambda'} = 2c^2h \int_o^{\lambda_c} \lambda^{-5} \left[\exp\left(\frac{hc}{\lambda k T_{cyo}}\right) - 1\right]^{-1} d\lambda$	Planck law
ε_{cyo}	E13	Cavity emissivity	$\varepsilon_{cyo} = 1 - \rho_{cyo}$	NASA SP-164 thermal radiation heat transfer
ρ_{do}	C14	Detector transfer function, reflectivity	$\rho_{do} = \rho_{do}(\lambda, T_d)$	Empirical
$N_{do, \Delta\lambda}$	B14	Detector blackbody radiance	$N_{do, \Delta\lambda} = 2c^2h \int_o^{\lambda_c} \lambda^{-5} \left[\exp\left(\frac{hc}{\lambda k T_{do}}\right) - 1\right]^{-1} d\lambda$	Planck law
ε_{do}	E14	Detector emissivity	$\varepsilon_{do} = 1 - \rho_{do}$	NASA SP-164 thermal radiation heat transfer
$N'_{cyo, \Delta\lambda}$	B15	Cavity blackbody radiance	$N'_{cyo, \Delta\lambda'} = 2c^2h \int_o^{\lambda_c} \lambda^{-5} \left[\exp\left(\frac{hc}{\lambda k T_{cyo}}\right) - 1\right]^{-1} d\lambda$	Planck law
ε'_{cyo}	E15	Cavity emissivity	$\varepsilon'_{cyo} = 1 - \rho'_{cyo}$	
$N'_{r40, \Delta\lambda}$	B16	Concentrator secondary blackbody radiance	$N'_{r40, \Delta\lambda} = 2c^2h \int_o^{\lambda_c} \lambda^{-5} \left[\exp\left(\frac{hc}{\lambda k T_{r40}}\right) - 1\right]^{-1} d\lambda$	Planck law
ε'_{r40}	E16	Concentrator secondary emissivity	$\varepsilon'_{r40} = \begin{cases} 1 - \rho'_{r40} & \text{reflective system} \\ 1 - \tau_{r40} - \rho'_{r40} & \text{refractive system} \end{cases}$	NASA SP-164 thermal radiation heat transfer
ξ'_{r4}	Z16	Concentrator secondary formfactor	$\xi'_{r4} = \frac{A'_{r4}}{A_i}$	Geometrical configuration

The radiance can be evaluated from

$$N_\lambda = 2c^2 h\lambda^{-5}\left[\exp\left(\frac{hc}{\lambda kT}\right)-1\right]^{-1}$$

If the values

$$c = 2.997929 \times 10^{8} \quad \text{m sec}^{-1} \text{ (ref. 2)}$$

$$h = 6.6252 \times 10^{-34} \text{ W sec}^2 \text{ (ref. 2)}$$

$$k = 1.38046 \times 10^{-23} \text{ W sec deg}^{-1} \text{ (ref. 2)}$$

are assumed precise for the purpposes of this definition, then

$$N_{i,\Delta\lambda} = \int_{14.0\mu}^{16.28\mu} \frac{11908.901\, d\lambda}{\lambda^5\, e^{14387.867/\lambda T} - 1} \quad W/m^2\text{-sr}$$

if λ is in meters and T is in °K.

Since N is a function of T, N can be evaluated to determine the temperature (therefore, spectral distributions) which give particular radiance levels within the specified range.

Space radiance: There has been no precise measurement of radiation from space in the 14.0 to 16.3-micron spectral region. (This constitutes a valid area for experimental investigation for infrared measurements of space and celestial bodies.) Such measurements have been hindered by absorption of the atmosphere and by self radiance of instruments flown in space. Radiances from the sun and moon are so large that they are considered as pertinent elements of stray light since they definitely would prevent accurate space reference when the sun or moon was imaged into the field of view. These celestial objects, therefore, are not considered in this subsection.

The models generally assumed for space, therefore, are relatively simple and consist of multiple-point sources at relatively high temperatures (stars and planets) superimposed on a general field which is a black body at a very low temperature.

Thus, the general model adopted for this study assumes a radiance given by N as in the description of earth radiance plus specific components at specified directions in a celestial coordinate system. Generally, these components are given in terms of a star catalog and are tabulated with irradiance values rather than radiance since the sources are generally of unknown diameter which is much less than the size of any practical field of view. A truly

complete description would include larger area sources such as interstellar clouds, and nebulae, but adequate data for such a description is lacking.

Therefore, the general form for space is expressed as an irradiance in W/m^{-2} at the aperture calculated as

$$H_{total} = N\zeta + H_{\alpha,\ \delta} \quad \text{where}$$

N is inband radiance as a function of temperature T as in the earth-radiance description,

The form factor, ζ, for converting radiance to irradiance depends on the shape and size of the field of view.

$H_{\alpha,\ \delta}$ is cataloged irradiance from an object at a given right ascension (α) and declination (δ).

Earth-radiance simulator: Basically, the earth-radiance simulator uses a calibration system that consists of a source featuring a continuous temperature variation in the range $77°K \leq T \leq 300°K$, and an off-axis paraboloidal reflector producing a nealy parallel beam of radiation, thus simulating an extended source at infinity. The source temperature is controlled by a platinum resistance-thermometer interpolation standard, but certainly is subject to measurement errors. Flux reflected from the collimating element passes all the way through the radiometer and provides an output signal at the detector in the same manner as an external earthbound source of radiation. Since the input signal, by virtue of measuring the temperature, is known to a certain degree of accuracy, it can be used for calibration of the radiometer output. This means that, if the calibrator output is measured in W/m^2-sr. one obtains a relation of the form

$$E_{det} = m \times F_{cal}$$

where E_{det} = voltage obtained by irradiation of the detector

F_{cal} = calibrator output flux

It is evident that only the radiant flux-to-voltage conversion factor m is a function of errors encountered by propagating the input signal through the radiometer. Error in the calibrator output cannot be removed at all. Therefore, it is obligatory to design the calibration unit in a manner such that unavoidable errors are not affecting substantially the conversion factor. For this reason, mandatorily, errors involved in operating the calibrator must be established. There errors are primarily due to

- Nonuniformity and time-dependent degradation of the collimator's reflectivity and a slight temperature dependence of reflectance. In the IR region of interest, wavelength dependence of reflectivity is not expected to pose problems;

- Inaccuracies in determining actual temperatures of the calibrator source and the reflector

In addidion, radiation emitted by the source and the collimator, like that of any other surface, obviously is subject to photon-flux-density noise.

One can define:

- A source radiance

$$N_{cal,\Delta\lambda} = N_{cal\,o,\Delta\lambda}\left(1 \pm \frac{\Delta N_{cal,\Delta\lambda}}{N_{cal\,o,\Delta\lambda}}\right)$$

$$\Delta N_{cal,\Delta\lambda} = \Delta N_{cal,\Delta\lambda}\,(T_{cal})$$

where $N_{cal\ o,\ \Delta\lambda}$ = nominal radiance at temperature T_{cal} within the IR region of interest, $\Delta\lambda = \lambda_2 - \lambda_1$

- A reflector radiance

$$N_{ref,\Delta\lambda} = N_{ref\,o,\Delta\lambda}\left(1 \pm \frac{\Delta N ref,\Delta\lambda}{N_{ref\ o,\Delta\lambda}}\right)$$

$$\Delta N_{ref,\Delta\lambda} = \Delta N_{ref,\Delta\lambda}\,(T_{ref})$$

where T_{ref} = temperature of collimator surface

- A collimator surface reflectivity

$$\rho_{ref} = \rho_{ref\,o}\left(1 \pm \frac{\Delta\rho_{ref}}{\rho_{ref\,o}}\right)$$

- where $\Delta\rho_{ref} = \Delta\rho_{ref}\,(T_{ref};\ r_{ref};\theta_{ref})$

and the polar coordinates (r_{ref}, θ_{ref}) are used to express possible nonuniformities in the reflectance distribution,

- A collimator-surface emissivity

$$\epsilon_{ref} = \epsilon_{ref\,o}\left(1 \pm \frac{\Delta\rho_{ref}}{\epsilon_{ref\,o}}\right)$$

where $\epsilon_{refo} = 1 - \rho_{refo}$

Hence, accumulated radiometer input power from the calibration system is

$$\left[\rho_{refo} N_{calo,\Delta\lambda}\left(1 \pm \frac{\Delta\rho_{ref}}{\rho_{refo}}\right)\left(1 \pm \frac{\Delta N_{cal,\Delta\lambda}}{N_{calo,\Delta\lambda}}\right)\right.$$

$$\left. + \xi_{ref}\,\epsilon_{refo} N_{refo,\Delta\lambda}\left(1 \pm \frac{\Delta\rho_{ref}}{\epsilon_{refo}}\right)\left(1 \pm \frac{\Delta N_{ref,\Delta\lambda}}{N_{refo,\Delta\lambda}}\right)\right]$$

where

$\xi_{ref} = A_{ref}/A_{cal}$ = form factor

A_{ref}, A_{cal} = actual reflector and calibrator aperture areas, respectively

Earth-radiance simulator (alternate approach): The alternate approach for the earth-radiance simulation uses a sufficiently large extended source for calibration of the radiometer, thus avoiding the need for collimating optics. The extended source is simply a blackbody cavity cooled down with liquid nitrogen; temperature variation is obtained by heating the cavity up by means of radiation transfer. Precision temperature control is provided by use of a platinum resistance-thermometer interpolation standard.

Reasoning about the emitted radiation, as in the case of the primary approach, one can describe immediately radiometer input from the extended-source-calibration system:

$$N_{calo,\Delta\lambda}\left(1 \pm \frac{\Delta N_{cal,\Delta\lambda}}{N_{calo,\Delta\lambda}}\right)$$

where

$N_{cal\ o,\Delta\lambda}$ = nominal cavity radiance in interval $\Delta\lambda$

$\Delta N_{cal,\Delta\lambda} = \Delta N_{cal,\Delta\lambda}(T_{cal})$

Space-radiance simulator: A space radiance simulator could consist of a large black plate sufficiently cooled down by liquid helium. Certainly this will provide temperatures below 5C°K. Since, at 50°K, the blackbody radiance of any surface is about three orders of magnitude lower than the minimum apparent radiance to be recognized by the radiometer, errors in determining the actual temperature of the simulator, and nonuniformities of emittance distribution will play only an insignificant role, that is, errors introduced by the space simulator are considered negligible.

Inflight calibrator: Initial modelling of the calibration system considered the highest inflight calibration level only. Intermediate levels could be achieved by use of an attenuator or alternate calibration schemes. The calibration system envisaged now consists of a source and a collimating mirror, and is a through-the-optics approach. The collimated energy fills a fraction of the total radiometer aperture. To achieve attenuation, a first approach made use of a perforated off-axis paraboloidal reflector as described below.

To determine signal and error propagation through a conceptual inflight calibration system, the system is assumed to consist of a temperature-controlled source and an off-axis portion of a paraboloidal reflector for collimating the source output, that is, simulating irradiance from a target scene at a very large distance from the radiometer. The source may be shielded by a circular field stop. The paraboloidal reflector is supposed to be rotatable around its optical axis in a stepwise fashion to enable a five-level attenuation of the calibrator beam: high, medium high, medium low, low, and zero. Attenuation is achieved by appropriately perforating the reflector portions in actual use; the zero level is obtained by a complete cutoff of the paraboloid. Thus, the attenuator does not contribute a radiance term to the calibrator output which is identical to the radiometer input N_i.

Specifically, one obtains

$$N_i = \epsilon_r N_r \times \eta_a \times \rho_m + \zeta_m \epsilon_m N_m$$

where

ϵ_r = source emissivity

η_a = attenuator efficiency factor = ratio of actual to circular beam area (supposing the use of a field stop)

ρ_m = mirror reflectivity

ϵ_m = $(1 - \rho_m)$ = mirror emissivity

ζ_m = mirror form factor = ratio of the actually used area of the paraboloidal reflector's off-axis portion to that of its projection into a plane passing through the paraboloidal apex

N_r, N_m = blackbody radiances (W/cm^{-2} - sr) of source and reflector, respectively

ε_r is considered to be a function of the wavelength λ only. η_a and ζ_m are assumed to be affected substantially by environmental conditions. All other quantities are subject to error-producing uncertainties like bias, drift, surface, and nonuniformities. In addition, N_r and N_m are characterized by correlated photon-noise terms; although the photon noise is taken into account at the detector at the end of the p ropagation chain through the radiometer, it is shown in the error model for more generality (Figure 11). Of course, noise propagates through the entire system in a manner that is completely different from that of the other errors; that is, one has

$$\sigma_i^2 = (\sigma_r \eta_a \rho_m)^2 + \sigma_m^2$$

where

σ_r, σ_m, σ_i = rms-values of noises corresponding to the source, reflector and radiometer input radiances, respectively

If $\Delta\lambda = \lambda_2 - \lambda_1$ denotes the spectral width of the bandpass filter, the radiance errors

$$\Delta N_{n,\Delta\lambda} = N_{T,\Delta\lambda}\ (T)$$

$$\Delta N_{m,\Delta\lambda} = N_{m,\Delta\lambda}\ (T)$$

are dependent on uncertainties in determining the actual temperature T(°K); the reflectivity ρ_m is affected by the environment, expressed by the time t, slightly by the temperature, and by nonuniform distributions, expressed by polar coordinates (r_m, θ_m) in a conveniently chosen coordinate system. Defining

$$\Delta\rho_m = \Delta\rho_m\ (t; T; r_m\ \theta_m)\ ,$$

one obtains

$$N_{r,\Delta\lambda} = N_{ro,\Delta\lambda}\left(1 \pm \frac{\Delta N_{r,\Delta\lambda}}{N_{ro,\Delta\lambda}}\right)$$

$$N_{m,\Delta\lambda} = N_{mo,\Delta\lambda}\left(1 \pm \frac{\Delta N_{m,\Delta\lambda}}{N_{mo,\Delta\lambda}}\right)$$

$$\rho_m = \rho_{mo}\left(1 \pm \frac{\Delta\rho_m}{\rho_{mo}}\right)$$

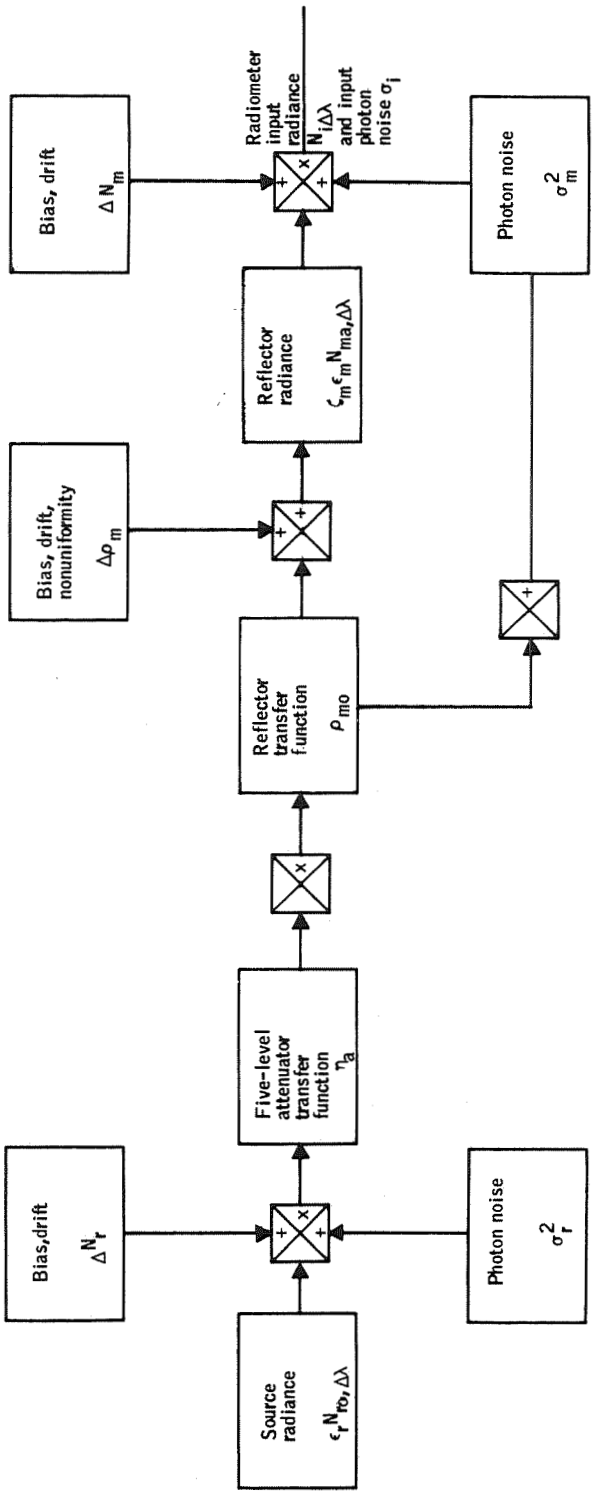

Figure 11. Inflight Calibration System Error Model

$$\epsilon_m = \epsilon_{mo}\left(1 \mp \frac{\Delta\rho_m}{\epsilon_{mo}}\right)$$

where $\epsilon_{mo} = 1 - \rho_{mo}$, and all the other parameters indexed by a zero denote nominal quantities. Consequently, one has

$$N_{i,\Delta\lambda} = \epsilon_r \eta_a \rho_{mo} N_{ro,\Delta\lambda}\left(1 \pm \frac{\Delta\rho_m}{\rho_{mo}}\right)\left(1 \pm \frac{\Delta N_{m,\Delta\lambda}}{N_{ro,\Delta\lambda}}\right)$$

$$+ \zeta_m \epsilon_{mo} N_{mo,\Delta\lambda}\left(1 \mp \frac{\Delta\rho_m}{\epsilon_{mo}}\right)\left(1 \pm \frac{\Delta N_{m,\Delta\lambda}}{N_{mo,\Delta\lambda}}\right)$$

The second approach applies

- A small extended source
- An attenuating stop in the diverging beam
- An off-axis paraboloidal reflector

The signal and error flow model for this type of inflight calibrator is shown in Figure 12. Radiant output of this calibrator is derived easily.

$$N_{i,\Delta\lambda} = \left(N_{ico,\Delta\lambda}\left(1 \pm \frac{\Delta N_{ic,\Delta\lambda}}{N_{ico,\Delta\lambda}}\right) \times \tau_{ca} + N_{ao,\Delta\lambda}\left(1 \pm \frac{\Delta N_{a,\Delta\lambda}}{N_{ao,\Delta\lambda}}\right) \times \epsilon_{cao}\left(1 \pm \frac{\Delta\epsilon_{ca}}{\epsilon_{cao}}\right) \times \zeta_{ca}\right)$$

$$\times \rho_{cco}\left(1 \pm \frac{\Delta\rho_{cc}}{\rho_{cco}}\right) + N_{co,\Delta\lambda}\left(1 \pm \frac{\Delta N_{c,\Delta\lambda}}{N_{co,\Delta\lambda}}\right) \times \epsilon_{cco}\left(1 \mp \frac{\Delta\rho_{cc}}{\epsilon_{cco}}\right) \zeta_{cc}$$

where all the Δ quantities represent systematic errors, and

$N_{ico,\Delta\lambda}$ = nominal source radiance in bandpass-filter wavelength interval (emissivity assumed to be 1.0)

τ_{ca} = attenuator transfer function, a transmissivity

$N_{ao,\Delta\lambda}$ = nominal attenuator blackbody radiance in interval $\Delta\lambda$

ϵ_{cao} = $1 - \rho_{cao}$ = nominal attenuator emissivity

ρ_{cao} = nominal attenuator reflectivity

ζ_{ca} = $1 - \tau_{ca}$ = attenuator blockage factor

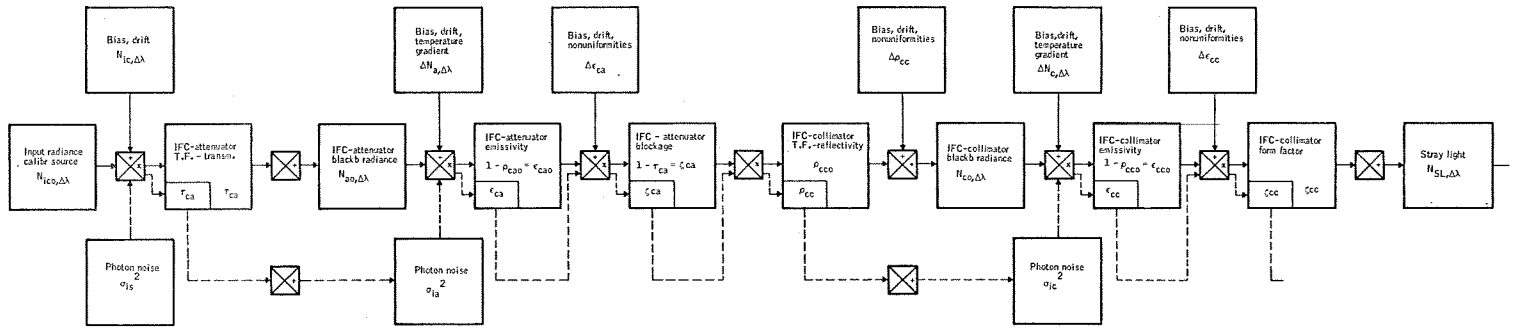

Figure 12. Signal and Error Model for Inflight Calibration Subsystem

ρ_{cco} = IFC-collimator transfer function, a nominal reflectivity

$N_{io,\Delta\lambda}$ = nominal collimator blackbody radiance in interval $\Delta\lambda$

ϵ_{cco} = $1 - \rho_{cco}$ = nominal collimator emissivity

ρ_{cco} = nominal collimator reflectivity

ζ_{cc} = collimator form factor = ratio of actual collimator area to that of its projection into a plane through the collimator apex

Stray light - near axis: Stray light for purposes of this model is constituted by input radiance imaged within the field of view but which does not arise from the target within the field of view. Such stray light is due to diffraction and aberration of the image. If completely uniform targets of the same extent outside the field of view were always viewed, this type of stray light would produce a signal which could be disregarded from consideration as a possible offset error since the same conditions would always occur. If the radiometer views a target such as a "cold" area surrounded by warmer areas, this type of stray light could be of significance.

Stray light off-axis: To describe analytically the stray light from off-axis objects outside the field of view, one may apply derivations of Zanoni and Hill (ref. 1). According to this article, it is supposed that stray light emanates from a circular source at infinity, and is completely incoherent; that is, the circular source is considered to be a superposition of an infinity of point sources. Assuming uniform radiant intensity distribution over the source area, the point sources are characterized by diffraction patterns that are identically shaped, but dislocated with respect to each other. Then, it is evident that the diffraction pattern of the extended source consists of the superposition of individual point source diffraction patterns. Also, it is obvious that the circular source's diffraction pattern will extend over the periphery of the disk's geometrical image.

To take these facts into account, the region in the focal plane that corresponds to the field of view is described by a circular area of radius a; denoting the focal length of the radiometer by f, the field-of-view angle is determined by

$$\tan \alpha = a/f$$

Similarly, for a stray-light source outside the field of view, that is, at $\phi > \alpha$, one obtains the center location of the image at distance

$$R_i = f \tan \phi$$

from the optical axis. Although not reflecting reality, it may be assumed that the geometrical image of the stray-light source is a circle of radius b in the focal plane; denoting the small angular subtend of the source by $2\Delta\phi$, one has

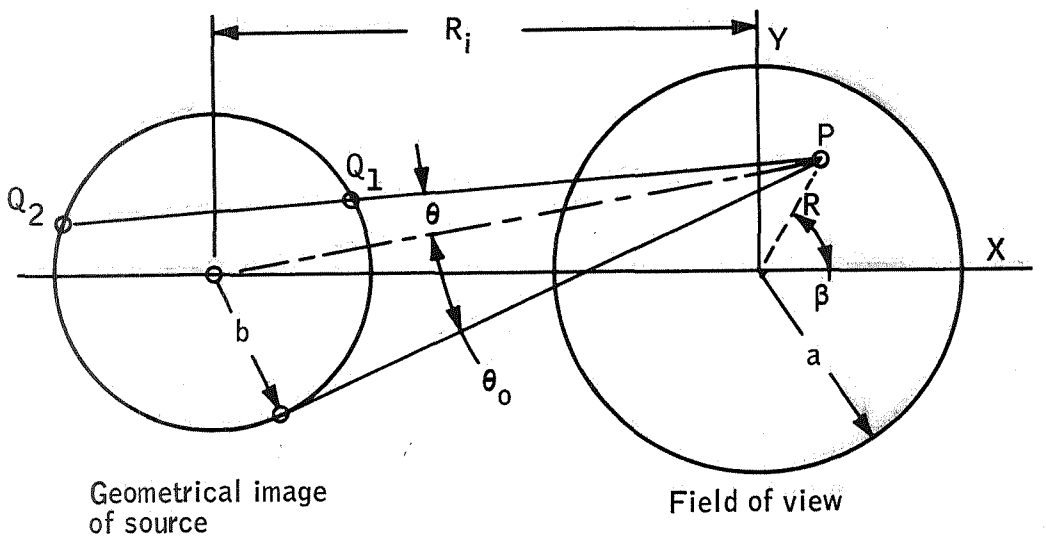

Figure 13. Location of Geometrical Stray-Light Source Image Relative to Field of View

λ = wavelength (m)

$N_{o,\lambda}$ = radiance at the pattern center , i.e., at $\rho = 0$

$N_{o,\lambda}$ may be expressed by the spectral blackbody radiance (W m^{-2} sr^{-1} $m^{-1}_{\Delta\lambda}$, Planck's law) and by the spectral emissivity $\epsilon(\lambda)$ of the stray-light source, that is, by

$$N_{o,\lambda} = 2c^2 h \epsilon(\lambda) \lambda^{-5} \left[\exp\left(\frac{hc}{\lambda kT}\right) - 1 \right]^{-1}$$

where

c = light velocity = 3×10^8 $msec^{-1}$

h = Planck's constant = 6.63×10^{-34} W sec^2

k = Boltzmann's constant = 1.38×10^{-23} W sec deg^{-1}

T = source temperature (°K)

However, $N_{o,\lambda}$ usually cannot be computed a priori since neither the temperature, T, nor the emissitivy, $\epsilon(\lambda)$ will be known.

The spectral radiance at the observation point P is obtained by integration:

$$b \approx f\Delta\phi$$

The situation encountered is illustrated in Figure 13

Now, diffracted radiances of all points Q within the geometrical source image contribute to radiance observable at any point P (R, β) within the field of view, where $0 \leq R \leq \alpha$, $0 \leq \beta \leq 2\pi$. Introducing, with respect to an origin at P, polar coordinates (r, θ), one obtains the relationship

$$\overline{CP}^2 = b^2/\sin^2\theta_o = R_i^2 + R^2 - 2R_i R\cos(\pi - \beta), \text{ or}$$

$$\sin\theta_o = f\Delta\phi\,(f^2\tan^2\phi + R^2 + 2fR\tan\phi\cos\beta)^{-1/2}$$

and has

$$b\,\frac{1-\sin\theta_o}{\sin\theta_o} \leq r \leq b\,\frac{1+\sin\theta_o}{\sin\theta_o}$$

$$-\theta_o \leq \theta \leq \theta_o$$

At points denoted by Q_o, Q_1, Q_2 in Figure 13, one has

$$r_o = b\cot\theta_o$$

$$r_1 = b\left(\frac{\cos\theta}{\sin\theta_o} - \sqrt{1 - \frac{\sin^2\theta}{\sin^2\theta_o}}\right)$$

$$r_2 = b\left(\frac{\cos\theta}{\sin\theta_o} + \sqrt{1 - \frac{\sin^2\theta}{\sin^2\theta_o}}\right), \text{respectively}$$

From the Fresnel-Kirchhoff integral, the Fraunhofer diffraction pattern for every point Q is derived (ref 3, for example)

$$N(w) = N_{o,\lambda}\left[\frac{2J_1(z)}{z}\right]^2$$

where

$J_1(z)$ = first-order Bessel function of first kind

z = $D\pi w/\lambda$

D = aperture diameter (m)

w = $\sin\gamma \approx \rho/f$

$$N_\lambda(R,\beta) = \frac{2}{b^2\pi}\int_0^{\theta_o}\int_{r_1(\theta)}^{r_2(\theta)} N(w)\, r\,dr\,d\theta$$

where, according to Figure 13, $w \approx r/f$, that is, $z \approx D\pi r/f\lambda$. Explicitly, the radiance in a wavelength interval, $\Delta\lambda = \lambda_2 - \lambda_1$, and observable within the field of view becomes

$$N_{SL,\Delta\lambda} = \frac{16c^2h}{a^2b^2\pi^2}\int_{\lambda_1}^{\lambda_2} \epsilon(\lambda)\,\lambda^{-5}\left[\exp\left(\frac{hc}{\lambda kT}\right)-1\right]^{-1}\int_0^{2\pi}\int_0^{a}\int_0^{\theta_o}\int_{r_1(\theta)}^{r_2(\theta)} \frac{J_1^2\left(\frac{D\pi r}{f\lambda}\right)}{r}\,dr\,d\theta\,dR\,d\beta\,d\lambda$$

Primary optics (off-axis paraboloidal mirror): Optical performance is described by the resolution obtainable. Since the use of an off-axis paraboloidal radiometer does not provide corrections for geometric-optical aberrations, the resolution is rather defined by the image blur than by the Rayleigh limit. As long as the image blur is smaller than or equal to the detector area, an output error due to the actual optical performance is not encountered; this even includes effects of

- Inhomogeneities in the surface finish and
- Nonuniformity of the reflectivity and emissivity

However, earth and space environments, especially when longer operation periods are to be considered, will very well produce degradation effects on the optical performance. This is certainly true if any large-scale deformation of the optical surface is encountered due to variations in such factors as time, temperature, and pressure; small-scale surface deformations due to particle bombardment, for example, are expected to have a very much lower influence.

It appears that radiometric performance is of much greater importance than optical. If the radiating mirror surface is considered as a perfect Lambertian diffuser, the radiometric performance is determined by

- Real area of the radiation source as compared with a flat circular surface passed perpendicularly to the optical axis through the mirror apex
- The solid angle subtended by the detector area at the reflector vertex
- Instantaneous reflectivity and emissivity of the mirror surface
- Actual temperature of the radiator

The form factor ζ_p, - that is, the ratio of real source area to that of the replacing flat, - usually is obtained by integration of the paraboloid analytic equation. Aside from certainly being subject to computational errors and inaccuracies in the integration procedure, the form factor is considered not affected substantially by short-term temperature and pressure fluctuations. Even the effect of long-period environmental variations is expected to be minimal. For these reasons, the form factor may be supposed to remain constant.

The solid angle subtended at the reflector vertex is defined essentially by the detector area divided by the square of the radiometer effective focal lenght. Whereas the detector area is considered a design constant for its essentially constant operation temperature, effective focal length is subject to minor changes due to short-term environmental effects. It is expected that even long-term surface deformations will not affect the focal length appreciably. Therefore, the solid angle subtended at the paraboloid apex also may be assumed to remain constant.

The reflectivity ρ_p determining the amount of radiant flux propagated through the primary optics, and the emissivity $\varepsilon_p = 1 - \rho_p$ determining the radiant-flux contribution of the mirror to the total flux receivable are evidently subject to degradations during the life time of the radiometer. These degradations are due to

- Chemical reactions with the environment on and near to the earth*
- Physical and chemical reactions with the environment outside the earth's denser atmosphere

In addition, due to nonuniform coating, ρ_p can be measured only to a certain degree of accuracy. Finally, ρ_p also may be slightly temperature dependent. For these reasons, denoting the nominal reflecitivity by ρ_{po} and the nominal $\varepsilon_{po} = 1 - \rho_{po}$, one may express

$$\rho_p = \rho_{po}\left(1 \pm \frac{\Delta\rho_p}{\rho_{po}}\right), \text{ and}$$

$$\varepsilon_p = \varepsilon_{po}\left(1 \mp \frac{\Delta\rho_p}{\varepsilon_{po}}\right)$$

where

$$\Delta\rho_p = \Delta\rho_p\,(t\,;\,T_p\,;\,r_p\,\varepsilon\,\theta_p)^{**}$$

In this expression, t represents the time elapsed since the mirror has been coated, that is, the dependence on the environment; T_p indicates the slight temperature dependence, and r_p, θ_p, coordinates in a conveniently chosen

polar system, describe the nonuniformity of the reflectance distribution. It appears obvious that the reflector has to undergo sufficient laboratory tests to determine percentage errors to be taken into account.

Radiance from the primary optics is only a function of the actual temperature. Of course, this temperature can be measured or estimated to a certain degree of accuracy. Therefore, one may express

$$N_{p,\Delta\lambda} = N_{po,\Delta\lambda}\left(1 \pm \frac{\Delta N_{p,\Delta\lambda}}{N_{po,\Delta\lambda}}\right)^{***}$$

*It is assumed that the mirror surface can be protected from the impact of dust particles and from careless handling.
**Notice that, in the IR wavelength interval considered, there is only a negligibly small dependence on the wavelength λ .
***Since the mirror radiant flux is later propagated through a bandpass filter, only the radiance contribution within $\Delta\lambda$ is to be considered and not the total radiance $N_{p,tot.}$.

where $N_{po,\Delta\lambda}$ = nominal radiance of mirror surface at temperature T_p within IR wavelength interval considered, $\Delta\lambda = \lambda_2 - \lambda_1$

$$\Delta N_{p,\Delta\lambda} = \Delta N_{p,\Delta\lambda}(T_p)$$

Hence the mirror contributions to the total output receivable consist of

- A multiplying factor

$$\rho_p = \rho_{po}\left(1 \pm \frac{\Delta\rho_p}{\rho_{po}}\right)$$

applied to the radiant flux incident upon the reflector, and of

- An additive radiance factor

$$N_{p,\Delta\lambda} = \zeta_p \varepsilon_{po} N_{po,\Delta\lambda}\left(1 \mp \frac{\Delta\rho_p}{\varepsilon_{po}}\right)\left(1 \pm \frac{\Delta N_{p,\Delta\lambda}}{N_{po,\Delta\lambda}}\right)$$

To demonstrate the generality of the error model conceived, an alternate approach for the primary optics is taken into consideration. In this approach, the off-axis paraboloidal mirror is replaced by a multiple-element component incorporating reflective as well as refractive elements. Without claiming the feasibility of such a design, one may assume the primary optics to consist of a modified Gregorian system, as shown in Figure 14. In detail, the design is described by

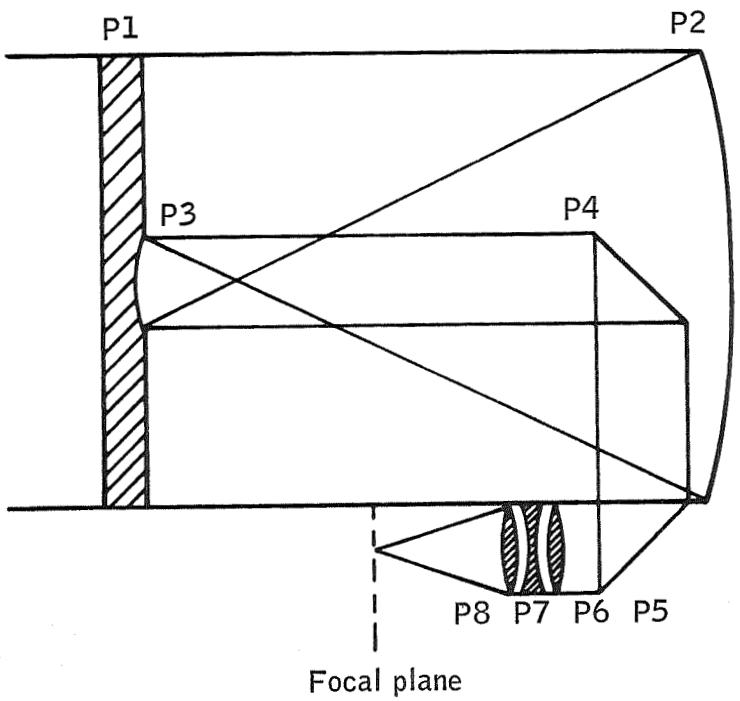

Figure 14. Example of Multiple-Element Primary Optics

p1 = refractive element (corrector plate, lowpass filters, etc.)
p2 = primary image-forming mirror
p3 = secondary collimating mirror
p4, p5 = beam-folding mirrors
p6, p7, p8 = reimaging refractive elements

In describing the error model of the multiple-element primary optics, one has to remember that each element, pm, contributes to the total output receivable at the detector face with

- A multiplying factor (transfer function)

$$\eta_{pm} = \eta_{pmo}\left(1 \pm \frac{\Delta\eta_{pm}}{\eta_{pmo}}\right), \text{ and}$$

- An additive factor (surface radiance term)

$$N_{pm} = \zeta_{pm}\,\epsilon_{pmo}\,N_{pmo,\Delta\lambda}\left(1 \mp \frac{\Delta\eta_{pm}}{\epsilon_{pmo}}\right)\left(1 \pm \frac{\Delta N_{pm,\Delta\lambda}}{N_{pmo,\Delta\lambda}}\right)$$

In these expressions, one uses the notations

η = efficiency factor, being equal to the reflectivity, ρ, of reflective or to the transmissivity, $\tau = 1 - \alpha - \rho$, of refractive elements

ϵ = emissivity, being equal to $(1 - \rho)$ of reflective or to the absorptivity α of refractive elements; α is supposed to be a function of the wavelength λ only and not subject to errors

ζ = form factor, expressed as the ratio of real surface area to its circular projection upon a plane passing through the real surface apex; ζ is assumed essentially to be constant

N = radiance $(W/cm^2 - sr)$

$\Delta\lambda$ = $\lambda_2 - \lambda_1$ defines the transmission region of the bandpass filter

Quantities indexed by a zero represent nominal values, subject to error quantities Δ (such as uncertainty, bias, drift, nonuniformity) which may be dependent on time t, temperature T, environment degradation, and other parameters; for example, one may define.

$$\Delta\eta = \Delta\eta\,(t;\, T;\, r,\, \theta)$$

where r, θ = polar coordinates describing possible nonuniformities,

$$\Delta N = \Delta N\,(T)$$

It must be noticed that every radiance is characterized additionally by a correlated photon-noise term. These noise terms propagating through the total system must be taken into account in a manner completely different from that described above. Since this is done at the end of the propagation chain, i.e., at the detector, there is no need for considering photon noises particularly at the moment.

In detail, if N_i denotes the input-radiance to the radiometer, one obtains at the output of the primary optics

$$\begin{aligned}\underline{N_o} = &\Big(\Big(\Big(\Big(\Big(\Big(\Big(N_i\,\tau_{p1} + N_{p1}\,\zeta_{p1}\,\epsilon_{p1}\Big)\,\rho_{p2} + N_{p2}\,\zeta_{p2}\,\epsilon_{p2}\Big)\,\rho_{p3} \\ &+ N_{p3}\,\zeta_{p3}\,\epsilon_{p3}\Big)\,\rho_{p4} + N_{p4}\,\zeta_{p4}\,\epsilon_{p4}\Big)\,\rho_{p5} + N_{p5}\,\zeta_{p5}\,\epsilon_{p5}\Big)\,\tau_{p6} \\ &+ N_{p6}\,\zeta_{p6}\,\epsilon_{p6}\Big)\,\tau_{p7} + N_{p7}\,\zeta_{p7}\,\epsilon_{p7}\Big)\,\tau_{p8} + N_{p8}\,\zeta_{p8}\,\epsilon_{p8} \\ = &\; N_i \times \prod_{m=1}^{8} \eta_{pm}\end{aligned}$$

$$+ \left[\sum_{k=1}^{7} N_{pk}\, \zeta_{pk}\, \epsilon_{pk} \times \prod_{m=k+1}^{8} \eta_{pm} + N_{p8}\, \zeta_{p8}\, \epsilon_{p8} \right]$$

This result indicates that the multiple-element primary optics are very well replaceable by a single box in the error-propagation model when the multiplying and additive factors are properly defined by

$$\eta_p = \prod_{m=1}^{8} \eta_{pm} \text{ , and}$$

$$N_{p,\Delta\lambda} = \sum_{k=1}^{7} N_{pk,\Delta\lambda}\, \zeta_{pk}\, \epsilon_{pk} \times \prod_{m=k+1}^{8} \eta_{pm} + N_{p8,\Delta\lambda}\, \zeta_{p8}\, \epsilon_{p8}$$

respectively.

Notice that in these expressions

$$N_{pm} = N_{pmo} \left(1 \pm \frac{\Delta N_{pm}}{N_{pmo}}\right) \text{ for both reflective and refractive elements}$$

$$\eta_{pm} = \rho_{pm} = \rho_{pmo} \left(1 \pm \frac{\Delta \rho_{pm}}{\rho_{pmo}}\right)$$

$$\epsilon_{pm} = 1 - \rho_{pm} = \epsilon_{pmo} \left(1 \mp \frac{\Delta \rho_{pm}}{\epsilon_{pmo}}\right)$$

$$\epsilon_{pmo} = 1 - \rho_{pmo} \text{ for reflective elements}$$

$$\eta_{pm} = \tau_{pm} = 1 - \alpha_{pm} - \rho_{pm} = \tau_{pmo} \left(1 \mp \frac{\Delta \rho_{pm}}{\tau \rho_{pmo}}\right)$$

$$\tau_{pmo} = 1 - \alpha_{pm} - \rho_{pmo}$$

$$\epsilon_{pm} = \alpha_{pm}(\lambda) \text{ for refractive elements}$$

Of course, similar considerations are applicable to the other optical components of the overall radiometer design, that is, to the calibrator optics and to the relay system's collimator and concentrator.

Modulation System: It appears that the modulation system is probably the most crucial element in the sequence of the radiometer components since the modulation function affects the propagation of the flux and the errors involved. The effect of the modulation system is best understood by considering the chopper action with respect to the very closely positioned field stop. This field stop is a rectangular opening in a screen that is obscured by a sinusoidally driven rectangular chopper plate. Since the sinusoidal chopper action cannot provide an on/off-type obscuration of the field stop, it is necessary to determine the characteristics of the time-dependent modulation function. Only in this way, the actually reflecting and emitting modulator area, that is, the blockage factor ζ_m can be found.

The dynamics involved may be considered from an analytic-geometrical point of view. In this application the origin of a Cartesian coordinate system is placed at the fixed rotation center of the sinusoidal motion of the chopper level arm (Figure 15). Instantaneous angular deviation of the lever arm from the zero position is expressed by

$$\phi = \phi_o \sin \omega_c t$$

where

ϕ_o = maximum angular deviation

ω_c = chopper frequency

Then, the equation of the instantaneous lever arm position is given by

$$x \sin \phi - y \cos \phi = 0$$

If the dimensions of the chopper plate are denoted by

l_m = lever-arm length between origin and chopper-plate center

$w_m h_m$ = half width and half height of chopper plate, respectively,

then, the equations of the lower and upper chopper-plate edges are

$$x \sin \phi - y \cos \phi - h_c = 0, \text{ and}$$

$$x \sin \phi - y \cos \phi + h_c = 0, \text{ respectively}$$

The field-stop center is located at the point $(l_m, 0)$ and characterized by w_f, h_f = half-width and half-height of field stop (or better of detector image), respectively.

When the chopper operation starts from the zero position, the field stop remains completely obscured until the lower chopper plate edge passes through the right lower corner of the field stop, $(l_m + w_f, - h_f)$. At this moment, one has

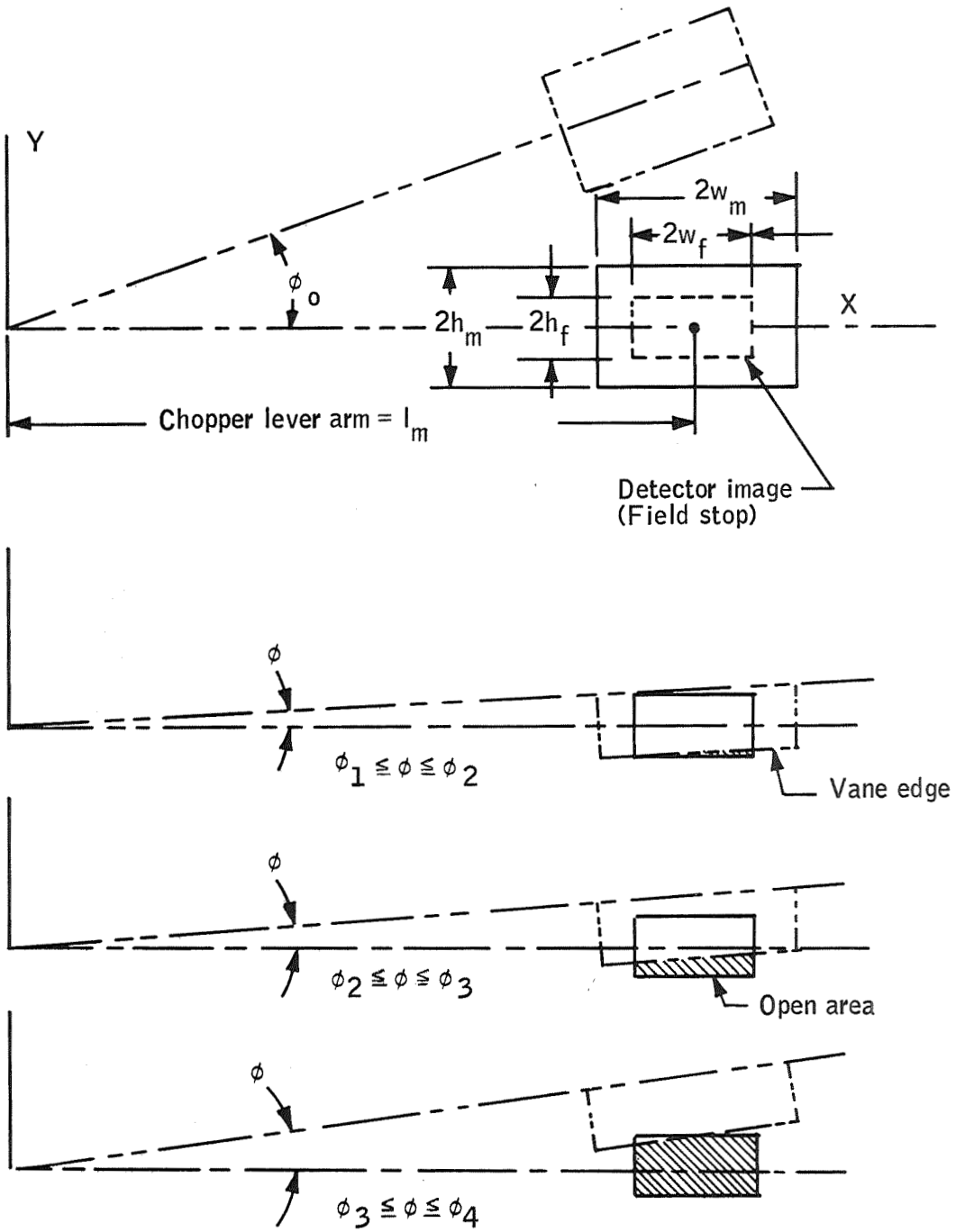

Figure 15. Field-Stop Obscuration by Chopper Motion

$$(l_m + w_f) \sin \phi_1 + h_f \cos \phi_1 - h_m = 0$$

whence ϕ_1 can be computed. Now the field stop begins to open. The lower chopper plate edge intersects both the right and the lower field stop edges until the chopper edge passes through the left lower field stop corner $(l_m - w_f, -h_f)$ where one has

$$(l_m + w_f) \sin \phi_2 + h_f \cos \phi_2 - h_m = 0$$

It is easily seen that, for $\phi_1 \leq \varphi \leq \phi_2$, the open field-stop area is a triangle. If the lower chopper edge is intersected with $x_2 \equiv l_m + w_f$ and $Y_1 \equiv -h_f$, one obtains

$$y_2 = \frac{1}{\cos \phi} \left[(l_m + w_f) \sin \phi - h_m\right] \text{ and}$$

$$x_1 = \frac{1}{\sin \phi} \left[-h_f \cos \phi + h_m\right] \text{ respectively}$$

Thus, the area of the triangle becomes

$$A_1 = \frac{1}{2} (x_2 - x_1)(y_2 - y_1) = \frac{1}{\sin 2\phi} \left[(l_m + w_f) \sin \phi + h_f \cos \phi - h_m\right]^2$$

When ϕ exceeds ϕ_2, the lower chopper edge intersects generally with $x_1 \equiv l_m - w_f$ and $x_2 \equiv l_m + w_f$, as illustrated in Figure 15, until the chopper edge passes through the upper-right field-stop corner $(l_m + w_f, h_f)$. Of course, this defines a limiting value for ϕ. The open field-stop area is always a trapezoid until this limiting value is reached. However, to find the analytic expression for this area, one must consider that the values of y_1 and y_2 corresponding to x_1 and x_2, respectively, can have negative and positive signs. However, defining the trapezoidal area as the sum of a rectangle and a triangle, it can be shown that one has in every case

$$A = (x_2 - x_1)(h_f + y_1) + \frac{1}{2}(x_2 - x_1)(y_2 - y_1) = (x_2 - x_1)\left(h_f + \frac{y_1 + y_2}{2}\right)$$

since

$$x_2 = l_m + w_f \,, \quad y_2 = \frac{1}{\cos \phi} \left[(l_m + w_f) \sin \phi - h_m\right]$$

$$x_1 = l_m - w_f \,, \quad y_1 = \frac{1}{\cos \phi} \left[(l_m - w_f) \sin \quad - h_m\right]$$

one obtains

$$A_2 = \frac{2w_f}{\cos\phi}\left[l_m \sin\phi + h_f \cos\phi - h_m\right] \; ; \phi_2 \leqq \phi \leqq \phi_3 ; (l_m + w_f)\sin\phi_3 - h_f \cos\phi_3 - h_m = 0$$

The field-stop area becomes completely open for $\phi \geqq \phi_4$ where ϕ_4 is defined by

$$(l_m - w_f)\sin\phi_4 - h_f \cos\phi_4 - h_m = 0$$

For $\phi_3 \leqq \phi \leqq \phi_4$, the obscured area is a triange obtainable from intersecting lower chopper edge with the upper-left field-stop edges. From

$$x_2 = \frac{1}{\sin\phi}\left[h_f \cos\phi + h_m\right] \; , \; y_2 = h_f$$

$$x_1 = l_m - w_f \; , \; y_1 = \frac{1}{\cos\phi}\left[(l_m - w_f)\sin\phi - h_m\right]$$

one obtains the open field-stop area

$$A_3 = 4 w_f h_f - \frac{1}{2}(x_2 - x_1)(y_2 - y_1) = 4 w_f h_f - \frac{1}{\sin 2\phi}\left[(l_m - w_f)\sin\phi - h_f \cos\phi - h_m\right]$$

Now it is possible to define the form factor ζ_m and the corresponding transmission factor $\tau_m = 1 - \zeta_m$ by

$$\zeta_{m1} = 1 \qquad \tau_{m1} = 0 \qquad \text{for } 0 \leqq \phi \leqq \phi_1$$

$$\zeta_{m2} = 1 - \frac{A_1}{4 w_f h_f} \qquad \tau_{m2} = \frac{A_1}{4 w_f h_f} \qquad \text{for } \phi_1 \leqq \phi \leqq \phi_2$$

$$\zeta_{m3} = 1 - \frac{A_2}{4 w_f h_f} \qquad \tau_{m3} = \frac{A_2}{4 w_f h_f} \qquad \text{for } \phi_2 \leqq \phi \leqq \phi_3$$

$$\zeta_{m4} = 1 - \frac{A_3}{4 w_f h_f} \qquad \tau_{m4} = \frac{A_3}{4 w_f h_f} \qquad \text{for } \phi_3 \leqq \phi \leqq \phi_4$$

$$\zeta_{m5} = 0 \qquad \tau_{m5} = 1 \qquad \text{for } \phi_4 \leqq \phi \leqq \phi_0$$

where, in general and specifically, one has

$$\phi = \phi_o \sin \omega_c t$$

$$(l_m + w_f) \sin\phi_1 + h_f \cos\phi_1 - h_m = 0$$

$$(l_m - w_f) \sin\phi_2 + h_f \cos\phi_2 - h_m = 0$$

$$(l_m + w_f) \sin\phi_3 - h_f \cos\phi_3 - h_m = 0$$

$$(l_m - w_f) \sin\phi_4 - h_f \cos\phi_4 - h_m = 0$$

$$A_1 = \frac{1}{\sin 2\phi}\left[(l_m + w_f) \sin\phi + h_f \cos\phi - h_m\right]^2$$

$$A_2 = \frac{2\, w_f}{\cos\phi}\left[l_m \sin\phi + h_f \cos\phi - h_m\right]$$

$$A_3 = 4\, w_f\, h_f - \frac{1}{\sin 2\phi}\left[(l_m - w_f) \sin\phi - h_f \cos\phi - h_f\right]^2$$

Of course, the modulation functions, ζ_m and τ_m, are symmetrical to the zero chopper position. This can be shown easily by considering negative values of ϕ and using the upper chopper edge as an intersecting line.

Modulation factors are considered not affected substantially by short-term temperature and pressure fluctuations causing surface deformations, and in addition are supposed to be relatively insensitive to long-term environmental variations. In this view, they can be handled as analytically determinable functions of time or its equivalent, the angular deviation ϕ of the chopper's lever arm from its zero position. Furthermore, it is not expected that the angular subtense of the detector face as seen from the axial point of the chopper plane will appreciably change with a long-term variation of the environment. For this reason, the subtended solid angle can be assumed to remain constant.

Optical elements behind the chopper, that is, the field-stop screen, the collimator and concentrator of the secondary optics, and the bandpass filter produce a certain amount of radiant flux incident upon the actual chopper surface. Reflectivity ρ_m of the chopper determines the amount of this incident flux that can be propagated back through the secondary optics. On the other hand, the emissivity $\varepsilon_m = 1 - \rho_m$ defines the radiant-flux contribution of the actual chopper area to the total flux receivable. Both, ρ_m and ε_m, are subject to long-term environmental degradations to be experienced during the radiometer's lifetime in space. Moreover, by nonuniform coating, $\varkappa_m$ can be determined to a certain degree of accuracy; $\varkappa_m$ also may be temperature dependent. For these reasons, the reflectivity and the emissivity are expressed by

$$\rho_m = \rho_{mo}\left(1 \pm \frac{\Delta\rho_m}{\rho_{mo}}\right), \text{ and}$$

$$\epsilon_m = \epsilon_{mo}\left(1 \mp \frac{\Delta\rho_m}{\epsilon_{mo}}\right), \text{ respectively}$$

where

$$\Delta\rho_m = \Delta\rho_m\,(t\,;\,T_m\,;\,r_m,\,\theta_m)$$

ρ_m, ϵ_m = nominal reflectivity and emissivity, respectively; t represents the time elapsed since the chopper surface has been prepared; T_m indicates the presumably slight temperature dependence; and $(r_m,\ \theta_m)$ are polar coordinates in a conveniently chosen coordinate system describing the non-uniform reflectance distribution.

Of course, chopper-plate radiance is a function of the actual temperature T_m, however, which can be determined to a certain degree of accuracy. Hence, this radiance is expressible by

$$N_{m,\Delta\lambda} = N_{m,\Delta\lambda}\left(1 \pm \frac{N_{m,\Delta\lambda}}{N_{mo,\,\Delta\lambda}}\right)$$

where $N_{mo,\,\Delta\lambda}$ = nominal radiance of actual chopper surface of temperature T_c within the IR wavelength interval considered, $\Delta\lambda = \lambda_2 - \lambda_1$. By using immediately $N_{m,\,\Delta\lambda}$ instead of the total radiance $N_{m,\,tot,}$ the propagation through the bandpass filter to be passed through later is taken into account.

$$\Delta N_{m,\,\Delta\lambda} = \Delta N_{m,\ \Delta\lambda}\,(T_m)$$

From these particular derivations, one obtains chopper contributions to the total output receivable:

- The power incident from the primary optics and propagated through the open portion of the modulation system must be multiplied by the factor

  $$\tau_m = \tau_m\,(\phi) \text{ or its equivalent } \tau_m = \tau_m\,(t)$$

  expressing the short-term dependence on the chopper frequency.

- The power incident from the elements behind the chopper must be multiplied by the factor

$$\zeta_m(t)\ \rho_{mo}\left(1 \pm \frac{\Delta\rho_m}{\rho_{mo}}\right)$$

- The radiance of the chopper itself must be added

$$\zeta_m(t)\ \epsilon_{mo}\ N_{mo,\Delta\lambda}\left(1 \mp \frac{\Delta\rho_m}{\epsilon_{mo}}\right)\left(1 \pm \frac{\Delta N_{m,\Delta\lambda}}{N_{mo,\Delta\lambda}}\right)$$

Field stop: The field stop is supposed to be a rectangular opening, in a totally absorbing screen, reflecting the angular dimensions of the required field-of-view in azimuth and elevation. For easy alinement and adjustment the image of the field-stop area, as obtained by the relay optics, preferably should be larger than the detector area. In this aspect, the screen area outside the field stop is not contributing any amount of erroneous radiation falling on the detector face. On the other hand, the effect of the time-dependent transmissivity, a function of the combined action of chopper and field stop, already has been taken into account by virtue of the transmission factor

$$\tau_m = \tau_m(t)$$

an analytical function that is not supposed to be subject to significant errors.

However, so far it has not been taken into consideration that the area of the rectangular field stop is evidently different from the size of the image blur in the primary optics focal plane. To take this into account, one must define:

- A form factor

$$\zeta_f = A_{fs}/A_b$$

where

A_{fs} = total field-stop area, and

A_b = image-blur area

This form factor enters the error-propagation equation as an essentially constant multiplier since A_b is determined by the optical performance of the primary optics, and A_{fs} may be slightly dependent on the screen temperature.

Relay optics collimator (off-axis paraboloidal mirror): Arguments used in considering the primary optics are valid equally for the first element of the secondary optics. This means that one has to define the reflectivity

$$\rho_{s1} = \rho_{s10}\left(1 \pm \frac{\Delta\rho_{s1}}{\rho_{s10}}\right)$$

and the emissivity

$$\epsilon_{s1} = \epsilon_{s10}\left(1 \mp \frac{\Delta\rho_{s1}}{\epsilon_{s10}}\right)$$

where, neglecting the certainly trivial wavelength dependence,

$$\Delta\rho_{s1} = \Delta\rho_{s1}\,(t;\, T_{s1};\, r_{s1},\, \theta_{s1})$$

ρ_{s10}, ϵ_{s10} = nominal values of reflectivity and emissivity, respectively. The time t represents the long-term effect of the environment; T_{s1} accounts for the slight temperature dependence; and the polar coordinates (r_{s1}, θ_{s1}), referred to a conveniently chosen coordinate system, are used to describe the nonuniform reflectance distribution.

The radiance of the collimator, a function of the actual temperature only, contributes to the power output of the radiometer in a twofold manner:

- Direct radiation falls on the next element in the deisgn sequence, the bandpass filter
- Indirect radiation impinges on the actual chopper surface where it is reflected backward such that it passes, after reflection at the collimator, through the spectral filter

However, in both cases one can express the radiance by

$$N_{s1,\Delta\lambda} = N_{s10,\Delta\lambda}\left(1 \pm \frac{\Delta N_{s1,\Delta\lambda}}{N_{s10,\Delta\lambda}}\right)$$

where

$N_{s10,\,\Delta\lambda}$ = nominal collimator radiance at temperature T_{s1} within IR wavelength interval $\Delta\lambda = \lambda_2 - \lambda_1$

$\Delta N_{s1,\Delta\lambda} = \Delta N_{s1,\,\Delta\lambda}(T_{s1})$

From this derivation, it follows that collimator contributions to the total radiometer output are describable

- By a multiplying factor

$$\rho_{s1} = \rho_{s10}\left(1 \pm \frac{\Delta\rho_{s1}}{\rho_{s10}}\right)$$

that applies to

- Total radiation passed through the open field-stop area
- Radiation of the actual chopper area
- Total indirect radiation reflected toward the chopper and
- Total indirect radiation reflected by the chopper

- By an additive term

$$\zeta_{s1}\,\epsilon_{s10}\,N_{s10,\Delta\lambda}\left(1 \mp \frac{\Delta\rho_{s1}}{\epsilon_{s10}}\right)\left(1 \pm \frac{\Delta N_{s1,\Delta\lambda}}{N_{s10,\Delta\lambda}}\right)$$

where

ζ_{s1} = form factor of the collimator surface

This additive term describes both

- Direct radiation toward the bandpass filter
- Indirect radiation toward the chopper

Relay optics collimator (refractive components): If a refractive instead of a reflective component is used in the relay optics assembly, the reflectivity ρ_{s1} must be replaced by a transmissivity τ_{s1}, a function of wavelength λ that is defined by the compound absorptivity α_{s1} of the component's particular elements and by the surface reflectivities ρ_{s1}. It is supposed that ρ_{s1} is not strongly dependent on λ in the IR region of interest. However, exposed lens surfaces certainly are affected by the environment over longer periods of time t. An inherent nonuniformity of the reflectance distribution expressed by polar coordinates (r_{s1}, θ_{s1}) also may be subject to time-dependent variations due to long-term environmental effects, e. g., occurrence of scattering centers due to particle impact. Furthermore, there may exist a slight dependence on the component temperature T_{s1}. On the other hand, it can be assumed that the absorptivity α_{s1} (and consequently the emissivity ϵ_{s1}) is only a function of λ since it relates to the internal molecular structure

of the lens materials which supposedly is not affected by the environment. Taking these considerations into account and defining a nominal transmissivity by

$$\tau_{s10} = 1 - \alpha_{s1}(\lambda) - \rho_{s10}$$

one obtains an expression for the actual transmissivity

$$\tau_{s1} = \tau_{s10}\left(1 \mp \frac{\Delta\rho_{s1}}{\tau_{s10}}\right)$$

where $\Delta\rho_{s1} = \Delta\rho_{s1}(t\,;\, T_{s1}\,;\, r_{s1},\, \theta_{s1})$. The emissivity is simply given by

$$\epsilon_{s1}(\lambda) = \alpha_{s1}(\lambda)$$

Radiance for both the direct and indirect paths is only a function of temperature uncertainties; i. e., one has

$$N_{s1,\Delta\lambda} = N_{s10,\Delta\lambda}\left(1 \pm \frac{\Delta N_{s1,\Delta\lambda}}{N_{s10,\Delta\lambda}}\right)$$

where

$$\Delta N_{s1,\Delta\lambda} = \Delta N_{s1,\Delta\lambda}(T_{s1})$$

Collimator contributions to the total radiometer output now are described as

- A multiplying factor

$$\tau_{s1} = \tau_{s10}\left(1 \mp \frac{\Delta\rho_{s1}}{\tau_{s10}}\right)$$

must be applied to

- Total radiation passed through the open field-stop area, as well as to the direct radiation of the actual chopper area
- Total indirect radiation passing through the collimator toward the chopper
- Total indirect radiation reflected by the chopper

In determining the additive power terms, it is to be realized that the form factors encountered probably will be different for the front and back surfaces of the collimator assembly. Denoting these front- and back-surface form factors by subscripts f and b, respectively, one obtains

- Additive term for direct radiation

$$\zeta_{s1b}\, \epsilon_{s1}(\lambda)\, N_{s10,\Delta\lambda} \left(1 \pm \frac{\Delta N_{s1,\Delta\lambda}}{N_{s10,\Delta\lambda}}\right)$$

- Additive term for indirect radiation

$$\zeta_{s1f}\, \epsilon_{s1}(\lambda)\, N_{s10,\Delta\lambda} \left(1 \pm \frac{\Delta N_{s1,\Delta\lambda}}{N_{s10,\Delta\lambda}}\right)$$

Spectral filter: With respect to the filter, derivations are quite similar to those pertaining to reflecting surfaces. The only difference is that the mirror reflectivity must be replaced by the filter transmissivity, a function of wavelength that is defined by the filter's absorptivity α_f and surface reflecitivity ρ_b. However, it can be supposed that ρ_b is not strongly dependent on the wavelength λ. Furthermore, it may be assumed that the absorptivity (and therefore the emissivity ϵ_b), aside from certainly being a function of the wavelength, is not subject to substantial environment degradation since it is due to the molecular structure of the filter material. If one defines the surface reflectivity by

$$\rho_b = \rho_{bo} \left(1 \pm \frac{\Delta\rho_b}{\rho_{bo}}\right)$$

where

$$\Delta\rho_b = \Delta\rho_b (t\,;\, T_b\,;\, r_b\,,\, \theta_b)$$

one obtains

$$\tau_b = \tau_{bo} \left(1 \mp \frac{\Delta\rho_b}{\tau_{bo}}\right)$$

where

and

$$\tau_{bo} = 1 - \alpha_b(\lambda) - \rho_{bo}$$

$$\epsilon_b(\lambda) = \alpha_b(\lambda)$$

Usually, in defining the error quantity $\Delta\rho_b$, the time dependence t stays for environmental effects near the earth and in space which, however, may be considered minimal. On the other hand, it is not expected that the filter temperature T_b and the nonuniformity of the surface reflectance distribution, expressed by the polar coordinates $(r_b,\ \theta_b)$, will affect the reflectivity substantially. For these reasons, the percentage error of the filter's transmissivity may become very small.

More careful consideration must be directed toward the radiance contributions of the filter itself, for, although comprising a direct and an indirect component the first one, directed toward the relay optics' concentrator in the sensitivity range of the detector, $\Delta\lambda = \lambda c - 0$ (λ_c = cut-off wavelength), must refer to the radiation emitted, whereas the second component, by virtue of the filtering process involved, requires only the coverage of the wavelength interval $\Delta\lambda$. One must, therefore, define

- Direct-radiance component

$$N_{b,\Delta\lambda'} = N_{bo,\Delta\lambda} \left(1 \pm \frac{\Delta N_{b,\Delta\lambda'}}{N_{bo,\Delta\lambda'}}\right)$$

- Indirect-radiance component

$$N_{b,\Delta\lambda} = N_{bo,\Delta\lambda} \left(1 \pm \frac{\Delta N_{b,\Delta\lambda}}{N_{bo,\Delta\lambda}}\right)$$

where

$N_{bo,\Delta\lambda'}$, $N_{bo,\Delta\lambda}$ = nominal radiances spectrally filtered in wavelength intervals $\Delta\lambda'$ and $\Delta\lambda$, respectively, and

$$\Delta N_{b,\Delta\lambda'} = \Delta N_{b,\Delta\lambda'} (T_b)$$

$$\Delta N_{b,\Delta\lambda} = \Delta N_{b,\Delta\lambda} (T_b)$$

According to these physical characteristics, spectral filter contributions to the total radiometer output are described as follows:

- Multiplying factor

$$\tau_b = \tau_{bo} \left(1 \mp \frac{\Delta\rho_b}{\tau_{bo}}\right)$$

$$\tau_{b_o} = 1 - \alpha_b (\lambda) - \rho_{bo}$$

ρ_{bo} = **nominal filter surface reflectivity**

This multiplying factor is to be applied to

Total radiation passed through the open field-stop area

Accumulated direct radiation from the actual chopper area and the relay optics collimator

Total indirect radiation reflected by the chopper

Total indirect radiation pointing toward the chopper

- Additive direct power term

$$\epsilon_b(\lambda)\ N_{bo,\Delta\lambda'}\left(1 \pm \frac{\Delta N_{b,\Delta\lambda'}}{N_{bo,\Delta\lambda'}}\right)$$

- Additive indirect term

$$\epsilon_b(\lambda)\ N_{bo,\Delta\lambda}\left(1 \pm \frac{\Delta N_{b,\Delta\lambda}}{N_{bo,\Delta\lambda}}\right)$$

Relay optics concentrator (off-axis paraboloidal mirror): Derivations concerning the realy optics second element are equal to those for the collimator except that radiances are different in forward and backward directions. This means that one has to consider

- A reflectivity

$$\rho_{s2} = \rho_{s20}\left(1 \pm \frac{\Delta\rho_{s2}}{\rho_{s20}}\right)$$

- An emissivity

$$\epsilon_{s2} = \epsilon_{s20}\left(1 \mp \frac{\Delta\rho_{s2}}{\epsilon_{s20}}\right)$$

- Radiances

$$N_{s2,\Delta\lambda'} = N_{s20,\Delta\lambda'}\left(1 \pm \frac{N_{s2,\Delta\lambda'}}{N_{s20,\Delta\lambda'}}\right)$$

$$N_{s2,\Delta\lambda} = N_{s20,\Delta\lambda}\left(1 \pm \frac{N_{s2,\Delta\lambda}}{N_{s20,\Delta\lambda}}\right)$$

where all quantities exhibiting the subscript 0 represent nominal values.

The expression $\Delta\rho_{s2} = \Delta\rho_{\tilde{s}2}(t; T_{s2}; r_{s2}, \theta_{s2})$ is a function of long-term environmental changes with time t, and slightly dependent on the actual temperature T_{s2}; the polar coordinates r_{s2}, θ_{s2}, referred to a conveniently chosen system, indicate possible nonuniformities in the reflectance distribution.

$$\Delta N_{s2,\Delta\lambda'} = \Delta N_{s2,\Delta\lambda'}(T_{s2})$$

$$\Delta N_{s2,\Delta\lambda} = \Delta N_{s2,\Delta\lambda}(T_{s2})$$

constitute radiance error quantities due to uncertainties in determing the nominal temperature T_{s2}, and are related to the total and filtered wavelength intervals, respectively.

Conclusively, the following contributors of the relay optics concentrator to the radiometer output are obtained:

- Multiplying factor

$$\rho_{s2} = \rho_{s20} \left(1 \pm \frac{\Delta\rho_{s2}}{\rho_{s20}}\right)$$

to be applied to

  - Total radiation passed through the open field-stop area, including the accumulated direct radiation from the actual chopper area, the relay optics collimator, and the spectral filter
  - Indirect radiation of the cavity in the detector envelope pointing toward the chopper
  - Total indirect radiation reflected by the chopper

- Additive direct term

$$\zeta_{s2}\, \epsilon_{s20}\, N_{s20,\Delta\lambda'} \left(1 \mp \frac{\Delta\rho_{s2}}{\epsilon_{s20}}\right) \left(1 \pm \frac{\Delta N_{s2,\Delta\lambda'}}{N_{s20,\Delta\lambda'}}\right)$$

- Additive indirect term

$$\zeta_{s2}\, \epsilon_{s20}\, N_{s20,\Delta\lambda} \left(1 \mp \frac{\Delta\rho_{s2}}{\epsilon_{s20}}\right) \left(1 \pm \frac{\Delta N_{s2,\Delta\lambda}}{N_{s20,\Delta\lambda}}\right)$$

where ζ_{s2} = form factor of concentrator surface.

Relay optics concentrator (refractive component): Referring to the derivations for the relay optic's refractive collimator and its reflective concentrator, contributors of the refractive concentrator to the radiometer output can immediately be indicated.

- One has a multiplying factor

$$\tau_{s2} = \tau_{s20} = \left(1 \mp \frac{\Delta\rho_{s2}}{\tau_{s0}}\right)$$

where

$$\tau_{s20} = 1 - \alpha_{s2}(\lambda) - \rho_{20}$$

$$\rho_{s2} = \rho_{s20} \left(1 \pm \frac{\Delta\rho_{s2}}{\rho_{s20}}\right)$$

$$\Delta\rho_{s2} = \Delta\rho_{s2} \; (t \; ; T_{s2} \; ; r_{s2} \; , \theta_{s2})$$

This multiplying factor is to be applied to

- Total radiation passed through the open field-stop area, as well as to the accumulated direct radiation from the actual chopper area, the relay optics collimator and the spectral filter
- Indirect radiation of the cavity in the detector envelope pointing toward the chopper
- Total indirect radiation reflected by the chopper
- Additive direct term

$$\zeta_{s_{2b}} \epsilon_{s2} \; (\lambda) \; N_{s20,\Delta\lambda'} \left(1 \pm \frac{\Delta N_{s2,\Delta\lambda'}}{N_{s20,\Delta\lambda'}}\right)$$

- Additive indirect term

$$\zeta_{s2f} \; \epsilon_{s2} \; (\lambda) \; N_{s20,\Delta\lambda} \left(1 \pm \frac{N_{s2,\Delta\lambda}}{N_{s20,\Delta\lambda}}\right)$$

where

ζ_{s2f}, ζ_{s2b} = form factors of front and back surfaces, respectively, of concentrator-lens assembly

$\epsilon_{s2}(\lambda) = \alpha_{s2}(\lambda)$

$\Delta N_{s2,\Delta\lambda'} = \Delta N_{s2,\Delta\lambda'}(T_{s2})$ error in radiance with $\Delta\lambda' = \lambda_c - 0$ due to temperature undertainty

$\Delta N_{s2,\Delta\lambda} = \Delta N_{s2,\Delta\lambda}(T_{s2})$ error in radiance within wavelength interval $\Delta\lambda = \lambda_2 - \lambda_1$

subscript zero characterizes nominal radiance values.

Cavity: The detector is enclosed in a very narrow shield that is kept at approximately the same low temperature as the detector itself. This shield is called a cavity and has a dual purpose:

- It rejects or at least minimizes every background radiation from the space outside of the detector's field of view
- It helps maintain the desired detector temperature

The cavity has a hole in front of the detector allowing the radiation within the field of view to pass through. Since the detector's field of view is well defined by the cold stop, the transmissivity of the cavity is unity.

The energy emitted from the inside walls of the shield usually is small enough as to be negligible. However, for precision long-wavelength radiometers it may become important.

In the indirect-propagation chain, radiation from the outside walls of the shield normally will not contribute to the overall radiation receivable. Thus, in this chain the cavity can be considered to represent a blackbody radiator of very low temperature.

From this description it is seen that the cavity is characterized

- By a multiplicative transfer function

$$\tau_{cy} = 1$$

- By an additive direct radiance term

$$N_{cyo,\Delta\lambda'}\,\epsilon_{cyo}\left(1 \pm \frac{\Delta N_{cy,\Delta\lambda'}}{N_{cyo,\Delta\lambda'}}\right)\left(1 \pm \frac{\Delta\epsilon_{cy}}{\epsilon_{cyo}}\right)$$

where

$N_{cyo,\Delta\lambda'}$ = nominal blackbody radiance in $\Delta\lambda' = \lambda_c - \lambda$

λ_c = cutoff wavelength (m) of detector sensitivity

ϵ_{cyo} = nominal cavity wall emissivity

- By an additive indirect radiance term

$$N'_{cyo,\Delta\lambda}\,\epsilon'_{cyo}\left(1 \pm \frac{\Delta' N'_{cy}}{N'_{cyo,\Delta\lambda}}\right)\left(1 \pm \frac{\Delta\epsilon'_{cy}}{\epsilon'_{cyo}}\right)$$

where

$N'_{cyo,\Delta}$ = nominal blackbody radiance in $\Delta = \lambda_2 - \lambda_2$; i.e., in the spectral range of the bandpass filter

ϵ'_{cyo} = nominal cavity emissivity ≈ 1

Cold stop: The function of the cold stop is to restrict the acceptance cone for radiation receivable from all sources in front of the cavity. It is essential that the size of the projected cold stop is always smaller than the optical element at the projection point. In this manner, it is possible to assure that no warm baffle or mirror support vignettes the field or causes radiance at an undesirably high level due to a high emissivity. The general description of the projection of the cold stop and the exact geometry has not been generated, although it appears possible to obtain it in a fairly general form.

Of course, the cold stop does not contribute any radiance terms; it is only characterized by an efficiency factor that represents the solid angle of the acceptance cone, and for this reason, transforms radiance into irradiance.

As shown in reference 4, the solid angle Ω can be calculated from the half-cone apex angle ϕ. The result is

$$\eta_{cs} = \Omega = 2\pi (1 - \cos \phi) = 4\pi \sin^2 \phi/2$$

It must be noted that the apex angle of the cavity's radiation cone certainly will be larger than the angle 2ϕ. The effective solid angle for the cavity radiation is the difference between an outer solid angle Ω' and Ω where Ω' may even be as large as 2π (hemisphere). In this case one obtains

$$\Omega_{cy} = 2\pi - 2\pi (1 - \cos \phi) = 2\pi \cos \phi$$

This fact may be taken into account by defining the cavity form factor by

$$\zeta_{cy} = \Omega_{cy}/\Omega = \frac{\cos \phi}{1 - \cos \phi}$$

that applies to the cavity radiance term (direct chain).

Detector: The optical transducer taken into consideration to date is a background-limited photoconductive device that is operated from a constant current-bias supply. Since the detector resistance is inversely proportional to the photon flux (photons $\sec^{-1}$ m^{-2}) or irradiance produced by the cold-stop, transfer function first must be converted into photon flux; the appropriate multiplicative conversion factor is represented by the detector area $A_d(m^2)$.

From the total flux available only a portion will be absorbed by the detector; the remaining portion will be reflected. This means that a detector transfer function or efficiency factor η_d must be assigned to the transducer. In addition, the detector will be characterized by a quantum efficiency factor η_q; in the model, this quantum efficiency factor is assumed to be unity.

Since the actual resistance at the time of flux incidence is unknown, it must be referenced to a resistance that is determined experimentally under rather well-known measurement conditions. This implies that one has to express the actual detector resistance by

$$R_d = \frac{1}{F_{eff}} F_{cal} R_m$$

and, therefore, the output voltage by

$$E_o = \frac{1}{F_{eff}} F_{cal} R_m i_b$$

where

F_{eff} = effective incident flux passed through the radiometer in normal operation

F_{cal} = calculated flux that defines the measurement conditions

R_m = measured resistance under the condition of the calculated incident flux

i_b = constant bias current

one has

$$F_{eff} = H A_d \eta_{do} \left(1 \pm \frac{\Delta \eta_d}{\eta_{do}}\right)$$

$$F_{cal} = F_{calo} \left(1 \pm \frac{\Delta F_{cal}}{F_{calo}}\right)$$

$$i_b = i_{bo} \left(1 \pm \frac{\Delta i_b}{i_{bo}}\right)$$

Signal processing: With respect to the signal processing, only the functions of the electrical filter and the preamplifier are described. The electrical filter is usually a complex frequency response function $G_o(\omega)$ where $\omega = 2\pi\rho$ = circular electrical frequency. An example of such a frequency response function is

$$G_o(\omega) = \frac{1}{(1 + R_d/R_i) + j\omega C_i R_d}$$

where

R_d = detector resistance

R_i = amplifier input resistance

C_i = amplifier input capacitance

The amplifier is characterized by a constant gain factor C_a.

Both $G_o(\omega)$ and C_a act as multiplying factors on the detector output voltage E_o. Thus, the preamplifier output voltage due to the signal is given by

$$E_{Ao} = E_o G_o (\omega) C_a$$

The total preamplifier output voltage E_A must take into account the noise output voltage E_{AN}, i.e., one has

$$E_A = E_{Ao} + E_{AN}$$

Radiance propagation. -- To understand radiation propagation through the radiometric system, it is necessary to explain first the meaning of the term "input radiance." Figure 16 illustrates schematically the situation encountered in orbit. The unknown quantity to be measured by the radiometer is the radiance of the target scene on earth. During the period of not pointing toward the earth, the radiometer measures the space radiance and the various levels of the inflight calibrator radiance. Figure 17 shows the input radiances involved in ground calibration. Contrary to orbital operation, the simulated earth radiance is a well-defined quantity that can be measured and used for calibration of the radiometer output. The simulated space radiance also has a well-determined value and is used together, for a certain time span, with the inflight calibrator's radiances. Generation of the input radiance by the five-level inflight calibrator is shown schematically in Figure 18. Notice that systematic error quantities can be assigned only to simulator and calibrator radiances.

Stray light from objects outside the radiometer's field of view is a special type of input for which systematic errors cannot be assigned. It may be explained by applying diffraction theory as shown previously.

As the input radiance and the stray light propagates through the various radiometer elements, they are multiplied (reduced) successively by transfer functions and pick up an additional radiance term at each element passed through. At some stations, the radiation is reflected partially backwards until it meets a final station where it is again reflected in the direction toward the detector. The last of these backward-reflecting stations is the detector face itself. The radiation reflected here is subject also to multiplying transfer functions and additive radiance terms. Thus, two radiation-propagation chains, called direct and indirect chains, are to be considered. The detector responds to the combined radiance of both chains. Although the modulator transfer function is actually a time-dependent function, it is assumed, for simplifying the description of the radiation propagation, that the modulator operates only in either the chopper-open or the chopper-closed modes.

As shown later for the specific case of a multiple-element collector, each group (or subgroup) can be represented

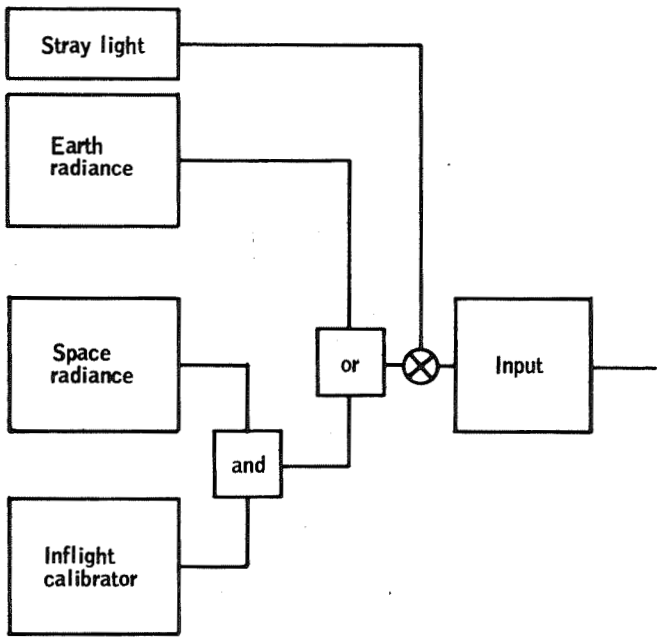

Figure 16. Generation of Input Radiance in Orbit

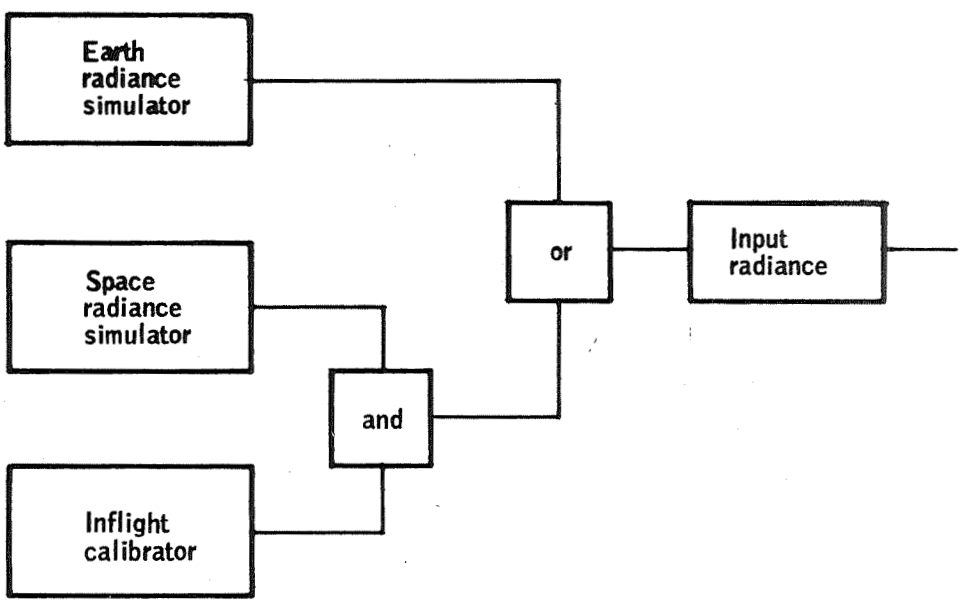

Figure 17. Generation of Input Radiance at Ground Calibration

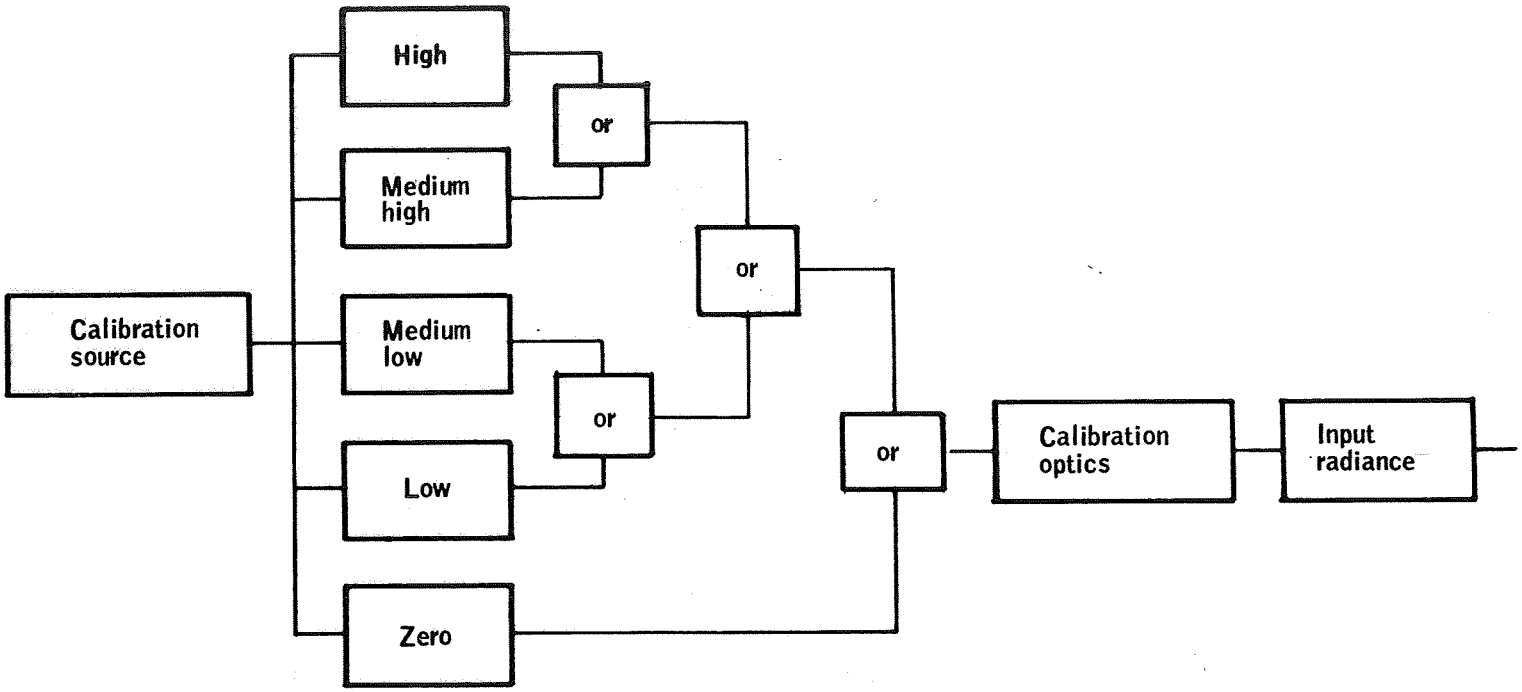

Figure 18. Generation of Input Radiance by Five-Level Inflight Calibrator

- By a multiplicative transfer function η
- By an additive radiance term $N_{\Delta\lambda}$

if appropriate definitions are applied; for example, one may obtain

$$\eta = \prod_{m=1}^{M} \eta_m$$

$$N_{\Delta\lambda} = \sum_{k=1}^{M-1} \left(N_{k,\Delta\lambda}\ \epsilon_k\ \xi_k\right)^* \prod_{m=k+1}^{M} \eta_m + \left(N_{M,\Delta\lambda}\ \epsilon_M\ \zeta_M\right)$$

This fact alleviates the general description of the radiance propagation since it allows referring to the compressed model (Figure 9).

As seen from Table 10, the direct radiation-propagation chain works as follows.

The input radiance enters the collector optics which contributes an additional radiance term. The purpose of this group is to collect the radiation passed through, concentrate it, and transmit it to the modulator in the focal plane of the collector. After reaching the modulator, the radiation is chopped to create an a-c signal at the detector, and to allow the system to differentiate between instrumental radiation behind the modulator (closed-mode operation) and signal and instrumental radiation of the total radiometer (open-mode operation). In open-mode operation the radiation passes through the modulator ($\tau_m = 1$) and enters the relay optics. These optics collect the radiation, add another radiance term, and relay the signal to the detector. In closed-mode operation the incident radiation cannot pass through the modulator ($\tau_m = 0$). Now, the modulator radiance appears and enters the relay optics, passes through them, and finally is collected at the detector. In each mode a portion of the radiation incident at the detector is reflected and contributes to the indirect radiation.

The indirect propagation chain starts with the reflected (attenuated) radiation from the detector face. After adding a detector radiance term, the radiation propagates through the relay optics and is focussed at the modulator location. In open-mode operation, it passes through the modulator until it finally is reflected toward the detector by the inflight calibrator attenuator. In this mode, the radiation afterwards is attenuated by the multiplicative transfer functions of all elements between the attenuator and the detector; however, additive radiance terms no longer appear. On the other hand, in closed-mode operation the indirect radiation incident at the chopper is reflected toward the detector by the modulator itself and, without experiencing additional radiance terms, propagates through the relay optics until it is finally collected at the detector.

The signal and systematic error propagation is described in detail below.

Chopper-open operation mode:

- Direct radiation-propagation chain

$$E_{out} = \left(\left(N_{io}\left(1 \pm \frac{\Delta N_i}{N_{io}}\right)\eta_{po}\left(1 \pm \frac{\Delta \eta_p}{\eta_{po}}\right) + N_s + N_{po}\left(1 \pm \frac{\Delta N_p}{N_{po}}\right)\right) \times \eta_{mo}\left(1 \pm \frac{\Delta \eta_m}{\eta_{mo}}\right) \times \eta_{ro}\left(1 \pm \frac{\Delta \eta_r}{\eta_{ro}}\right) + N_{ro}\left(1 \pm \frac{\Delta N_r}{N_{ro}}\right)\right) \times \eta_c \times \eta_{do}\left(1 \pm \frac{\Delta \eta_d}{\eta_{do}}\right) \times \eta_D$$

- Indirect radiation-propagation chain

$$E'_{out} = \left(\left(N_{io}\left(1 \pm \frac{\Delta N_i}{N_{io}}\right)\eta_{po}\left(1 \pm \frac{\Delta \eta_p}{\eta_{po}}\right) + N_s + N_{po}\left(1 \pm \frac{\Delta N_p}{N_{po}}\right)\right)\eta_{mo}\left(1 \pm \frac{\Delta \eta_m}{\eta_{mo}}\right) \times \eta_{ro}\left(1 \pm \frac{\Delta \eta_r}{\eta_{ro}}\right) + N_{ro}\left(1 \pm \frac{\Delta N_r}{N_{ro}}\right)\right) \times \left(\left(\left(\left(\left(\left(\eta'_{do}\left(1 \pm \frac{\Delta \eta_{d'}}{\eta_{do'}}\right) + N_{do}\left(1 \pm \frac{\Delta N_d}{N_{do}}\right)\right)\eta_{ro}\left(1 \pm \frac{\Delta \eta_r}{\eta_{ro}}\right) + N'_{ro}\left(1 \pm \frac{\Delta N'_r}{N_{ro'}}\right)\right) \times \eta_{mo}\left(1 \pm \frac{\Delta \eta_m}{\eta_{mo}}\right) + N_{mo}\left(1 \pm \frac{\Delta N_m}{N_{mo}}\right)\right)\eta_{po}\left(1 \pm \frac{\Delta \eta_p}{\eta_{po}}\right) + N_{po}\left(1 \pm \frac{\Delta N_p}{N_{po}}\right)\right) \times \eta_{ao}\left(1 \pm \frac{\Delta \eta_a}{\eta_{ao}}\right) \times \eta_{po}\left(1 \pm \frac{\Delta \eta_p}{\eta_{po}}\right) \times \eta_{mo}\left(1 \pm \frac{\Delta \eta_m}{\eta_{mo}}\right) \times \eta_{ro}\left(1 \pm \frac{\Delta \eta_r}{\eta_{ro}}\right) \times \eta_c \times \eta_{do}\left(1 \pm \frac{\Delta \eta_d}{\eta_{do}}\right) \times \eta_D\right)$$

- Combined radiation propagation

$$E^*_{out} = E_{out} + E'_{out}$$

$$= \left(\left[N_{io} \left(1 \pm \frac{\Delta N_i}{N_{io}}\right) \eta_{po} \left(1 \pm \frac{\Delta \eta_p}{\eta_{po}}\right) + N_s + N_{po} \left(1 \pm \frac{\Delta N_p}{N_{po}}\right) \right] \eta_{mo} \left(1 \pm \frac{\Delta \eta_m}{\eta_{mo}}\right) \right.$$

$$\left. \times \eta_{ro} \left(1 \pm \frac{\Delta \eta_r}{\eta_{ro}}\right) + N_{ro} \left(1 \pm \frac{\Delta N_r}{N_{ro}}\right) \right)$$

$$\times \left\{ 1 + \left\{ \left[\left(\left[\left(\left[\left(\eta'_{do} \left(1 \pm \frac{\Delta \eta_{d'}}{\eta_{do'}}\right) + N_{do} \left(1 \pm \frac{\Delta N_d}{N_{do}}\right) \right) \eta_{ro} \left(1 \pm \frac{\Delta \eta_r}{\eta_{ro}}\right) + N'_{ro} \left(1 \pm \frac{\Delta N'_s}{N'_{ro}}\right) \right] \right. \right. \right. \right.$$

$$\left. \times \eta_{mo} \left(1 \pm \frac{\Delta \eta_m}{\eta_{mo}}\right) + N_{mo} \left(1 \pm \frac{\Delta N_m}{N_{mo}}\right) \right) \eta_{po} \left(1 \pm \frac{\Delta \eta_p}{\eta_{po}}\right) + N_{po} \left(1 \pm \frac{\Delta N_p}{N_{po}}\right) \Big]$$

$$\left. \left. \times \eta_{ao} \left(1 \pm \frac{\Delta \eta_a}{\eta_{ao}}\right) \times \eta_{po} \left(1 \pm \frac{\Delta \eta_p}{\eta_{po}}\right) \times \eta_{mo} \left(1 \pm \frac{\Delta \eta_m}{\eta_{mo}}\right) \times \eta_{ro} \left(1 \pm \frac{\Delta \eta_r}{\eta_{ro}}\right) \right\} \right\}$$

$$\times \eta_c \times \eta_{do} \left(1 \pm \frac{\Delta \eta_d}{\eta_{do}}\right) \times \eta_D$$

Chopper-closed operation mode:

- Direct radiation-propagation chain

$$\overline{E_{out}} = N_{ro} \left(1 \pm \frac{\Delta N_r}{N_{ro}}\right) \times \eta_c \times \eta_{do} \left(1 \pm \frac{\Delta \eta_d}{\eta_{do}}\right) \times \eta_D$$

- Indirect radiation-propagation chain

$$\overline{E'_{out}} = N_{ro} \left(1 \pm \frac{\Delta N_r}{N_{ro}}\right)$$

$$\times \left(\left(\left(\eta'_{do} \left(1 \pm \frac{\Delta \eta'_d}{\eta'_{do}}\right) + N_{do} \left(1 \pm \frac{\Delta N_d}{N_{do}}\right) \right) \eta_{ro} \left(1 \pm \frac{\Delta \eta_r}{\eta_{ro}}\right) + N'_{ro} \left(1 \pm \frac{\Delta N'_s}{N'_{ro}}\right) \right) \right.$$

$$\left. \times \eta'_{mo} \left(1 \pm \frac{\Delta \eta_{m'}}{\eta_{mo'}}\right) + N'_{mo} \left(1 \pm \frac{\Delta N_{m'}}{N_{mo}}\right) \right) \eta_{ro} \left(1 \pm \frac{\Delta \eta_r}{\eta_{ro}}\right) \times \eta_o \times \eta_{do} \left(1 \pm \frac{\Delta \eta_d}{\eta_{do}}\right) \times \eta_D$$

- Combined radiation propagation

$$\overline{E^*_{out}} = \overline{E_{out}} + \overline{E'_{out}} = N_{ro}\left(1 \pm \frac{\Delta N_r}{N_{ro}}\right)$$

$$x\left\{1 + \left\{\left[\left(\eta'_{do}\left(1 \pm \frac{\Delta \eta'_d}{\eta'_{do}}\right) + N_{do}\left(1 \pm \frac{\Delta N_d}{N_{do}}\right)\eta_{ro}\left(1 \pm \frac{\Delta \eta_r}{\eta_{ro}}\right) + N'_{ro}\left(1 \pm \frac{\Delta N'_r}{N'_{ro}}\right)\right.\right.\right.$$

$$\left.\left.\left. x\,\eta_{mo}\left(1 \pm \frac{\Delta \eta'_m}{\eta_{mo'}}\right) + N'_{mo}\left(1 \pm \frac{\Delta N'_m}{N_{mo'}}\right)\right\}\eta_{ro}\left(1 \pm \frac{\Delta \eta_r}{\eta_{ro}}\right)\right\} x\,\eta_c\, x\,\eta_{do}\left(1 \pm \frac{\Delta \eta_d}{\eta_{do}}\right) x\,\eta_D$$

Similar expressions can be obtained for the expanded signal and error flow model (Figure 10). Aside from being too lengthy, these expressions will not represent reality because, in specific applications, many of the transfer functions become unity and associated radiances vanish.

Noise propagation. -- To obtain an idea how photon noise, associated with each radiance term and denoted in the usual fashion by a variance σ^2, propagates through the radiometric system, one may refer preferably to the generalized compressed signal and error flow model of Figure 9. In this model, as well as in the expanded model of Figure 10, the noise propagation is indicated by dashed lines.

The particular photon noises are affected by transfer functions of the system. As long as one stays within the optical path, transfer functions for photon noises turn out to be identical to those of the radiances with which they are correlated.

To find the noise propagation, one must discriminate again the chopper-open from the chopper-closed operation mode. In each of these modes, one encounters the direct and the indirect propagation chains.

Following the dashed lines in the model of Figure 10, one obtains the following expressions for photon-noise input on the detector:

Chopper-on operation mode:

- Direct photon-noise propagation chain

$$\sigma_o^2 = \left(\left(\sigma_i^2 \eta_p + \sigma_p^2\right)\eta_m \eta_r + \sigma_r^2\right)$$

- Indirect photon-noise propagation chain

$$\sigma_o'^2 = \left(\left(\left(\left(\sigma_o^2 \eta_d + \sigma_d'^2\right)\eta_r + \sigma_r'^2\right)\eta_m + \sigma_m'^2\right)\eta_p + \sigma_p'^2\right)\eta_a \; x \; \eta_p \eta_m \eta_r$$

- Combined photon-noise propagation

$$\sigma_o^{*2} = \left(\left(\sigma_i^2 \eta_p + \sigma_p^2\right)\eta_m \eta_r + \sigma_r^2\right) \times \left(1 + \left(\left(\left(\left(\eta_d + \sigma_d'^2\right)\eta_r + \sigma_r'^2\right)\eta_m + \sigma_m'^2\right)\eta_p + \sigma_p'^2\right)\eta_a \eta_p \eta_m \eta_r\right)$$

Chopper-closed operation mode:

- Direct photon-noise propagation chain

$$\bar{\sigma}_o^2 = \sigma_r^2$$

- Indirect photon-noise propagation chain

$$\bar{\sigma}_o'^2 = \left(\left(\left(\bar{\sigma}_o^2 \eta_d + \sigma_d'^2\right)\eta_r + \sigma_r'^2\right)\eta_m + \sigma_m'^2\right)\eta_r$$

- Combined photon-noise propagation

$$\bar{\sigma}_o^{*2} = \left(\left(\left(\sigma_r^2 \eta_d + \sigma_d'^2\right)\eta_r + \sigma_r'^2\right)\eta_m + \sigma_m'^2\right)\eta_r$$

Now it is necessary to obtain an analytic expression for the photon noise and to find the relation that converts this noise into a noise voltage.

According to Planck's radiation law, radiance normal to the emitting surface is given by

$$N_\lambda = \frac{dN}{d\lambda} = 2c^2 h \lambda^{-5}\left[\exp\left(\frac{hc}{\lambda kT}\right) - 1\right]^{-1} \text{ measured in } W/m^3 - sr$$

or

$$Q_\lambda = \frac{\lambda}{hc} N_\lambda = 2c \lambda^{-4}\left[\exp\left(\frac{hc}{\lambda kT}\right) - 1\right]^{-1} \text{ photons } sec^{-1}\ m^{-3}\ sr^{-1}$$

Thus

$$N = \int_{\lambda_1}^{\lambda_2} N_\lambda\, d\lambda \quad W/m^2 - sr$$

$$Q = \int_{\lambda_1}^{\lambda_2} Q_\lambda\, d\lambda \quad \text{photons } sec^{-1}\ m^{-2}\ sr^{-1}$$

where

h = Planck's constant = 6.63×10^{-34} W sec^2

k = Boltzmann's constant = 1.38×10^{-23} W sec deg^{-1}

c = light velocity = 3×10^{8} msec^{-1}

λ = wavelength (m)

T = temperature (°K)

According to reference 5, the mean-square fluctuation in Q_λ (variance) is defined by the Bose-Einstein relation

$$\overline{(\Delta Q)_\lambda^2} = Q_\lambda \exp\left(\frac{hc}{\lambda kT}\right)\left[\exp\left(\frac{hc}{\lambda kT}\right) - 1\right]^{-1} = Q_\lambda \left[1 - \exp\left(-\frac{hc}{\lambda kT}\right)\right]^{-1}$$

$$= 2c\lambda^{-4} \exp\left(\frac{hc}{\lambda kT}\right)\left[\exp\left(\frac{hc}{\lambda kT}\right) - 1\right]^{-2} = 2c\lambda^{-4} \exp\left(-\frac{hc}{\lambda kT}\right)\left[1 - \exp\left(-\frac{hc}{\lambda kT}\right)\right]^{-2}$$

The classical result

$$\overline{(\Delta Q)_\lambda^2} \approx Q_\lambda$$

is obtained for $\exp\left(\frac{hc}{\lambda kT}\right)$ being large enough. Therefore, it is worthwhile to evaluate $\exp\left(\frac{hc}{\lambda kT}\right)$ for actually encountered conditions:

$$\lambda = 15\mu = 1.5 \times 10^{-5} \text{ m}, \quad T = 20, 75, 150, 300°K$$

$$\frac{hc}{\lambda} = 1.326 \times 10^{-20} \text{ W sec}$$

T	kT (W sec)	$\frac{hc}{\lambda kT}$	$\exp\left(\frac{hc}{\lambda kT}\right)$	$\exp\left(-\frac{hc}{\lambda kT}\right)$
20	2.76×10^{-22}	~48.04	$\sim 7 \times 10^{20}$	$\sim 1.4 \times 10^{-21}$
75	1.035×10^{-21}	~12.92	$\sim 4 \times 10^{5}$	$\sim 2.3 \times 10^{-6}$
150	2.07×10^{-21}	~6.46	$\sim 4 \times 10^{2}$	$\sim 2.5 \times 10^{-3}$
300	4.14×10^{-21}	~3.23	$\sim 2 \times 10^{1}$	$\sim 5 \times 10^{-2}$

Under the actual conditions, the classical result is always permissible. Hence, the rms value becomes

$$\sigma_\lambda \approx \sqrt{Q_\lambda}$$

Apparently, it is permissible also to express the variance by

$$\overline{(\Delta Q)^2} = \sigma_\lambda^2 \approx 2c\,\lambda^{-4} \exp\left(-\frac{hc}{\lambda kT}\right)$$

The error made is, even at T = 300°K, small (< 10%). This simplification facilitates the evaluation of the variance in finite wavelength intervals.

One obtains

$$\sigma^2_{\Delta\lambda'} = 2c \int_0^{\lambda_c} \lambda^{-4} \exp\left(-\frac{hc}{\lambda kT}\right) d\lambda$$

$$= 2c \left(\frac{kT}{hc}\right)^3 \exp\left(-\frac{hc}{\lambda_c kT}\right)\left[\left(\frac{hc}{\lambda_c kT}\right)^2 + 2\frac{hc}{\lambda_c kT} + 2\right]$$

by substituting

$$\lambda = \frac{hc}{kT} Z^{-1}\,;\; d\lambda = -\frac{hc}{kT} Z^{-2}\, dZ$$

$$\lambda = 0 \leftrightarrow Z \to \infty;\; \lambda = \lambda_c \leftrightarrow Z_c = -\frac{hc}{\lambda_c kT}$$

$$\lambda^{-4} = \left(\frac{kT}{hc}\right)^4 Z^4$$

$$\int_0^{\lambda_c} \lambda^{-4} \exp\left(-\frac{hc}{\lambda kT}\right) d\lambda = -\left(\frac{kT}{hc}\right)^3 \int_\infty^{Z_c} Z^2 \exp(-Z)\, dZ$$

$$= -\left(\frac{kT}{hc}\right)^3 \exp(-Z)\,(-Z^2 - 2Z - 2)\Big|_\infty^{Z_c} \quad \text{(ref. 3)}$$

Similarly

$$\sigma^2_{\Delta\lambda} = 2c \int_{\lambda_1}^{\lambda_2} \lambda^{-4} \exp\left(-\frac{hc}{\lambda kT}\right) d\lambda$$

$$= 2c \left(\frac{kT}{hc}\right)^3 \left\{\exp\left(-\frac{hc}{\lambda_2 kT}\right)\left[\left(\frac{hc}{\lambda_2 kT}\right)^2 + 2\frac{hc}{\lambda_2 kT} + 2\right]\right.$$

$$\left. - \exp\left(-\frac{hc}{\lambda_1 kT}\right)\left[\left(\frac{hc}{\lambda_1 kT}\right)^2 + 2\frac{hc}{\lambda_1 kT} + 2\right]\right\}$$

$$= 2\frac{kT}{h}\left\{\exp\left(-\frac{hc}{\lambda_2 kT}\right)\left[2\left(\frac{kT}{hc}\right)^2 + 2\frac{kT}{hc}\lambda_2^{-1} + \lambda_2^{-2}\right]\right.$$

$$\left. - \exp\left(-\frac{hc}{\lambda_1 kT}\right)\left[2\left(\frac{kT}{hc}\right)^2 + 2\frac{kT}{hc}\lambda_1^{-1} + \lambda_1^{-2}\right]\right\}$$

From the mean-square fluctuation in the photon-flux density per steradian, one obtains the mean-square fluctuation at the detector area A_d, in the solid angle $\Delta\Omega$, and in the electrical bandwidth $\Delta\nu$

$$\sigma^2_{\Delta\lambda} = 2\,\Delta\nu\,\Delta\Omega\,A_d\left(\eta_{q,\Delta\lambda}\,\sigma^2_{\Delta\lambda} + \eta_{q,\Delta\lambda'}\,\sigma^2_{\Delta\lambda'}\right)$$

where $\eta_{q,\Delta\lambda}$ and $\eta_{q,\Delta\lambda'}$ are the mean quantum efficiencies of the responsive element in the intervals $\Delta\lambda$ and $\Delta\lambda'$, respectively. These quantum efficiencies are assumed to be unity in the models.

To convert the photon noise which initially is given in terms of photons per sec into a voltage, one may argue that the average number of carriers defined by

$$\bar{n} = \tau_p F_{eff}$$

where

τ_p = lifetime

F_{eff} = effective photon flux (photons sec^{-1})

The mean square number of carries is, on the other hand,

$$\overline{\Delta n^2} = \tau_p^2 F_{eff}$$

The current generated by the photons is

$$i = \bar{n} q\,\mu\frac{A}{\ell}V = q\,\mu\frac{A}{\ell}V\tau_p F_{eff}$$

where

q = elementary charge

μ = mobility

A = cross-sectional area

ℓ = length

V = voltage applied

It follows that the resistance is

$$R_d = \frac{\ell}{\mu q A} \frac{1}{\bar{n}} = \frac{\ell}{\mu q A} \frac{1}{\tau_p F_{eff}}$$

The noise current becomes

$$\overline{\Delta i_n^2} = \overline{\Delta n^2}\, q^2 \mu^2 \frac{A^2}{\ell^2} V^2 = \tau_p^2 F_{eff}\, q^2 \mu^2 \frac{A^2}{\ell^2} V^2$$

and the noise voltage

$$\overline{\Delta V_n^2} = R_d^2 \overline{\Delta i_n^2} = \frac{\ell^2}{\mu^2 q^2 A^2} \frac{}{\tau^2 F_{eff}^2} \tau_p^2 F_{eff}\, q^2 \mu^2 \frac{A^2}{\ell^2} V^2$$

$$= \frac{1}{F} V^2 = \frac{i_b R_d^2}{F_{eff}}$$

$$= i_p^2 q^2 \mu^2 \frac{A^2}{\ell^2} \tau_p^2 F_{eff}\text{, if a constant-bias current is applied}$$

Now

$$R_d = R_m \frac{F_{cal}}{F_{eff}}$$

Hence,

$$\overline{\Delta V_n^2} = i_p^2 R_m^2 \frac{F_{cal}^2}{F_{eff}^3}$$

This expression is to be related to the unit bandwidth; that is, one obtains finally

$$\sigma_p^2 = 2 \Delta\nu\, i_b^2 R_m^2 \frac{F_{cal}^2}{F_{eff}^3} \left(1 + \omega^2 \tau_c^2\right)^{-1}$$

where

$\omega = 2\pi\nu$ = circular electrical frequency

$\tau_c = \frac{1}{\omega_c}$ = time constant

In addition to this squared photon-noise voltage, one has to consider the detector and amplifier-noise voltages.

The current noise, also sometimes called modulation noise (ref. 1), is not well understood. According to reference 5, this current noise can be expressed by the mean-square voltage

$$\overline{E_N^2} = K\, i_b^{\alpha}\, R_d^2\, \nu^{-\beta}\, \Delta\nu$$

where

K = constant that is dependent on the detector material and its size

i_b = bias current

$R_d = R_m \frac{F_{cal}}{F_{eff}}$ = actual detector resistance

R_m = measured resistance under experimental conditions defined by the calculated flux F_{cal}

$\alpha \approx 2$

β = constant varying between 0.8 and 2 (ref.

ν = frequency

$\Delta\nu$ = noise-equivalent bandwidth

For simplification, α and β are taken to be 2 and 1, respectively, in the generalized expanded signal and error flow model. Of course, K cannot be specified generally, Thus,

$$\sigma_c^2 = K R_m^2 \frac{F_{cal}^2}{F_{eff}^2} i_b^2\, \nu^{-1}\, \Delta\nu$$

Defining the detector resistance by

$$R_d = R_m \frac{F_{cal}}{F}$$

where R_m = measured resistance under the experimental conditions that are determined by a calculatef flux F_{cal}, one obtains according to reference 1,

- **Shot noise**

$$\sigma_s^2 = 2\Delta\nu\, q\, R_d^2\, i_b = R_m^2 \frac{F_{cal}^2}{F^2}\, i_b\, 2\, q\, \Delta\nu$$

- **Photon noise**

$$\sigma_b^2 = 2\Delta\nu R_d^2\, i_b^2\, (1 + \omega^2\, \tau^2)^{-1} = R_m \frac{F_{cal}^2}{F^2}\, i_b^2\, 2\, \Delta^{\nu} (1 + \omega^2\, \tau^2)^{-1}$$

- **Generation/recombination noise**

$$\sigma_g^2 = 2\Delta\nu\; R_d^2\, i_b^2\, \frac{\tau_2}{n}\, (1 + \omega^2\, \tau_c^2)^{-1}$$

where

$\tau_c = \frac{1}{\omega_c}$ = time constant

ω_c = chopping frequency

$n = \tau_p F$ = charge-carrier density

τ_p = lifetime

$$\sigma_g^2 = \frac{1}{F} R_m^2 \frac{F_{cal}^2}{F^2}\, i_b^2\, \frac{2\tau_c\, \Delta\nu}{\tau_b\, (1 + \omega^2\, \tau_c^2}$$

- **Thermal noise**

$$\sigma_t^2 = 4\Delta\nu\; k\; T_d\, R_d = R_m \frac{F_{cal}}{F}\, 4\, k\; T_\alpha\, \Delta\nu$$

where

k = Boltzmann constant

T_d = detector temperature

$\Delta\nu$ = noise-equivalent bandwidth

The total detector-noise output is given then by

$$E_{oN}^2 = \sigma_p^2 + \sigma_s^2 + \sigma_g^2 + \sigma_t^2 + \sigma_o^2$$

If the signal is generally defined by

$$E_o = C_a G_o(\omega)$$

where C_a = amplifier gain, the total noise voltage can be described by

$$E_N = C_a^2 \left[\left| G_o(\omega) \right|^2 E_{oN}^2 + \left| G_a(\omega) \right|^2 E_{AN}^2 \right]$$

where E_{AN} characterizes the amplifier noise, and

$$\left| G_a(\omega) \right| = \frac{R_d}{R_i} \left| G_o(\omega) \right|$$

R_d/R_i = matching function

R_i = amplifier input resistance

Recommendations. -- The expanded signal and error model (Figure 10)

- Relates the radiance terms in the direct radiation-propagation chain behind the relay optics collimator to the sensitivity interval $\Delta\lambda'$ of the detector
- Relates radiances in the indirect radiation propagation chain after reflection at the detector to the bandpass-filter transmission range $\Delta\lambda$ only

Careful inspection, however, indicates that the direct radiation passing through the bandpass filter after reflection at the detector must be related to $\Delta\lambda$. On the other hand, the portion of the indirect radiation that is reflected toward the detector at the bandpass filter must be related to $\Delta\lambda'$.

It appears that there are two ways to overcome this minor deficiency:

- Steps taken to split up the partial direct and indirect propagation chains mentioned above have not been completely successful since the radiance terms involved must not appear more than once in the final signal. Therefore, it is recommended that efforts made up to date for improving the model be continued.
- The expanded model is completely correct if it uses spectral radiances $N\lambda$, emissivities, reflectivities, and transmissivities instead of wavelength-interval integrated radiances, $N_{\Delta\lambda}$ and $N_{\Delta\lambda'}$, and averaged emissivities, reflectivities, and transmissivities. In this case, the final state of the model must be modified as shown in Figure 19; that is one would have to apply an integration operator, $F_{eff} = \int_0^{\lambda c} F_\lambda \eta_c \eta_q \, d\lambda$, at the end of the chain. This means, however, that the computation program would become very much more

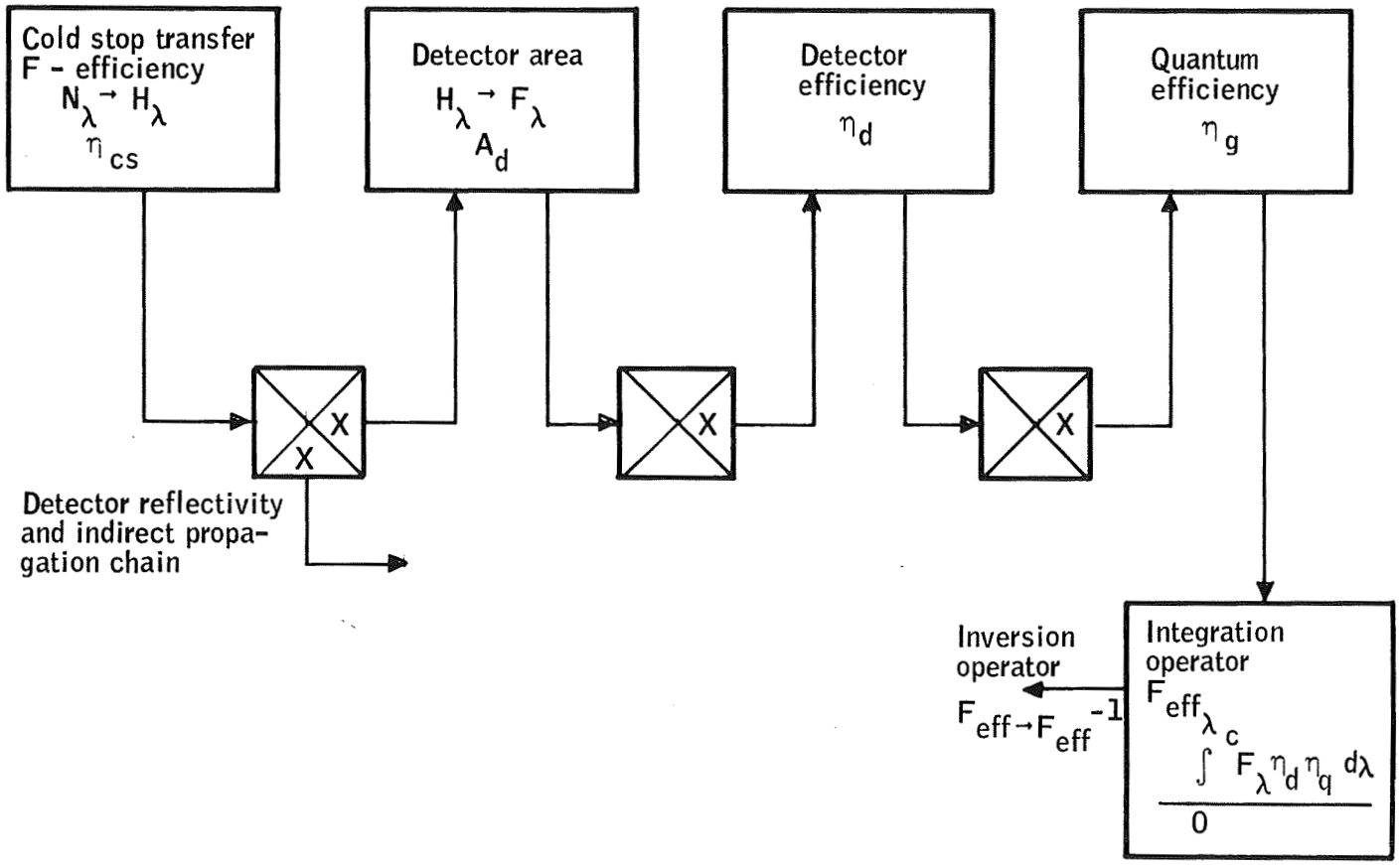

Figure 19. Modification of Final Model Stage Needed to Consider Propagation of Spectral Radiances

tedious. Nevertheless, investigation of this possibility of circumventing the deficiency of the present model is recommended.

The expanded model shown in Figure 10 is restricted to use of a specific inflight calibrator in front of the collector optics, and especially to a specific detector. For this reason, it is highly recommended to indicate, for example, by appropriate overlays the modifications needed for

- Changing the inflight-calibrator configuration or its location
- Applying other types of detectors
  - Constant-bias voltage photoconductors
  - Photovoltaic cells
  - Photoemissive devices if other than infrared wavelength intervals are to be taken into consideration
  - Bolometers
  - Thermopiles
- The expanded model indicates that the radiance terms may be affected by temperature gradients. An attempt already has been made to obtain an analytic expression for the temperature gradient.

  If an element x in the radiation-propagation chain is affected by a temperature gradient, one may determine the effect on the radiance $N(T_x)$ by differentiation of Planck's law of monochromatic radiation; that is, by

$$\frac{d}{dT_x}\frac{dN(T_x)}{d\lambda} = 2c^2h\,\lambda^{-5}\frac{d}{dT_x}\left[\exp\left(\frac{hc}{\lambda kT_x}\right)-1\right]^{-1}$$

$$= 2c^2h\,\lambda^{-5}\left(\frac{hc}{\lambda k}\right)\exp\left(\frac{hc}{\lambda kT_x}\right)\left\{T_x\left[\exp\left(\frac{hc}{\lambda kT_x}\right)-1\right]\right\}^{-2}$$

$$= 2\frac{c^3h^2}{kT_x^2}\lambda^{-6}\exp\left(-\frac{hc}{\lambda kT_x}\right)\left[1-\exp\left(-\frac{hc}{\lambda kT_x}\right)\right]^{-2}$$

  Integration over λ in the wavelength interval $\Delta\lambda = \lambda_2 - \lambda_1$ yields

$$\Delta N_{\Delta\lambda}(T_x) = 2\frac{c^3h^2}{kT_x^2}\int_1^2 \lambda^{-6}\exp\left(-\frac{hc}{\lambda kT_x}\right)\left[1-\exp\left(\frac{hc}{\lambda kT_x}\right)\right]^{-2} d\lambda$$

Since in the wavelength intervals of interest and for the temperature range to be considered $\exp\left(-\frac{hc}{\lambda kT_x}\right)$ is a small quantity compared to unity, it is believed permissible to evaluate only the approximate integral

$$\int_{\lambda_1}^{\lambda_2} \lambda^{-6} \exp\left(-\frac{hc}{\lambda kT_x}\right) d\lambda = -\left(\frac{kT_x}{hc}\right)^5 \int_{Z_1}^{Z_2} Z^4 \exp(-Z)\, dZ$$

$$= -\left(\frac{kT_x}{hc}\right)^5 \exp(-Z)\left(-Z^4 - 4Z^3 - 12Z^2 - 24Z - 24\right)\Big|_{Z_1}^{Z_2}$$

Hence,

$$\Delta N_{\Delta\lambda}(T_x) = 2\frac{c^2h}{T_x}\left\{\exp\left(-\frac{hc}{\lambda_2 kT_x}\right)\left[24\left(\frac{kT_x}{hc}\right)^4 + 24\left(\frac{kT_x}{hc}\right)^3\lambda_2^{-1} + 12\left(\frac{kT_x}{hc}\right)^2\lambda_2^{-2} + 4\left(\frac{kT_x}{hc}\right)\lambda_2^{-3} + \lambda_2^{-4}\right]\right.$$

$$\left. - \exp\left(-\frac{hc}{\lambda_1 kT_x}\right)\left[24\left(\frac{kT_x}{hc}\right)^4 + 24\left(\frac{kT_x}{hc}\right)^3\lambda_1^{-1} + 12\left(\frac{kT_x}{hc}\right)^2\lambda_1^{-2} + 4\left(\frac{kT_x}{hc}\right)\lambda_1^{-3} + \lambda_1^{-4}\right]\right\}$$

$$= 2\,kc\left(\frac{kT_x}{hc}\right)^3\left\{\exp -\left(\frac{hc}{\lambda_2 kT_x}\right)\left[\left(\frac{hc}{\lambda_2 kT_x}\right)^4 + 4\left(\frac{hc}{\lambda_2 kT_x}\right)^3 + 12\left(\frac{hc}{\lambda_2 kT_x}\right)^2 + 24\left(\frac{hc}{\lambda_2 kT_x}\right) + 24\right]\right.$$

$$\left. - \exp\left(-\frac{hc}{\lambda_1 kT_x}\right)\left[\left(\frac{hc}{\lambda_1 kT_x}\right)^4 + 4\left(\frac{hc}{\lambda_1 kT_x}\right)^3 + 12\left(\frac{hc}{\lambda_1 kT_x}\right)^2 + 24\left(\frac{hc}{\lambda_1 kT_x}\right) + 24\right]\right\}$$

The expression $2\,kc\left(\frac{kT_x}{hc}\right)^3$ becomes a small quantity for $T_x = 300°K$ ($\approx 7.5 \times 10^{-2}$). Thus, the effect of the temperature gradient ($\approx 1.52 \times 10^{-5}$) in the wavelength interval $\Delta\lambda = (1.628 - 1.4) \times 10^{-5}$ m on the radiance ($\approx 1.51 \times 10^{-3}$) can be considered small for this high temperature. However, this effect needs to be evaluated for lower temperatures.

Other methods of describing temperature gradients should be considered, and it is recommended that attention be devoted to this important effect in the future.

- The present model may be called dc in the sense that it computes power incident on the detector and amplifier-output voltage independent of optical resolutions and actual detector configuration.

This is equivalent to assuming a uniform extended source at the input. In radiometers requiring high spatial resolution, it is essential to consider the optics transfer function, the actual detector size; that is, not only its area and position, the filter and amplifier transfer functions, and the spatial description of the target scene and the noise. These items are further discussed in a subsequent section entitled Transfer Function Model.

Rules for Application

General rules. -- It has been mentioned already that the expanded signal and error flow model comprises two radiation propagation chains:

- The direct propagation chain represented by the top line of Figure 10 starts with the input radiance box at the upper left of the illustration. The input radiance propagates through various elements of the model to the detector at the upper right of the figure. As the radiation passes through, energy from the optical elements in the direct chain is assed successively, thus contributing to the total irradiance incident on the detector.

- A portion of the total direct radiance is reflected by the detector backwards, as indicated in the bottom line of Figure 10 by arrows pointing from the right to the left. The second-from-the-top line, with arrows pointing to the left, contains only multiplicative transfer functions necessary to take into account the propagation of radiation reflected backwards from specific elements in the direct chain; that is, spoke, spike, window, modulator, and bandpass filter. Similar primary reflections from the same elements occur in the bottom line. The second-from-the-bottom line contains the collected radiance terms as they loop back to the detector. As the reflected portion of the total direct radiation propagates through the elements of the model's bottom line, it picks up additional radiance terms. The total radiance receivable at the detector that is caused by the primary reflections described is called indirect radiation.

As an example of how the model must be read, consider that portion of the direct chain which begins at "Input Radiance" and ends with the "Spoke Blockage"; that is, the "Collector Prim" input.

One obtains:

$$\text{Spoke Output} = N_{so,\Delta\lambda} = \left\{\left[N_{io,\Delta\lambda}\left(1 \pm \frac{N_{i,\Delta\lambda}}{N_{io,\Delta\lambda}}\right) + N_{SL,\Delta\lambda}\right] \times \tau_a \times \tau_{s1} + N_{s10,\Delta\lambda}\left(1 \pm \frac{\Delta N_{s1,\Delta\lambda}}{N_{s10,\Delta\lambda}}\right) \times \epsilon_{s10}\left(1 \pm \frac{\Delta\epsilon_{s1}}{\epsilon_{s10}}\right) \times \zeta_{s1}\right\} \times \ldots$$

As an example of the indirect-radiation contributions, that portion of the chain may be considered which also is affected by the spoke. The collector output in the model bottom line is denoted by $N_{co,\Delta\lambda}$. Then neglecting the systematic errors, one obtains for the inflight calibration in action

- **Term from direct radiation**

$$(N_{i,\Delta\lambda} + N_{SL,\Delta\lambda}) \times \rho_{s1} \times \zeta_{s1} \times \rho_{cc}$$

- Term from bottom line

$$\left(N'_{co,\Delta\lambda} \times \tau_{s1} + N_{s1} \times \epsilon_{s1} \times \zeta_{s1}\right) \times \rho_{cc} + N_{cc,\Delta\lambda} \times \epsilon_{cc} \times \zeta_{cc}$$

- Term from spoke reflection in bottom line

$$N'_{co,\Delta\lambda} \times \rho'_{s1} \times \zeta_{s1}$$

- Combined signal

$$\Big(\Big(\Big(\Big(\Big(N_{i,\Delta\lambda} + N_{SL,\Delta\lambda}\Big) \times \rho_{s1} \times \zeta_{s1} \times \rho_{cc}$$
$$+ \left(N'_{co,\Delta\lambda} \times \tau_{s1} + N_{s1} \times \epsilon_{s1} \times \zeta_{s1}\right) \times \rho_{cc} + N_{cc,\Delta\lambda} \times \epsilon_{cc} \times \zeta_{cc}\Big)$$
$$\times \rho_{ca} \times \zeta_{ca} \times \rho_{cc} \times \tau_a \times \tau_{s1}\Big)$$
$$+ N'_{co,\Delta\lambda} \times \rho'_{s1} \times \zeta_{s1}\Big) \times \eta_{p1} \times \ldots$$

For the inactive inflight calibrator, one has to use $\zeta_{ca} = 0$ such that only the third term from the spoke reflection in the bottom line propagates through the system.

A crucial element in the model is the modulator which, most generally, is described by a time-dependent transfer function. Considering only the completely closed and completely open operation modes, one has to define

$$\zeta_m = 1, \quad \tau_m = 0 \quad \text{for the chopper-closed mode, and vice versa}$$

$$\zeta_m = 0, \quad \tau_m = 1 \quad \text{for the chopper-open mode}$$

If specific radiometer configurations are to be considered, some of the parameters used in the expanded model appropriately must be defined as shown in the next subsection.

Special considerations. -- The generalized expanded signal and error flow model is applied to the radiometer configurations specified in Table 13.

TABLE 13.- SPECIFIC RADIOMETER CONFIGURATIONS[a] CONSIDERED

Configuration number	Collector optics	Relay optics
1	Lowpass filter supported Cassegrainian	Cassegrainian pair
2	Lowpass filter supported Newtonian	Cassegrainian pair
3	Off-axis paraboloid	Off-axis paraboloidal pair
4	Single lens	Single-lens pair
5	Spike-window supported Cassegrainian	Single-lens pair
6	Spike-supported Newtonian	Single-lens pair
7	Off-axis paraboloid	Single-lens pair
8	Spoke supported Cassegrainian	Cassegrainian pair
9	Spoke supported Newtonian	Cassegrainian pair

[a]In all conceptual configurations the bandpass filter is located in the collimated beam of the relay optics.

To facilitate the computerization, the flow chart was modified slightly as shown in Figure 20, although this modification does not reflect the physical reality. The computer program is further simplified as follows:

- The radiation term splitup at the bandpass-filter locations in the direct and indirect propagation chains is omitted. This means that, in the direct propagation chain, the detector sensitivity range is used instead of the bandpass-filter transmission range for the radiation impinging on and reflected from the detector. It is assumed that passing the radiation later through the bandpass filter will cancel the effect of this modification.
  In the indirect propagation chain, on the other hand, the detector sensitivity range is replaced by the bandpass-filter transmission range for the radiation reflected backwards to the detector from the filter; it is anticipated that the effect of this modification will be small because of the low temperatures of the detector and the cavity, and especially because of the very small detector reflectivity.

- Second and higher-order reflection terms at the detector and at other stations in the chains are not taken into account at this moment.

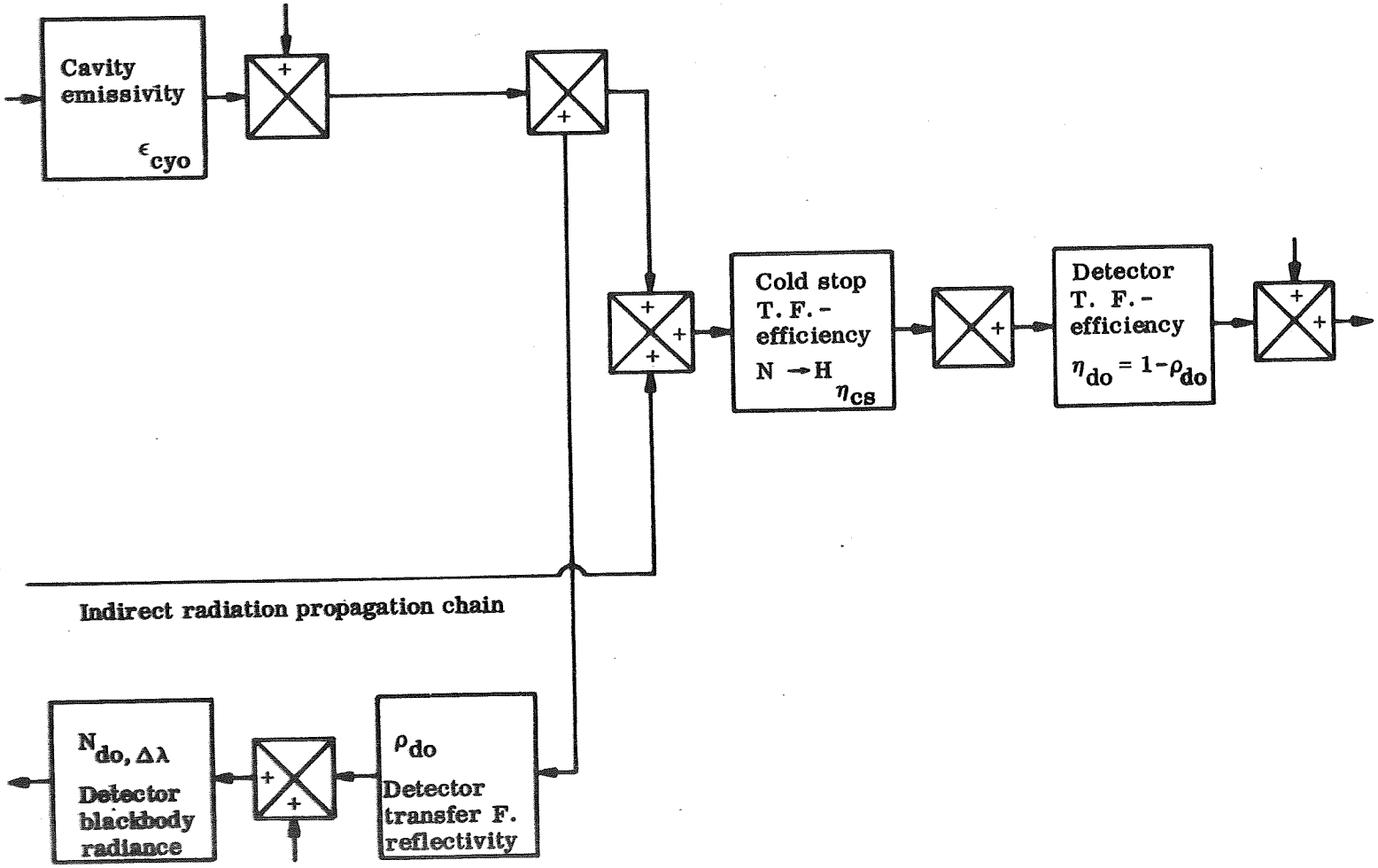

Figure 20. Flow Modification to Facilitate Computation

- Quantum efficiency is assumed to be equal for both wavelength intervals to be considered, and is specifically supposed to be unity.

Model parameters belonging to the nine configurations are presented in Table 14, which describes them not only by their model denotations, but also by the corresponding computer variables. In this table a check mark replaces the model denotation; efficiency factors are either transmissivities or reflectivities, both being related in many cases to blockages or emissivities, respectively.

The model itself assumes the use of a photoconductive detector with constant-bias current. However, other sensor types, like constant-voltage photoconductive detectors, photovoltaic detectors, and bolometers, can be handled easily by corresponding overlays since the optical train does not change at all. To find the output voltage of the photoconductive detector applied, the actual detector voltage is expressed by

$$R_d = R_m F_{cal} F^{-1} \tag{1}$$

where R_m = measured detector resistance under the experimental conditions of the calculated photon flux F_{cal},

F = actually incident flux (photons sec^{-1})

Denoting the bias current by i_b, one obtains the detector output voltage

$$E_D = R_d i_b \tag{2}$$

To obtain the noise voltage at the detector output, one has generally to consider

- Photon noise

$$\sigma_\rho^2 = 2\Delta\nu E_d^2 F^{-1} (1 + \omega^2 \tau_c^2)^{-1} \tag{3}$$

where $\Delta\nu$ = noise-equivalent bandwidth

- Shot noise

$$\sigma_s^2 = 2\Delta\nu q R_d E_d \tag{4}$$

where $q = 1.6 \times 10^{-19}$ amp sec = electron charge

- Current noise

$$\sigma_c^2 = K \Delta\nu E_d^2 \nu^{-1} \tag{5}$$

where K = constant depending on detector size and material

ν = electrical frequency

TABLE 14.- MODEL PARAMETERS FOR NINE CONFIGURATIONS

Model denotation	Computer Variable	Configuration number									Element and radiance sum
		1	2	3	4	5	6	7	8	9	
Direct-radiation terms											
$N_{i,\Delta\lambda}$	B0	$\surd$	$\surd$	$\surd$	$\surd$	$\surd$	$\surd$	$\surd$	$\surd$	$\surd$	Input radiance
$N_{SL,\Delta\lambda}$	BS0	$\surd$	$\surd$	$\surd$	$\surd$	$\surd$	$\surd$	$\surd$	$\surd$	$\surd$	
τ_a	CT0	$\surd$	$\surd$	1	1	$\surd$	$\surd$	1	$\surd$	$\surd$	X0
τ_{s1}	CT1	τ_ℓ	τ_ℓ	1	1	1	1	1	$1-\zeta_{s1}$	$1-\zeta_{s1}$	Spoke or low-pass filter support
$N_{s1,\Delta\lambda}$	B1	$N_{\ell,\Delta\lambda}$	$N_{\ell,\Delta\lambda}$	0	0	0	0	0	$\surd$	$\surd$	
ϵ_{s1}	E1	ϵ_ℓ	ϵ_ℓ	0	0	0	0	0	$1-\rho_{s1}$	$1-\rho_{s1}$	
ζ_{s1}	Z1	1	1	0	0	0	0	0	$\surd$	$\surd$	X1
η_{p1}	CE2	ρ_{p1}	ρ_{p1}	ρ_{p1}	τ_{p1}	ρ_{p1}	ρ_{p1}	ρ_{p1}	ρ_{p1}	ρ_{p1}	Collector primary
$N_{p1,\Delta\lambda}$	B2	$\surd$	$\surd$	$\surd$	$\surd$	$\surd$	$\surd$	$\surd$	$\surd$	$\surd$	
ϵ_{p1}	E2	$1-\rho_{p1}$	$1-\rho_{p1}$	$1-\rho_{p1}$	$\surd$	$1-\rho_{p1}$	$1-\rho_{p1}$	$1-\rho_{p1}$	$1-\rho_{p1}$	$1-\rho_{p1}$	
ζ_{p1}	Z2	$\surd$	$\surd$	$\surd$	$\surd$	$\surd$	$\surd$	$\surd$	$\surd$	$\surd$	X2
η_{p2}	CE3	ρ_{pa}	ρ_{p2}	1	1	ρ_{p2}	ρ_{p2}	1	ρ_{p2}	ρ_{p2}	Collector secondary
$N_{p2,\Delta\lambda}$	B3	$\surd$	$\surd$	0	0	$\surd$	$\surd$	0	$\surd$	$\surd$	
ϵ_{p2}	E3	$1-\rho_{p2}$	$1-\rho_{p2}$	0	0	$1-\rho_{p2}$	$1-\rho_{p2}$	0	$1-\rho_{p2}$	$1-\rho_{p2}$	
ζ_{p2}	Z3	$\surd$	$\sec\phi$	0	0	$\surd$	$\sec\phi$	0	$\surd$	$\sec\phi$	X3
τ_{s2}	CT4	1	1	1	1	1	$1-\zeta_{s2}$	1	1	1	Spike support
$N_{s2,\Delta\lambda}$	B4	0	0	0	0	0	$\surd$	0	0	0	
ϵ_{s2}	E4	0	0	0	0	0	$1-\rho_{s2}$	0	0	0	
ζ_{s2}	Z4	0	0	0	0	0	$\surd$	0	0	0	X4

TABLE 14.- MODEL PARAMETERS FOR NINE CONFIGURATIONS (CONTINUED)

Model denotation	Computer Variable	Configuration number									Element and radiance sum
		1	2	3	4	5	6	7	8	9	
Direct-radiation terms											
τ_w	CT5	1	1	1	1	√	1	1	1	1	Window support
$N_{w,\Delta\lambda}$	B5	0	0	0	0	√	0	0	0	0	
ϵ_w	E5	0	0	0	0	√	0	0	0	0	X5
τ_m	CT6	$1-\zeta_m$	$1-\zeta_m$	$1-\zeta_m$	$1-\zeta_m$	$1-\zeta_m$	$1-\zeta_m$	$1-\zeta_m$	$1-\zeta_m$	$1-\zeta_m$	Modulator
$N_{m,\Delta\lambda}$	B6	√	√	√	√	√	√	√	√	√	
ϵ_m	E6	$1-\rho_m$	$1-\rho_m$	$1-\rho_m$	$1-\rho_m$	$1-\rho_m$	$1-\rho_m$	$1-\rho_m$	$1-\rho_m$	$1-\rho_m$	
ζ_m	Z6	√	√	√	√	√	√	√	√	√	X6
ζ_f	CT7	√	√	√	√	√	√	√	√	√	Field stop X7
η_{r1}	CE8	ρ_{r1}	ρ_{r1}	ρ_{r1}	τ_{r1}	τ_{r1}	τ_{r1}	τ_{r1}	ρ_{r1}	ρ_{r1}	Collimator secondary
$N_{r1,\Delta\lambda}$	B8	√	√	√	√	√	√	√	√	√	
ϵ_{r1}	E8	$1-\rho_{r1}$	$1-\rho_{r1}$	$1-\rho_{r1}$	√	√	√	√	$1-\rho_{r1}$	$1-\rho_{r1}$	
ζ_{r1}	Z8	√	√	√	√	√	√	√	√	√	X8
τ_{r2}	CT9	√	√	1	1	1	1	1	√	√	Collimator primary
η_{r2}	CE9	ρ_{r2}	ρ_{r2}	1	1	1	1	1	ρ_{r2}	ρ_{r2}	
$N_{ra,\Delta\lambda}$	B9	√	√	0	0	0	0	0	√	√	
ϵ_{r2}	E9	$1-\rho_{r2}$	$1-\rho_{r2}$	0	0	0	0	0	$1-\rho_{r2}$	$1-\rho_{r2}$	
ζ_{r2}	Z9	√	√	0	0	0	0	0	√	√	X9
τ_b	CT10	√	√	√	√	√	√	√	√	√	Bandpass filter
$N_{b,\Delta\lambda}$	B10	√	√	√	√	√	√	√	√	√	
ϵ_b	E10	√	√	√	√	√	√	√	√	√	X10

TABLE 14.- MODEL PARAMETERS FOR NINE CONFIGURATIONS (CONTINUED)

Model denotation	Computer Variable	Configuration number									Element and radiance sum
		1	2	3	4	5	6	7	8	9	
Direct-radiation terms											
τ_{r3}	CT11	√	√	1	1	1	1	1	√	√	Concentrator primary
η_{r3}	CE11	ρ_{r3}	ρ_{r3}	1	1	1	1	1	ρ_{r3}	ρ_{r3}	
$N_{r3,\Delta\lambda'}$	B11	√	√	0	0	0	0	0	√	√	
ϵ_{r3}	E11	$1-\rho_{r3}$	$1-\rho_{r3}$	0	0	0	0	0	$1-\rho_{r3}$	$1-\rho_{r3}$	
ζ_{r3}	Z11	√	√	0	0	0	0	0	√	√	X11
η_{r4}	CE12	ρ_{r4}	ρ_{r4}	ρ_{r4}	τ_{r4}	τ_{r4}	τ_{r4}	τ_{r4}	ρ_{r4}	ρ_{r4}	Concentrator secondary
$N_{r4,\Delta\lambda'}$	B12	√	√	√	√	√	√	√	√	√	
ϵ_{r4}	E12	$1-\rho_{r4}$	$1-\rho_{r4}$	$1-\rho_{r4}$	√	√	√	√	$1-\rho_{r4}$	$1-\rho_{r4}$	
ζ_{r4}	Z12	√	√	√	√	√	√	√	√	√	X12
τ_{cy}	CT13	1	1	1	1	1	1	1	1	1	Cavity
$N_{cy,\Delta\lambda'}$	B13	√	√	√	√	√	√	√	√	√	
ϵ_{cy}	E13	√	√	√	√	√	√	√	√	√	X13 = Y1
Indirect-radiation terms											
ρ_d	C14	√	√	√	√	√	√	√	√	√	Detector
$N_{d,\Delta\lambda}$	B14	√	√	√	√	√	√	√	√	√	
ϵ_d	E14	√	√	√	√	√	√	√	√	√	X20
τ_{cy}	CT13	1	1	1	1	1	1	1	1	1	Cavity
$N'_{cy,\Delta\lambda}$	B15	√	√	√	√	√	√	√	√	√	
ϵ'_{cy}	E15	√	√	√	√	√	√	√	√	√	X21

TABLE 14.- MODEL PARAMETERS FOR NINE CONFIGURATIONS (CONTINUED)

Model denotation	Computer Variable	Configuration number									Element and radiance sum
		1	2	3	4	5	6	7	8	9	
Indirect-radiation terms											
η_{r4}	CE12	ρ_{r4}	ρ_{r4}	ρ_{r4}	τ_{r4}	τ_{r4}	τ_{r4}	τ_{r4}	ρ_{r4}	ρ_{r4}	Concentrator secondary
$N'_{r4,\Delta\lambda}$	B16	√	√	√	√	√	√	√	√	√	
ϵ'_{r4}	E16	$1-\rho_{r4}$	$1-\rho_{r4}$	$1-\rho_{r4}$	√	√	√	√	$1-\rho_{r4}$	$1-\rho_{r4}$	
ζ'_{r4}	Z16	ζ_{r4}	ζ_{r4}	ζ_{r4}	√	√	√	√	ζ_{r4}	ζ_{r4}	X22
τ_{r3}	CT11	√	√	1	1	1	1	1	√	√	Concentrator primary
η_{r3}	CE11	ρ_{r3}	ρ_{r3}	1	1	1	1	1	ρ_{r3}	ρ_{r3}	
$N'_{r3,\Delta\lambda}$	B17	√	√	0	0	0	0	0	√	√	
ϵ'_{r3}	E17	$1-\rho_{r3}$	$1-\rho_{r3}$	0	0	0	0	0	$1-\rho_{r3}$	$1-\rho_{r3}$	
ζ'_{r3}	Z17	ζ_{r3}	ζ_{r3}	0	0	0	0	0	ζ_{r3}	ζ_{r3}	X24
τ_b	CT10	√	√	√	√	√	√	√	√	√	Bandpass filter
$N'_{b,\Delta\lambda}$	B18	√	√	√	√	√	√	√	√	√	
ϵ'_b	E18	√	√	√	√	√	√	√	√	√	X25
τ_{r2}	CT9	√	√	1	1	1	1	1	√	√	Collimator primary
η_{r2}	CE9	ρ_{r2}	ρ_{r2}	1	1	1	1	1	ρ_{r2}	ρ_{r2}	
$N_{r2,\Delta\lambda}$	B9	√	√	0	0	0	0	0	√	√	
ϵ'_{r2}	E19	$1-\rho_{r2}$	$1-\rho_{r2}$	0	0	0	0	0	$1-\rho_{r2}$	$1-\rho_{r2}$	
ζ'_{r2}	Z19	ζ_{r2}	ζ_{r2}	0	0	0	0	0	ζ_{r2}	ζ_{r2}	X27
η_{r1}	CE8	ρ_{r1}	ρ_{r1}	ρ_{r1}	τ_{r1}	τ_{r1}	τ_{r1}	τ_{r1}	ρ_{r1}	ρ_{r1}	Collimator secondary
$N_{r1,\Delta\lambda}$	B8	√	√	√	√	√	√	√	√	√	
ϵ'_{r1}	E20	$1-\rho_{r1}$	$1-\rho_{r1}$	$1-\rho_{r1}$	√	√	√	√	$1-\rho_{r1}$	$1-\rho_{r1}$	
ζ'_{r1}	Z20	ζ_{r1}	ζ_{r1}	ζ_{r1}	√	√	√	√	ζ_{r1}	ζ_{r1}	X28

TABLE 14.- MODEL PARAMETERS FOR NINE CONFIGURATIONS (CONTINUED)

Model denotation	Computer Variable	Configuration number									Element and radiance sum
		1	2	3	4	5	6	7	8	9	
Indirect-radiation terms											
ζ'_f	CT21	$\surd$	$\surd$	$\surd$	$\surd$	$\surd$	$\surd$	$\surd$	$\surd$	$\surd$	Field stop X29
τ_m	CT6	$1-\zeta_m$	$1-\zeta_m$	$1-\zeta_m$	$1-\zeta_m$	$1-\zeta_m$	$1-\zeta_m$	$1-\zeta_m$	$1-\zeta_m$	$1-\zeta_m$	Modulator
$N_{m,\Delta\lambda}$	B6	$\surd$	$\surd$	$\surd$	$\surd$	$\surd$	$\surd$	$\surd$	$\surd$	$\surd$	
ϵ'_m	E22	$1-\rho'_m$	$1-\rho'_m$	$1-\rho'_m$	$1-\rho'_m$	$1-\rho'_m$	$1-\rho'_m$	$1-\rho'_m$	$1-\rho'_m$	$1-\rho'_m$	
ζ_m	Z6	$\surd$	$\surd$	$\surd$	$\surd$	$\surd$	$\surd$	$\surd$	$\surd$	$\surd$	X30
τ_w	CT5	1	1	1	1	$\surd$	1	1	1	1	Window support
$N_{w,\Delta\lambda}$	35	0	0	0	0	$\surd$	0	0	0	0	
ϵ'_w	E23	0	0	0	0	$\surd$	0	0	0	0	X31
τ_{s2}	CT4	1	1	1	1	1	$1-\zeta_{s2}$	1	1	1	Spoke support
$N_{s2,\Delta\lambda}$	B4	0	0	0	0	0	$\surd$	0	0	0	
ϵ'_{s2}	E24	0	0	0	0	0	$1-\rho_{s2}$	0	0	0	
ζ_{s2}	Z4	0	0	0	0	0	$\surd$	0	0	0	X32
η_{p2}	CE3	ρ_{p2}	ρ_{p2}	1	1	ρ_{p2}	ρ_{p2}	1	ρ_{p2}	ρ_{p2}	Collector secondary
$N_{p2,\Delta\lambda}$	B3	$\surd$	$\surd$	0	0	$\surd$	$\surd$	0	$\surd$	$\surd$	
ϵ'_{p2}	E25	$1-\rho_{p2}$	$1-\rho_{p2}$	0	0	$1-\rho_{p2}$	$1-\rho_{p2}$	0	$1-\rho_{p2}$	$1-\rho_{12}$	
ζ_{p2}	Z25	ζ_{p2}	$\sec\phi$	0	0	ζ_{p2}	$\sec\theta$	0	ζ_{p2}	$\sec\phi$	X33
η_{p1}	CE2	ρ_{p1}	ρ_{p1}	ρ_{p1}	τ_{p1}	ρ_{p1}	ρ_{p1}	ρ_{p1}	ρ_{p1}	ρ_{p1}	Collector primary
$N_{p1,\Delta\lambda}$	B2	$\surd$	$\surd$	$\surd$	$\surd$	$\surd$	$\surd$	$\surd$	$\surd$	$\surd$	
ϵ'_{p1}	E26	$1-\rho_{p1}$	$1-\rho_{p1}$	$1-\rho_{p1}$	$\surd$	$1-\rho_{p1}$	$1-\rho_{p1}$	$1-\rho_{p1}$	$1-\rho_{p1}$	$1-\rho_{p1}$	
ζ'_{p1}	Z26	ζ_{p1}	ζ_{p1}	ζ_{p1}	$\surd$	ζ_{p1}	ζ_{p1}	ζ_{p1}	ζ_{p1}	ζ_{p1}	X34

TABLE 14.- MODEL PARAMETERS FOR NINE CONFIGURATIONS (CONTINUED)

Model denotation	Computer Variable	Configuration number									Element and radiance sum
		1	2	3	4	5	6	7	8	9	
Indirect-radiation terms											
τ_{s1}	CT1	τ_ℓ	τ_ℓ	1	1	1	1	1	$1-\zeta_{s1}$	$1-\zeta_{s1}$	Spoke support
$N_{s1,\Delta\lambda}$	B1	$N_{\ell,\Delta\lambda}$	$N_{\ell,\Delta\lambda}$	0	0	0	0	0	$\surd$	$\surd$	
ϵ'_{s1}	E27	ϵ'_ℓ	ϵ'_ℓ	0	0	0	0	0	$1-\rho'_{s1}$	$1-\rho'_{s1}$	
ζ_{s1}	Z1	1	1	0	0	0	0	0	$\surd$	$\surd$	X35
ρ_{ca}	C28	$\surd$	$\surd$	$\surd$	$\surd$	$\surd$	$\surd$	$\surd$	$\surd$	$\surd$	IFC-Attenuator
ζ_{ca}	Z28	$\surd$	$\surd$	$\surd$	$\surd$	$\surd$	$\surd$	$\surd$	$\surd$	$\surd$	X36
Secondary and higher order indirect-radiation terms											
ρ_d	C14	$\surd$	$\surd$	$\surd$	$\surd$	$\surd$	$\surd$	$\surd$	$\surd$	$\surd$	
τ_{cy}	CT13	1	1	1	1	1	1	1	1	1	
η_{r4}	CE12	ρ_{r4}	ρ_{r4}	ρ_{r4}	τ_{r4}	τ_{r4}	τ_{r4}	τ_{r4}	ρ_{r4}	ρ_{r4}	
τ_{r3}	CT11	$\surd$	$\surd$	1	1	1	1	1	$\surd$	$\surd$	
η_{r3}	CE11	ρ_{r3}	ρ_{r3}	1	1	1	1	1	ρ_{r3}	ρ_{r3}	
τ_b	CT10	$\surd$	$\surd$	$\surd$	$\surd$	$\surd$	$\surd$	$\surd$	$\surd$	$\surd$	
τ_{ra}	CT9	$\surd$	$\surd$	1	1	1	1	1	$\surd$	$\surd$	
η_{r2}	CE9	ρ_{r2}	ρ_{r2}	1	1	1	1	1	ρ_{r2}	ρ_{r2}	
η_{r1}	CE8	ρ_{r1}	ρ_{r1}	ρ_{r1}	τ_{r1}	τ_{r1}	τ_{r1}	τ_{r1}	ρ_{r1}	ρ_{r1}	
ζ'_f	CT21	$\surd$	$\surd$	$\surd$	$\surd$	$\surd$	$\surd$	$\surd$	$\surd$	$\surd$	
τ_m	CT6	$1-\zeta_m$	$1-\zeta_m$	$1-\zeta_m$	$1-\zeta_m$	$1-\zeta_m$	$1-\zeta_m$	$1-\zeta_m$	$1-\zeta_m$	$1-\zeta_m$	
τ_w	CT5	1	1	1	1	$\surd$	1	1	1	1	
τ_{s2}	CT4	1	1	1	1	1	$1-\zeta_{s2}$	1	1	1	

TABLE 14.- MODEL PARAMETERS FOR NINE CONFIGURATIONS (CONTINUED)

Model denotation	Computer Variable	Configuration number									Element and radiance sum
		1	2	3	4	5	6	7	8	9	
Secondary and higher order indirect-radiation terms											
η_{p2}	CE3	ρ_{p2}	ρ_{p2}	1	1	ρ_{p2}	ρ_{p2}	1	ρ_{p2}	ρ_{p2}	
η_{p1}	CE2	ρ_{p1}	ρ_{p1}	ρ_{p1}	τ_{p1}	ρ_{p1}	ρ_{p1}	ρ_{p1}	ρ_{p1}	ρ_{p1}	
τ_{s1}	CT1	τ_{ℓ}	τ_{ℓ}	1	1	1	1	1	$1-\zeta_{s1}$	$1-\zeta_{s1}$	
ρ_{ca}	C28	$\surd$	$\surd$	$\surd$	$\surd$	$\surd$	$\surd$	$\surd$	$\surd$	$\surd$	
ζ_{ca}	Z28	$\surd$	$\surd$	$\surd$	$\surd$	$\surd$	$\surd$	$\surd$	$\surd$	$\surd$	
Main chain of efficienty terms of direct-radiation side loops											
ρ_{b}	C10	$\surd$	$\surd$	$\surd$	$\surd$	$\surd$	$\surd$	$\surd$	$\surd$	$\surd$	
τ_{r2}	CT9	$\surd$	$\surd$	1	1	1	1	1	$\surd$	$\surd$	
η_{r2}	CE9	ρ_{r2}	ρ_{r2}	1	1	1	1	1	ρ_{r2}	ρ_{r2}	
η_{r1}	CE8	ρ_{r1}	ρ_{r1}	ρ_{r1}	τ_{r1}	τ_{r1}	τ_{r1}	τ_{r1}	ρ_{r1}	ρ_{r1}	
ζ_{f}''	CT22	$\surd$	$\surd$	$\surd$	$\surd$	$\surd$	$\surd$	$\surd$	$\surd$	$\surd$	
τ_{m}	CT6	$1-\zeta_{m}$	$1-\zeta_{m}$	$1-\zeta_{m}$	$1-\zeta_{m}$	$1-\zeta_{m}$	$1-\zeta_{m}$	$1-\zeta_{m}$	$1-\zeta_{m}$	$1-\zeta_{m}$	
τ_{w}	CT5	1	1	1	1	$\surd$	1	1	1	1	
τ_{s2}	CT4	1	1	1	1	1	$1-\zeta_{s2}$	1	1	1	
η_{p2}	CE3	ρ_{p2}	ρ_{p2}	1	1	ρ_{p2}	ρ_{p2}	1	ρ_{p2}	ρ_{p2}	
η_{p1}	CE2	ρ_{p1}	ρ_{p1}	ρ_{p1}	τ_{p1}	ρ_{p1}	ρ_{p1}	ρ_{p1}	ρ_{p1}	ρ_{p1}	
τ_{s1}	CT1	τ_{ℓ}	τ_{ℓ}	1	1	1	1	1	$1-\zeta_{s1}$	$1-\zeta_{s1}$	
τ_{a}	CT0	$\surd$	$\surd$	1	1	$\surd$	$\surd$	1	$\surd$	$\surd$	
ρ_{ca}	C28	$\surd$	$\surd$	$\surd$	$\surd$	$\surd$	$\surd$	$\surd$	$\surd$	$\surd$	
ζ_{ca}	Z28	$\surd$	$\surd$	$\surd$	$\surd$	$\surd$	$\surd$	$\surd$	$\surd$	$\surd$	

TABLE 14.- MODEL PARAMETERS FOR NINE CONFIGURATIONS (CONTINUED)

Model denotation	Computer Variable	Configuration number									Element and radiance sum
		1	2	3	4	5	6	7	8	9	
Main Chain of efficiency terms common to both the direct-radiation side loops and indirect-radiation											
τ_a	CT0	√	√	1	1	√	√	1	√	√	
τ_{s1}	CT1	τ_ℓ	τ_ℓ	1	1	1	1	1	$1-\zeta_{s1}$	$1-\zeta_{s1}$	
η_{p1}	CE2	ρ_{p1}	ρ_{p1}	ρ_{p1}	τ_{p1}	ρ_{p1}	ρ_{p1}	ρ_{p1}	ρ_{p1}	ρ_{p1}	
η_{p2}	CE3	ρ_{p2}	ρ_{p2}	1	1	ρ_{p2}	ρ_{p2}	1	ρ_{p2}	ρ_{p2}	
τ_{s2}	CT4	1	1	1	1	1	$1-\zeta_{s2}$	1	1	1	
τ_w	CT5	1	1	1	1	√	1	1	1	1	
τ_m	CT6	$1-\zeta_m$	$1-\zeta_m$	$1-\zeta_m$	$1-\zeta_m$	$1-\zeta_m$	$1-\zeta_m$	$1-\zeta_m$	$1-\zeta_m$	$1-\zeta_m$	
ζ_f'''	CT23	√	√	√	√	√	√	√	√	√	
η_{r1}	CE8	ρ_{r1}	ρ_{r1}	ρ_{r1}	τ_{r1}	τ_{r1}	τ_{r1}	τ_{r1}	ρ_{r1}	ρ_{r1}	
τ_{r2}	CT9	√	√	1	1	1	1	1	√	√	
η_{r2}	CE9	ρ_{r2}	ρ_{r2}	1	1	1	1	1	ρ_{r2}	ρ_{r2}	
τ_b	CT10	√	√	√	√	√	√	√	√	√	
τ_{r3}	CT11	√	√	1	1	1	1	1	√	√	
η_{r3}	CE11	ρ_{r3}	ρ_{r3}	1	1	1	1	1	ρ_{r3}	ρ_{r3}	
η_{r4}	CE12	ρ_{r4}	ρ_{r4}	ρ_{r4}	τ_{r4}	τ_{r4}	τ_{r4}	τ_{r4}	ρ_{r4}	ρ_{r4}	
τ_{cy}	CT13	1	1	1	1	1	1	1	1	1	
Side-loop efficiency terms of direct-radiation chain											
ρ_m	C6	√	√	√	√	√	√	√	√	√	
ζ_m	Z6	√	√	√	√	√	√	√	√	√	
ρ_w	C5	0	0	0	0	0	0	0	0	0	

TABLE 14.- MODEL PARAMETERS FOR NINE CONFIGURATIONS (CONCLUDED)

Model denotation	Computer Variable	Configuration number									Element and radiance sum
		1	2	3	4	5	6	7	8	9	
ρ_{s2}	C4	0	0	0	0	0	√	0	0	0	
ζ_{s2}	Z4	0	0	0	0	0	$1-\tau_{s2}$	0	0	0	
ρ_{s1}	C1	0	0	0	0	0	0	0	√	√	
ζ_{s1}	Z1	1	1	0	0	0	0	0	$1-\tau_{s1}$	$1-\tau_{s1}$	
Side-loop efficiency terms of indirect-radiation chain											
ρ_{s1}'	C27	0	0	0	0	0	0	0	√	√	
ζ_{s1}	Z1	1	1	0	0	0	0	0	√	√	
ρ_{s2}'	C24	0	0	0	0	0	√	0	0	0	
ζ_{s2}	Z4	0	0	0	0	0	√	0	0	0	
ρ_{w}'	C23	0	0	0	0	√	√	0	0	0	
ρ_{m}'	C22	√	√	√	√	√	√	√	√	√	
ζ_{m}	Z6	√	√	√	√	√	√	√	√	√	
ρ_{b}'	C18	√	√	√	√	√	√	√	√	√	

Model detonation	Computer Variable	Element	Output designation
Signal flow from cavity to amplifier for every configuration			
η_{cs}	CE30	Cold stop	Y3 = total irradiance
η_{d}	CE31	Detector efficiency	
A_{d}	A31	Detector area	Y4 = total flux
R_{m}	RM32	Measured detector resistance	
F_{cal}	FC32	Calculated flux (measurement condition)	RD = actual resistance
i_{b}	BC32	Bias current	Y5 = detector output voltage = amplifier input voltage

- Generation/recombination noise

$$\sigma_{gr}^2 = 2\,\Delta\nu\,E_d^2\,\tau_c\,\tau_p\,F(1+\omega^2\tau_c^2)^{-1} \tag{6}$$

where τ_c = time constant = ω_c^{-1}

ω_c = chopper frequency

τ_ρ = lifetime defining the average number of charge carriers

$$\bar{n} = \tau_\rho F$$

$\omega = 2\pi\nu$ = circular frequency

- Thermal noise, subject to temperature fluctuations

$$\sigma_t^2 = 4\Delta\nu k\,T_d R_d \tag{7}$$

where $k = 1.38 \times 10^{-23}$ watt sec deg^{-1} = Boltzmann constant

T_d = detector temperature

Consequently, one has the total detection noise

$$\sigma_d^2 = \sigma_p^2 + \sigma_s^2 + \sigma_c^2 + \sigma_{gr}^2 + \sigma_t^2 \tag{8}$$

To obtain the total noise, one has to add the matched amplifier noise; that is, $(R_d/R_i)^2\sigma_a^2$, where R_i = amplifier input impedance.

This means that the total noise becomes

$$\sigma^2 = \sigma_d^2 + (R_d/R_i)^2\sigma_a^2 \tag{9}$$

Then, the noise voltage is given by

$$E_N = \sigma = \left[\sigma_d^2 + (R_d/R_i)^2\sigma_a^2\right]^{1/2} \tag{10}$$

Now, if the frequency response of the amplifier is described generally by a function $G_a(\omega)$, e.g., by $G_a(\omega) = \left[(1 + R_d/R_i)^2 + j\,C_iR_d\right]^{-1}$ where C_i denotes the amplifier input impedance, and if the amplifier gain is C_a, then, the amplifier voltage becomes

$$E_o = C_a\left[E_d\,G_a(\omega) + E_n|G_a(\omega)|\right] \tag{11}$$

The model denotations and the corresponding new computer variables needed in Equations (1) through (11) are shown in Table 15.

TABLE 15. - SIGNAL AND NOISE PROPAGATION VARIABLES

Model denotation	Computer Variable	Analytical expression	Description
Noise propagation from detector to amplifier for every configuration			
F	Y4		Actually incident photon flux
R_m	RM32		Measured detector resistance at experimental conditions defined by F_{cal}
F_{cal}	FC32		Calculated flux incident upon detector
R_d	RD	$R_d = R_m F_{cal} F^{-1}$	Actual detector resistance
i_b	BC32		Bias current
E_d	ED	$E_d = R_d i_b$	Detector output voltage
$\Delta\nu$	DFREQ		Noise-equivalent bandwidth
q	ECHARG	$q = 1.6 \times 10^{-19}$ amp sec = universal const.	Electron charge
σ_s^2	DNS	$\sigma_s^2 = 2 \Delta\nu q R_d E_d$	Shot noise
K	CONST		Constant depending on detector size and material
ν	FREQ		Electrical frequency
σ_c^2	DNC	$\sigma_c^2 = K \Delta\nu E_d^2 \nu^{-1}$	Current noise
σ_p^2	DNP	$\sigma_p^2 = 2\Delta\nu E_d^2 F^{-1} (1 + \omega^2 \tau_c^2)^{-1}$	Photon noise
τ_c	TAUC	$\tau_c = \omega_c^{-1}$	Time constant for chopping frequency cy ω_c
τ_p	TAUP		Lifetime defining the average carriers $\bar{n} = \tau_p F$
ω	OMEGA	$\omega = 2\pi\nu$	Circular frequency $2\pi\nu$
σ_g^2	DNGR	$\sigma_g^2 = 2\Delta\nu E_d^2 \tau_c \left[\tau_p F(1 + \omega^2 \tau_c^2)\right]^{-1}$	Generation/ recombination noise

TABLE 15. - SIGNAL AND NOISE PROPAGATION VARIABLES (Concluded)

Model denotation	Computer Variable	Analytical expression	Description
Noise propagation from detector to amplifier for every configuration			
k	BOLTZ	$k = 1.38 \times 10^{-23}$ watt sec deg^{-1} = universal const.	Boltzmann constant
T_d	DTEMP		Detector temperature (deg K)
σ_t^2	DNT	$\sigma_t^2 = 4\Delta\nu kT_d R_d$	Thermal noise
σ_d^2	DN	$\sigma_d^2 = \sigma_s^2 + \sigma_c^2 + \sigma_p^2 + \sigma_g + \sigma_t^2$	Detector noise
σ_a^2	AN		Amplifier noise
R_i	RI		Amplifier input impedance
σ^2	TN	$\sigma^2 = \sigma_d^2 + (R_d/R_i)^2 \sigma_a^2$	Total noise = sum of detector noise and matched amplifier noise
E_n	EN	$E_n = \sigma = \left[\sigma_d^2 + (R_d/R_i)^2 \sigma_a^2\right]^{1/2}$	Total noise voltage
$G_a(\omega)$	GA	e.g., $G_a(\omega) = \left[(1 + R_d/R_i)^2 + j\omega C_i R_d\right]^{-1}$	Frequency response function (C_i = ampl. input capacitance)
E_{ai}	EAI	$E_{ai} = E_d G_a(\omega) + E_n \lvert G_a(\omega) \rvert$	
C_a	CA		Amplifier gain
E_{av}	EAO	$E_{ao} = C_a E_{ai}$	Amplifier output voltage

Table 16 describes the computer equations to be applied in evaluating the error model.

TABLE 16. - COMPUTER EQUATIONS NEEDED FOR ERROR-MODEL EVALUATION

X0 = CTO * (BO + BSO)	X35 = X34 * CT1 + B1 * E27 * Z1
X1 = X0 * CT1 + B1 * E1 * Z1	X36 = X35 * C28 * Z28
X2 = X1 * CE2 + B2 * E2 * Z2	X40 = X9 * C10 * CT9 * CE9 * CE8 * CT22 * CT6
X3 = X2 * CE3 + B3 * E3 * Z3	X41 = X5 * C6 * Z6
X4 = X3 * CT4 + B4 * E4 * Z4	X42 = (X40 + X41) * CT5
X5 = X4 * CT5 + B5 * E5	X43 = X4 * C5
X6 = X5 * CT5 + B6 * E6 * Z6	X44 = (X42 + X43) * CT4
X7 = X6 * CT7	X45 = X3 * C4 * Z4
X8 = X7 * CE8 + B8 * E8 * Z8	X46 = (X44 + X45) * CE3 * CE2 * CT1
X9 = X8 * CT9 * CE9 + B9 * E9 * Z9	X47 = X0 * C1 * Z1
X10 = X9 * CT10 + B10 * E10	X48 = (X46 + X47) * CTO * C28 * Z28
X11 = X10 * CT11 * CE11 + B11 * E11 * Z11	X50 = (X36 + 47) * CTO
X12 = X11 * CE12 + B12 * E12 * Z12	X51 = X34 * C27 * Z1
X13 = X12 * CT13 + B13 * E13	X52 = (X50 + X51) * CT1 * CE3 * CT4 * CE2
Y1 = X13	X53 = X31 * C24 * Z4
X20 = Y1 * C14 + B14 * E14	X54 = (X52 + X53) * CT5
X21 = X20 * CT13 + B15 * E15	X55 = X30 * C23
X22 = X21 * CE12 + B16 * E16 * Z16	X56 = (X54 + X55) * CT6
X23 = X22 * CT11	X57 = X29 * C22 * Z6
X24 = X23 * CE11 + B17 * E17 * Z17	X(1) = X56
X25 = X24 * CT10 + B18 * E18	X(2) = X57
X26 = X25 * CT9	X58 = X(J) * CT23 * CE8 * CT9 * CE9 * CT10
X27 = X26 * CE9 + B9 * E19 * Z19	X59 = X24 * C18
X28 = X27 * CE8 + B8 * E20 * Z20	X60 = (X58 + X59) * CT11 * CE11 * CE12 * CT13
X29 = X28 * CT21	Y2 = X60
X30 = X29 * CT6 + B6 * E22 * Z6	Y3 = (Y1 + Y2) * CE30
X31 = X30 * CT5 + B5 * E23	Y4 = Y3 * CE31 * A31
X32 = X31 * CT4 + B4 * E24 * Z4	RD = RM32 * FC32/Y4
X33 = X32 * CE3 + B3 * E25 * Z25	
X34 = X33 * CE2 + B2 * E26 * Z26	

TABLE 16. - COMPUTER EQUATIONS NEEDED FOR ERROR-MODEL EVALUATION (Concluded)

```
ED = RD * BC32
DNS = 2 * DFREQ * ECHARG *
      ED * RD
DNC = CONST * DFREQ * ED *
      ED/FREQ
DNP = 2 * DFREQ * ED * ED/Y4/
      (1 + OMEGA * OMEGA * TAUC *
      TAUC)
DNGR = 2 * DFREQ * ED * ED/Y4 *
       TAUC/TAUP/(1 + OMEGA *
       OMEGA * TAUC * TAUC)
DNT = 4 * DFREQ * BOLTZ *
      DTEMP * RD
DN = DNS + DNC + DNP + DNGR + DNT
TN = DN + AN * RD * RD/RI/RI
EN = SQRT (TN)
EAI = ED * GA + EN * ABS(GA)
EAO = CA * EAI
```

In defining input radiance, it has been shown that one must consider simulators and especially the inflight calibrator. To show how these subsystems can be handled in the model and the computer program, the inflight calibrator is taken as an example. Symbols used in the model were already described, and the corresponding computer variables are summarized in Table 17. Supposedly, the computer is handling the inflight calibrator output radiance by a subroutine as shown in the equations of Table 18.

TABLE 17. - INFLIGHT CALIBRATOR SIGNAL-FLOW SYMBOLS

Model denotation	Computer variable	Element	Output designation of stepwise computation and analytic expression
$N_{ic,\Delta\lambda}$	BCO	Calibration source: input radiance	
τ_{ca}	CTA	IFC-attenuator transmissivity	
$N_{a,\Delta\lambda}$	BAO	IFC-attenuator blackbody radiance	
ϵ_{ca}	EA	IFC-attenuator emissivity	$\epsilon_{ca} = 1 - \rho_{ca}$
ζ_{ca}	Z28	IFC-attenuator blockage factor	X01; $\zeta_{ca} = 1 - \tau_{ca}$
ρ_{cc}	CO	IFC-collimator reflectivity	
$N_{c,\Delta\lambda}$	BOO	IFC-collimator blackbody radiance	
ϵ_{cc}	EO	IFC-collimator omissivity	$\epsilon_{cc} = 1 - \rho_{cc}$
ζ_{cc}	20	IFC-collimator form factor	X02

TABLE 18. - INFLIGHT CALIBRATION COMPUTER EQUATIONS (SUBROUTINE)

X01 = CTA * BCO + BAO * EA * Z28
X02 = X01 * CO + BOO * EO * ZO
BO = X02 (Transfer to main program)

Model Application

The analytical model was previously described analytically and graphically. The arithmetic caluclations required to get a feeling for the model behavior, and to explore a particular configuration, are extensive enough to require some automation. Thus, a computer program was written using the TYMSHARE time-sharing service which allows a rapid and efficient description of the system and determination of effects of parameter variation. The use of a time-sharing system allows the user to change any parameters at will, determine the effect of the change, and quickly reconfigure and run again. Easy program changes are also possible, allowing one to compute the quantities of immediate interest without having a large and complicated program.

The basic outputs are power on the detector and signal and noise out of the amplifier for the modulator in both open (transmitting) and closed positions.

This program was used to look at the analytical model's description of three baseline radiometers and the test-bed model proposed for Part II of the program. These systems are described and representative calculations presented herein.

Baseline systems. -- Three radiometer configurations were selected for exploration with the analytical model, both as a means of exercising the model and as a guidance for the Part II experimentation. The three configurations are

- An all-reflective, off-axis system
- A Cassegrain collector optics with off-axis reflective relay optics
- A Cassegrain collector optics with refractive relay optics

Figures 21, 22, and 23 are schematic drawings of the three systems. Table 19 indicates nominal parameter values for these systems. Table 20 includes a complete list, except for the detector and electrical filter, of the analytical variables and their assignments for the three baseline systems.

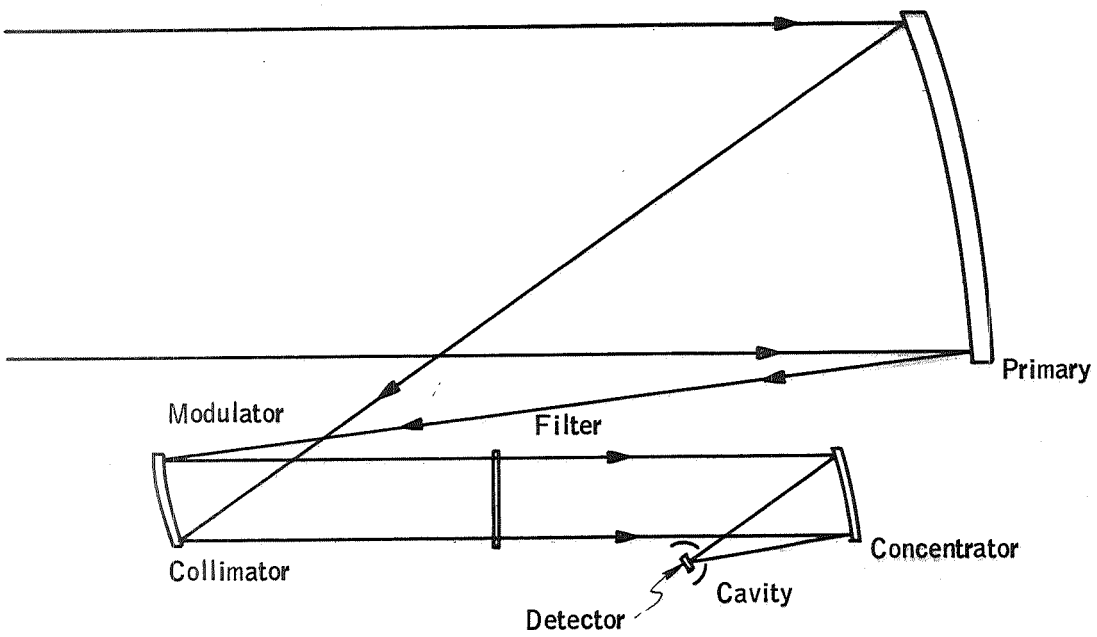

Figure 21. Off-Axis System

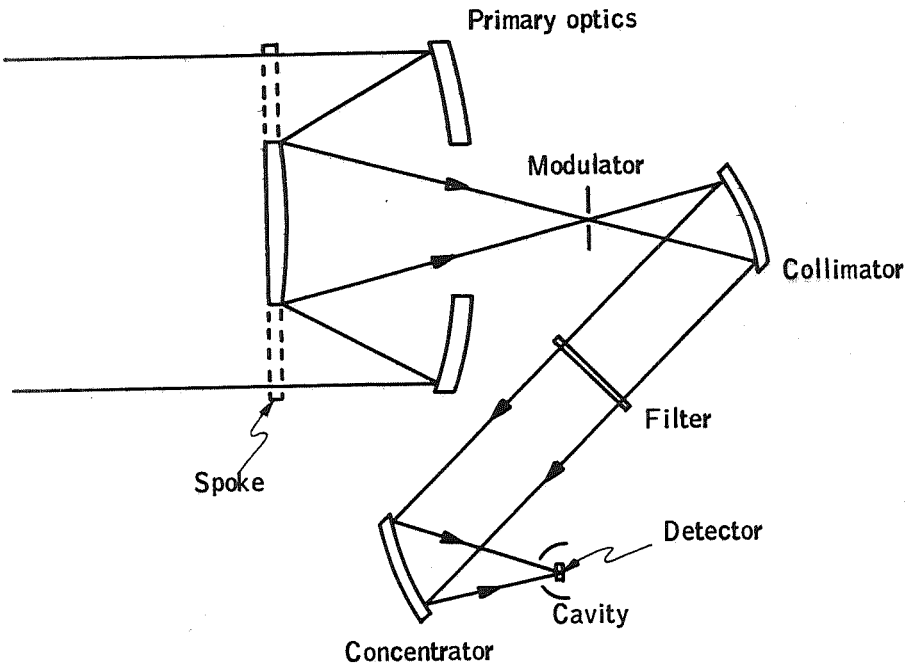

Figure 22. Cassegrainian and Reflective System

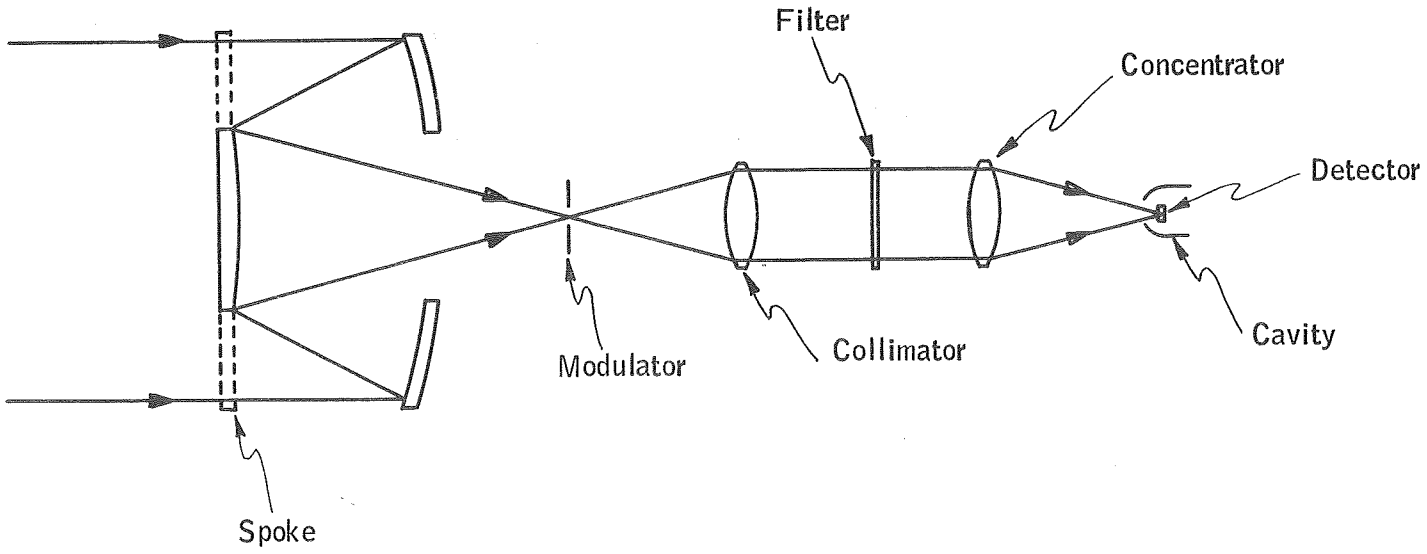

Figure 23. Cassegrainian and Refractive System

TABLE 19. - NOMINAL PARAMETER VALUES FOR BASELINE RADIOMETER MODELS

Parameter	Value
Primary optics reflectivity	0.986
Spoke emissivity	0.94
Primary optics temperature	200°K
Modulator temperature	200°K
Modulator emissivity	0.05
Collimator reflectivity (reflective)	0.986
Collimator reflectivity (refractive)	0.05
Collimator transmission (refractive)	0.9
Collimator temperature	80°K
Filter transmission	0.7
Filter reflectivity	0.1
Filter temperature	80°K
Concentrator reflectivity (reflective)	0.986
Concentrator reflectivity (refractive)	0.05
Concentrator transmission (refractive)	0.90
Concentrator temperature	80°K
Cavity temperature	15°K
Detector temperature	15°K
Detector reflectivity	0.2
f/no.	2.0

TABLE 20. - ANALYTICAL VARIABLES ASSIGNED TO BASELINE RADIOMETER SYSTEMS

Model denotation	Computer variable	Configuration number[a]		
		1	2	3
Direct radiation terms				
$N_{i,\Delta\lambda}$	B0	✓	✓	✓
$N_{SL,\Delta\lambda}$	BS0	✓	✓	✓
τ_a	CT0	1	✓	✓
τ_{s1}	CT1	1	$1-\zeta_{s1}$	$1-\zeta_{s1}$
$N_{s1,\Delta\lambda}$	B1	0	✓	✓
ϵ_{s1}	E1	0	$1-\rho_{s1}$	$1-\rho_{s1}$

[a]Check mark means that parameter is identical to model denotation.

TABLE 20. - ANALYTICAL VARIABLES ASSIGNED TO BASELINE RADIOMETER SYSTEMS (CONTINUED)

Model denotation	Computer variable	Configuration number		
		1	2	3
Direct radiation terms				
ζ_{s1}	Z1	0	✓	✓
η_{p1}	CE2	ρ_{p1}	ρ_{p1}	ρ_{p1}
$N_{p1, \Delta\lambda}$	B2	✓	✓	✓
ϵ_{p1}	E2	$1-\rho_{p1}$	$1-\rho_{p1}$	$1-\rho_{p1}$
ζ_{p1}	Z2	✓	✓	✓
η_{p2}	CE3	1	ρ_{p2}	ρ_{p2}
$N_{p2, \Delta\lambda}$	B3	0	✓	✓
ϵ_{p2}	E3	0	$1-\rho_{p2}$	$1-\rho_{p2}$
ζ_{p2}	Z3	0	✓	✓
τ_{s2}	CT4	1	1	1
$N_{s2, \Delta\lambda}$	B4	0	0	0
ϵ_{s2}	E4	0	0	0
ζ_{s2}	Z4	0	0	0
τ_{w}	CT5	1	1	1
$N_{w, \Delta\lambda}$	B5	0	0	0
ϵ_{w}	E5	0	0	0
τ_{m}	CT6	$1-\zeta_{m}$	$1-\zeta_{m}$	$1-\zeta_{m}$
$N_{m, \Delta\lambda}$	B6	✓	✓	✓
ϵ_{m}	E6	$1-\rho_{m}$	$1-\rho_{m}$	$1-\rho_{m}$
ζ_{m}	Z6	✓	✓	✓
ζ_{f}	CT7	✓	✓	✓

TABLE 20. - ANALYTICAL VARIABLES ASSIGNED TO BASELINE RADIOMETER SYSTEMS (CONTINUED)

Model denotation	Computer variable	Configuration number		
		1	2	3
Direct radiation terms				
η_{r1}	CE8	ρ_{r1}	ρ_{r1}	τ_{r1}
$N_{r1, \Delta\lambda}$	B8	✓	✓	✓
ϵ_{r1}	E8	$1-\rho_{r1}$	$1-\rho_{r1}$	✓
ζ_{r1}	Z8	✓	✓	✓
τ_{r2}	CT9	1	1	1
η_{r2}	CE9	1	1	1
$N_{r2, \Delta\lambda}$	B9	0	0	0
ϵ_{r2}	E9	0	0	0
ζ_{r2}	Z9	0	0	0
τ_{b}	CT10	✓	✓	✓
$N_{b, \Delta\lambda}$	B10	✓	✓	✓
ϵ_{b}	E10	✓	✓	✓
τ_{r3}	CT11	1	1	1
η_{r3}	CE11	1	1	1
$N_{r3, \Delta\lambda'}$	B11	0	0	0
ϵ_{r3}	E11	0	0	0
ζ_{r3}	Z11	0	0	0
η_{r4}	CE12	ρ_{r4}	ρ_{r4}	τ_{r4}
$N_{r4, \Delta\lambda'}$	B12	✓	✓	✓
ϵ_{r4}	E12	$1-\rho_{r4}$	$1-\rho_{r4}$	✓
ζ_{r4}	Z12	✓	✓	✓
τ_{cy}	CT13	1	1	1
$N_{cy, \Delta\lambda'}$	B13	✓	✓	✓
ϵ_{cy}	E13	✓	✓	✓

TABLE 20. - ANALYTICAL VARIABLES ASSIGNED TO BASELINE RADIOMETER SYSTEMS (CONTINUED)

Model denotation	Computer variable	Configuration number		
		1	2	3
Indirect radiation terms				
ρ_d	C14	✓	✓	✓
$N_{d,\Delta\lambda}$	B14	✓	✓	✓
ϵ_d	E14	✓	✓	✓
τ_{cy}	CT13	1	1	1
$N'_{cy,\Delta\lambda}$	B15	✓	✓	✓
ϵ_{cy}'	E15	✓	✓	✓
η_{r4}	CE12	ρ_{r4}	ρ_{r4}	τ_{r4}
$N'_{r4,\Delta\lambda}$	B16	✓	✓	✓
ϵ_{r4}'	E16	$1-\rho_{r4}$	$1-\rho_{r4}$	✓
ζ_{r4}'	Z16	✓	✓	✓
τ_{r3}	CT11	1	1	1
η_{r3}	CE11	1	1	1
$N_{r3,\Delta\lambda}'$	B17	0	0	0
ϵ_{r3}'	E17	0	0	0
ζ_{r3}'	Z17	0	0	0
τ_b	CT10	✓	✓	✓
$N_{b,\Delta\lambda}'$	B18	✓	✓	✓
ϵ_b'	E18	✓	✓	✓
τ_{r2}	CT9	1	1	1
η_{r2}	CE9	1	1	1
$N_{r2,\Delta\lambda}$	B9	0	0	0

TABLE 20. - ANALYTICAL VARIABLES ASSIGNED TO BASE-LINE RADIOMETER SYSTEMS (CONTINUED)

Model denotation	Computer variable	Configuration number		
		1	2	3
Indirect radiation terms				
ϵ_{r2}'	E19	0	0	0
ζ_{r2}'	Z19	0	0	0
η_{r1}	CE8	ρ_{r1}	ρ_{r1}	τ_{r1}
$N_{r1, \Delta\lambda}$	B8	✓	✓	✓
ϵ_{r1}'	E20	$1-\rho_{r1}$	$1-\rho_{r1}$	✓
ζ_{r1}'	Z20	ζ_{r1}	ζ_{r1}	✓
ζ_f'	CT21	✓	✓	✓
τ_m	CT6	$1-\zeta_m$	$1-\zeta_m$	$1-\zeta_m$
$N_{m, \Delta\lambda}$	B6	✓	✓	✓
ϵ_m'	E22	$1-\rho_m'$	$1-\rho_m'$	$1-\rho_m'$
ζ_m	Z6	✓	✓	✓
τ_w	CT5	1	1	1
$N_{w, \Delta\lambda}$	B5	0	0	0
ϵ_w'	E23	0	0	0
τ_{s2}	CT4	1	1	1
$N_{s2, \Delta\lambda}$	B4	0	0	0
ϵ_{s2}'	E24	0	0	0
ζ_{s2}	Z4	0	0	0
η_{p2}	CE3	1	1	1
$N_{p2, \Delta\lambda}$	B3	0	0	0
ϵ_{p2}'	E25	0	0	0
ζ_{p2}'	Z25	0	0	0

TABLE 20. - ANALYTICAL VARIABLES ASSIGNED TO BASE-LINE RADIOMETER SYSTEMS (CONTINUED)

Model denotation	Computer variable	Configuration number		
		1	2	3
Indirect radiation terms				
η_{p1}	CE2	ρ_{p1}	ρ_{p1}	τ_{p1}
$N_{p1, \Delta\lambda}$	B2	✓	✓	✓
ϵ_{p1}'	E26	$1-\rho_{p1}$	$1-\rho_{p1}$	✓
ζ_{p1}'	Z26	ζ_{p1}	ζ_{p1}	✓
τ_{s1}	CT1	1	$1-\zeta_{s1}$	$1-\zeta_{s1}$
$N_{s1, \Delta\lambda}$	B1	0	✓	✓
ϵ_{s1}'	E27	0	$1-\rho_{s1}'$	$1-\rho_{s1}'$
ζ_{s1}	Z1	0	✓	✓
ρ_{ca}	C28	✓	✓	✓
ζ_{ca}	Z28	✓	✓	✓
Main chain of efficiency terms of direct radiation side loops				
ρ_b	C10	✓	✓	✓
τ_{r2}	CT9	1	1	1
η_{r2}	CE9	1	1	1
η_{r1}	CE8	ρ_{r1}	ρ_{r1}	τ_{r1}
ζ_f'	CT22	✓	✓	✓
τ_m	CT6	$1-\zeta_m$	$1-\zeta_m$	$1-\zeta_m$
τ_w	CT5	1	1	1
τ_{s2}	CT4	1	1	1
η_{p2}	CE3	1	ρ_{p2}	ρ_{p2}
η_{p1}	CE2	ρ_{p1}	ρ_{p1}	ρ_{p1}

TABLE 20. - ANALYTICAL VARIABLES ASSIGNED TO BASE-LINE RADIOMETER SYSTEMS (CONTINUED)

Model denotation	Computer variable	Configuration number		
		1	2	3
Main chain of efficiency terms of direct radiation side loops				
τ_{s1}	CT1	1	$1-\zeta_{s1}$	$1-\zeta_{s1}$
τ_a	CT0	1	✓	✓
ρ_{ca}	C28	✓	✓	✓
ζ_{ca}	Z28	✓	✓	✓
Main chain of efficiency terms common to both direct radiation side loops and indirect radiation				
τ_a	CT0	1	✓	✓
τ_{s1}	CT1	1	✓	✓
η_{p1}	CE2	ρ_{p1}	ρ_{p1}	ρ_{p1}
η_{p2}	CE3	1	ρ_{p2}	ρ_{p2}
τ_{s2}	CT4	1	1	1
τ_w	CT5	1	1	1
τ_m	CT6	$1-\zeta_m$	$1-\zeta_m$	$1-\zeta_m$
ζ_f'	CT23	✓	✓	✓
η_{r1}	CE8	ρ_{r1}	ρ_{r1}	τ_{r1}
τ_{r2}	CT9	1	1	1
η_{r2}	CE9	1	1	1
τ_b	CT10	✓	✓	✓
τ_{r3}	CT11	1	1	1
η_{r3}	CE11	1	1	1
η_{r4}	CE12	ρ_{r4}	ρ_{r4}	τ_{r4}
τ_{cy}	CT13	1	1	1

TABLE 20. - ANALYTICAL VARIABLES ASSIGNED TO BASE-LINE RADIOMETER SYSTEMS (CONCLUDED)

Model denotation	Computer variable	Configuration number		
		1	2	3
Side loop efficiency terms of direct radiation chain				
ρ_m	C6	✓	✓	✓
ζ_m	Z6	✓	✓	✓
ρ_w	C5	0	0	0
ρ_{s2}	C4	0	0	0
ζ_{s2}	Z4	0	0	0
ρ_{s1}	C1	0	✓	✓
ζ_{s1}	Z1	0	$1-\tau_{s1}$	$1-\tau_{s1}$
Side loop efficiency terms of indirect radiation chain				
ρ_{s1}'	C27	0	✓	✓
ζ_{s1}	Z1	0	✓	✓
ρ_{s2}'	C24	0	0	0
ζ_{s2}	Z4	0	0	0
ρ_w'	C23	0	0	0
ρ_m'	C22	✓	✓	✓
ζ_m	Z6	✓	✓	✓
ρ_b'	C18	✓	✓	✓

The test-bed model, designed for Part II of this program, was also analyzed. A schematic drawing and nominal parameter values are given in Figure 24 and Table 21, respectively.

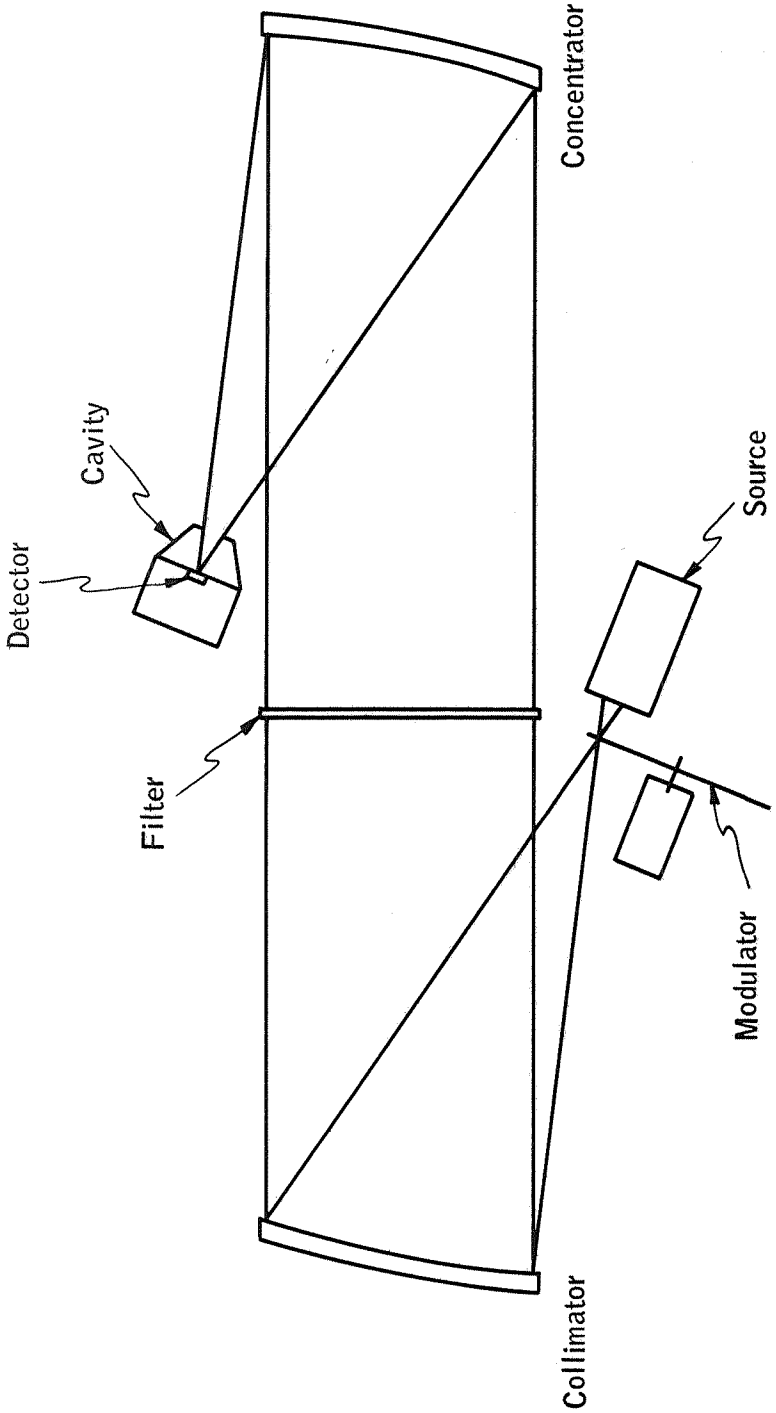

Figure 24. Test Bed System

TABLE 21. - NOMINAL PARAMETER VALUES FOR TEST-BED RADIOMETER MODEL

Parameter	Value
Source radiance	0.0
Modulator emissivity	0.7
Modulator temperature	125°K
Collimator reflectivity	0.986
Collimator temperature	80°K
Filter transmission	0.7
Filter emissivity	0.2
Filter temperature	80°K
Concentrator reflectivity	0.986
Concentrator temperature	80°K
Cavity temperature	15°K
Detector temperature	15°K
Detector reflectivity	0.2
f/number	2.0

Results. -- Results obtained on the four configurations are presented primarily in the form of graphs. These show power, in watts, passing through the detector surface for the modulator open (P_o) and closed (P_c) normalized to the power with the modulator closed as a function of temperature and emissivity. The normalizing power, which enables a conversion to actual watts by a multiplication, is listed on each graph. On each graph there is also an indication of the power due to the minimum and maximum input radiances of a typical ARRS application. (P_{Bo}min and P_{Bo}max). $B_o$min = 5 x 10^{-3} W/m^2-sr.

Temperature variations: For a radiometer with an inflight calibrator, one of the primary error sources is temperature uncertainty. Figures 25, 26, 27, and 28 show the effect of temperature variation of the major components and indicate configuration dependent behavior of the systems. These plots show gross variations of the type that would help choose a configuration. Figures 28 and 29, on the other hand, explicitly present the differential power on the detector and its rate of change with temperature. This data is the primary means of determining the effects of tolerances and uncertainties. Although only two plots of differential power are included, the data can be generated for any parameter quite easily.

As an example of the use of the rate of change plots, consider the differential power uncertainty due to a filter temperature uncertainty of 0.1°K at a temperature of 100°K. From Figure 28

$$\frac{d\Delta P}{dT_f} = 4 \times 10^{-3}/°K$$

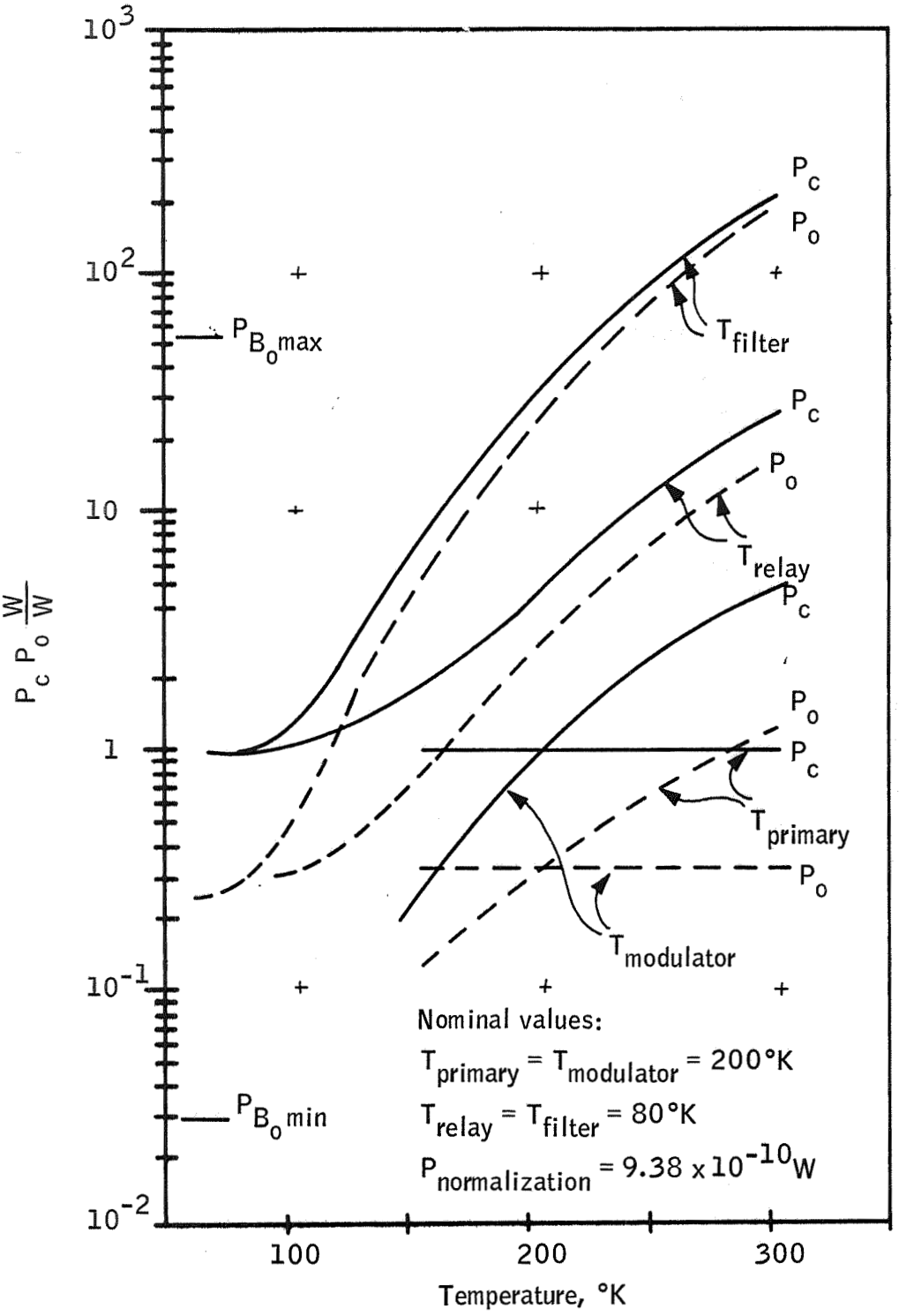

Figure 25. Normalized Power on Detector for Modulator Open and Closed versus Temperature on Various Elements, Off-Axis System

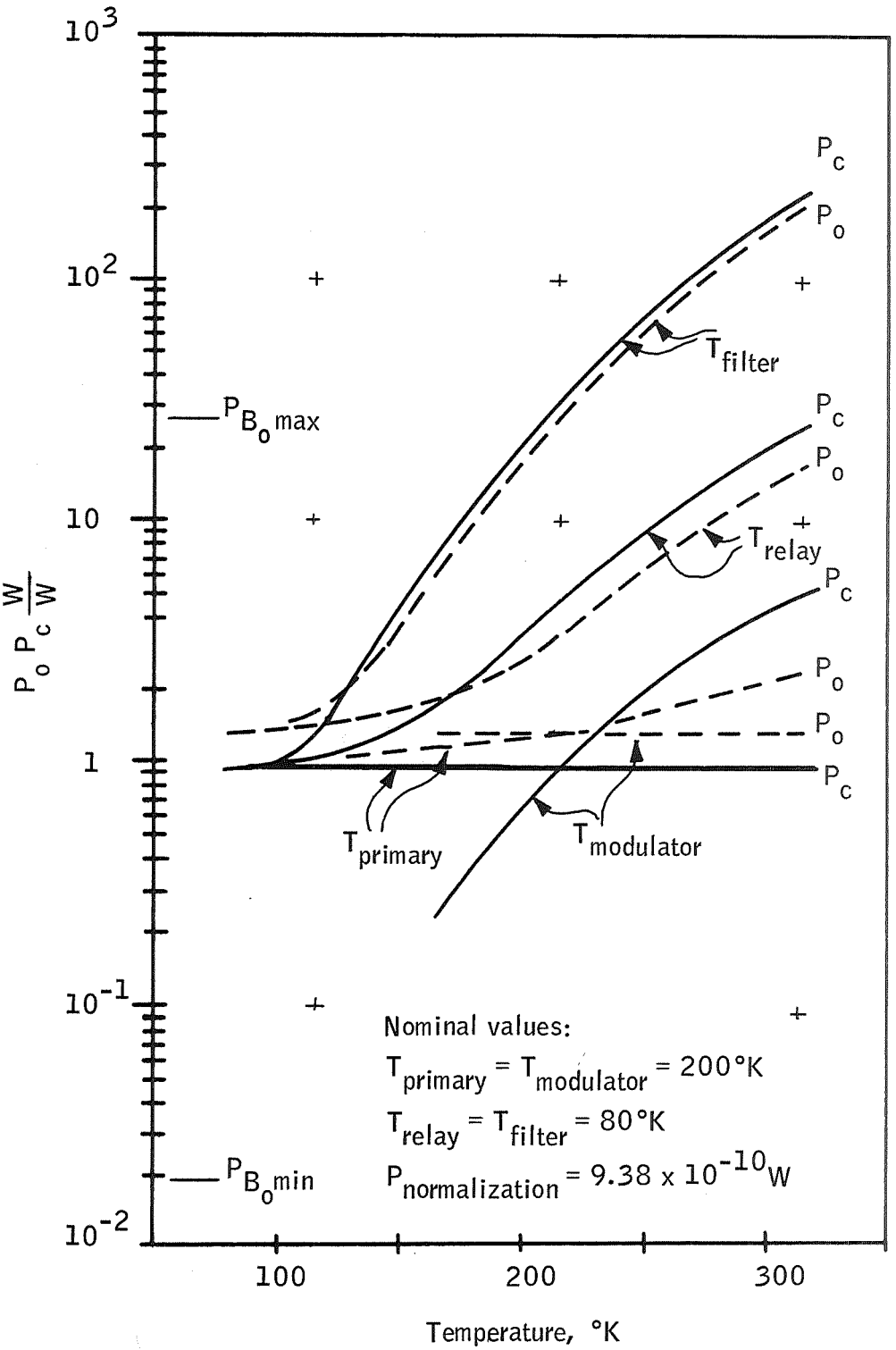

Figure 26. Normalized Power on Detector for Modulator Open and Closed versus Temperature on Various Elements, Cassegrain and Reflective System

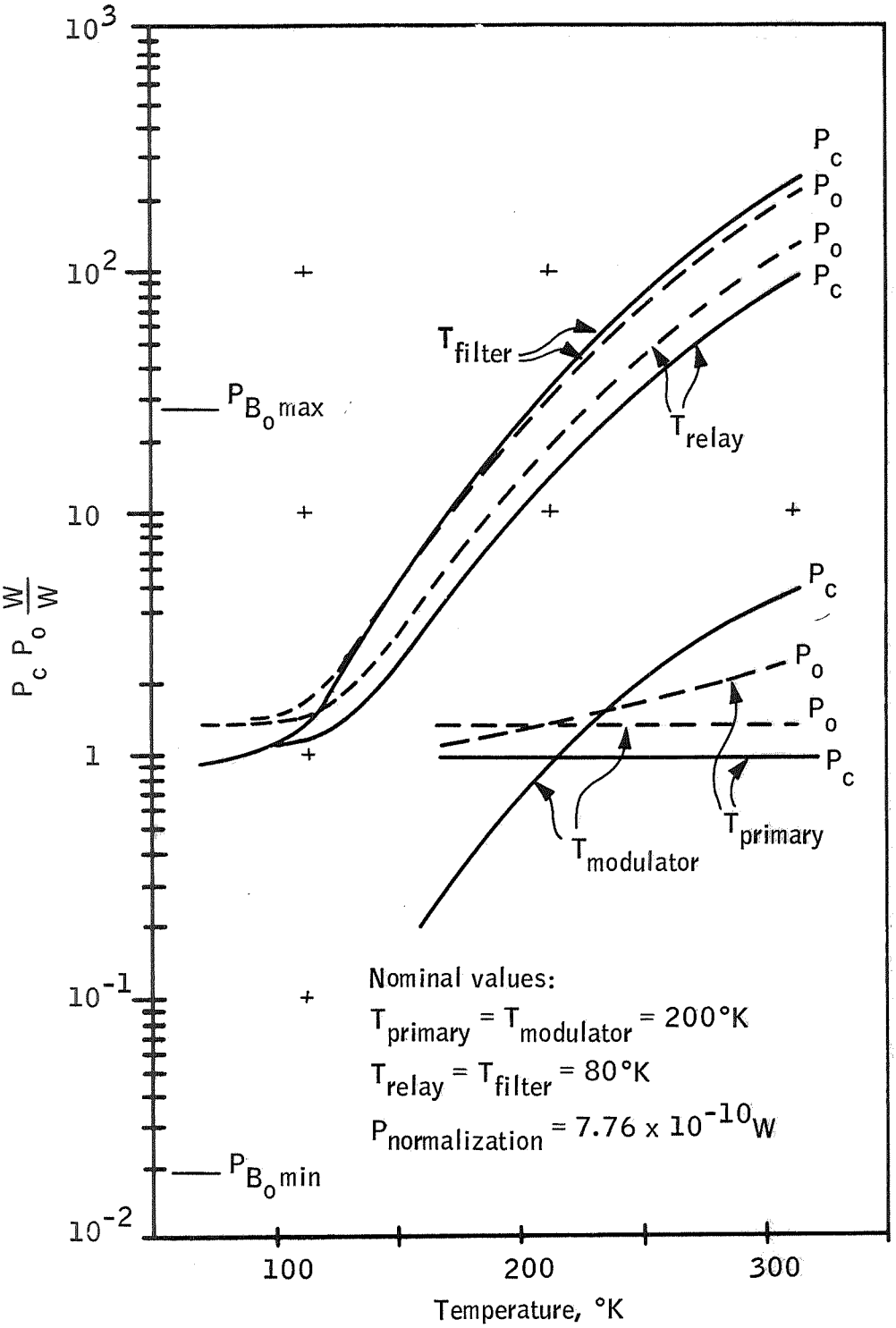

Figure 27. Normalized Power on Detector for Modulator Open and Closed versus Temperature on Various Elements, Cassegrain and Reflective System

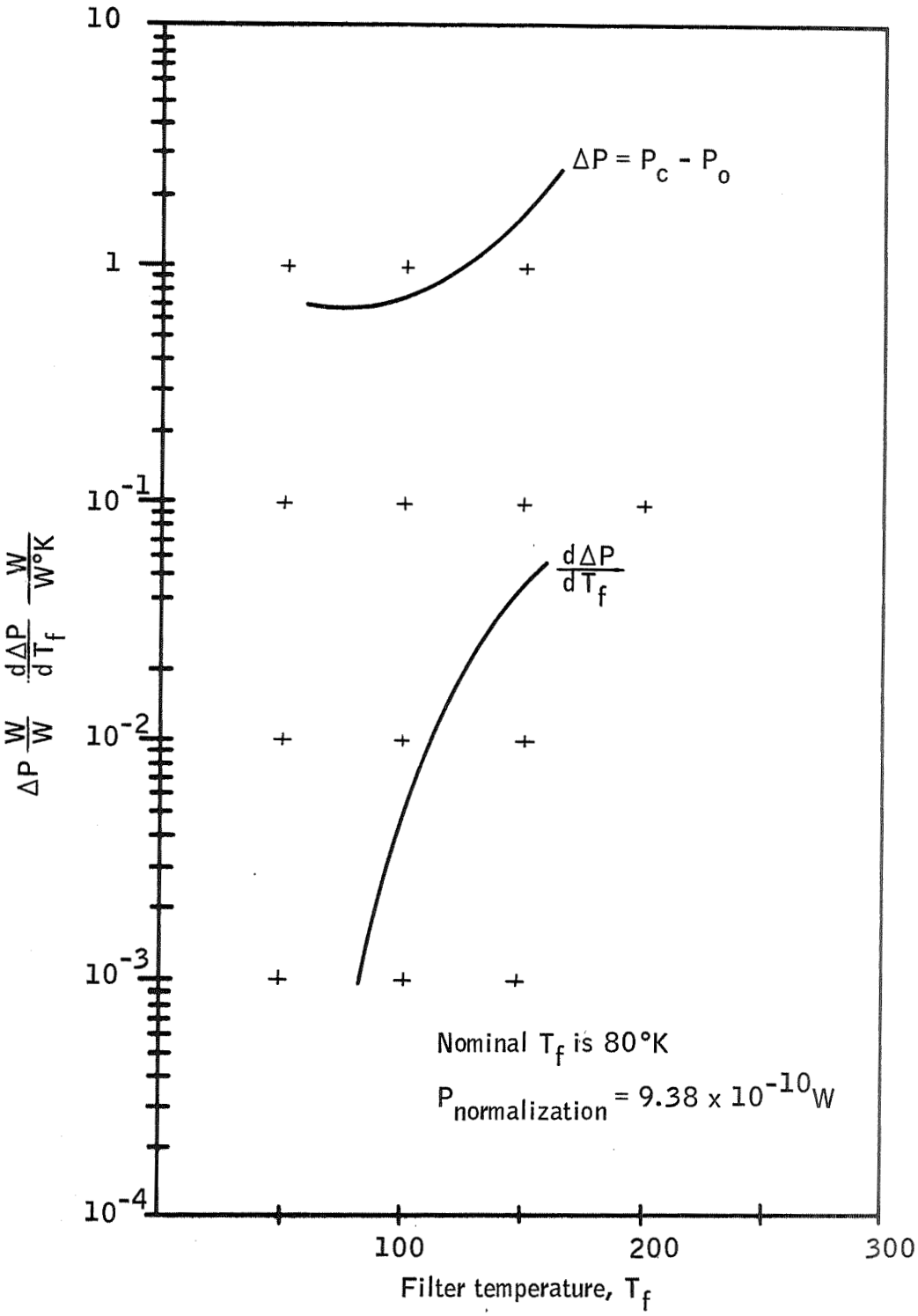

Figure 28. Differential Power on Detector and Its Derivative versus Filter Temperature, Off-Axis System

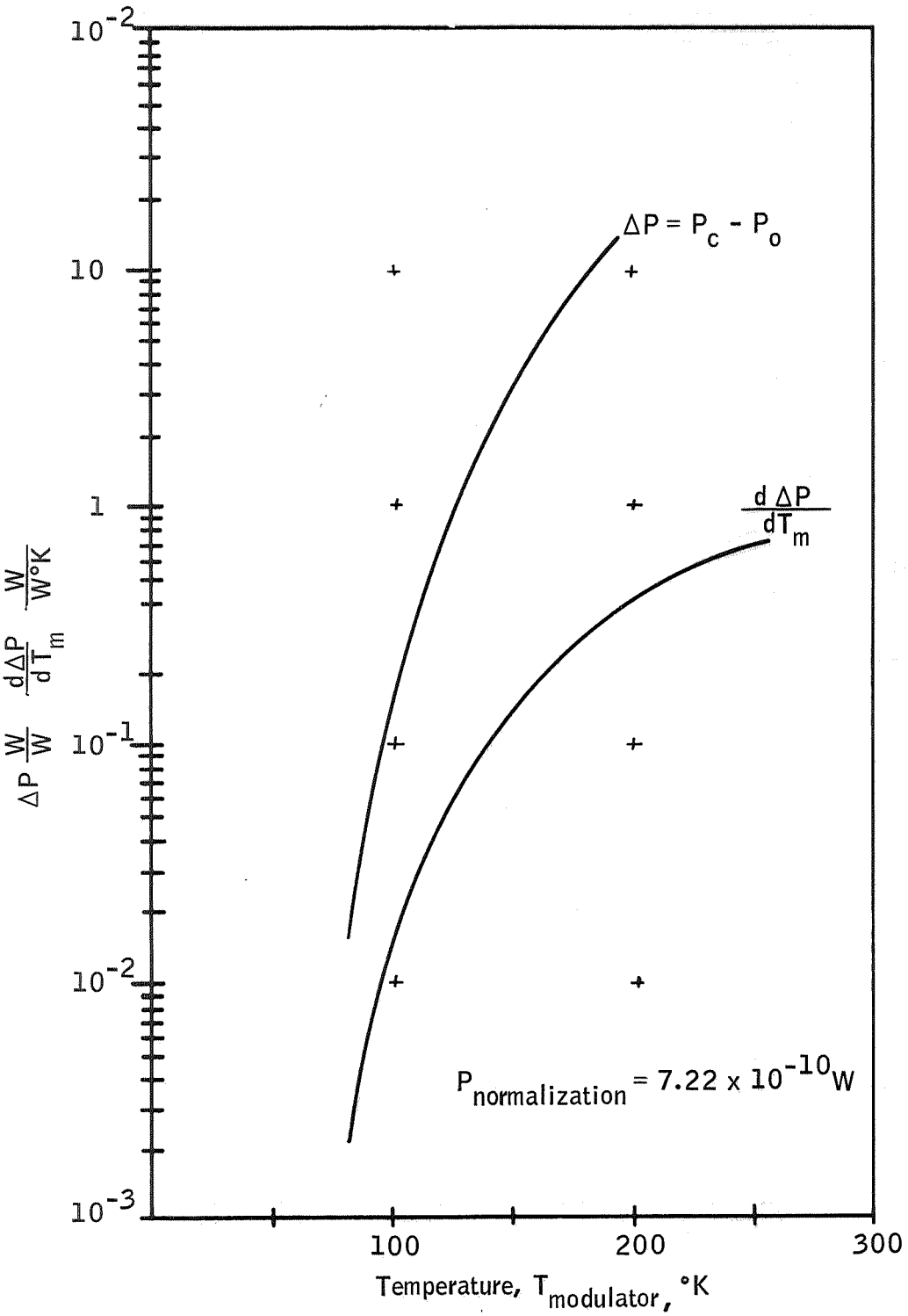

Figure 29. Differential Power on the Detector and Its Derivative versus Modulator Temperature, Test-Bed Model

and since

$$d\Delta P = \left(\frac{d\Delta P}{dT_f}\right)' dT_f$$

the power uncertainty, $d\Delta P$, is 4×10^{-3} (0.1) = 4×10^{-4} W/W. With the normalization power of 9.38×10^{-10} W, $d\Delta P$ is 3.75×10^{-13} W.

Emissivity variations: Variations of emissivity of a surface can affect the system in varying degrees depending on the percentage of power coming from that surface. Thus, even though some cases may be quite easy to calculate, it is useful to be able to determine generally the effects of emissivity variations. Figures 30, 31, and 32 show the effect of varying emissivities on power at the detector. Figure 32 in particular shows that some emissivity effects are not particularly simple.

Other parameter variations: There are many parameters other than temperature and emissivity in a radiometer, of course, but these two have been emphasized for two reasons:

- This is primarily a radiance propagation model and temperature and emissivity are the primary parametrics contributing to radiance.
- The detector and electronics are not sufficiently defined to allow computations.

It is also necessary to note that some parameters are functions of others. In particular reflectivities and emissivities for a reflecting surface are related by by $\epsilon + \rho = 1$. A transmitting surface in addition has a transmission resulting in $\epsilon + \rho + \tau = 1$.

Detector reflectivity is another parameter that has been varied in these computations. The results are of interest primarily in that they show the effects of return loops in the analytical model. In Figure 33, both curves would be linear without the second-order effects.

System uncertainties: Once parameter (or component) uncertainties have been determined, they can be used to determine system uncertainties. The effects of parameter uncertainties are calculated identically to the example in the temperature variations subsection; that is, compute rate of change of output with parameter variation, multiply by parameter uncertainty, and the result is the output uncertainty due to that parameter uncertainty. The uncertainties from all sources are then combined appropriately depending on the way they contribute to the total uncertainty. The three most common methods are worst case, root-sum-square, or a combination of these.

Test-bed radiometer application: Temperatures and emissivities were varied in the most adverse direction and the differential power uncertainty

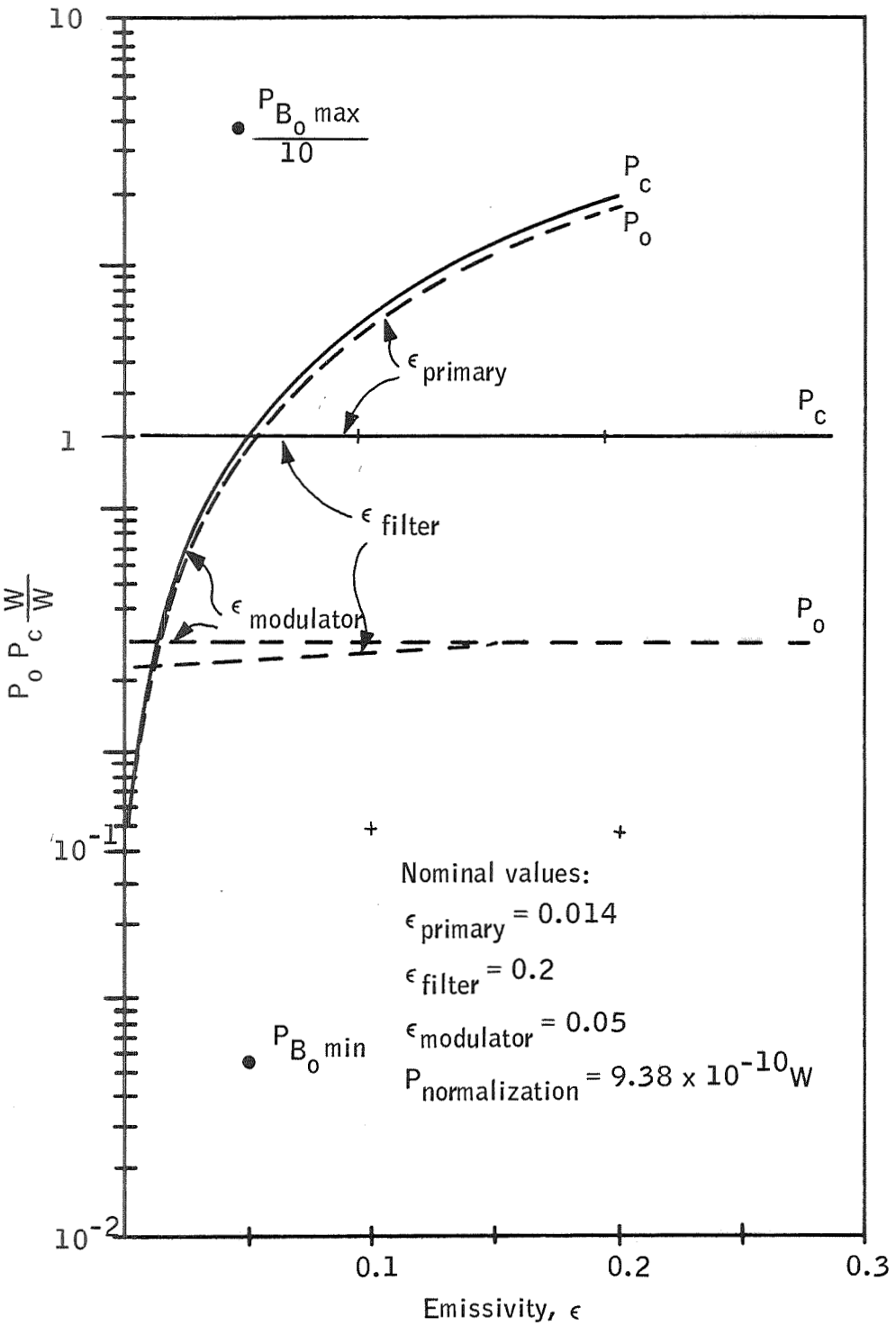

Figure 30. Normalized Power versus Emissivity, Off-Axis System

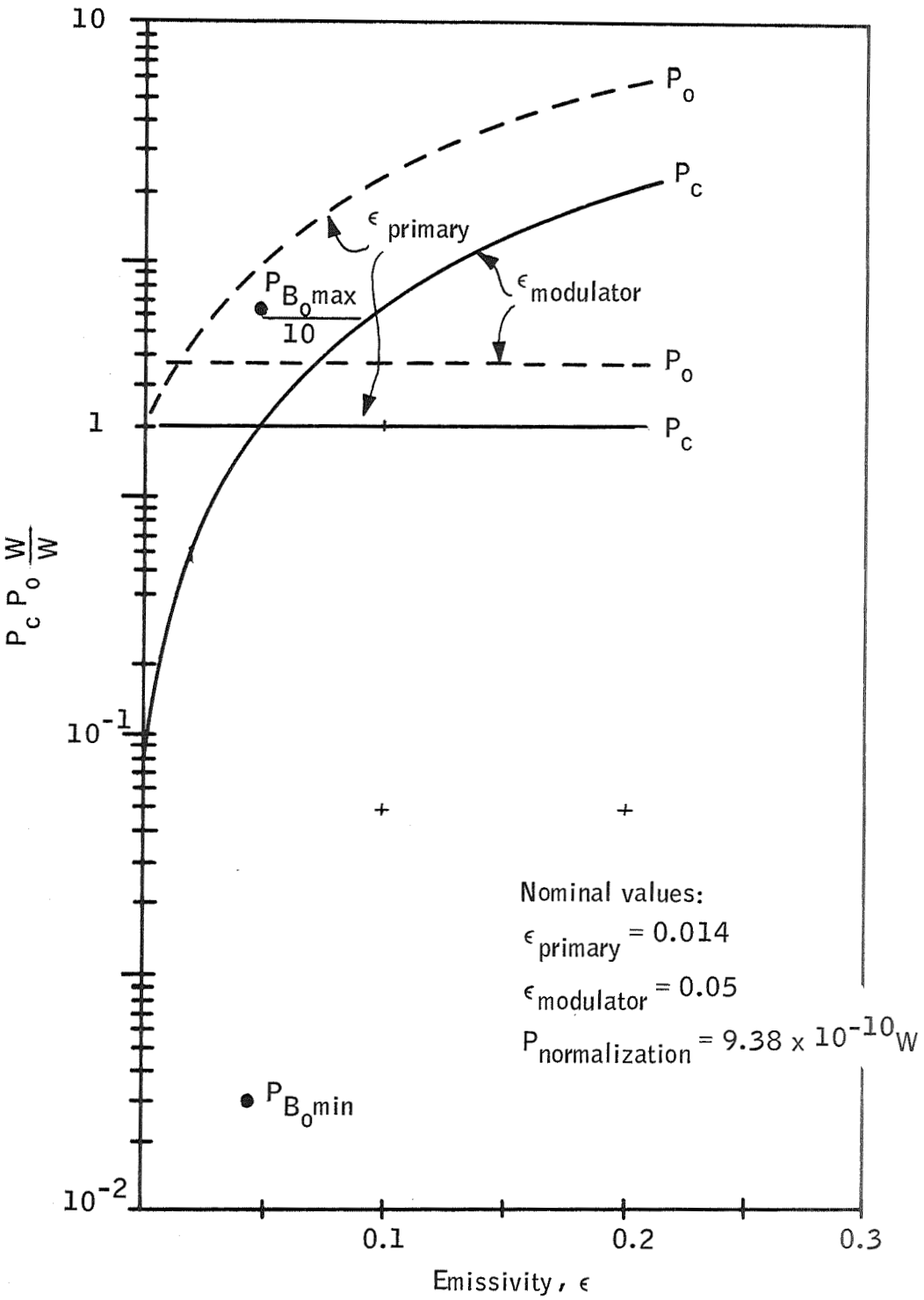

Figure 31. Normalized Power versus Emissivity, Cassegrain and Refractive System

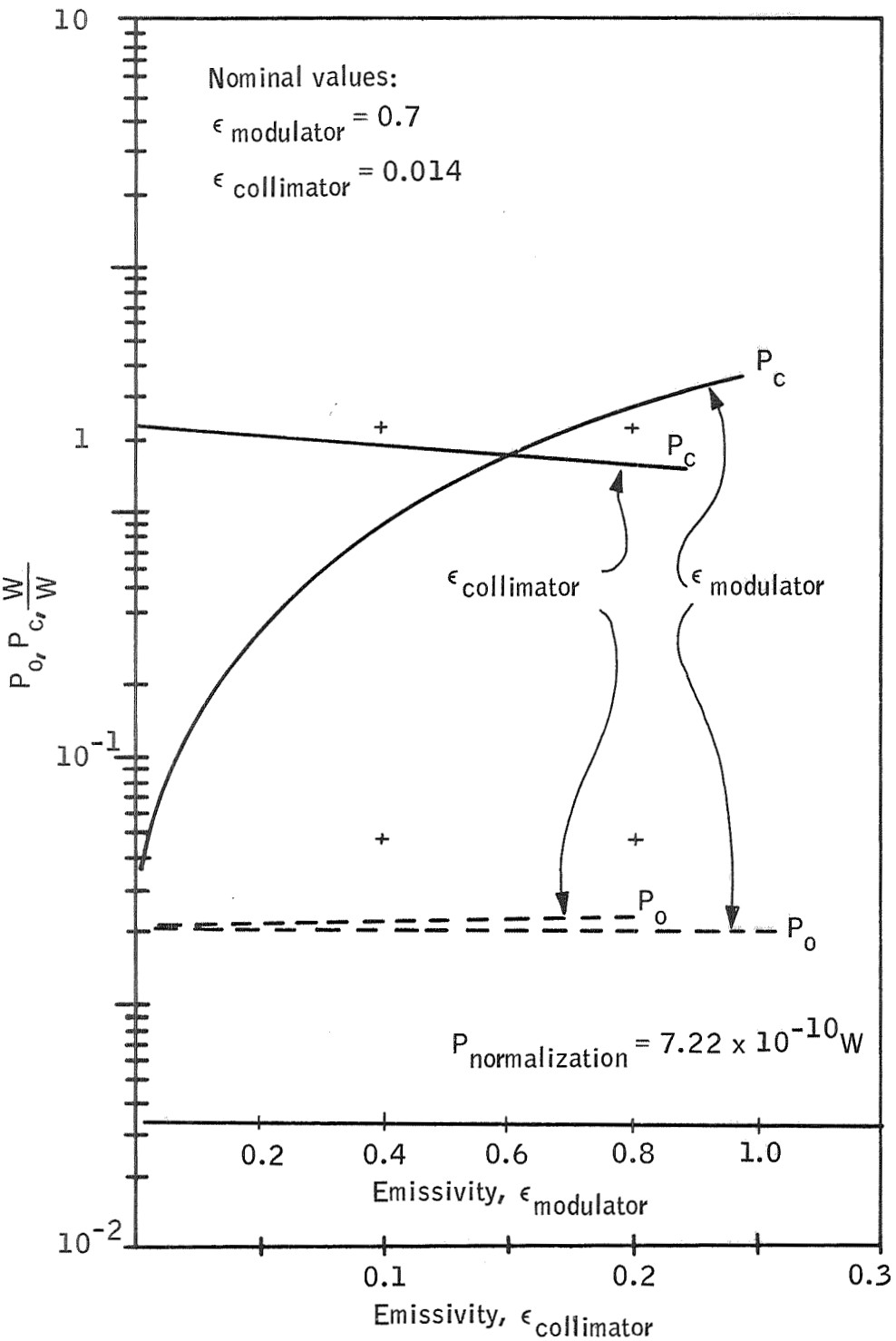

Figure 32. Normalized Power on Detector versus Emissivity, Test-Bed Model

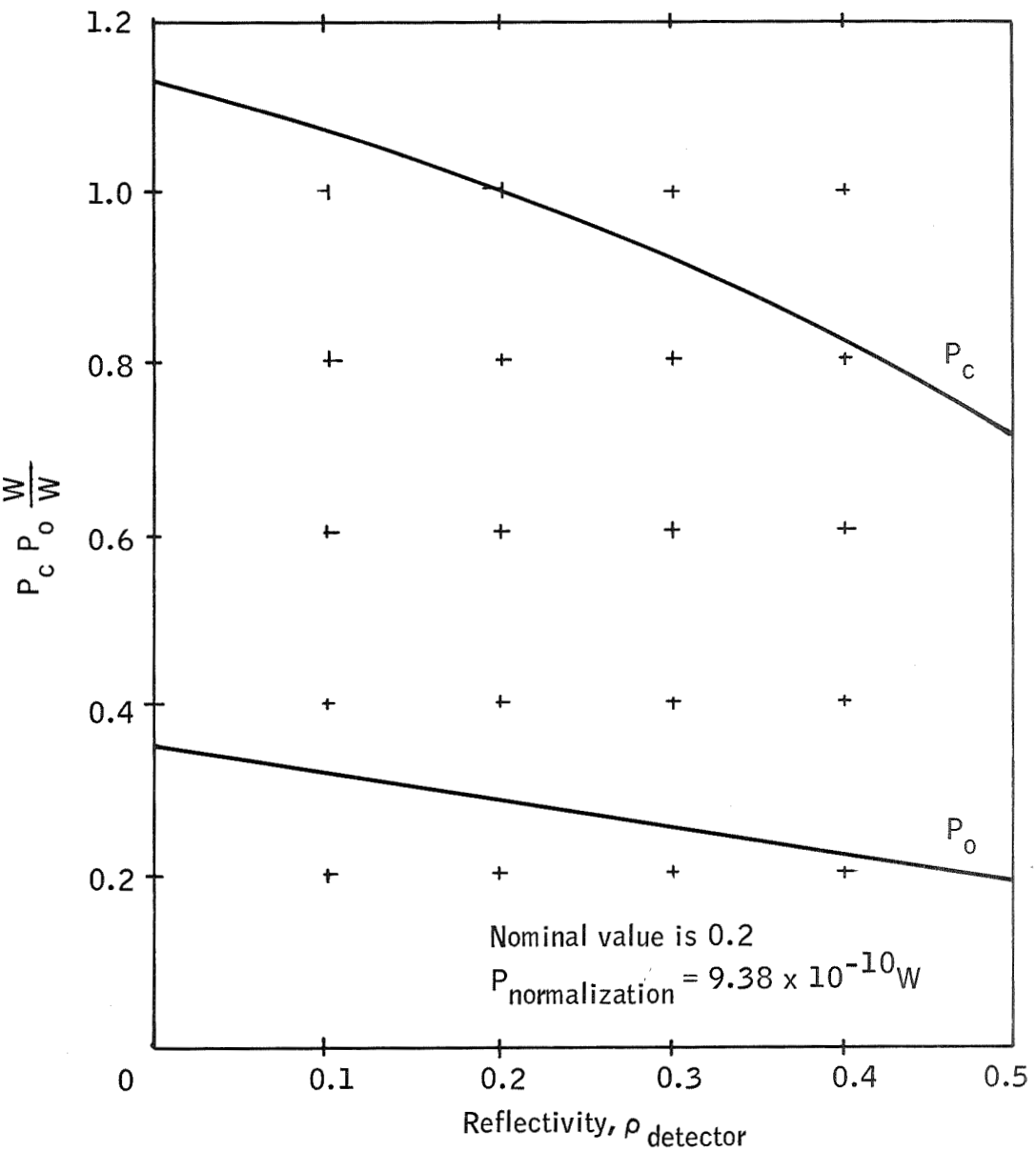

Figure 33. Normalized Power Crossing Surface of Detector versus Detector Reflectivity, Off-Axis System

summed. The results are as noted in Table 22. The sensitivity of the test-bed model to temperature change was evaluated. With all other components at nominal temperatures, the temperature of the filter, concentrator, collimator, and modulator was changed over the baseline range of 80 to 300°K. The resultant change in output power to the detector is illustrated in Figure 34.

One point worth noting is that relative measurements are more accurate than the absolute. As noted in Table 22, the relative uncertainty is only 0.606 %, and this is mainly due to uncertainty of modulator temperature.

TABLE 22. - TEST-BED MODEL UNCERTAINTIES

Parameter	Parameter uncertainty	Differential power uncertainty	Short-term relative uncertainties
Modulator emissivity	0.007 (1%)	0.93%	
Modulator temperature	0.1°K	0.60	0.6
Collimator emissivity	0.005	0.56	
Collimator temperature	0.03°K	0.002	0.002
Filter emissivity	0.002 (1%)	0.03	
Filter temperature	0.03°K	0.002	0.002
Concentrator emissivity	0.005	0.49	
Concentrator temperature	0.03°K	0.002	0.002
Total		2.63%	0.606%

Summary. -- With the short computer program it was possible to quickly manipulate the model and determine the consequences of the design decisions. An examination of the graphs presented indicates the variety of information easily obtainable and in addition suggests additional data that is of interest. This is one of the values of the analytical model and the primary rationale for using it with the aid of a digital computer.

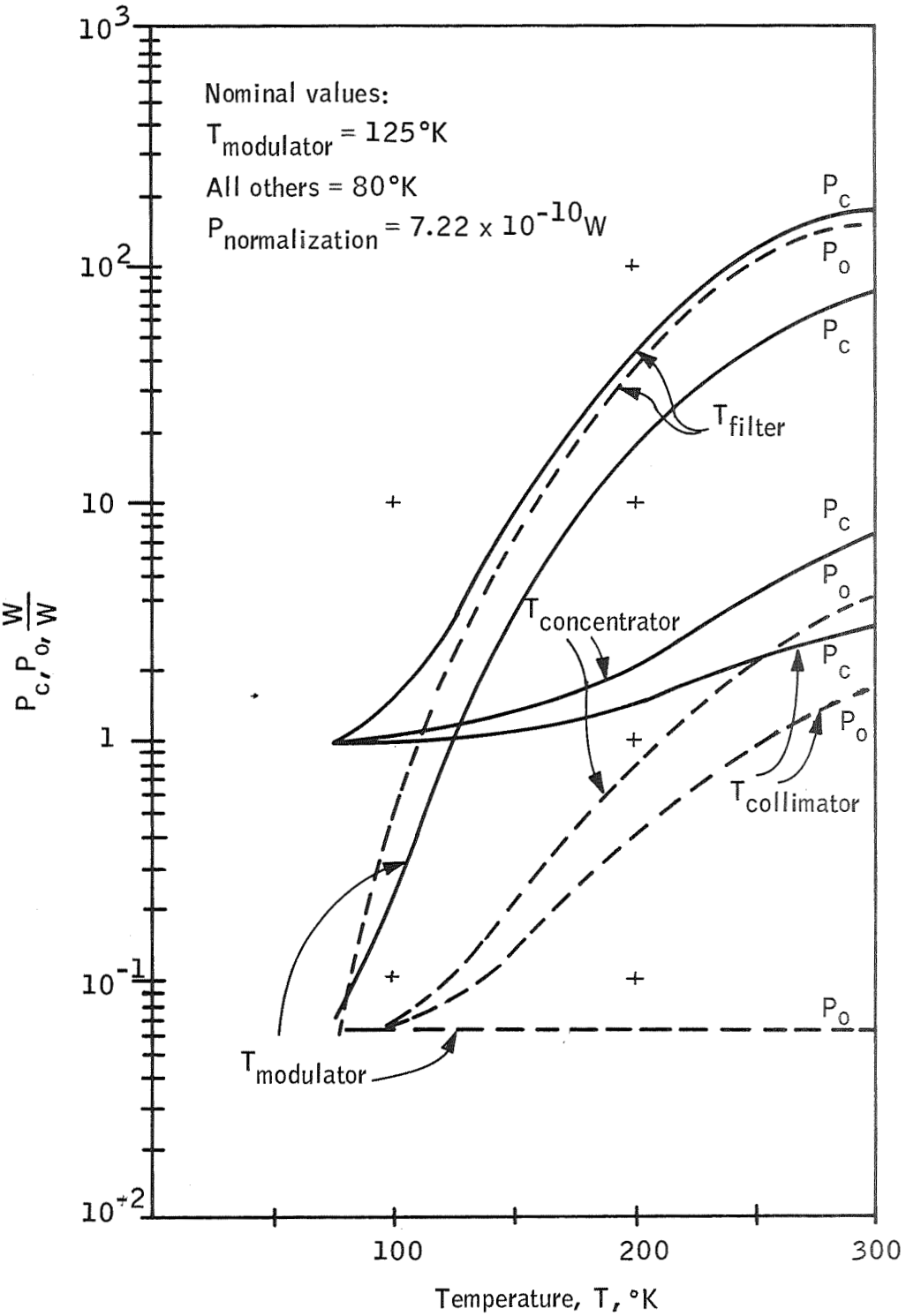

Figure 34. Normalized Power on Detector for Modulator Open and Closed versus Temperature of Various Elements, Test-Bed Model

TRANSFER FUNCTION MODEL

The previous section described an analytical model used to determine the propagation of radiant signal and noise through a radiometer, and the conversion of that radiant signal and noise into a usable electrical signal. That model was intentionally limited in its scope to include only radiant transfer and to exclude the effects of radiometer dynamics and of signal conditioning, transmittal, and reconstruction; it is then seen to be applicable to "dc radiometry", or the situation where the input radiance is emitted from an infinite, extended, constant source. If the source is time and space varying, as is the general case, then the radiometer frequency response and the methods of signal conditioning, transmittal, reconstruction, and interpretation become significant in the preservation of accuracy and precision. This determines the requirement for a transfer function model which can account for these effects. The transfer function model must then describe all of the operations that are performed on the input signal to reproduce that signal at the system output (system includes all elements in a measurement process from actual measurement through display of the measured quantity).

OBJECTIVES

Three major problem areas exist in the design, evaluation, and eventual performance of the radiometric system in terms of its transfer function - aliasing, distortion, and the set of effects of perturbations, tolerances, drifts, and transients.

Aliasing, or sampling, error results from those residual, unaccounted for higher-frequency terms that violate the initial premise of a bandlimited input signal. Signal frequencies beyond the nominal system cutoff are there either because they were not anticipated or because of a system bandwidth constraint. The opening premise is always that the signal spectrum bounds are known; one of the ARRS objectives is to quantify, to three places, the effect of some bounded signal energy outside the nominal pass band. Signal frequencies near but less than the cutoff frequency are invaribly distorted due to the less than ideal character of the on-board analog filtering. Traditionally, this is corrected on the ground by removing the effect by division by the known transfer function in the frequency domain or deconvolution in the time domain. To attempt input-output subtraction for error analyses, it was necessary to explore such correction techniques, during which it became apparent that only with great care could such a process approach 0.1 percent reproduction in time. The problem of correction for distortion is discussed in Appendix E.

Establishment of a sufficiently sensitive analytical tool to determine the effects of small variations, assumed unknown, in the various factors comprising the transfer function is also required.

The objectives of the effort in transfer function modeling, then, are to

- Derive a model of the measurement system transfer function
- Perform analyses to provide an understanding of aliasing and distortion effects
- Perform perturbation analyses to quantify effects of tolerances, drifts, and transients

APPROACH

The starting point for deriving the model was an existing computerized radiometer model simulation (RMS).

Inputs to this time domain model were time varying scene radiance. Using multiple convolutions containing transfer function parameters, this model produced time varying radiometric outputs. To investigate correction for signal distortion in the frequency domain, two approaches were available -- add features (e. g., Fourier transform routine) to the existing time domain model or derive a completely new frequency domain model. Both approaches were used with only partial success achieved with the frequency domain model (FDM). The FDM was derived but was never successfully computerized to permit a comprehensive analysis of correction techniques. The FDM derivation and the model itself is described below to provide continuity with future efforts.

A Fourier transform routine was added to the existing time domain model (TDM) and correction techniques were investigated.

The TDM was applied in a two-step analysis, outlined below and described in a subsequent section.

Step 1: aliasing and distortion analysis. -- The purpose of this exercise was to

- Quantify aliasing errors in the time domain
- Determine predictability of aliasing from error frequency spectra and FDM
- Determine effectiveness of correction techniques

Step 2: perturbation analysis. -- Computation was performed of the effects of

- Blur function change (defocussing)
- Chopper frequency shifts
- Chopper waveform changes
- Gate versus no-gate
- Chopper phase
- Filter shifts

MODEL DESCRIPTION

Frequency Domain Model (FDM)

The FDM is presented in four parts - detector output, signal processing, noise processing, and integrated model. In each category, an analytical expression suitable for computer programming and describing an output in the frequency domain was derived using standard convolution and transform techniques.

Detector output. -- The chopper-modulated optical radiometer system is shown schematically in Figure 35. Generally, the optics may consist of lenses, mirrors, aperture stops, and field stops. All of these elements are not necessarily placed in front of the chopper, but some may be between chopper and detector. The chopper can be considered as a stop whose position is varying with time. Therefore, an optics-chopper, time-dependent, point-spread function can be defined as

$$a = a\left[\theta, \psi, x, y, x_c(t), y_c(t), \lambda\right] \tag{12}$$

where

θ, ψ = coordinates in object plane

x, y = coordinates in detector plane

$x_c(t), y_c(t)$ = coordinates defining position of the chopper in chopping plane

λ = wavelength of radiation

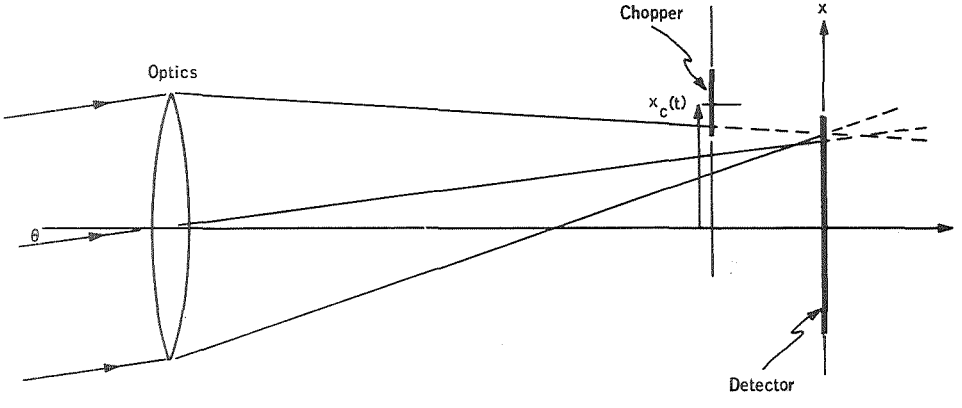

Figure 35. Chopper-Modulated Optical Radiometer System

In Figure 35, θ, x, and $x_c(t)$ are illustrated. The point-spread function (Equation 12) gives the energy-distribution at the wavelength λ in the detector plane x-y from a point object at (θ, ψ) in the object plane for the position $[x_c(t), y_c(t)]$ of the chopper in the chopping plane. For a particular optical configuration, the point-spread function is a function of six variables $(\theta, \psi$ x, y, t, $\lambda)$. Changing chopping plane and/or detector plane will give a different optics-chopper spread function.

Generally, the scene is not a point object, but an extended and nonuniform object

$$s = s(\theta', \psi', \lambda) \tag{13}$$

where θ', ψ' = coordinates in the scene's coordinate system.

A single plane contains (θ', ψ') and (θ, ψ), but their origins are separated by $[\theta_s(t), \psi_s(t)]$ for a scene moving with respect to the radiometer (e.g., a radiometer scanning a fixed scene). In Equation (13) the scene is assumed not to vary with time (in its own coordinate system $\theta' - \psi'$). Figure 37 gives the relation between θ', θ, θ_s, ψ', ψ, and ψ_s; therefore,

$$s(\theta', \psi', \lambda) = s[\theta - \theta_s(t), \psi - \psi_s(t), \lambda] \tag{14}$$

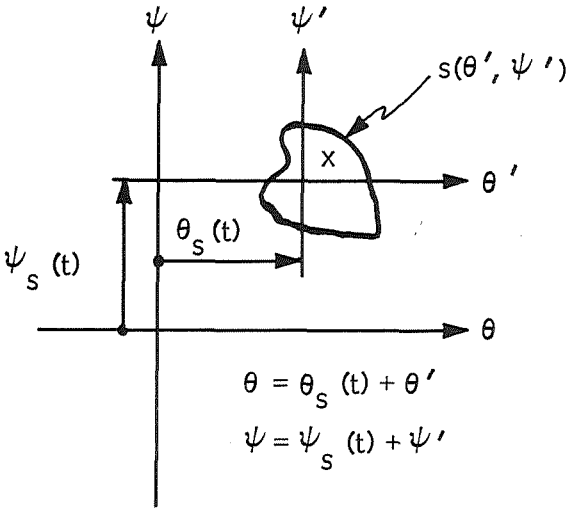

Figure 36. Image Energy Distribution in Detector Plane

The image plane energy distribution is found by integrating the product of the scene distribution times the optics/chopper point spread function over the scene coordinates, as in Equation (15).

$$f(x, y, t, \lambda) = \int_{\psi}\int_{\theta} s[\theta - \theta_s(t),\ \psi - \psi_s(t), \lambda]\ a[\theta, \psi, x, y, x_c(t),\ y_c(t), \lambda] d\theta d\psi \tag{15}$$

The detector output signal is then found by integrating, over the limits of the detector area, the product of the image plane energy distribution times the detector response, given by b (x, y, λ), as in Equation (16):

$$s_d(t) = \int_{\lambda}\int_{y}\int_{x} f(x, y, t, \lambda)\ b(x, y, \lambda)\ dxdyd\lambda = \tag{16}$$

$$\int_{\lambda}\int_{y}\int_{x}\int_{\psi}\int_{\theta} s[\theta - \theta_s(t),\ \psi - \psi_s(t)]\ a[\theta, \psi, x, y, x_c(t),\ y_c(t)]\ b(x, y, \lambda) d\theta d\psi dx dy d\lambda$$

Equation (16) is the most general form of the time dependent detector output. However, in the general form shown, Equation (16) is not amenable to efficient computer usage and does not give the output in the frequency domain as required. Certain limiting assumptions will now be applied to achieve a usable function describing the detector output frequency content. These assumptions are that

- Chopping is done in the detector plane.
- The optics point-spread function is space invariant; i.e., varying object position causes the image plane energy distribution to shift position but not change shape.
- Scanning is done only in the θ direction with constant scan velocity $\dot{\theta}$.
- The scene is constant in the direction normal to scan, the ψ direction.
- Chopping is done in a manner that produces a nearly square wave output from the detector.
- Spectral integration over the wavelength limits of the instrument response will be dropped for simplicity but understood to be finally required.

With the above assumptions, the optics/chopper point-spread function is separable into an optics line-spread function (since the scene is constant normal to the scan direction) and a periodic chop wave as follows:

$$a[\theta, \psi, x, y, x_c(t),\ y_c(t),\ \lambda] = O(x-\theta)\ c(t) \tag{17}$$

where

$O(x-\theta)$ = one dimensional optics line spread function

$c(t)$ = chop wave = $\begin{cases} 1, & \text{chopper open} \\ 0, & \text{chopper closed} \end{cases}$

The scene function reduces to

$$s(t) = s(\theta - \dot{\theta}t) \tag{18}$$

and the detector response reduces to

$$b(x, y, \lambda) = b(x) \tag{19}$$

The time-dependent detector output, previously given by Equation (16), then reduces to Equation (20),

$$s_d(t) = c(t) \int_x \int_\theta s(\theta - \dot{\theta}t) \; O(x-\theta) \; b(x) \; d\theta dx \tag{20}$$

Transformation to the frequency domain is now readily accomplished as follows. Using an intermediate variable, s'(t), [the integral part of Equation (20)] the detector output is:

$$s_d(t) = c(t) \; s'(t) \tag{21}$$

The Fourier transform of Equation (21) gives

$$S_d(f) = C(f) * S'(f) \tag{22}$$

where * denotes convolution.

The chop wave, c(t), is periodic and, using standard Fourier expansions, can thus be represented by

$$c(t) = \sum_{n=-\infty}^{\infty} c_n \, \epsilon^{\, j2\pi \, n \, f_c \, t} \tag{23}$$

where f_c = chop frequency

and

$$c_n = f_c \int_0^{1/f_c} c(t) \; \epsilon^{\, -j \, 2 \, \pi \, n \, f_c \, t} \tag{24}$$

The frequency domain representation of the chop wave is the Fourier transform of Equation (23)

$$C(f) = \sum_{n=-\infty}^{\infty} C_n \; \delta(f - n f_c) \tag{25}$$

where δ = Dirac delta function.

The term s'(t) in Equation (21) can be shown to transform into

$$S'(f) = M(f)\, S(f) \tag{26}$$

where

M(f) = optics/detector transfer function = O(f) B(f), and

S(f) = scene frequency distribution

Then, substituting Equations (25) and (26) into Equation (22), the detector output in the frequency domain becomes

$$S_d(f) = \sum_{n=-\infty}^{\infty} C_n\, M(f - nf_c)\, S(f - nf_c \tag{27}$$

Equation (27) is the desired representation of the detector output spectra. It will be used again later when the frequency domain representation of the detector signal processing electronics has been derived.

Detector signal processing. -- A linear detector signal processing system is shown in Figure 37. Since it includes the detector amplifier, $H_1(t)$ has a bandpass character. As will be shown under detector noise processing, it is important that $H_1(f)$ filters out the detector 1/f noise if g(t) has a d-c component. Typically, g(t) is a demodulating and/or gating wave to demodulate the modulated detector output $s_d(t)$ and/or to gate out the chop transients. One reason for this possible gating is to reduce the effect of extraneous, unpredictable, modulated chopper radiation during the transient. Other reasons are reduction of chopper instability effects, reduction of chop-modulator phase instability effects, and, less likely, reduction of frequency instability effects in chop and demodulator waves, all shown to be critical in the analysis presented in Appendix G. If g(t) has a demodulating effect, then $h_2(t)$ is typically a lowpass filter or integrator. If, however, g(t) does not have this effect, then $h_2(t)$ is chosen as a bandpass filter to pass the still modulated signal. To digitize the output from $h_2(t)$ for telemetry transmission, d(t) is a sampling pulse train. A reconstruction filter $h_3(t)$ is at the receiving station. This filter typically is an interpolation filter with a flat frequency response from zero frequency to half sampling frequency and zero response beyond this latter frequency.

The output of the system in Figure 37 is given by

$$s_o(t) = \left[\left(\left\{[s_d(t) * h_1(t)]\; g(t)\right\} * h_2(t)\right) d(t)\right] * h_3(t) \tag{28}$$

where * denotes convolution.

Convolution and multiplication in time domain is equivalent to multiplication and convolution, respectively, in the frequency domain. The Fourier transform of the signal output is thus

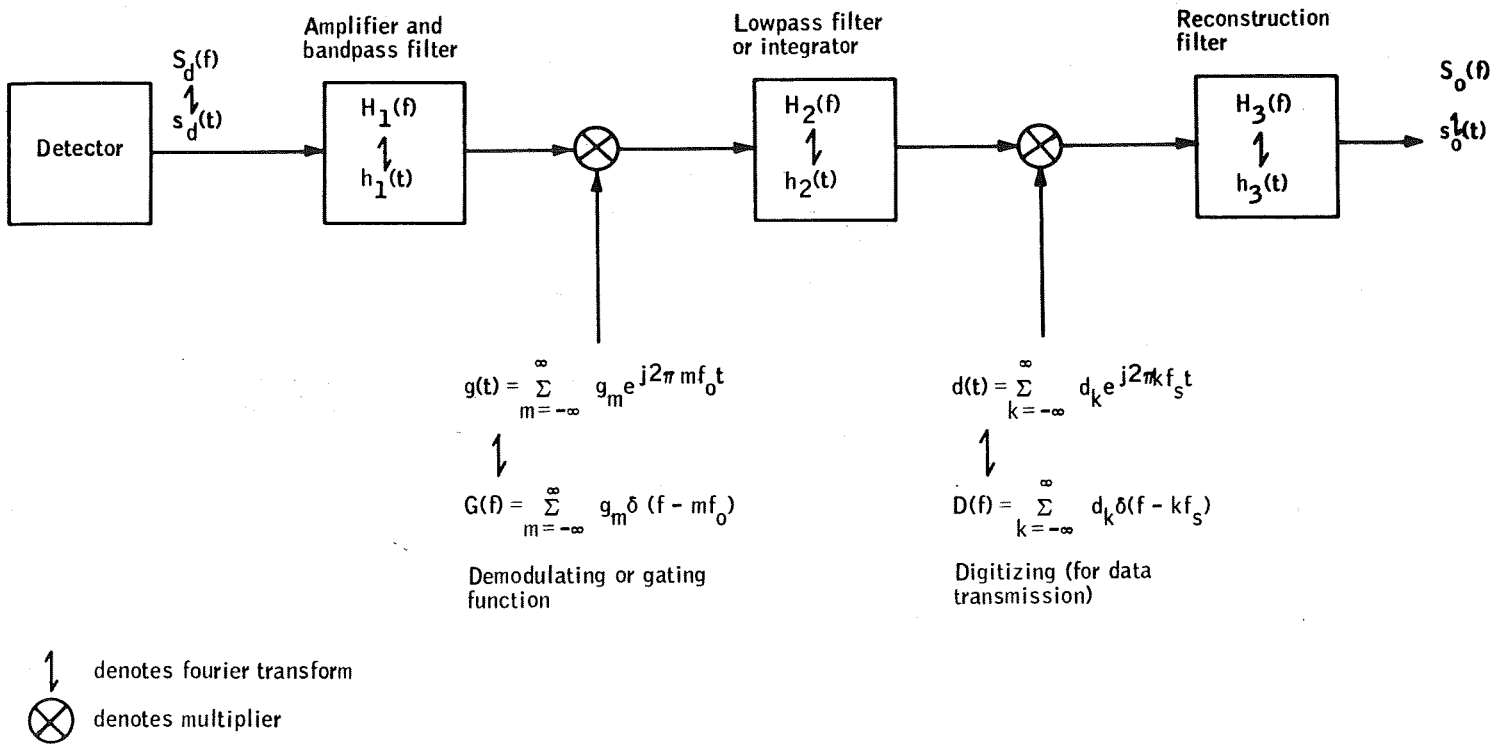

Figure 37. Detector Signal Processing

$$S_o(f) = \left[\left(\left\{[S_d(f)\ H_1(f)] * G(f)\right\} H_2(f)\right) * D(f)\right] H_3(f) \tag{29}$$

As g(t) and d(t) are periodic, one can write

$$g(t) = \sum_{m=-\infty}^{\infty} g_m\ e^{jm2\pi f_o t} \tag{30}$$

$$d(t) = \sum_{k=-\infty}^{\infty} d_k\ e^{jk2\pi f_s t} \tag{31}$$

where

$1/f_o$ = period of g(t)

$1/f_s$ = period of d(t)

$$g_m = f_o \int_o^{1/f_o} g(t)\ e^{-jm2\pi f_o t}\ dt \tag{32}$$

$$d_k = f_s \int_o^{1/f_s} d(t)\ e^{-jk2\pi f_s t}\ dt \tag{33}$$

From Equations (31) and (32) the Fourier transforms of g(t) and d(t), respectively, are obtained

$$G(f) = \sum_{m=-\infty}^{\infty} g_m\ \delta(f - mf_o) \tag{34}$$

$$D(f) = \sum_{k=-\infty}^{\infty} d_k\ \delta(f - kf_s) \tag{35}$$

The first convolution in Equation (29) then becomes

$$[S_d(f)\ H_1(f)] * G(f) = \sum_{m=-\infty}^{\infty} \left\{g_m [S_d(f)\ H(f)] * \delta(f - mf_o)\right\}$$

$$= \sum_{m=-\infty}^{\infty} g_m\ S_d(f - mf_o)\ H(f - mf_o) \tag{36}$$

Similarly for the second convolution,

$$\left(\left\{[S_d(f)\, H_1(f)] * G(f)\right\} H_2(f)\right) * D(f) = \left[H_2(f) \sum_{m=-\infty}^{\infty} g_m S_d(f-f_o)\, H_1(f-mf_o)\right] * D(f)$$

$$= \sum_{k=-\infty}^{\infty} d_k \left[H_2(f) \sum_{m=-\infty}^{\infty} g_m S_d(f-mf_o)\, H_1(f-mf_o)\right] * \delta(f-kf_s) \tag{37}$$

$$= \sum_{k=-\infty}^{\infty} d_k H_2(f-kf_s) \sum_{m=-\infty}^{\infty} g_m S_d(f-mf_o-kf_s)\, H_1(f-mf_o-kf_s)$$

and the Fourier transform of the output signal is thus

$$S_o(f) = H_3(f) \sum_{k=-\infty}^{\infty} \sum_{m=-\infty}^{\infty} d_k\, g_m\, S_d(f-mf_o-kf_s)\, H_1(f-mf_o-kf_s)\, H_2(f-kf_s) \tag{38}$$

Detector noise processing.--The expression for the mean square of the output noise $n_o(t)$ in Figure 38 will be in terms of the detector noise power spectral density $\Phi_{nn}(f)$, the transfer functions $H_1(f)$ and $H_2(f)$, the Fourier series coefficients g_m, and the fundamental frequency f_o of g(t).

Let $\langle\ \rangle$ denote expectation value and * denote convolution. The output noise in Figure 38 is given by

$$n_o(t) = \{[n(t) * h_1(t)]\, g(t)\} * h_2(t) \tag{39}$$

The mean square noise at time t_o is thus

$$\sigma_{t_o}^2 = \left\langle n_o^2(t)\right\rangle = \left\langle [\{[n(t_o) * h_1(t_o)]\, g(t_o)\} * h_2(t_o)]^2\right\rangle \tag{40}$$

Making the substitution

$$n_2(t_o) = \{[n(t_o) * h_1(t_o)]\, g(t_o)\} \tag{41}$$

in Equation (40) yields

$$\sigma_{t_o}^2 = \left\langle [n_2(t_o) * h_2(t_o)]^2\right\rangle = \left\langle \left[\int_u n_2(t_o-u)\, h_2(u)du\right]^2\right\rangle$$

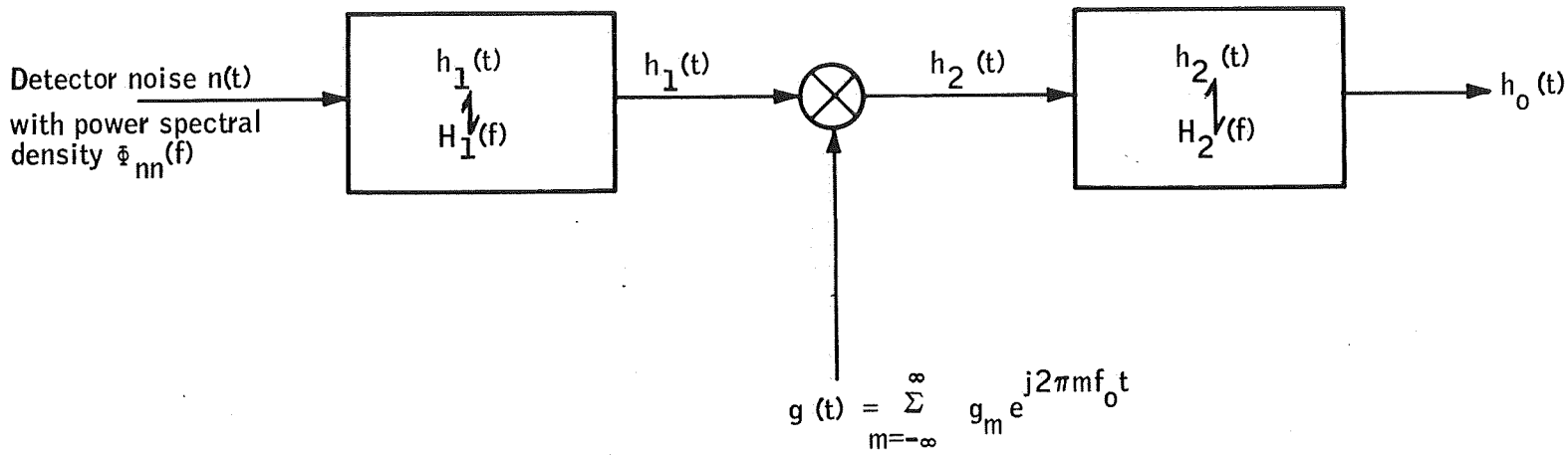

Figure 38. Detector Noise Processing

$$= \left\langle \left[\int_u n_2(t_o-u)\, h_2(u)du \right] \left[\int_v n_2(t_o-v)\, h_2(v)dv \right] \right\rangle \tag{42}$$

$$= \left\langle \iint_{u\,v} n_2(t_o-u)\, n_2(t_o-v) h_2(u)\, h_2(v)\, dvdu \right\rangle$$

$$= \iint_{u\,v} \left\langle n_2(t_o-u)\, n_2(t_o-v)\, h_2(u)\, h_2(v) \right\rangle dudv$$

$$= \iint_{u\,v} \left\langle n_2(t_o-u)\, n_2(t_o-v) \right\rangle h_2(u)\, h_2(v)\, dvdu$$

Make the substitution

$$n_1(t) = n(t) * h_1(t) \tag{43}$$

Then

$$n_2(t) = n_1(t)\, g(t) \tag{44}$$

And

$$\left\langle n_2(t_o-u)\, n_2(t_o-v) \right\rangle = \left\langle n_1(t_o-u)\, g(t_o-u)\, n_1(t_o-v)\, g(t_o-v) \right\rangle$$

$$= \left\langle n_1(t_o-u)\, n_1(t_o-v) \right\rangle g(t_o-u)\, g(t_o-v) \tag{45}$$

As the detector noise $n(t)$ is a stationary random process, so is $n_1(t)$. One can therefore write

$$\left\langle n_1(t)\, n_1(t+\tau) \right\rangle = \phi_{n_1 n_1}(\tau) = \int_{-\infty}^{\infty} \Phi_{n_1 n_1}(f)\, e^{j2\pi f\tau}\, df \tag{46}$$

where $\phi_{n_1 n_1}(\tau)$ is the auto-correlation function of the process $n_1(t)$, and $\Phi_{n_1 n_1}(f)$ is the corresponding power spectral density which is obtained as

$$\Phi_{n_1 n_1}(f) = \Phi_{nn}(f)\, |H_1(f)|^2 \tag{47}$$

Substituting Equation (47) into (46) yields

$$\left\langle n_1(t_o-u)\, n_1(t_o-v) \right\rangle = \int_{-\infty}^{\infty} \Phi_{nn}(f)\, |H_1(f)|^2\, e^{j2\pi f(u-v)}\, df \tag{48}$$

Combining (48), (45), and (42) yields

$$\sigma^2_{t_o} = \int_u \int_v \left[\int_f \Phi_{nn}(f) |H_1(f)|^2 \, e^{j2\pi f(u-v)} df \right] g(t_o-u)\, g(t_o-v)\, h_2(u)\, h_2(v)\, dv\, du$$

$$= \int_f \Phi_{nn}(f) \, |H_1(f)|^2 \left[\int_u g(t_o-u)\, h_2(u)\, e^{j2\pi fu}\, du \right] \left[\int_v g(t_o-v)\, h_2(v)\, e^{-j2\pi fv}\, dv \right] df \qquad (49)$$

$$= \int_f \Phi_{nn}(f) \, |H_1(f)|^2 \left| \int_v g(t_o-v)\, h_2(v)\, e^{-j2\pi fv}\, dv \right|^2$$

As

$$g(t) = \sum_{m=-\infty}^{\infty} g_m \, e^{j2\pi m f_o t} \qquad (50)$$

One has

$$\int_v g(t_o-v)\, h_2(v)\, e^{-j2\pi fv}\, dv$$

$$= \sum_{m=-\infty}^{\infty} g_m \int_v h_2(v)\, e^{j2\pi m f_o (t_o-v)}\, e^{-j2\pi fv}\, dv$$

$$= \sum_{m=-\infty}^{\infty} g_m \, e^{j2\pi m f_o t_o} \int_v h_2(v)\, e^{-j2\pi v (f+mf_o)}\, dv \qquad (51)$$

$$= \sum_{m=-\infty}^{\infty} g_m \, e^{j2\pi m f_o t} \, H_2(f+mf_o)$$

Combining Equations (49) and (51) thus yields

$$\sigma^2_{t_o} = \int_{-\infty}^{\infty} \Phi_{nn}(f) \, |H_1(f)|^2 \left| \sum_{m=-\infty}^{\infty} H_2(f+mf_o)\, g_m \, e^{j2\pi m f_o t_o} \right|^2 df \qquad (52)$$

Usually the detector noise power spectal density $\Phi_{nn}(f)$ is increasing for decreasing f due to so-called 1/f noise. Equation (52) shows that there are two ways that the mean square noise $\sigma^2_{t_o}$ can be made small for the processing system in Figure 38, either by making $H_1(f)$ a highpass filter or making the sum highpass in character. The latter condition is satisfied by letting g(t) have a small or no d-c component, $g_o \approx 0$, if $H_2(f)$ is a lowpass filter. If $H_2(f)$ is a bandpass filter, the d-c component of g(t) should be large compared to the other components (g_m, $m \neq 0$).

If $H_2(f)$ is a bandpass filter with reasonably sharp cutoff, the noise out from this filter is bandlimited to a good approximation. Therefore, if to the noise processing in Figure 38 is added d(t) and $h_3(t)$ as in Figure 37, where d(t) is a sampler and $h_3(t)$ is an ideal reconstruction filter, the noise output of $h_3(t)$ will then be approximately equal to the noise output of $h_2(t)$.

If the input noise is a Gaussian random process, the output will also be a Gaussian process. The detector noise was assumed stationary above; however the output noise is not stationary because of the time-varying multiplier g(t). In other words, the probability distribution of the output noise for each t_o is Gaussian if the input is a Gaussian process, but the probability distribution is a function of t_o.

The bounds on output mean square noise $\sigma^2_{t_o}$ for all times t_o are computed in Appendix F and are shown to satisfy

$$1.0\ N_o(f_o/2) \lesssim \sigma^2_{t_o} \lesssim 1.4\ N_o(f_o/2)$$

($N_o = \Phi_{nn}(f)$ for white noise)

Integrated Model. -- The complete frequency domain model of the total system output consists of the combination of Equations (27), giving the detector output, and (38), giving the signal processed output. For clarity and completeness, these equations and their proper combining will be given here with definitions of terms available in the previous paragraphs.

Equation (38) gave the system output signal as

$$S_o(f) = H_3(f) \sum_{k=-\infty}^{\infty} \sum_{m=-\infty}^{\infty} d_k g_m S_d(f-mf_o-kf_s) H_1(f-mf_o-kf_s) H_2(f-kf_s) \quad (53)$$

The detector output, S_d, was given by Equation (27) as

$$S_d(f) = \sum_{n=-\infty}^{\infty} c_n \; M(f - nf_c) \; S \; (f - nf_c) \tag{54}$$

The final form of the signal output is then found by properly combining Equation (54) with Equation (53) and rearranging to obtain

$$S_o(f) = H_3(f) \sum_n \sum_m \sum_k \bar{c}_{n-m} g_{m-k} d_k \; S_i(f-nf_o) \; M(f-nf_o) \; H_1(f-mf_o) \; H_2(f-kf_o) \tag{55}$$

Equation (55) is the final form of the frequency domain model of the signal. The complete FDM consists of Equation (55) and Equation (52), which gives the noise output.

Time Domain Model

The digital RMS program using time-domain simulation yields the time response and its Fourier transform of the radiometer signal processing system for any time-varying input and system parameters. The system that the RMS program was used to simulate for ARRS is shown in Figure 39. Note here that the "near square wave" chopping approximation is used.

The radiance input to the system is given as a time function, which can be tied to a radiance in space via the radiometer scan velocity. For this application, the input variability is one dimensional and the optics are specified by their line-spread function. As the optics in the simulation runs were assumed diffraction limited with a circular aperture, the line spread function involves the first-order Struve function. The parameter inputs to this function are aperture size and wavelength, which then give the line-spread function with angle as variable. The line-spread function is assumed space-invariant; that is, it is independent of the position of a line object with respect to the optical axis.

The program computes an optics-detector line-spread function by convolving the optics line-spread function with the one-dimensional detector response, the latter being assumed constant over the entire detector. For each input the (unchopped) detector output is then given as the convolution of the input function and the optics-detector line-spread function. There is a normalization built into the program such that the infinite integral over the optics line-spread function is unity when angle (in radians) is the variable. This corresponds to the modulation transfer function of the optics having a response of unity at zero frequency. With this normalization the unchopped detector output is equal to the detector width (in radians) for a unit d-c input.

The detector output as a function of time is then multiplied by the chop wave. The parameters of the chop wave are turn on, on, turn off, off times, and phase relation between input and chop wave.

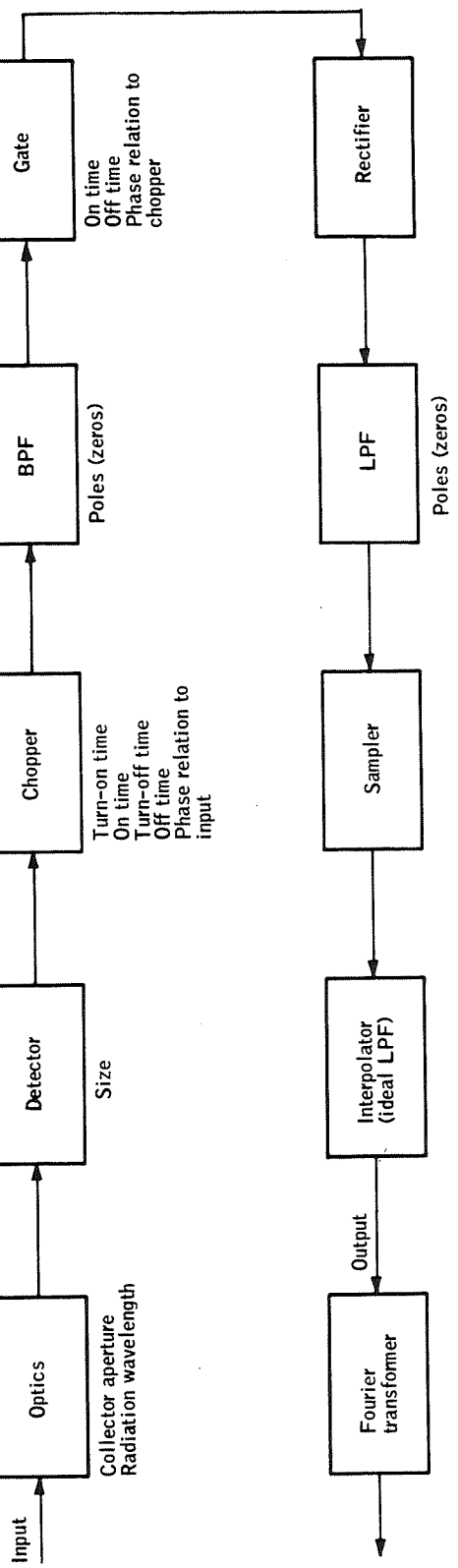

Figure 39. RMS Program Block Diagram

The program solves the differential equation for the bandpass filter with the chopper output as input to the bandpass filter. The bandpass filter output can be obtained as the solution to a differential equation as the bandpass filter is specified by its poles and zeros.

The signal is then multiplied by a gate wave synchronous with the chop wave. On time, off time, and phase relation between gate and chop waves are parameters.

Rectification is accomplished by taking the absolute value of the signal. Another and often preferable, way of rectifying is sometimes used in an actual system. The signal in this case would be multiplied by a rectifying wave, synchronous with the chop wave and gate wave. This synchronous rectification scheme should also be simulated, as these two schemes are not equivalent due to the distorting effect of the bandpass filter.

The simulation of the lowpass filter is analogous to that of the bandpass filter.

Sampling is done by taking the value of the lowpass filter output at evenly spaced intervals with the frequency of the chop wave.

The interpolation by ideal lowpass filtering is accomplished by adding the impulse responses excited by the impulse train output from the sampler. For a given time span of the output no truncation, either in the summation or in impulse responses, is done. The only parameter of the ideal lowpass filter is the cutoff frequency, which is equal to half chop frequency.

Because of the character of the input (finite impulse train) to the ideal lowpass filter, the Fourier transform of the filter output is computed analytically by the program.

Model Application

As mentioned previously in the discussion of transfer function model approach, a two-step analysis was conducted; one dealing with aliasing and distortion analysis, called "step 1" below, and the other dealing with perturbation analysis, called "step 2".

Subsequent paragraphs present details of steps 1 and 2 and significant conclusions drawn from the results. Related transfer function model analyses are presented in Appendix G.

Step 1: Aliasing and distortion analysis. -- This initial set of computations was performed with nominal system parameters as listed below.

- Optics line-spread function =

$$\begin{cases} \dfrac{H_1\left(\frac{2\pi D}{\lambda}\theta\right)}{\left(\frac{2\pi D}{\lambda}\right)\theta^2}, & \text{for } |\theta| < \theta_o \\ 0, & \text{for } |\theta| > \theta_o \end{cases}$$

where

$H_1(x)$ = first-order Struve function

λ = wavelength = $2\pi/4200$ cm $\approx 14.96\,\mu$

D = aperture diameter = 40 cm

θ = coordinate in rad

- Detector width = β = 0.0096°
- Scan rate = $\dot{\phi}$ = 19.2°/ sec
- Chop frequency = f_c = 4000 Hz
- Chop wave 1:2:1:2 for turn on, on, turn off, and off time ratio
- Bandpass filter: two-pole Butterworth with 3 dB cutoff at 0.1 x 4000 Hz and 5 x 4000 Hz

$$H_1(s) = \frac{K_1 s^2}{\left[(s+\omega_1)^2 + \omega_1^2\right]\left[(s+\omega_2)^2 + \omega_2^2\right]}$$

$K_1 = 1.575 \times 10^{10}$

$\omega_1 = 88800$

$\omega_2 = 1776$

- Gate wave: 1:2:1:2 for off, positive on, off, and negative on time ratio. Synchronous with chop wave.
- Lowpass filter: two-pole Chebychev, 0.1 dB ripple, with 3 dB cutoff at 2000 Hz

$$H_2(s) = \frac{K_2}{(s+\omega_3)^2 + \omega_4^2}$$

$K_2 = 1.285 \times 10^8$

$\omega_3 = 7390$

$\omega_4 = 8600$

- Sampling frequency = f_c = 4000 Hz
- Reconstruction filter = $H_3(f) = \begin{cases} 1, & |f| < f_c/2 = 2000 \text{ Hz} \\ 0, & |f| > f_c/2 = 2000 \text{ Hz} \end{cases}$
- Correction factor

$$H(f) = M(f)\, H_2(f) \sum_{m=-\infty}^{\infty} c_{-m}\, g_m\, H_1(f - mf_c)$$

$$M(f) = \frac{2}{\pi}\left[\cos^{-1}\frac{\lambda|f|}{\dot{\phi}} - \frac{\lambda|f|}{\dot{\phi}D}\sqrt{1 - \left(\frac{\lambda|f|}{\dot{\phi}D}\right)^2}\right]\frac{\sin \pi(f/\dot{\phi})\alpha}{\pi(f/\dot{\phi})}$$

$$c_m = \frac{1}{m\pi}\, e^{-jm\pi(a+b)} \sin m\pi(a+b)\, \frac{\sin m\pi a}{m\pi a}$$

$a + b = 1/2$ $\qquad g_m = \begin{cases} (-1)^{(m+1)/2}\, \frac{2j}{m\pi} \sin m\pi b, & m \text{ odd} \\ 0, & m \text{ even} \end{cases}$

$a = 1/6$ = trapezoidal chop wave rise (or fall) time, expressed as fractional part of chop wave period

$b = 1/3$ = trapezoidal chop wave on (or off) time, fractional part of chop wave period

for the above parameters, the input data were sine waves with frequencies 0.4 f_c, 0.5 f_c, 0.6 f_c, 0.8 f_c fc, 1.2 f_c, and a duration time sufficient to reach a steady-state condition.

Typical examples of Step 1 outputs are presented in Figures 40, 41, and 42 for three frequencies near the nominal system cutoff. Note that the reconstructed output is that prior to correction; peculiarities of the particular family of systems being simulated prevented meaningful use of the correction factor, as will be discussed later in this section.

Figure 40 depicts the response of the system to an input sunusoid at 0.4 f_c. At the detector output the envelope is attenuated significantly but not as much as the higher frequency sine wave, a disparity normally removed at the end by the correction factor. The short time to reach steady-state response is approximately one cycle and represents the optics blur function width. At the system output, however, some leading and trailing edge overshoot is evident and is related to the electronic filter transient response. This latter effect would also normally be removed by correction. In Figure 41, the input signal is precisely at the first zero in the detector spatial frequency response and, accordingly, produces only the envelope at the detector output. However, the reconstructed system output exhibits decidedly anomalous behavior -- a ripple term at 0.5 f_c which should not be passable by the system. This term is present in varying degrees for all the runs made and is related to the problem of performing a meaningful correction for distortion.

Figure 42 shows the response of the system to a sine wave at 0.6 f_c, above the nominal cutoff frequency. Here the detector-optics combination has a response (analogous to the first lobe in the sin x/x function) but reversed in sign. This can be seen by close inspection of the middle curve. The reconstructed output is the aliasing signal produced by the imperfect but representative character of the electronic filtering prior to sampling. Note that the output frequency is $f_c - 0.6\ f_c = 0.4\ f_c$, which is in the information bandwidth and has become indistinguishable from a true signal at 0.4 f_c. This is an uncorrectable error and is in no way to be confused with the above mentioned anomalous behavior. The following is a summary of typical aliasing effects:

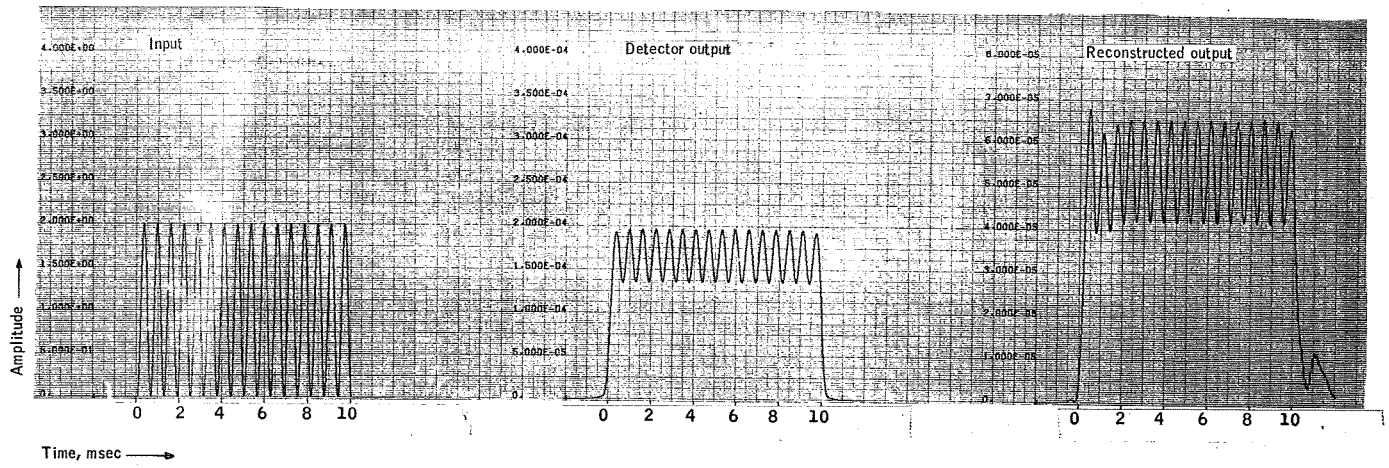

Figure 40. Step 1 Computer Output for Input Frequency $0.4\ f_c = 1600$ Hz

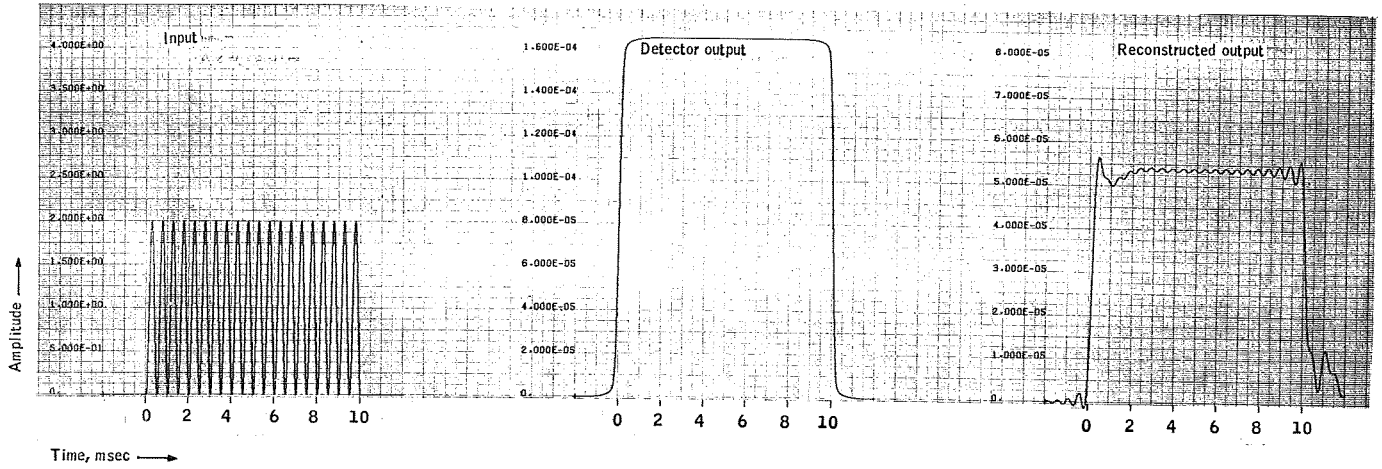

Figure 41. Step 1 Computer Output for Input Frequency $0.5\ f_c = 2000$ Hz

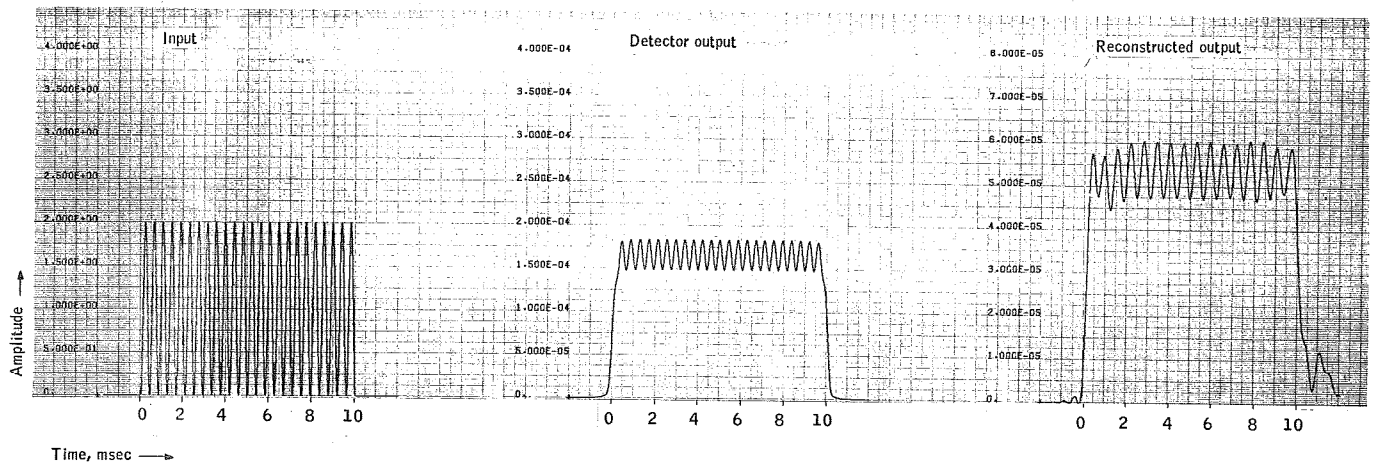

Figure 42. Step 1 Computer Output for Input Frequency $0.6\ f_c = 2400$ Hz

Input signal frequency	Output signal frequency	Output signal magnitude normalized to input
0.6 f_c	0.4 f_c	0.53
0.8 f_c	0.2 f_c	0.15
1.2 f_c	0.2 f_c	0.05

These results indicate the care which must be taken to recover one percent radiometric measurement accuracy, even at very low frequencies. In making the initial assumption of a band-limited input signal spectrum, the amount of signal energy outside the nominal limits should be known to be less than a few percent. More study is necessary, however, to better quantify this error source for an appropriate range of electronic filter and chopping rate combinations.

The difficulty experienced with the correction factor noted above may be explained as follows. The ripple term produced at 0.5 f_c occurs in the system after the detector. The correction factor, which includes the detector response, has a zero at 0.5 f_c. Therefore, the process of division by the correction factor in the frequency domain blows up near 0.5 f_c and the resultant spectrum cannot be transformed back into the time domain. Figure 43 illustrates this problem for a signal at 1/8 f_c (500 Hz). The source of this effect turned out to be real; it is associated with the synchronous rectification technique used, where synchronism was made with signal zero-crossing rather than with the chopper wave itself. Because of unavoidable assymetries produced by the bandpass filter, this rectification scheme produces subharmonics of the chop frequency proportional to the signal components that are also subharmonics - but not necessarily the same ones - of the chop wave.

Investigation of this effect produced an alarming number of ways in which spurious submultiples of the chop frequency could be produced. The solutions to this problem range from exercising great care during design and test to the brute-force approach of using a very high chopping rate. The latter is strongly recommended to the extent practical.

In Appendix G, the variation of an aliased signal output as a function of the input signal phase is noted. To explore this effect, the Step 1 runs were repeated for five different phase relations, representing shifts of 0, 0.05, 0.15,

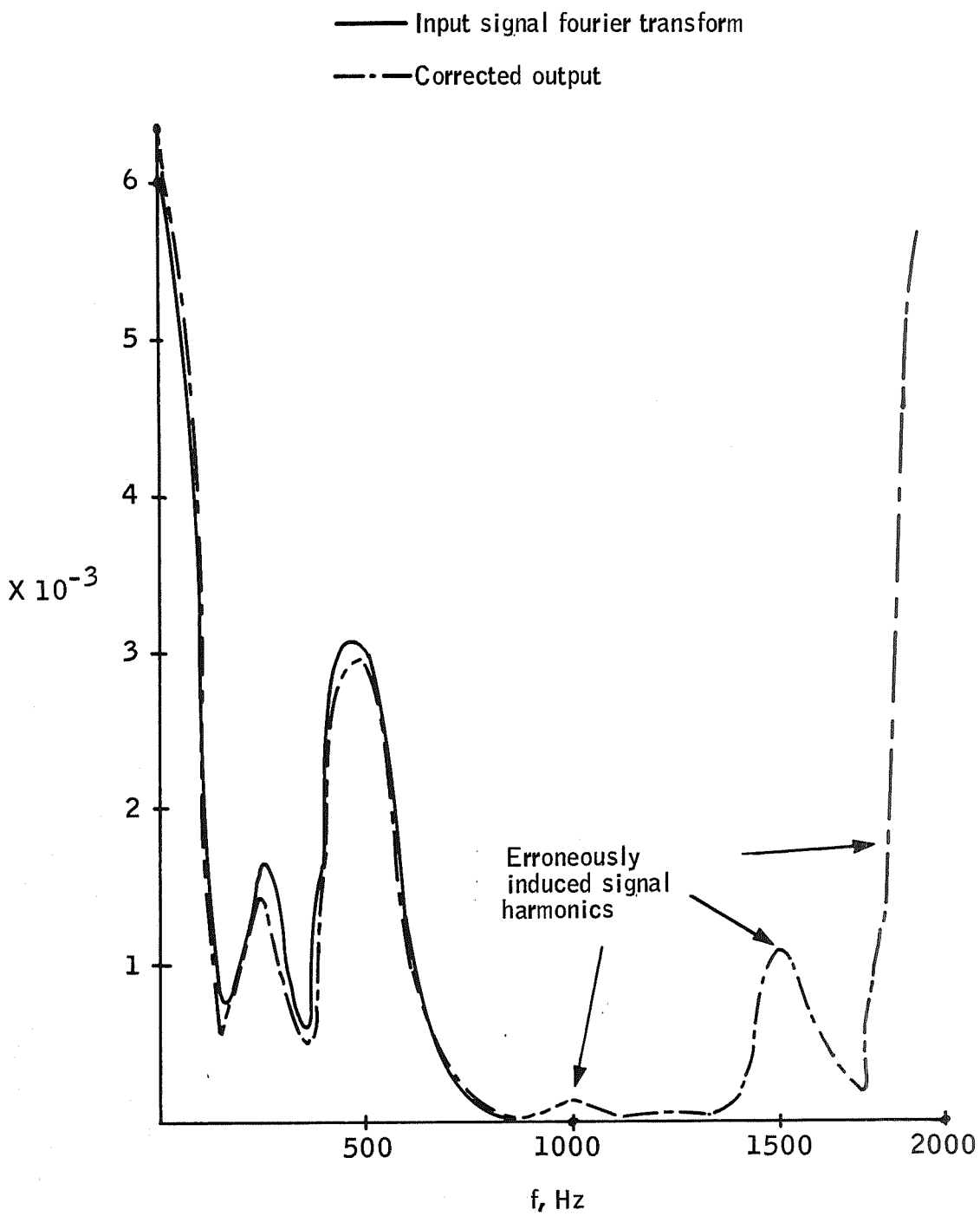

Figure 43. Input Signal Fourier Transform and Corrected Output Spectrum

0.10, and 0.20 relative to the chop wave period, Figures 44 and 45 show two of these runs for 0.4 and 0.6 f_c. In Figure 44, note that the well-behaved character of the output for this inband signal does not persist for other than zero signal-chopper phase relations. A small oscillation at 0.1 f_c can be noted at the intermediate phasings, probably due to aliasing terms associated with the leading and trailing edges. In Figure 45 the entire output sine wave is aliasing error. Hence this figure shows the total phase dependence of aliasing, which is surprisingly small. This phase dependence would produce a "noise" or short-term repeatability type of error and, as summarized in Figure 46, should be gratifyingly small for reasonable out-of-band signal levels.

Step 2: Perturbation analysis -- Two types of variability were analyzed - gross variations (e.g., x2) representing design ranges and small changes typical of tolerancing and drifts. Table 23 summarizes the computer runs made in this area and the printouts published.

Two frequencies were used as shown in Figure 47. This figure depicts an entire flow for the nominal system parameters used in Step 2.

Note that the ripple term of 0.5 f_c is much larger in the $f_c/6$ (666 2/3 Hz) output than in the $f_c/2.5$ (1600 Hz) output. This is particularly obvious in the last curves in the flow, the corrected frequency spectra. Other features displayed in these figures are

- Assymmetry and overshoot produced by the bandpass filter
- Imperfect on-board carrier suppression (lowpass)
- The presence of the ripple term on the trailing edge of the fc/6 reconstructed output
- The spurious harmonics in the fc/6 uncorrected spectrum and the results after correction

Figures 48 through 60 show the results of variations in blur function, chop frequency, chop and gate waveforms, and lowpass filter. These are discussed in the following paragraphs.

Figures 48 through 51 show the effects of combined blur circle and detector size variation up to a factor of two. The attenuation associated with the optical transfer function (product of detector and optics MTF) is precisely as expected (see Figures 49 and 51), and it is interesting to note that the ripple term is also reduced. This is because the variations in the assymetries produced by the bandpass filter, which couple with the rectifier to produce the ripple term, are reduced by the blurring.

Figures 52 through 55 are some of the outputs for chopping frequency variations. For these runs the gate and sample waves, reconstruction filter, and correction factor were all varied in consonance with the chopper wave, thus isolating the aliasing effects. As can be seen, the signal is progressively cleaner for higher rates and, as verified by the frequency spectra, the spurious harmonics are driven to zero.

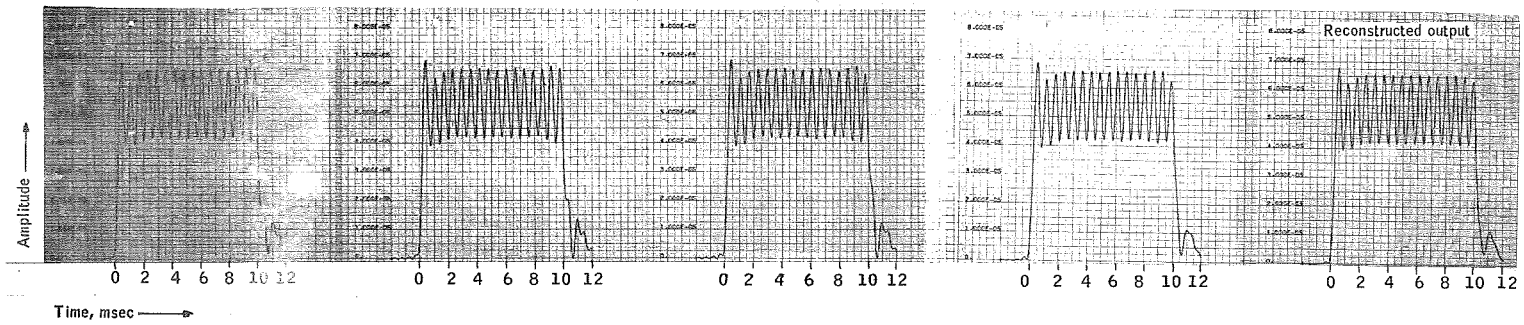

Figure 44. Reconstructed Output for Five-Phase Relations Between Input and Chop Wave. $f = 0.4\ f_c = 1600$ Hz

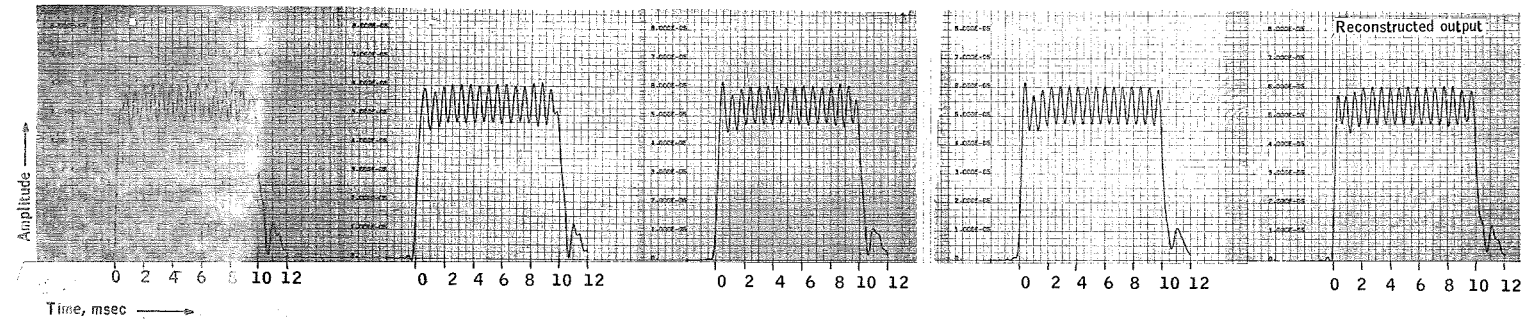

Figure 45. Reconstructed Output for Five-Phase Relations Between Input and Chop Wave. $f = 0.6\ f_c = 2400$ Hz

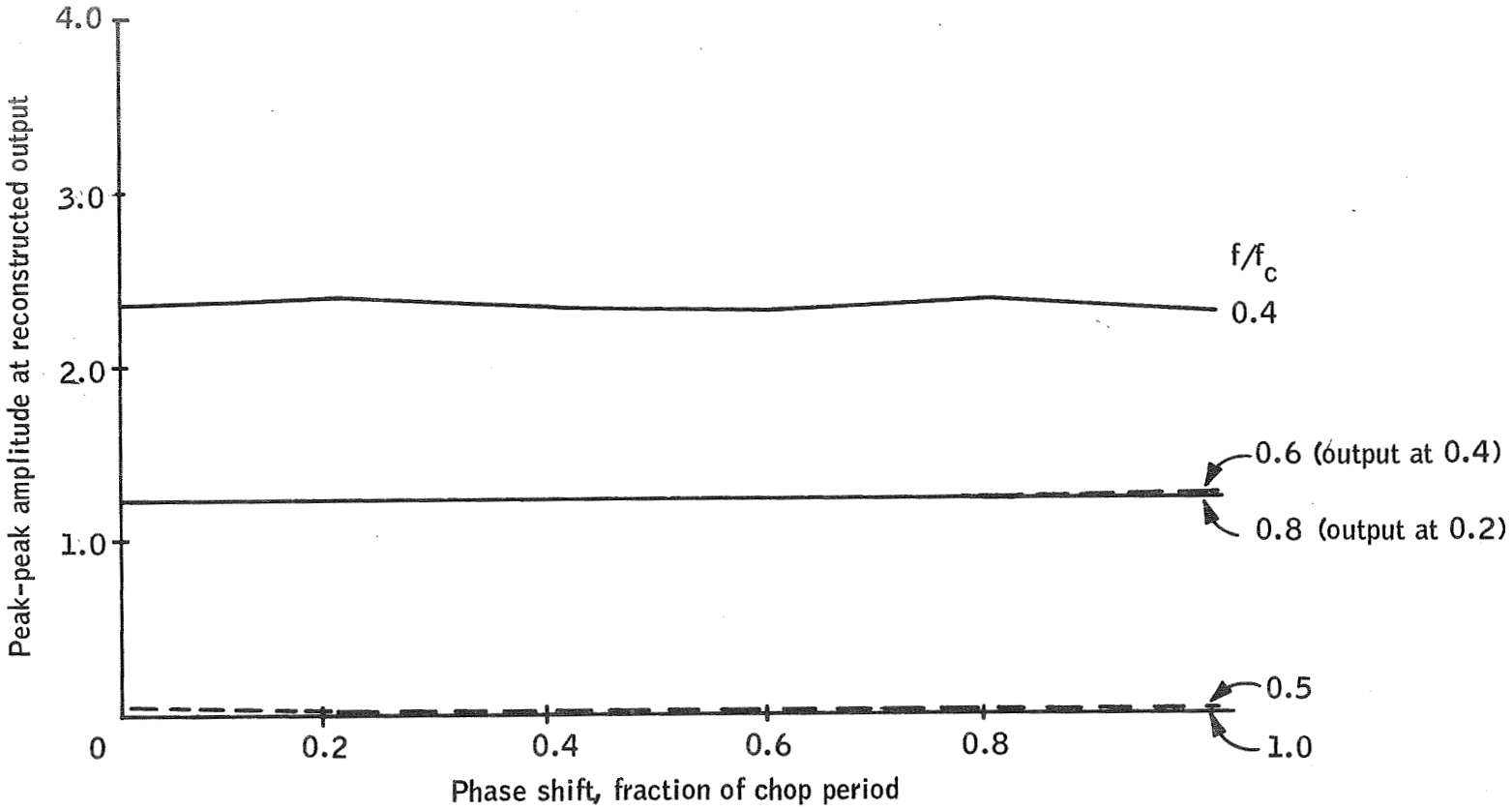

Figure 46. Phase Shift Effects

TABLE 23. - STEP 2: COMPUTER RUNS

Perturbation	Bandpass filter	Gate	Longpass filter	Plot
Optics / detector spread				
1.1x (Nominal width)				A, F, G, H
1.5x (Nominal width)				A, F, G, H
2x (Nominal width)				A, F, G, H
Chop wave				
1.1x (Nominal f_c)		1)		F, G
1.5x (Nominal f_c)	6)	1)		F, G
2x (Nominal f_c)	7)	1)		F, G
turn-on / on / turn-off / off				
$\frac{8}{48}$ $\frac{16}{48}$ $\frac{8}{48}$ $\frac{16}{48}$		3), 4), 5)		F, G
$\frac{15}{96}$ $\frac{35}{96}$ $\frac{15}{96}$ $\frac{81}{96}$ a)		2), 3)		F, G
$\frac{8}{48}$ $\frac{22}{48}$ $\frac{6}{48}$ $\frac{14}{48}$ b)		2), 3), 4), 5)		F, G
Bandpass filter				
High cutoff 0.9x	8)			F, G
Low cutoff 1.1x	9)			F, G
Lowpass filter				
3dB ripple Chebychev			10)	E, F, G
13) Cutoff 0.9x [0.1dB]			11)	F, G
14) Cutoff 0.9x [3dB]			12)	F, G
Nominal cases (two)				A, B, C, D, E, F, G, H

a) Corresponds to $\frac{\Delta A}{A} = 2.8\%$; b) Corresponds to $\frac{\Delta A}{A} = 11.3\%$

$\frac{\Delta A}{A}$ = chopper amplitude shift

TABLE 23. - STEP 2: COMPUTER RUNS (Concluded)

Input: Sine waves $666\frac{2}{3}$ Hz (8 cycles), 1600 Hz (20 cycles)

Nominal system parameters as defined in Step 1

1) Gate wave synchronous with chopper.

		Off	+On	Off	-On
2)	Nominal gate wave	$\frac{8}{48}$	$\frac{16}{48}$	$\frac{8}{48}$	$\frac{16}{48}$
3)	No gate	0	$\frac{24}{48}$	0	$\frac{24}{48}$
4)	+On, -on = 0.8x (nominal)	$\frac{11}{48}$	$\frac{13}{48}$	$\frac{11}{48}$	$\frac{13}{48}$
5)	+On, -on = 0.5x	$\frac{16}{48}$	$\frac{8}{48}$	$\frac{16}{48}$	$\frac{8}{48}$

6)	$\omega_1 = 133100$	$\omega_2 = 2660$	$K_1 = 3.54 \times 10^{10}$
7)	$\omega_1 = 177600$	$\omega_2 = 3552$	$K_1 = 6.3 \times 10^{10}$
8)	$\omega_1 = 79900$	$\omega_2 = 1776$	$K_1 = 1.276 \times 10^{10}$
9)	$\omega_1 = 88800$	$\omega_2 = 1598$	$K_1 = 1.575 \times 10^{10}$
10)	$\omega_3 = 3440$	$\omega_4 = 8110$	$K_2 = 8.02 \times 10^{7}$
11)	$\omega_3 = 6660$	$\omega_7 = 7740$	$K_2 = 1.042 \times 10^{8}$
12)	$\omega_3 = 3095$	$\omega_4 = 7300$	$K_2 = 6.50 \times 10^{7}$

A	Detector output
B	Chopper output
C	Bandpass filter output
D	Gate/rectify output
E	Lowpass filter output
F	Reconstructed output (time)
G	Fourier transform of rec. output
H	Fourier transform of corrected output

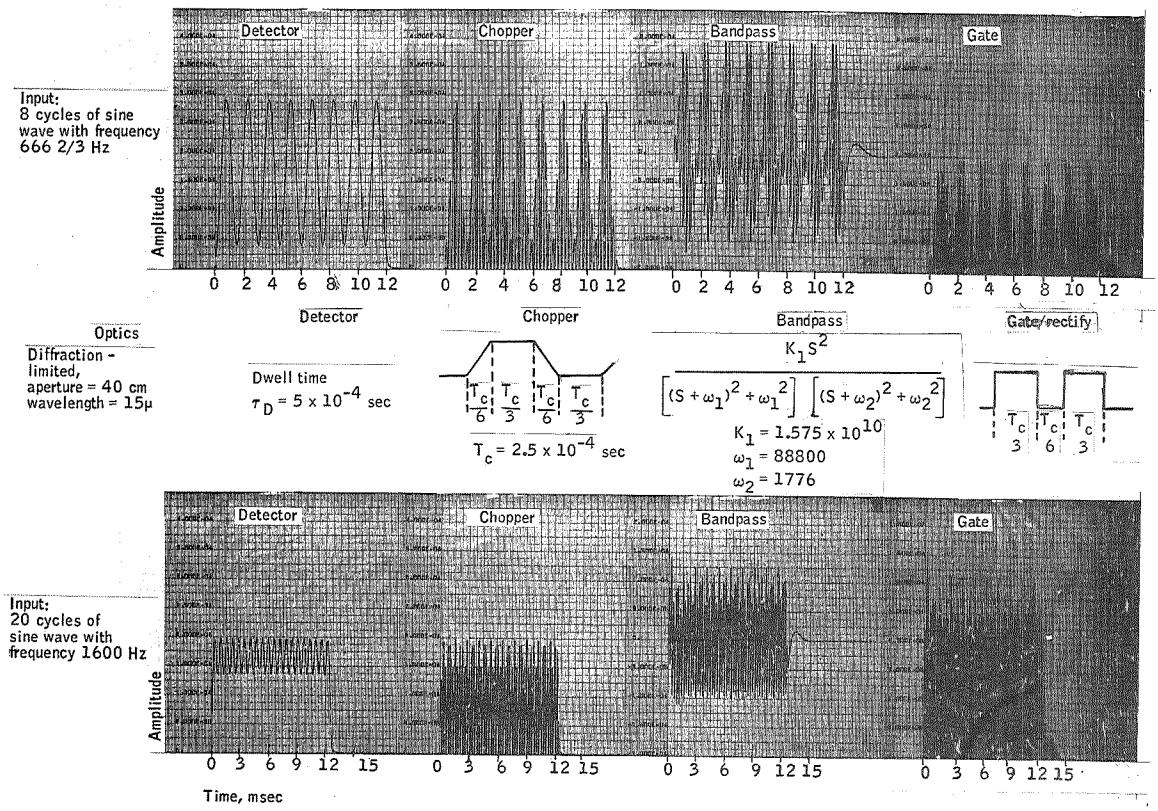

Figure 47. Step 2 Nominal Computer Run Outputs

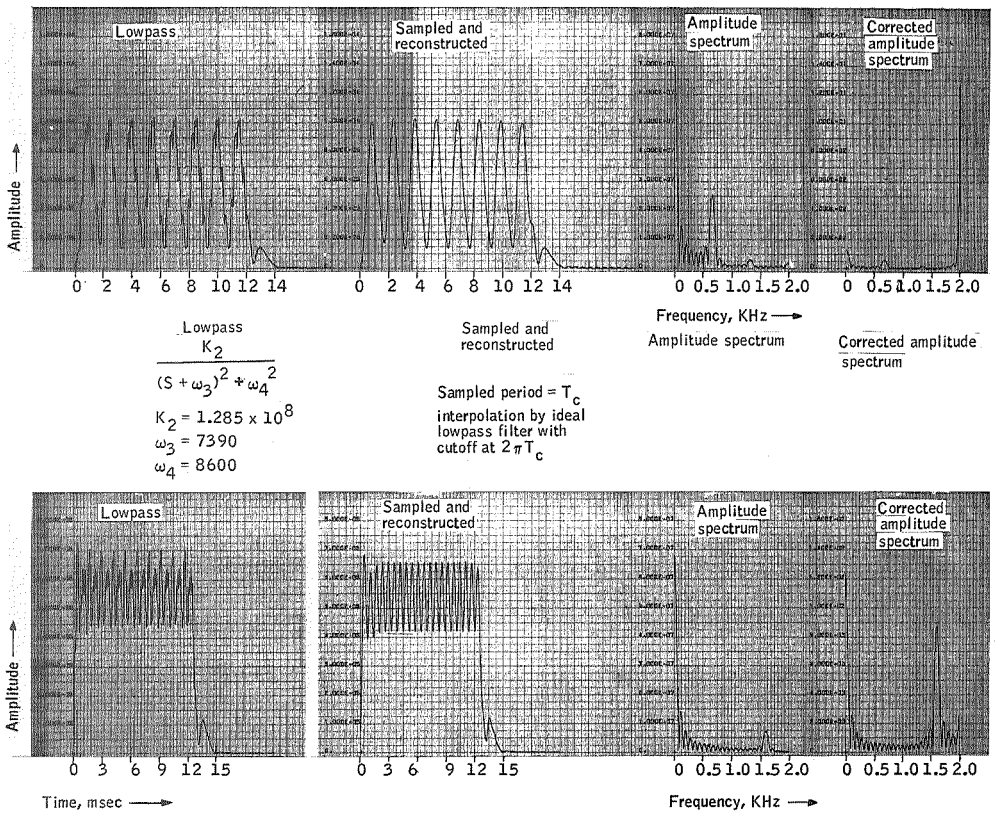

Figure 47. Step 2 Nominal Computer Run Outputs (Concluded)

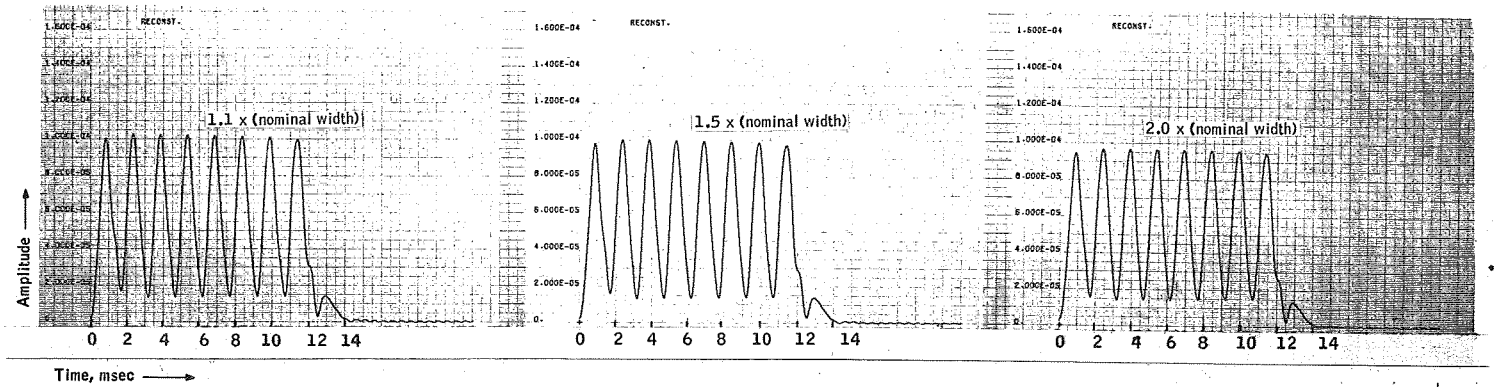

Figure 48. Effect of Change in Detector/Optics Spread Function on Reconstructed Output for Input Frequency of $f_c/6 = 667$ Hz

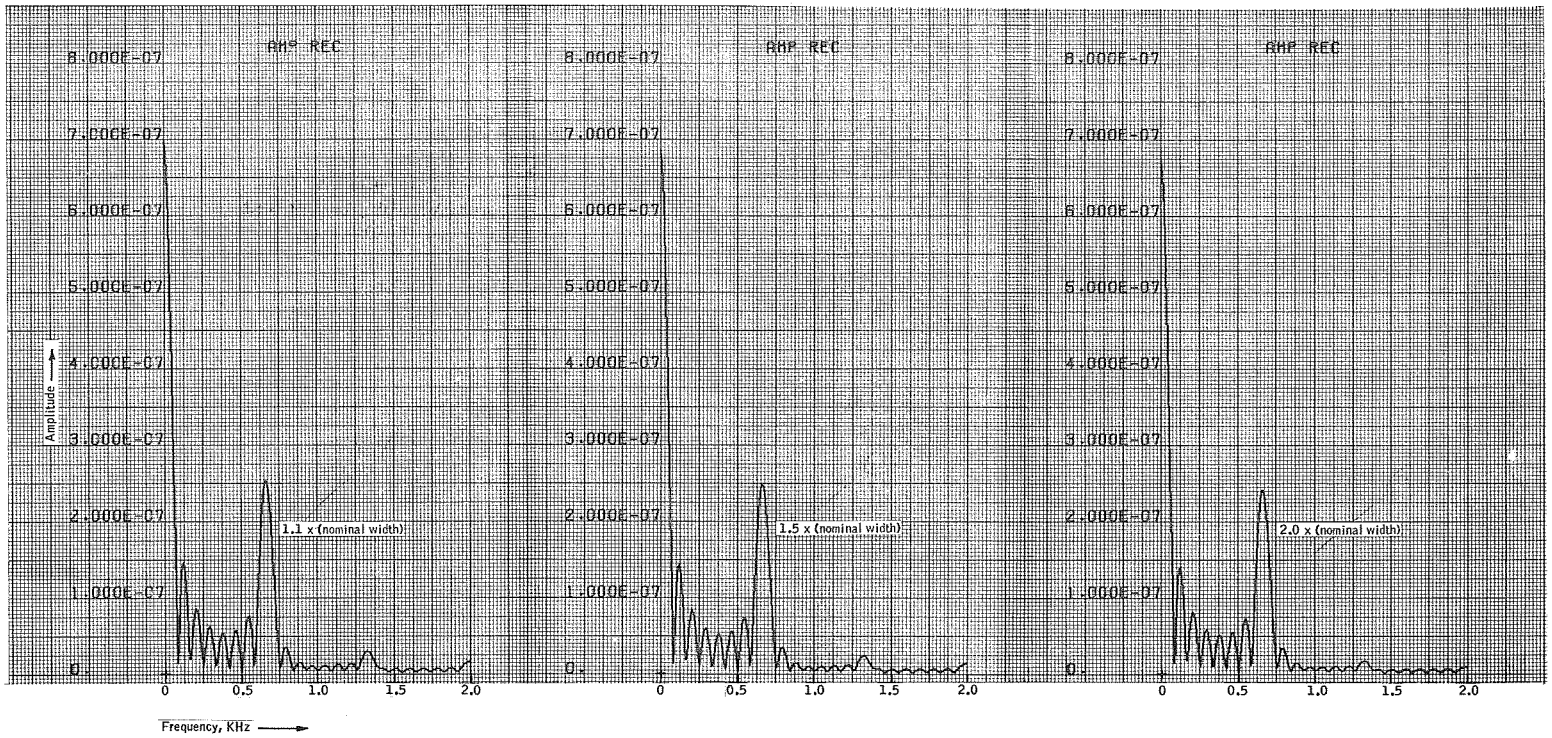

Figure 49. Effect of Change in Detector/Optics Spread Function on Amplitude Spectrum of Reconstructed Output for Input Frequency of $f_c/6$ = 667 Hz

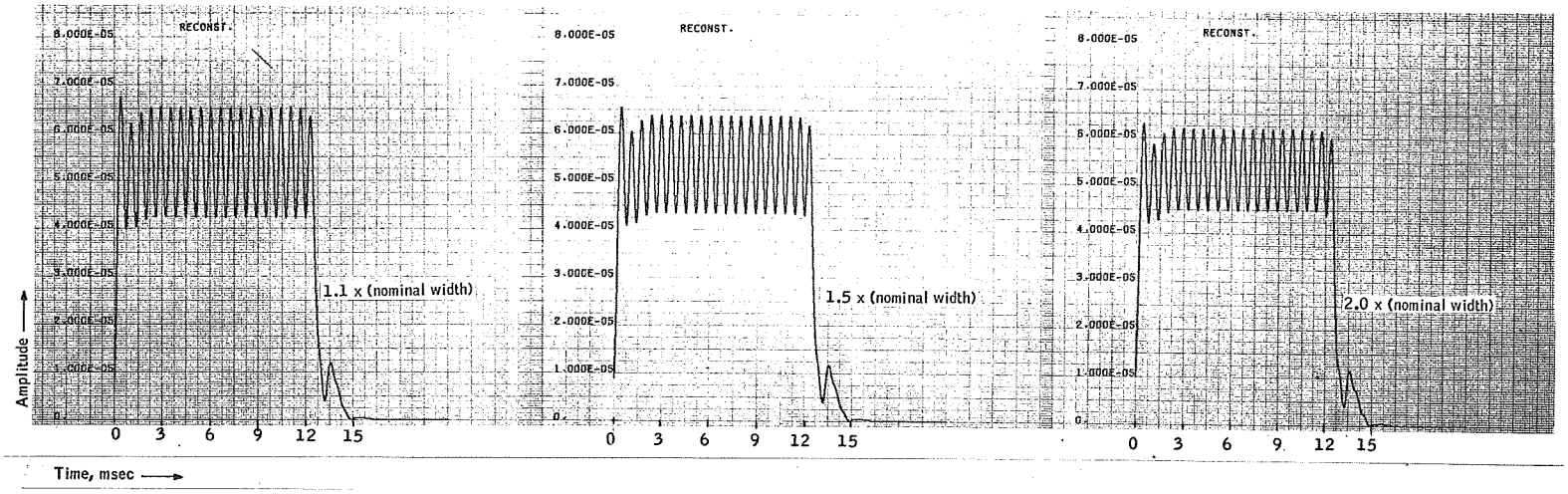

Figure 50. Effect of Change in Detector/Optics Spread Function on Reconstructed Output for Input Frequency of $f_c/6$ = 667 Hz

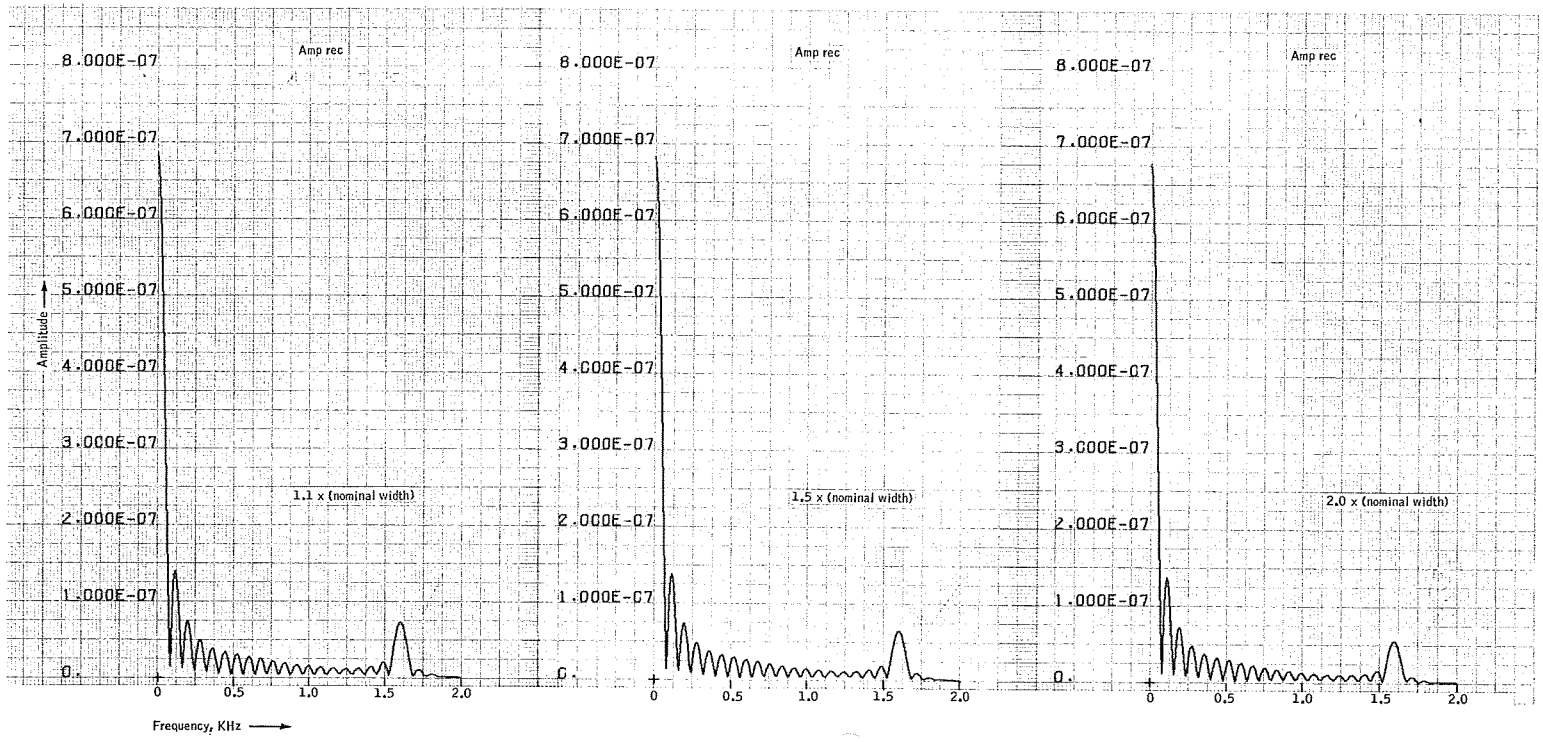

Figure 51. Effect of Change in Detector/Optics Spread Function on Amplitude Spectrum of Reconstructed Output for Input Frequency $0.4\ f_c$ = 1600 Hz

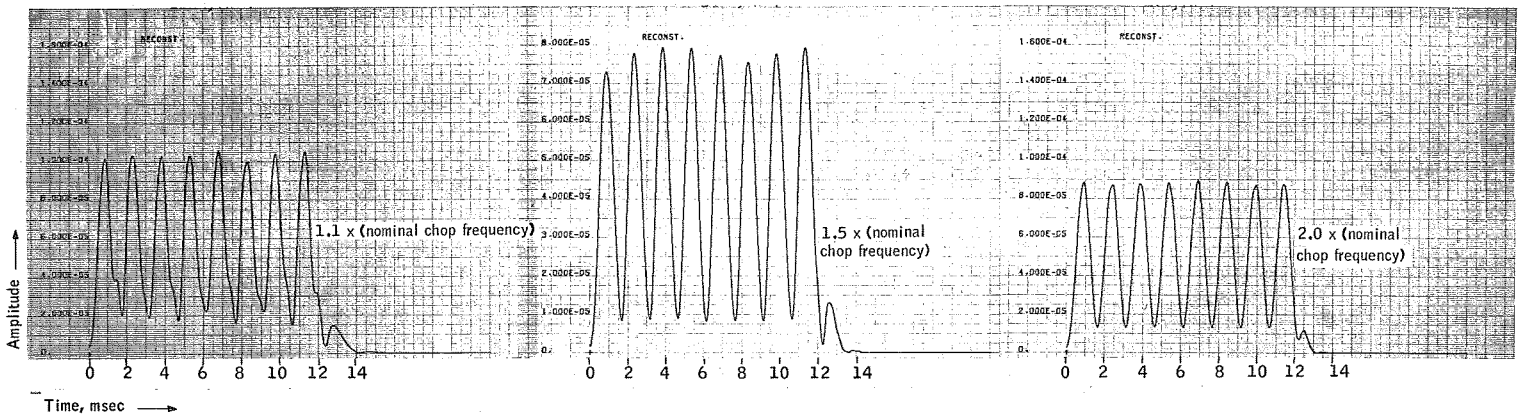

Figure 52. Effect of Change in Chop Frequency on Reconstructed Output for Input Frequency of $f_c/6$ = 667 Hz

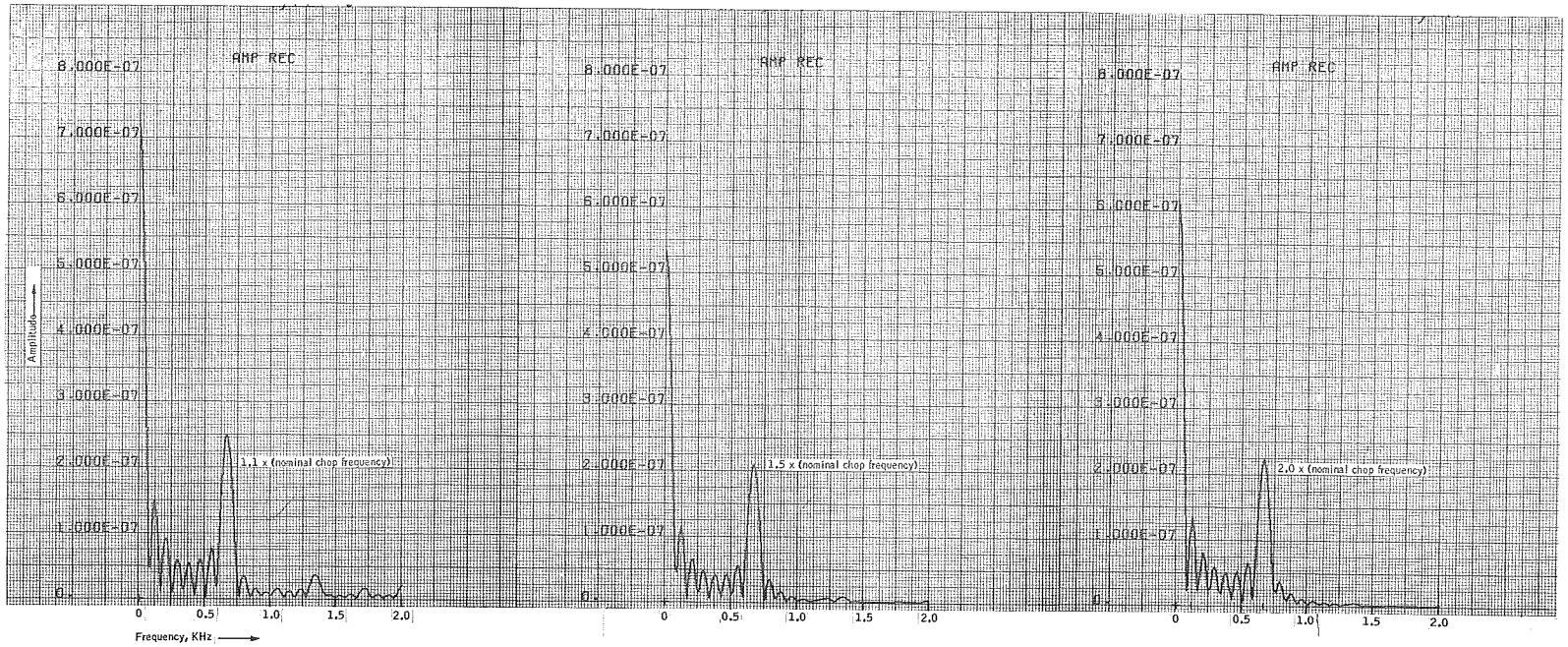

Figure 53. Effects of Change in Chop Frequency on Amplitude Spectrum of Reconstructed Output for Input Frequency of $f_c/6$ = 667 Hz

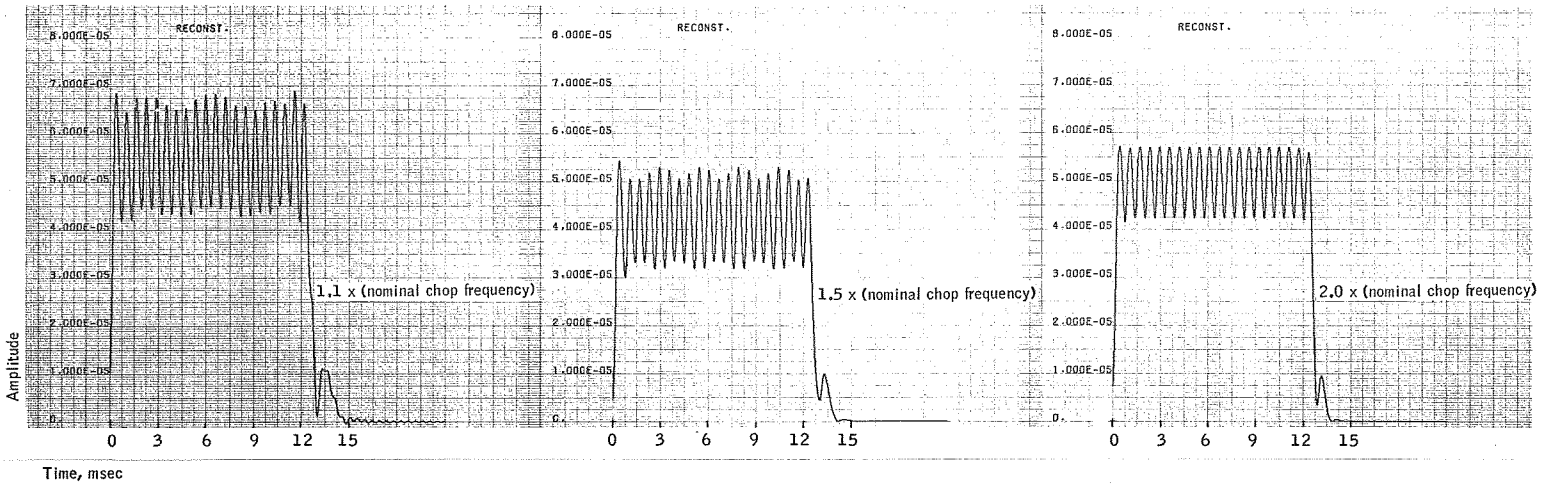

Figure 54. Effect of Change in Chop Frequency on Reconstructed Output for Input Frequency of 0.4 f_c = 1600 Hz

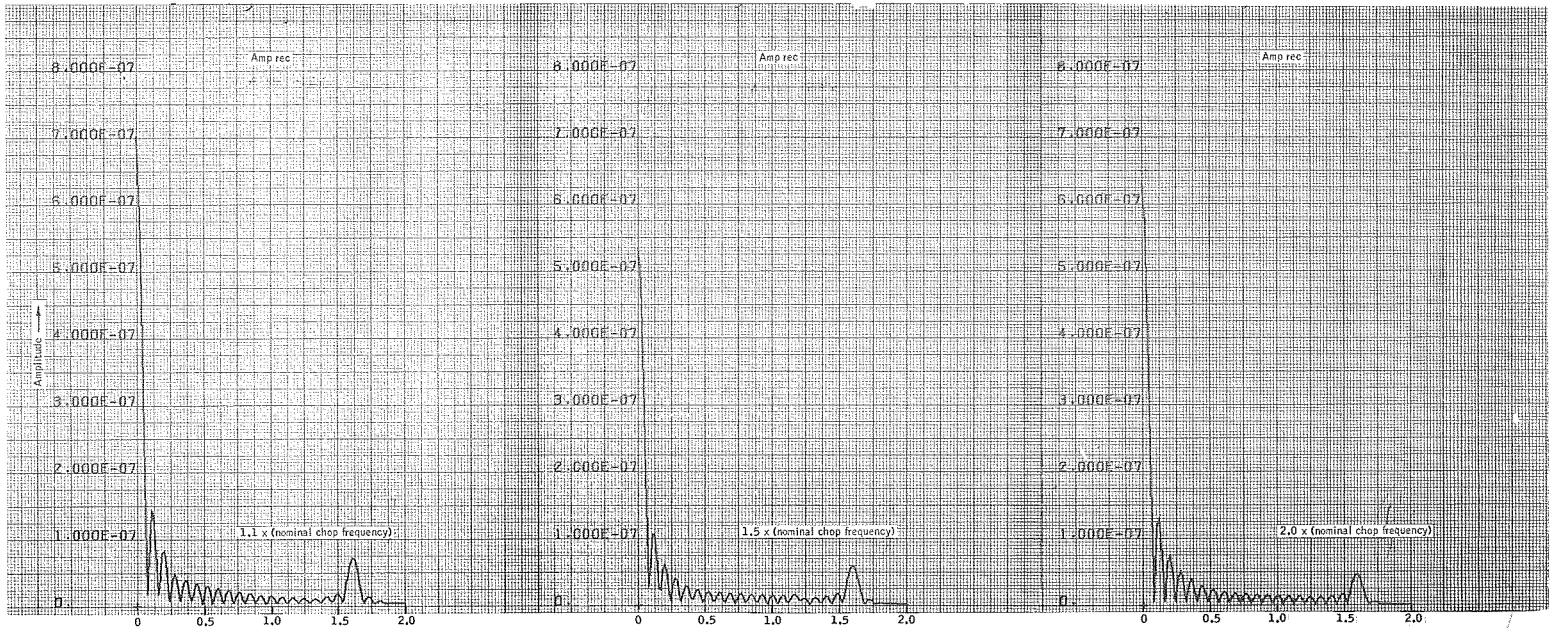

Figure 55. Effect of Change in Chop Frequency on Amplitude Spectrum of Reconstructed Output for Input Frequency of 0.4 f_c = 1600 Hz

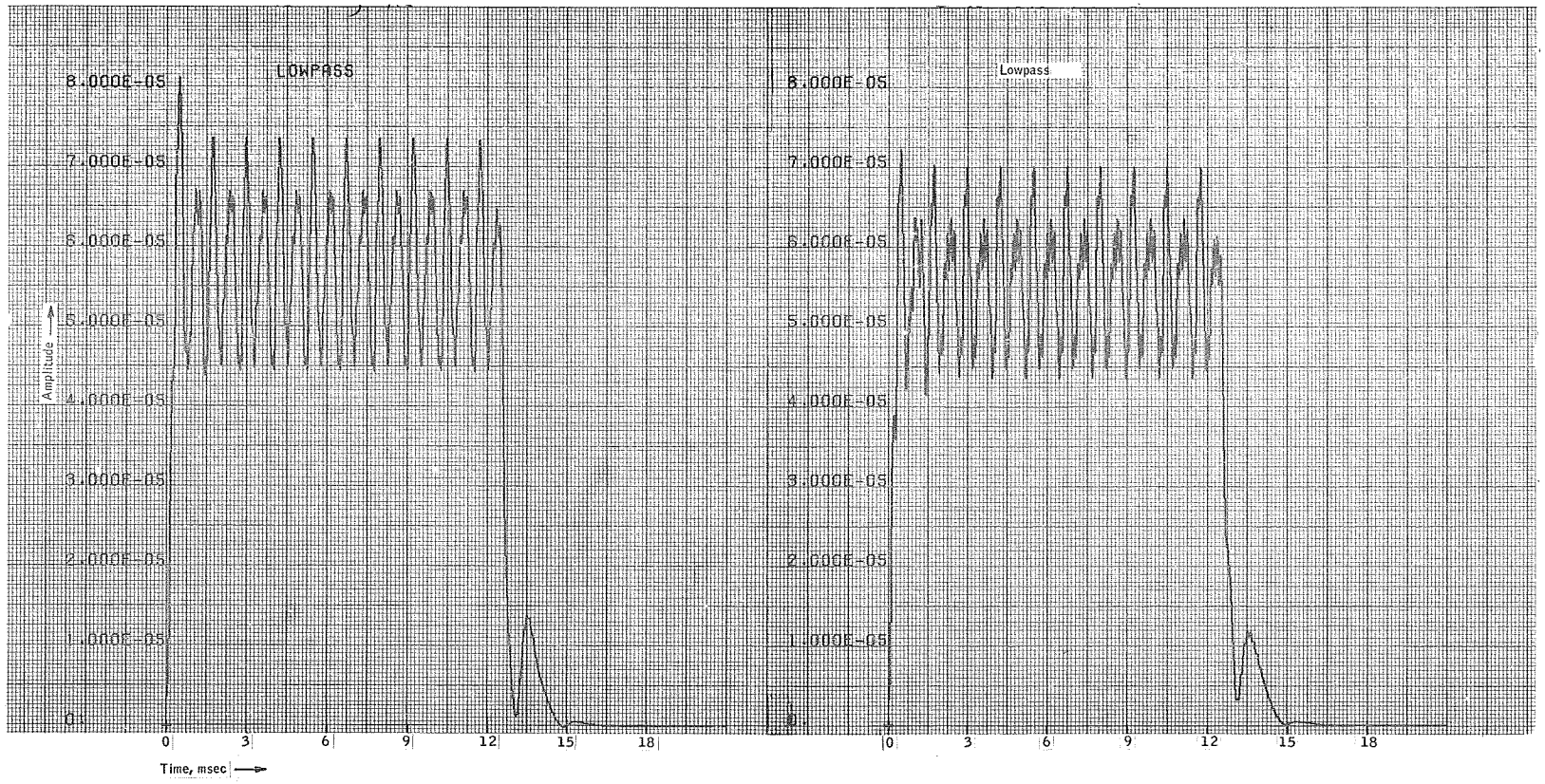

Figure 56. Effect of Change in Lowpass Filter on Lowpass Filter Output

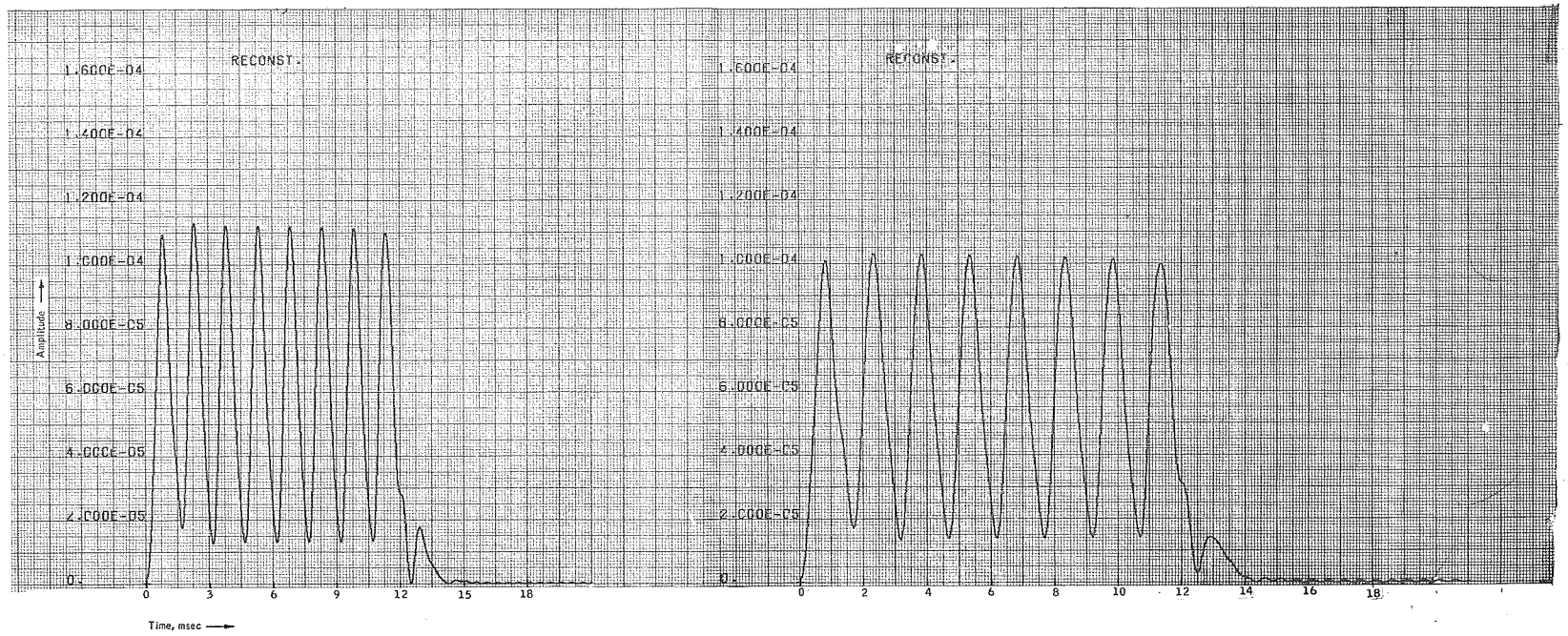

Figure 57. Effect of Change in Lowpass Filter on Reconstructed Output for Input Frequency $f_c/6$ = 667 Hz

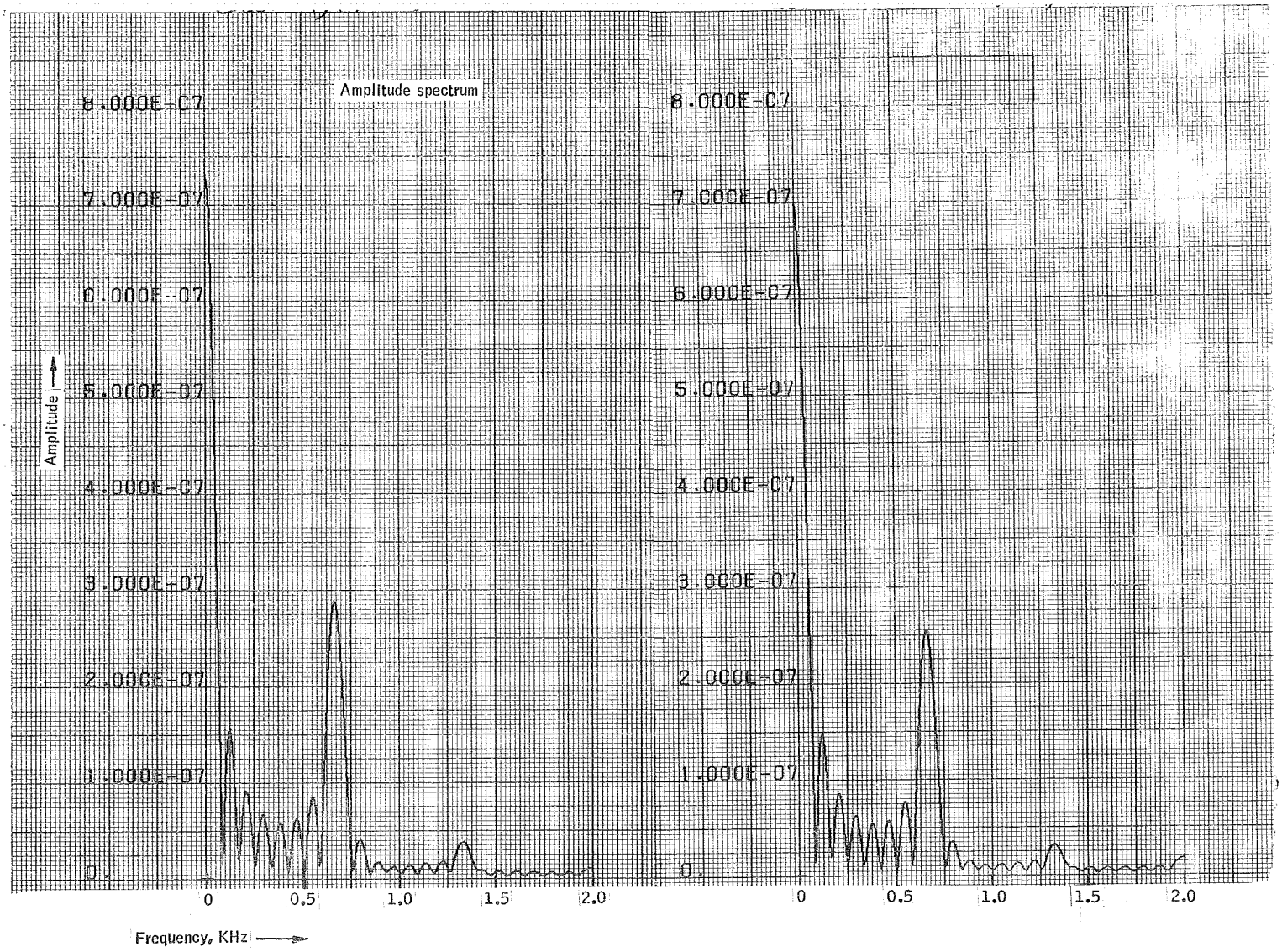

Figure 58. Effect of Change in Lowpass Filter on Amplitude Spectrum of Reconstructed Output for Input Frequency $f_c/6$ = 667 Hz

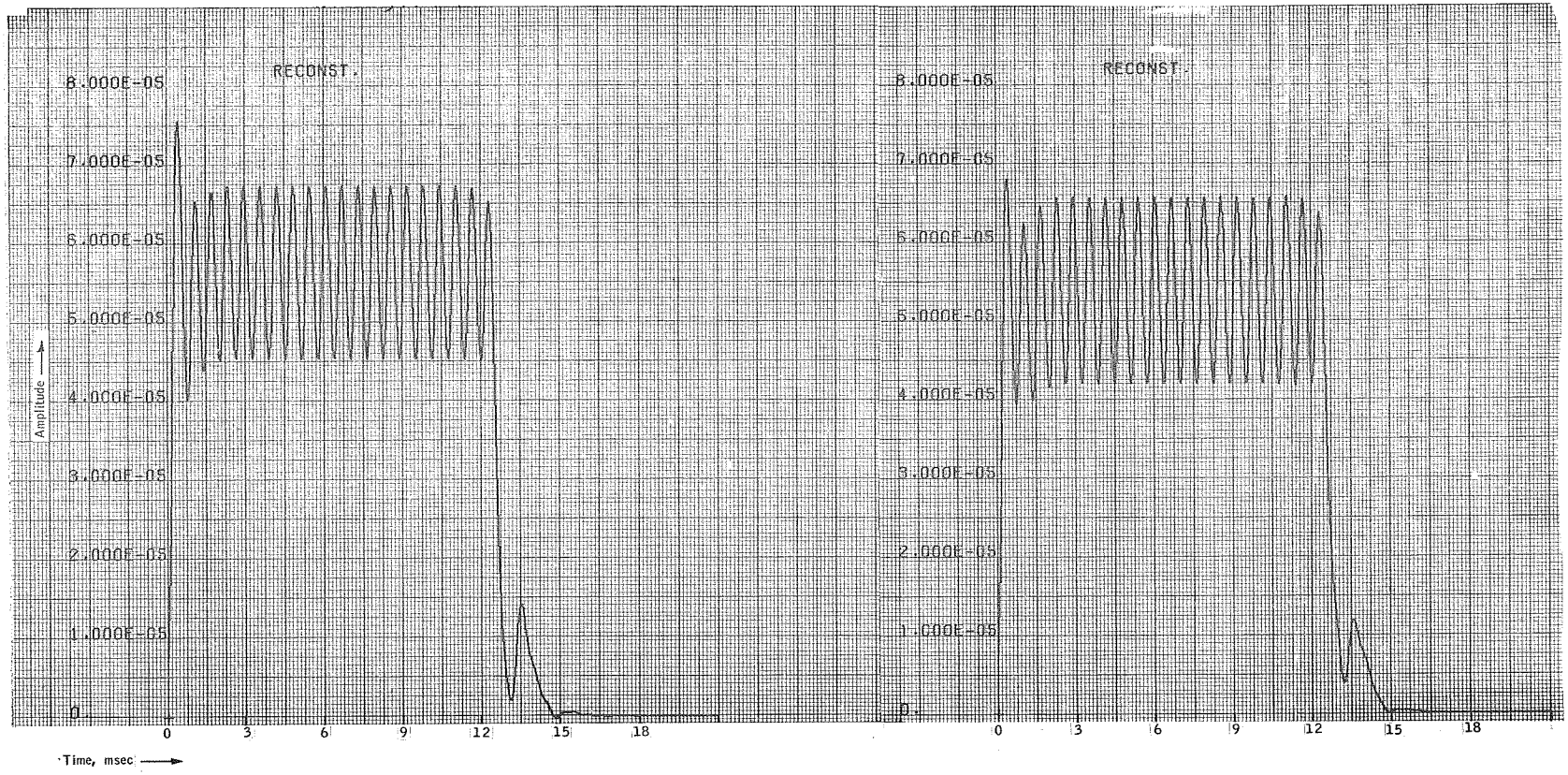

Figure 59. Effect of Change in Lowpass Filter on Reconstructed Output for Input Frequency 0.4 f_c = 1600 Hz

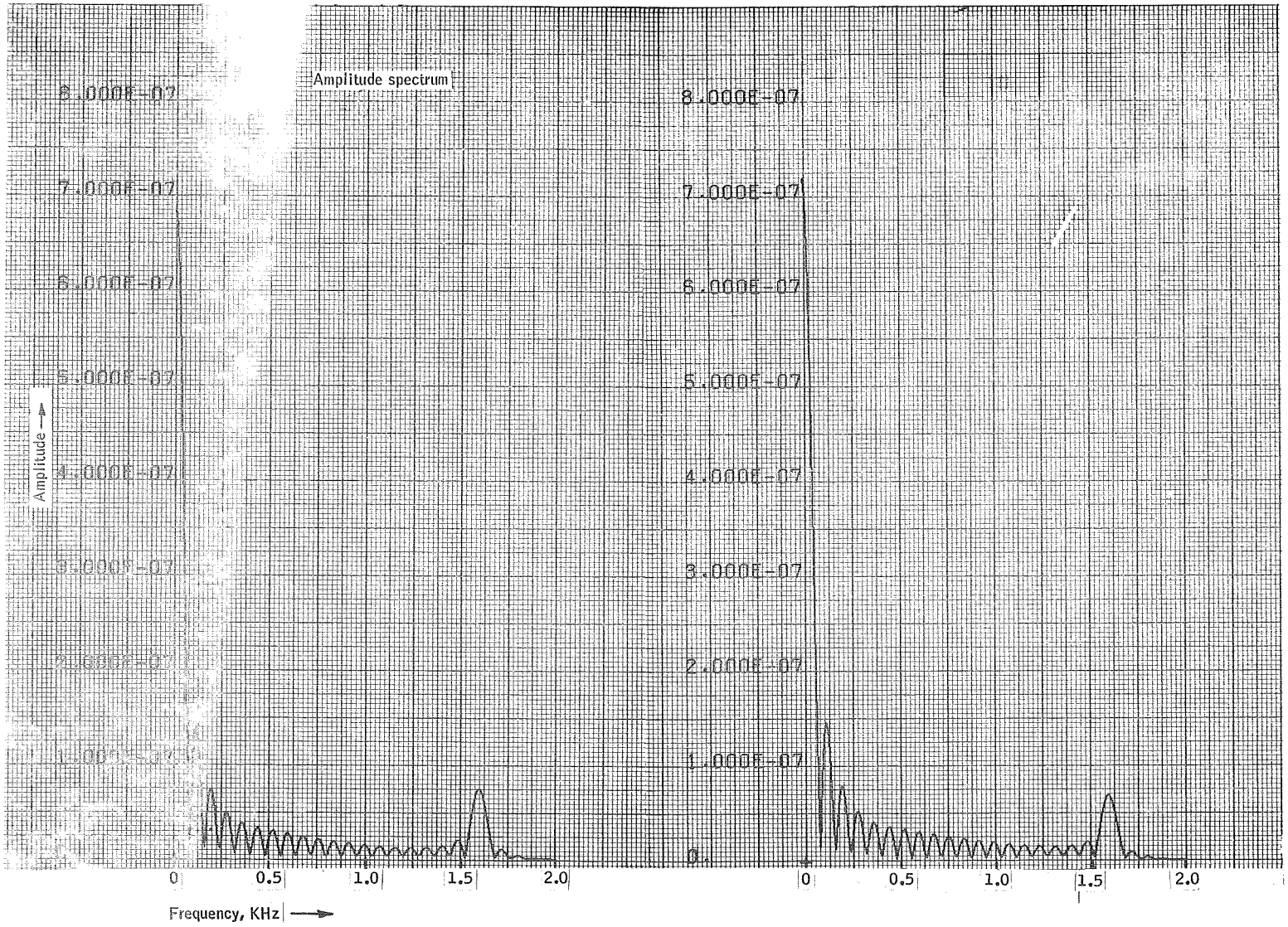

Figure 60. Effect of Change in Lowpass Filter on Amplitude Spectrum of Reconstructed Output for Input Frequency 0.4 f_c = 1600 Hz

Figures 56 through 60 depict lowpass filter variations where in each case the curve on the right is the original unvaried output. The variation shown is in the manner in which in-band ripple is traded against sharpness of cut-off. In the original run the filter has 0.1 db in-band ripple and a very gentle roll-off. The variation is to 3 db ripple and a very sharp roll-off. The expected result would be a pronounced (up to 3 db) effect on the uncorrected amplitude and a cleaner (less ripple) signal. Inspection of the curves shows the lower frequency term more affected, indicating more filter ripple at that frequency.

Summary and Conclusions

The RMS program is operational, including a precise fourier transform routine which had to be developed for this application. Input modelling improvements included the programming and use of the Struve line spread function to handle in two dimensions a scene with one-dimensional variability. The spatial extent and point density required for the $\leq 0.1\%$ precision goal were analyzed, defined, and used. The program was then used to uncover and attempt to define radiometric measurement errors associated with the system transfer function and its response to unknown signal dynamics. The following results were obtained:

- Aliasing is a serious problem - margins in chopping rate and on-board memory should be allowed proportionate to the uncertainty in input signal high-frequency components.
- Spurious Harmonics are easily introduced even with reasonable care in the design; increased chopping frequency is again the only sure cure.
- Blur function, filter, and chop wave variability produce readily predictable results from tools such as the FDM approximations.

CALIBRATION

PRIMARY CALIBRATION SYSTEM

Calibration Requirements

A basic requirement for the radiometric system is the ability to measure the radiance of interest with the maximum possible accuracy. Since the accuracy of measurement can be no greater than the accuracy of the primary calibration, the calibration source and method are extremely critical. As discussed in the NASA Report CR-66429 from the NAS 1-6010 program, the following conditions of calibration must be met to assure that the desired accuracy is achieved:

1) The radiance of the source within the calibration apparatus in the 14- to 16.3-μ band must be known within one percent of its actual value (accuracy), and its radiance must not vary in excess of 0.1 percent (precision).

2) The calibration source must appear to be at inifnity as viewed by the radiometer so that it simulates the conditions of field measurement and that no error is introduced by an uncertainty in the radiometer field of view (fov).

3) A means of varying the source radiance must be provided so that the radiometer may be calibrated at radiance values equivalent to the radiance range of its intended operation.

4) The radiometer must be calibrated at a sufficient number of points to define completely the calibration curve of the instrument.

5) A known zero reference for calibration must be provided so that the effect of thermally emitted radiation by the optical components of the radiometer may eliminated.

From the above conditions, the following criteria for the ARRS program were established as objectives or requirements for which a primary calibration method is proposed:

a) A system accuracy of 0.03 W/m^3-sr (1σ)

b) A repeatability of 0.005 W/m^2-sr (1σ)

c) A dynamic range of 10 W/m^2-sr

d) An operating temperature range of 80°K to 300°K

e) A spectral region of 14 to 16.3 μ, which implies operation in a vacuum to eliminate atmospheric absorption

f) Configured as an extended calibration source as opposed to a point source.

Approach

The basic calibration techniques considered included

1) Simulating an extended source at infinity, using collimating optics
   a) A fixed temperature source which is a melting-point standard
   b) A fixed temperature source with attenuators (diffuser, aperture plate, neutral density filter, etc.)
   c) A variable-temperature source with platinum resistance thermometers used as temperature standards
2) Using an extended source at the radiometer aperture with no optics
   a) Variable temperature capability

Each of the above methods will provide only a partial measurement and contains some deficiency:

1a) Will not allow calibration points throughout the operating range of interest.

1b) A diffuser or neutral density filter has not been developed which has the required demonstrated characteristics. A variable aperture size would result in a point-source measurement and would require exact knowledge of the radiometer angular response function.

1c) This concept varies the radiance and spectral content simultaneously with temperature. The capability depends on indirect proof that the thermometer temperature is the actual radiating temperature. It also requires a precise knowledge of the collimator mirror reflectance.

2a) Requires low thermal gradients over large areas. In addition, coupling to a radiometer creates a problem.

Of the above configurations only 1c), variable temperature source with collimating optics, was the source developed to the level of accuracy required for the ARRS effort. Accordingly, the design of the Primary Calibration System (PCS) was developed around this concept.

During Phase A, Part II of NASA Contract NAS1-6010, the calibration source development program concluded with the construction and some testing of a feasibility model of a blackbody source demonstrating the practicality of precise LWIR absolute calibration using a source continuously variable in temperature from 80°K to 300°K. The purpose of the ARRS Part I primary calibration activities was (based on this prior effort) to develop the design of an

operational system to provide a large collimated beam of calibrated long wavelength IR radiation to a radiometer such that the system utility and accuracy is relatively independent of the radiometer configuration. This effort included the following activities:

- System concept design
- Optics design and system layout
- Source design - upgrading of feasibility model into an operational model
- Vacuum and cooling systems - support equipment definition
- Error analyses - radiance, thermal, triple-point cell feasibility
- Mirror reflectance measurement - development of a suitable measurement technique with applicability for eventual use in situ

Design improvements incorporated into the PCS include the following:

- Enlargment of the source to 3 mr extent
- Improvement of the source thermal-control operation
- Capability of comparison with alternate radiance sources such as a water triple-point cell
- Variable aperture adjustment of linearity checks
- Interface with a standard flanged chamber for radiometric system measurements

General PCS Description

The PCS is contained within a cylindrical stainless-steel vacuum sealed chamber 42 inches in diameter by 16 feet long. Figure 61 shows the physical layout of the chamber and its elements. These elements include the following:

- A variable-temperature blackbody source and its surrounding guard heater assembly
- A variable-temperature, variable-aperture plate
- A variable-speed rotating chopper
- Access for an alternate source, such as a water triple-point cell

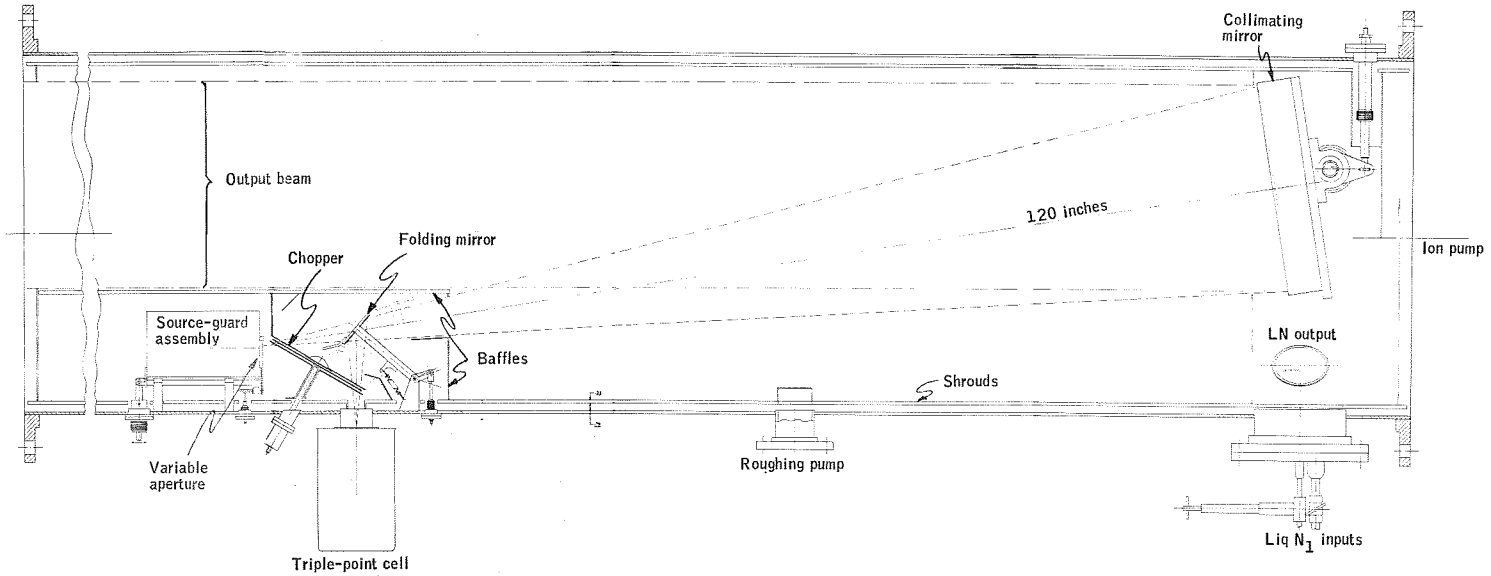

Figure 61 Primary Calibration System

- A 25-inch diameter off-axis parabola for producing a 24-inch collimated beam of calibrated radiance
- Liquid-nitrogen-cooled shrouds and baffles throughout the chamber
- A liquid-nitrogen, closed-cycle cooling system
- A two-stage vacuum system
- A standard flange interface for interconnecting radiometers or test measurement devices such as a reflectometer

Detailed PCS Description

Source-guard assembly. -- Figure 62 shows a detailed layout of the source-guard assembly. The source is fabricated from high-purity, oxygen-free copper to assure minimum outgassing and thermal gradient effects. A two-stage, recessed off-axis cone with a length-to-diameter (L/D) ratio of 12.45 and an aperture of 1.75 cm is machined into the copper block. This configuration was established during the NAS1-6010 program and was verified by the cavity emittance study on contract NAS 1-8447. The cavity is designed to be machined on-axis with respect to the block, with the result that in the PCS installation it is operated 9° off-axis, thus assuring proper emissivity characteristics. The cavity is coated with a nominally specularly reflecting black paint with an emittance of 0.95. This paint, coupled with the cavity geometry, will provide a source emittance of 0.99999. This extremely high emittance was experimentally verified by the Emittance Measurement study.

Platinum resistance thermometers are installed at opposite ends of the source to measure precisely the source temperature and gradient structure. These platinum resistance thermometers will be calibrated to the International Practical Temperature Scale and traceable to the NBS. Calibration accuracy obtainable is shown in Figure 63. The thermometer installation will use a split carrier with berylium-copper leaf spring thermal contact. The thermometer is a tight slip-fit in the split-ring, which runs the length of the thermometer. The thermometers are of a four-lead configuration designed for operation with a Mueller bridge. Lead configuration allows removal of the lead resistance from the measurement. The leads will be heat stationed to the rear of the source block to minimize thermal electromotive force (emf) effects.

Cooling passages for liquid nitrogen flow around the source for source cooling are provided with helical milled slots around the circumference of the source block. An outer copper sleeve is welded to the source block, which provides a sealed jacket around it and to which the source liquid nitrogen cooling lines are attached. Provisions for source heating are made by a spray-on resistive heater applied to the outer circumference of the copper sleeve. The source heater was sized at 260 W as a result of thermal analysis presented in Appendix H.

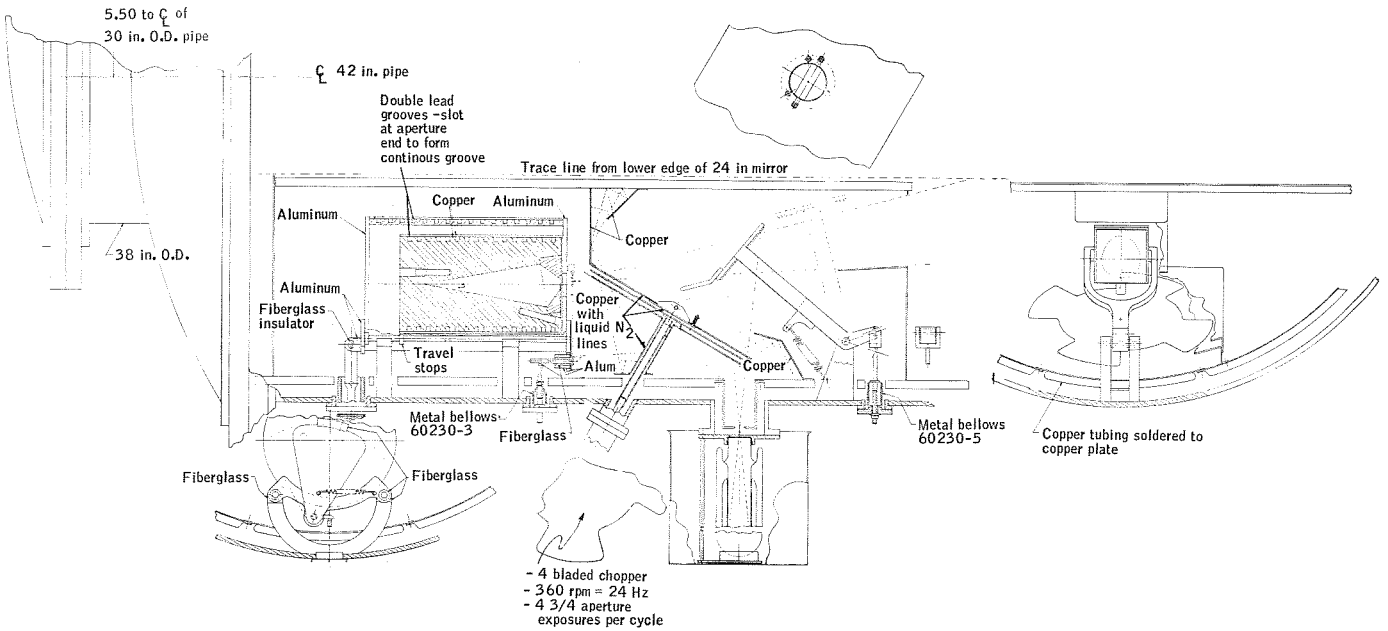

Figure 62 Primary Calibration System Source - Chopper Assembly

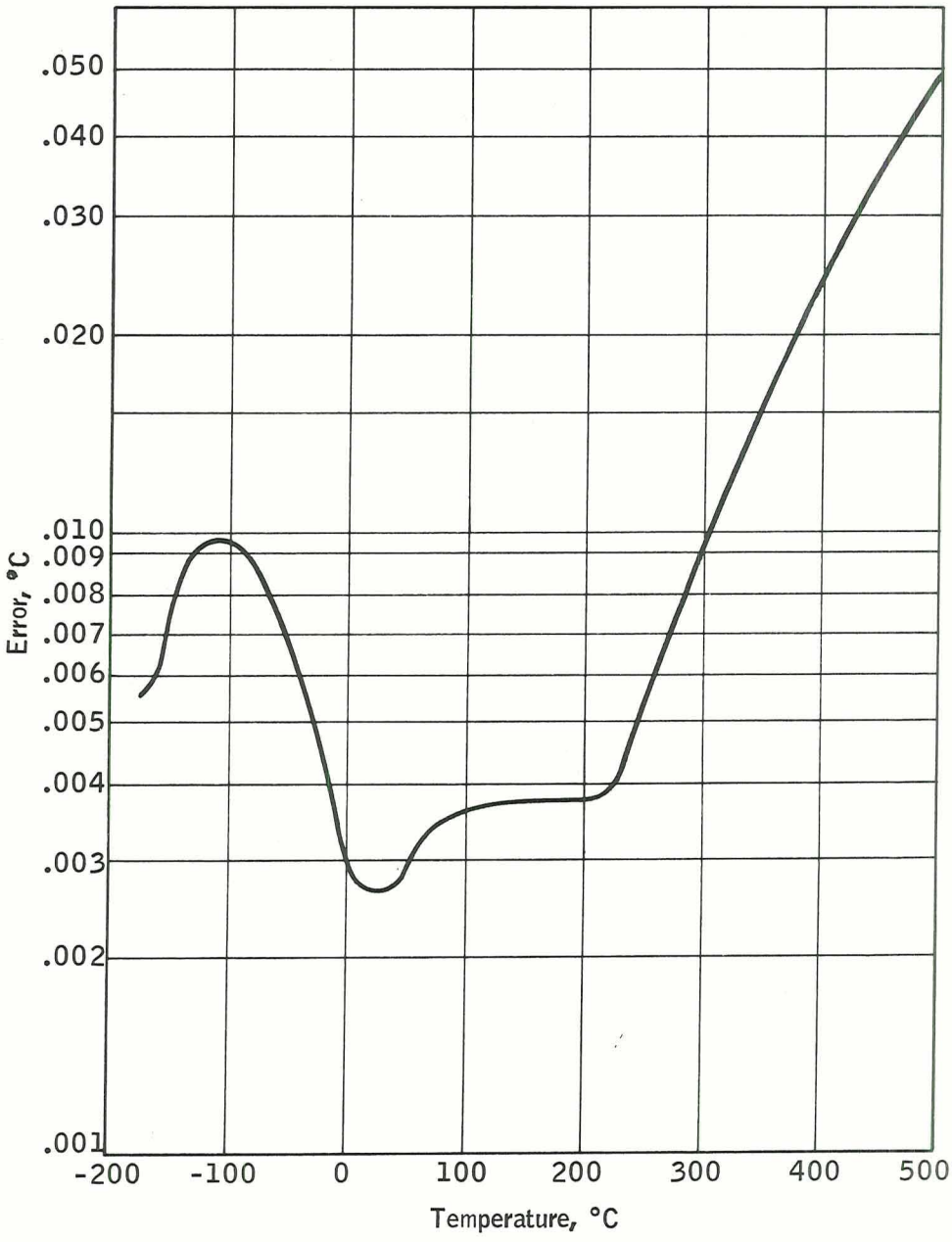

Figure 63. Calibration Accuracy of Platinum Thermometer (From Rosemount Engineering Company, Temperature Standard 162D)

The guard assembly consists of a multi-element aluminum circular cylinder which surrounds the copper source. The inner portion of the guard cylinder contains milled helical slots similar to the source for liquid-nitrogen coolant flow. An outer sleeve is welded to the slotted cylinder to seal the passages. The sleeve OD and end caps of the guard are coated with a spray-on heater material to provide warmup and temperature control of the source-guard assembly. The guard heater is sized at 100 W from thermal analysis presented in Appendix H. A thermocouple on the guard provides the sensing point to which the guard temperature is controlled.

Longitudinal movement of the source-guard assembly along the system optical axis will allow the defining aperture to be located at the collimating mirror focal point. This is provided by a sliding mount which is thermally stable yet well isolated from the outer chamber. The mount is constructed of aluminum with fiberglass inserts for thermal isolation. Adjustment from outside the chamber is accomplished through a sealed bellows linkage.

Variable aperture. -- Figure 62 shows the layout for the source variable aperture that will be used to vary the source radiance subtense at a particular source temperature. This will check radiometer detector linearity over various aperture extents. A series of precisely machined aperture holes will be indexed in front of the source cavity. Each of these holes is a known, defining aperture size. The defining aperture is capable of up to 1-cm diameter which will provide a 3-mr source extent. Temperature control of the aperture plate will be accomplished by flow-rate control of a liquid-nitrogen cooling line attached to the aperture plate. Control of the aperture plate position is accomplished through a linkage and sealed bellows to the outside of the chamber.

Chopper. -- Figure 62 shows the chopper layout. This chopper is configured as a four-segment rotating blade which intercepts and modulates the variable-temperature source beam or an external radiation source alternatively. The chopper is driven by a bellows drive mechanism which effectively thermally isolates the blade from the driving mechanism by a fiberglass shaft coupling. Blade chopping rate will be capable of being varied from 10 Hz to 25 Hz. The portion of the blade intercepting the beam is made highly specularly reflective to minimize blade self-emission and to direct the reflected intercepted rays precisely to a cold trap so that they may be absorbed away from the field of view (fov) of the optical system. This is accomplished by orienting the blade at an angle with respect to the radiation beam being chopped. A light source-detector block assembly also chopped by the blade will be used to provide a synchronous reference output signal for interfacing with a phase-lock electronics readout system.

The chopper blade will be radiatively cooled with highly absorbant aluminum baffles located on either side of the chopper blade and around the shaft. Liquid nitrogen lines will be attached to the baffles for cooling.

A means will be provided to conductively cool the chopper blade during the cooldown sequence. A center section of the upper baffle adjacent to the chopper blade is movable but spring restrained. It will be conductively cooled by

running a flexible liquid-nitrogen line directly to it. The folding mirror positioning mechanism will be used, with a small extension, to push the cold baffle to physically contact the chopper blade. Prior to starting the chopper, the mirror mechanism will be moved back into place, thereby releasing the conductive element away from the blade.

Folding mirror. -- Figure 62 shows the layout of the folding mirror and mount assembly. The mirror is rotated into the optical path of the PCS source cone such that an external radiation source - i.e., the triple-point cell - can be folded into the optical system. This mirror will be of high reflective quality gold-coated cervit, with a reflectance of at least 0.98, calibrated to 0.1%. The mirror will be conductively cooled with a liquid nitrogen line attached to its mounting plate. A fiberglass bushing provides good thermal isolation to the outer chamber. Movement is provided with an externally adjustable, bellows-linkage mechanism.

External source interface. -- A flanged interface connection will be provided by the chamber to allow an external radiance source to be introduced into the PCS optical system. A variable-sized, cold aperture stop will define the radiance FOV of the source. The chopper blade is positioned to chop the radiation in a similar fashion as with the variable-temperature blackbody source. Possible alternate sources which may have application for an absolute temperature/emission comparison with the PCS source are a water triple-point cell, a monochromator, and an independent blackbody radiance source. Further discussion of the triple-point cell is presented later.

Collimating mirror and mount. -- The collimating mirror is a critical element in the PCS because of its use in the optical system. Reflective characteristics of the mirror - i.e., reflectance and uniformity - directly affect the PCS performance. For this reason, considerable care was taken when designing and mounting the mirror. The mirror is configured as an off-axis parabola with its centerline 9° off its optic axis and with a focal length of 120 inches. The mirror material is premium grade cervit, known for its extremely low thermal expansion coefficient. Dimensions of the mirror are 25 inches in diameter by 4 inches thick with a clear aperture diameter of 24 inches. The mirror is coated with high purity gold over chrome, with a reflectance of at least 0.985, calibrated to 0.1%. The measurement of the mirror reflectance was studied and is described later. It will be performed in situ with the use of a reflectometer.

Figure 64 presents the method for mounting the mirror. The aluminum mirror mounting plate is supported by a 2-inch OD stainless steel tube (3/16-inch wall) which runs through two pillow blocks with fiberglass temperature isolating inserts. At each end of the 2-inch tube are slip-fit steel extensions with a flattened shaft protruding through slotted plates which are bolted and vacuum sealed to the chamber. A steel bellows is fastened to these pieces to achieve a seal. External adjustment screws are used to adjust for axial and/or angular azimuth position (±1°). Freedom of movement of ±5° in elevation is needed to perform the in situ reflectance measurement. Elevation adjustment is achieved by an external adjustment screw which transmits vertical motion through a

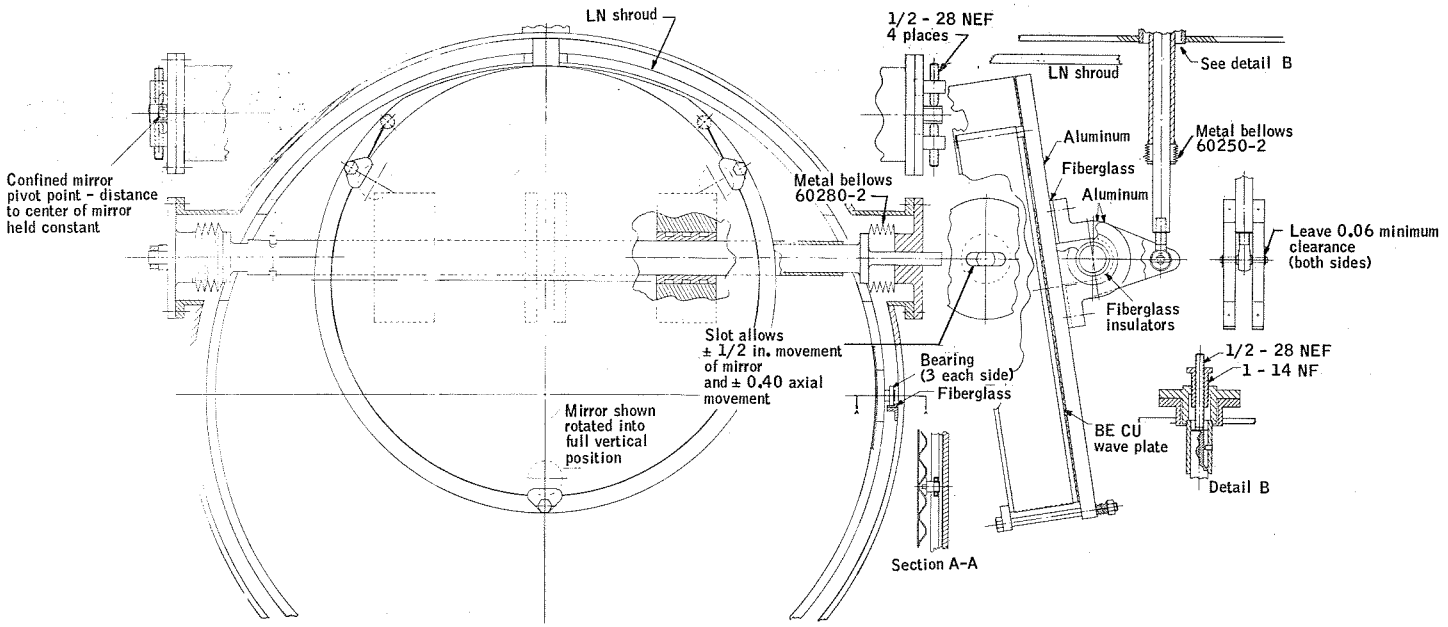

Figure 64 Collimating Mirror and Mount

bellows seal to a crank arm mounted on the mirror mount plate. The crank arm pivots around the 2-inch support tube and gives angular motion to the mirror around this point. Vertical adjustment tube, shaft, and bellows are made of stainless steel. The crank arm is made of steel with fiberglass inserts. The mirror is supported on the mounting plate by means of a steel band sling and three spring-loaded clips, located directly opposite cushioning pads.

For cooling purposes the mirror mounting plate will have liquid nitrogen cooling lines mechanically fastened to it. The back surface of the mirror will rest on pads, and there will also be a berylium-copper wave plate between it and the aluminum mounting plate for high thermal conductance.

Shrouds and baffles. -- Shrouds and baffles were strategically placed throughout the PCS chamber to eliminate stray radiation and emission from within the optical system FOV. These shrouds and baffles are shown in Figures 61, 62, and 63 and consist of the following:

- Main shroud - fabricated in one section - three parallel feed sections
- C-shaped shrouds at the chamber source end
- Mirror cooling coil
- Mirror front baffle
- Rear-ion pump baffle
- Folding mirror cooling coil
- Triple-point cell aperture
- Chopper baffles
- Source aperture coil
- Source cooling coil
- Guard cooling coil
- Front baffle - behind the source
- Output beam baffle between source and collimated beam
- C-shroud bottom plate

Each of the shrouds is made from two embossed, stainless-steel sheets. When the sheets are electric resistance welded together into a panel, the embossed areas become channels for liquid nitrogen cooling.

Figure 65 shows the interconnections for liquid nitrogen coolant flow. All shrouds and baffles are coated with high absorptivity paint ($\alpha > 0.9$) to provide as black a surface as possible. The shroud surfaces viewing the chamber walls are electropolished for low emissivity ($\varepsilon < 0.1$) to minimize radiative coupling. The large circular shrouds are mounted to the chamber walls by bearings and fiberglass insulated tracks, which provide a convenient means of installing the shrouds in the chamber.

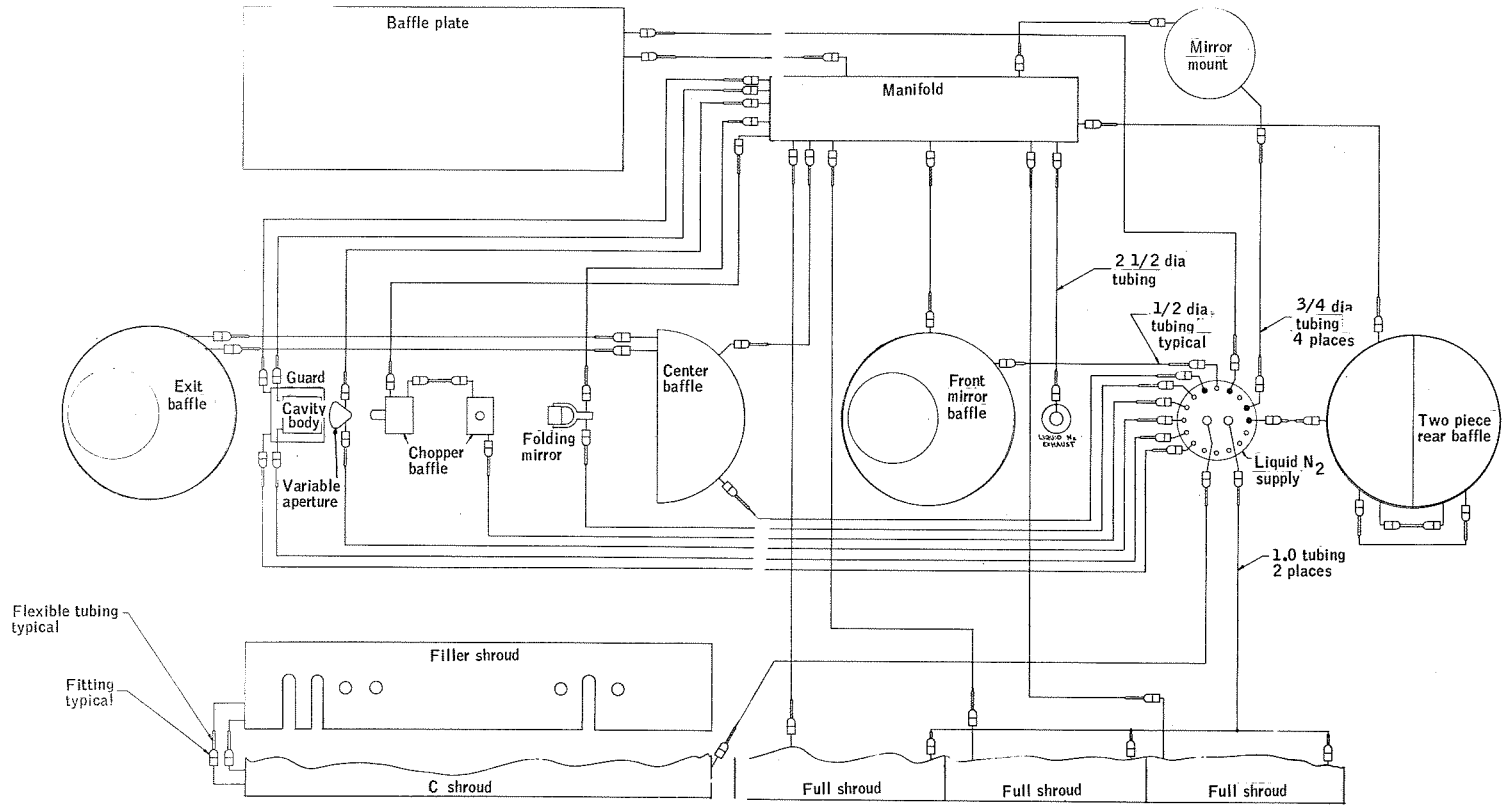

Figure 65 Liquid Nitrogen Tubing Schematic

Cooling System. -- The PCS cooling system will be a closed-cycle system consisting of a supply dewar, transfer line, phase separator, and pump (see Figure 66). The liquid nitrogen will flow from the supply dewar at approximately 50 psi to the cooled elements in the chamber and then to the phase separator. Here gases will be vented and the liquid nitrogen returned to the dewar. Separate valves and lines will control the coolant flow to each of the elements within the chamber. A layout of these valves is shown in Figure 67. The transfer lines will be physically spaced to prevent conduction coupling problems. A common manifold within the chamber will combine all the exit lines to a single large (2.5-inch) line which will exit through a header to the phase separator. A detailed cooling analysis of the PCS is discussed later.

Vacuum chamber. -- The PCS vacuum chamber consists of a 13-foot-long, 42-inch-diameter, 5/16-inch wall tube with standard vacuum seal flanges at either end (see Figure 68). Standard flanges are also provided for the roughing pump and liquid nitrogen header connections. A 2-foot-long, 42-inch-diameter extension is provided on one end of the chamber to house the ion pumping modules. The opposite end contains a flanged extension to which a 30-inch-diameter radiometer or reflectometer housing is attached. Special machined flanges for adjustment bellows and mountings are welded to the chamber walls. All chamber materials are type 304 stainless steel for weldability and corrosion resistance. All surfaces are polished for cleanliness and low emissivity.

The chamber will be mounted on a stand of structurally-reinforced steel construction which provides necessary access to the chamber adjustments. Chamber and stand are shown in Figure 69.

Vacuum system. -- The PCS vacuum system consists of two stages - a mechanical roughing pump and an ion pumping system. The 100-cfm roughing pump will pump down to a level of $\approx 50\ \mu$; its flanged connection is midway between the optical elements of the PCS. A failsafe valve and liquid nitrogen cooled trap will prevent any oil from backstreaming into and contaminating the chamber. The ion system will contain on the order of forty 25-liter-per-second pumping modules to achieve a pressure of 10^{-6} torr. Figure 70 shows the location of the pumping modules within the flanged housing of the 2-foot chamber extension. Cooled baffles are provided between the chamber end and the pumping modules to prevent contamination problems.

Electrical system. -- Figure 71 shows the electrical schematic diagram for the PCS. Interconnections to the chamber will be through hermetic seal MIL-STD connectors.

A proportional temperature controller will be provided to control the guard heater assembly heater power and temperature. A Mueller bridge will be used to precisely measure the platinum resistance thermometer resistances. A simple nulling bridge will be used to measure the various thermocouple voltages throughout the chamber, monitoring the temperatures of interest.

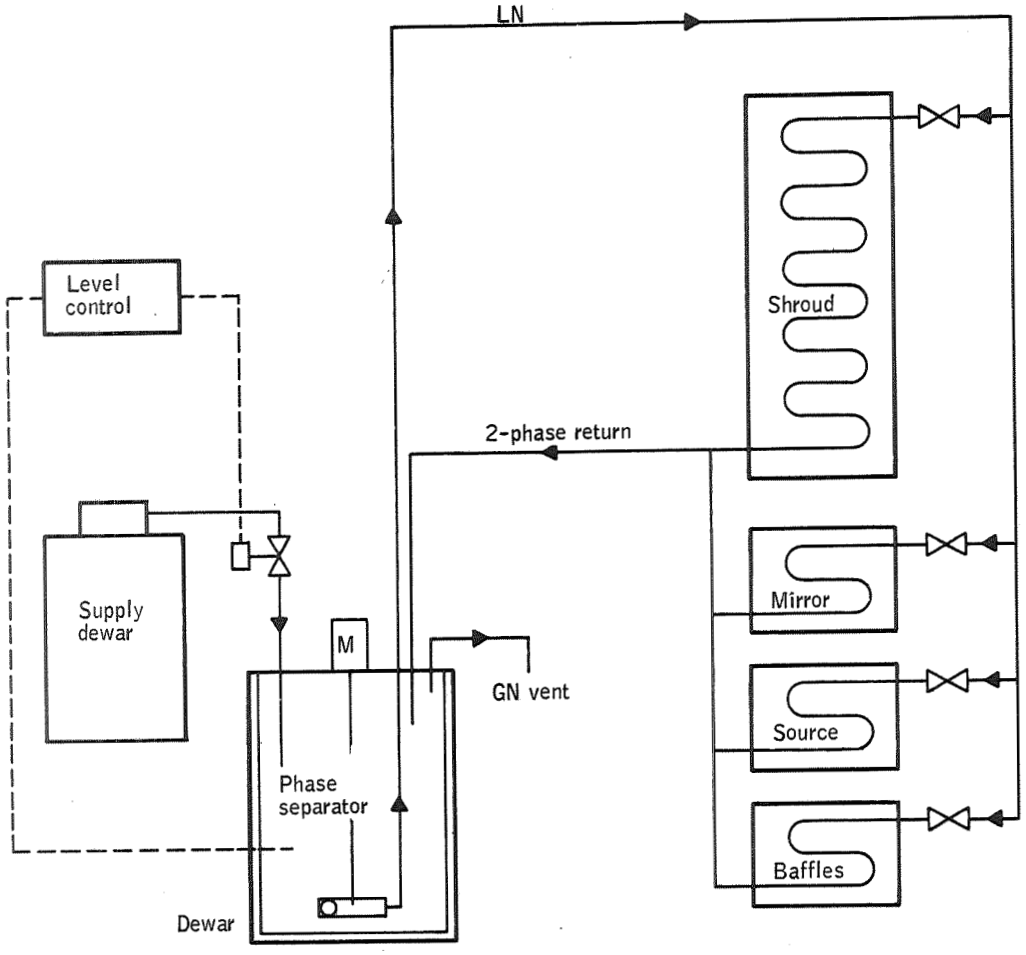

Figure 66. Liquid Nitrogen Handling System

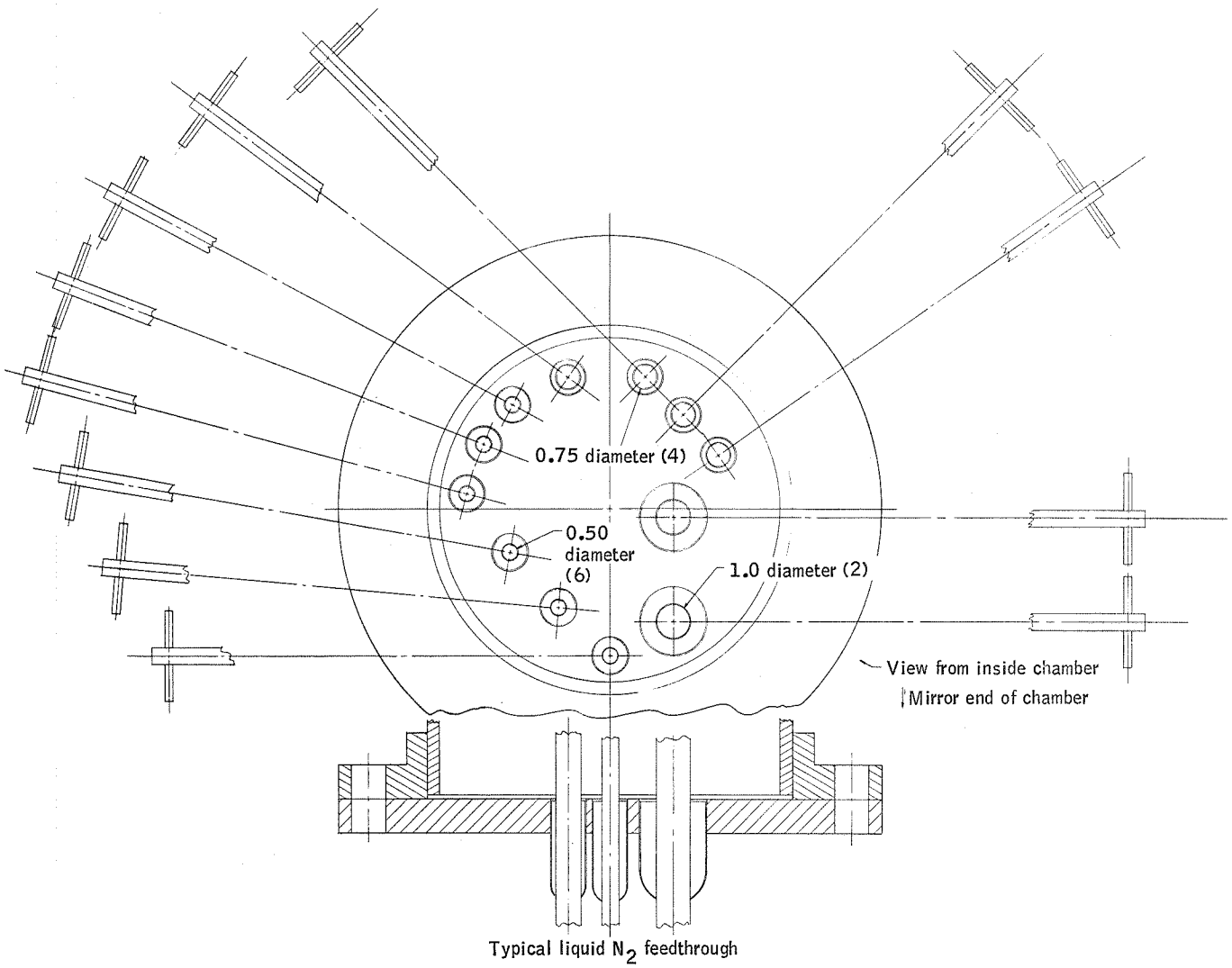

Figure 67 Liquid Nitrogen Valve Layout

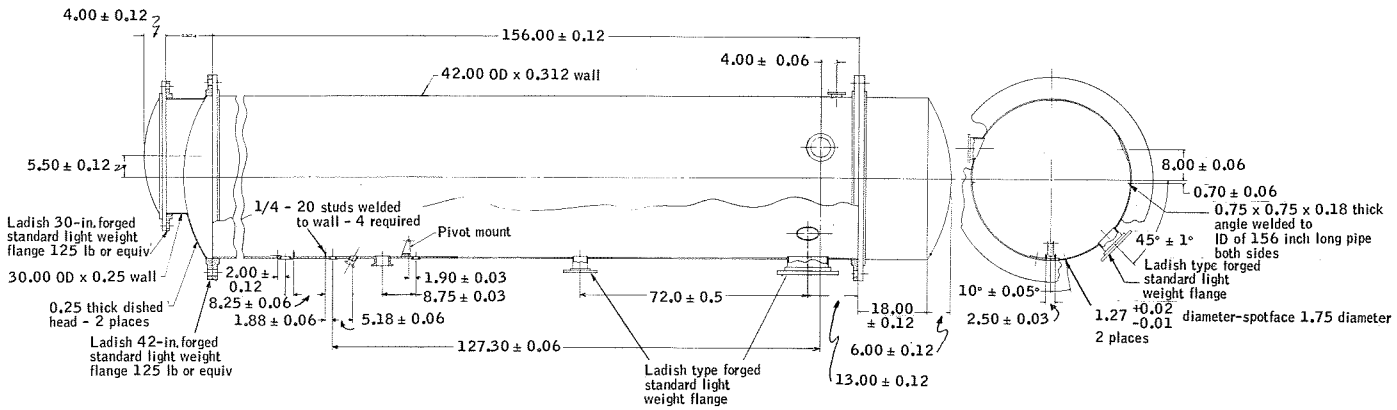

Figure 68 PCS Vacuum Chamber

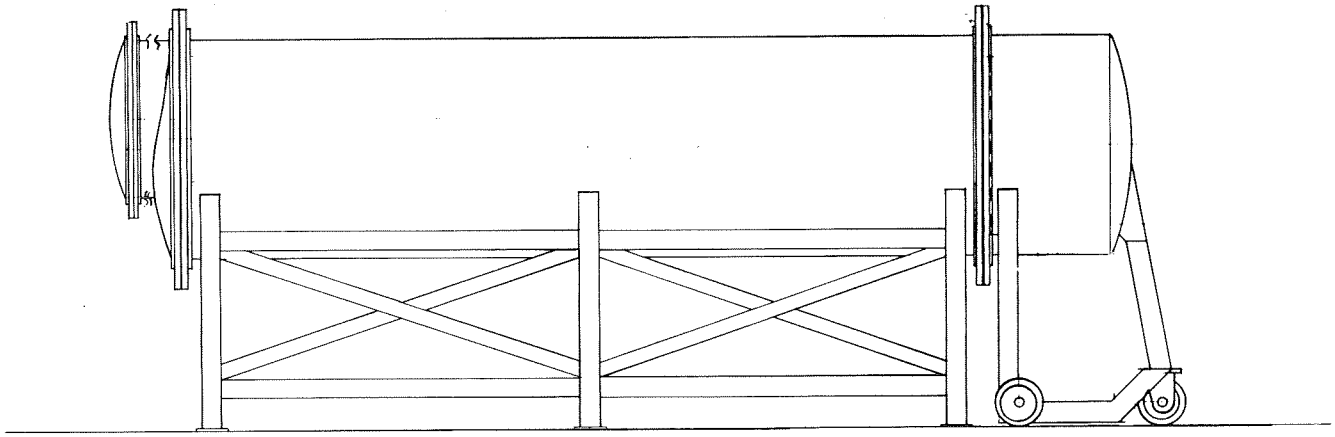

Figure 69. PCS Vacuum System

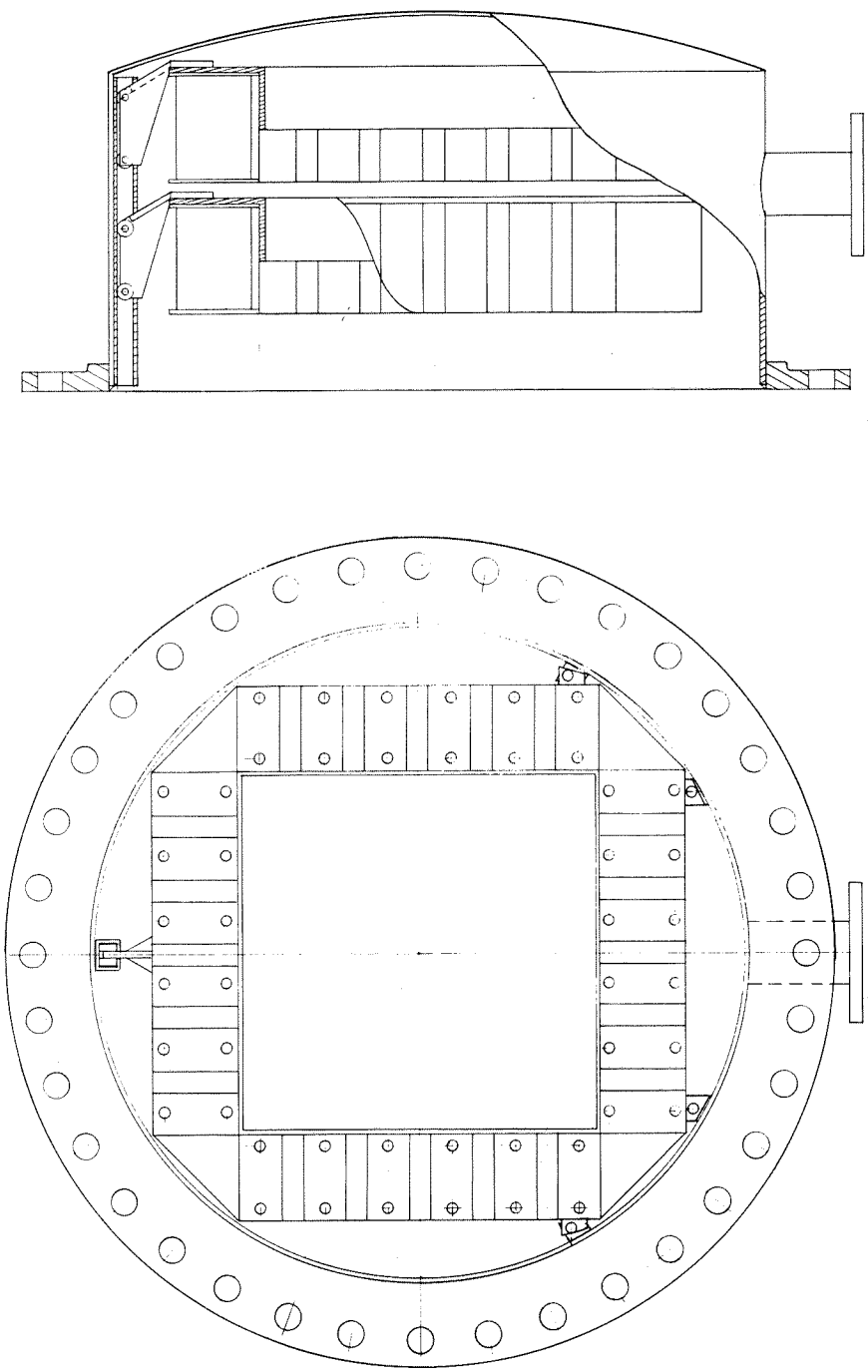

Figure 70. PCS Vac-Ion Pumps

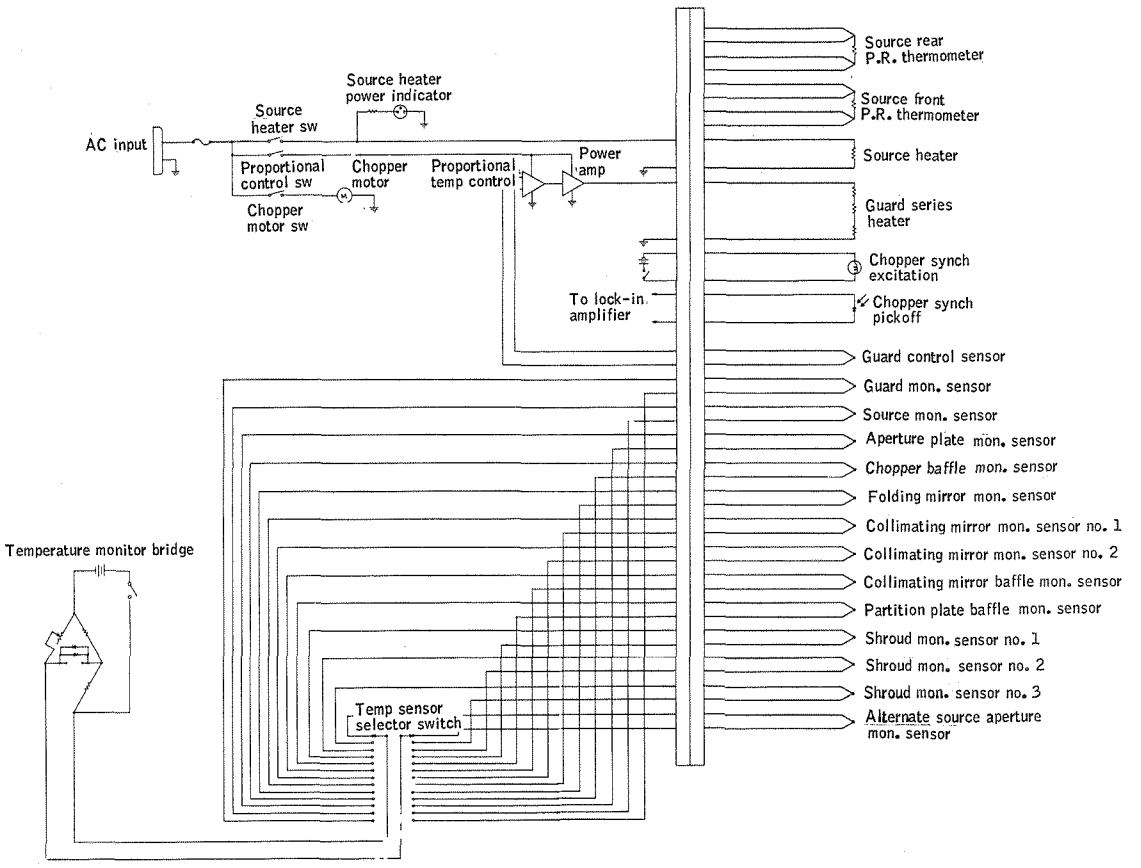

Figure 71 Primary Calibration Schematic

PCS - radiometer interface.--The output of the PCS will be a collimated, 24-inch-diameter radiation beam with well defined radiation characteristics. The beam spread due to aberrations will not exceed 0.1 mr at $\lambda = 15\mu$. This is discussed in the radiance error analysis in a later section of this report. The spatial distribution of the output beam will be uniform or calibrated to within 0.1% over the 24-inch beam diameter. This will be verified by making radiometric measurements of the beam using the test radiometer discussed in a separate section. The radiometer under test will be attached to the PCS with a flanged, 30-inch-diameter tube which will provide a vacuum seal to the PCS. The radiometer will be separately cooled by the PCS cooling system through proper flow rate control of the liquid nitrogen to its cooled elements.

In place of the radiometer under calibration and test, a variety of infrared elements can also be evaluated, such as collecting optics, filters, and cooled detectors.

PCS sequence of operation.--During the operation of the PCS, a particular operational sequence will be required. This sequence is as follows:

1) The mechanical roughing pump will be turned on and operated to pump the chamber down to $\approx 50\mu$. This should be accomplished within 0.5 hour. The pump will then be turned off.

2) The main shrouds will be cooled with liquid nitrogen down to $\approx -30°C$. This will condense out the water vapor which may be present within the chamber.

3) The mirrors and other elements within the chamber will next be cooled. The cryogenic pumping effect from the cooldown will drop the chamber pressure level to $\approx 10^{-4}$ torr. Overall cooldown time will be designed to be accomplished within 10 hours.

4) The ion pumps will be activated to maintain the desired pressure level. Their operation will take care of small chamber leaks and outgassing effects.

For warmup of the source guard assemblies to a particular operating point, a manually controlled heater-monitoring procedure will be used. When the desired temperature is reached, the source heater will be turned off and the proportional controller will be used to maintain the guard assembly temperature at the desired operating point. The close radiative coupling between the source and guard will cause the source temperature to stabilize within a fraction of a degree of the guard temperature.

For returning the chamber to ambient pressure, a means will be provided for backfilling the chamber with dry nitrogen gas. This will minimize contamination and water vapor condensation effects.

Error Analysis

Radiance Error Analysis. -- A radiance error analysis was performed on the PCS to determine the various contributors of radiance errors and their magnitudes. These errors are separated into two types which will cause inaccuracies in the calibrated radiometer response function. Bias errors are caused by unwanted, signal-independent, effective radiance; this type of error would raise or lower the calibration response function from its true value. Scale errors are a function of source radiance and collimator reflectance and are expressed as a percentage of radiance. These errors multiply the response curve by a constant which rotates the calibrated response function from its true value.

Both of these types of errors can be either time dependent or constant in time.

Bias errors: Bias errors are caused in the calibration system by radiation from a source other than the blackbody which is chopped by the source chopper. The radiometer cannot, of course, differentiate between this radiation and the source radiation, thus resulting in an error.

Figure 72 diagrammatically demonstrates the nature of this error. This figure is an example of the radiance waveform as it is chopped by the source chopper. Amount A in the figure is due to radiation emitted from the various components of the chamber and radiometer which impinges on the radiometer detector when the chopper is in the "open" position with the source at liquid nitrogen temperature. Besides the source zero level radiation, amount A also includes collimator emission, PCS chamber stray radiation, radiometer mirror emission, and radiometer stray radiation, none of which are chopped by the source chopper. Amount B represents radiation emitted by the various components of the chamber which impinges on the radiometer with the chopper in the "closed" position. This radiation includes the effects of blade emission, chamber emission reflected off the chopper blade, and radiometer emission reflected off the blade, as illustrated in Figure 73.

With the source at LN_2 temperature a waveform such as the solid line in Figure 72 would result. If the blackbody source is heated to some higher temperature, the dotted waveform of the figure will result. Because the chopped, stray radiation is adding to the radiometer output when the chopper is covering the blackbody source, the zero level, A, is not measured. This analysis is based on the fact that there is no measurement of A and that B is nearly equal to A. The value of B then becomes the bias error.

The contributors to the bias error B were calculated by using the following assumed set of conditions:

- All components except the radiometer are at 77°K
- Blackbody source temperature is 77°K
- The temperature of the radiometer is at 300°K

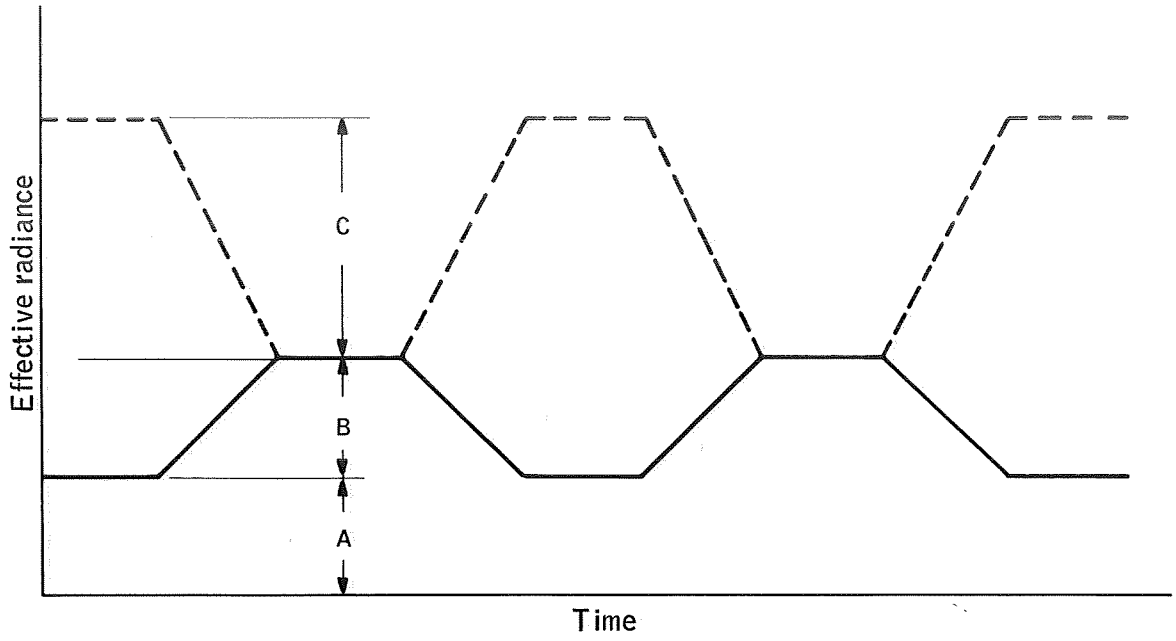

Figure 72. Example of Calibration Bias Error

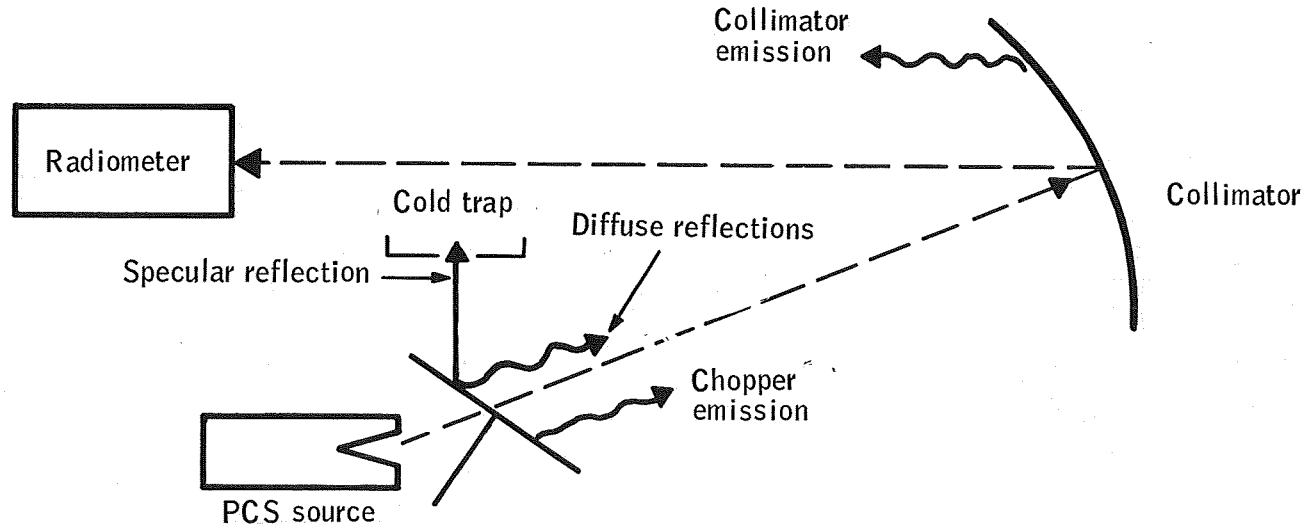

Figure 73. Bias Error Sources

- The chopper blade is a specular reflector and Lambertian radiator with the following characteristics:

$$\rho_{specular} = 0.9^{*}$$

$$\rho_{diffuse} = 0.05^{*}$$

$$\epsilon = 0.05^{**}$$

- The vacuum chamber is a Lambertian radiator with an emissivity of 1.0

- The collimator is a specular reflector and Lambertian radiator with $\rho = 0.98$ and $\epsilon = 0.02$ (established by the mirror reflectance measurement discussed herein).

- The collimator is the only element which can radiate directly into the radiometer since it completely fills the fov.

Bias error calculations are summarized as follows:

- Chopper self emission

$$N(\lambda = 14\text{-}16.3\mu,\ T = 77°K,\ \epsilon = 0.1) = 1.6 \times 10^{-4}\ W/m^2\text{-sr}$$

- Collimator self emission

$$N(\lambda = 14\text{-}16.3\mu,\ T = 77°K,\ \epsilon = 0.02) = 3.0 \times 10^{-5}\ W/m^2\text{-sr}$$

- Radiometer emission reflected off chopper blade. Only the diffuse component is reflected into the FOV. The specular component is absorbed by a cold trap.

$$N_{rad}(\lambda = 14\text{-}16.3\mu,\ T_{rad} = 300°K,\ \epsilon_{rad} = 1.0) = 15.1\ W/m^2\text{-sr}$$

$$H_{ch} = N_{rad} \times \frac{1}{4f^2} = 15.1 \left(\frac{1}{4 \times 25}\right) 1.5 \times 10^{-1}\ W/m^2$$

$$N_{refl} = \frac{H_{ch} \times \rho}{\pi}\ diff = \frac{1.5 \times 10^{-1} \times 0.05}{\pi} = 2.39 \times 10^{-3}\ W/m^2\text{-sr}$$

- Chamber radiation reflected by chopper

$$N(\lambda = 14\text{-}16.3\mu)\ T = 77°K,\ \epsilon = 1.0,\ \rho_{tot} = 0.95)$$
$$= 1.52 \times 10^{-3}\ W/m^2/sr$$

*Handbook of Materials, Mantell, Table 6-1.
**Handbook of Materials, Mantell, Table 35-5.

- Total linear sum

$$N_T = 1.6 \times 10^{-4} + 3.0 \times 10^{-5} + 2.39 \times 10^{-3} + 1.52 \times 10^{-3}$$
$$= 4.0 \times 10^{-3} \text{ W/m}^2\text{-sr}$$

Scale errors: Scale errors are a function of the calibration source and are expressed as a percentage of that radiance. The set of conditions on which each of the errors was calculated is described with each contributor. The contributors to scale errors are as follows:

- An error in the knowledge in the temperature of the adjustable temperature source. As shown in Figure 63, the temperature may be measured within 0.01°C at any temperature within the range which is required (80°K to 300°K). Figure 74 shows the dependence of blackbody radiance error versus temperature for a temperature measurement error of 0.01°C. At 100°K, the radiance calibration error is 0.04%.

- Error in collimator reflectance. The reflectance error is calculated at 0.1% from the mirror reflectance measurement and analysis discussed herein.

- Source emittance. The error in calculated radiance is directly proportional to the error in emittance. Source emittance error is determined to be less than 0.01%, based on the PCS source having the identical geometry and cone surface as the off-axis cone tested in the Emittance Measurement Study performed under contract NAS 1-8447.

The total scale error is calculated as follows:

$$N = N_{bb}(T)\ \epsilon_{bb}\ \rho_{mirror}$$

$$\frac{\Delta N}{N}(\text{scale error}) = \frac{\epsilon\rho\ \Delta N_{bb}\ (\Delta T)}{\epsilon\ \rho N_{bb}} + \frac{N_{bb}\ (T)\ \epsilon\ \Delta\ \rho}{\epsilon\ \rho N_{bb}} + \ldots$$

$$\frac{\Delta N}{N} = \frac{\Delta N_{bb}\ (\Delta T)}{N_{bb}\ (T)} + \frac{\Delta\epsilon}{\epsilon} + \frac{\Delta\rho}{\rho}$$

For independent error sources,

$$\frac{\Delta N}{N} = \sqrt{\left(\frac{\Delta N_{bb}}{N_{bb}}\right)^2 + \left(\frac{\Delta\epsilon}{\epsilon}\right)^2 + \left(\frac{\Delta\rho}{\rho}\right)^2}$$

The algebraic sum and rss scale errors versus temperature are shown in Figure 75.

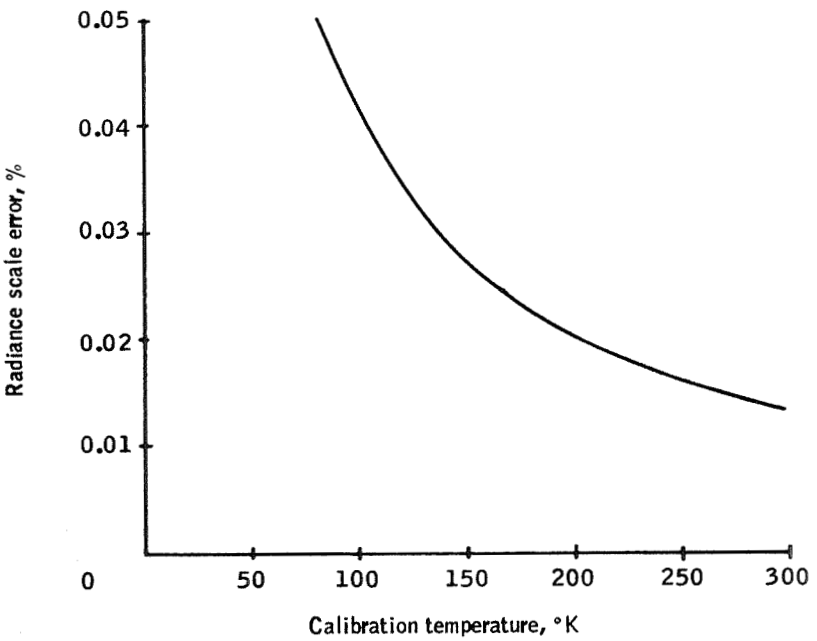

Figure 74. Blackbody Radiance Error versus Temperature for $\Delta T = 0.01°K$

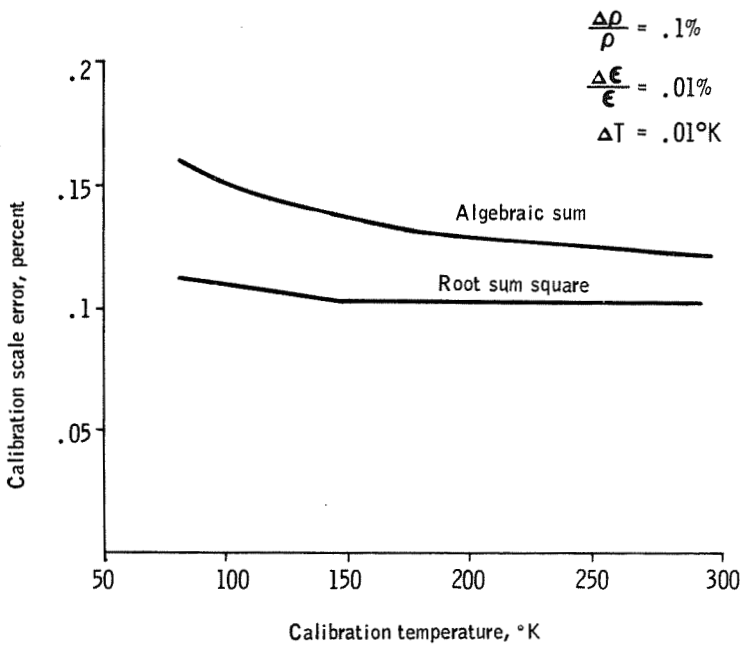

Figure 75. Calibration Scale Error versus Calibration Source Temperature

Diffraction and geometrical aberrations. -- When calibrating a radiometer system, a uniform infinite, extended source is simulated by one that covers a solid angle larger than the radiometer detector projected onto the source so that the detector will see the uniform source only. However, due to diffraction and geometrical aberrations in the radiometer optics, the projection of a uniform-response, finite-size detector will not generally be uniform in response and finite in size. The integral over the detector response in the physical detector plane (with angle as the variable) and the integral over the projected detector in the source plane (still with angle as the variable) are the same, however. Thus, the projected detector response will have tails outside the source. The ratio between the integral over these tails and the total integral is an error which is introduced by assuming the source to be sufficiently large (larger than the detector response function), or assuming first-order optics with no diffraction and geometrical aberrations. The projected detector response is a function of detector size, radiometer optics, and PCS collimator.

The deviation from first-order optics is due to diffraction and geometrical aberrations whose effects will be treated separately. It will be shown that the geometric effects in the PCS can be neglected for the parameters of interest.

Diffraction effects: Assume a point detector on-axis in a perfect radiometer optical system. The projection of this detector by the PCS off-axis paraboloid has then the following projected response if Fraunhofer diffraction is assumed:

$$R(\omega) = \frac{\pi a^2}{\lambda^2}\left[\frac{2J_1(ka\omega)}{ka\omega}\right]^2 \tag{56}$$

where

a = aperture radius

λ = wavelength

$k = 2\pi/2$

ω = the angle (in radians) off-axis

Assume that the source has an angular radius of ω_o. The fraction of the projected detector response contained within the source area is then

$$L(\omega_o) = \frac{\pi a^2}{\lambda^2}\int_0^{2\pi}\int_0^{\omega_o}\left[\frac{2J_1(ka\omega)}{ka\omega}\right]^2 \omega d\omega d\phi = 2\int_0^{ka\omega_o}\frac{J_1^2(x)}{x}\,dx \tag{57}$$

From reference 7

$$2\frac{J_1^2(x)}{x} = \frac{d}{dx}\left[J_o^2(x) + J_1^2(x)\right] \tag{58}$$

So

$$\mathbf{L}(\omega_o) = 1 - J_o^2(ka\omega_o) - J_1^2(ka\omega_o) \tag{59}$$

Because $\mathbf{L}(\omega_o)$ is an ever decreasing function and $\mathbf{L}(\omega_o)$ changes very little from one dark ring to the next for large $ka\omega_o$, we will consider such $ka\omega_o$ that $J_1(ka\omega_o) = 0$. Thus,

$$\mathbf{L}(\omega_o) \approx 1 - J_o^2(ka\omega_o) \tag{60}$$

But for large x we have

$$J_o(x) \approx \sqrt{\frac{2}{\pi x}} \cos\left(x - \frac{\pi}{4}\right) \tag{61}$$

When $J_1(x_n) = 0$, we have maxima for $J_o(x_n)$. Therefore,

$$J_o(x_n) \approx \sqrt{\frac{2}{\pi x_n}} \tag{62}$$

For large $ka\omega_o$ we thus have

$$\mathbf{L}(\omega_o) \approx 1 - \frac{2}{\pi(ka\omega_o)} \tag{63}$$

For (focal length = 120 inches, source size = 1 cm)

$$\lambda = 15\mu$$

$$a = 12 \text{ in.}$$

$$\omega_o = \frac{0.5}{120 \times 2.54} = 1.67 \times 10^{-3} \text{ rad} = 1.67 \text{ mr}$$

we have

$$\mathbf{L}(1.67) \approx 1 - 3.0 \times 10^{-3} \tag{64}$$

That is, we are losing 0.3% of the response function. This is equivalent to saying that angular intensity distribution of the collimated PCS output is down 0.3% at the center.

We will now assume a point detector 0.5 mr off-axis and we want to find the fraction of the response function that is lost due to diffraction. As the exact solution is difficult to get due to asymmetry, we will bound the fraction with the source sizes indicated in Figure 76.

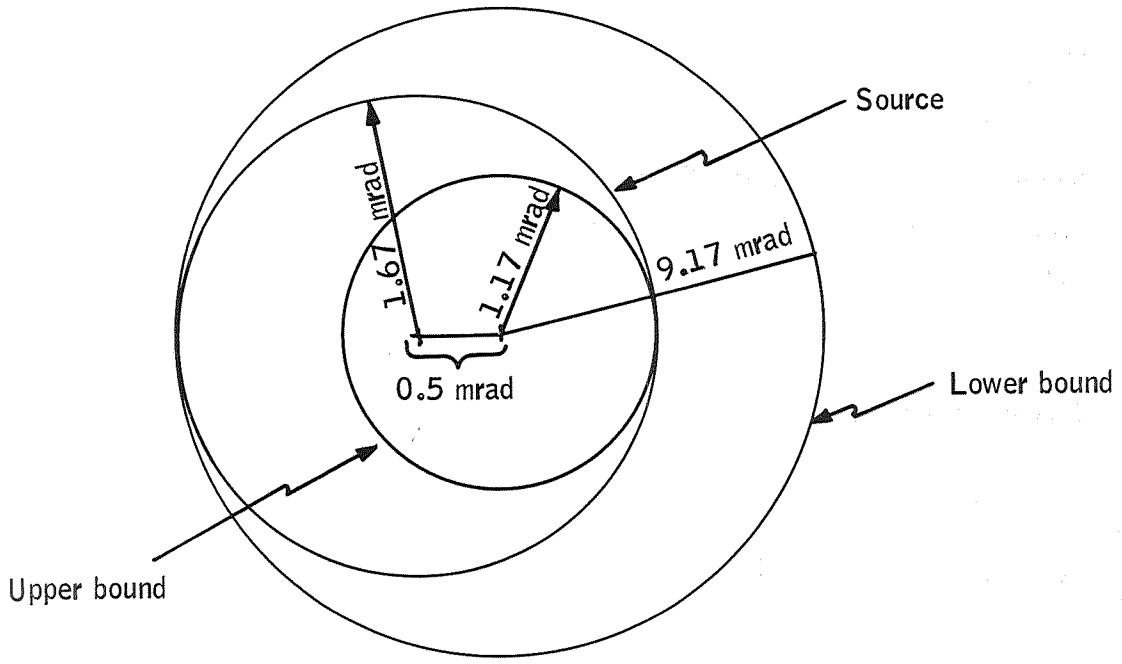

Figure 76. Diffraction Bounds, 0.5 mr Off-Axis

We then get for the upper bound; if assuming the regular Frauenhofer pattern,

$$L(1.17) \approx 1 - 4.3 \times 10^{-3} \tag{65}$$

And the lower bound,

$$L(2.17) \approx 1 - 2.3 \times 10^{-3} \tag{66}$$

For an extended detector 1 mr in diameter with perfect radiometer optics, a conservative estimate seems to be that between 0.3% and 0.4% of the detector response is lost due to diffraction in the PCS system. In other words, by assuming first-order optics an error between 0.3% and 0.4% is introduced for a diffraction-limited 24 inch, f/5 PCS collimator with a 3.33 mr source and a perfect radiometer with a 1 mr circular fov.

Geometrical aberration effects: The PCS collimator is an f/5 off-axis paraboloid, which is made as through it were a piece of approximately an f/2 on-axis paraboloid. For a paraboloidal reflector we have two geometrical aberration effects, coma and astigmatism. A conservative estimate of these aberrations for the f/5 off-axis reflector will be to consider the coma and astigmatism for the on-axis f/2 reflector. The formulas for sagittal coma and astigmatism are (ref. 8), respectively,

$$\text{coma}_s = \frac{U_P}{16(f/\#)^2} \tag{67}$$

$$\text{astigmatism} = \frac{U_P^2}{2(f/\#)^2} \quad \text{(stop at mirror surface)} \tag{68}$$

For 0.5 mr off-axis ($U_P = 0.5 \times 10^{-3}$) and f/2 we have

$$\text{coma}_s = \frac{0.5 \times 10^{-3}}{16 \times 2^2} = 7.8 \times 10^{-6} \text{ rad} = 7.8 \times 10^{-3} \text{ mr} \tag{69}$$

$$\text{astigmatism} = \frac{0.5^2 \times 10^{-6}}{2 \times 2} = 6.0 \times 10^{-8} \text{ rad} = 6.0 \times 10^{-5} \text{ mr} \tag{70}$$

The sagittal coma is one third of the total coma blur or

$$\text{coma}_t = 3 \times 7.8 \times 10^{-3} = 0.023 \text{ mr} \tag{71}$$

Coma will thus not spread the projected detector response any further than to 0.5 + 0.023 = 0.523 mr off-axis, as compared with the source size 1.67 mr. The astimatism is two orders of magnitude smaller than the sagittal coma; therefore, it is believed that the total astimatic blur (100% blur circle) is smaller than the total coma blur.

Combined effect: Compared to diffraction effects, the geometrical aberrations in the PCS system are thus negligible for a 1 mr fov radiometer detector. When nonperfect radiometer optics are used, their diffraction and geometric aberrations have to be considered. Assuming the PCS to be limiting the optical blurring, the error introduced by assuming first-order optics is between 0.3% and 0.4%.

Error summary. -- The PCS radiance errors may be summarized as follows:

- Bias errors (linear sum) = 4.0×10^{-3} W/m^2-sr
- Scale errors at 100°K (rss) = 0.11%
- Diffraction errors with a 1-mr fov radiometer detector = 0.4%
- Geometrical aberration errors with a 1-mr fov radiometer detector are relatively negligible
- Combined total scaling error (rss) = $\sqrt{(0.11)^2 + (0.4)^2} = 0.41\%$

Thermal Analysis

A thermal analysis effort was performed to support the design of the PCS during part I of the ARRS program. The analysis included nodal break-up and computer solutions of the system's components and assemblies. The major areas of study included

- Sizing the source and guard heaters and determining their required temperature control system characteristics
- Source thermal gradient characteristics
- Transient and steady-state analysis of the chopper blade cooldown characteristics
- System steady-state cooling load
- System transient cooling load and cooldown time

Source thermal analysis. -- The PCS source was thermally analyzed using a 10-node thermal resistance network representing the source-guard heater thermal model. From this model, the transient behavior of the source-guard assembly was determined and the heater sizes were determined to obtain proper thermal response characteristics. The source heater was sized at 260 W and the guard heater at 100 W. A proportional control system was considered in the analysis, and the resultant temperature differential between the source and guard was calculated to be 0.3°F. Supporting analyses are presented in Appendix H.

Source thermal gradients. -- Net heat flow out of the source block aperture results in an axial temperature gradient within the block, and thus on the surface of the off-axis cone cavity. A significant temperature gradient could produce an error in the radiance calculation for the source aperture; that is, the assumption of an isothermal source will be invalid. The source axial temperature graident may be determined by calculating the axial heat flow through the block.

The temperature levels of the source, guard, and other PCS components near steady state were obtained from the computer solution. Although steady-state temperature levels were not achieved at 20 hours, it is believed that the system is near enough to steady state such that the temperature differences between components given in the computer output are representative of steady-state temperature level differences.

The copper source block receives thermal energy from the guard heater (see Figure 77). It suffers heat loss by conduction to the chamber (70°F) and by radiation to the aperture plate, mirror, radiometer, and shrouds (all assumed at liquid nitrogen temperature of -322°F). The source block heat flows were determined from the final temperature levels in the computer solution and the thermal math model conductances.

• Heat flow rate from the guard heater to the source	0.5008 BTU/hr
• Heat flow rate lost to the chamber mirror, aperture, and shrouds	0.4252 BTU/hr
Difference	0.0756 BTU/hr

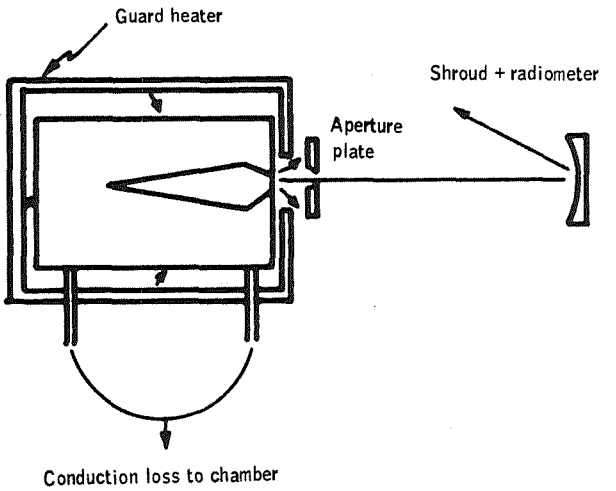

Figure 77. Source Heat Flow

The difference between the two heat flow rates is the energy being stored in the source block; this should be reflected in a source block temperature rise. The rate of change of source temperature from the computer solution printout is 0.0111°F/hr. Dividing the heat flow difference given above by the source block's total thermal capacitance listed in the thermal model yields a temperature rise rate of

$$\frac{Q}{C} = \frac{0.0756 \text{ BTU/hr}}{7.5 \text{ BTU/°F}} = 0.0101\text{°F/hr}$$

Thus, this check indicates that the approximate heat balance values on the source tabulated above are reasonably correct.

The net heat flow from the block out the aperture is then 0.4252 BTU/hr or 124 mW. A conservative estimate of the source temperature gradient (an upper bound) can be made by assuming that this entire flow originates at the rear and flows through the block to the aperture location. This procedure results in an upper bound on source axial temperature gradient, since in actual fact the majority of the source heat flow is added to the block along its periphery and at the front. The axial gradient can be calculated by the following analysis:

$$\Delta T_{source} = \frac{Q_{source}}{K_{source}}$$

where

$$K_{source} = \frac{K_{cu} A}{\Delta x}$$

K_{cu} = thermal conductivity of copper, 230 BTU/hr-ft

A = heat flow area, $\pi(2.5)(2) = 5\pi$ in.^{2}

Δx = heat flow path length, 8 in.

Q = 0.4252 BTU/hr (from computer solution)

Thus, $\Delta T = 0.0113°F = 0.0063°C$.

This temperature gradient results in a temperature error of ±0.003°C on the effective average source temperature (see Figure 78). As discussed in NASA CR 66614, this temperature error is commonly relegated to an effective emissivity error, holding the source average temperature as an invariant parameter. Using this approach, Figure 79 indicates that the cavity monochromatic radiance will be in error of approximately 0.003% at 300°K, and 0.03% at 100°K.

Thus, source thermal gradients appear to be small, and they result in negligible errors in the cavity radiant flux.

Chopper thermal analysis. -- As noted in the discussion of the PCS radiance analysis, the chopper thermal emission is a direct contributor to the total bias error. Transient and steady-state thermal analyses were performed on the chopper to ascertain if its cooldown rate and steady-state equilibrium temperature were compatible with the operational requirements and the other cooled elements in the PCS.

Results of the transient analysis, as described in Appendix A, show that an undesirably long time, in excess of 10 hours, will be required for the chopper blade to achieve an equilibrium temperature of 80°K during the cooldown sequence by radiative cooling. A conduction path with 1% of the blade area in contact with a cold baffle will cause the blade to cool down to liquid nitrogen temperature in less than 0.5 hour.

System steady-state cooling load. -- The PCS steady-state thermal losses were calculated and are summarized in Table 24. The calculations are presented in Appendix J.

The total dissipation of 667 W leads to a nitrogen consumption of 16 liters/hr, as follows:

$$\dot{v} = \frac{P}{\gamma \rho} = \frac{(667W) \times (3.41 \text{ BTU/hr/W})}{(85.4 \text{ BTU/lb}) \times (1.8 \text{ lb/liter})} = 16 \text{ liters/hr}$$

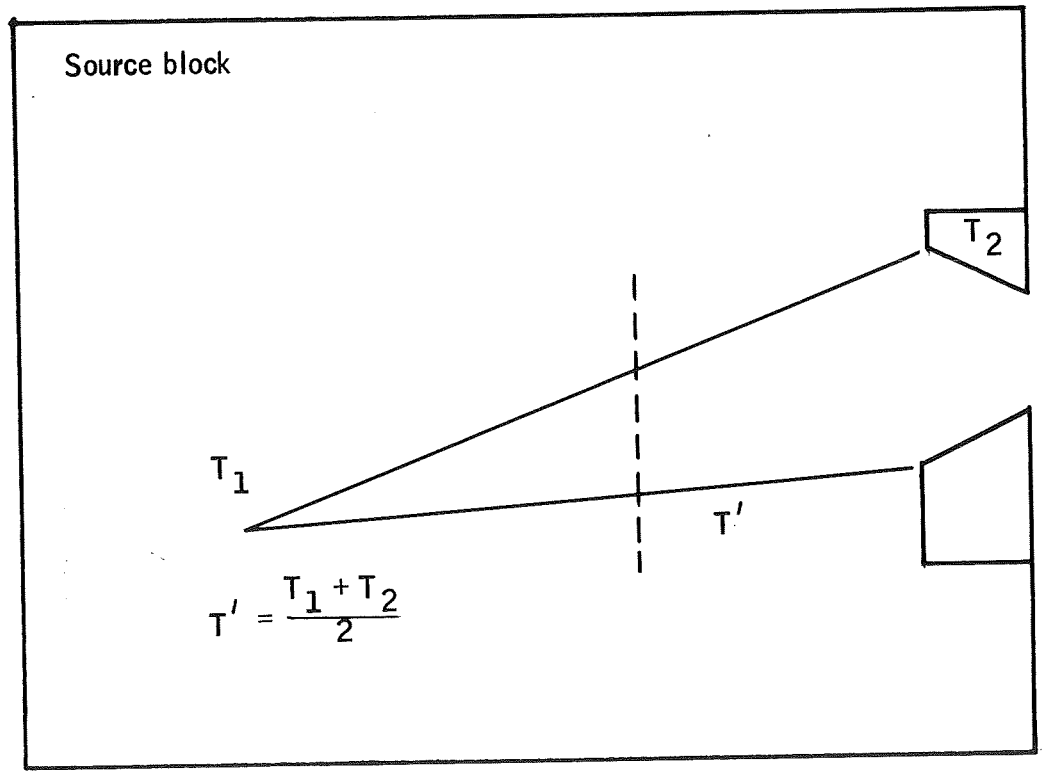

Figure 78. Average Source Temperature, T' ±0.003°C

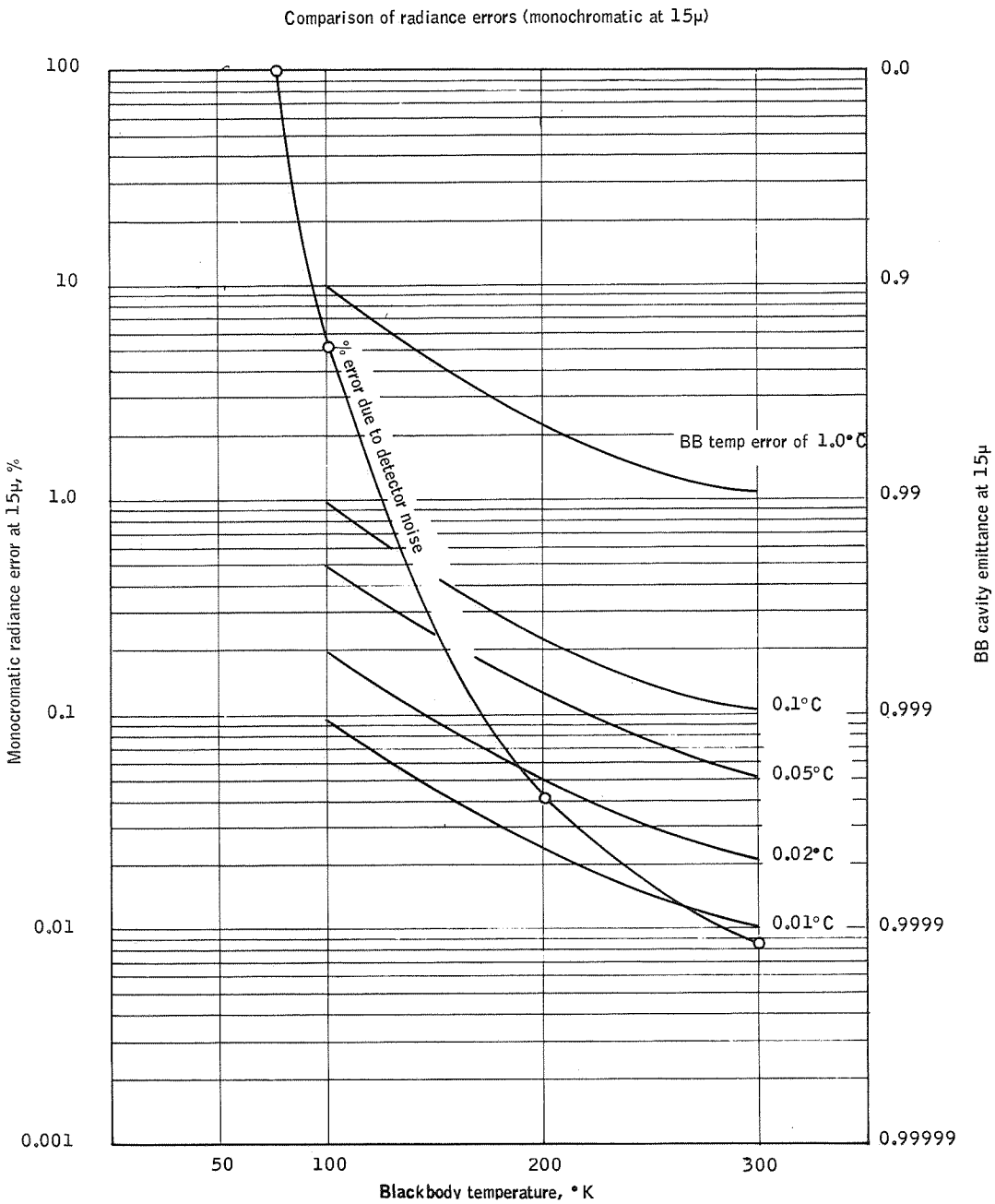

Figure 79. Radiance Error Due to Temperature Error

TABLE 24. - TOTAL STEADY-STATE PCS LOSSES

1. Main shroud (includes two "c" shrouds)	322 W
2. Mirror cooling coil	279 W
3. Mirror front baffle	0.5 W
4. Source aperture and chopper baffles	2.3 W
5. Front baffle	11.5 W
6. Rear ion pump	20 W
7. Folding mirror	0.5 W
8. Output beam baffle	30 W
	~667 W

where:

P = heat load

γ = LN_2 heat of vaporization

ρ = LN_2 density

Estimated system losses are 1 liter/hr in piping transfer line conduction losses, 25 liters/hr in feed-through line conduction losses, and 20 liters/hr in circulating pump conduction losses, totalling 46 liters/hr.

Total estimated flow rate is then 16 + 46 = 62 liters/hr. This compares to the present LRC chamber which, when throttled down to a minimum flow rate to maintain liquid nitrogen temperatures, consumed the contents of a 115-liter tank per day.

In addition to avoiding the high consumption rate of an open system venting into the atmosphere, the closed-cycle system offers a further advantage. The closed-cycle system will maintain positive pressure, thereby keeping the nitrogen in a liquid state. No gaseous nitrogen is allowed to form, which could cause localized warm areas in the circulating system due to vapor lock.

System transient cooling analysis. -- The detailed transient analysis is presented in Appendix J, and the results are summarized in Table 25. Cooldown time for the main shrouds was calculated to be five hours and the main collimating mirror 5.6 hours. These are limiting elements in the PCS cooldown process.

TABLE 25. - SUMMARY OF DETAILED TRANSIENT ANALYSIS RESULTS

Item	Transient Cooling Load (liters/hr)
Mirror	14.5
Main shrouds	15
Source and guard	27
Others (steady-state load)	54
Total	110.5

Triple-Point Cell Analysis

Objective. -- An investigation was made to determine whether a water triple-point cell, normally used for calibrating thermometers, can be used as an absolute radiance comparison and calibration point within the operating range of the PCS.

The purpose of using such a standard cell is to obtain a correlation between the blackbody source radiance and an absolute standard of radiance traceable to NBS. The water triple-point cell would add confidence to the theoretical level of radiance calculated from source temperature which is measured by NBS traceable platinum resistance thermometers.

Three potential problem areas initially were anticipated:

1) The method of correlating energy distributions of the triple-point cell and blackbody source could prove difficult.

2) The cell would be used in combination with a folding mirror. The effect of this mirror on the cell's radiation beam would have to be determined.

3) The effect of the hostile vacuum environment on cell operation would have to be evaluated.

During Part I the investigation concerned itself primarily with the third problem area. Specific objectives were as follows:

- The region of constant temperature within the cell
- The amount and region of constant emissivity within the cell
- The effects of exposing the cell to a vacuum

- The heat loads which would occur in interfacing the cell with the chamber at liquid nitrogen temperature
- The orientation limitations for operating the cell

Cell installation. -- The cell under consideration is manufactured by Trans-Sonics Inc., Burlington, Massachusetts. Type 130B is illustrated in Figure 80 and exhibits the following properties:

- Region of constant temperature is bottom two-thirds of cell
- The inner well may be exposed to a vacuum
- The cell can operate up to 20° of arc from vertical
- Any modifications of the cell must be made by Honeywell

The proposed installation of the triple-point cell in the PCS is shown in Figure 80. The neck is cut down; the cell is then installed on a mounting flange using rubber seals and a support frame. To place the cell in use, powdered dry ice is poured into the inner well to freeze a mantle of ice around the tube. Next, a 3/8-inch-diameter rod at room temperature is inserted into the well until the ice mantle has melted away from the well wall (as evidenced by free rotation of the ice mantle when the jacket is rotated sharply). Then, under normal use, water is poured into the well to assure good thermal contact.

If the cell is to be used in a vacuum, the inner well is empty rather than being filled with water, and the flange is bolted to the primary calibration chamber as shown in Figure 81. A beaker of water and ice is then raised to submerge the cell completely. The chamber is pumped down, and, if a thin layer of water remains between the ice mantle and inner wall, the bottom two-thirds of the cell can be used as an absolute reference at 0.010°C.

The installation is characterized by the following properties:

- The LN_2 shroud forms an aperture so that the radiometer sees only the interior of the cell.
- The cell is positioned so that the folded beam extending from the collimating mirror focuses on the aperture and receives only rays originating from the bottom two-thirds of the well.
- The cell is completely submerged in icewater in accordance with NBS standard procedure for triple-point cell operation.
- Limited contact with supporting members and the vacuum seal reduces heat conductivity paths to a minimum.
- A glass container for the icewater permits viewing of the ice mantle during operation.

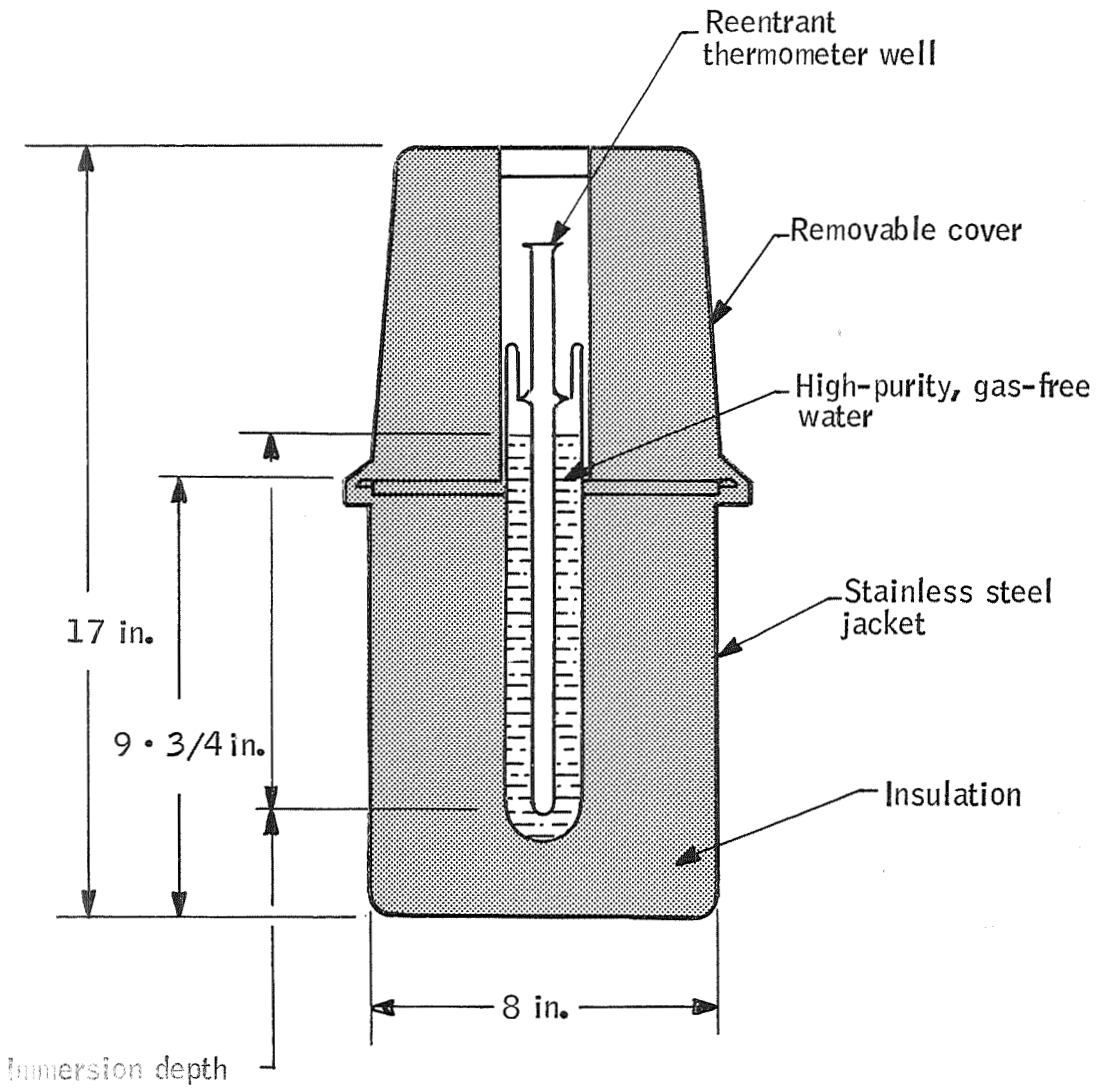

Figure 80 Trans-Sonics, Triple-Point Cell

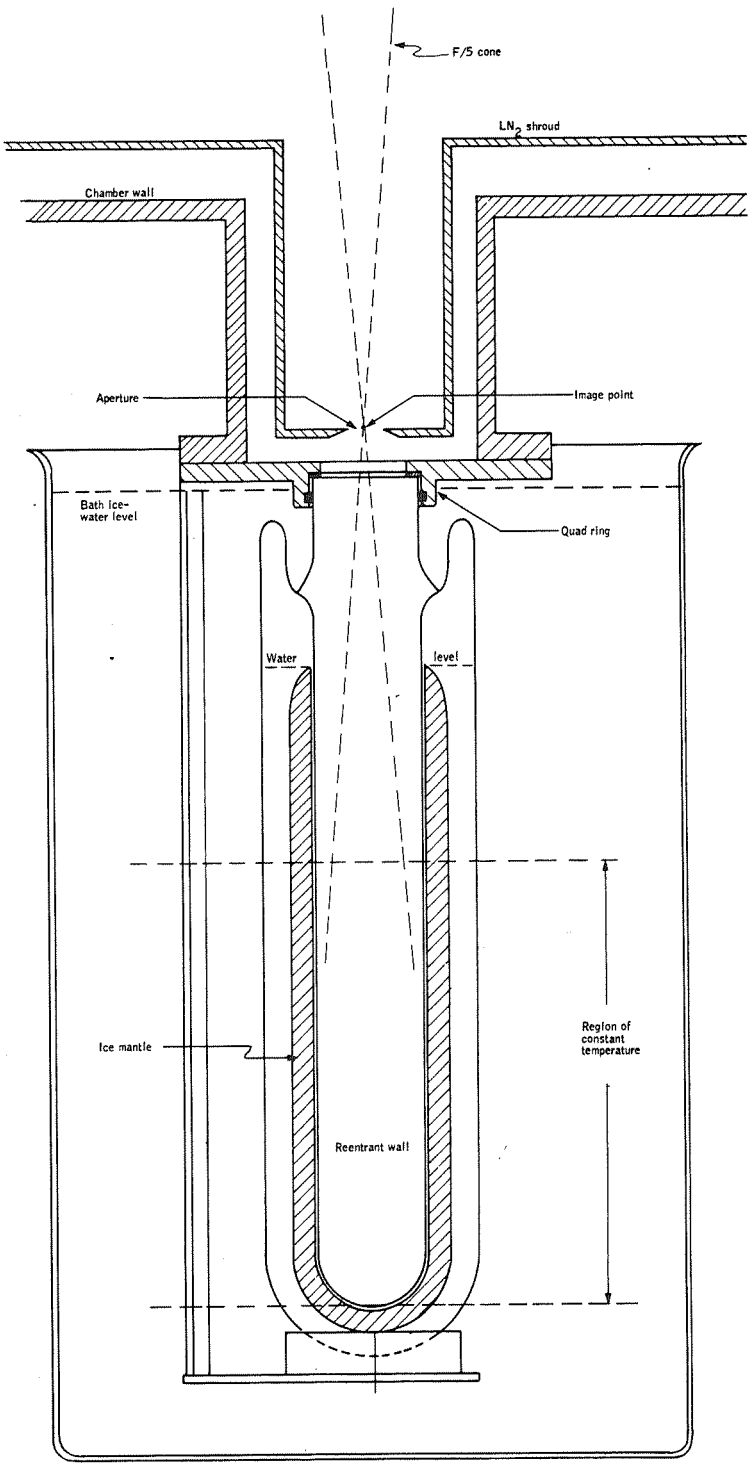

Figure 81. Triple-Point Cell Installation

- The cell is initially locked in a support frame to prevent damage during handling.

- The universal flange allows connection to other reference sources.

Thermal analysis. -- Because the cell's inner well is to be exposed to a vacuum rather than filled with water in the atmosphere, the resulting thermal effects were analyzed. Along with this, the cell's radiative properties were studied.

The thermal models for analysis were adapted from the installation shown in Figure 81.

Initial model: To obtain a rough measure of heat flow, the model diagrammed in Figure 82 was analyzed for a steady-state condition. Heat flow was assumed to be strictly radial in Regions I and II, and vertical in Region III.

- Part 1: Heat Flow In. Heat transfer at the air-beaker interface and resistances of the glass and water are taken into account: Result:

$$\boxed{Q_{in} \approx 30 \text{ BTU/hr}}$$

- Part 2: Heat Radiated from Wall. Assume maximum net radiation - i.e., the cavity radiates to 0°K.

where:

N = Blackbody irradiance at 32°F
$= 3.1 \times 10^{-2}$ W/cm^2

ϵ = Cavity emittance
$= 0.995 \approx 1$

A_s = Source aperture area
$= 7.91$ cm^2

Result:

$$Q_{rad} = 0.25 \text{ W}$$

$$\boxed{Q_{rad} = 0.85 \text{ BTU/hr}}$$

Modified model: The connection of the triple-point cell to the primary calibration chamber wall was considered in this analysis. Figure 83. shows

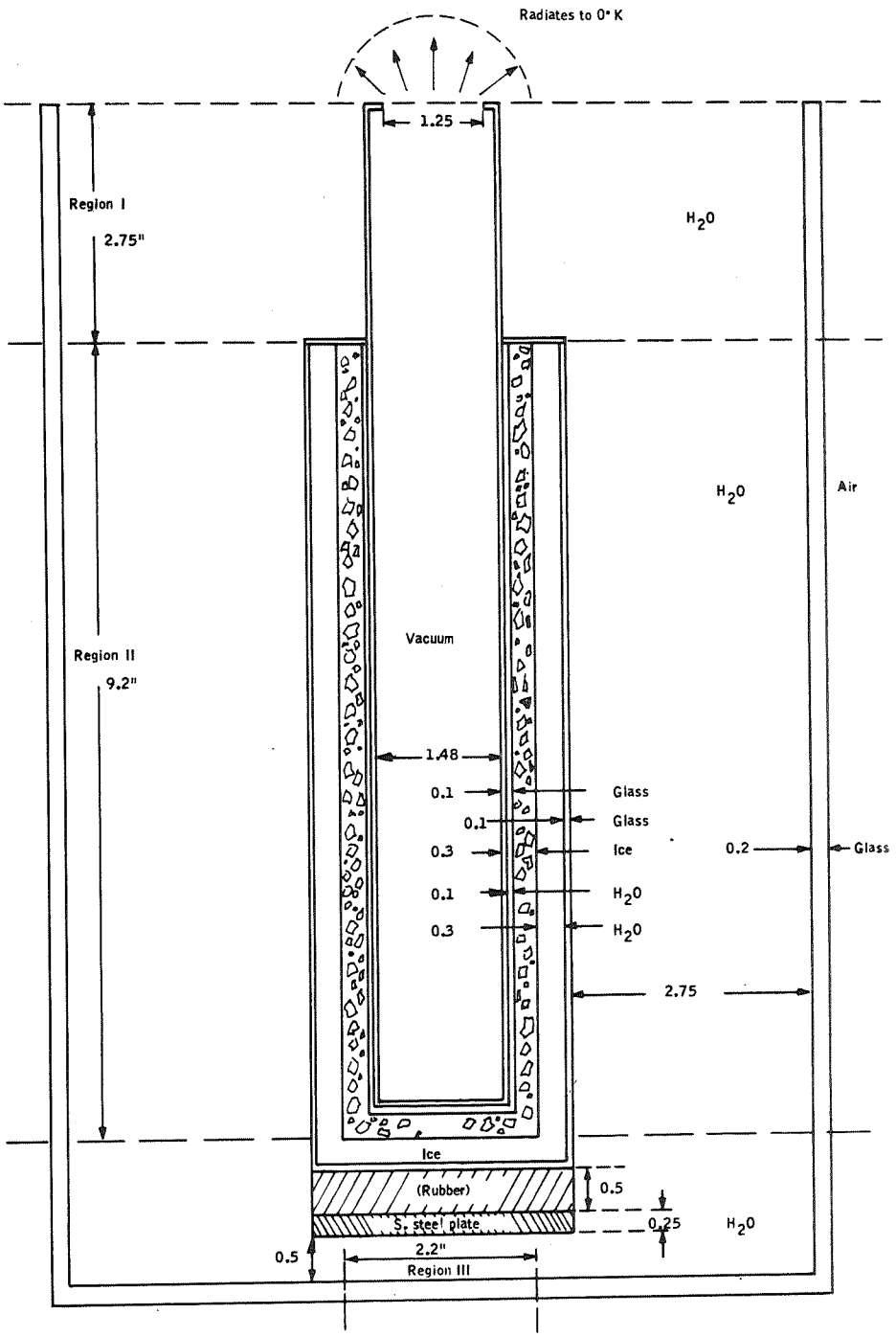

Figure 82. Triple-Point Cell Initial Model for Thermal Analysis

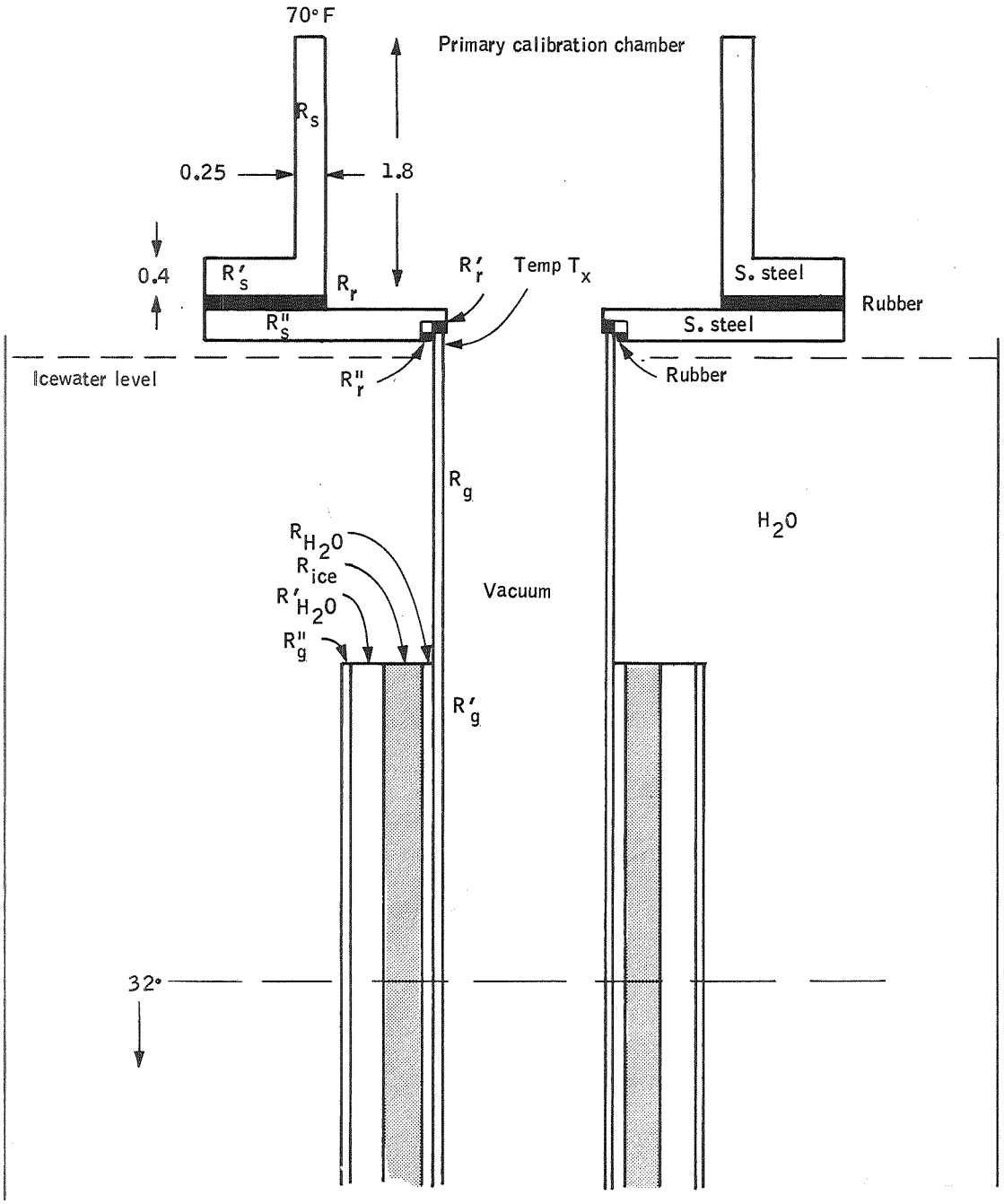

Figure 83. Triple-Point Cell - Modified Thermal Model

the assumed configuration. Heat conduction from the chamber wall at 70° down through the cell is used to obtain an estimate of the temperature T_x at the top of the cell. It is concluded that T_x can be as high as 40°F (worst-case estimate).

Further analysis shows that the incorporation of cooling coils in the water bath and around the perimeter of the cell-chamber interconnect flange can reduce the temperature T_x to below 33°F.

Radiative properties: A cursory radiation analysis indicates that the inner well can be made to radiate with an emissivity of at least 0.9995. This figure is obtained under the following assumptions:

- The aperture at the top of the well is 0.75 inch.
- Only first reflections are considered.
- A copper conical cavity (with L/D = 3) is placed at the bottom of the wall.
- The conical cavity has an emittance of 0.993 at 15μ (this number is extrapolated from experimental data taken at 10.6μ).
- The emittance of the glass is 0.90.
- All surfaces are diffuse except for the cone placed on the bottom.

A significant conclusion is that neither the incoming radiation at 70°K nor the temperature at the top of the cell has a significant effect on the cell's emissivity, provided the bottom two-thirds of the well is uniformly at 32°F.

Results:

Temperature, top third of cell	Emissivity of cell
34°F	0.9956
42°F	0.9959

Ice mantle analysis: The greatest difficulties with a triple-point cell appear to center around the behavior of the ice mantle. The following analysis points up some of these difficulties.

Consider a 1-inch section of the beaker-icewater, bath-cell located about half way between the top and bottom of the cell:

Assume:

- A uniform mantle has been formed under normal conditions so that a layer of water exists between the mantle and the well wall.

- Heat flow is only radial. That is, neglect heat flow down the well wall.

- The well instantaneously is exposed to a vacuum and a temperature field at 70°K.

The portion of Q_{in} which reaches the ice serves to melt it at its outer surface. None of this heat travels through the ice.

As heat is radiated from the well wall, a gradient forms across it. Heat flows from the water layers into the glass and a gradient is formed across it. Since the water is in contact with ice at 32° on the outside, the water in contact with the well wall turns to ice as it loses heat to the wall.

When the layer of water freezes out to the mantle, the ice begins to conduct to provide Q_{rad}. At this point the mantle grows or diminishes in size depending on the relationship between Q_{in} and Q_{rad}.

Compute T' for the condition illustrated in Figure 84 . Resistances through which Q_{rad} flows are

$$R_{H_2O} = 0.73 \frac{H_r \cdot °F}{BTU}$$

$$R_g = 0.40 \frac{H_r \cdot °F}{BTU}$$

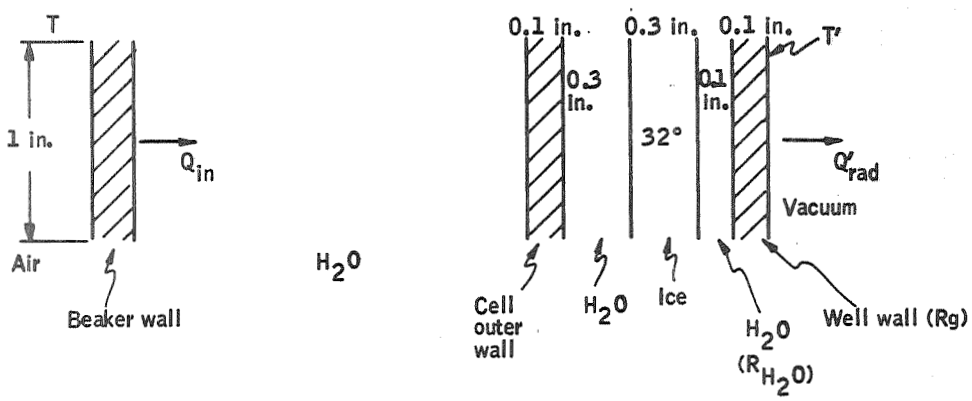

Figure 84. Triple-Point Cell Assembly Cross Section

Then

$$Q'_{rad} = K\Delta T = \frac{32 - T'}{R_{H_2O} + R_g}$$

where

$$Q'_{rad} \approx \frac{1}{8} Q_{rad} = \frac{1}{8}(0.85) \frac{BTU}{hr}$$

for the 1-inch section under consideration.

$$\left(\frac{1}{8}\right)(0.85) = \frac{32 - T'}{1.13}$$

$$T' = 32 - (1.13)\ (0.85) \left(\frac{1}{8}\right) = 32 - 0.12$$

$$\boxed{T' \approx 31.9°F}$$

Now consider the limits of accuracy in determining T'. Well wall thickness is not specified by the manufacturer and cannot be measured accurately. Inner melt thickness at any given time cannot be measured. Therefore, a conservative estimate of error limits is

$$\text{well wall thickness} = 0.1 \pm 0.05 \text{ inch}$$

$$\text{inner melt thickness} = 0.1 + 0.1 \ - 0.25 \text{ inch}$$

Then,

$$0.35 < R_{H_2O} < 1.1$$

$$0.30 < R_g' < 0.80$$

$$0.66 < R_{H_2O} + R_g' < 1.9$$

and

$$31.8°F \leq T' \leq 31.9°F$$

In practice, analytical accuracy is worse than this because heat flowing down from the top of the tube will cause a continuous change in the shape of the ice mantle and inner melt, resulting in a changing temperature gradient down the radiating well wall.

The following conclusions may be drawn from the foregoing analysis:

1. The triple-point cell, with its inner wall evacuated and looking at 80°K, no longer behaves as an absolute temperature reference.

2. It is unlikely that the temperature gradient along the inner wall can be kept constant as a function of time because the shape of the ice mantle cannot be controlled.

3. The temperature inside the well cannot be determined analytically to an accuracy greater than ±0.1°F.

4. Items No. 2 and 3 make it imperative that the temperature in the well be monitored when the cell is in operation if the cell is to be installed as in Figure 81.

Required cell modifications. -- Two possible modifications of the triple-point cell could make it feasible as an absolute temperature standard in the PCS.

The modifications suggested are shown in Figure 85. One possibility is to reduce the size of the inner well opening and thereby reduce the amount of radiation from the well. This would slow down or stop the freezing of the inner melt and could reduce the temperature gradient between the inner surface of the mantle and the well interior to within the limits of accuracy required.

The second possibility is to install a heating baffle which will radiate into the well the same amount of heat which is being lost through the hole. These two modifications can be used in combination as the figure shows.

Reduced aperture: Using the model described in the foregoing analysis, it is possible to quickly obtain an estimate of the size opening required to assure that this well wall temperature is within 0.0005°F of the triple-point temperature, 32.018°F.

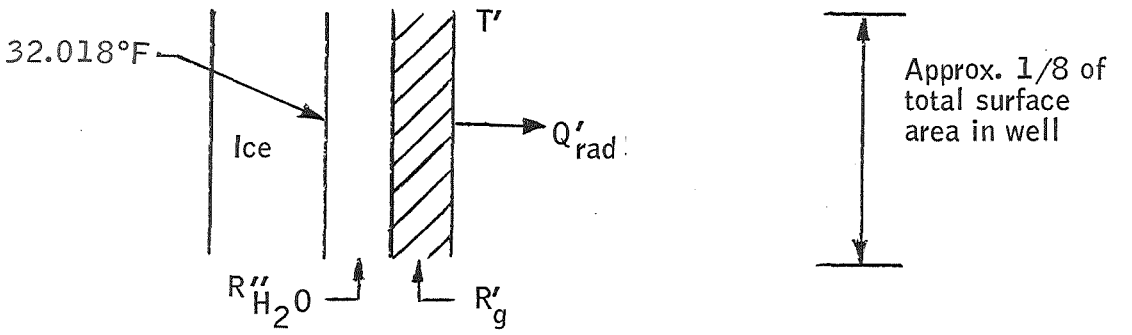

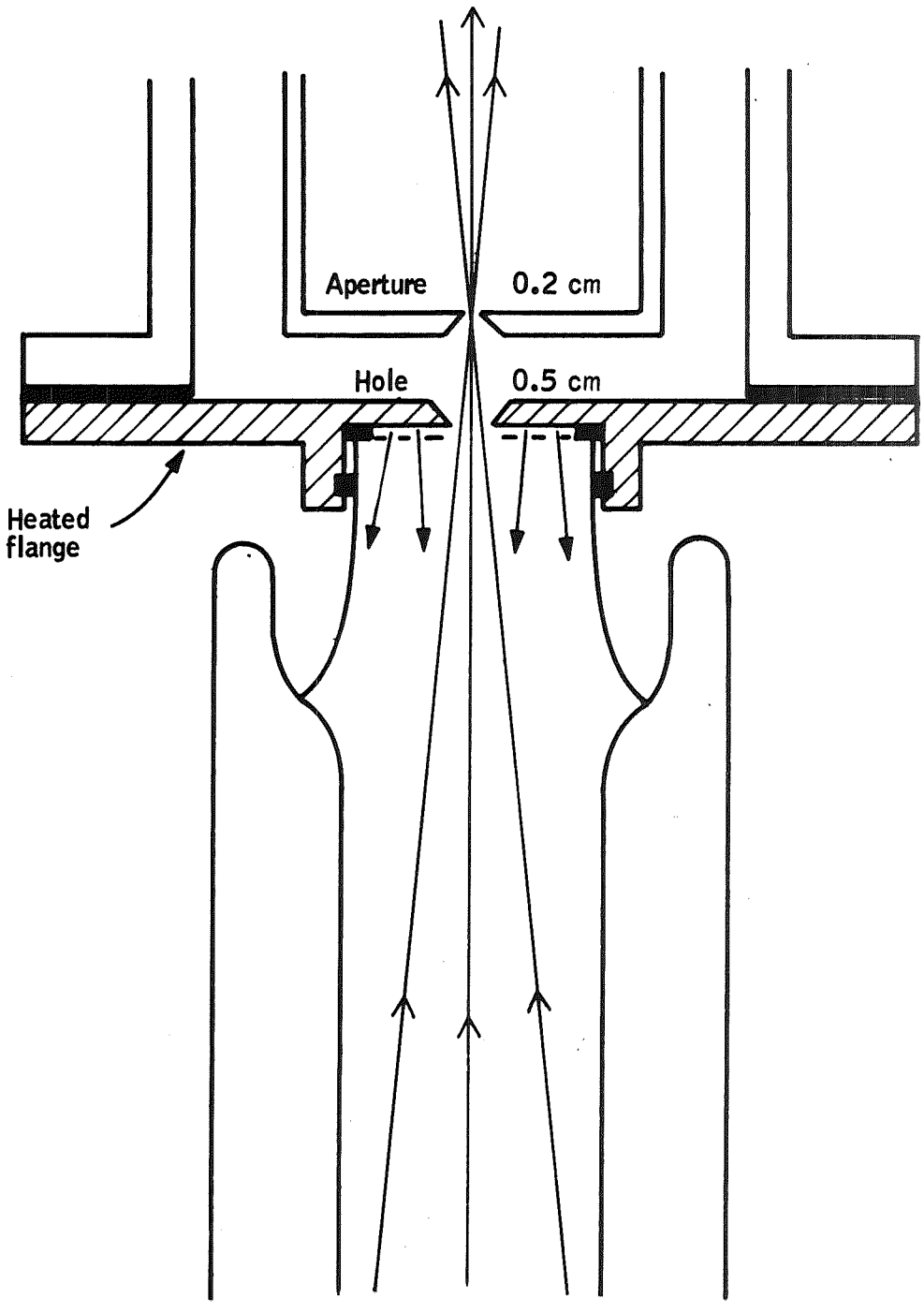

Figure 85. Triple-Point Cell Mount Modification

Thickness of the inner melt and the well wall are not accurately known. It was determined that

$$0.6\, R_{H_2O} + R'_g = \frac{2\ hr\cdot°F}{BTU}$$

We wish to find Q_{rad} such that

$$32.013 < T' < 32.018°F$$

By definition of the triple point, $T_{ice} = 32.018°F$ at its inner surface. Now, we can find an approximate value for Q'_{rad}:

$$Q'_{rad} = \frac{\Delta T}{(R''_{H_2O} + R'_g)_{max}}$$

$$Q'_{rad} = \frac{0.005°F}{\frac{2\ hr\cdot°F}{BTU}} = 0.0025\ \frac{BTU}{hr}$$

$$Q'_{rad} = 0.735\ mW$$

Then $$Q_{rad} = 8\, Q'_{rad} = 5.9\ mW$$

since Q'_{rad} was calculated for about 1/8 the total surface area inside the well.

Now

$$A_s = \frac{Q_{rad}}{N\epsilon}$$

$$\frac{5.9 \times 10^{-3}\ W}{(3.1 \times 10^{-2}\ W/cm^2)\ (1)}$$

$$\approx 0.2\ cm^2$$

and

$$\text{diameter} = 2\sqrt{\frac{\Delta s}{\pi}}$$

$$\boxed{\text{hole diameter} \approx 0.5\ cm}$$

This means that the LN_2 shroud aperture must be

aperture diameter $\approx$ 0.2 cm

Note that this analysis assumes a static condition with an inner melt of uniform thickness. In reality the condition is dynamic and the inner melt is continually changing shape.

Note also that this analysis is made for a section at the center of the cell. Conditions may be radically different at the top and bottom of the cell.

Radiative heater: Time limitations have precluded a quantitative investigation of this possibility. The following arguments provide some justification:

- Relative sizes of the hole and aperture can be adjusted so that no radiation from the heater is included in the f/5 cone.
- Since Q_{rad} is so small, the heater can operate very close to 32.018°F. Therefore, its effect on the uniformity of the B. B.-cell radiation at 32.018°F should be very small.
- Since the flange is metal and connected to chamber at 70°F, it may supply more radiative heat than is necessary and may have to be cooled with a coil around the outside.
- If the net heat flow in balances the heat flow out, the ice melt should remain relatively stable and uniform.

Conclusions and recommendations. -- The analyses have thus far indicated that the triple-point cell is potentially feasible as a radiance standard in the PCS chamber. It is recommended that the following analyses be done.

- The heater baffle temperature necessary to maintain equilibrium remains to be determined. Because of the small quantity of heat under consideration, all possible flow paths must be taken into account.
- When the heater temperature is determined, its effect on the quality of the cavity emittance should be evaluated.
- Conductive heat flow down the inner wall and the presence of a copper slug in the bottom will tend to cause uneven melting of the mantle. Detailed analysis is required to evaluate the situation.

Design Verification

Several items were initially identified as requiring early verification, preferably during Part I, before the Part II phase could be performed. Those items identified were investigations into

1) A method for and demonstration of performing a collimator reflectance measurement to $\approx 0.1\%$ with suitability of mechanizing the measurement for in situ use with the PCS

2) Investigation of performing a cavity emittance measurement of the PCS variable temperature blackbody source and the expected emittance level achievable

3) Investigation of the source temperature measurement to verify the accuracy and gradient condition of temperature through the blackbody source.

Discussions of the above investigations are presented in this section of the report.

Collimator reflectance measurement. --

Objective: The objectives of the collimator reflectance measurement effort were to define and experimentally verify a technique which could be used to perform in situ reflectance measurements of the PCS collimator with an accuracy of $\pm 0.1\%$.

While PCS collimator reflectance measurements will be made in a vacuum environment, the experimental verification of a measurement technique was conducted in a laboratory ambient environment in an LWIR wavelength interval which minimized atmospheric absorption effects; i.e., $\approx 9\mu$ to 12μ. This approach was used to permit a maximum of experimenting and diagnostic testing within the schedule constraints. Furthermore, a technique found to be capable of 0.1% accuracy reflectance measurement in the laboratory atmosphere was expected to be capable of better accuracy in vacuum conditions where errors caused by variable emission surroundings and atmospheric variabilities would not exist.

Test configuration evolution: Under Contract NAS 1-6010, analysis of the modified Strong method indicated the feasibility of 0.1% accuract reflectance measurements. The technique finally established differs considerably from that initially considered, and there were several steps involved in the evolution of the final technique. These steps are described in the following paragraphs to provide information concerning the problems inherent in a 0.1% accurate reflectance measurement.

Modified Strong method: Initially, the scheme which seemed to give most promise for a reflectance measurement good to 0.1 percent was the modified Strong method illustrated in Figure 86. Here a blackbody source radiation beam is chopped and passed through a beam splitter and an optical

system made up of three mirrors. Two of the mirrors are collimating off-axis parabolic mirrors, while the third is a large polished flat.

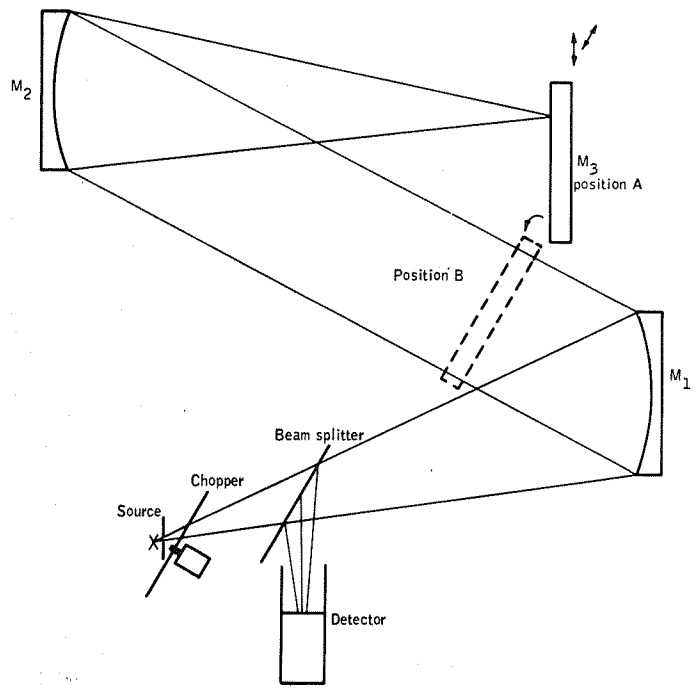

Figure 86. Modified Strong Method

The reflectance of mirror M_2 is determined by ratioing the detector response energies for the two positions of mirror M_3 located at A and B. This ratio is given by

$$\frac{S_A}{S_B} = \frac{H_\lambda \tau_{BS} \rho M_1^2 \rho M_2^2 \rho M_3 \rho_{BS}}{H_\lambda \tau_{BS} \rho M_1^2 \rho M_3 \rho_{BS}} = \rho M_2^2$$

or

$$\rho M_2 = \sqrt{\frac{S_A}{S_B}}$$

where

S_A, S_B = detector energy response for M_3 in positions A and B, respectively

H_λ = source energy in the wavelength region being considered

ρM_1, ρM_2, ρM_3 = mirror reflectances

τ_{BS}, ρ_{BS} = beam splitter transmittance and reflectance, respectively

This method assumes that H_λ, τ_{BS}, ρM_1, ρM_3, and ρ_{BS} do not change during the movement of M_3 between positions A and B.

An alternate approach to the method just described is the technique shown in Figure 87 . In this scheme the source is placed at a distance from M_1 equal to twice its focal length (radius of curvature of M_1 at parabola center). The same area on M_3 is illuminated in the two positions and the effect of M_3 reflectance variations and the different geometry eliminated from the measurement.

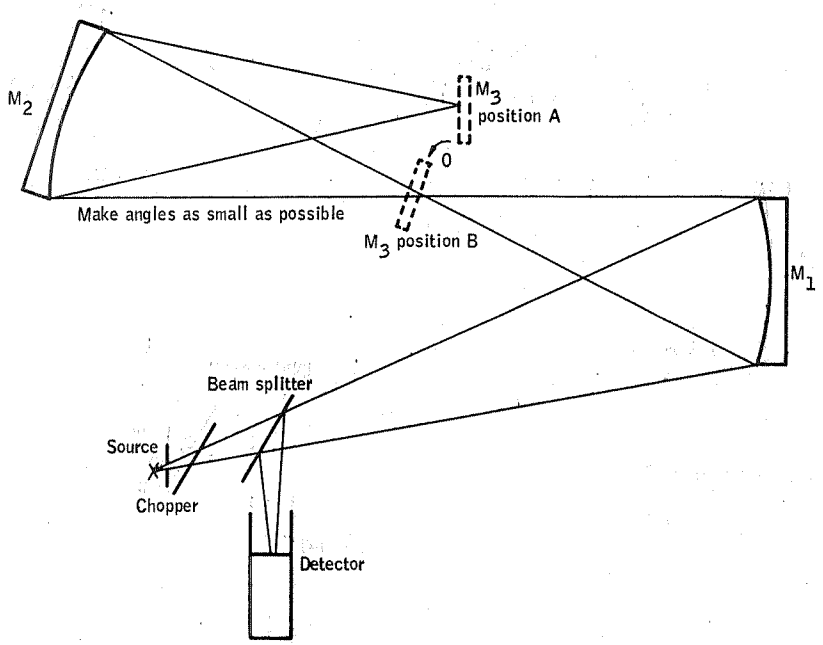

Figure 87. Alternate Method

Source and detector sizing: The original plan was to operate using a small source and to collect all of its energy on a relatively large detector (thermopile). However, the practicality of large area detector response nonuniformities created a significant problem in alignment repeatability requirements.

Measurements of thermopile response uniformity showed wide variations across the detector active area, and preliminary analysis indicated the need for repeating image placement on the detector to fractional arc sec precision when mirror M_3 was moved from position A to position B.

It was then decided to operate with a large uniform source and relatively small detector - a scheme which offered the following advantages:

- Eliminated the effects of detector sensitivity variations
- Reduced errors caused by system alignment instability
- Improved the signal-to-noise ratio by a factor of 5

Rooftop reflector: Preliminary analysis of the modified Strong method indicated that use of a beam splitter prevented alignment with a visible light source, caused a sufficient signal loss (effective double-pass transmission of ≈ 0.16) that signal-to-noise ratio was predicted to be marginal, and caused multiple internal reflections which were not analyzed in detail but were expected to cause significant problems. An effort was then made to find a means to provide beam separation without using a beam splitter. This effort resulted in replacing the beam splitter with a rooftop reflector as in Figure 88. With the source placed slightly off axis, relative to mirror M_1, and with the source beam reflected back through the optical system at a different off-axis angle, sufficient angular beam separation would exist that the roof top reflector could separate the output and return beams. With this modification, the modified Strong method (Figure 86) and the alternate method (Figure 87) became known as Configuration 1 (Figure 89) and Configuration 2 (Figure 90), respectively.

The advantage of such an approach is the elimination of the beam splitter disadvantages, including an increase in signal-to-noise ratio by a factor of ≈ 5. The main disadvantage is that the output and return beams do not occupy identical areas of either mirror M_1 or M_2. It was expected that there would be sufficient overlap of the output and return beams that negligible error would result and that the error magnitude could be experimentally determined by scanning the output and return beams over the mirror surfaces. However, further analysis and experimentation showed that these expectations could not be realized for all positions of mirror M_3 in Figures 86 and 87.

Analysis and preliminary experimentation with 6-inch parabolic mirrors revealed the following problems:

1) With a beamsplitter in the system, the witness flat is placed at the calibration mirror's focal point (position A). When a rooftop reflector is used in place of the beamsplitter, the incident and reflected beams must be separated at the reflector. To achieve this separation, the witness flat must be moved back of the calibration mirror's focal point with the result that the return beam is not collimated. This leads to erroneous results because the return beam is collimated when the witness flat is in position B.

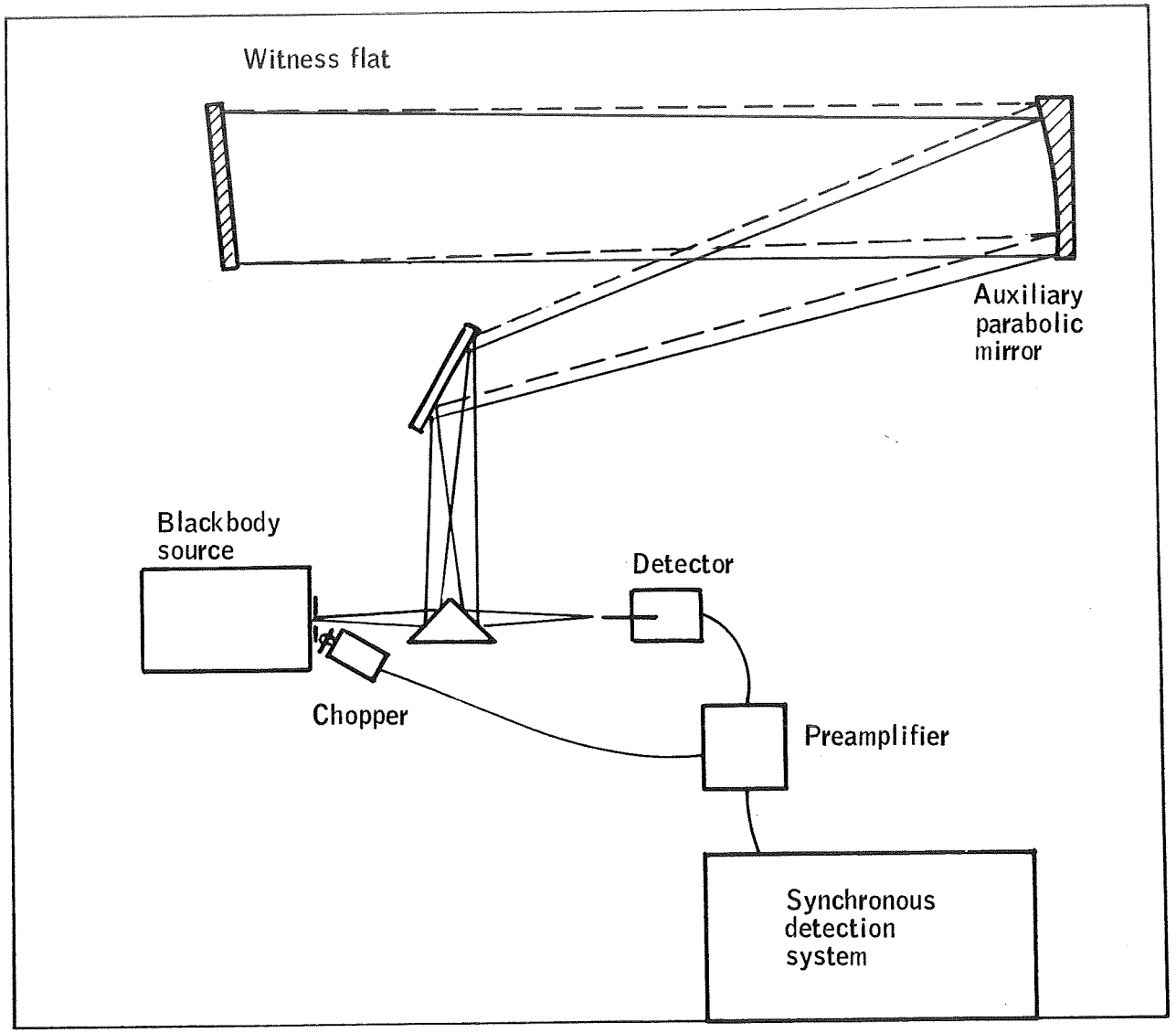

Figure 88. Beam Separation with Rooftop Reflector

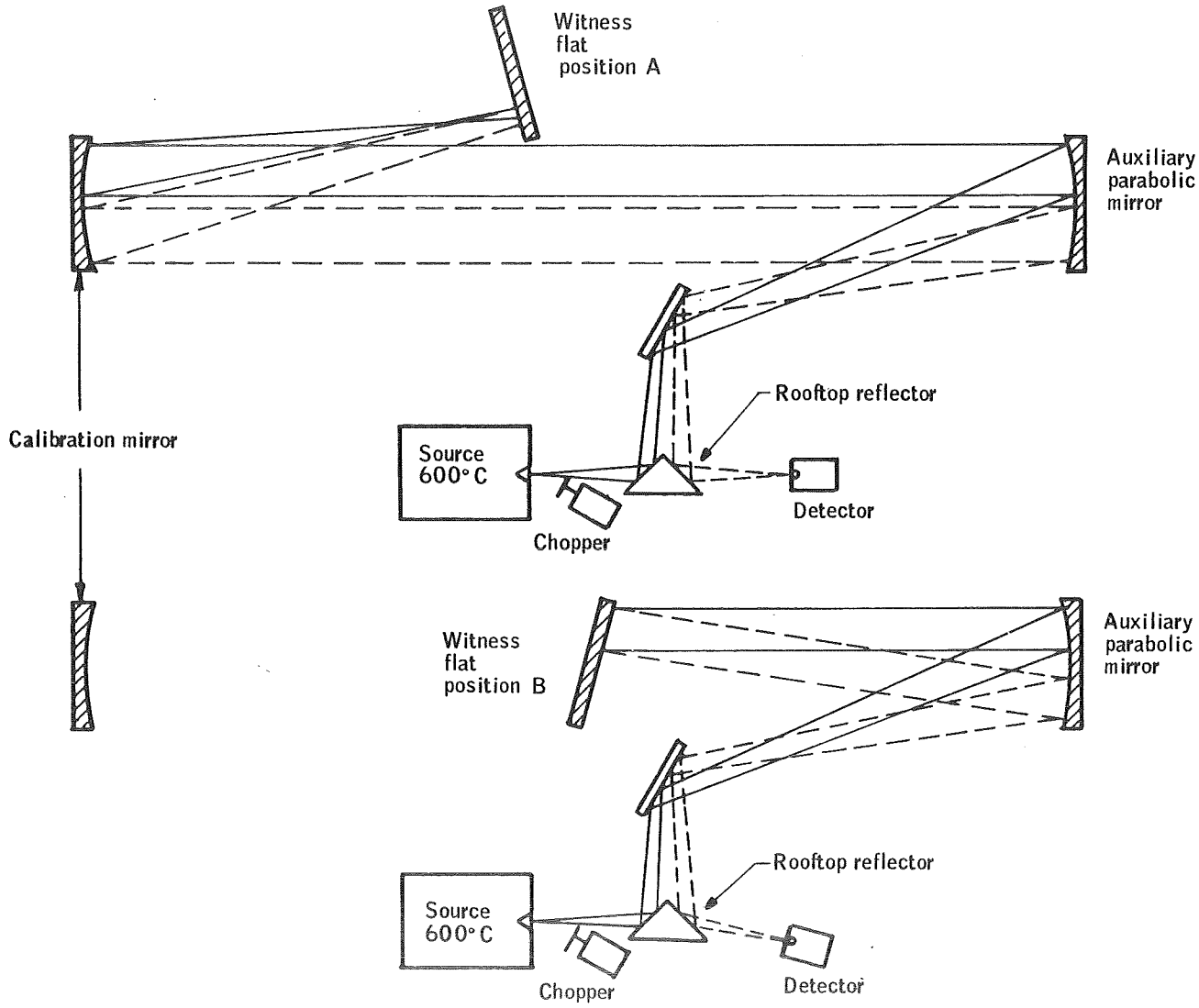

Figure 89. Configuration 1

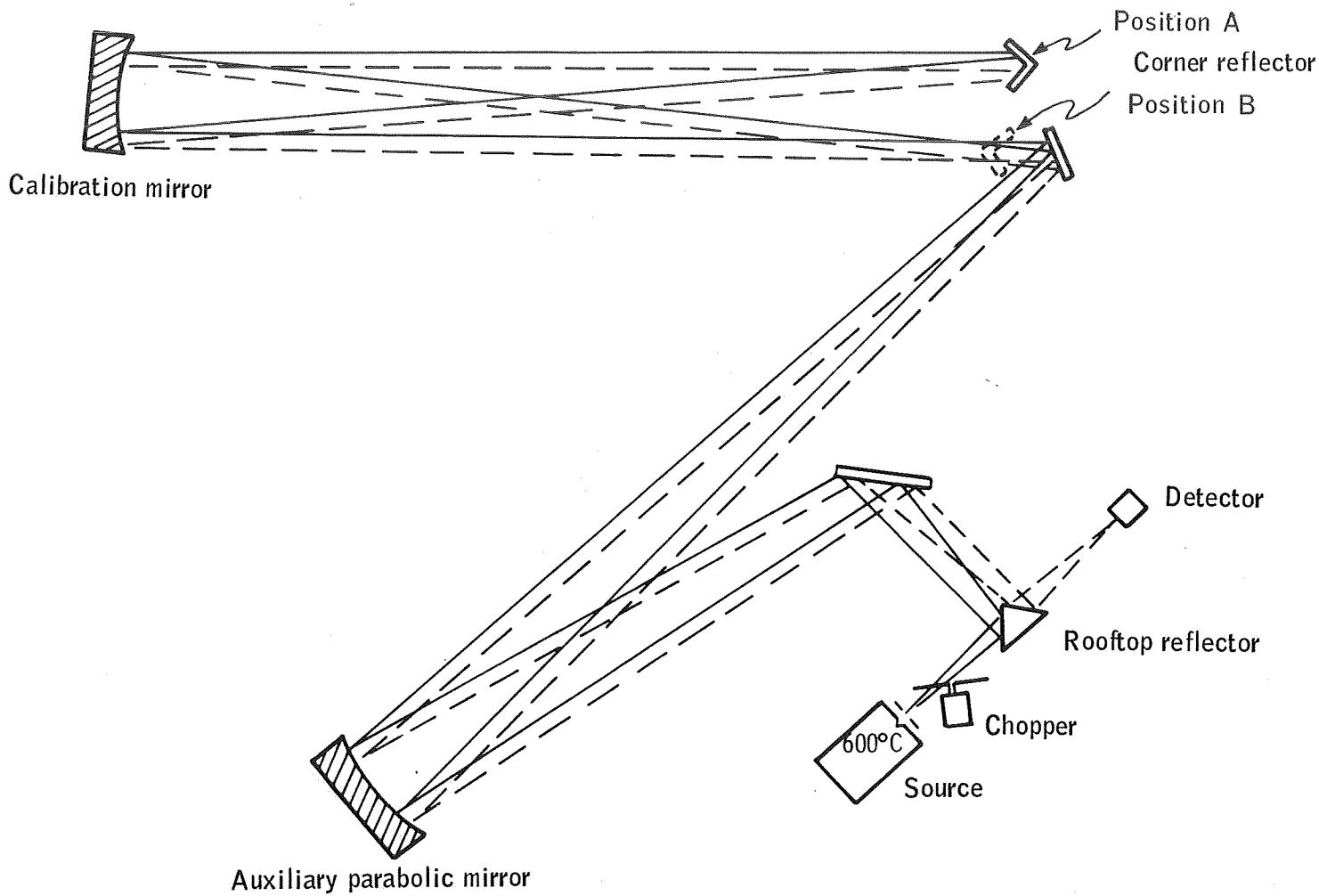

Figure 90. Configuration 2

2) An additional result of the positioning change is that the source image at the detector changes positions when the witness flat is moved from position A to position B.

3) An inherent deficiency of the modified Strong method is that the witness flat reflectance must be uniform over its entire area. This is necessary because the flat is placed at a focal point in position A and in the collimated beam if position B. That is, only a small portion of the mirror is filled in position A whereas the entire mirror is filled in position B.

4) Incorporation of a rooftop reflector in the modified Strong method requires complete separation of the incident and return beams to obtain complete angular separation, as shown in Figure 88. The effect is demonstrated in Figure 91 which traces the path of rays from the source through the system and on to the detector. Reflections from the parabolic mirrors are folded back for simplicity. In this figure the witness flat is placed beyond the focal point and set so that the top ray of the incident cone is coincident with the bottom ray of the return cone. If the witness flat is tilted counterclockwise so that the beams begin to overlap, the image cone envelops the source. Thus, it is not possible to achieve separation of image and source for the rooftop reflector if the beams overlap.

Figure 92 describes the same setup except that the witness flat is now moved in front of the focal point. If the witness flat is tilted counterclockwise so that the beams begin to overlap, the source cone envelops the image. Again, separation and overlap cannot be achieved simultaneously.

It follows that the beams must intercept opposite halves of the parabolic mirrors and must be less than 4 inches in diameter to achieve separation of source and image. Therefore, it is not possible with Configuration 1 to measure the total reflectance of the calibration mirror.

Configuration 3a: Because of the problems caused by both the beamsplitter and rooftop reflector, it was decided to look for a simpler, more basic method of measurement.

A scheme was devised which did not use either a beamsplitter or corner reflector; this scheme is illustrated in Figure 93. In this technique the detector is physically translated from one source image (formed by auxiliary mirror) to the other source image (formed by auxiliary mirror plus calibration mirror). However, since the detector signal is governed by the image f/No. cone, it would have been necessary to exactly duplicate or measure the image f/No. cone with the detector in positions A and B. This problem was overcome by interchanging, in Figure 93, the source and detector; this configuration is the final one used and is discussed in the following paragraphs.

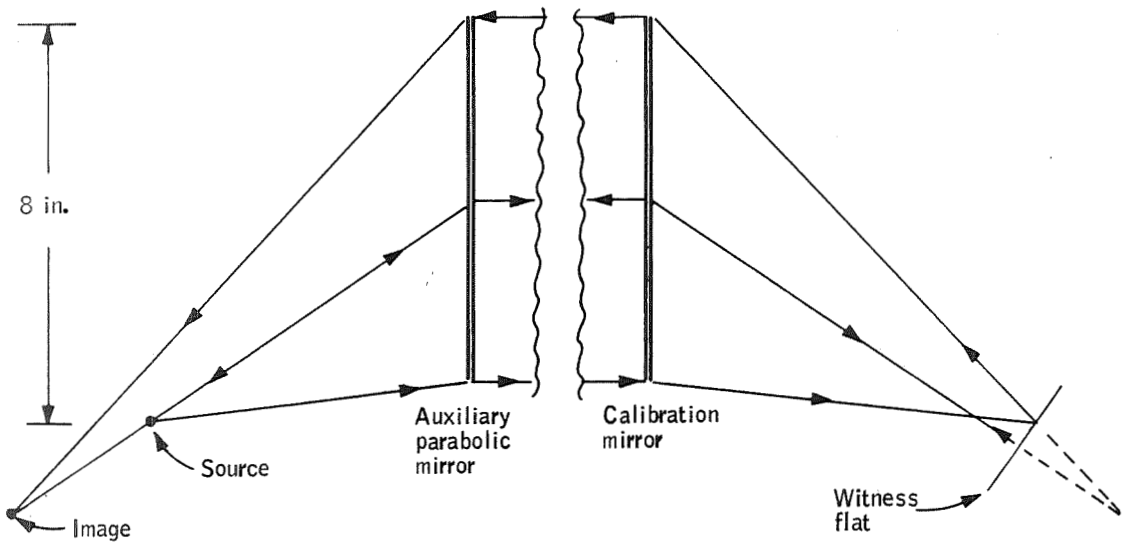

Figure 91. Beam Overlap, Configuration 1 (Witness Flat Behind Focus)

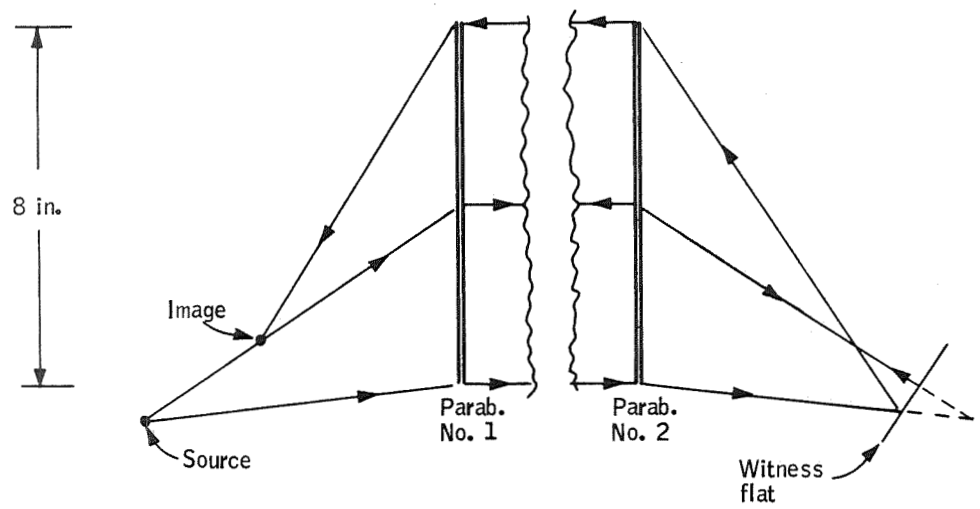

Figure 92. Beam Overlap, Configuration 1 (Witness Flat Before Focus)

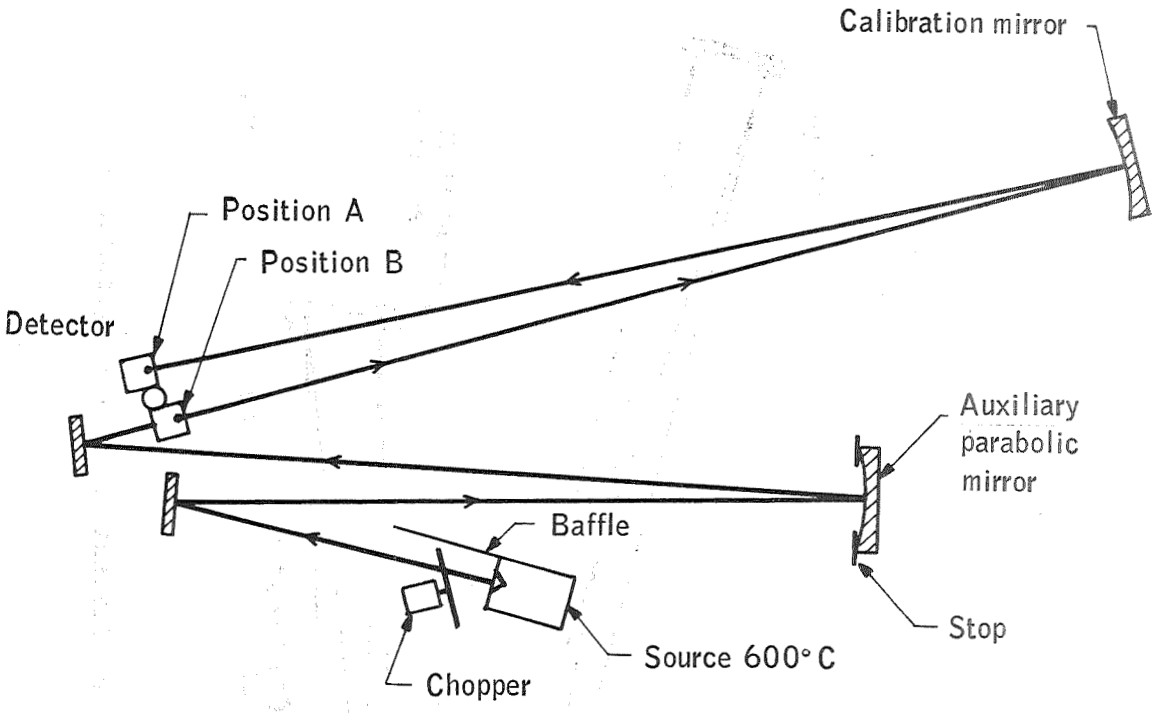

Figure 93. Mirror Reflectance Measurement, Configuration 3a

Final test configuration (configuration 3b): Configuration 3b (Figure 94) is similar to Configuration 3a except that the source-chopper and detector are interchanged. The detector now is stationary and its fov is defined by the auxiliary parabola stop.

The source is set at position B at the radius of curvature of the auxiliary parabolic mirror and 2° off axis. The beam is stopped to an 8-inch diameter at this mirror and focused on the detector. When the source is rotated 180° to position A (radius of curvature of the calibration mirror), the beam intercepts the calibration mirror, is focused at position B, continues on to the auxiliary parabola, and is refocused on the detector. The ratio of the detector signal at position A to the signal at position B is the reflectance of the calibration mirror.

Scanning of the source in a horizontal and vertical direction is accomplished by moving the source in the image plane of the calibration mirror. This arrangement offers all the advantages of configuration 3a and eliminates the problem of critical alignment. Since the detector fov remains constant, the essential requirement for the source aperture position is that the detector be imaged completely within it (assuming a uniform source). The larger the source compared to the detector, the easier to align the system.

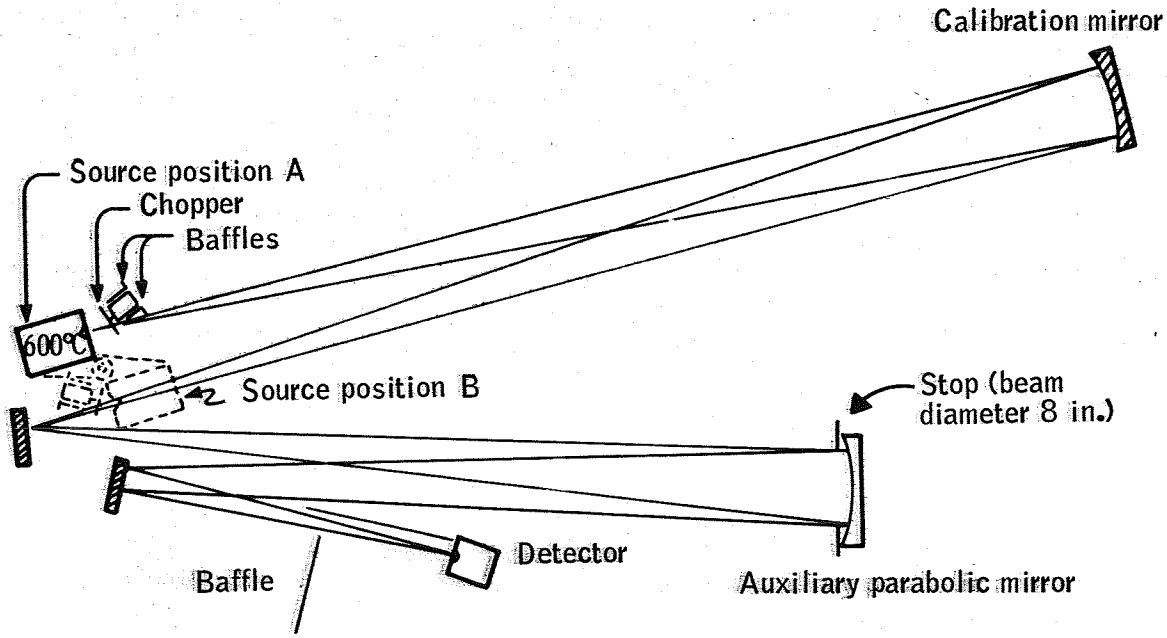

Figure 94. Mirror Reflectance Measurement, Configuration 3b

Configuration 3b offers the following advantages over the first two schemes:

1) The system is simpler and easier to align.

2) The beam limiting stop is at the auxiliary parabolic mirror; therefore, diffraction effects are minimized.

3) Because the calibration mirror is filled, a true value for its total reflectance is obtained.

4) The signal-to-noise ratio is doubled.

5) The beam is reflected only 3 to 4 times; therefore, the effects of aberrations and mirror surface irregularities are minimized.

In spite of these significant improvements, Configuration 3b suffers from three minor deficiencies:

1) The source must move through 180°.

2) The detector cannot look directly at the source; therefore, detector-source-amplifier drift cannot be checked instantaneously.

3) The reflectance is the ratio of two signals rather than the square root of a ratio as in the first two configurations; therefore, error sources produce larger reflectance errors by a factor of 2.

Optical system: The optical system is illustrated in Figures 95 through 99. These are detailed as follows:

- Figure 95 -- System aligned in Position A. Fixtures from left to right - auxiliary parabolic mirror; detector; baffle; second folding mirror; first folding mirror; blackbody source mounted on fixture with horizontal, vertical, and rotational movement capability; chopper; and calibration mirror.

- Figure 96 -- System aligned in Position B (source rotated 180°, chopper moved in front of source).

- Figure 97 -- Close-up of source in Position A. Fixtures from left to right - detector, baffle, second folding mirror, first folding mirror, blackbody source, and chopper.

- Figure 98 -- Close-up of 10-inch parabolic mirrors. Left to right - calibration mirror and auxiliary mirror with system limiting stop.

- Figure 99 -- System electronics (Brower preamplifier and chopper not shown).

Figure 95 System Aligned in Position A

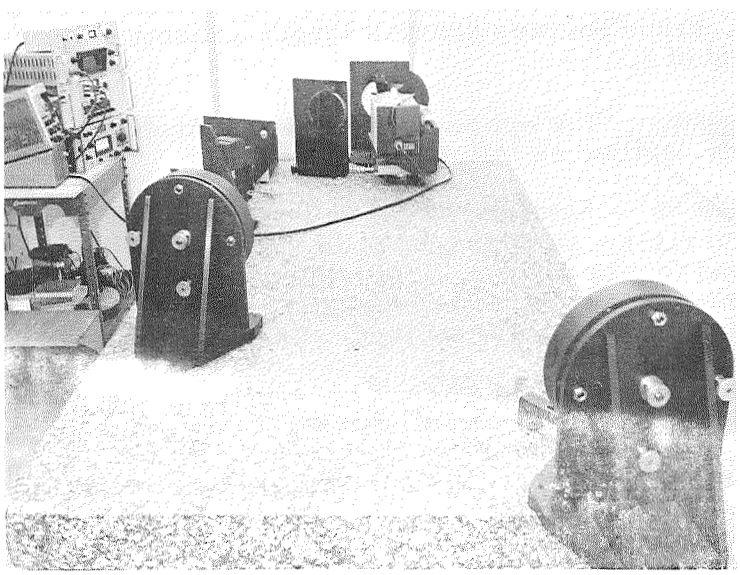

Figure 96 System Aligned in Position B

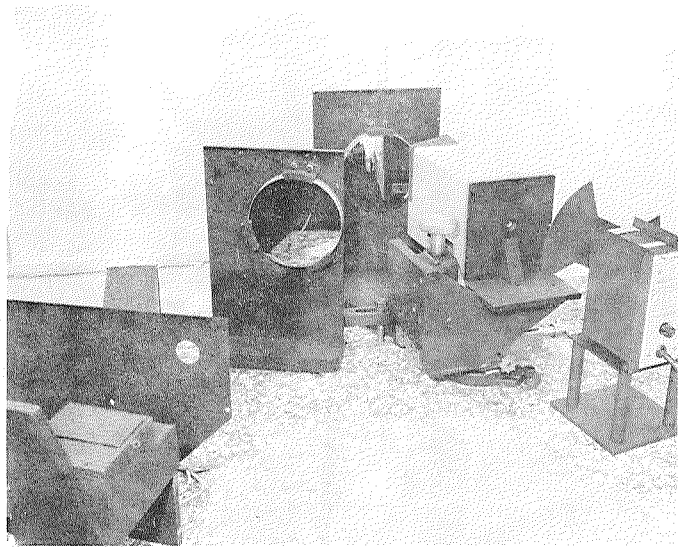

Figure 97 Close-Up of Source in Position A

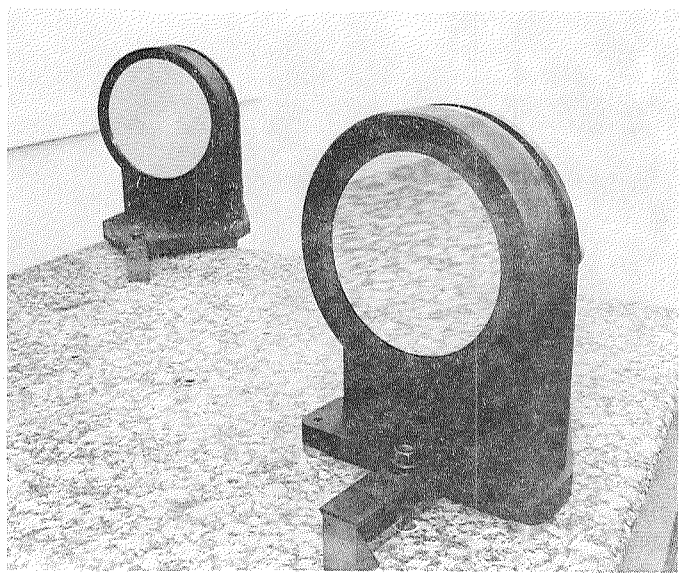

Figure 98 Close-Up of 10-Inch Parabolic Mirrors

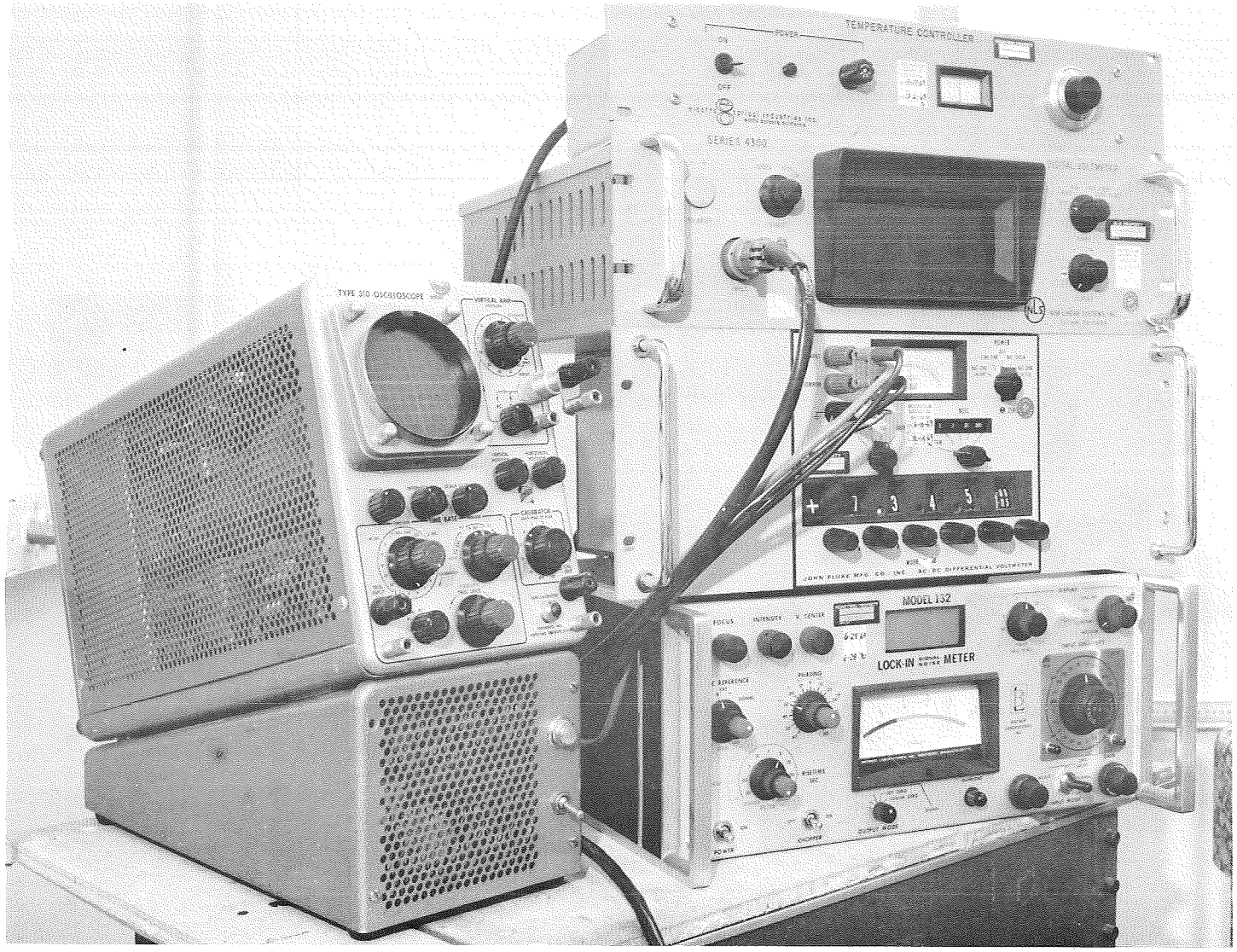

Figure 99 System Electronics

The optical system is set up on a 4 x 8 x 1.5 foot-thick granite slab having a ground top surface of laboratory grade (0.0004-inch total variance over the surface). The slab is isolated from ground vibration, and a matrix of threaded bolt holes over the surface allows all fixtures to be bolted down.

The blackbody source has a temperature range of 50-600°C, with aperture sizes up to 0.4 inch.

The two 8-inch mirrors are ground from 10-inch cervit blanks into 40-inch focal length parabolas with centers 9° off-axis, and are coated with high-vacuum, high-purity gold. The mirrors are mounted on fixtures illustrated in Figure 100, and are adjustable for elevation and train. Surface irregularities are less than 1/10 λ in the 10-μ region.

The two small mirrors are 6-inch optical flats (high-purity gold coated) which are mounted vertically on nonadjustable fixtures.

Immediately in front of the detector is a germanium filter with a passband of 9μ to 12.3μ.

Baffles isolate the detector from stray radiation so that it sees only the auxiliary parabolic mirror. The chopper is baffled so that radiation reflected into the system from its back surface is insignificant.

Electronics: The electronic system is described by the block diagram of Figure 101. Figure 102 is a signal processing diagram which represents the physical processing of the signal from the blackbody source to the data display equipment. Table 26 lists the important properties of the individual electronic blocks.

Results: The measured reflectance of the off-axis paraboloid tested was 0.985. A small plane mirror, with a reflectance of 0.9766 ±0.001 measured at Michelson Laboratory, NOL China Lake, was also measured in a modified configuration indicated by Figure 103 and found to have a reflectance of 0.977. This result supports the accuracy and precision figures quoted below.

Accuracy refers to the difference between the average value of a set of reflectance measurements; precision or repeatability refers to the data spread in that set of measurements. Precision is controllable in that those individual errors which are time varying or random can be reduced by repeated measurement. Accuracy cannot be treated similarly. The quantitative description of accuracy and precision is given in the following paragraphs. Error sources are listed in Table 27 as accuracy or precision error sources.

Accuracy: Stray-light problems arose when experimenting with the early configurations. The detector signal was sensitive to the position of people near the test setup and sensitive in different amounts with the source in

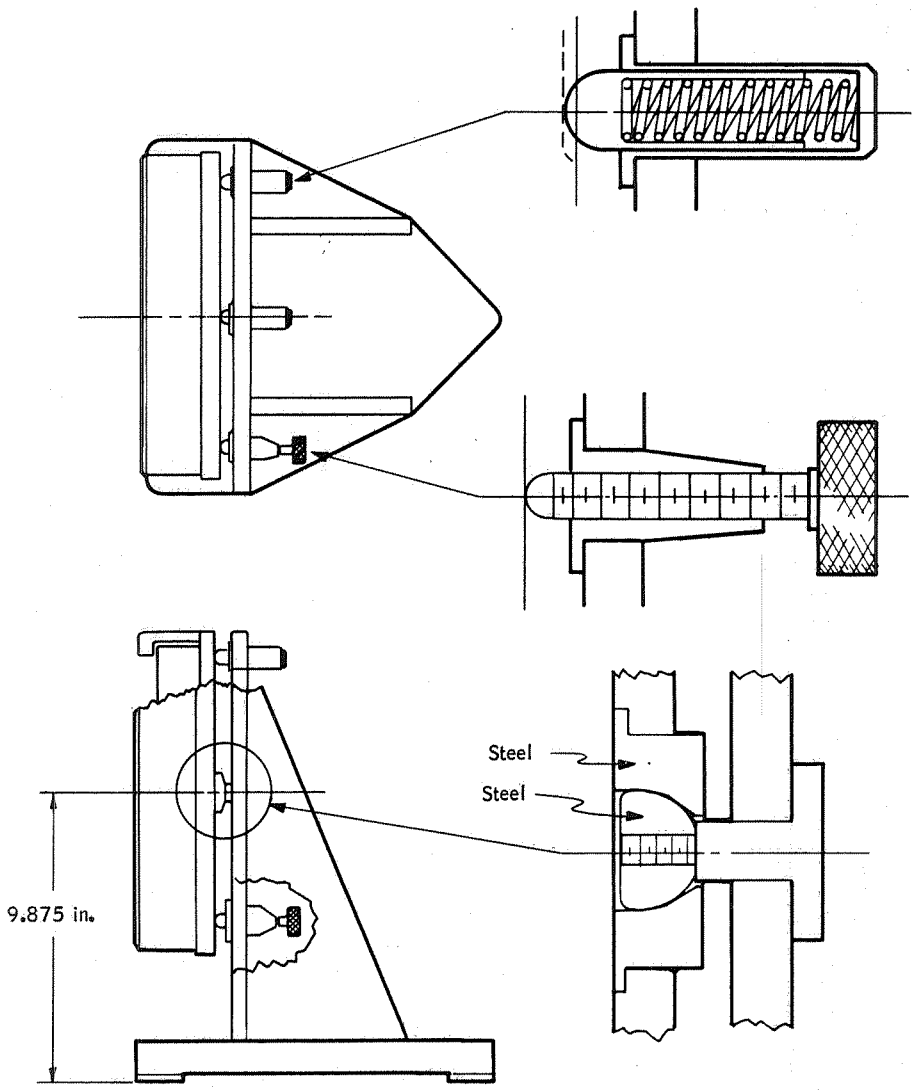

Figure 100. Ten-Inch-Diameter Parabolic Mirror Fixture

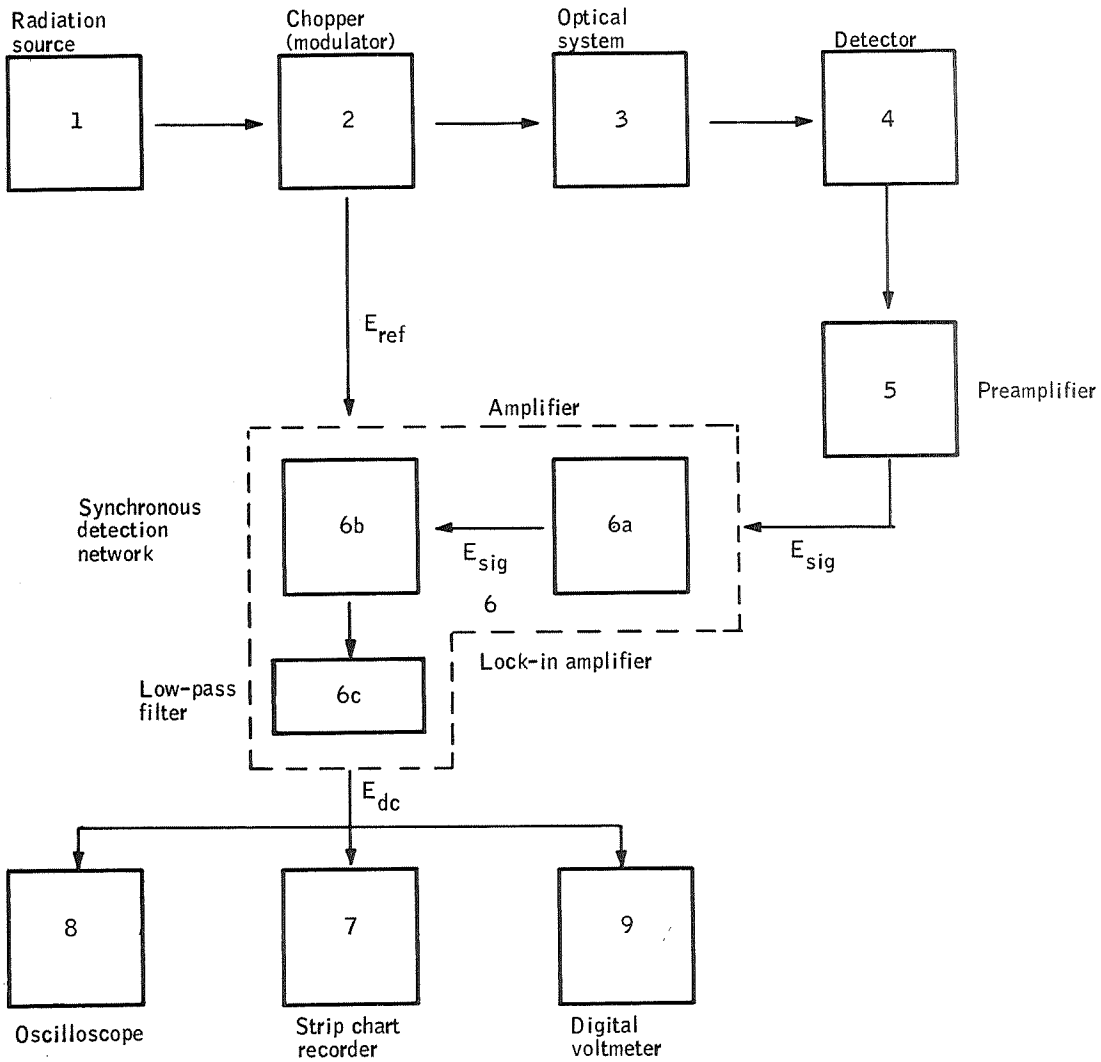

Figure 101. Reflectance Measurement Electronic Network Block Diagram

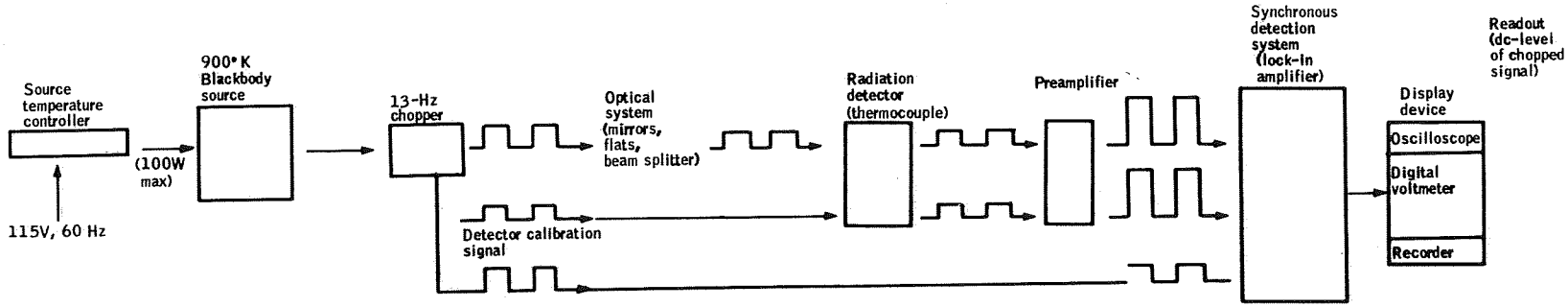

Figure 102. Reflectance Measurement Electronic Network Signal Processing Block Diagram

TABLE 26. - PROPERTIES OF THE ELECTRONIC BLOCK DIAGRAM COMPONENTS

Component	Description
Radiation source	Electro-Optical blackbody source,- Model 141
	Temperature range 50 to 600°C
	Model 210B temperature controller - linear proportional, true null
	Long-term stability 0.1°C, short-term stability 0.02°C
	Sensing element - platinum resistance thermometer
	Temperature monitor - chromel alumel T/C
Chopper	Brower Model 312A
	Blade designed for 1.5 - 20 Hz chopping rate
	Minimum reference signal 100 mV peak-to-peak
Optical system	
• Four mirror elements	Two 8-inch-diameter cervit off-axis parabolas
	Two mirror flats
	All coated with ultra-high-vacuum, high-purity gold
• Filter	OCLI germanium, 9 to 12.3μ
Detector	
• Thermocouple	Charles Reeder & Co., Model RP-3W
	Responsibity 14 to 18 V/W
	Time constant 0.008 sec
	Impedance 10Ω
	Detector size 2 mm x 0.2 mm
Preamplifier	Brower Model 261
	Impedance matched to detector impedance
	Noise < 0.2 nV rms

TABLE 26. - PROPERTIES OF THE ELECTRONIC BLOCK DIAGRAM COMPONENTS (CONCLUDED)

Component	Description
Synchronous detection system	Brower lock-in amplifier Model 132 Frequency range 0.5 Hz to 3 KHz Gain > 1 000 000 Output 0 to 10 Vdc Minimum input level • Signal channel 1 nV for full-scale response • Reference channel 100 mV peak-to-peak Input impedance (signal channel) 400KΩ Linearity ±1% of full scale Zero drift ±0.5% full scale/hr
Stripchart recorder	Sanborn Model 150 Chart speed, 0.25 mm/sec to 25 mm/sec Full scale 100 mV
Oscilloscope	Tektronix Type 310
Digital voltmeter	NLS Model 4300 Voltage range 5 digits to 10 to 10^3 full scale Accuracy 0.1% of reading

position A compared to position B. This effect was caused by diffuse reflection of chopper source radiation off surfaces seen by the detector other than the auxiliary mirror. Baffles were then placed as shown in Figure 94 in an attempt to minimize the problem. Hand-held baffles were then introduced into the system at various locations that could be seen by the detector, and no change in signal level existed. A 40°C source was also introduced into the system at critical points, and no signal change existed. Since the resolution on signal readings exceeded 1 part in 4000 and stray radiation produced no measurable change in the signal, the error attributed to this source is less than 0.025%.

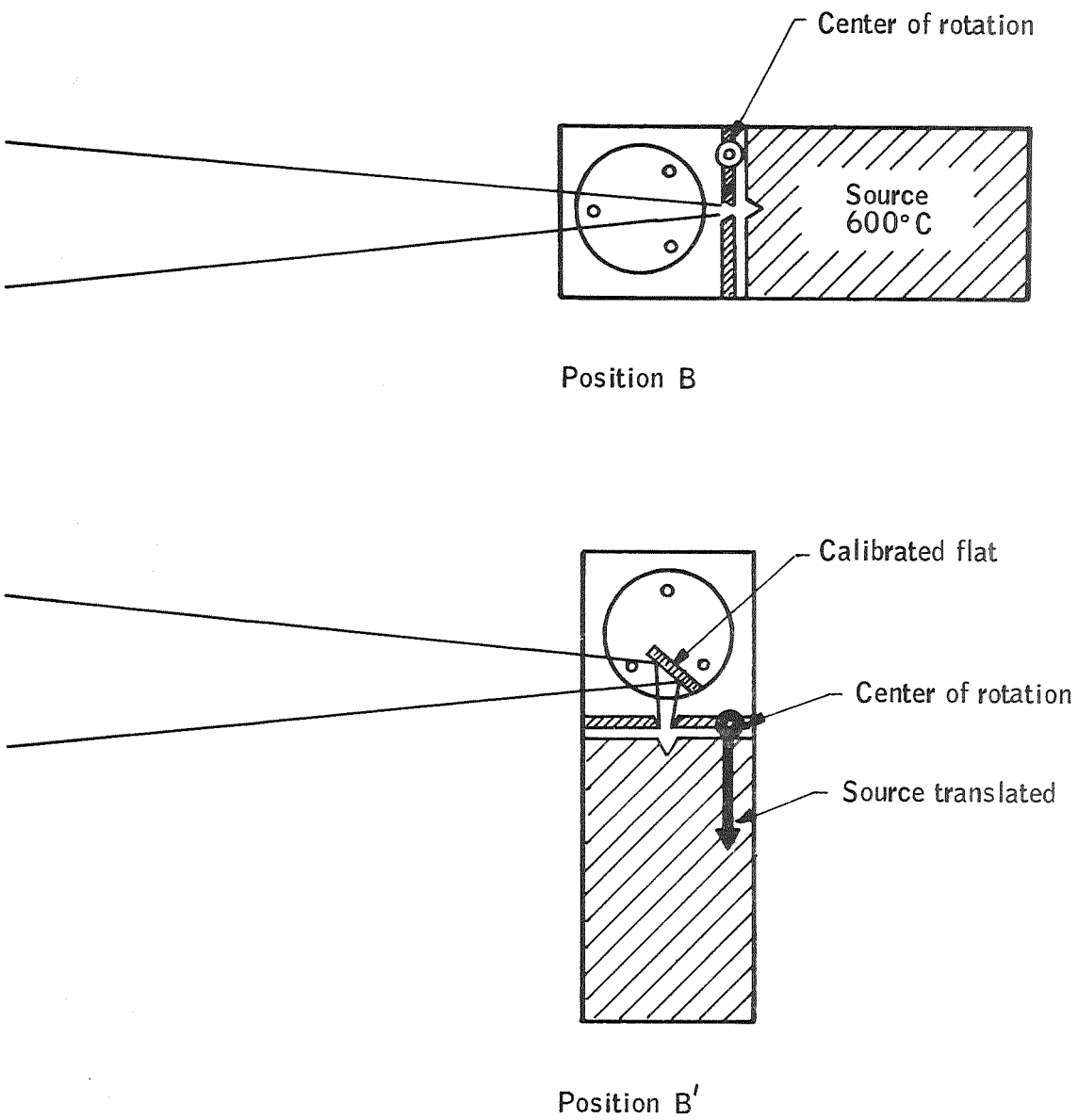

Figure 103. Calibrated Flat Reflectance Measurement

TABLE 27. - ERROR SOURCES

Accuracy	Precision
Stray light	Detector and electronics noise
Atmospheric absorption	Detector and electronics drift
Initial misalignments	Source temperature drift
Diffraction	Position repeatability
	Alignment repeatability
	Ambient temperature variations

Atmospheric absorption produced an error which was never fully compensated for, even by flushing the system with dry nitrogen. The experiment spectral region was initially set at 9 to 12μ, the atmospheric window region, in which preliminary calculations showed that the path length difference would produce a transmittion difference ≈0.1%, which could be corrected to result in an error of only ≈0.025%. These initial calculations were based on H_2O as the only significant absorber in the window region.

This prediction was not realized. In the normal laboratory ambient atmosphere, the reflectance was found to have a daily cyclical variation of ±1% - 0.95 during the day and 0.97 at night. The peak-to-peak short-path signal variation was 3% the longer path signal varied 5%. Because the variation was path length dependent, the effect was judged to be caused by varying atmospheric constituents. It was also believed that the spectral filter may have had significant leaks outside the passband. Addition of IRTRAN 2 to block out a known filter leak at ≈20μ had no effect on the readings. A spectral scan of the filter showed that it had no short wavelength leaks. The problem was then determined to be in the passband, but the atmospheric constituent which caused a 5% degradation of transmission over the relatively short path could not be identified and remains unknown. A polyethylene tent was constructed and the system was flushed with dry nitrogen. The daytime reflectance value obtained then changed to ≈0.985 from 0.950 and repeated at night. The average of four readings taken over two days and nights is 0.9853. A second set of readings taken with a greater but unknown N_2 pressure in the tent produced a reflectance of 0.9866. Thus, the technique is very sensitive to atmospheric effects. Note that this does not affect the PCS in situ reflectance measurement since that will be performed under vacuum conditions. However, reflectance measurements made in laboratory ambient atmospheres can only be made to the 0.1% level of accuracy after the atmospheric effects are better understood and steps taken to reduce them to a tolerable level.

Misalignments cause error because of the nonuniformities of the blackbody source, and optics nonuniformities including nonuniform mirror reflectance and aberrations. If different parts of the auxiliary mirror and source are used between source positions A and B, erroneous readings could then be

obtained because of the above nonuniformities. However, scans of the source (Figures 104 through 107) show that sufficient uniformity exists to effectively eliminate this as a source of error. Aberrations and nonuniformities of mirror reflectance are also eliminated since effects of aberrations would show up as a source nonuniformity, and different parts of the auxiliary mirror were of necessity used in obtaining the curves shown. Over the identified region of constant intensity, the nonuniformity is only ±0.044%, a value which does not include compensation for signal resolution (i.e., noise in signal). The positioning and alignment techniques used allow initial centering of the detector fov well within the so-called constant intensity region. However, within that region the detector fov position with the source in position A and in position B is unknown. Thus, the worst condition must be assumed, which is that an effective uncompensateable difference in apparent source radiance of ≈0.04% exists from position A to position B.

Effects of diffraction are considered to be negligible. While diffraction acts in such a way to cause an apparent loss in signal of ≈0.45%, using the method derived under PCS error analysis, the limiting aperture stop is located at the fixed auxiliary mirror. Thus, diffraction losses are the same with the source in both positions A and B.

Total inaccuracy, given by the rss of the above individual contributors and relative to measurement in a vacuum, is 0.047%.

Precision: Contributors to precision error, or nonrepeatability, are identified in Table 27 and will not be discussed individually here. Rather, overall measurement precision is obtained by analysis of the spread of repeated measurements. Table 28 shows measurements obtained over several days at two different N_2 partial pressures. At the lower pressure, the maximum data spread is ±0.04% and the standard deviation is ±0.036%. At the higher pressure, the maximum spread is ±0.07% and the standard deviation is ±0.056%. Thus, the measurement precision, on a statistical basis, is <0.06% 1σ.

Cavity emittance measurement. -- Measurement of the blackbody source cavity emittance for the PCS had been identified as a component test to be conducted during the Part I phase of the ARRS program. However, prior to entering into such tests directly, parallel related efforts were reviewed. The analytical results of the off-axis cone fonfiguration of a blackbody source (reference CR-66614) indicated an expected emissivity of >0.99999. To obtain experimental verification of this and to develop a technique for measuring the directional emittance of blackbody cavities, a Cavity Emittance Study was conducted as a separate program under NASA Contrast NAS 1-8447. This program was completed with the following conclusions obtained:

- Error analyses, which were verified, proved the measurement technique to be capable of providing highly precise values of emittance. The experiment demonstrated that five significant figures could be resolved in the emittance of high-emittance cavities.

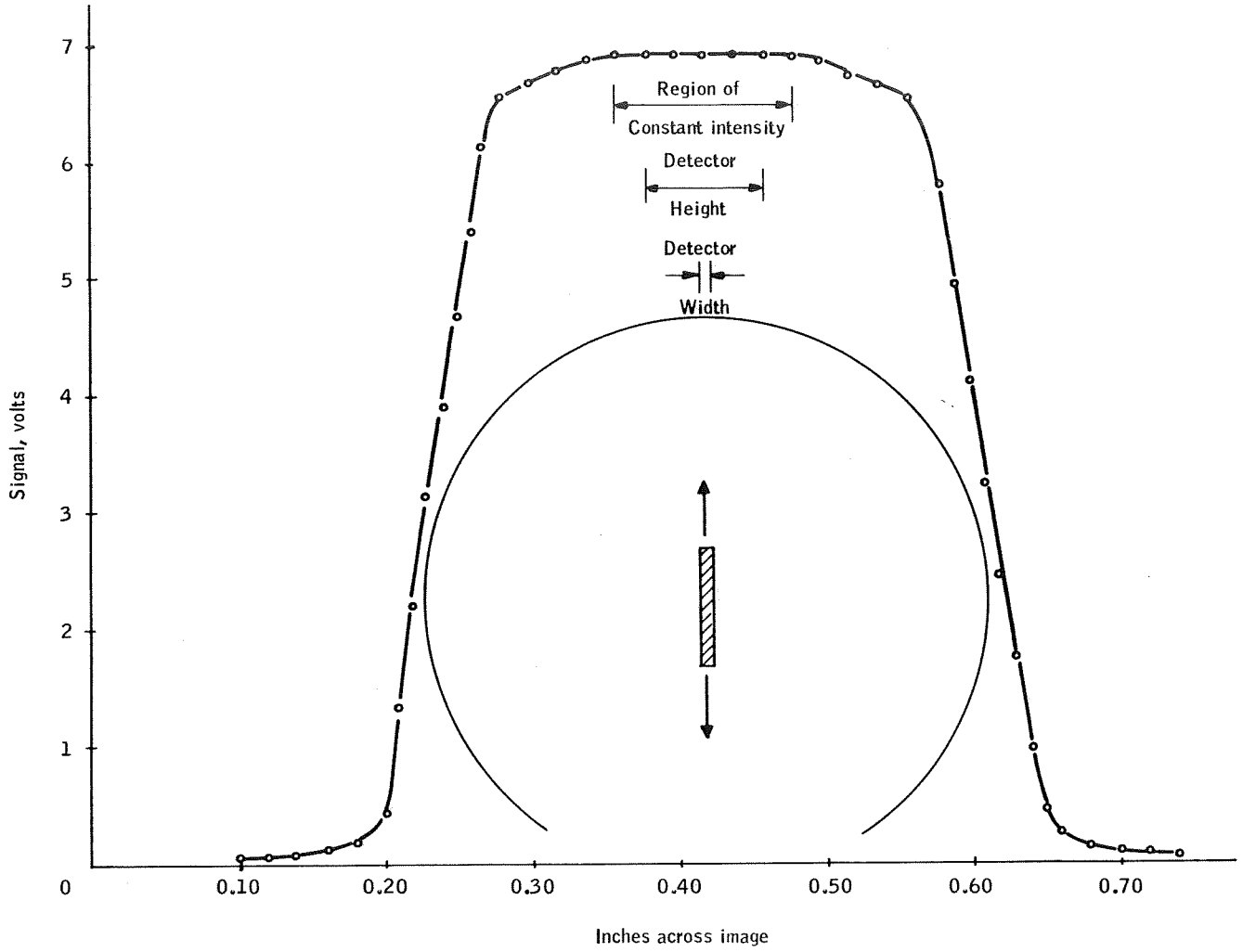

Figure 104. Source Scan, Calibration Mirror In, Vertical

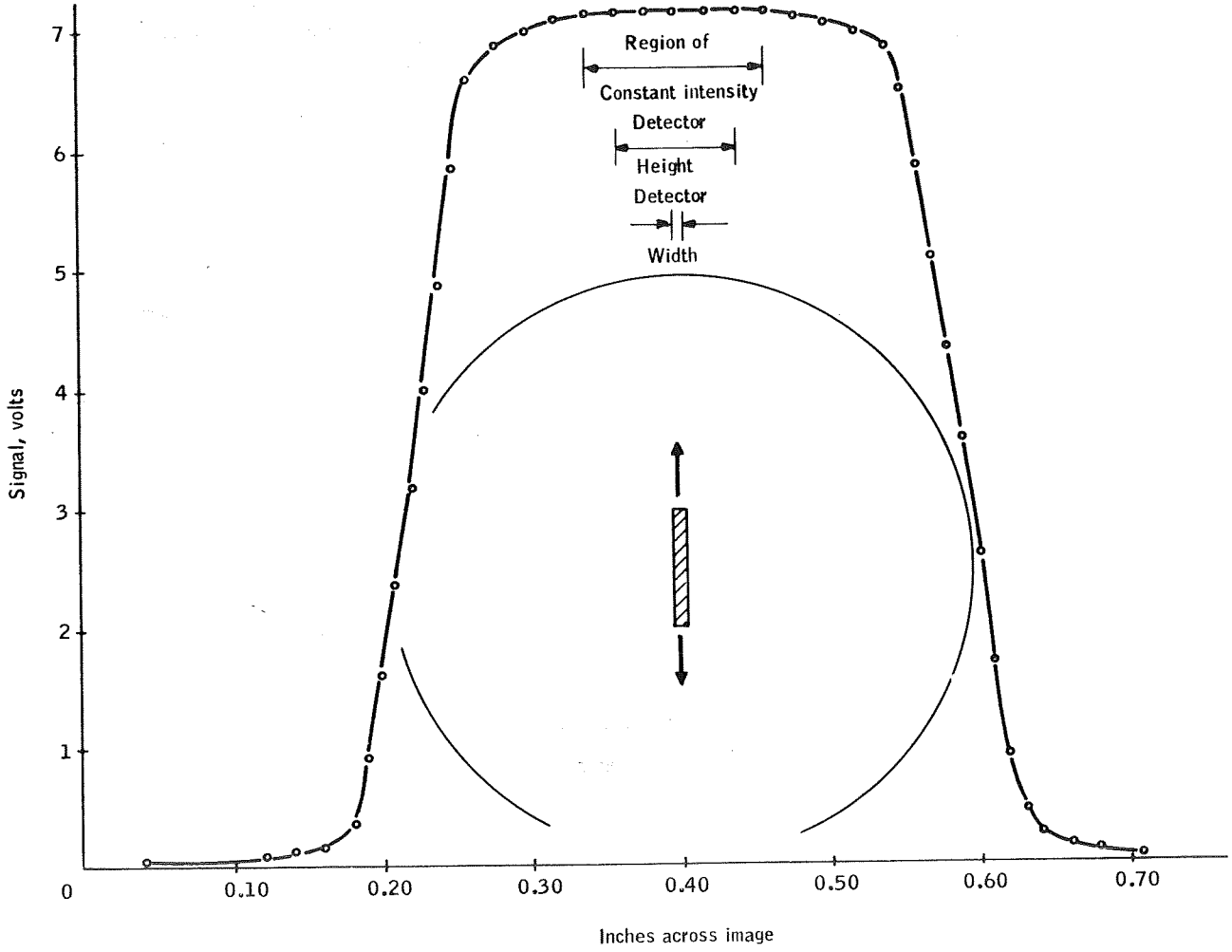

Figure 105. Source Scan, Calibration Mirror Out, Vertical

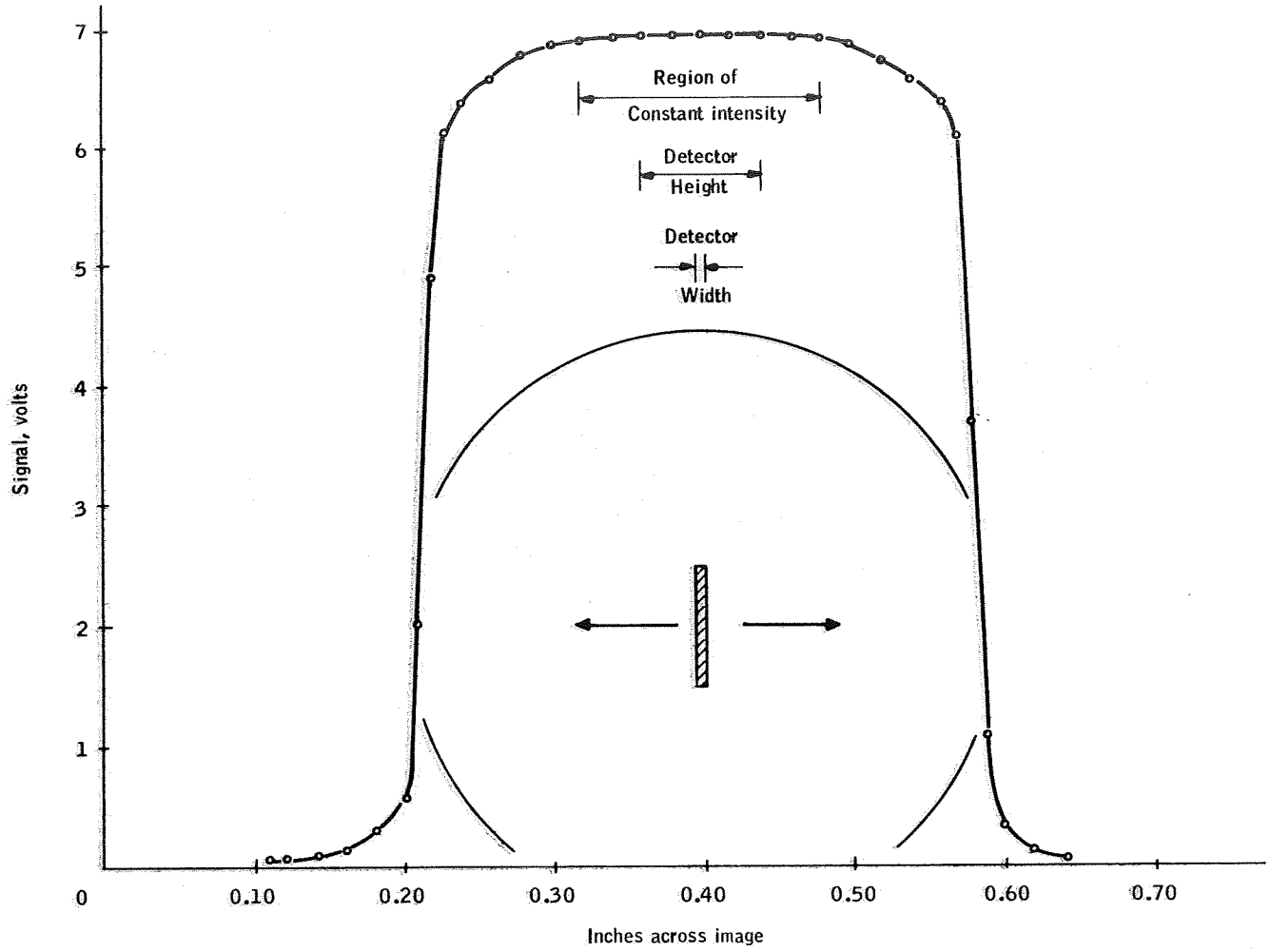

Figure 106. Source Scan, Calibration Mirror In, Horizontal

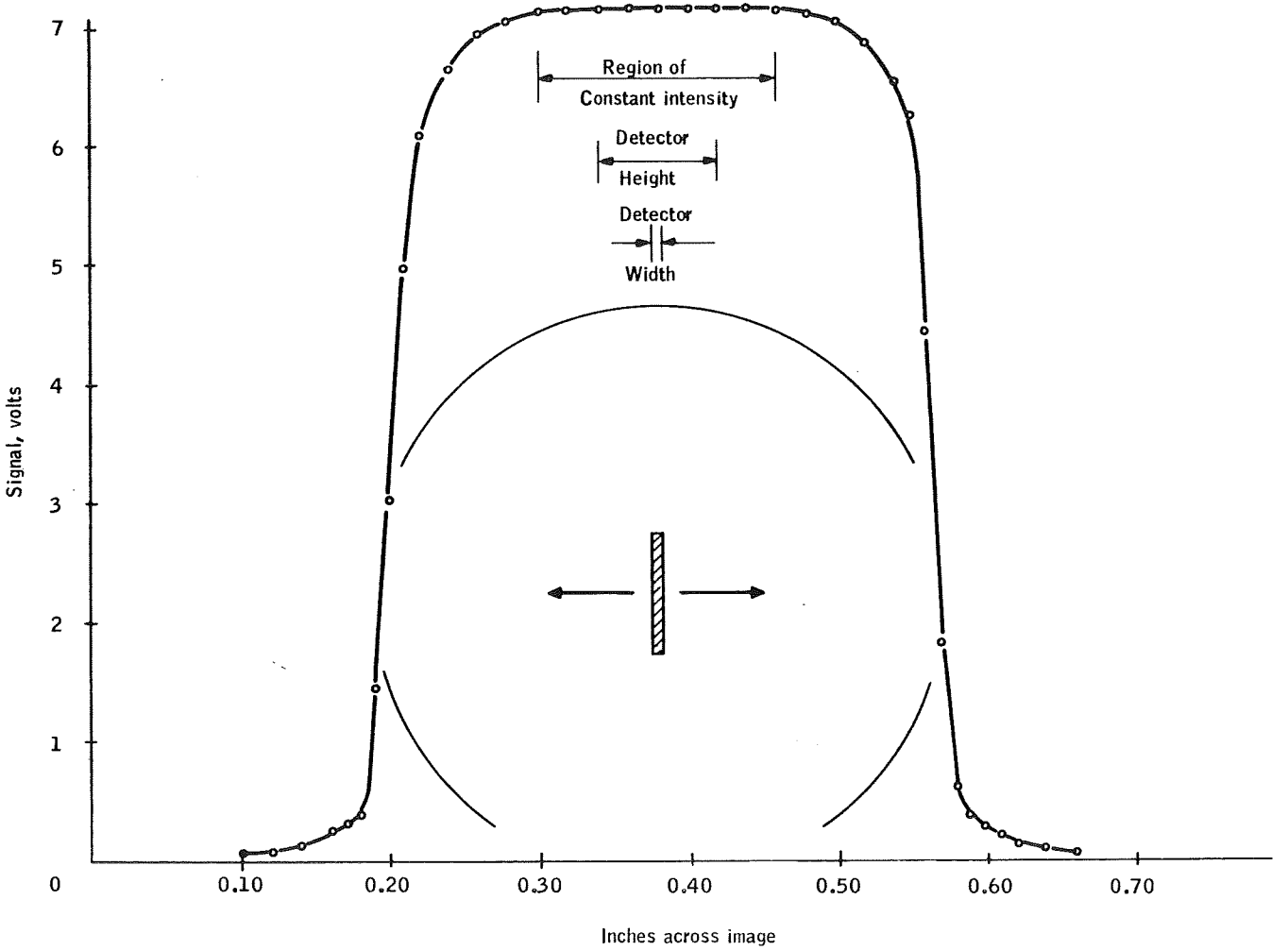

Figure 107. Source Scan, Calibration Mirror Out, Horizontal

TABLE 28. - REFLECTANCE VALUES

Time			Reflectance
1700	8/8/69	Low N_2	0.9856
2200	8/8/60		0.9855
2240	8/8/69		0.9848
0030	8/9/69		0.9852
			Ave. = 0.9853
1530	8/11/69	High N_2	0.9867
1540	8/11/69		0.9870
1550	8/11/69		0.9865
1600	8/11/69		0.9871
1610	8/11/69		0.9857
			Ave. = 0.9866

- A cavity with a 12.45 L/D ratio off-axis cone had an emittance greater than 0.99999 when coated with nominally specularly reflecting or nominally diffusely reflecting black paints.

These conclusions indicated that a separate PCS source cavity emittance component test would not be required. The cavity configuration of the PCS source is identical to that of the Cavity Emittance Measurement (CEM) program, with a cavity L/D ratio of 12.45 and a cone off-axis angle of 10°. The cavity size was scaled up by approximately a factor of 1.75 (to 1.75 cm dia aperture) to obtain the aperture size needed for the PCS requirements. The emittance characteristics, however, are still valid insofar as these characteristics are independent of cavity volume, if the cavity has isothermal surfaces. This condition is shown to be adequately satisfied by the source gradient analysis discussed in this report.

In addition, a limitation of the CEM setup prevented the emittance measurement of the PCS source cavity. The CEM thermopile detector sensitive area is limited to measuring cavities with apertures up to the order of 0.5 cm diameter. The PCS source, with a cavity aperture diameter of 1.75 cm, dictated the need for a much larger CEM detector, which was not available.

Source temperature measurements. -- Results of Contract NAS 1-6010 platinum resistance thermometer testing were reviewed because unexplained variations on the order of 20 millidegrees were noted. This occurred during the testing of the feasibility model variable temperature source at LRC.

The variations were suspected to be caused by a lack of annealing and subsequent mishandling of the particular thermometers which had evidenced the change. Later, after proper annealing, these thermometers were checked within the copper source and were found to track each other within 6 millidegrees C, which is both an allowable and expected termpeature gradient (ref. source gradient analysis). It further established strong evidence that the original thermometers had been disturbed through mishandling or improper operation. Consequently, it was decided to forego further component testing of the thermometers. Proper handling procedures relating to the thermometers and PCS will be observed to prevent a recurrence of the above problem; reappearance of the temperature gradient will be considered an indication to recalibrate the thermometers.

Results and Conclusions

The PCS Part I program was completed with the following results obtained:

- A layout design from which an operational PCS can be fabricated and integrated into a high precision LWIR Radiometric System
- Supportive analyses to establish radiance characteristics, thermal behavior, and procedures of operation for a PCS
- Component investigations and tests to establish techniques and methods for measuring collimator reflectance and quantifying source emittance and temperature characteristics

PCS design. -- The PCS design has evolved into a specific configuration, such that a variable-temperature blackbody source radiates to an off-axis parabolic mirror, which in turn radiates a collimated beam of energy 24 inches in diameter and whose radiation characteristics are well defined. The PCS is contained within a vacuum chamber 42 inches in diameter by 13 feet long and interfaces with a radiometer chamber with a 30-inch-diameter flange interface. All PCS elements were defined to the extent that procurement and fabrication can proceed upon authorization to build an operational system.

Radiance error analysis. -- The PCS radiance errors were classed and separated into four types - bias errors, scale errors, diffraction errors, and aberration errors. Their totals were calculated to be

- Bias error total (linear sum) = 4.0×10^{-3} W/cm^2-sr
- Scale error total (rss at 100°K) = 0.11%
- Diffraction errors = 0.4%.
  Scale and diffraction rss errors = 0.41%
- Geometrical aberration errors are calculated to be relatively negligible.

Source thermal control analysis. -- Source and guard assembles were analyzed thermally to determine heater parameters and performance characteristics. The heaters were sized such that they will warm up the source-guard assembly at a rate of 1°C/minute and will proportionally control the source temperature to within 0.17°C of a preselected temperature.

Source thermal gradient analysis. -- The source was analyzed for gradients through it under operating conditions. Maximum gradients were conservatively calculated to be more than 0.007°C.

PCS chopper thermal analysis. -- Cooldown of the chopper blade may take an excessively long period of time if radiative cooling only is considered. By conductively cooling the blade, the cooldown time is reduced to 0.5 hour or less. After cooldown is achieved, the blade will be maintained at 80°K through radiative coupling to the cooled baffles.

PCS thermal analysis. -- A transient and steady-state thermal analysis was performed for the PCS. Results of the analysis indicated a steady-state cooling load of 62 litters/hr of liquid nitrogen and a transient load of 110 liters/hr, with the collimating mirror requiring the longest time for cooldown, $\approx$5.6 hours.

Triple point cell analysis. -- An analysis was performed to establish the feasibility of using a water triple-point cell as an absolute means of comparison with the variable temperature blackbody source as a temperature/emittance standard. The analysis indicated several operational problems, and some additional investigations are in order.

Collimator reflectance. -- A procedure and test setup were developed to make a precise reflectance on a parabolic mirror. Several methods were attempted before a workable configuration was devised. Potential for attaining 0.1 percent accuracy was achieved by obtaining correlation with the measured reflectance to within 0.01 percent for a flat mirror previously measured at Michelson Laboratories.

Source temperature, emissivity. -- Parallel activities at LRC and Honeywell have provided high confidence in the expected blackbody source performance. Thermal gradients less than 6 millidegrees C were measured through the blackbody source during typical operation. The Cavity Emittance Measurement program has established directional emittance values of >0.99999 for cones with similar geometry and surface finish as the PCS source.

Conclusions. -- Results of the PCS Part I program have firmly established and defined a straightforward design definition of the primary calibration function for the ARRS program. Previous areas of some concern--such as the fabrication of a large collimating mirror, accurately knowing its reflectance, and the thermal behavior of the blackbody source--were all thoroughly investigated and questions were resolved. Some further investigations are recommended in the following section. In all other respects,

however, the PCS is considered to be ready for fabrication, testing, and use as an operational part of a precision LWIR Radiometric System.

Recommendations for Further Study

In addition to the basic PCS design, supportive analysis, and component program testing performed during the ARRS Part I program, several additional areas of investigation are indicated. They include the following specific tasks:

- Triple-point cell gradient analysis
- Triple-point cell component tests
- Reflectometer design, fabrication, and checkout

INFLIGHT CALIBRATION

Requirements

Inflight calibration is required to detect any changes which occur in the radiometer transfer function so that primary calibration can be preserved over the life of the mission. The following conditions must be satisfied to assure an acceptable inflight calibration system:

1) The source must include a means of attenuation such that the radiant power in the 14-to 16-μ band which impinges on the detector surface equals the power which the detector would receive when measuring the horizon radiance.

2) The source must have a sufficient number of radiant power levels to check the entire radiance range of the horizon. These attenuation levels are necessary for the detection of nonlinear variations of the system.

3) The source must be situated within the system such that at least one radiant power level will traverse the entire radiometer system. This requirement will assure detection of any changes which occur in the optical system as well as changes in the more complex elements such as the detector and electronics.

4) The radiance of the source must be sufficiently stable over the one-year period to assure that calibration errors due to variations in the radiometer system do not exceed required tolerances.

5) The temperature of the calibration source must not impose an excessive heat dissipation requirement on the thermal design of the spacecraft.

6) A method of calibration at a zero level must be included so that the effect of thermally emitted radiations by the optical elements of the system may be eliminated.

Specific requirements placed on the inflight calibrator from considerations of the ARRS baseline design parameters are

1) Maximum calibrator level equivalent to apparent background radiance of 10 W/m^2-sr

2) Bounding temperature range for all calibrator elements 60 to 300°K, except source

3) Calibration bias error at all levels shall be less than maximum allowable system error of 3×10^{-2} W/m^2-sr (1 sigma) and, as a goal, the long-term error shall be less than 1.0×10^{-2} W/m^2-sr (1 sigma)

4) Calibration scale error shall be less than 0.1 percent

5) A minimum of 5 calibration levels shall be provided and spread over the complete ARRS dynamic range

6) Calibration technique must accommodate a detector fov of 0.2 x 1.0 mr

Inflight Calibrator (IFC) Concept

Various methods of accomplishing inflight calibration (IFC) were evaluated qualitatively. Introduction of a calibration signal after the chopper into the secondary reimaging system does not account for parameter changes of the primary optic system and chopper, in addition to requiring a chopper of its own. Since we can expect, as a minimum, longterm changes in mirror stability, this concept was excluded. The mode selected required introduction of the IFC ahead of the primary optics. This mode ensures maximum reduction of radiometer gain changes resulting from transfer-function parameter changes.

With that mode, the concept design of the IFC was developed consistent with the following goals:

- Multilevel through-the-optics system, including all essential radiometer components

- Attenuator for various calibration levels integral with calibrator

- No insertion of elements or changes of operating mode of radiometer from primary optics to output to ensure consistency of radiometer transfer function
- Minimum coupling between radiometer and calibrator unit
- Maximum configuration independence

The essential difference in radiometer configurations affecting the IFC is the difference in types of primary optics. For an off-axis primary system with no blockages, the calibrator mirror could be as large as the primary mirror. For a blocked f/No. = 2 cassegrain primary, the largest calibrator clear aperture will be approximately 30 percent of the primary aperture. This case represents the limitation on the ratio of calibrator-optics diameter to primary-optics diameter suitable for all types of primaries.

Concept tradeoffs. -- Four mechanizations of a five-level IFC were considered. All four used the basic technique of collimating radiance from a small blackbody source through a portion of the radiometer aperture and through the complete radiometer optical system. The mechanisms vary in achieving the five required calibration levels from a single temperature source. Four concepts were considered to determine the most suitable for mechanization:

- A cooled aperture plate with appropriately sized holes is used to stop down the IFC collimator in specific steps (see Figure 108).
- A five-position rotating disc is used to insert into the path of the source radiation three partially reflective collimators (see Figure 109). The reflectivity would be designed to span the range from 0 to 100 percent (see Figure 109).
- Same as second item above except that all mirrors are highly reflective and the total reflectance of each mirror is controlled by perforating each mirror to produce desired effective collecting (and collimating) area.
- A single collimator is used and the calibration radiance is varied by moving the source relative to the collimator (see Figure 110).

Table 29 contains tradeoff considerations used in concept selection.

Recommended concept. -- The cooled aperture plate with appropriately sized holes was selected as the recommended concept. Figures 111 and 112 show the recommended IFC configuration. The highest IFC level corresponds to an input radiance of 10 W/cm^2-sr, the peak value of the ARRS dynamic range. From that level the attenuator produces additional levels of 1/5, 1/25, and 1/125 of peak. A logarithmic scale is used to bracket the expected ranges of detector nonlinearities considering the required range of detector characteristics within the ARRS boundary parameters. Any particular selection of operating parameters could lead to a reconsideration of the values of levels. The concept consists of the following components:

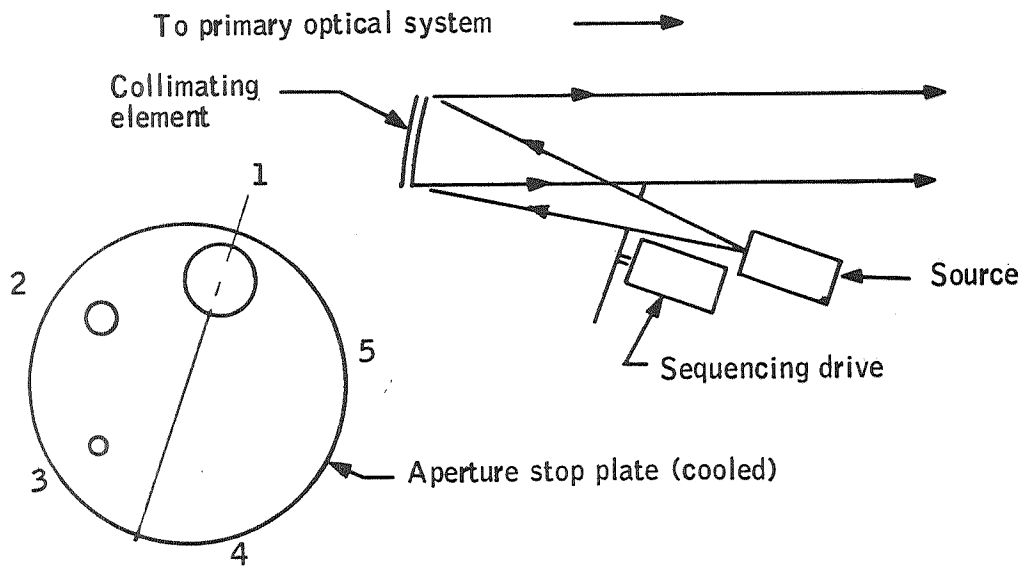

Figure 108. Cooled Aperture Plate Mechanization

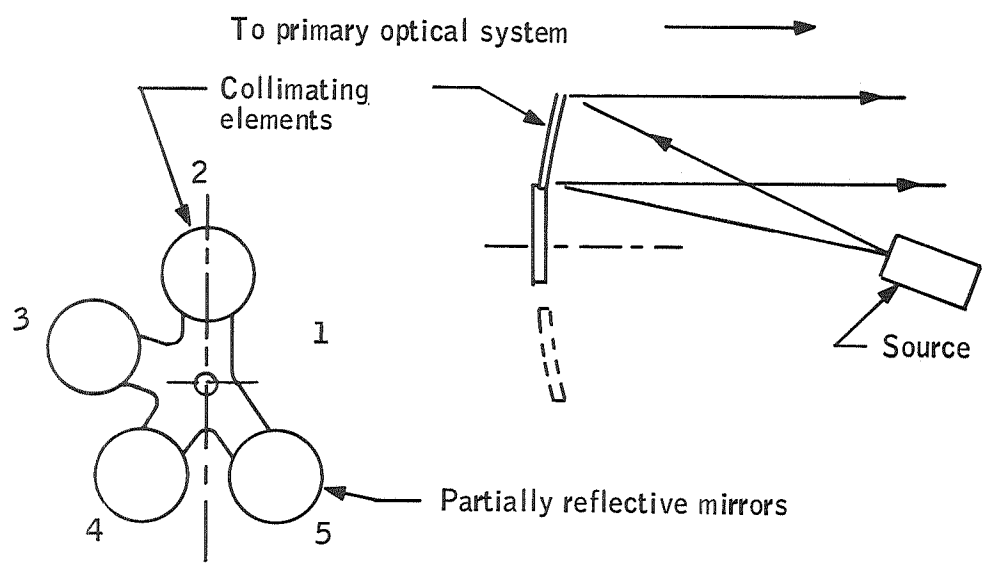

Figure 109. Partially Reflective Mechanization

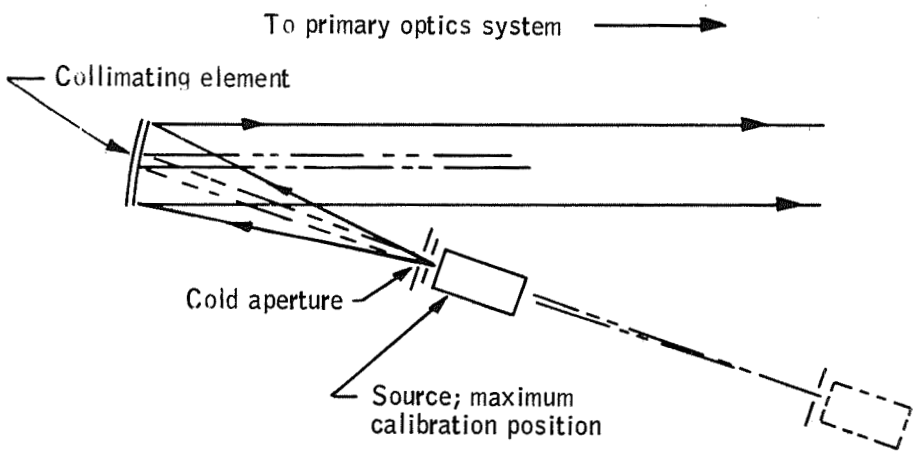

Figure 110. Movable-Source Mechanization

- Source
- Defining aperture
- Cold iris for defining illumination angle
- Collimating optics
- Mechanism for moving collimating optics in and out of primary system
- Mechanism for changing size of iris, or moving source, or changing aperture stop

The Noise Equivalent Radiance (NER) specified for ARRS is 5×10^{-3} W/m^2 -sr. If we consider the maximum radiometer-input-flux uncertainty ($\Delta N_{\Delta\lambda}$) allowable as two NERs referred to the aperture, then the percent-error budget of calibrator radiance at each calibrator level is

Level		Percent of calibrator flux equal to $\Delta N_{\Delta\lambda}$
1	$10^{-2}/10$	0.1
2	$10^{-2}/2$	0.5
3	$10^{-2}/0.4$	2.5
4	$10^{-2}/0.08$	12.5

TABLE 29. - INFLIGHT-CALIBRATION-CONCEPT TRADEOFFS

Method	Advantages	Disadvantages
Cooled-aperture plate	1. Simpler to mechanize and maintain alinement 2. Calibration levels adjusted readily by changing aperture plate	1. Requires two moving parts: aperture plate and collimating mirror 2. Minimum calibration level is dependent on temperature of aperture plate but this calibration level permits a maximum percent error
Partially reflective mirrors	1. Constant f/No system 2. Requires that only one optical element be moved	1. Difficult to obtain desired reflectances. Obtainable calibrator levels are controlled by substrate-material limitations 2. Emissivity is different for each mirror since $\epsilon = 1-\rho-\tau$. This results in high emissivity for low-reflectivity mirrors. If emittance is to be held down, mirrors must be cooled to very low levels – difficult to achieve with this rotating component 3. Alignment (and accuracy) uncertainties are high
Perforated mirrors	1. Ratio of reflected energy to emitted energy from the mirror remains a constant	1. Shaped holes or infinitely thin mirrors are required to minimize coupling of the radiometer to itself 2. For low calibration levels, there is a structural problem in that there is too little mirror surface at low calibration levels 3. Has similar mechanical disadvantages as the partially reflective mirror with the same misalinement and accuracy implication
Movable source	1. Single stop reduces uncertainties 2. Provides continuous calibration	1. Difficult to mechanize. Initial design indicates approximately 10 inches of motion required with precise location and measurement of stops. Also, there is a problem in moving fast enough to achieve ARRS cycling 2. Out-of-focus image of the detector becomes large at the source aperture as the source moves farther from the cold stop. Therefore, this requires a cold stop which moves with the source. At minimum calibration level, accuracy becomes dependent on temperature of the cold stop, but this level permits a maximum percent error 3. Good thermal isolation of the source from the cold stop is required

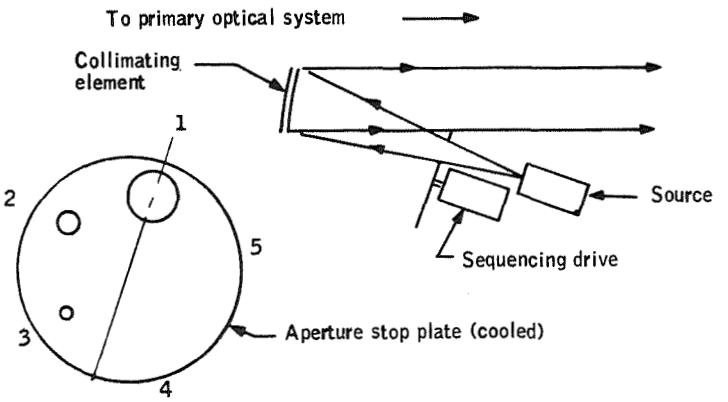

Figure 111. Recommended IFC Configuration

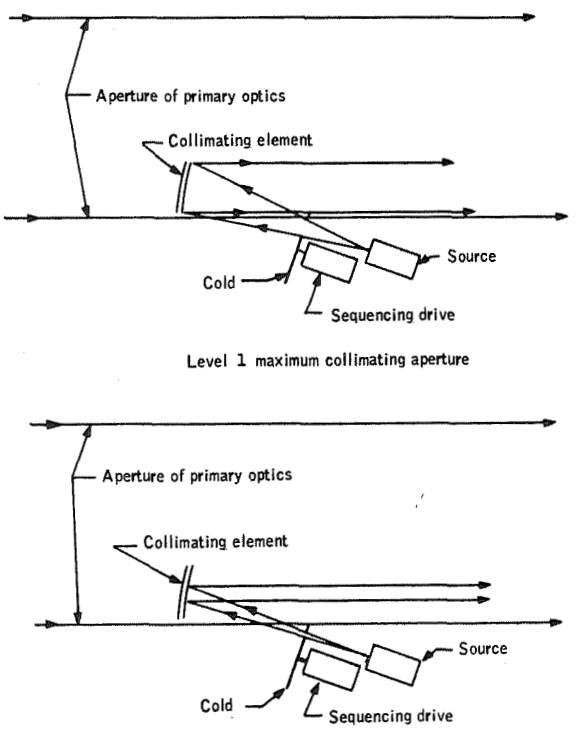

Figure 112. Schematics of Levels 1, 2, 3 and 4

Source temperature optimization: The temperature of the source should be as low as possible to minimize power and thermal-insulation requirements. It must be high enough to generate a radiance which at the maximum calibration level provides an input flux to the radiometer equivalent to the maximum background flux expected at the input. For the selected configuration, the calculations to determine required source temperature are as follows:

H = $\Delta_1\Delta_2 N_{io,\Delta\lambda}$ W/m^2 (incoming energy)

$\Delta\lambda$ = spectral interval from 14.0 to 16.3 μ

$N_{io,\ \Delta\lambda}$ = radiance of background in W/m^2-sr

$\Delta_1\Delta_2$ = angular subtence of radiometer (instantaneous field of view)

Assumptions

- Calibration signal introduced ahead of primary optics
- Source aperture has larger angular subtence than radiometer; therefore, radiometer defines effective source aperture
- Aperture plate shall be at a common temperature
- Primary optic system is a clear-aperture configuration (off-axis parabola), however, aperture plate and source temperature area can be modified to accommodate other configurations

Output of calibrator for above levels can be written as

$$H_{cal} = H_1 + H_2 + \ldots H_n$$

where

H_1 = source contribution

H_2 = mirror contribution

H_3 = aperture-plate-contribution

Source emission

$$H_1 A_{oc} = \Delta_1\Delta_2(fl_c^2)\,\epsilon_{co}\,N_{ico,\Delta\lambda}\frac{A_{oc}}{fl_c^2}\rho_{cco}\zeta_{oc}\tau_{ca}$$

fl_c = focal length of calibrator collimating optics

ϵ_{co} = source emissivity

$N_{ico, \Delta\lambda}$ = blackbody in-band radiance of source

A_{oc} = total aperture of collimating mirror

ρ_{cco} = reflectivity of collimating mirror

ζ_{cc} = form factor of mirror

ζ_{oc} = source form factor

τ_{ca} = fraction of mirror illuminated by source (aperture plate defined)

$$H_1 A_{oc} = \Delta_1 \Delta_2 \, \epsilon_{co} \, N_{ico, \Delta\lambda} \, A_{oc} \, \rho_{cco} \, \zeta_{oc} \, \tau_{ca}$$

Mirror emission

$$H_2 A_{oc} = \Delta_1 \Delta_2 \, A_{oc} \, (1 - \rho_{cco}) \, N_{co, \Delta\lambda} \, \zeta_{cc}$$

where

$N_{co, \Delta\lambda}$ = blackbody radiance of mirror

ζ_{cc} = form factor of mirror, $\epsilon_{cco} = 1 - \rho_{cco}$

Aperture plate emission

$H_3 A_{oc} = \Delta_1 \Delta_2 \, A_{oc} \, \epsilon_{cao} \, N_{ao, \Delta\lambda} \, \zeta_A \, (1 - \tau_{ca}) \, \rho_{cco}$

ζ_A = Aperture Form Factor

where

ϵ_{cao} = aperture-plate emissivity = $1 - \rho_{cao}$

$N_{ao, \Delta\lambda}$ = blackbody radiance of aperture plate

ζ_{ca} = blockage factor of attenuator = $1 - \tau_{ca}$

For the calibrator to match the radiometer input conditions

$$HA_{op} = H_{cal}A_{oc}$$

Thus

$$A_{op}\,\Delta_1\Delta_2\,N_{io,\,\Delta\lambda} = \Delta_1\Delta_2\,\epsilon_{co}\,N_{ico,\,\Delta\lambda}\,A_{oc}\,\rho_{cco}\,\zeta_{oc}\,\tau_{ca} + \Delta_1\Delta_2\,A_{oc}\,(1-\rho_{cco})\,N_{co,\,\Delta\lambda}\cdot\zeta_{cc} + \Delta_1\Delta_2\,A_{oc}\,\epsilon_{cao}\,N_{ao,\,\Delta\lambda}\,\zeta_{ca}(1-\tau_{ca})\,\rho_{cco}$$

$$N_{io,\,\Delta\lambda} = \frac{Aoc}{Aop}\left[\epsilon_{co}\,N_{ico,\,\Delta\lambda}\,\rho_{cco}\,\tau_{ca} + (1-\rho_{cco})\,N_{co,\,\Delta\lambda}\,\zeta_{cc} + \epsilon_{cao}\,N_{ao,\,\Delta\lambda}\,\zeta_{A}\,(1-\zeta_{ca})\,\rho_{cco}\right]$$

for unity form factors

$$N_{io,\,\Delta\lambda} = \frac{Aoc}{Aop}\left[\epsilon_{co}\,\rho_{cco}\,\tau_{ca}\,N_{ico,\,\Delta\lambda} + (1-\rho_{cco})\,N_{co,\,\Delta\lambda} + \epsilon_{cao}\,(1-\tau_{ca})\,N_{ao,\,\Delta\lambda}\,\rho_{cco}\right]$$

At peak IFC level, the above expressions reduce to

$$N_{io,\,\Delta\lambda\,max} = \frac{Aoc}{Aop}\,\epsilon_{co}\,\rho_{cco}\,N_{ico,\,\Delta\lambda}$$

where

$\tau_{ca} = 1$ and $(1-\rho_{cco})\,N_{co,\,\Delta\lambda}$ is small compared to the energy reflected off the mirror.

IFC source radiance which produces the same detector signal as the peak signal radiance is then given by

$$N_{ico,\,\Delta\lambda} = N_{io,\,\Delta\lambda\,max}\,\frac{Aop}{Aoc}\,\frac{1}{\epsilon_{co}\,\rho_{cco}}$$

For applicable IFC parameters of $\frac{Aoc}{Aop} = (0.3)^2$, $\epsilon_{co} = 0.998$, and $\rho_{cco} = 0.986$, required IFC source radiance is

$$N_{ico,\Delta\lambda} = 10\left|\frac{1}{(0.09)(0.998)(0.986)}\right| = 112.5\ W/m^2\text{-sr}$$

Calculation of balckbody radiance over the source-temperature range of interest appears in Table 30. Optimum source temperature is obtained by matching source temperature (and radiance) to equivalent radiance of the maximum anticipated background as in Figure 113. From Figure 113, the required source temperature is 670°K.

Aperture-plate and collimator: For level 4, the total emittance source is the aperture plate and mirror:

$$\xi_{ca} = 1;\ \tau_{ca} = 0$$

$$N_{io,\Delta\lambda} = \frac{Aoc}{Aop}\left[(1 - \rho_{cco})\, N_{co,\Delta\lambda} + \epsilon_{cao}\, N_{ao,\Delta\lambda}\, \rho_{cco}\right]$$

Let

$$N'_{io,\Delta\lambda} = \frac{Aoc}{Aop}\, \epsilon_{cao}\, N_{ao,\Delta\lambda}\, \rho_{cco}$$

Assuming mirror emission

$(1 - \rho_{cco})\, N_{co,\Delta\lambda}$ is negligible

$N'_{io,\Delta\lambda} = 10/125\ W/m^2\text{-sr} = 8 \times 10^{-2}\ W/m^2\text{-sr}$

$\rho_{cco} = 0.986$

$\epsilon_{cao} = 0.98$ (black aperture plate)

Step 1. Compute maximum temperature of aperture plate

$$N_{ao,\Delta\lambda} = N_{io,\Delta\lambda}\, \frac{Aoc}{Aop}\, \epsilon_{cao}\, \rho_{cco}$$

where

$$(1 - \rho_{cco})\, N_{co,\Delta\lambda} < \epsilon_{cao}\, N_{ao,\Delta\lambda}\, \rho_{cco}$$

$$N_{ao,\Delta\lambda} = \frac{10^{-3}}{125} \times \frac{1}{0.09} \times \frac{1}{0.965}$$

TABLE 30.–BLACKBODY RADIANCE

Temp °K	$W_{\Delta\lambda}$ Watts m^{-2}	$N_{ico,\Delta\lambda}$ Watts m^{-2} st^{-1}	$\Delta W_{\Delta\lambda}$ Watts m^{-2} °K	$\frac{\Delta W}{W}$
550	2.3386×10^{2}	74.439	0.89772	0.00384
600	2.7967×10^{2}	89.021	0.93317	0.00334
650	3.2707×10^{2}	104.108	0.96192	0.00294
700	3.7577×10^{2}	119.610	0.98549	0.00262
750	4.2555×10^{2}	135.455	1.0050	0.00236
800	4.7622×10^{2}	151.584	1.0213	0.00214

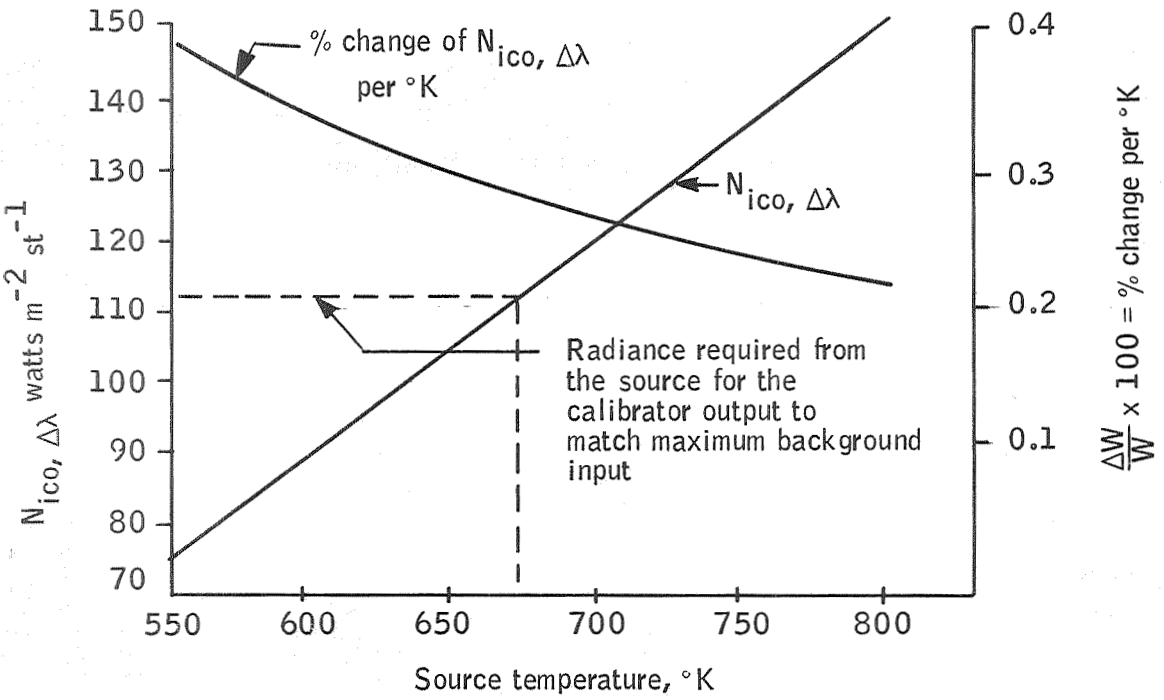

Figure 113. Source Temperature Optimization

$$N_{ao,\Delta\lambda} = 92 \text{ W/m}^2\text{-sr}$$

This corresponds to T = 160°K (maximum temperature at the aperture plate).

Bounding value for collimating optic check at maximum temperature - bound 300°K

$$N''_{io,\Delta\lambda} = \frac{Aoc}{Aop} (1 - \rho_{cco}) N_{co,\Delta\lambda}$$

$$N''_{io,\Delta\lambda} = 0.09\ (0.008)\ 15. = 1.08 \times 10^{-2} \text{ W/m}^2\text{-sr}$$

A gross measurement of the collimating mirror temperature would allow correction for this term. Even at 300°K, a 50° decrease in collimating mirror temperature would be equivalent to a change equal to the system NER.

Selection of calibration levels: The ARRS input covers almost three orders of magnitude of input-signal range. Depending on how the radiometer is modeled, the detector output signal could vary from one to three orders of magnitude. For this broad range, a geometric progression of calibration levels was selected. If the spread of calibrator level is insufficient, the knee of the system response function may not be determinable. Therefore, a geometric progression was used to provide a wide spread of calibration levels. When particular system parameters have been established, an optimum selection of calibration levels is feasible.

IFC Engineering Model

General description. -- The engineering/model IFC is mounted on a base plate designed to work on an optical rail (see Figures 114, 115 and 116). The collimating mirror is mounted on a pivoting, counterweighted cell. The mirror is positioned for the calibration cycle by a stepping motor and a stop.

A cooled five-position aperture disc also is positioned by means of a stepping motor. The cooling shroud for the disc is isolated thermally to minimize the heat load on the cooling device.

The blackbody source and its cold-plate aperture are mounted at the focal point of the collimating mirror.

All three subassemblies are aligned to each other and to the centerline of the optical rail for ease of positioning with other optical equipment for testing.

Source: The Electro-Optical Industries blackbody model 121 will have to be modified to meet the 0.1°C stability for 1 year at the 600°C requirement. The modified blackbody will be identified as model 1944.

A miniature controller model 210, battery operated, as modified to be compatible with source requirements, can be provided.

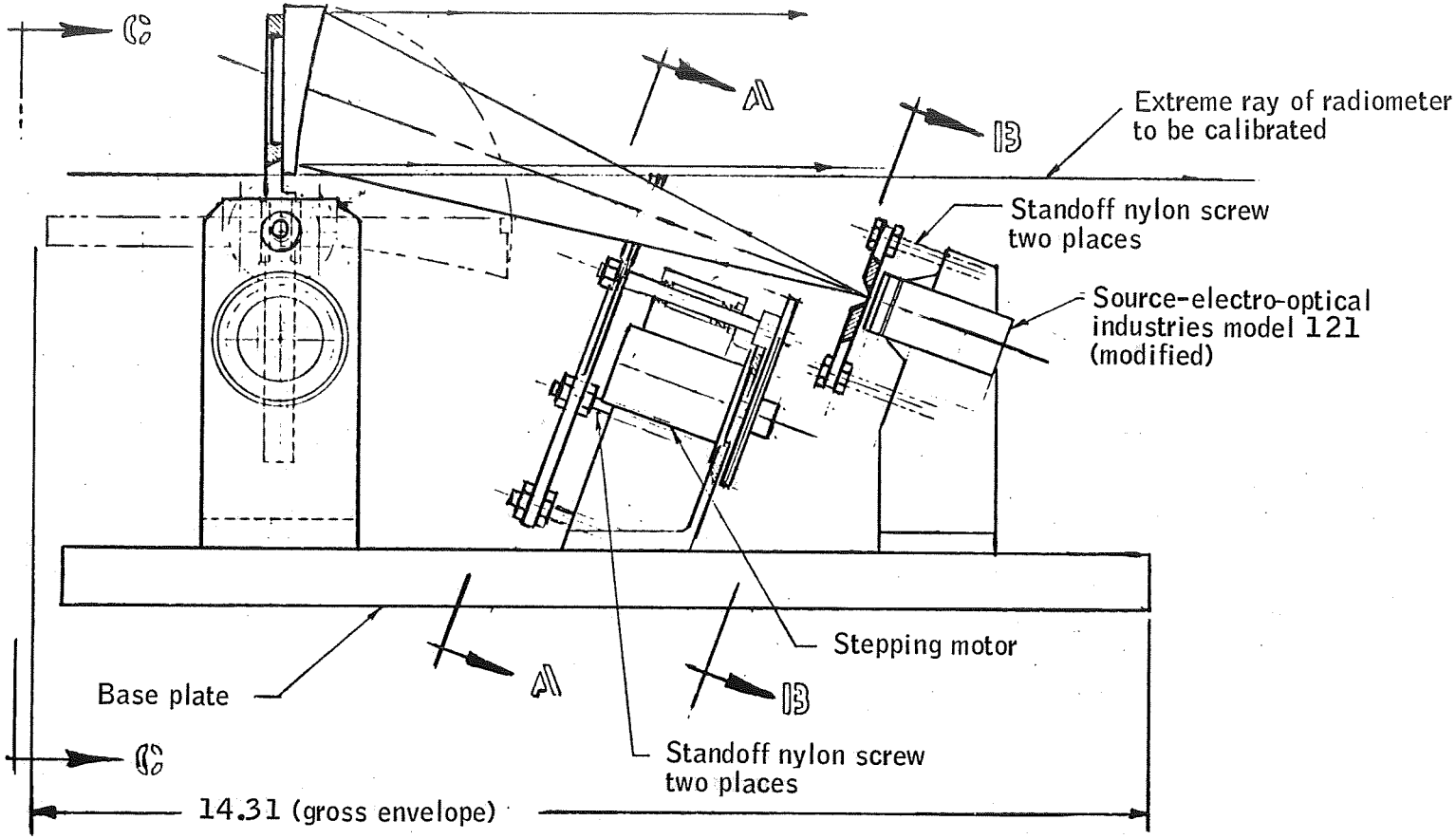

Figure 114. Inflight Calibrator Model for Optical Rail Mounting

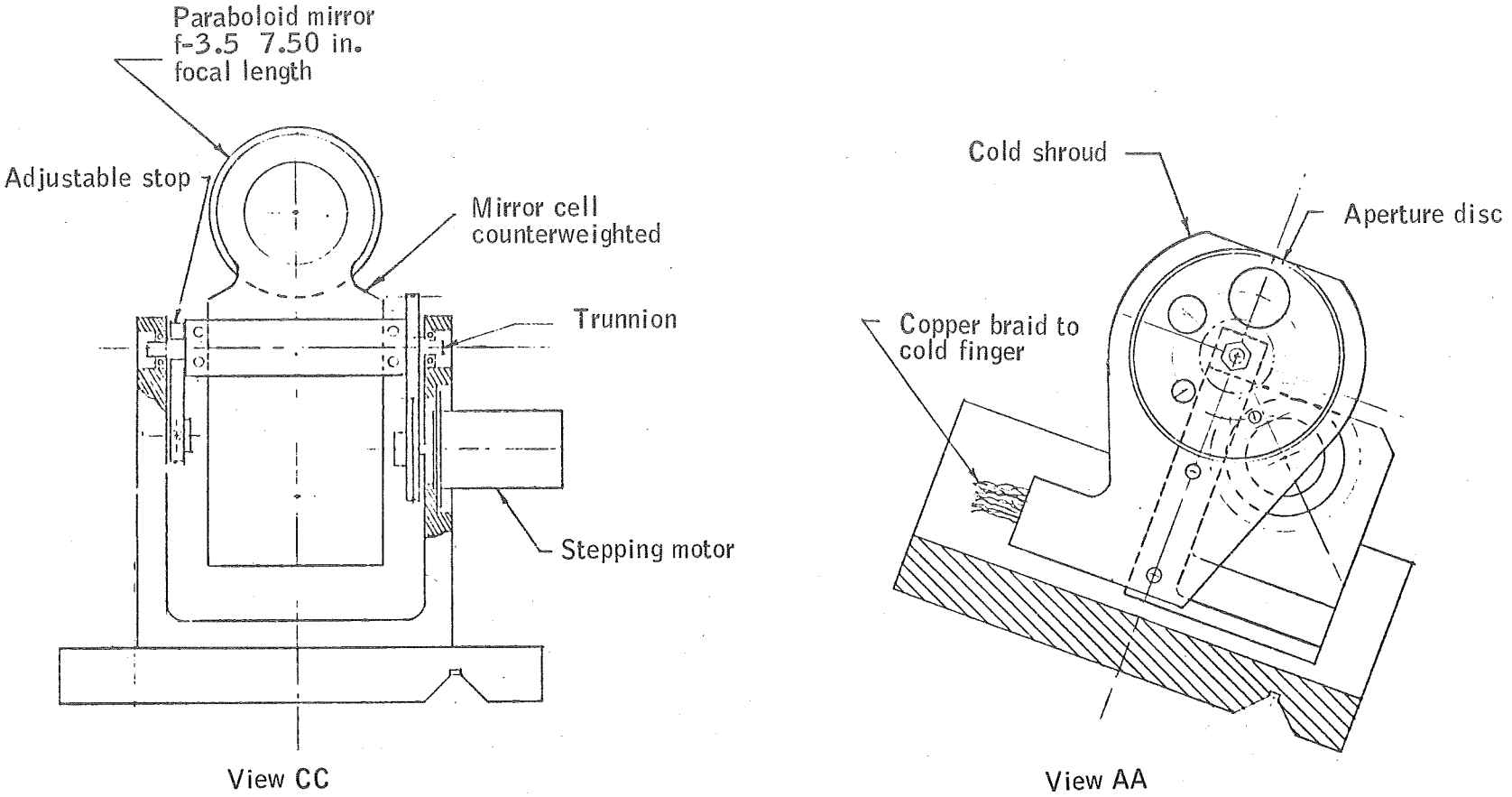

Figure 115. Auxiliary Views of Inflight Calibrator Model

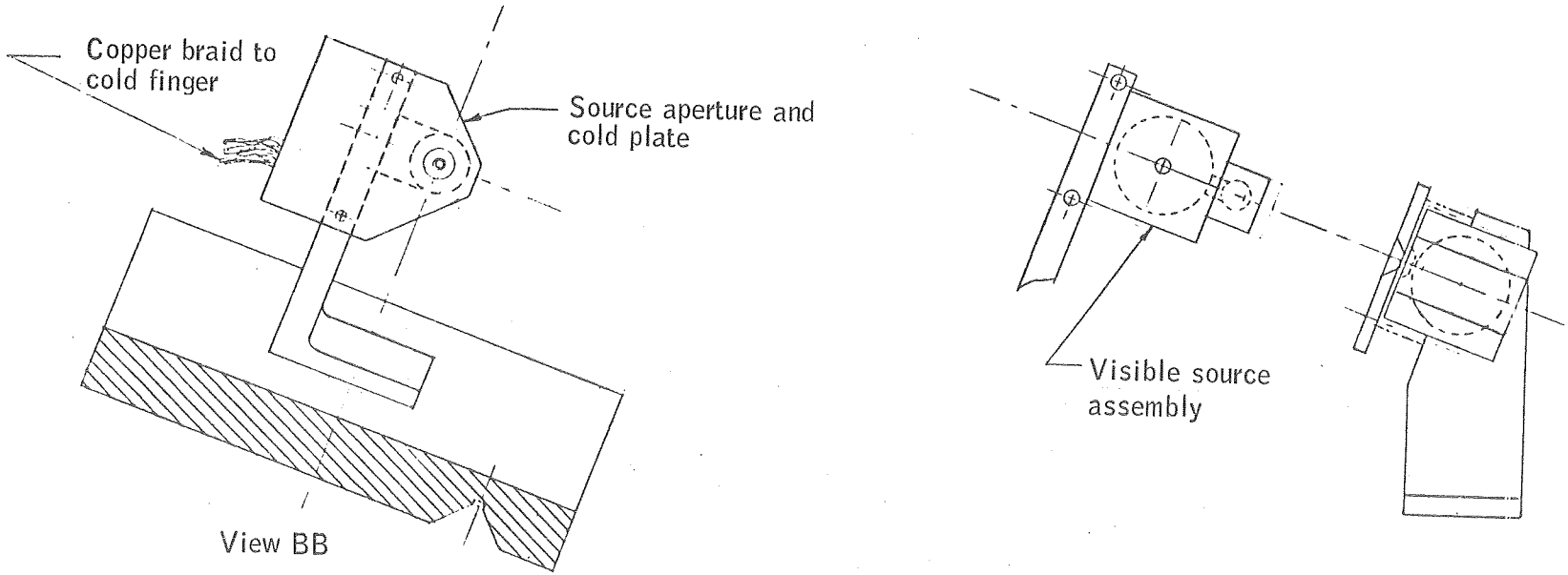

Figure 116. Source Configurations of Inflight Calibrator Model

The source is an insulated package 1.25 x 0.75 x 1.75 inches, weighing 4 oz. The cavity is 0.080 inch in diameter, with a nominal fov of 10°.

Aperture stop: The aperture stop is a thin copper disc mounted on a cold-plate heat sink to eliminate the stop as a secondary source.

Aperture size is a function of the detector to be flooded and the intervening optical system since a magnification of the source results due to focal lengths of the collimating mirror and primary optics of the detection system.

Aperture disc: The aperture disc provides the four levels of energy required for the calibration by changing the effective aperture. The lowest of these four is accomplished by looking at the disc itself as a source. The aperture disc is black on the surface facing the paraboloid mirror and is also black on the opposite face except for one spot at the blank position of the disc.

The disc is housed in a cold shroud. This shroud consists of a thin plate covering the disc except for the opening corresponding to the maximum aperture. The surface of the shroud looking at the disc is blackened for maximum radiation coupling of the shroud to the disc. The heavy section at the rim of the shroud provides a good thermal path to the heat sink.

The disc is run through a calibration sequence each time the collimating mirror is positioned to direct energy to the detector. This sequence would start with the blank or disc as the source and work through the small aperture to the maximum aperture and back to the blank position. This position would be maintained between calibration sequences to eliminate stray addition in a radiometer application.

Sequencing the disc is most readily done with a stepping motor. These units are programmed easily for a specific number of steps as well as time at station. In addition, an inherent cogging provides a detent action at the chosen stop points. This type of unit was developed for, and proven in, various applications in the space environment.

Collimating mirror assembly: The 7.5-inch focal length off-axis paraboloid mirror is fabricated of Cer-Vit material and mounted in a Cer-Vit counter balanced cell. The cell is held in position on a trunnion that is coupled by means of an antibacklash gear to a stepping motor. The mirror assembly is deployed against an adjustable stop for alinement in the operating position, and the detenting action of the stepping motor holds the assembly against the stop. This effect is applicable in the nonenergized condition of the motor.

The mirror is proportioned and held in such a way that the primary optics of a radiometer would see nothing but the mirror surface.

Thermal effects: The IFC as a flight unit would be operated at the vehicle-interface temperature of 200°K. Therefore, various elements should be aligned to compensate for this condition and all tests would be run in this condition.

Effects of temperature variation of each element would change the energy through the system. The heat load of the source and two stepping motors would be coupled to the structure to minimize fluctuation of temperature of elements in the optical path.

Selection of calibration levels: The only uniquely selected calibration level is the maximum level. For this level, the source temperature was selected to match the maximum radiance signal for a ratio of diameter of calibration collimating optic to primary optics of 0.3. Actual selection of optic ratios is determined for a particular configuration and, hence, source temperature can be configuration dependent. Intermediate levels are selected to minimize interpolation errors. These intermediate levels depend on the radiometer responsivity function. A typical set of aperture-defining openings was selected in this report as an example. The minimum calibration level uses the aperture plate as the apparent source. This permits operation of the aperture plate at its maximum temperature of 160°K. Output levels of the calibrator were chosen as a geometric progression on the tentative assumption that the system output response would range over two orders of magnitude with a definite knee at the low-radiance end.

Error Analysis

Engineering model. -- Uncertainty of radiance from the inflight calibration consists of the sum of the uncertainties of its components as propagated through the system. The major uncertainties are described analytically below:

IFC uncertainty	Resultant output uncertainty
Source emittance	$\pm \Delta\epsilon_c \, \rho_{cco} \, N_{ico, \Delta\lambda} \, \tau_{ca}$
Mirror reflectance	$\pm \Delta\rho_{cc} \, \epsilon_{co} \, N_{ico, \Delta\lambda} \, \tau_{ca}$
Source temperature	$\pm \Delta N_{ic, \Delta\lambda} \, \epsilon_{co} \, \rho_{cco} \, \tau_{ca}$
Mirror temperature	$\pm \Delta N_{c, \Delta\lambda} \, \epsilon_{cco}$
Mirror emittance	$\pm \Delta \epsilon_{cc} \, N_{co, \Delta\lambda}$
Aperture-plate emittance	$\pm \Delta \epsilon_{ca} \, N_{ao, \Delta\lambda} \, \rho_{cco} \, (1 - \tau_{ca})$
Aperture-plate temperature	$\pm \Delta N_{a, \Delta\lambda} \, \epsilon_{cao} \, \rho_{cco} \, (1 - \tau_{ca})$
Mirror temperature (for nonilluminated portion)	$\pm \Delta \, \rho_{cc} \, N_{ao, \Delta\lambda} \, \epsilon_{cao} \, (1 - \tau_{ca})$

Symbols used are defined in Table 31. Table 32 is a summation of errors.

TABLE 31.- SYMBOLS AND VALUES ASSIGNED

Symbol	Definition and value
$N_{io,\Delta\lambda}$	Input inband radiance
ϵ_{co}	Source emissivity = 0.9999
$\Delta\epsilon_c$	Source emissivity uncertainty = 0.0001
ρ_{cco}	Calibrator-mirror reflectivity = 0.986
$\Delta\rho_{cc}$	Calibrator-mirror-reflectivity uncertainty = 0.001
τ_{ca}	Fraction of mirror illuminated by source
$\Delta\tau_{ca}$	Uncertainty of τ_{ca}
$N_{ico,\Delta\lambda}$	Blackbody inband radiance of source at 680°K = 112.5 W/m^2-sr
$\Delta N_{ic,\Delta\lambda}$	Uncertainty of $N_{iso,\Delta\lambda}$; $\frac{N_{ic,\Delta\lambda}}{N_{iso,\Delta\lambda}}$ = 0.275 %/°K
ϵ_{cco}	Calibrator-mirror emissivity = 0.014
$\Delta\epsilon_{cc}$	Uncertainty of ϵ_{cco} = ±0.001
ϵ_{cao}	Aperture-plate emissivity = 0.95
$\Delta\epsilon_{ca}$	Uncertainty of ϵ_{cao} = ±0.02
$N_{ao,\Delta\lambda}$	Blackbody inband radiance of the aperture plate; at 160°K = 0.91 W/m^2-sr
$\Delta N_{a,\Delta\lambda}$	Uncertainty of $N_{ao,\Delta\lambda}$; for 2°K uncertainty = 6.68×10^{-2} W/m^2-sr
$N_{co,\Delta\lambda}$	Blackbody inband radiance of calibrator mirror at 280°K = 11.9 W/m^2-sr
$\Delta N_{c,\Delta\lambda}$	Uncertainty of $N_{oc,\Delta\lambda}$; for 20°K uncertainty = 3 W/m^2-sr
A_{oc}	Area of Calibrator mirror
A_{op}	Area of primary mirror

All form factors are equated to 1.0

$$\frac{A_{oc}}{A_{op}} = (0.3)^2 = 0.09$$

TABLE 32.- ERROR SUMMATION

Term	Numeral values of factors			Level 1 $\tau_{ca} = 1$ $1 - \tau_{ca} = 0$	Level 2 $\tau_{ca} = 0.2$ $1 - \tau_{ca} = 0.8$	Level 3 $\tau_{ca} = 0.04$ $1 - \tau_{ca} = 0.96$	Level 4 $\tau_{ca} = 0$ $1 - \tau_{ca} = 1$	Comments
$\pm \epsilon_c \rho_{cco} N_{\lambda co, \Delta\lambda} \tau_{ca}$	$\pm\Delta\epsilon_c$ 0.0001	ρ_{cco} 0.986	$N_{\lambda co, \Delta\lambda}$ 112.0	$\pm 1.11 \times 10^{-2}$	$\pm 0.219 \times 10^{-2}$	$\pm 0.0496 \times 10^{-2}$	0	Uncertainty in source emittance
$\pm\Delta\rho_{cc} \epsilon_{co} N_{\lambda co, \Delta\lambda} \tau_{ca}$	$\pm\Delta\rho_{cc}$ 0.001	ϵ_{co} 0.9999	$N_{\lambda co, \Delta\lambda}$ 112.0 x	$\pm 11.25 \times 10^{-2}$	$\pm 2.25 \times 10^{-2}$	$\pm 0.45 \times 10^{-2}$	0	Uncertainty in mirror reflectance
$\pm\Delta N_{\lambda c, \Delta\lambda} \epsilon_{co} \rho_{cco} \tau_{ca}$	$\pm\Delta N_{\lambda c, \Delta\lambda}$ 3.10 x 10	ϵ_{co} 0.9999	ρ_{cco} 0.992	$\pm 3.08 \times 10^{-2}$	$\pm 0.62 \times 10^{-2}$	$\pm 0.12 \times 10^{-2}$	0	Source temperature uncertainty +0.1°K
$\pm\Delta N_{c, \Delta\lambda} \epsilon_{cco}$	$\pm\Delta N_{c, \Delta\lambda}$ 3.00	ϵ_{co} 0.014	1	$\pm 4.2 \times 10^{-2}$	$\pm 4.2 \times 10^{-2}$	$\pm 4.2 \times 10^{-2}$	$\pm 4.2 \times 10^{-2}$	Mirror-temperature uncertainty ±20°K at 280°K
$\pm\Delta\epsilon_{co} N_{co, \Delta\lambda}$	$\pm\Delta\epsilon_{cc}$ 0.001	$N_{cc, \Delta\lambda}$ 11.9	1	$\pm 1.19 \times 10^{-2}$	$\pm 1.19 \times 10^{-2}$	$\pm 1.19 \times 10^{-2}$	$\pm 1.19 \times 10^{-2}$	Mirror emittance uncertainty
$\pm\Delta\epsilon_{ca} N_{ao, \Delta\lambda} \rho_{cco} (1 - \tau_{ca})$	$\pm\Delta\epsilon_{ca}$ 0.020	$N_{ao, \Delta\lambda}$ 0.910	ρ_{co} 0.986	0	$\pm 1.43 \times 10^{-2}$	$\pm 1.72 \times 10^{-2}$	$\pm 1.79 \times 10^{-2}$	Aperture-plate emittance uncertainty
$\pm\Delta N_{a, \Delta\lambda} \epsilon_{cao} \rho_{cco} (1 - \tau_{ca})$	$\pm\Delta N_{a, \Delta\lambda}$ 6.68×10^{-2}	ϵ_{cao} 0.95	ρ_{cco} 0.986	0	$\pm 5.0 \times 10^{-2}$	$\pm 6 \times 10^{-2}$	$\pm 6.25 \times 10^{-2}$	Aperture-plate temperature uncertainty ±2° at 160°K
$\pm\Delta\rho_{cc} N_{ao, \Delta\lambda} \epsilon_{cao} (1 - \tau_{ca})$	$\pm\Delta\rho_{cc}$ 0.001	$N_{ao, \Delta\lambda}$ 0.91	ϵ_{cao} 0.95	0	$\pm 0.07 \times 10^{-2}$	$\pm 0.09 \times 10^{-2}$	$\pm 0.09 \times 10^{-2}$	Mirror-reflectance uncertainty
$\frac{A_{oc}}{A_{op}} = 0.09$	$(3\sigma)\Sigma$			18.45×10^{-2}	12.60×10^{-2}	11.44×10^{-2}	11.14×10^{-2}	
	$\Delta N_{i, \Delta\lambda} = \Sigma / \frac{A_{op}}{A_{oc}}$ W/m²-sr			1.66×10^{-2}	1.13×10^{-2}	1.03×10^{-2}	1.0×10^{-2}	3σ value referred to input
Uncertainties				0.55×10^{-2} 0.3375×10^{-2} 0.2160×10^{-2}	0.38×10^{-2} 0.0696×10^{-2} 0.3084×10^{-2}	0.34×10^{-2} 0.0162×10^{-2} 0.3270×10^{-2}	0.33×10^{-2} 0.0027×10^{-2} 0.3315×10^{-2}	1σ total 1σ scale 1σ bias

Long-term goals are: scale: 1×10^{-2} $(W/m^2\text{-sr})$
bias: 3×10^{-2}

Uncertainty of the radiance from the calibrator referred to the radiometer input is the sum of component uncertainties multiplied by the ratio of the area of calibrator optics to the area of the primary optics.

$$\Delta N_{i,\Delta\lambda} = \frac{A_{oc}}{A_{op}} \Big[(\pm\Delta\epsilon_{co})\ \rho_{cco}\ N_{ico,\Delta\lambda}\ \tau_{ca} + (\pm\Delta\rho_{cc})\ \epsilon_{co}\ N_{ico,\Delta\lambda}\ \tau_{ca} + (\pm\Delta N_{ic,\Delta\lambda})\ \epsilon_{co}\ \rho_{cco}\ \tau_{ca} + (\pm\Delta N_{c,\Delta\lambda})\ \epsilon_{cco} + (\pm\Delta\epsilon_{cc})\ N_{co,\Delta\lambda} + (\pm\Delta\epsilon_{ca})\ N_{ao,\Delta\lambda}\ \rho_{cco}\ (1 - \tau_{ca}) + (\pm\Delta N_{a,\Delta\lambda})\ \epsilon_{cao}\ \rho_{cco}\ (1 - \tau_{ca}) + (\pm\Delta\rho_{cc})\ N_{ao,\Delta\lambda}\ \epsilon_{cao}\ (1 - \tau_{ca}) \Big]$$

Diffraction effects. -- The IFC considered here consists of

- A small extended source assumed to be circular in shape and to radiate completely incoherently, but uniformly, over its surface
- Attenuating field stops in common location
- Collimating optics (Figure 117)

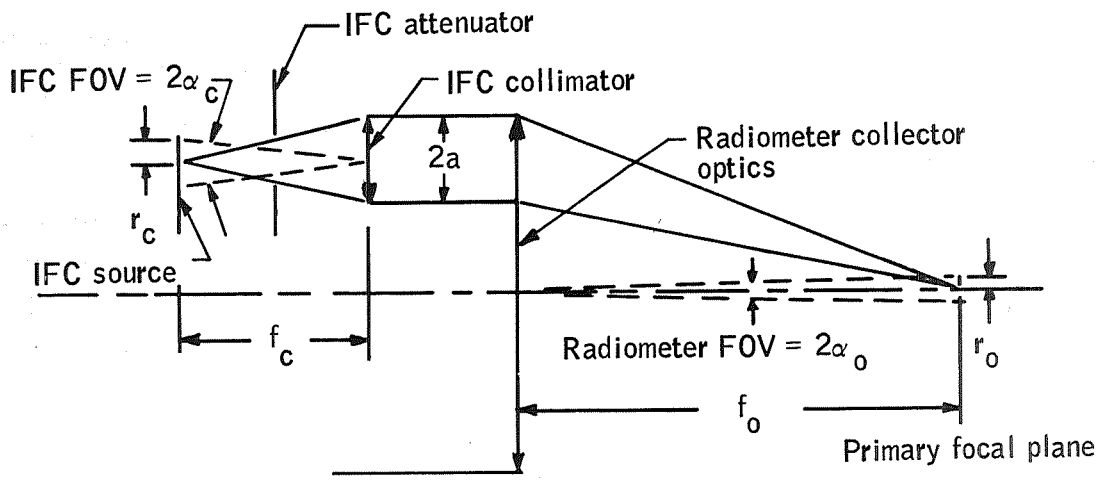

Figure 117. Schematic of Inflight Calibration

The geometrical image of the calibration source in the focal plane of the collector optics is superimposed to the rectangular detector image formed by the relay optics. However, instead of considering this actual image, the total circular fov of the radiometer is used for the derivation of the diffraction effects due to the IFC. This fov is supposed to be smaller than the geometrical image of the calibration source such that some misalinement can be tolerated. For example, having a half-field angle of $\alpha_o = 5 \times 10^{-4}$ rad and a focal length of $f_o = 50$ cm for the collector optics, one obtains the radius of the fov circle

$$r_o = 2.5 \times 10^{-2} \text{ cm}$$

On the other hand, using a half-field angle of $\alpha_c = 1.5 \times 10^{-3}$ rad and a focal length of $f_c = 18.75$ cm for the IFC collimator, one obtains a calibration source radius of

$$r_c = 2.8125 \times 10^{-2} \text{ cm}$$

and, consequently, a source image radius of

$$r_i = r_c f_o / f_c = 7.5 \times 10^{-2} \text{ cm}$$

that is

$$r_i = 3 r_o$$

Before deriving the diffraction effects, it is advantageous, if not necessary, to consider the geometrical relationships between source size, field-stop extension, effective aperture, and total collimator aperture. The situation encountered is illustrated in Figure 118. For analysis, a Cartesian coordinate system with origin at the source center is used.

Defining the source size by $y = \pm y_s$, one may denote the field-stop location by $x = x_f$ and its extension by $y = \pm y_f$. Location of the collimator optics is at $x = x_c = f_c$. A ray emerging from $y = +y_s$ and passing through the field-stop points $x = x_f$, $y = \pm y_f$ intersects the collimator aperture plane at

$$y_{c1} = y_s + (y_f - y_s) f_c / x_f$$

and

$$y_{c2} = y_x - (y_f + y_s) f_c / x_f$$

respectively.

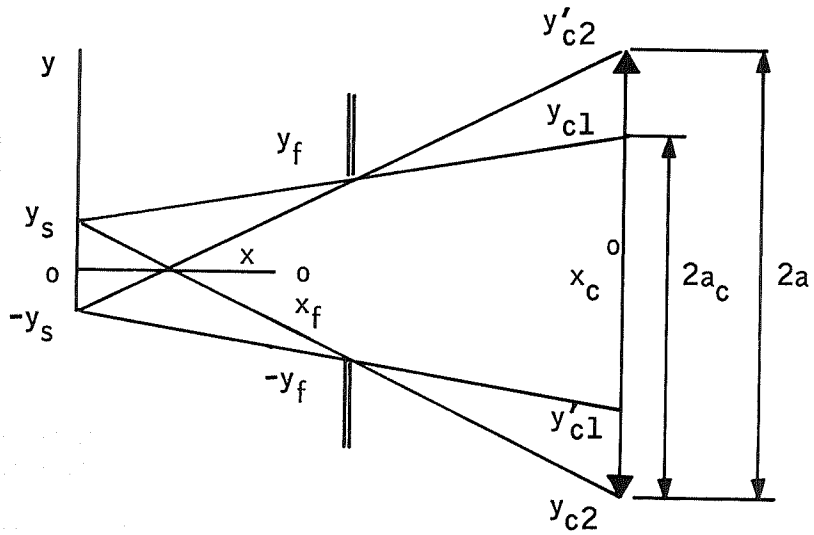

Figure 118. Geometrical Relationship Between Source Size, Field-Stop Extension, Effective Aperture, and Collimator Aperture

On the other hand, a ray emerging from $y = -y_s$ and passing through the same field-stop points has intersection points with the collimator aperture plane

$$y_{c1} = -y_{c1}$$

and

$$y_{c2} = -y_{c2}$$

respectively.

Consequently, the effective aperture radius is given by

$$a_c = \frac{y_{c1} - y_{c2}}{2} = y_f f_c / x_f$$

that is, a_c is independent of the source size. Total collimator aperture is determined by the maximum field-stop extension, $y = \pm y_{fmax}$, and expressed by

$$a = \frac{(y'_{c2} - y_{c2})_{max}}{2} = -y_{c2_{max}}$$

$$= (y_{f_{max}} + y_s)\, f_c/x_f - y_s = a_{c_{max}} + (f_c - x_f)\, y_s/x_f$$

It is seen that, depending on the source size, the collimator aperture is always larger than the maximum effective aperture. The attenuator transmission factor is defined by

$$\tau_{ca} = (a_c/a_{c_{max}})^2$$

$$= (y_f/y_{f_{max}})^2$$

As shown in Figure 119, the collimator and, consequently, the collector optics also receive for any $y_f < y_{f_{max}}$ radiation from all points of the source. For this reason, extension of the source image remains unchanged; the intensity of this image varies with τ_{ca}.

It was shown (ref. 9) that the diffraction pattern of a bar-type incoherently radiating source generated by a slit or double-slit aperture can be obtained by integration of the point-source pattern over the geometrical image of the source. Of course, this principle applies also to the circular source, the radiation of which is diffracted by a circular aperture. Whereas in the first case the integration is easily performable, it is quite difficult in the latter one. Nevertheless, Nagaoka (ref. 10) arrived at approximate solutions for some specific configurations encountered in the image plane, and Zanoni and Hill (ref. 2) found an exact solution for the case of the fov being outside of the source image.

The specific configuration to be handled here applies to the case where the radiometer's fov is smaller than and completely inside of the source image, as illustrated in Figure 120. Referring to a fixed Cartesian coordinate system (W, Y) with origin at the radiometer's fov center O, an arbitrary point P within this fov may be described by polar coordinate (R, β) where $0 \leqq R \leqq r_o$, $0 \leqq \beta \leqq 2\pi$. The center C of the geometrical source image may be displaced by the amount D. Then, an arbitrary point Q within the area of the geometrical source image may be described by polar coordinates (r, θ) referred to P as origin and to $d = \overline{PC}$ as baseline for measuring the angle θ. One obtains easily

$$d = (D^2 - 2DR\cos\beta + R^2)^{1/2}$$

where $D - r_o \leqq d \leqq D + r_o$, a relationship that is completely independent of the polar coordinates of Q.

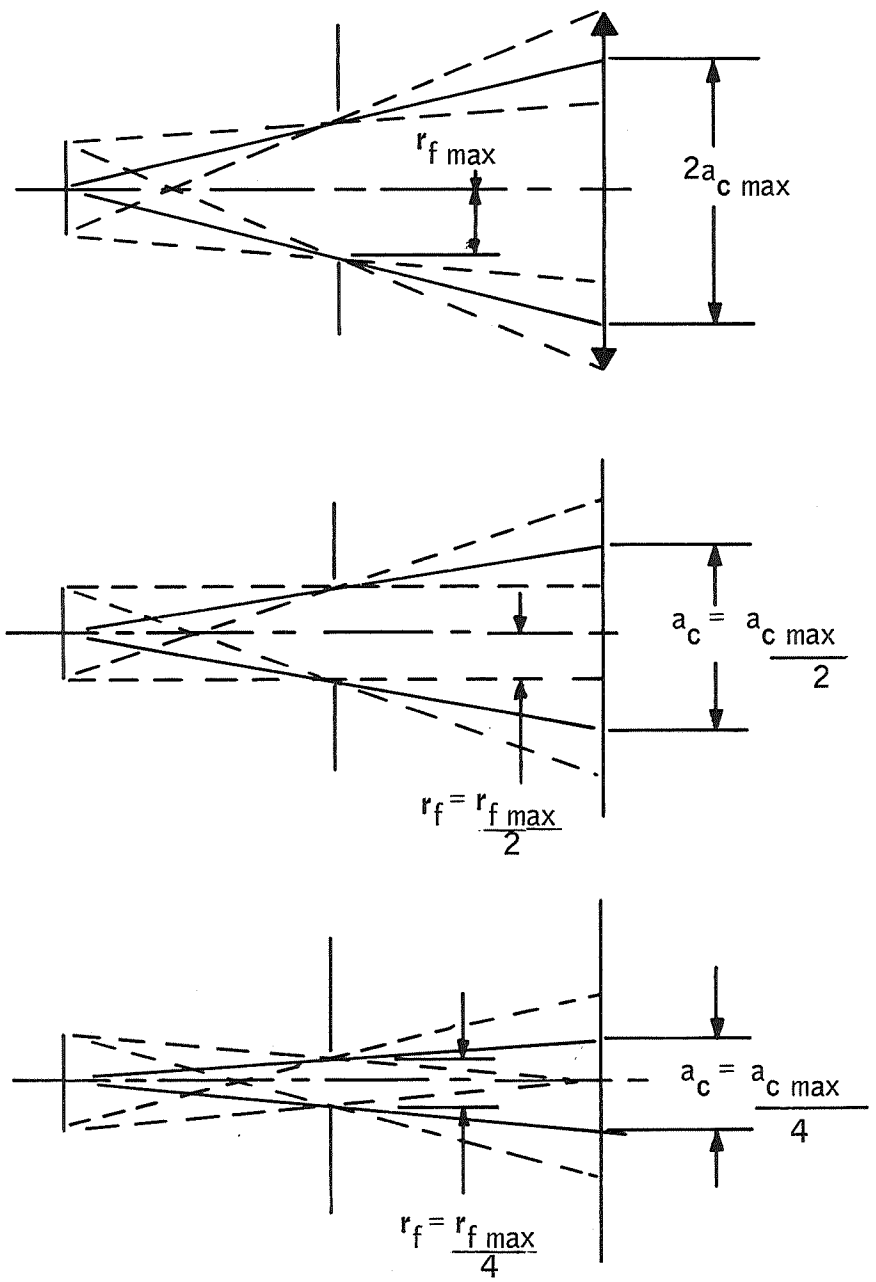

Figure 119. Variation of Effective Aperture with Field-Stop Extension

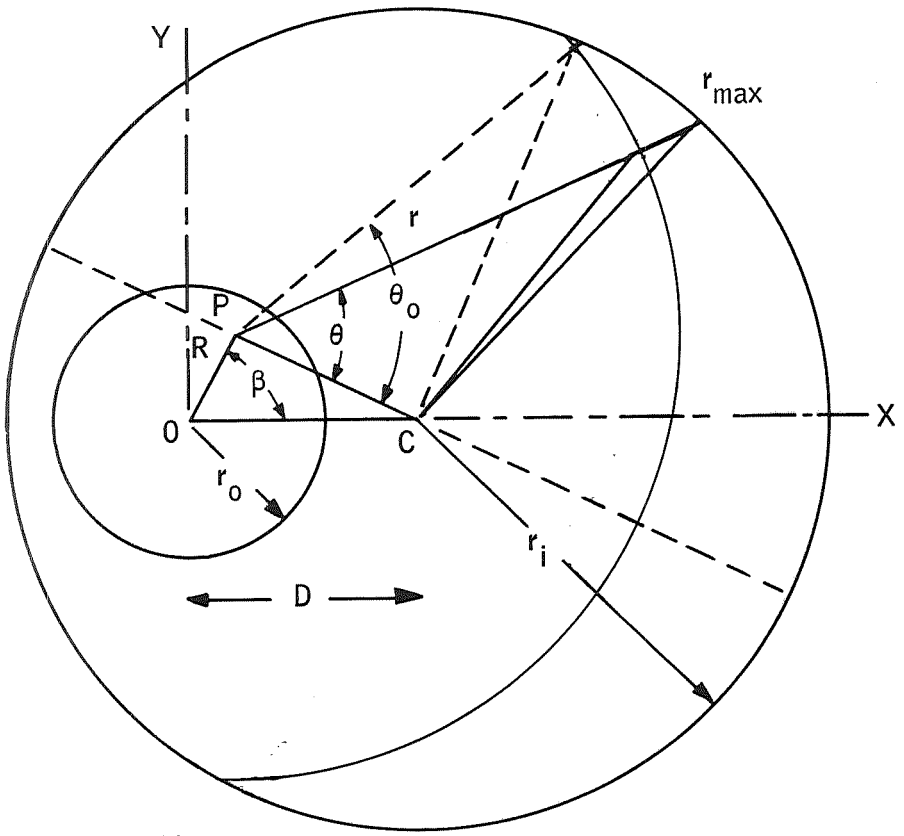

Figure 120. Actually Encountered Configuration for Deriving the Diffraction Pattern Due to Extended Source of Inflight Calibrator

The geometrical image of a particular point within the extended source is represented by Q; i.e., it is the center of a diffraction pattern defined by

$$N_\lambda(w) = \bar{N}_{o,\lambda} \left[\frac{2 J_1 \left(\frac{2\pi}{\lambda} a_c w \right)}{\frac{2\pi}{\lambda} a_c w} \right]^2 \quad \text{(for example, see ref. 4)}$$

where $N_{o,\lambda}$ = central spectral radiance (W/m^2-sr-m $\Delta\lambda$)

$$= \tau_{ca} \eta_{co} \, 2 c^2 h \lambda^{-5} \left[\exp \frac{ch}{\lambda k T} - 1 \right]^{-1}$$

$$\tau_{ca} = (r_f / r_{f_{max}})^2$$

r_f, $r_{f_{max}}$ = actual and maximum aperture-stop radius

η_{co} = IFC-collimator efficiency factor

= ρ_{co} = reflectivity of reflective, or

= τ_{co} = transmissivity of refractive collimator, respectively

c = light velocity = 3×10^8 m sec^{-1}

h = Planck's constant = 6.63×10^{-34} W sec^2

λ = wavelength (m)

k = Boltzmann's constant = 1.38×10^{-23} W sec deg^{-1}

T = source temperature (deg K)

J_1 = first-order Bessel function of first kind

a_c = effective aperture radius (m)

$w = \sin \phi \approx r/f_o$

f_o = collector focal length (m)

Since every point along a circle through Q with origin at P contributes the same amount of radiance, one obtains the accumulated radiance

$$N_\lambda (R,\beta) = \frac{1}{r_i^2 \pi} \int_{-\theta_o}^{\theta_o} \int_{o}^{r} N_\lambda (w)\ r\ dr\ d\theta$$

Unfortunately, θ_o becomes a function of r because it is defined by

$$\theta_o = \cos^{-1} \left(\frac{r_i^2 - d^2 - r^2}{2rd} \right)$$

For this reason, the integral cannot be evaluated in the usual way - i.e., by performing first the integration over θ and subsequently that over r - if the range of $-\pi \leqq \theta_o \leqq \pi$ is to be covered.

However, vice versa, r can be expressed as a function of θ if the radial line connecting P and Q is extended to the periphery of the geometrical source image. By doing this, one obtains

$$r_i^2 = r_{max}^2 + d^2 - 2\, r_{max}\, d \cos \theta$$

or

$$r_{max} = d\cos\theta \pm (d^2\cos^2\theta + r_i^2 - d^2)^{1/2}$$

$$= d\cos\theta \pm r_i\left(1 - \frac{d^2}{r_i^2}\sin^2\theta\right)^{1/2}$$

i.e., a well-defined function of θ. Inspecting this expression, it is found that it must have the values

$$r_{max} = d + r_i \text{ for } \theta = 0, \text{ and } r_{max} = -d + r_i \text{ for } \theta = \pm\pi$$

that is, one generally has

$$r_{max} = d\cos\theta + r_i(1 - \kappa^2\sin^2\theta)^{1/2}$$

if one denotes $\kappa = d/r_i$. Thus, one can express r_{max} in terms of Jakobi's elliptical functions

$$r_{max} = d \times \text{cnu} + r_i \times \text{dnu} \quad \text{(ref. 11, for example)}$$

However, since the integrations involved in any way will have to be performed with the aid of digital computers, this academic substitution is of no help. What is really important is the fact that θ varies now from zero to $\pm\pi$ and r from zero to the above defined value of r_{max} and that the integration over r can very well be performed before that over θ.

Consequently, the original integral now is transformed into

$$N_\lambda(R,\beta) = \frac{1}{r_i^2\pi}\int_{-\pi}^{\pi}\int_{o}^{r_{max}} N_\lambda(w)\, r\, dr\, d\theta$$

$$= \frac{2}{r_i^2\pi}\int_{o}^{\pi}\int_{o}^{r_{max}} N\ (w)\ r\, dr\, d\theta$$

$$= N_{o,\lambda}\,\frac{8}{r_i^2\pi}\int_{o}^{\pi}\int_{o}^{r_{max}} \frac{J_1\left(\frac{2\pi}{\lambda}\frac{a_c}{f_o}r\right)}{\left(\frac{2\pi}{\lambda}\frac{a_c}{f_o}r\right)^2}\ r\, dr\, d\theta$$

Introducing the integration variables

$$z = \frac{2\pi}{\lambda} \frac{a_c}{f_o} r \quad , \quad dz = \frac{2\pi}{\lambda} \frac{a_c}{f_o} \, dr$$

results in

$$N_\lambda (R,\beta) = N_{o,\lambda} \frac{2}{\pi} \left(\frac{f_o \lambda}{r_i a_c \pi} \right)^2 \int_o^\pi \int_o^{z_{max}} \frac{J_1^2 (z)}{z} \, dz \, d\theta$$

$$= -N_{o,\lambda} \frac{1}{\pi} \left(\frac{f_o \lambda}{r_i a_c \pi} \right)^2 \int_o^\pi \int_o^{z_{max}} \frac{d}{dz} \left[J_o^2 (z) + J_1^2 (z) \right] dz \, d\theta$$

$$= N_{o,\lambda} \frac{1}{\pi} \left(\frac{f_o \lambda}{r_i a_c \pi} \right)^2 \int_o^\pi \left[1 - J_o^2 (z_{max}) - J_1^2 (z_{max}) \right] d\theta$$

Now, the total spectral radiance experienced within the radiometer's fov is obtained again by integration:

$$N_\lambda = \frac{1}{r_o^2 \pi} \int_o^{2\pi} \int_o^{r_o} N_\lambda (R,\beta) \, R \, dR \, d\beta$$

$$= N_{o,\lambda} \left(\frac{f_o \lambda}{r_o r_i a_c \pi^2} \right)^2 \int_o^{2\pi} \int_o^{r_o} \int_o^\pi \left[1 - J_o^2 (z_{max}) - J_1^2 (z_{max}) \right] d\theta \, R \, dR \, d\beta$$

Finally, total radiance becomes

$$N_{tot,\Delta\lambda} = \tau_{ca} \eta_{co} 2c^2 h \left(\frac{f_o}{r_o r_i a_c \pi^2} \right)^2 \int_{\lambda_1}^{\lambda_2} \int_o^{2\pi} \int_o^{r_o} \int_o^\pi \lambda^{-3} \left[\exp\left(\frac{ch}{\lambda kT} \right) - 1 \right]^{-1} \exp$$

$$x \left[1 - J_o^{\,2} (z_{max}) - J_1^{\,2} (z_{max}) \right] d\theta \, R \, dR \, d\beta$$

It is to be mentioned that the actual fov determined by the area of the detector's geometrical image can be taken into account easily by describing this area by

$$-a \leqq X_p \leqq a, \quad -b \leqq Y_p \leqq b$$

by defining

$$d = D^2 - X_p^2 - Y_p^2 \quad ^{1/2}$$

and by replacing

$$Rd\,R d\beta \text{ by } dX_p\, dY_p$$

and

$$r_o^2\,\pi \text{ by } 4\,a\,b$$

COMPONENT TEST

A careful literature search was conducted to determine the amount of information available on parametric measurements of components required for ARRS. Component data substantiation obtained is shown in Table 33. This investigation led to the need for tests where data were not available. The objectives of the component test program are to provide accurate documented data on the operating characteristics of various ARRS components considered for use.

These tests will determine if the actual operating characteristics meet the ARRS requirements or if a design tradeoff is required. The data obtained will also be used for insertion into the error analysis to evaluate effects of parametric uncertainties on the operating characteristics of the ARRS radiometer system.

A comprehensive survey of available component test data and the results of component error from the radiometer system error analysis indicated that more complete data were required for components listed below:

- Mirror reflectance
- IFC source
- Chopper
- Spectral filter
- Detector
- Detector mount

Vacuum aging tests of mirror reflectance and IFC source stability are continuing past final report publication and the results will be presented in an addendum. Effects of environment cycling on mirror reflectance are presented here. Chopper, filter, and detector tests were identified and defined, but component procurement lead times prevented running of tests during Part I; however applicable tests are described. Proposed detector mount tests were identified and defined, and are discussed below. The tests were not run because the performance characteristics of the detector mount were determined to be heavily dependent on the specific operating characteristics of the radiometer. The proposed tests would therefore be used as part of development tests for a detector mount designed for a specific application.

In addition to these areas, special attention was given to data on refractive materials, an area in which tests were thought to be required. However, sufficient data were obtained to render the tests unnecessary, as previously discussed.

TABLE 33.- CONTRIBUTIONS TO MEASUREMENT UNCERTAINTY WITHOUT CALIBRATION (SHORT-TERM)

Component characteristic	Uncertainty	Documented source
1. Mechanical dimensions of precise (< 1 in.) parts or apertures	0.0001 in.	Leitz Model UWM Toolmaker Microscope Catalog 81-10/a Engl Pg 7
2. Mechanical dimensions of precise large Parts (< 1 in.) or apertures	0.001 in.	Starret Catalog 27: Outside Micrometers, 436 series; Inside Micrometers, 124 series
3. Mirror reflectivity (0.98622)	0.00568	LMSC tests[a]
4. Mirror emissivity (1-reflectivity)	0.00586	Same as mirror reflectivity
5. Emissivity of painted (black or gray) solid objects (No measurable temperature dependence at 14 to 16μ for 3M or Cat-A-Lac black paint in 10^{-7} mm vacuum.) 3M emissivity = 0.94	1%	b
6. Transmission of window materials 14 to 16μ, germanium (1.6 mm) T 40% R 38% KRS 5 (2 mm) T 75% R 20% IRTRAN 6 (77° or 298°K) T 97% R 2%	1%	c, d, e
7. Bandpass-filter transmission	1%	e
8. Bandpass-filter spectral characteristics	0.05%	
9. Blackbody radiance, f (t)	0.03°K	f
10. Temperature gradients	To be determined	Design dependent
11. Mechanical/optical alinement of, and from factors due to, thermo-elastic effects, operator mis-alinement	g	Design dependent
12. Chopper stability (amplitude or frequency shift)	g	Design dependent (component tests required)
13. Detector uncertainties	g	Component tests required
14. Electrical filter uncertainties	g	Design dependent

TABLE 33.–CONTRIBUTIONS TO MEASUREMENT UNCERTAINTY WITHOUT CALIBRATION (SHORT-TERM)(Continued)

[a]The uncertainty calculated below is based on data obtained from initial LMSC tests conducted at NOL, China Lake.

- The mirrors were ordered to have a reflectance of 0.99
- It was assumed all OCLI and PE mirrors are acceptable

Nonimal value received	0.98622 ± 0.00213
Uniformity uncertainty	0.00124
Measurement uncertainty	0.00231
Total uncertainty	± 0.00568

This total uncertainty represents that associated with the nominal value and the range to be expected for similarly manufactured mirrors shortly after receipt.

After measurement (which would not normally be made for new mirrors), uncertainty reduces to 0.00124 + 0.00231 = 0.00355.

[b]Stierwalt, D. L., Infrared Spectral Emittance Measurements of Optical Materials Appl. Optics 5, No. 12, 1911, Dec. 1966

Uses Beckmann IR-3 Spectrophotometer with 1.0% uncertainty.

[d]Calculated values IRTRAN 6, LMSC TRD, Refractive Materials Based on MIL Handbook-141 Par. 17.

[e]Beckman Instruction Manual 1416-C Nov. 1965 For IR12 Infrared Spectrophotometer.

1.0% absolute accuracy; 0.2% of reading for single beam or with calibration in double beam.

Wave number accuracy:

±0.2 cm^{-1}	(0.05%)	at 400 cm^{-1}	(25μ)
±0.3 cm^{-1}	(0.0405%)	at 740 cm^{-1}	(13.5μ)
±0.4 cm^{-1}	(0.0037%)	at 1330 cm^{-1}	(7.45μ)
±0.5 cm^{-1}	(0.00225%)	at 2220 cm^{-1}	(4.45μ)

TABLE 33.- CONTRIBUTIONS TO MEASUREMENT UNCERTAINTY WITHOUT CALIBRATION (SHORT-TERM) (Concluded)

[f]Accuracy of temperature measurements: Precision platinum resistance thermometers (-183 to 400°C), as they are manufactured today, are capable of reproducing temperatures in the range -183 to -400°C to within 0.001°K for very long periods of time (tested to 1600 hours). At temperatures between 400 and 630°C, this time is considerably reduced but is still in the order of a few hundred hours. Ref: Berry, R.J., The Stability of Platinum Resistance Thermometers at Temperatures Up to 630°C, in Temperature, Its Measurement and Control in Science and Industry, Vol. 3, Part 1, Reinhold Publishing Corp., New York, 1962.

Germanium resistance thermometers (1 to 100°K): Many thermal sensing elements were cycled between helium temperature and room temperature up to 50 times with no evidence of changes in calibration of as much as 10^{-4}°K. Two thermometers were in continuous use for three years with no change in the original calibration curves. Ref.: Kunzler, Geballe and Hull, Germanium Resistance Thermometers, in Temperature, Its Measurement and Control in Science and Industry, Vol. 3, Part 1, Reinhold Publishing Corp., New York, 1962.

Thermistors 4.2 to 200°K: Thermal cycling up to 100 times causes drift in calibration curves of a few tenths of 1 K. Reproducibility of calibration curve is in the range of 30 millidegrees. After prolonged cycling, no further drifts occur for several thousand cycles. After 200 days, drifts were of the order of 100 millidegrees K. Sensitivity 10^{-4}°K, reliability $\sim$ 0.030°K in thermal cycling up to 300°K. Ref.: Sachse, Measurement of Low Temperatures With Thermistors, in Temperature, Its Measurement and Control in Science and Industry, Vol. 3, Part 2, Reinhold Publishing Corp., New York, 1962.

[g]To be determined.

MIRROR REFLECTANCE

The recommended concept of inflight calibration uses an off-axis parabolic reflector that collimates radiance from the IFC source into a portion of the radiometer collecting aperture. Inflight calibration stability is consequently dependent on the stability of the reflectance of the IFC mirror, since any changes in its reflectance produce a one-to-one change in the IFC signal, and these changes are undetectable. Similarly, instabilities in the uniformity of reflectance of the radiometer primary and relay reflectors also propagate into inflight calibration instabilities; if that part of the collecting aperture used by inflight calibration varies in reflectance by a different magnitude than the total aperture which is used for collecting scene radiance, an undetectable IFC error results. Since the IFC stability requirement is 0.1%, it is imperative that the IFC reflectance stability and primary and relay reflectance uniformity stability be better than 0.1%. Literature surveys have not produced data on which can be based a substantial prediction of that order of reflectance stability over the expected ARRS environment. Tests were therefore required.

Both Optical Coating, Inc., and Perkin-Elmer claim to be able to produce gold-coated mirrors with reflectance of 0.99 or better with uniform reflectance. However, neither company has the facilities to measure reflectance stability to the required precision of 0.1%. Michelson Laboratory of Naval Weapons Center (NWC), China Lake, California has a published capability (refs. 12 and 13) to make 0.1% accurate reflectance measurements. Gold-coated mirror samples were measured at Michelson Laboratory and the reflectance proved to be 98.4 to 98.8%.

References 14, 15, 16, and 17 indicate that optical properties of space-borne optical components can be affected by the following environmental conditions:

- Micrometeroid bombardment
- Condensation of outgassed materials
- Radiation
- Extreme temperature conditions
- Temperature and vacuum cycling

In addition, reference 13 shows measured 0.3% reflectance degradation caused by aging in air. The references do not cite pure aging effects (i.e., the effects of long-term operation in low-temperature vacuum operation). However, because of the stringent stability requirement on reflectance of 0.1%, it is prudent to add such an environment to the above list as a potentially harmful environment.

Relative to the above environments, the literature indicates that while radiation damage is probable, there are insufficient data to determine the magnitude of expected degradation. While reflectance degradation over the temperature cycling dictated by ARRS parameter bounds is not expected, nothing could be found in the literature to substantiate this quantitatively. References 15 and 16 point out that solid materials in a hard vacuum sublime at a rate proportional to their vacuum pressure and temperature; however, no data were found for gold at temperatures and vacuum pressures applicable to ARRS. Consideration was given to the possible damage caused by micrometeorites and the subsequent effects on reflectance. References 13 and 14 indicate that this effect will be negligible and can be ignored. According to reference 14, even if we are very conservative and take the average micrometeorite crater diameter as 50μ (0.002 inch), the area of one crater would be 3.14×10^{-6} inch^2, and the sum of 400 crater areas accumulated during the period of one year $1.26 \cdot 10^{-3}$ inch^2. Related to the test area of 2 inch^2, the damage is only 0.063%. Note that the crater area is considered, thereby taking into account most crazing that will be caused my micrometeoroid impact. Reflectance degradation will thus be no greater than 0.063%.

A first-order analysis, assuming that the distribution of scattered radiance is Lambertian, produced the result that noise equivalent radiance from earth self-emission, earth reflected sunlight, and direct sunlight would be at least an order of magnitude less than the ARRS error requirement. Therefore, test in this area is not recommended.

Recommendation was made to determine effects on mirror reflectance of temperature cycling, thermal vacuum cycling, sublimation, radiation, and low-temperature vacuum aging.

The mirrors measured were high-vacuum, gold-coated mirror blanks of a size consistent with the reflectance measurement equipment at Michelson Laboratory, NWC. Although ultra-high-vacuum, gold-coated mirrors exhibit a higher reflectance value than high-vacuum coated mirrors with the attendent desirable reduction in emissivity, the ARRS radiometer mirrors will be high-vacuum coated because equipment does not exist in industry to produce ultra-high-vacuum coatings. Both CERVIT and ULE quartz substrates were used to determine effects caused by different substrates.

Test Objectives

The objectives of these tests were to determine the effects of the environments on the reflectance of HV gold-coated Cervit and ULE quartz mirrors in the ARRS spectral region. Objectives of each environment are described below:

- Temperature cycle - To simulate the storage, transportation, and assembly temperature environment the mirrors are likely to experience.

- Thermal vacuum cycle - To simulate the thermal vacuum environment the mirrors are likely to experience in testing and operation. Soak temperatures and pressures were representative of the range of temperatures and pressures to be experiences by the ARRS mirrors (primary, secondary, or relay) in test or operation. Rates of change of environments were taken from reference 14 and are representative of the capabilities of the environmental test equipment rather than relating to expected ARRS environment rates of change which are dependent on parameters outside the scope of Part I considerations (e.g., specific mission or test related parameters dependent on prelaunch equipment to test equipment being used).

- Sublimation - The thermal vacuum cycles described above were also used on separate mirrors on both anodized and black-painted fixtures to determine the effects of outgassed anodize and paint which recondense on the optics.

- Radiation - Nuclear radiation environments simulating the total dosage of the radiation environment of the ARRS typical orbit were used. Dose rates were accelerated to simulate the total dosage of either one month or one year in orbit.

- Low temperature vacuum aging - Effects of long-term operation in vacuum at low temperature are being determined by subjecting seven mirrors to an extended vacuum environment at a temperature representative of ARRS operation.

Measurement requirements. -- The most significant requirement is the ability to measure reflectance with accuracy of 0.2% and precision of 0.1%.

Test procedures. -- On receipt from the manufacturers, the mirrors were taken to the NWC at China Lake, California, where their reflectance was measured in the Michelson Laboratory. To determine uniformity as well as absolute reflectance, two areas of 0.75 inch x 0.25 inch separated by 0.62 inch on a 1.5-inch diameter disc were measured.

The sample was then rotated 90° and the measurement repeated. After the measurements were performed and documented, the samples were returned for environmental simulation. Following that, the samples (numbered 1 through 12) were measured again at Michelson Laboratory to measure the difference which is the degree of reflectance degradation caused by the environmental simulation.

The environmental simulation was performed on a large number of samples in series to learn the effect of each environmental factor separately:

- One mirror went through the temperature cycle
- The second mirror went through thermal vacuum cycling
- The third mirror went through the same environment as the second but was mounted in a black anodized aluminum housing to test an eventually outgassing effect of the coating
- The fourth mirror underwent the radiation test
- The fifth mirror went along with the first four, and so received the sum of all environmental factors
- The sixth mirror remained untouched in its protective container as a reference

Table 34 shows a mirror/environment matrix. With a limited number of available mirrors, a condition brought on by having to order a particular quantity of blanks prior to finalizing the test approach, all combinations of environments were not run. However, one Cervit blank and one ULE quartz blank were subjected to the combined environment, including one-year radiation exposure.

Temperature cycle: Mirrors No. 1, 5, 7, and 11 were subjected to temperature cycling. Equipment is a Tenney Chamber, Model No. T3OUF-100550 -

- 70° to 160°F - Test chamber internal rate of temperature change was 1.5°F per minute. The temperature internal relative humidity was uncontrolled. The internal temperature was raised to a temperature of 160°F. The mirrors were exposed to this temperature for a period of four hours.
- Test chamber internal ambient temperature was reduced at a rate of -3.6°F per minute down to -60°F and was maintained at this level for 16 hours. At the conclusion of this soak period the test chamber cooling was turned off and the chamber internal absolute pressure was reduced to 87 mm Hg.
- After the third cycle, the test chamber internal conditions were returned to normal
- See Table 35 for test details of these three cycles

TABLE 34. - ENVIRONMENT SUMMARY

Mirror No.	Material	Source	Fixture coating	Environment			
				Temp cycle	Thermal-vac cycle	Sublimation	Radiation (months)
1	Cervit	HI		x			
2	Cervit	HI			x		
3	ULE	OCLI	Anodize			x	
4	ULE	OCLI	Anodize				1
5	ULE	OCLI	Anodize	x	x	x	12
6	ULE	OCLI		control			
7	ULE	PE		x			
8	ULE	PE			x		
9	ULE	PE	Paint			x	
10	ULE	PE	Paint				12
11	Cervit	HI	Paint	x	x	x	12
12	Cervit	HI		control		x	

TABLE 35. - THERMAL CYCLE DATA

	Time	Temp, °F	Condition	Hours
1st Cycle				
17 June 1969	10:00 AM	70	760 mm Hg 1.5°F/min	1
	11:00 AM	160		4
	3:00 PM	160	-3.6°F/min	1
	4:00 PM	-60		16-1/2
18 June 1969	8:30 AM	-60	87 mm Hg +1.2°F/min	3
2nd Cycle				
	11:30 AM	+160		4
	3:30 PM	+160	-3.6°F/min	1
	4:30 PM	-60		16
19 June 1969	8:30 AM	-60	87 mm Hg +1°F/min	3-1/2
3rd Cycle				
	12:00 N	+160		4
	4:00 PM	+160	-4.9°F/min	3/4
	4:45 PM	-60		16
20 June 1969	8:45 AM	-60	87 mm Hg +0.9°F/min	2-1/2
	11:15 AM	+70	760 mm Hg	

Thermal-vacuum cycling: Mirrors No. 2, 5, 8, and 11 were subjected to thermal-vacuum cycling.

- Chamber conditions were at normal atmospheric conditions
- Chamber pressure was reduced from sea level to 25 mm Hg in 90 seconds. During this period, the maximum pressure reduction rate was 15 mm Hg/sec for a maximum duration of 30 seconds. Pressure reduction was continued until a pressure of 6.5×10^{-6} mm Hg had been reached.

Note: The vacuum equipment has been programmed to function at the above stated rate. Thus, for the first cycle:

25 June 1969	9:07	Initiate pump down
	9:07	760 mm Hg
	9:07:30	310 mm Hg
	9:09:30	25 mm Hg
	11:27	6.5×10^{-6} mm Hg

- Temperature reduction was started at approximately the same time as evacuation. The temperature reduction rate of both the fixture and the chamber walls did not exceed 3°F/min (~2K/min). Temperature reduction was continued until an equilibrium temperature of -315°K was attained.

- Samples were soaked at these conditions for four hours.

- Test chamber internal conditions were then returned to normal atmospheric conditions. The chamber rate of pressure increase did not exceed 30 mm Hg/sec, and the rate of temperature increase did not exceed 3°F/min (~2°K/min).

- Test chamber internal condition then remained at this condition for eight hours.

- Cycle up to this step in procedure was repeated three times.

- See Table 36 for details of the four cycles.

Sublimation: Mirrors No. 3 and 5 in a black anodized fixture, and mirrors 9 and 11 in black painted fixtures, were subjected to the thermal-vacuum cycle after the fixtures had been subjected to outgas conditioning for six days in a vacuum.

- Chamber condition was a normal atmospheric condition.

- 9:50 initiate pump-down -- Chamber pressure was reduced to simulate ascent from sea level to 25 mm Hg in 90 seconds. During this period, the maximum pressure reduction rate was 15 mm Hg/sec for a maximum duration of 30 seconds. Pressure reduction was continued until a pressure of 6.5×10^{-6} mm Hg was reached.

  Note: The vacuum equipment has been programmed to function at the above stated rate. Thus, for the first cycle:

9:50	760 mm Hg
9:50:30	310 mm Hg
9:51:30	25 mm Hg
12:10	6.5×10^{-6} mm Hg

- Temperature reduction started at 10:10. The temperature reduction rate of both the fixture and the chamber walls was 2.9°F/min average.

- See Table 37 for details of these four cycles.

TABLE 36.- THERMAL-VACUUM CYCLING DATA

	Temp, °F	Time	Condition
First cycle			Chamber pressure
25 June 1969		9:07	Initiate Pump Down
		9:07	760 mm Hg
		9:07:30	310 mm Hg
		9:08:30	25 mm Hg
		11:27	6.5×10^{-6} mm Hg
			Temperature reduction
	75	9:35	Initiate Shroud Cooling
	-10	9:55	
	-30	10:10	
	-60	10:20	
	-90	10:30	2°F/min
	-125	10:40	
	-150	10:50	
	-180	11:00	
	-220	11:15	
	-250	11:23	
	-260	11:27	
	-315	11:45	Start 4-hour soak period
	-315	15:45	End of 4-hour soak period
	70	24:00	
Second cycle			Chamber pressure
26 June 1969		7:45	Initiate Pump Down
			Temperature reduction
	75	8:30	Initiate Shroud Cooling
	60	8:40	
	30	8:50	
	5	9:00	
	-25	9:10	
	-50	9:20	
	-95	9:37	
	-150	9:50	2.6°F/min
	-180	10:00	
	-200	10:10	
	-270	10:40	
	-315	11:00	Start 4-hour soak period
	-315	15:00	Complete 4-hour soak period
	70	24:00	

TABLE 36.- THERMAL-VACUUM CYCLING DATA (Concluded)

	Temp, °F	Time	Condition
Third cycle			Chamber pressure
27 June 1969		7:40	Initiate Pump Down
			Temperature reduction
	70	7:40	Initiate Cool-Down
	50	7:50	
	30	8:00	
	-30	8:20	
	-60	8:30	
	-90	8:40	2.75°F/min
	-120	8:50	
	-150	9:00	
	-175	9:10	
	-210	9:24	
	-260	9:40	
	-315	10:00	Start 4-hour soak period
	-315	14:00	End 4-hour soak period
	70	24:00	
Fourth cycle			Chamber pressure
30 June 1969		7:45	Initiate Pump Down
			Temperature reduction
	75	7:45	Initiate Shroud Cooling
	55	7:55	
	25	8:05	
	0	8:15	
	-15	8:18	
	-30	8:25	2.9°F/min
	-60	8:35	
	-90	8:45	
	-125	8:55	
	-150	9:05	
	-210	9:25	
	-315	10:00	Start 4-hour soak period
	-315	14:00	End 4-hour soak period
	70	24:00	
	70	8:00	
1 July 1969	End of test		

TABLE 37.- SUBLIMATION TEST DATA

	Temp, °F	Time	Condition
First cycle			
1 July 1969	75	10:10	
	10	10:35	
	-35	10:55	
	-55	11:05	
	-100	11:20	
	-150	11:35	
	-175	11:45	
	-220	12:00	
	-250	12:10	6.5×10^{-6} mm Hg
	-315	12:25	Start 4-hour soak period
	-315	16:20	End of-4 hour soak period
	70	24:00	760 mm Hg
End of first cycle			
Second cycle			
2 July 1969	70	7:40	760 mm Hg Pump Down
		7:40:30	310 mm Hg
		7:41:30	25 mm Hg
		12:00	6.5×10^{-6} mm Hg
	70	7:40	Initiate Shroud Cooling
	50	7:50	
	25	8:00	
	0	8:10	
	-25	8:20	
	-60	8:30	
	-90	8:40	
	-150	9:00	
	-175	9:10	
	-200	9:20	
	-230	9:30	
	-275	9:40	
	-300	9:50	
	-315	10:00	Start 4-hour soak period
	-315	12:00	6.5×10^{-6} mm Hg
	-315	14:00	End of 4-hour soak
	70	24:00	760 mm Hg

Temperature reduction rate was 2.75°F/minute average.
End of second cycle

TABLE 37.- SUBLIMATION TEST DATA (Concluded)

	Temp, °F	Time	Condition
Third cycle			
3 July 1969		7:40	760 mm Hg
		7:40:30	310 mm Hg
	75	7:40	Initiate Shroud Cooling
	50	7:50	
	25	8:00	
	0	8:10	
	-30	8:20	
	-60	8:30	
	-85	8:40	
	-130	8:50	
	-145	9:00	
	-175	9:10	
	-215	9:20	
	-230	9:30	
	-270	9:40	
	-315	10:00	Start 4-hour soak period;
	-315	14:00	6.5×10^{-6} TORR
	75	24:00	760 mm Hg
The temperature reduction rate was 2.8°F/minute average.			
End of third cycle			
Fourth cycle			
7 July 1969	75	7:40	Initiate Shroud Cooling
	50	7:50	
	-15	8:05	
	-30	8:20	
	-60	8:30	
	-120	8:50	6.5×10^{-6} TORR
	-150	9:00	
	-175	9:10	
	-220	9:20	
	-250	9:35	
	-275	9:45	6.5×10^{-6} TORR
	-315	10:00	Start 4-hour soak period
	-315	14:00	6.5×10^{-6} TORR
	70	24:00	
	70	7:40	760 mm Hg
The temperature reduction rate was 2.8°F/minute average.			
End of 4th cycle; end of test.			

Irradiation: Test equipment is a Febretion - Research Lab - Electron Acceleration with pulse time of 2×10^{-8} seconds at 2×10^{-6} rad intensity. This gives a dose rate of 10^{-4} rad/sec. The average electron energy is 1.5 MeV. In the X-ray mode, the intensity is reduced to 2×10^{3} rad or 10^{11} rad/sec. The normal beam is 1 cm diameter with Cobalt-60 as source, which produces 1.25 MeV photon-gamma rays with a dose rate of 10 rad/sec. Beam will accommodate three-inch-diameter disc.

- Mirror No. 4 in black anodized fixture simulation for one-month radiation exposure (refs. 12 and 17). Proton energy 20 keV 2.6×10^{10} protons/cm^2
- Mirror No. 5 in black anodized fixture
- Mirrors No. 10 and 11 in black painted fixtures
- Simulation for one year radiation exposure - 3.6×10^{11} protons/cm^2
- Proton energy 20 keV

Vacuum aging: Seven mirrors are being subjected to a vacuum aging environment, with test results to be presented in a final report addendum. This test was combined with the IFC source vacuum aging test and the test procedures are discussed under that section.

Test results. -- The reflectance of the mirrors was measured as described in reference 12. Using the instruments which are described in the reference, the specular reflectance at normal incidence can be measured with high precision. The major systematic error usually encountered in reflectance measurements are either reduced or eliminated. Therefore, by using these instruments it is possible to make measurements of high-reflectance samples through the visible and infrared regions of the spectrum which are good to ±0.001. The readout of each measurement was made with instruments discussed in reference 13.

The measurements were performed by E.J. Ashley, co-author of reference 13, and the results reviewed by Dr. Bennett. Initial reflectance measurements were made and then the sample was rotated 90° and the measurements were repeated to obtain data on the uniformity of the reflectance. Measurements were made on four samples from Optical Coating Laboratories, four samples from Perkin-Elmer, and six samples from Precision Magnetics, Inc.

The results of the initial reflectance measurements at 15.0μ are shown in Table 38. In the first column of the table, 1.0 means sample No. 1 and 1.9 means sample No. 1, rotated 90°; then 2.0 means sample No. 2 and 2.9 means No. 2 rotated 90°; etc. The results were reviewed and samples No. 3, 4, and 13 were measured again, because the first output results, the degree of uniformity, were doubtful. The reflectance values for the second measurements are also shown in the table. The average uniformities of all measurements

are 0.075% and, when using only the second readings for samples No. 3, 4, and 13, only 0.047%.

TABLE 38. -INITIAL REFLECTANCE OF SAMPLES AT 15μ

Sample [b, c]	Reflectance [a]	Mirror source	$\Delta(R_0, R_{90})$ [a]
1.0	98.562	Cervit	0.070
1.9	98.492		
2.0	97.828		
2.9	97.776		0.052
3.0-1	98.606	ULE quartz	
3.9-1	98.788		
3.0-2	98.805		
3.9-2	98.812		0.007
4.0-1	98.548		
4.9-1	98.782		
4.0-2	98.746		
4.9-2	98.793		0.047
5.0	98.672		
5.9	98.590		0.082
6.0	98.836		
6.9	98.719		0.117
7.0	98.570		
7.9	98.521		0.049
8.0	98.654		
8.9	98.614		0.040
9.0	98.588		
9.9	98.572		0.016
1000.0	98.445		
1090.0	98.409		0.036
1100.0	97.356	Cervit	
1190.0	97.480		0.124
1200.0	97.815		0.023
1290.0	97.792		
1300.0-1	97.698		
1390.0-1	97.480		0.000
1300.0-2	97.711		
1390.0-1	97.711		0.000
1400.0	97.666		0.001
1490.0	97.665		
	Average measured uniformity:		0.050%

[a] Last two digits are not reliable

[b] Samples denoted with a hyphen followed by a 1 or 2 denote cases where the reflectance measurements were repeated and the results of both measurements are shown.

[c] 1.0 indicates mirror #1 in its initial position in the measurement apparatus. 1.9 indicates mirror #1 90° rotated from its initial position in the measurement apparatus.

The second set of reading necessitated a second setup, and the average deviation of these three readings from the initial reflectances is 0.128%, which is approximately the stated accuracy of 0.1%. This is an indication of the maximum inaccuracy of the test since this was determined from selected worst-case data. The average accuracies determined from average data should be better than that determined for the above. The spectral reflectance as a function of wavelength of the OCLI samples is shown in Figure 121.

The results of the reflectance measurements on the samples after environmental testing are shown in Tables 39 and 40. The data shown in Table 40 are with the samples rotated 90° from the position of those data presented in Table 39. For these final data each measurement was repeated a second time to determine the precision of the data. These data are also presented in Tables 39 and 40. The average precision of the data from Tables 38 and 40 is 0.035%, which is less than the average uniformity, or precision, determined for the initial reflectances. The average uniformity for the final test tata is determined by the difference between the average of the data of Tables 39 and 40. This also is shown in Table 39, and the average uniformity is 0.030%.

TABLE 39.- REFLECTANCE OF SAMPLES AT 15μ AFTER TEST

Sample	Transmittance	Reflectance	ΔR	$\Delta(R_0, R_{90})$
1.0		98.317	0.062	0.007
1.0		98.379		
2.0		97.284	0.065	0.026
2.0		97.219		
3.0		98.544	0.098	0.004
3.0		98.446		
4.0		98.434	0.026	0.045
4.0		98.460		
5.0		98.522	0.018	0.029
5.0		98.504		
6.0		98.681	0.027	0.024
6.0		98.708		
7.0		98.368	0.039	0.021
7.0		98.407		
8.0		98.316	0.074	0.033
8.0		98.390		
9.0		98.428	0.014	0.020
9.0		98.442		
1000.0		98.440	0.028	0.053
1000.0		98.412		
1100.0		97.283	0.044	0.002
1100.0		97.327		
1200.0		97.694	0.050	0.045
1200.0		97.744		
		Average precision	0.045%	0.030% Average Noniformity

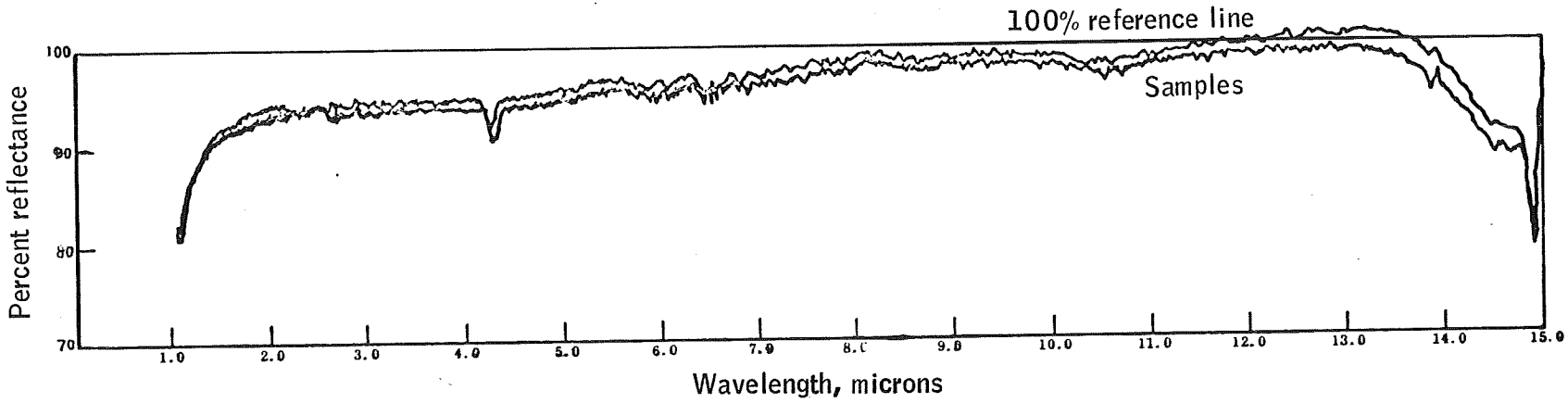

Figure 121. Spectral Reflectance of OCLI Mirror

TABLE 40. - REFLECTANCE OF SAMPLES AT 15μ
TEST ROTATED 90°

Sample	Transmittance	Reflectance[a]	ΔR
1.90[0]		98.370	
1.9		98.340	0.030
2.9		97.275	
2.9		97.299	0.024
3.9		98.500	
3.9		98.479	0.021
4.9		98.509	
4.9		98.485	0.014
5.9		98.561	
5.9		98.545	0.016
6.9		98.666	
6.9		98.681	0.015
7.9		98.440	
7.9		98.379	0.061
8.9		98.373	
8.9		98.400	0.027
9.9		98.471	
9.9		98.440	0.031
1090.0		98.467	
1090.0		98.492	0.025
1190.0		97.315	
1190.0		97.299	0.016
1290.0		97.772	
1290.0		97.757	0.015
		Average Precision 0.025%	

[a]Last two digits are not reliable

The average uniformity determined seems to be limited by the average precision determined by the initial and final tests and seems to be approximately 0.05%. The maximum inaccuracy in setup could be 0.13%, as determined from the three repeated measurements of the initial reflectance measurements.

A comparison of the initial and final reflectance measurements is given by Table 41. The test environment for each of the samples is summarized in Table 34. Samples 6 and 12 were used as control samples and were not exposed to any of the environments. An average drop in reflectance of 0.079% was observed for these control samples, which is within the stated accuracy of the measurement. Significant changes, on the order of twice the measurement accuracy of the equipment, are noted for samples 1, 2, 3, 4, and 8.

Sample 1, gold coating on Cervit substrate, was thermally cycled in ambient environment and shows a decrease in reflectance of 0.18%.

TABLE 41. - MIRROR REFLECTANCE TEST RESULTS

Mirror	Material	Source	Fixture Coating	Environment	First Measurement, %[a]	Second Measurement, %[a]	ΔR, %[a]
1	CERVIT	PM		Temperature Cycle	98.527	98.346	-0.181
2	CERVIT	PM		T/V Cycle	97.802	97.269	-0.533
3	ULE	OCLI	Anodize	Sublimation	98.808	98.493	-0.305
4	ULE	OCLI	Anodize	1 Mo Rad	98.769	98.470	-0.299
5	ULE	OCLI	Anodize	Temp., TV, Sub., 12 Mo Rad	98.631	98.533	-0.098
6	ULE	OCLI		(Control)	98.779	98.683	-0.096
7	ULE	PE		Temperature	98.546	98.398	-0.148
8	ULE	PE		T/V	98.634	98.370	-0.264
9	ULE	PE	Paint	Sublimation	98.580	98.445	-0.135
10	ULE	PE	Paint	12 Mo Rad	98.426	98.452	+0.026
11	CERVIT	PM	Paint	Temp., T/V Sub., 12 Mo Rad	97.418	97.306	-0.062
12	CERVIT	PM		Sub. (Control)	97.804	97.742	

[a]Last two digits are not reliable.

Sample 2, gold coating on Cervit substrate, was thermally cycled in vacuum and shows a quite significant change in reflectance of 0.53%. This was noticeable visually; the sample was observed to have a slightly darker tone to the gold color of the coating.

The slight degradation observed for sample 1, thermal cycling in ambient environment, could possibly have been enhanced by the thermal cycling in vacuum, but the test data are not conclusive since sample 11, a similar mirror to No. 1 which went through both these tests and also the sublimation and radiation test, did not degrade significantly.

Sample 3, gold coating on ultra-low-expansion quartz, shows significant degradation. This sample and also samples 4 and 5 were enclosed in a baffle assembly shown in Figure 122, which was coated with a black anodized material. Three similar mirrors, samples 9, 10, and 11, were mounted on similar baffle assemblies coated with a black paint.

Samples 3, 4, and 5 show significant degradation with an average change of -0.234% compared to the similar tested mirrors with painted baffle surfaces and an average change in reflectance of 0.067%. Thus, there seems to be no

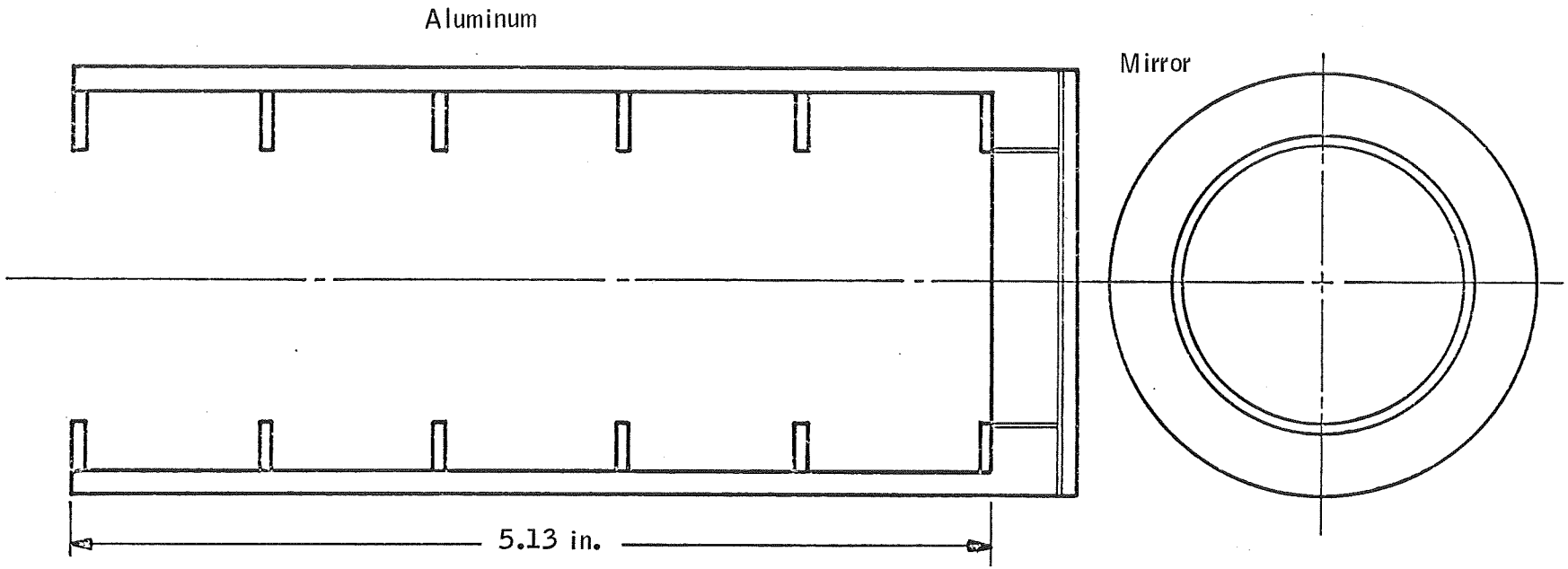

Figure 122. Baffle Assembly for Mirror Test

advantage of the hard anodized surface over the painted surface. Samples 3 and 4 actually show a fairly significant degradation, but this is not seen in the similar sample No. 5; therefore, the data are not very conclusive.

Sample 5, gold coating on ULE quartz, also showed significant degradation on thermal cycling in vacuum.

Table 34, the summary of the mirror environmental test, showed four mirrors being tested for each of the four environments. The average change in reflectances of the mirrors exposed to each environment was

- Temperature cycle - ambient - 0.132%
- Temperature cycle - vacuum - 0.252%
- Sublimation 0.162%
- Radiation 0.127%

Thus, the thermal cycling in vacuum appears to have the most significant effect on the reflectance stability. It is not clear, however, from the tests run that the environments affect reflectance in any given systematic or cyclical manner. It may be that the degradation observed is only an initial instability and that repeated environment cycling would tend to stabilize the reflectance value. This conclusion is supported by the data as presented in Table 42. Note that the mirrors with higher initial reflectance values degraded most except for mirror 2, which inhibited physical damage. This suggests that mirror reflectance might stabilize to a value of $\approx$ 98.5% and exhibit minimum degradation about that value. It is thus recommended that additional testing of the above type be done in which the reflectance degradation be determined as a function of the number of environment cycles.

No final conclusions will be made until the vacuum aging tests are completed; however, the following tentative observations are made:

- Initial mirror reflectance fails to meet the 99% specified by the vendors.
- The control mirrors, as expected, were among the three which degraded least.
- Mirrors subjected to all environments degraded less than most other mirrors. This was unexpected and yet is to be explained.
- Mirrors with higher initial reflectance tended to degrade the most.
- Mirror 2 was visibly degraded after the thermal-vacuum test, perhaps because of a defective coating. As expected its reflectance decreased most.

TABLE 42. - MIRROR REFLECTANCE TEST RESULTS IN ORDER OF DEGRADATION

First	ΔR(%)	Environment	Mirror
97.802	-0.533	T/V (darkened)	2 C
98.808	-0.305	Sublim. Anodize	3 O
98.769	-0.299	1 Mo Rad. Anodize	4 O
98.634	-0.264	T/V	8 P
98.527	-0.181	Temperature	1 C
98.546	-0.148	Temperature	7 C
98.580	-0.135	Sublimation	9 P
97.418	-0.112 (Paint)	Temp., T/V, Sub., 12 Mo. Rad.	11 C
98.631	-0.098 (Anod.)	Temp., T/V, Sub., 12 Mo. Rad.	5 O
98.777	-0.094	Control	6 O
97.804	-0.062	Control	12 C
98.426	+0.026	12 Mo. Radiance	10 P

INFLIGHT CALIBRATION SOURCE

The overall long-term accuracy of the radiometer is dependent on the emissivity stability and temperature stability of the calibration source. This dependence may be lowered somewhat by monitoring the temperature of the cavity and applying corrections for the radiance of the source. However, this is not desirable since other errors may be introduced into the calibration system.

Initial efforts to obtain a blackbody source for the inflight calibration system to meet the ARRS long-term stability requirements were directed toward designing a source. No commercially available source had been found to meet the ARRS requirements. The configuration of the source that was designed is shown in Figures 123 and 124. The cavity core was to be made from platinum to match the thermal expansion of the platinum wire sensors. This was contained in a gold bushing which matched the thermal expansion of the bridge

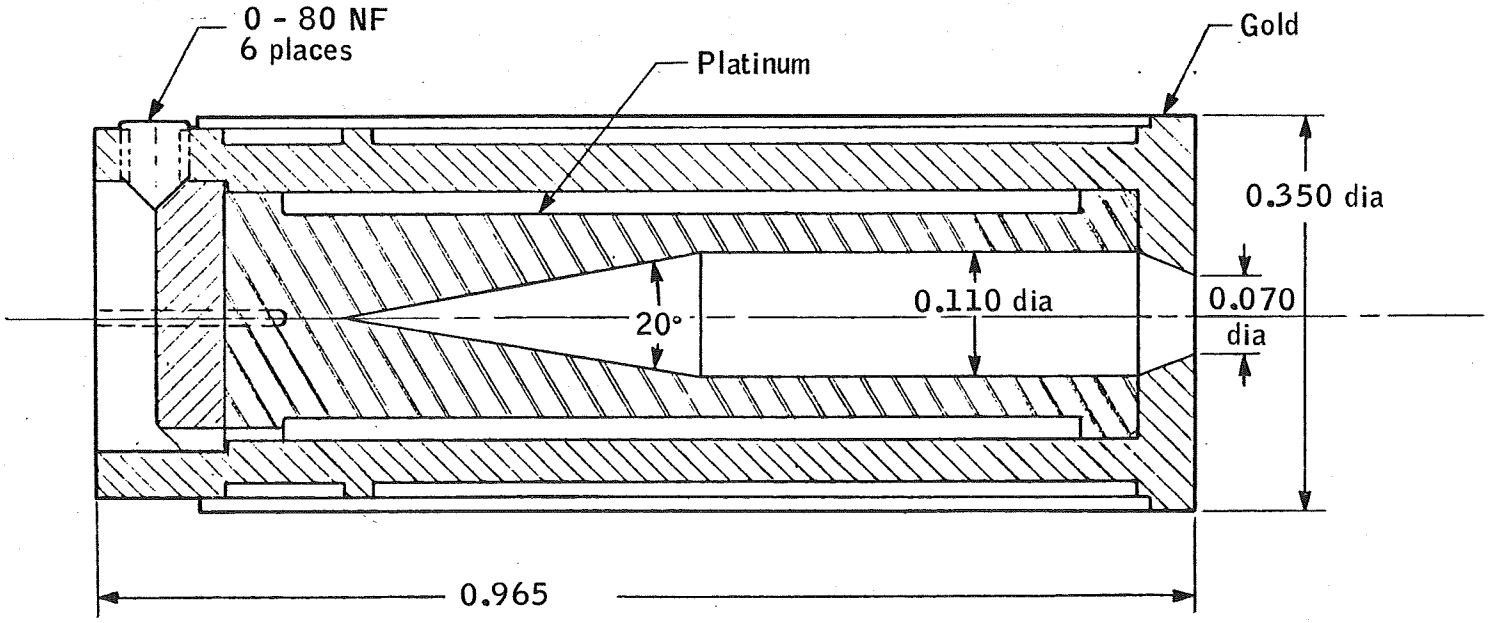

Figure 123. Blackbody Source Configuration

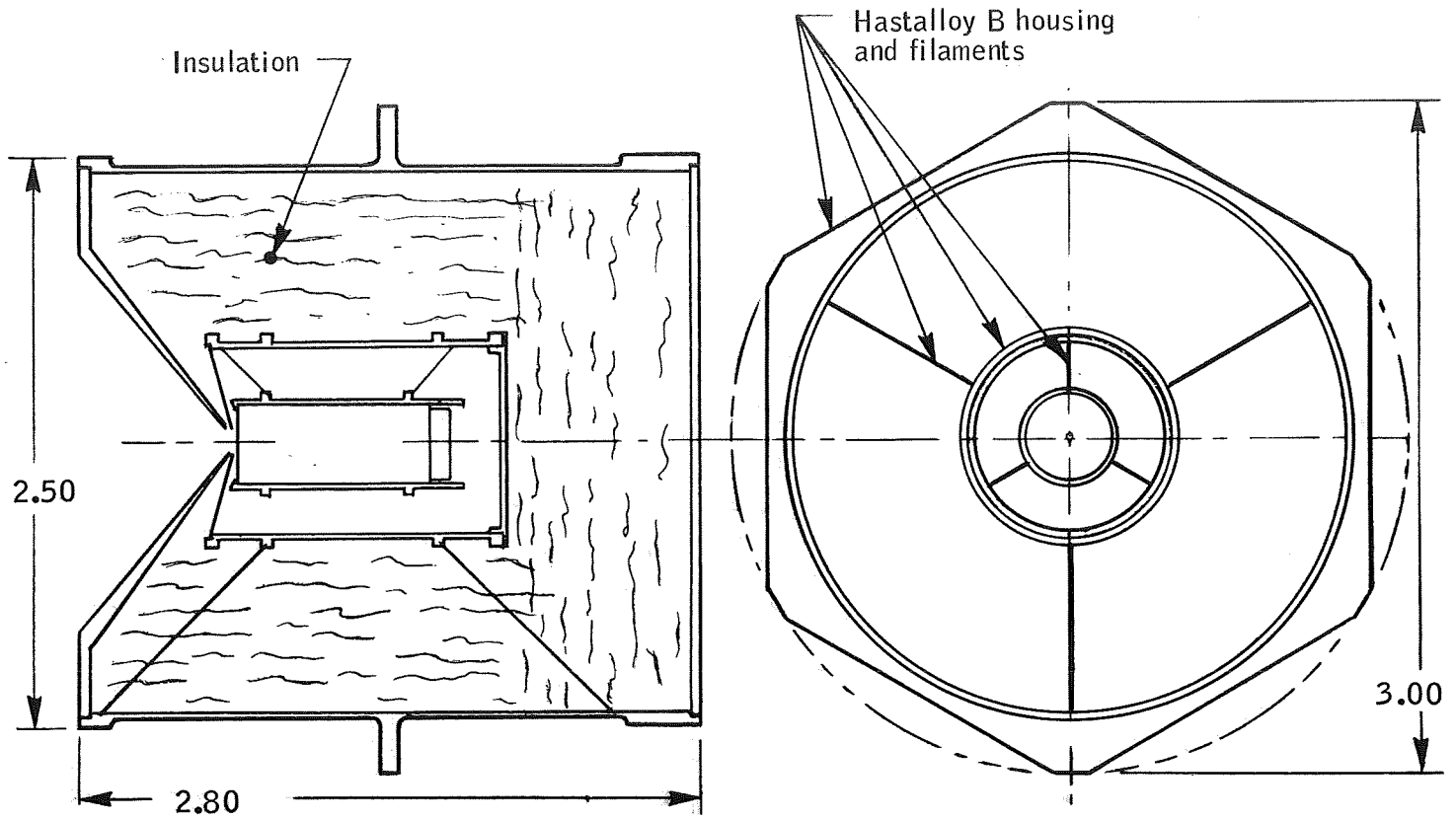

Figure 124. Blackbody Source Housing

resistors and had very good thermal transfer characteristics. The cavity was thermally isolated from the housing as shown in Figure 124 to minimize power requirements. A platinum monitor sensor was provided on the cavity to monitor the operating temperature.

Eventually a commerially available source was found that, with modifications, appeared to be able to meet the ARRS requirements. This was an Electro Optical Industries Model 121 blackbody source and controller. The manufacturer' s specifications for this source are given in Table 42. Discussions with Electro Optical Industries personnel led to a design which used no silicons that could come in contact with the control sensor and used a four-wire hook-up between the control sensor and the control bridge to minimize the effect of lead resistance drift.

TABLE 43.- SOURCE SPECIFICATIONS
Electro Optical Industries Model 1944

1.	Temperature range	50 to 600°C
2.	Cavity	0.080 in.
3.	Field-of-view	10°
4.	Control sensor	Platinum resistance thermometer
5.	Control sensor leads	4 wire
6.	Monitor sensor	Thermocouple Pt/Pt 10% Rh
7.	Control power	4 W
8.	Max input power	10 W
9.	Warmup time	10 min
10.	Dimensions	1.25 x 0.75 x 1.75 in.
11.	Weight	4 oz
12.	Cavity emittance	0.9999
13.	Cavity	Recessed cone
14.	Type of control	Linear proportional
15.	Stability (short term)	0.02°C
16.	Stability (long term)	0.1°C

Model 121 with the above modifications was then designated Model 1944. The temperature stability specifications show that this source meets the ARRS requirements for short periods. This source was not tested for extended operating periods in the ARRS IFC.

The stability of the cavity emittance is dependent only on the cavity geometry and the stability of the cavity coating . Electro Optical Industries personnel state the stability of the emittance of the cavity coating material at these temperatures (below 600°C) is 0.94 (±1)%. They calculate the emittance of the cavity, which is a 15° extended conical cavity, to be 0.9999. The 1% variation of the coating emittance is expected to vary the cavity emittance only a few digits in the last significant figure.

Thus, emissivity stability is expected to be of the order of ±0.0005, which satisfies the ARRS IFC error budget. Consequently, tests of emissivity stability are not required.

Test Objectives

Objectives of this test are to determine the long-term temperature stability of the Electro Optical Industries Model 1944 blackbody source operating in a vacuum. In addition, as discussed under mirror reflectance tests, a second objective is to determine the long-term degradation of mirror reflectance in a vacuum environment. Relative to reflectance effects, only the test environment is applicable; reflectance measurement techniques are those discussed under mirror reflectance tests.

Measurement Requirements

The requirements of the inflight calibration source as derived from analysis of the inflight calibration system are

- Source Temperature - 680°K
  - ► The minimum source temperature required to provide the maximum required calibration radiance level
- Source Temperature Stability < 0.3°C
  - ► At this stability level the error from this source becomes significant in comparison to the mirror reflectance instability error

Thus, the measurement resolution of the source temperature measurement should be of the order of 0.1°C.

Test Procedure

The source stability test was combined with a mirror vacuum aging test. The source and the mirror are placed in a configuration simulating the inflight calibration source and the collecting mirror (Figure 125). Another mirror is mounted so that it is shielded from direct exposure to the source and source cavity. The mirror exposed to the source cavity will be carefully examined for any contamination deposited from the source during the test. The unexposed mirror will act as a control surface.

The stability test will be performed in a hard vacuum of 10^{-5} torr or better using a vac-ion pumping system, which is inherently a very clean vacuum system and should introduce no contamination to the mirror itself. This test will be performed at ambient temperatures.

Thermal environment effect on the IFC source stability was discussed with Electro Optical Industries. Two extreme operating cases were considered - (1) connecting the source cavity to a 150°K heatsink, or (2) operation in a 150°K heatsink). These differences in operation will cause an increase of approximately 1 W connected to a heatsink as opposed to operation without

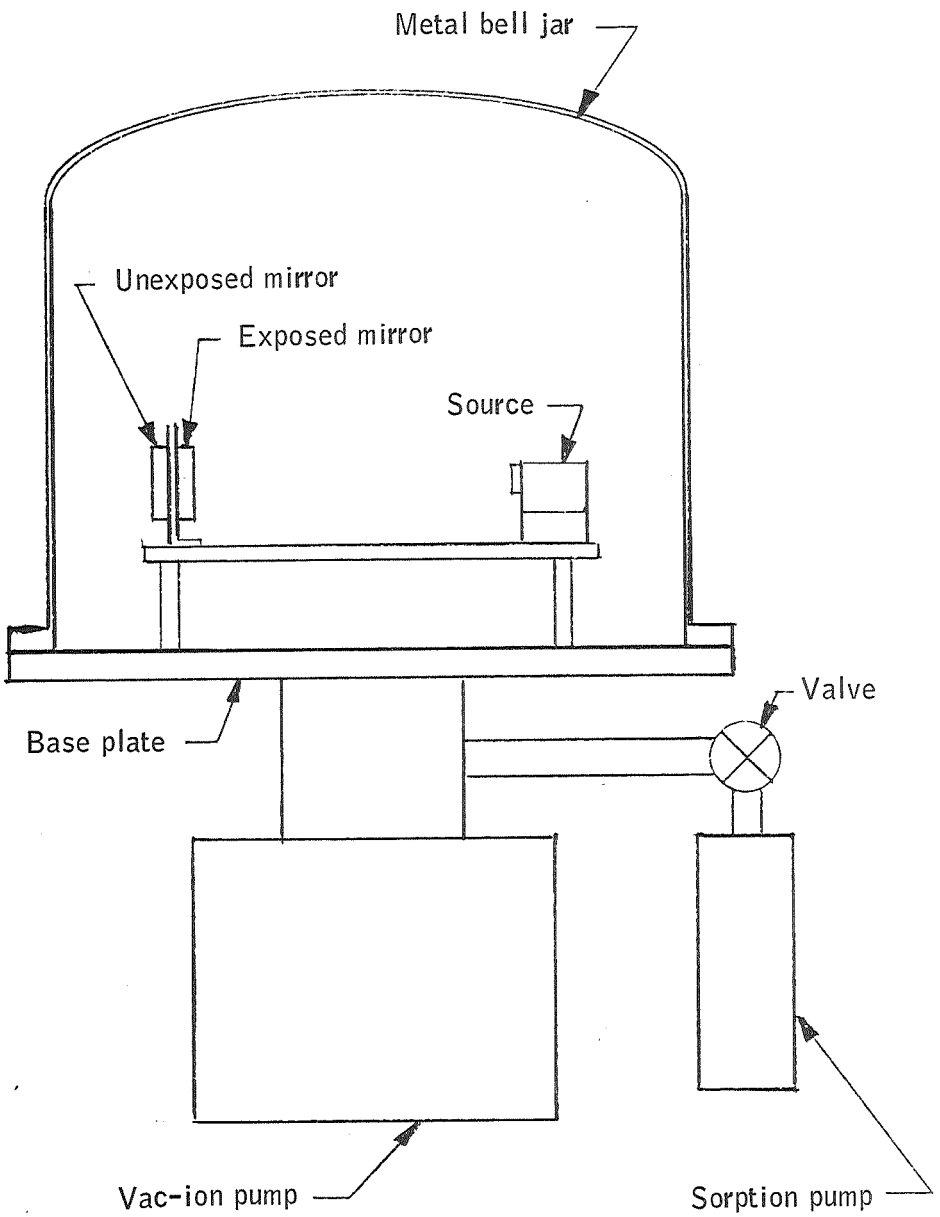

Figure 125. Source Stability and Mirror Aging Test

connection to a heatsink. This increase refers to the power required to maintain the source at 600°C, and would necessarily be somewhat less for the 680°K ARRS source operating temperature. The control point and operating temperature would be unaffected by the use or nonuse of the heatsink.

Source temperature will be monitored by attaching a platinum/platinum 10% rhodium thermocouple to the cavity material. The thermocouple is attached by Electro Optical Industries. The source design does not facilitate the attachment of any of the commercially available platinum resistance sensors. To obtain the desired temperature accuracy (resolution of 0.1°C), the thermocouple emf will be compared to a standard platinum resistance thermometer at the operating temperature of 680°K before and after the stability run. Comparison of the data before and after the stability run will show any drift of the thermocouple calibration which may be applied to the temperature stability data. If any significant temperature drifts occur during the test, the test may be temporarily stopped and the thermocouple recalibrated to determine if the drift was real or a change in thermocouple calibration. The relatively low operating temperature and operation at a set temperature should minimize the platinum thermocouple calibration drifts.

Output of the thermocouple is measured with a potentiometer which has sufficient accuracy to resolve the 0.1°C temperature accuracy required. The thermocouple emf may be calibrated to the desired accuracy by comparison against a standard platinum resistance thermometer.

The tests started September 1969 and are scheduled for completion according to the schedule of Figure 126.

CHOPPER

For ARRS the selected operating frequency is 4000 Hz. The torsional chopper was selected to provide the required chopping frequency. A torsional chopper operating at 4000 Hz had not been made, although American Time did not believe that making such a chopper would be a problem. An alternate solution is to operate at 2000 Hz and chop twice per cycle. No data are available on the operational characteristics of these choppers at ARRS operating temperatures.

Because no documented data are available, and there is an uncertainty as to the operational characteristics at the low ARRS operating temperatures, tests were devised for evaluation of the stability of these choppers.

Four torsional choppers are recommended for testing, two of which operate at 4000 Hz with one chop per cycle and two of which operate at 2000 Hz with two chops per cycle. The general configuration of these choppers is shown in Figure 127, and the specifications are given in Table 44.

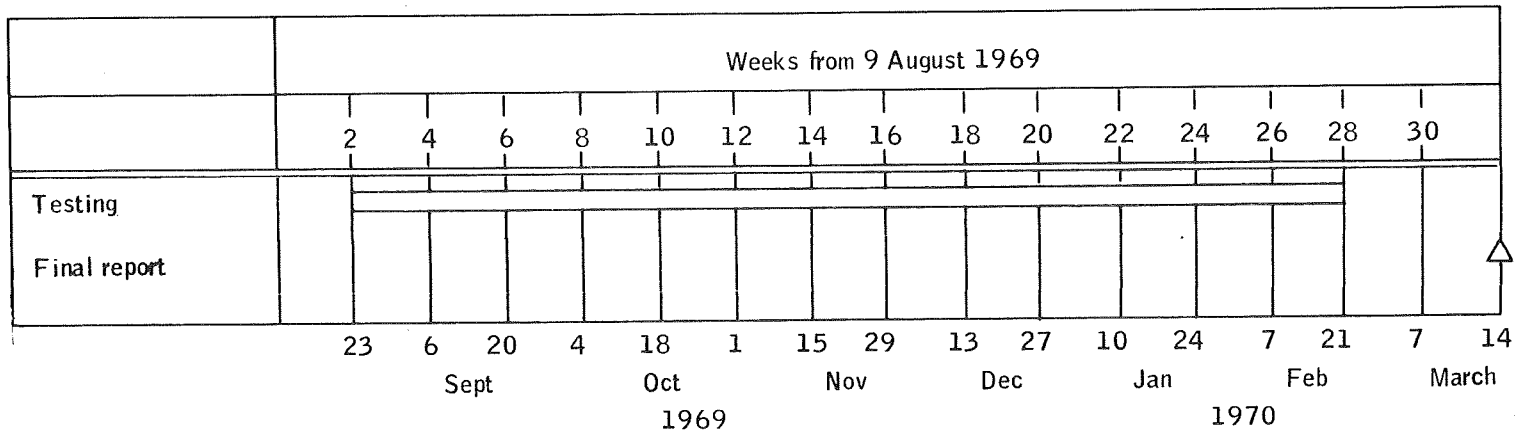

Figure 126. Mirror and IFC Source Aging Test Schedule

TABLE 44.- CHOPPER SPECIFICATIONS

	Specification 1	Specification 2
1. Torsional vibration frequency	4000 Hz	2000 Hz
2. Aperture chopping frequency	4000 Hz	4000 Hz
3. Aperture to be chopped -- 0.076 x 0.380		
4. Aperture open and blocked times to be equal		
5. Temperature -- units will operate from cryogenic temperature up to 85°C		
6. Altitude -- from 1000 feet to space		
7. Frequency accuracy -- 1% from 150° to 300°K is standard		
8. Drive circuit -- the chopper shall operate from a Model 4A driver or equivalent		
9. Reference signal at chopper frequency		

Measurement Requirements

Results of the analysis (Appendix G) performed to determine the errors generated by the chopper amplitude, null-point, phase, and frequency instabilities show that for

A = Amplitude

ΔA = Amplitude instability

ΔX = Null-point instability

$\Delta \phi$ = Phase instability

Δf = Frequency instability

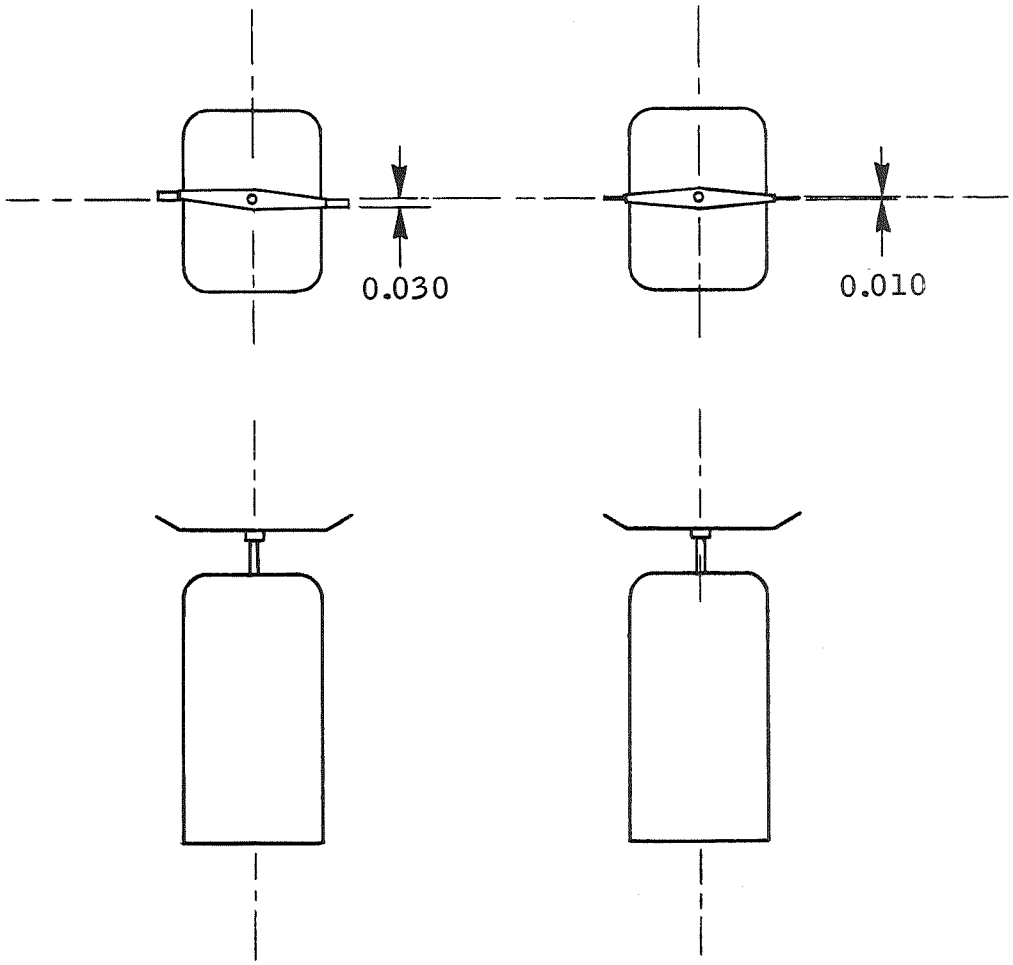

Figure 127. Chopper Configuration and Envelope

0.1% error contribution results from the following parameter magnitudes:

$$\Delta A/A = 0.005$$
$$\Delta X/A = 0.0003$$
$$\Delta \phi = 2.5°$$
$$\Delta f/f = 0.10$$

The effects of amplitude and frequency shifts will be removed by inflight calibration; thus, these effects are primarily of interest for short-term variations. Null-point shifts provide new frequency components which probably cannot be removed except in very special cases. Phase-shift effects are removed by calibration only if there are no unknown transients.

Thus, two types of measurements are indicated:

- Short-term effects -- Changes over time intervals of up to 10 seconds, with a time resolution of less than one cycle
- Long-term effects -- Period of interest is one year, with a time resolution of one minute

The requirements are to perform the test with the following resolution:

$$\frac{\Delta A}{A} \leq 5 \times 10^{-3} \text{ with } (2 \times 10^{-3} \text{ as a goal})$$

$$\frac{\Delta X}{A} \leq 2 \times 10^{-4} \text{ with } (1 \times 10^{-4} \text{ as a goal})$$

$$\Delta \phi \leq \pm 1°$$

$$\frac{\Delta f}{f} \leq 5 \times 10^{-2}$$

Any incompatibility of these requirements with either chopper technology or test capabilities would require steps to be taken in the radiometer design to resolve the problem (e.g., use of synchronous gate wave); the following measurements requirements then would apply:

$$\frac{\Delta A}{A} \leq 0.05$$

$$\frac{\Delta X}{A} \leq 0.05$$

$$\Delta \phi \leq \pm 10°$$

$$\frac{\Delta f}{f} \leq 0.05$$

Discussions with American Time indicate no measurements of this type were made at ambient temperatures or cryogenic temperatures, but they believe that the instability levels should be on the order of

$$\frac{\Delta A}{A} \sim 0.05\%$$

$$\frac{\Delta X}{X} \sim 0.05\%$$

$$\frac{\Delta f}{f} \sim 0.01\%$$

for extended operation at a set temperature. No indication of the phase stability was stated. American Time indicated that with the use of the new alloy under consideration, which has low hysteresis effects, that they believed these instability levels or lower could be attained.

Test Procedures

The chopper can be tested in the vacuum test chamber shown in Figure 128. The chamber houses an LN_2 Dewar reservoir constructed of stainless steel. The exterior surface of the reservoir is coated with a low emittance surface to minimize radiant transfer with the outer chamber walls. The interior surface is coated with 3M Black Velvet Paint. An inner chamber is provided to supply a uniform temperature shroud. The exterior surface of the inner shroud is covered with a heating element which is controlled to provide a stable temperature environment for the test chopper over the temperature range 80°K to 300°K. The vacuum chamber is a stainless steel chamber with provision for mounting the LN_2 Dewar inside and is provided with a vacuum valve for isolating a sorption vacuum pump from the vacuum chamber. The sorption pump was chosen to provide a vibration free vacuum system. The top of the vacuum chamber is provided with a window for visual observation of the chopper for optical measurements.

Figure 128 shows the experimental steup. The source aperture shown is located above the center of rotation of the chopper blade. Radiant energy from the aperture is incident on a specular reflecting portion of the chopper vane, rectangular in shape and approximately 1 x 2 mm in size, with the narrow width perpendicular to the plane of the incident beam. Energy reflected off the vane is incident on the detector. With the ratio of the source-to-reflector distance and reflector-to-detector distance as shown in Figure 128, we get a magnification of 10X of the movement of the reflector position, and of the reflector size, for a source aperture of 0.5 x 2 mm, at the detector position, as shown in Figure 129.

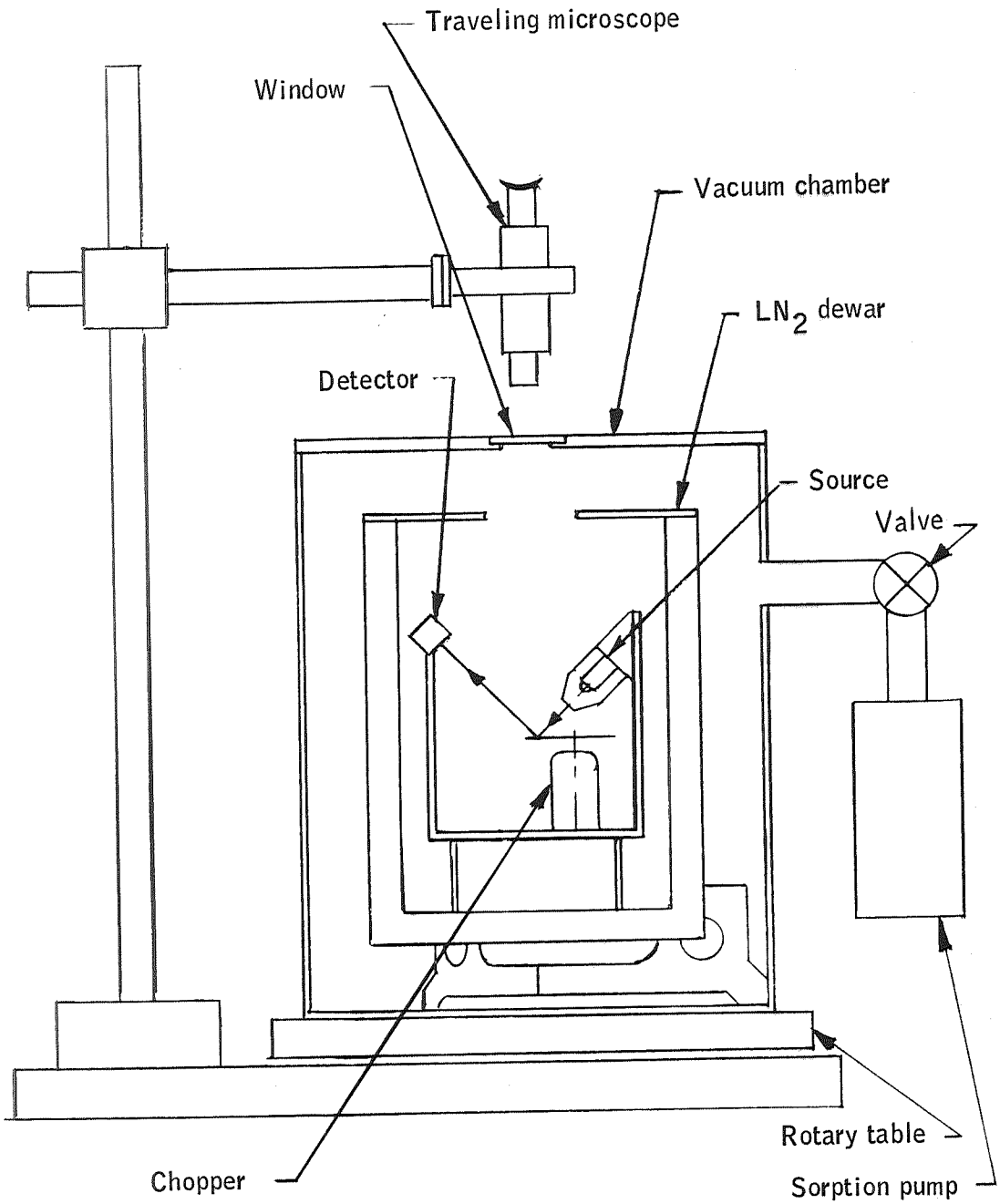

Figure 128. Chopper Test Setup

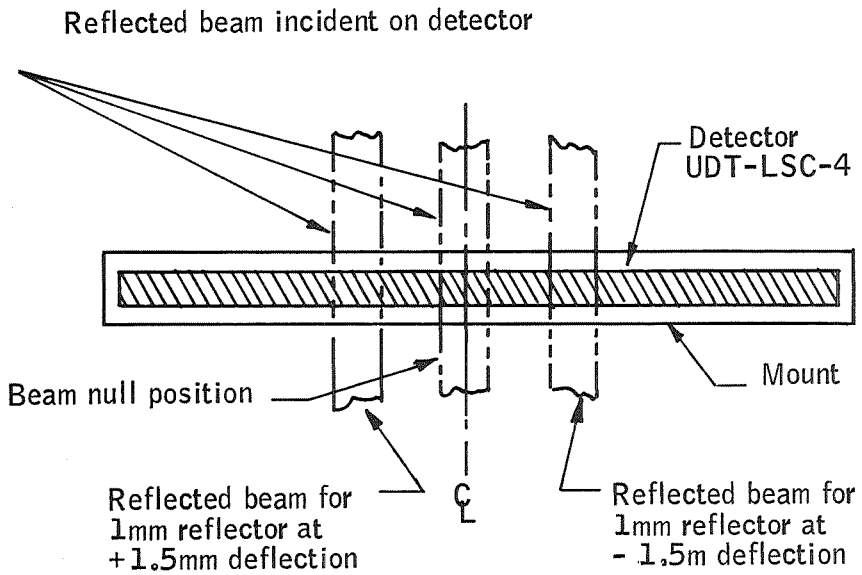

Figure 129. Reflected Beam Incident on Detector

The detector considered for the test is a United Detector Technology LSC-4. This is a single-axis, light-position-sensing silicon Schottky barrier photodiode. Characteristics of this silicon photodiode are shown in Table 45 and Figures 131 through 133.

TABLE 45. - CHARACTERISTICS OF POSITION DETECTOR

UDT Device No.	Active Area (Inches)	Dark Leakage Current (Microamp)	Capitance 90 to 5V Bias or Full Depletion (Picofarad)	Sensitivity at 8500 Å (μa/μw)	Noise Equivalent Power (10^3 Hz, 1 Hz, 8500 Å) (Picowatt)	Rise Time 25 OHM Load (Nanosecond)	Position Sensitivity (μa/m watt/MIL)
LSC/4	0.185 x 4	2.0	1200 to 3600	0.5	1.4	96	0.2

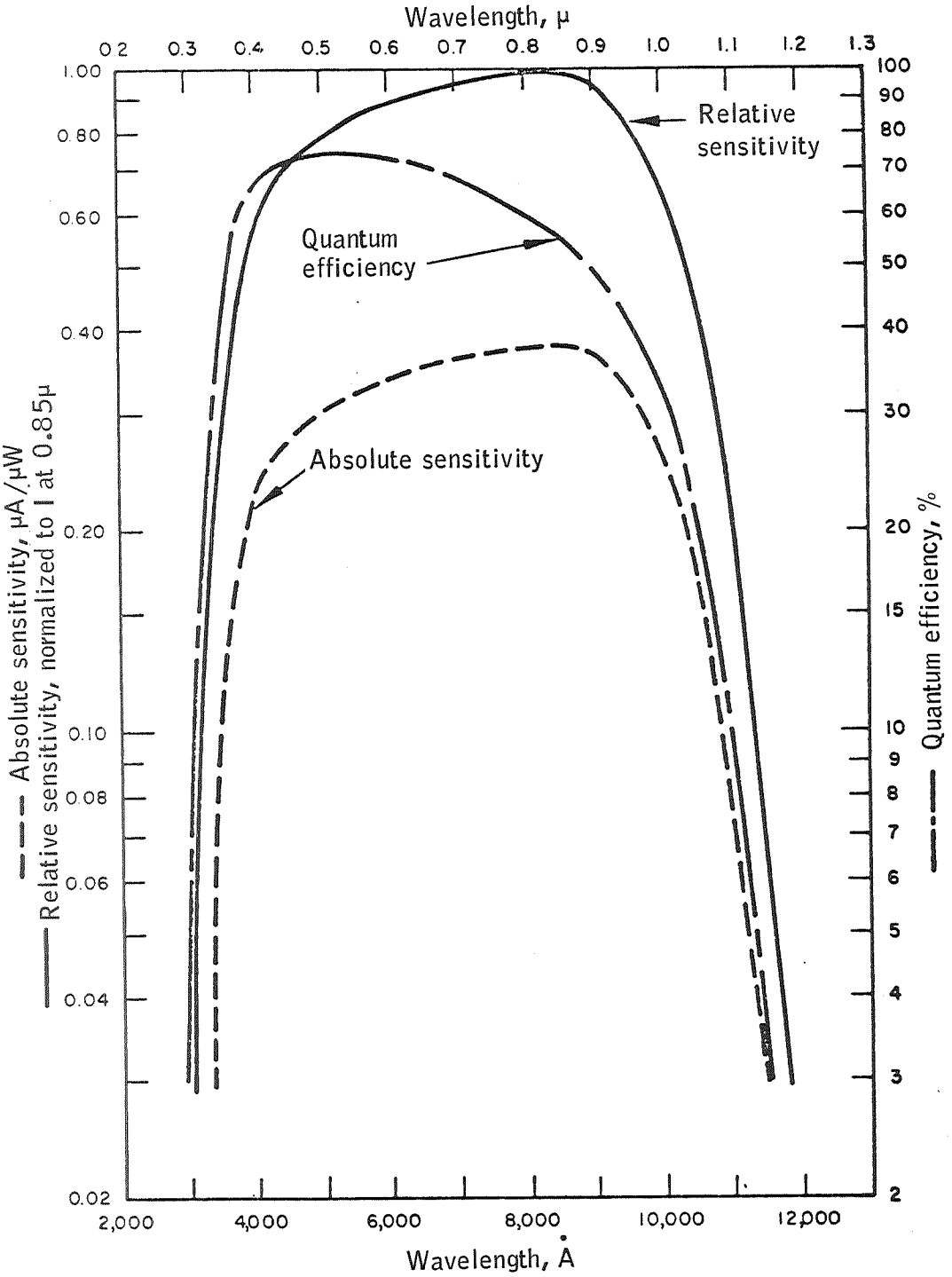

Figure 130. Spectral Characteristics of all Models of Pin Photodiodes

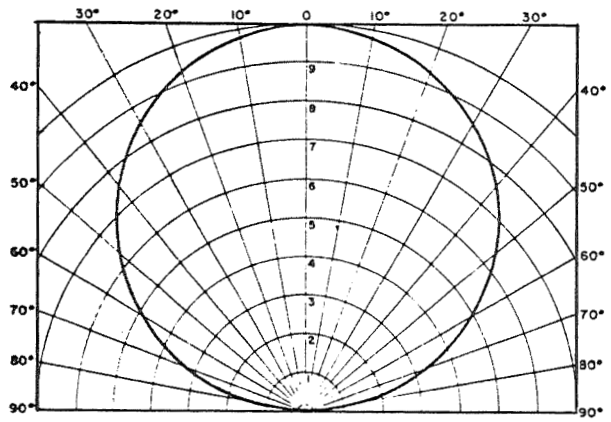

Figure 131. Relative Directional Sensitivity of Pin Photodiodes

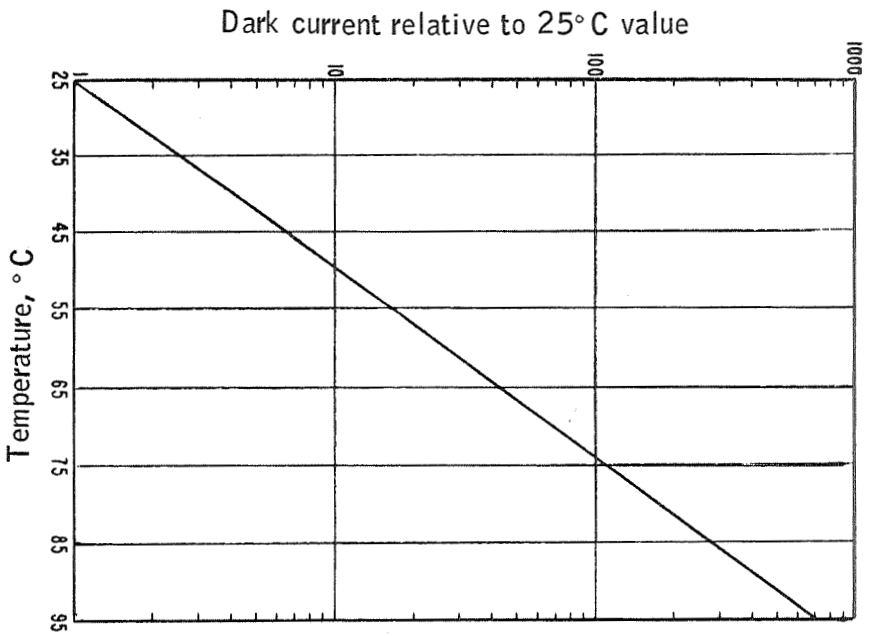

Figure 132. Dark Current at 10V Bias versus Temperature

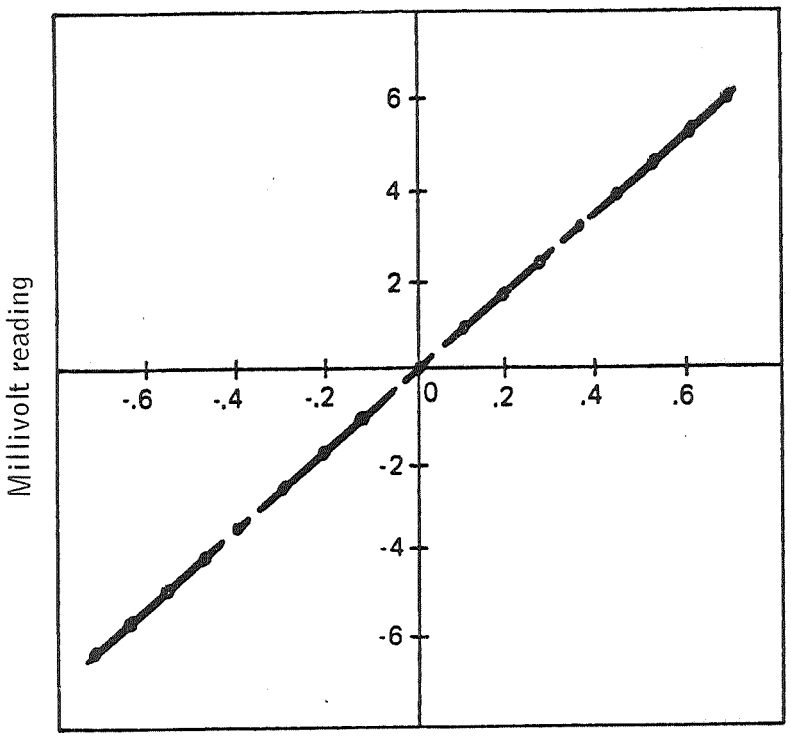

Spot diameter = 10 mil

Spot intensity = 10 μW

Figure 133. Typical Performance

The beam incident on the detector is an extended beam perpendicular to the axis of the detector. This was considered to minimize the effect of any vertical vibration of the chopper vane. Any variation in this direction will be due to nonumiformities of reflections along the length of the reflecting portion of the chopper blade.

Detector sensitivity is an inverse function of the beam diameter. Measurements on similar detectors (ref. 19) show that for a 0.6 mm diameter light probe the mean deviation in d-c output over the surface of the active area is ±2%, and measurements with a 1.0μ diameter probe gave mean deviations of 10% over the active surface area. For a 0.120-inch-diameter light beam probe there were very slight variations and these decreased with increasing spot size. For the case shown in Figure 129, the detector response for the large beam size shown is less than 1%.

The test circuit is shown in Figure 134. These photodetectors provide an electrical output signal specifying the position of an input light spot signal that is relative to fixed internal coordinates. When the input light spot is exactly at the device center, null signal is generated. At other positions, the signal is proportional to the light spot position from the center. The light beam may be any diameter since the position of the centroid of the light spot is indicated. A separate measure of the total light falling on the detector can be obtained from a meter placed between the battery and ground (Figure 134). Null position may be varied by varying the load resistors R_1 in Figure 134.

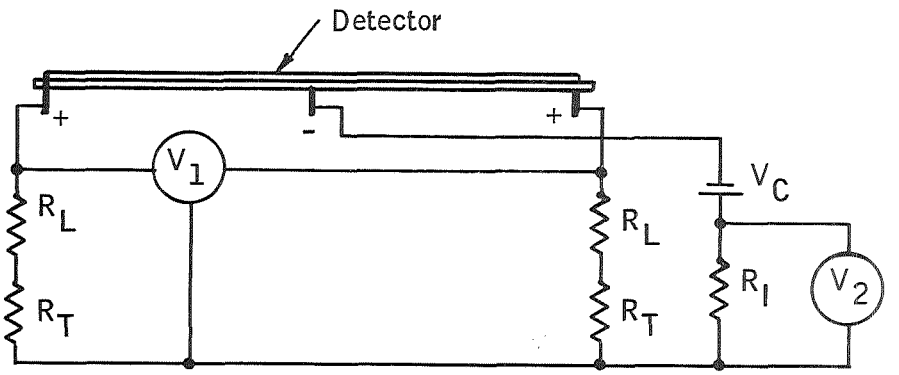

V_C = suppply voltage (2-50V)

R_L = position load resistors (1K-100K ohms)

R_T = position trim resistors (zero set)

R_I = intensity load resistor (50-1K ohms)

V_1 = position voltage indicator

V_2 = intensity voltage indicator

Figure 134. Measurement Circuit

A typical position detector performance is shown in Figure 133. This shows the output voltage across the X-axis load resistors, as the light spot is scanned across the X-axis. This shows approximately 6 mV output for 0.6 cm displacement for a 10-mil-diameter light spot of 10μW intensity.

This test setup can be easily calibrated to minimize the effects of drifts in detector sensitivity or changes in output intensity of the light source. Intensity of the light spot on the detector is monitored by V_2 in Figure 134, but this is really an indication of the light intensity and detector response. This is a d-c voltage and can be set at any level, and it may be reset at a calibrated setting each time measurements are made by varying the lamp power. Thus, the position sensitivity may be calibrated each time measurements are made.

As shown in Figure 134, the position of the center of the beam and the intensity of the beam modified by the responsivity of the detector as the beam traverses the detector may be displayed simultaneously on a scope. Thus, the intensity-responsivity, as a function of displacement, may also be determined and normalized. Therefore, we may minimize the variations of intensity and response on the displacement measurements.

The possible use of a small magnesium oxide coated integrating sphere, illuminated by a tungsten filament lamp, for a source is is being investigated. This would provide a very uniform source and minimize the intensity-responsivity variations.

Chopper frequency, amplitude, null point, and phase will be monitored as the chopper temperature is lowered from ambient (300°K) to liquid nitrogen temperatures (80°K). Each chopper will be run at 80°K for a period of four hours. The two most stable choppers then will be selected and each run for a period of two weeks at the operating temperature of 150°K. The following paragraphs give the procedures to be used to determine each of the chopper operating characteristics.

Frequency stability. -- Frequency of the chopper may be determined by monitoring the output of the detector, shown in Figure 127, by an electronic counter. The output of the counter may be fed into a digital-to-analog converter with a recorder output. The requirement of 0.05% accuracy poses no problem since the use of an electronic counter to measure the frequency should have a resolution of one cycle per second.

Null-point stability. -- Null-point stability may be determined from the test setup shown in Figure 127. With the chopper operating, the d-c component of the voltage monitored at V_1 (Figure 134) will be an indication of the drift of the null point of the chopper vane. The intensity-responsivity can be calibrated by making V_2 a calibration voltage. This minimizes drift considerations of source intensity and detector response.

Intensity-responsivity can be calibrated by setting the voltage V_2. The responsivity-intensity as a function of displacement can be normalized from the center position by observing a trace of the displacement signal and the intensity voltage V_2 simultaneously on a scope. The use of a d-c null volt-ammeter, which has 80 dB a-c rejection above 60 Hz with 0.1 μ V resolution, could be used for setting calibration response and reading the d-c displacement voltage.

Null-point displacement can be calibrated by providing a mount for the chopper and detector assembly which allows for small calibrated angular displacement of the chopper relative to the detector assembly. It appears that the required accuracy of $\Delta X/A \leq 3 \times 10^{-4}$ cannot be met by this setup. Use of the optical lever increases the beam size on the detector and thus increases the uniformity of the detector response but does not decrease displacement accuracy required at the detector. However, it does increase the displacement resolution at the detector since it magnifies the displacement. Displacement accuracy is still limited by calibration of the actual intensity-responsivity as a function of displacement. If uniformities of source intensity and the detector response are in the order of 2% and these could be amplified and normalized with 10% calibration error, then we would be able to make measurements on the order of 0.2% accuracy. The resolution attainable would depend on the noise level of the system and instabilities of the detector response and the lamp-source intensity. Thus, since the measurement requirements cannot be met by this method, the following optical test may be used to determine the null-point stability.

The null-point of the chopper vane at rest may be determined optically, using a rotary table, to the degree of resolution required. This would be accomplished by measuring the angle between a radial indexing line on the top of the chopper case and a radial indexing line on the chopper vane. This measurement would use a traveling microscope as shown in Figure 128 and a Litz No. 7610 Imperial Rotary/inclinable table with a stated accuracy of 5 seconds and readable to 1 sec of arc. Differential measurements over small differentials should be better than that for wide angles. For the resolution of 0.35×10^{-4} inches, as previously shown as required, at a radius distance of 0.625 inch as shown in Figure 127, the differential angular resolution required is $\Delta\phi \sim 10$ seconds. So more than sufficient resolution is available to determine the null-point with the desired resolution. This measurement could be made as a function of the chopper temperature from ambient to liquid nitrogen temperatures by using the test chamber as shown in Figure 128. Provision would be made in the cover plates in the interior chamber for visual observation of the top of the chopper. The vacuum chamber with its internal Dewar and chopper could be mounted on the rotary table. With the traveling microscope mounted about the windows, the angle between the indexing mark on the chopper case and the vane could be determined for a number of temperature points as the chopper temperature is lowered from ambient to 80°K.

Amplitude stability. -- Amplitude is determined by monitoring the peak-to-peak a-c voltage at V_1 of Figure 134 with an a-c voltmeter. An alternate

approach is to monitor the output coil voltage, but this is not a direct measure of the amplitude excursions of the chopper vane. As previously mentioned, accuracy on the order of 0.2% is achievable, which is sufficient to meet requirements of the amplitude measurements of $\Delta A/A$ of 5×10^{-3}.

Cycle-to-cycle variations may be observed by display on a scope. Intensity voltage may also be displayed as previously mentioned, and may be used to normalize the intensity-response of the displacement signal to correct for variations in response over beam intensity as a function of beam displacement.

Phase stability. -- The phase considered here is the phase relation between the chopper vane and the drive voltage. The output of the detectors and the drive voltage are fed into a phase detector, such as a lock-in amplifier. Phase detectors are being investigated to determine if we can obtain sufficient resolution to meet the measurement requirement.

Critical Equipment Requirements

American Time has stated they believe that the torsional choppers they make will meet the ARRS requirement. To date no measurements of the operating characteristics of these torsional choppers have been reported for ambient-temperature operation or at the low cryogenic temperatures required by ARRS. Since so little is known about the low-temperature operation of this type of chopper, it is necessary that evaluation tests be made.

If the choppers are unable to meet the ARRS requirements, a synchronous gate wave amplifier and the stability requirements would be relaxes to approximately a 5% level.

Tests were proposed to determine at what temperature and after what operating life performance stability degrades. Since the apparatus will meet all measurement requirements except that required for the null-point stability, these preliminary measurements will determine whether further testing with a higher level of accuracy is required.

SPECTRAL FILTER

Specifications for the bandpass filter to be evaluated are given in Table 46. Requirements for ARRS are minimum emissivity, stability of the uniformity of spectral transmittance, and spectral band stability. The filter characteristics which require better definition are

- Transmission
  - Uniformity of the transmission
  - Temperature stability of the transmission
  - Temperature stability of the nonuniformities of the transmission

TABLE 46.- BANDPASS FILTER SPECIFICATIONS

1.	Center wavelength shall be 15.0 (±0.030)μ; transmission at center wavelength shall be equal to or greater than 70%.
2.	The half-power bandwidth points shall be 14.0μ (±2%) and 16.3μ (±2%).
3.	The transmission at 13.5 and 16.8μ shall be less than 1%; the integrated out-of-band transmission shall be less than 0.01% below and above to 24μ.
4.	Vacuum - The component shall be capable of operating without degradation in a vacuum of 10^{-13} torr for a period of one year.
5.	Temperature - The component shall be capable of operating without degradation in a temperature range of 77°K to 300°K for one year.
6.	Humidity - The component shall be capable of operating without degradation in a humidity environment of 95% for 24 hours.
7.	Size - 1.75-inch diameter by 0.060-inch thickness.

- Spectral
  - Uniformity of the spectral bandwidth over the surface of the filter
  - Temperature stability of the spectral bandwidth
  - Temperature stability of the nonuniformities of the spectral bandwidth
- Reflectivity and emissivity magnitudes, uniformity, and temperature dependence in band and outside of band

Because the IFC illuminates only a portion of the bandpass filter, the nonuniformities, if any, have to be known.

Multilayer filters are designed by computers using layer material whose index of refraction is known at the "design temperature". Back layer thickness is varied by computer until the required transmission and spectral interval at the "design temperature" is obtained. Standard multilayer filters shift to shorter wavelengths when the film temperature is decreased. The wavelength shift of a multilayer filter is essentially a linear function of film temperature because the materials which form the various layers have indexes of refraction which vary linearly with temperature. Thus, the optical thickness of adjacent

layers can be perfectly matched only at one temperature, the "design temperature". Figure 24 of reference 20 predicts a wavelength shift between 1% and 2.5% for a filter at liquid nitrogen temperature.

According to OCLI, a 15-μ filter with a 1.8 half-power bandwidth and a temperature drift from 40° to 60°K would have a center wavelength shift of the order of ±0.125% with a change in peak transmission of the order of 2%. With a special design and manufacturing effort for a design goal of 100% uniformity, a uniformity of 0.5% may be attained for a 0.25-inch beam transversing a filter with a 0.9-inch clear aperture. The standard OCLI coating uniformity over a flat filter 0.5 inches in diameter is ±2%. The amount of nonuniformity is expected to change slightly with decreasing temperature; however, OCLI stated that the nonuniformity and uniformity are expected to remain constant with decreasing temperature. No quantitative data based on actual measurements are available, and OCLI does not have the facilities to make the desired measurements at cryogenic temperatures.

Results of a specific spectral stability error analysis, Appendix L, indicated that filter temperature and angular alignment instabilities produce negligible errors. However, that analysis did not cover all possible ARRS applications. Spectral band shifts with temperature should, therefore, be measured so that data will be available for ARRS applications other than the one used in Appendix L.

Test Objectives

The objective of the bandpass filter test is to measure the spectral transmittance and its uniformity in the temperature range of 300 to 80°K.

While it is desired to make reflectance and emittance tests also, it is not known at present if such tests are available. Conversations with personnel at the Naval Weapons Laboratory, Corona, California indicate that the laboratory may have the capability required. If this proves to be the case, a revision of this test will be proposed to include such tests.

Measurement Requirements

The most significant requirement is the ability to measure the spectral transmittance and its uniformity with an accuracy of 2% and a precision of 0.1%.

The precision of 0.1% is obtained for relative transmission values with the instrument readout on the Datex recorder. This precision resolution is dependent on the stability of the spectrometer source and the associated electronics and appears to be constant over a long enough time to enable 0.1% precision measurements.

Test Procedures

Apparatus that could be used for these tests consists of a Beckman IR-12 spectrophotometer and an Air Products and Chemicals, Inc. Cryotip model AC-3L heat exchanger. The outline of the heat exchanger is shown in Figure 135. The system schematic flow diagram is shown in Figure 136.

The present cryostat configuration cannot accommodate the 1.75-inch diameter filter; therefore, a sample mount and a larger vacuum shroud with infrared transmitting windows must be made. The vacuum shroud and sample mount are shown in Figure 137. The holder for mounting the cyrotip Dewar to the Beckman IR-12, shown in Figure 138, holds the cryotip Dewar with mounted sample in the spectrometer beam. This mount allows for movement of the cryotip Dewar with the mounted sample across the beam in the horizontal and vertical directions to provide uniformity measurements on the sample filter surface. Small apertures are placed in the spectrometer beam before and after the cryotop windows to define the beam size traversing the filter.

Spectral transmission of the filter from 2.5 to 20μ, the detector cutoff, will be measured using the full spectrometer beam size. These measurements will be made from ambient design temperature 300°K down to 80°K intervals.

Apertures as small as possible, compatible with the energy transmitted by the sample filter, will be interposed in the spectrometer beam before and after the cryostat windows. These apertures will define the size of the beam incident on the filter. The transmission uniformity measurements will be made at three wavelengths within the bandpass of the filter. The three wavelengths are the center wavelength, determined from the spectral bandpass measurements as a function temperature in the previous spectral measurements, and the two half-power points on either side of bandpass, also determined by the previous spectral measurements. These measurements will be made in a single-beam mode for maximizing the energy traversing the apertures and the filter. There is sufficient source and electronics stability to easily resolve 0.1%. With the spectrometer at a set wavelength, the filter in the cryotip mount will be moved across the spectrometer beam, horizontally and vertically through its center, to determine the relative uniformity. The resolution of the uniformity that can be attributed to the filter could also depend on the uniformity of the window material of the vacuum shroud.

The window material will be potassium bromide (KBr), which has very high transmission, more than 90% at 15μ. This material is slightly hygroscopic, but with careful handling moisture absorption can be minimized. The uniformity of the transmission of these windows, mounted in place on the cryotip Dewar, will be determined before the filter uniformity tests are run. The mount for the cryotip Dewar has provision for re-establishing cryotip Dewar position to better than 1/10 of the uniformity test beam diameter.

The filter uniformity measurements will be made at approximately the same temperatures as the spectral bandpass measurements.

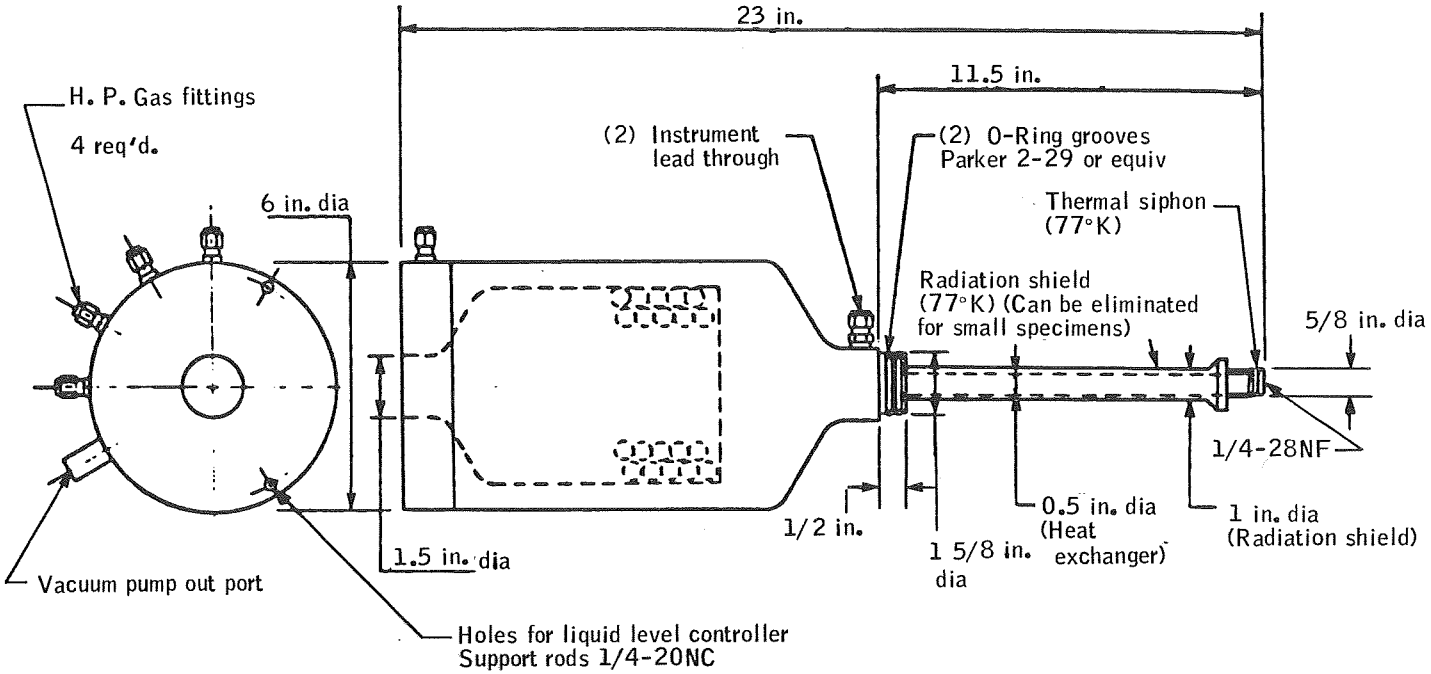

Figure 135. Heat Exchanger Outline

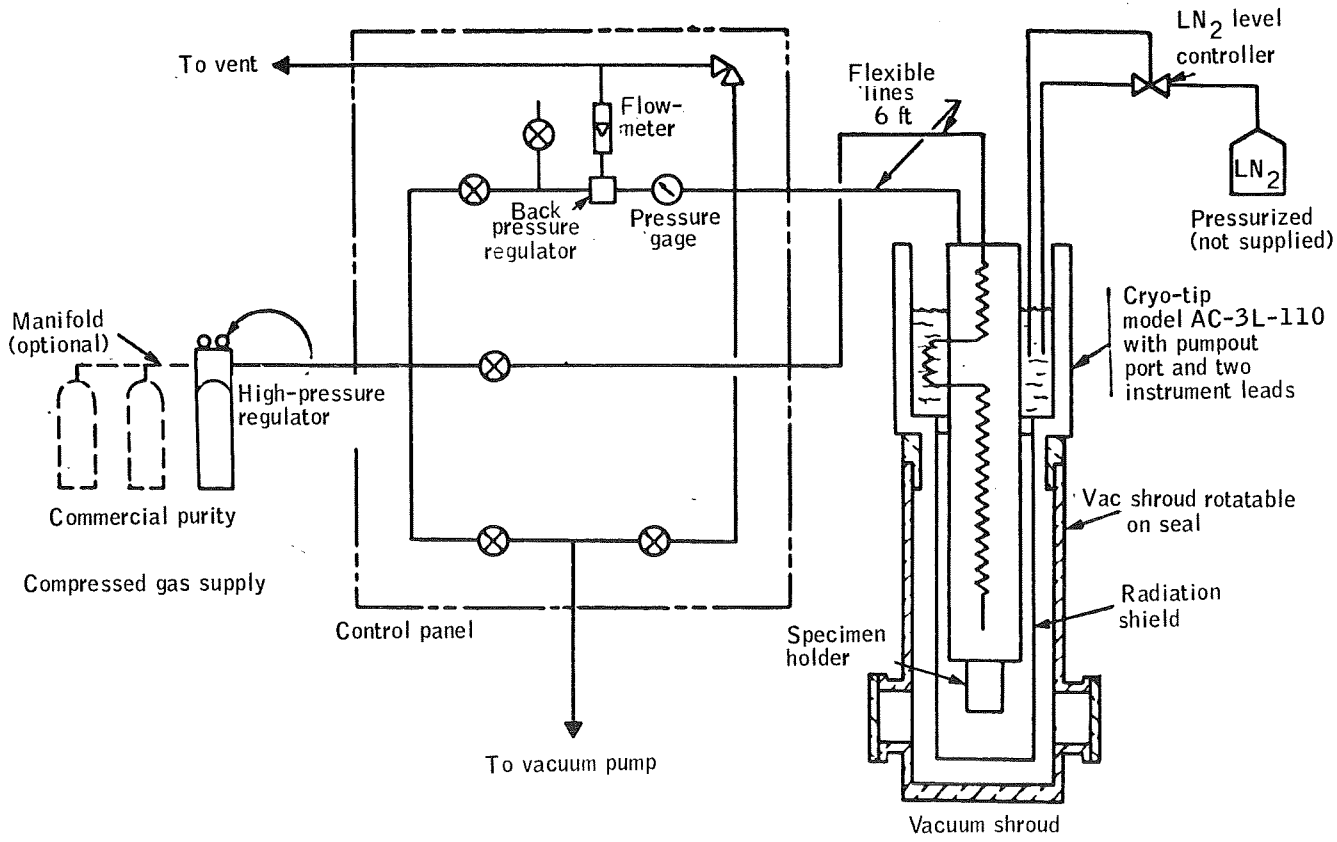

Figure 136. System Schematic Flow Diagram

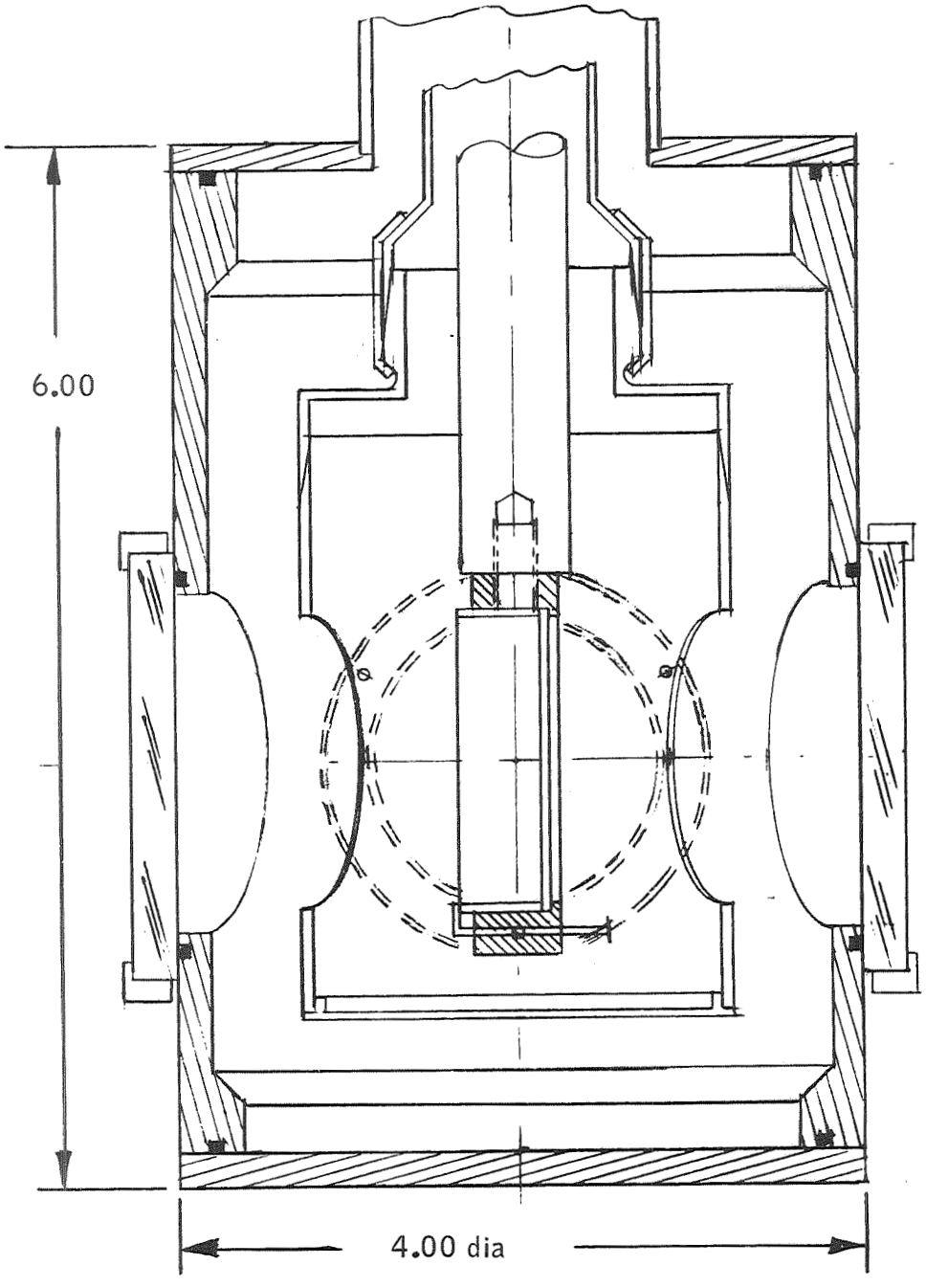

Figure 137. Cryostat Vacuum Shroud

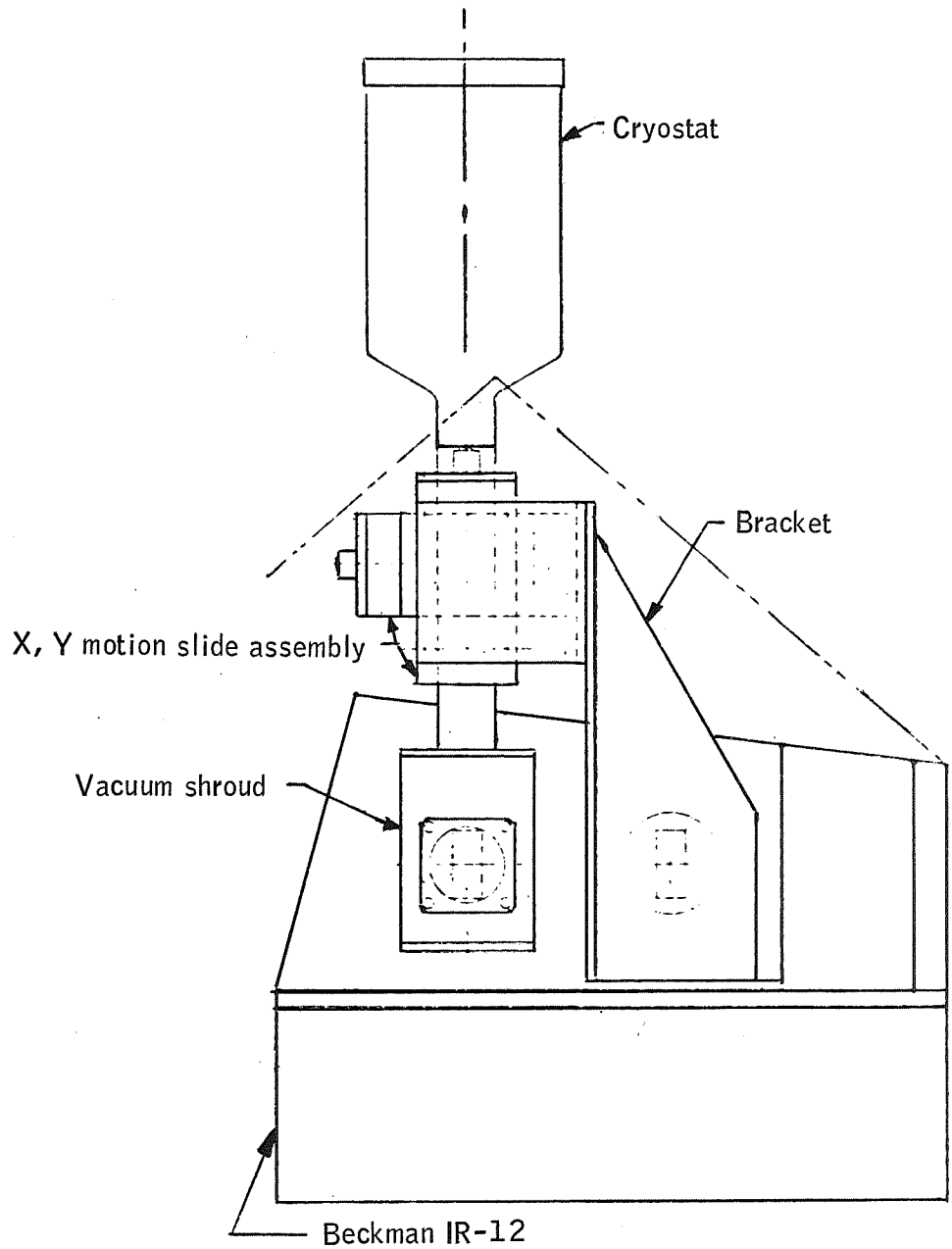

Figure 138. Filter Test Setup

DETECTOR

In the feasibility design study, NAS1 6010 (ref. 21), the Ge:Cd detector was selected as the prime detector approach. This detector subsequently was selected as an ARRS baseline component. Research of the literature indicated that very limited data are available on this detector type. Figures 139, 140, and Table 47 are extracted from a state-of-the-art brief by Santa Barbara Research Center (SBRC), dated January 1968.

Table 47 gives pertinent blackbody test data on representative SBRC Ge:Cd detectors made from two different single crystal ingots. One ingot had a Cd concentration of 2×10^5 Cd atoms/cm^3 while the other had 5×10^{15} atoms/cm^3.

These data reflect recent SBRC-developed techniques for increasing the Cd content in Ge:Cd by about one order of magnitude over that previously used. Detectors made from the more heavily doped material exhibit 500°K blackbody D*s approximately twice that of previous material; furthermore, the spectral response curve is found to be free of lattice absorption dips and the short wavelength response is improved. This condition is shown in Figure 139.

The D^*_{BB} versus temperature data shown in Figure 140 indicate that Ge:Cd is background limited at temperatures below 27°K under the condition of 60° fov of room temperature background radiation. This measurement was made with the previously doped material. Present-day material has a D^*_{BB} in the plateau region twice that shown by Figure 140.

The detector analytical model is based on theoretical detection physics. Real detectors only approach a detector analytical model in its operating characteristics, leaving some uncertainty in detector behavior between a detector analytical model and a real detector. In the radiometer analytical model the detector model uncertainty manifests itself in an output uncertainty. Measurement of the detector operating characteristics would provide information on the performance of a real detector and reduce the detector model uncertainties and the effect on the radiometer output uncertainty. In general these uncertainties are any anomalous functional change in a performance parameter such as the response versus irradiance curve. If the shape of this curve changes, then the number and/or levels of the inflight calibration points required for a certain accuracy may be changed. A detector test is recommended to search and evaluate such potential problem areas.

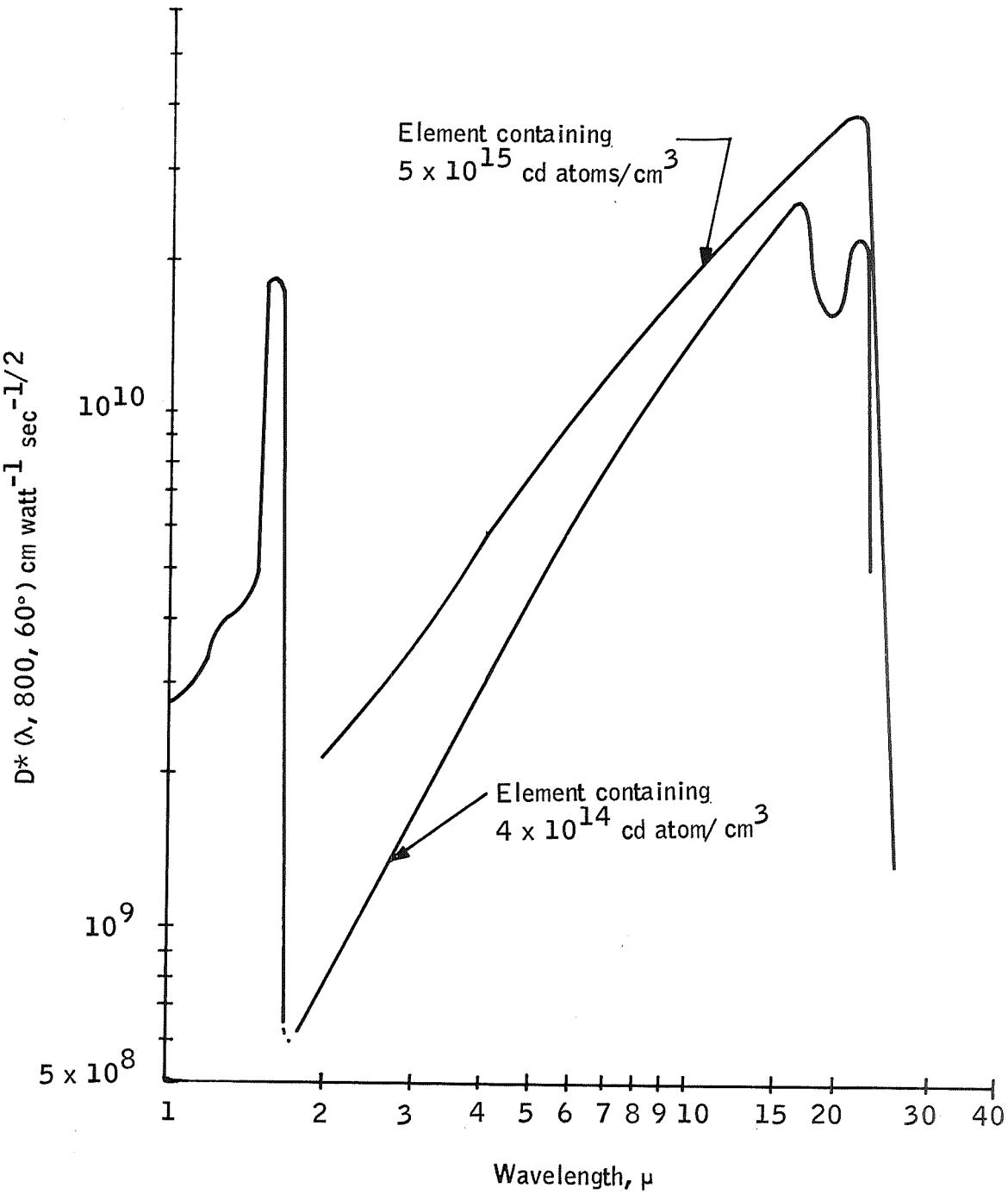

Figure 139. Spectral Detectivity for Two Ge:Cd Detector Elements

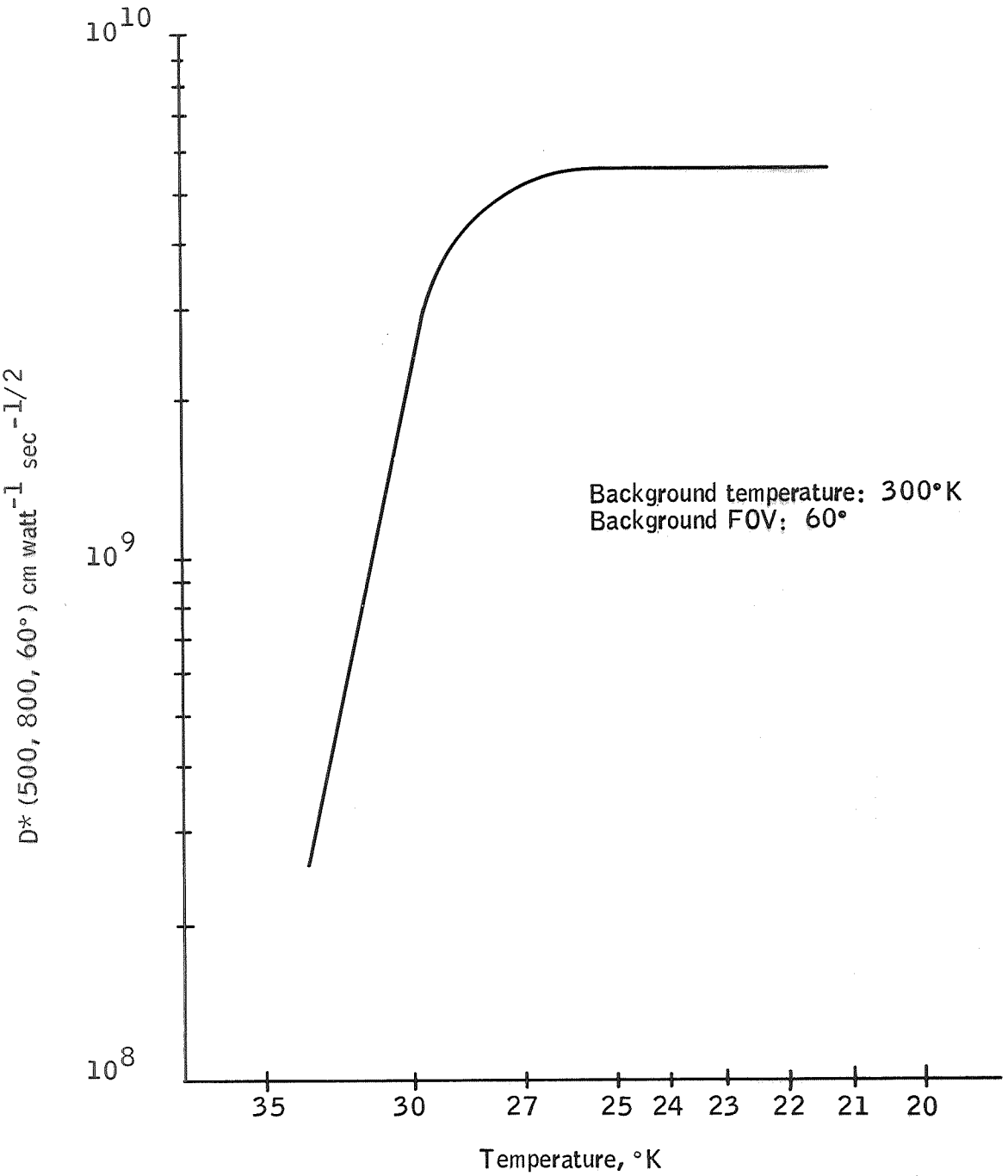

Figure 140. Detectivity versus Operating Temperature for Ge:Cd Detector

TABLE 47. - REPRESENTATIVE DATA[1] ON SBRC
Ge:Cd IR DETECTORS

Detector Number	2-A	2-B	2-C	4-9C	4-9
Cadmium concentration (atoms/cm^3)	2×10^{15}	2×10^{15}	2×10^{15}	5×10^{15}	5×10^{15}
Sensitive area (mm x mm)	2 x 2	2 x 2	2 x 2	2 x 2	0.5 x 1.7
Optimum bias voltage (V)	41	53	15	60	18
Optimum bias current (μamps)	500	300	75	2275	1000
d-c resistance at optimum (KΩ)	82	177	193	26	18
Field strength at optimum (V/cm)	205	265	73	300	360
Field of view (°)	30	30	30	60	40
Open circuit responsivity (V/W)	6.4×10^4	17.4×10^4	4.8×10^4	6.0×10^4	8×10^4
Open-circuit noise (1 Hz b.w.) ($V/Hz^{1/2}$)	0.81×10^{-6}	1.6×10^{-6}	0.72×10^{-6}	1.0×10^{-6}	0.55×10^{-6}
D* (500° 1800) (cm $Hz^{1/2}$/W)	1.6×10^{10}	2.4×10^{10}	1.3×10^{10}	1.2×10^{10}	1.4×10^{10}

$D^*(\lambda_m) \approx 2.5 \times D^*$ (500°)

$\lambda_m = 22\mu$

[1] All measurements made with detector cooled to liquid helium temperature.

Detector performance also affects design tradeoff considerations. Radiometer design characteristics that are strongly affected by the detector performance are the f number, optics type, and operating temperature. If the detector is BLIP at a given operating temperature, the radiometer NER is independent of f number since D*/f number $\approx$ constant. This leads to consideration of slowing the optical system down to achieve better fov and/or resolution. This slowing must, in turn, be traded off against the effects of tighter coupling to system temperature shifts and electronics problems associated with the higher impedances. If the detector is non-BLIP, however, optical speed will be emphasized. The actual operating characteristics of the detector are required to predict its performance within the different configurations under consideration.

Specifications for the Ge:Cd detector are given in Table 48. Small dimensions of the ARRS detector are the cause of another area of uncertainty. Detectors of this type with dimensions of 0.3 mm and smaller exhibit a double time constant at temperatures above 10°K. This test will provide a measure of the magnitude of this time constant so its effect can be anticipated.

TABLE 48. - DETECTOR SPECIFICATIONS

1. Detector - Ge:Cd	6. Bandpass - 500 Hz - best effort to 4000 Hz
2. Source - Santa Barbara Research Center	7. fov - 28°
3. Element size - 0.1 x 0.5 mm	8. Cooled preamp
4. Photon flux - 5×10^{12}	9. Standard heat sink package
5. D* - 5×10^{12} best effort to 1×10^{13}	

The change in signal levels anticipated for ARRS is quite large (earth to space backgrounds); therefore, consideration must be given to thermal gradients across the detector and "memory" or time constant. Calculations indicate that this is not a problem; however, a test is planned to investigate this effect.

The test outlined here will provide data for comparison with and augmentation of vendor information and supplemental information on response as a function of background flux at various detector temperatures and chopping frequencies up to 4000 Hz. The spectral response measurements on the detector are expected to be more accurate than vendor measurements. This improvement is obtained by the use of an improved standard reference flat-response detector.

Test Objectives

The detector characteristics to be determined by these tests include:

- Detector resistance versus background flux will be measured at various detector temperatures and bias. This is to verify that there is a direct linear relationship between background flux and detector resistance at temperatures below which the detector is background limited, and will determine the maximum temperature for background-limited operation for a given background flux.
- Detectivity (responsivity and noise) in the 14 to 15μ range will be measured as a function of background flux and chopping frequency and bias currents.
- Spectral dependence of responsivity in the 2 to 20μ range will be measured.
- Effects of high thermal loads on detection will be determined.

Measurement Requirements

Measurement data will be used to verify detector modeling. Required accuracy is approximately 5%. Accuracy obtainable is limited by the calibration of the InAs emitters (determining the blackbody flux on the detector passing through the Dewar window, and spike filter at approximately 15μ as described in the following procedure). With careful determinations of spectral transmissions of window and filter, the accuracy should be approximately 5%.

The ranges over which the measurements will be made are

- Background flux levels
  - The lowest background flux level is attained with the primary at 160°K and the cell shield at 50°K and gives a level of 1.7×10^{13}. The maximum signal level is 1.5×10^{16}.
- Chopping frequency range
  - The operating frequency determined for the radiometer system is 4000 Hz. The detector characteristics will be determined from below the knee of the frequency response curve to the operating frequency (~20 Hz to 4000 Hz).
- Temperature range
  - The detector characteristics will be determined for detector temperatures of 7° to 20°K with emphasis of 10° to 14°K ranges.

Test Procedure

A diagram of the test arrangement proposed for detector tests is shown in Figure 140. The test Dewar is a Texas Instruments "Cryoflask" Type CLF-3 in which the detector-preamplifier package and its cooled enclosure are mounted. With this Dewar and a temperature controller, the temperature of the detector can be varied from about 10° to 20°K.

Responsivity measurements are made using a variable temperature blackbody with variable frequency radiation chopper and a lock-in amplifier. Detector resistance will be determined by measuring the detector bias current with a vibrating-reed electrometer.

Noise measurements are made by closing the blackbody aperture and measuring the rms valve of the random fluctuations at the output of the lock-in amplifier with a long time-constant thermocouple-type RMS voltmeter. This method of measuring noise using the Lock-in Amplifier is very convenient since the instrument has a low-noise figure for the type of input impedances involved and the noise bandwidth can be varied over a wide range simply by varying the output time constant. The noise spectrum is easily obtained by using the instrument in the "internal mode" and varying the frequency of the tuned-amplifier stage. All apparatus shown in Figure 141 is currently set up and available for use.

Although it is desirable to vary the background radiation over a wide range (preferably from 10^{12} to 10^{16} photons/cm^2 second), it is totally impractical within the required time limit and budget to do so by using external blackbody temperature variations and cooled neutral density filters. A much more convenient and perhaps more accurate method of varying the background radiation on the detector is to use a calibrated InAs diode emitter inside the detector enclosure. Since the InAs diode emits at a much shorter wavelength (3.0μ at 4.2°K) than the absorption edge of the Ge:Cd detector, the use of the InAs emitter is a very effective way of placing a known background flux on the detector.

The blackbody source and chopper, and the intervening path to the Dewar, will have to be placed in a dry nitrogen purged atmosphere to reduce the attenuation of the 15μ radiation by the atmospheric CO_2 absorption in the 14 to 16.3 wavelength region.

To reduce the background level in the absence of emitter to approximately 10^{12} photons/cm^2 seconds, a cooled-spike filter peaked at 15μ and cooled neutral density filters will be used in conjunction with a narrow fov for the detector (5° to 10°). An accurate calibration of the InAs emitter for background energy at 15μ can then be obtained by placing a known source of blackbody radiation in the detector fov and measuring the resistance change of the detector. The emitter is then excited with a d-c current to produce the same change of resistance. When this procedure is repeated for several known levels of blackbody radiation, the emitter is then calibrated in terms of the 15μ radiation.

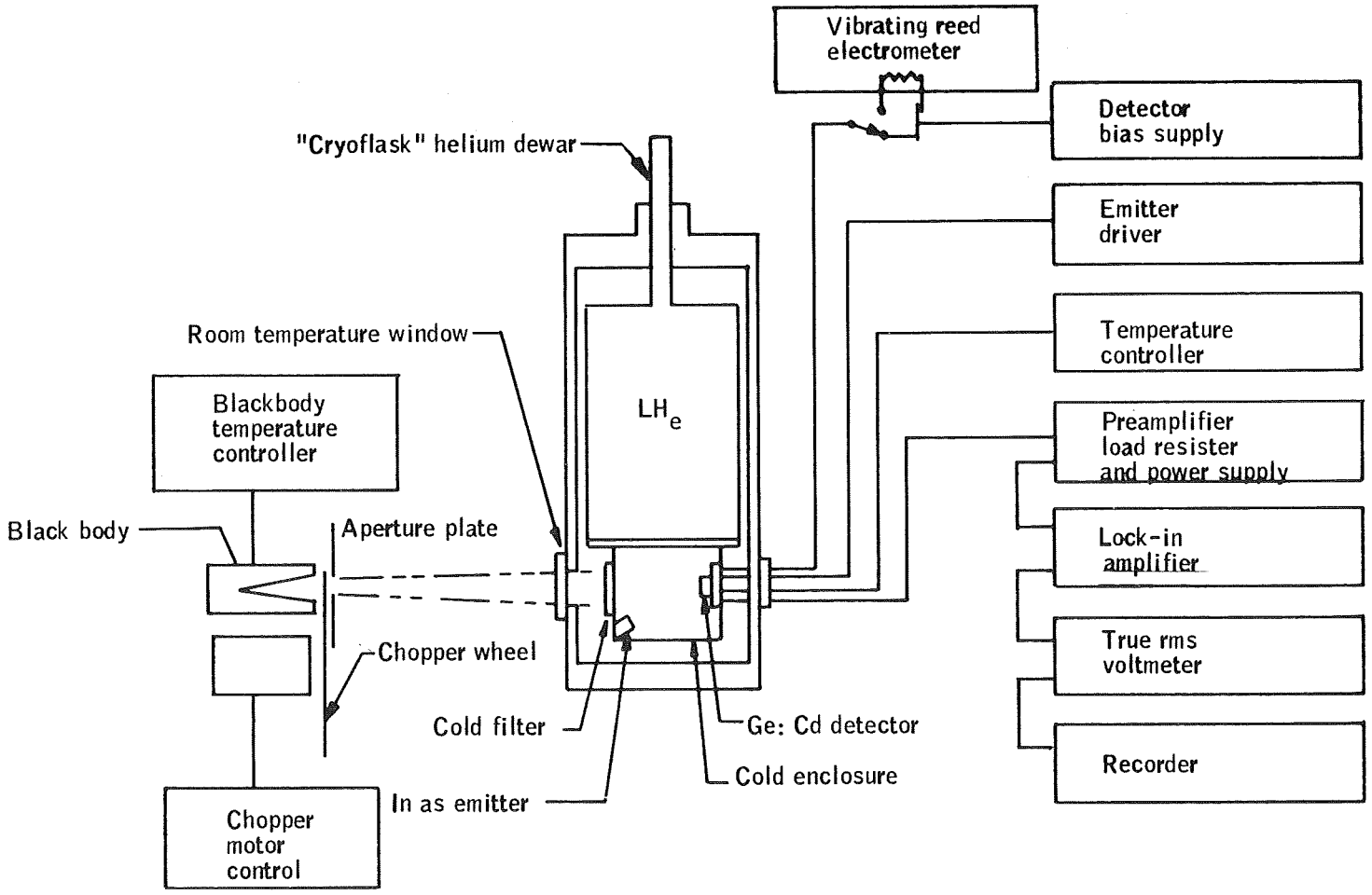

Figure 141. Schematic Diagram of Ge:Cd Detector Test

Due to the limited output of available InAs emitters, even at low temperatures ($n = 3 \times 10^5$ photons/second) there is doubt that the background photon flux can be extended to beyond approximately 5×10^{14} photons/cm^2-second using a single emitter. By the use of an appropriate lens and slightly focusing energy on the detector, the range should be extended to approximately 10^{16} using two emitters.

The alternative to using the 3μ emitted energy of the InAs emitters, calibrated at 16μ to provide the background photon flux levels, is to use an external source and calibrated neutral density filters to attenuate the ambient temperature background flux. This alternate would be an extremely time-consuming measurement process, because each filter would have to be calibrated at LHe temperatures and each background flux measurement would necessitate a new run to replace the neutral density filters. This also requires bringing apparatus back to ambient and replacing filters and recooling to liquid helium temperatures. The background flux levels are not continuously variable as with the use of the InAs emitter but are limited by the number of neutral density filters used. Thus, this alternate method would require approximately three times the helium and three times the labor required as using InAs emitters and would provide less information.

Use of a controlled blackbody cavity around the detector may also be used to provide the background flux. The cutoff wavelength of these type detectors are near the peak of the blackbody curve for these temperatures and thus the background flux is extremely sensitive to the temperature of the cavity as shown in Figure 142. This method would require the modification of existing equipment, and it would be extremely difficult to obtain data as accurate as the proposed test procedure.

Relative spectral response is determined using a Beckman IR-12 double beam spectrometer. The IR-12 is equipped with an external double-beam mount which separates the two beams after passing through the monochrometer and provides for a comparison of the response of two detectors. The usual method is to compare the response of the sample detector to that of a blackened vacuum thermocouple, which is assumed to have a flat response with wavelength. The spectral response of these detectors was shown to fall off quite rapidly past 10μ by Eisenman (ref. 22). Attempts were made to determine the relative response and to correct for the falloff.

These measurements will be made with the detector operating in its background limited condition. Absolute spectral response and D* are obtained by adjusting this relative response to the absolute responsivity and D* measurements made with the calibrated spike filter in the previous measurements.

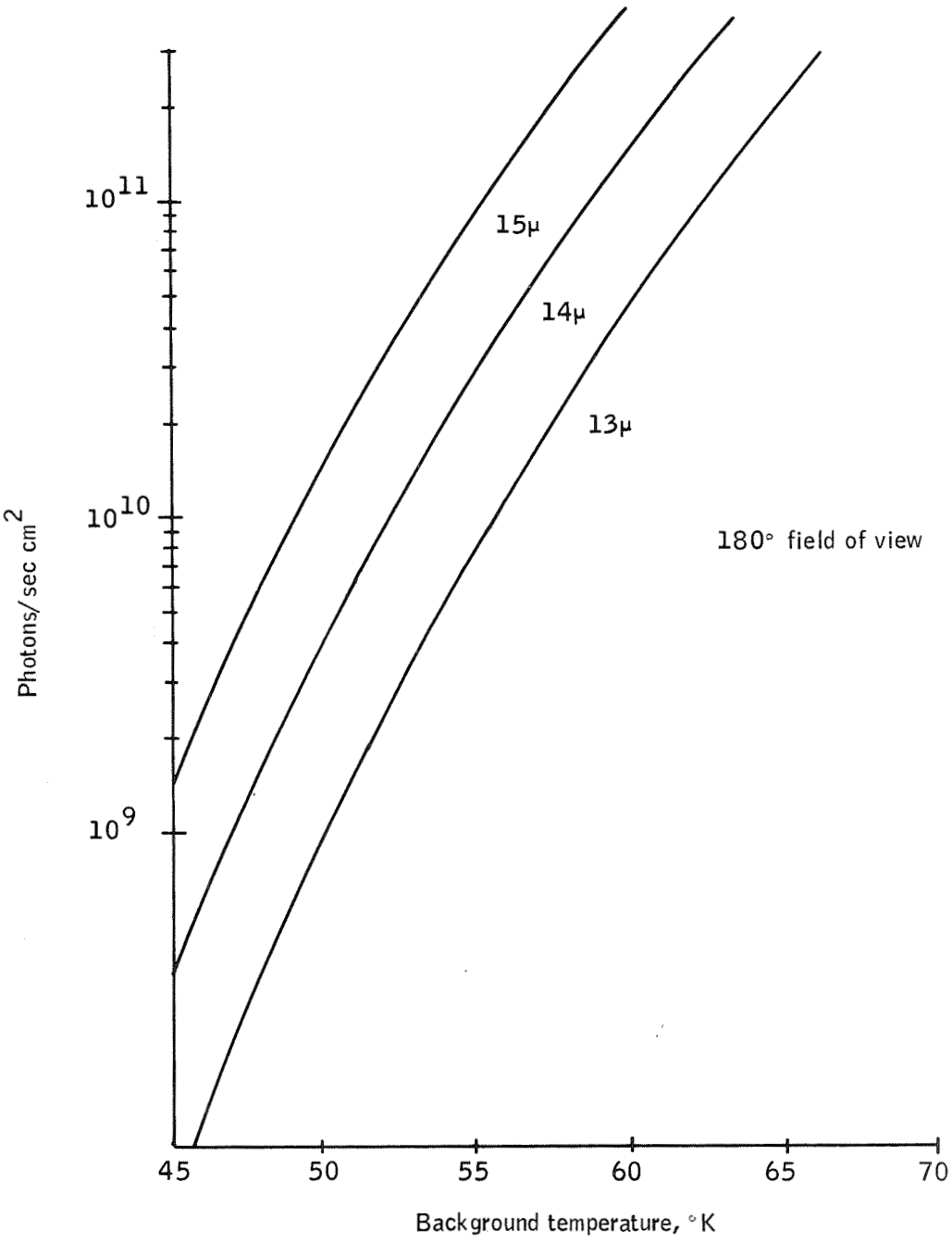

Figure 142. Absorbed Background Photon Flux versus Blackbody Background Temperature for Various IR Detector Cutoff Wavelengths

Effects of thermal gradients in the detector induced by the high-flux loads on the surface of the detector may be determined by removing the detector bias and observing the detector output while the detector is flooded with a high-flux load. Any voltage observed will be due to thermally induced electromagnetic forces.

The limiting accuracy for these measurements is the accuracy of the calibration of the InAs emitters. Most of the detector measurements may be made concurrently except for the relative spectral response which is determined as a separate test. The initial effort will be calibration of the InAs emitters against a blackbody with the detector test measurements following.

DETECTOR MOUNT

Alignment of the optical elements and the detector assembly is extremely critical. Relative motion between the detector and the lens will cause a shift in the focal point and consequent loss of signal. Studies conducted on similar radiometer systems indicate that serious defocusing can occur for dimensional changes along the optical path in the order of 0.1 to 1 mil. The budget for misalignment of the detector and field stop is 0.3 arc sec. At 20-inch focal length, 0.8 arc sec represents a motion of 0.0000774 inch, or somewhat less than 0.1 mil. The dimensional sensitivity of the system under study here is expected to be in the same range, but will not be determined until detailed analysis is done. The alignment of the secondary lens assembly and detector is especially difficult, since these components must be cooled from ambient temperature to operating temperatures of 60°K and 20°K, respectively. Substantial contraction of the elements takes place during this temperature reduction and emphasis must be placed on mounting techniques which minimize the cooldown deflections or which lead to highly predictable deflections.

The possible flight configurations of the detector assembly and the relay lens assemblies is severely limited by the requirements of low heatleak in order to minimize solid cryogen requirements. Of the many configurations studied, the best configuration for detector support appears to be one in which the detector is supported by taut filaments. Other configurations lead to much higher heat leaks. The design of the relay optics assembly is dictated by the same considerations; however, the cryogen requirements are not as severe and therefore there are more choices in the design. Two configurations which appear attractive are where

- Taut filaments are used, similar to the detector support
- Concentric fiberglas tubes are used for support of the relay optics assembly

Concentric fiberglas tubes are required to provide maximum thermal conduction path length and minimum thermal conductivity. Of these two choices, the taut filament system was closer for this test primarily because it is expected to result in less movement of the system when cooled to operating temperature and the heatleak is lower. This design is believed to be the best design to test because it is most representative of a flight system.

Calculations shown in Appendix K indicate the feasibility of meeting the extremely tight dimension and alignment requirements. To substantiate and further explore this area, tests are necessary on prototype assemblies. These tests require cooling to the operating temperatures with cryogenic fluids and the precise measurement of the location of the critical elements before and after cooldown. In addition to this primary test objective, the heatleak to the components can be measured to substantiate predictions on cooler requirements to maintain the assembly at operating temperature for one year.

Measurement of the heatleak to the components can be achieved as a byproduct of the main test objectives and will be valuable in the design of a flight system. These measurements can be made with a relatively small additional increase in cost and test time. Very little prior experience is available on the heat rates to assemblies such as these. The vast majority of operational or flight-type detectors in use now and in past years were cooled with closed-cycle refrigeration systems. These systems have large cooling capacities, of the order of several watts, so that detector support techniques do not have to concentrate on a low heatleak to the degree required here. The heatleak required for this detector assembly to result in a low-weight cryogen system are on the order of 10 mW, and as such require precise thermal design. Although some heatleak data are available on detector assemblies for similar systems, these data are limited and are generally for a complete system including heatleak from other sources such as insulation, etc. The specific measurement of the heatleak to detector and relay lens assemblies is considered to be highly desirable.

Test Objectives

The basic objective of the proposed tests is to determine the operating characteristics of the detector mount assembly when cooled to its cryogenic operating temperatures. The primary operating characteristics to be explored in these tests fall into the two broad categories of heat transfer effects and optical alignment effects. Included in the category of heat transfer effects are:

- Measurement of the heat transfer rate to the detector support assembly
- Temperature distribution in detector mount assembly

Determination of the heat transfer rates to the assembly is of paramount importance in the determination of the size and weight of the solid-cryogen cooling system anticipated for use with the radiometer system. The experimental determination of these heat transfer rates also provides a basis for assessing the accuracy of the analytical predictions used to size the solid-cryogen cooling system.

Determination of the temperature distribution in the assembly provides information on the ease of maintaining the assembly at the desired operating temperatures. The temperature gradient from the lens or detector assembly, down the flexible link connection and down the thermal link to the cryogen, will be determined and compared with predictions.

The optical alignment effects primarily consist of determining the dimensional change in the critical optical dimensions which results from cooldown from ambient temperature to operational temperature. The intent is to measure the location of the detector mount facing both axially and radially before and after cooldown. In addition, the radial and axial location of the secondary lens housing will be measured at various temperatures. The information gained from the tests will be used to determine the suitability of the mounting technique and the accuracy of the analytical predictions of thermal contraction of the components. The results will indicate the feasibility of using a passive alignment technique in which the optical elements are misaligned at room temperature so that cooldown contractions will bring the elements into focus at operating temperature.

Secondary objectives of the testing are to determine the resistance of various materials to the thermal cycling at cryogenic temperatures and to evaluate fabrication techniques.

Measurement Requirements

The measurement requirements fall into two categories.

- The change in position of the detector mount and the relay optics after cooldown must be measured. Autocollimators will be required to make these measurements. The desired accuracy of the measurements is 0.1 mil, which is believed to be within the capability of such a device, since measurements of 1 arc sec can be made.

- The heatleak to the detector assembly and to the relay optics housing must be determined by measurement of the boiloff rates. These boiloff rates will be measured with a precision wet test meter. Accuracies of ±3% can be obtained with this instrument, which is adequate for the test objectives. Temperature measurements will also be made at various locations as shown in Figure 143. Platinum resistance thermometers will be used in critical areas to obtain the required accuracy.

Test Procedures

A basic test setup that could be used is shown schematically in Figures 143 and 144. The test setup includes a vacuum chamber capable of pressures of 10^{-6} torr or better, which is used to contain the detector/lens assembly and the cryogens required for temperature control. Two cryogen containers will be used, one to hold liquid nitrogen and the other to hold liquid helium or liquid neon. These cryogen containers will be thermally isolated from the ambient environment by means of low thermal conductivity fiberglas support columns and multilayer insulation. By reducing the heatleak in this manner, the cryogen boiloff will be sensitive to heat inputs from the detector mount and secondary lens mount, allowing the heat rates to these components to be measured.

Detector and relay lens mount assemblies will be placed within the vacuum chamber on a removable flexible bellows assembly. The purpose of the bellows is to structurally disconnect the assembly from the vacuum chamber so that chamber cooldown and vibration will not have an effect on the positioning of the assembly. The assembly can be removed and replaced with alternative configurations without the removal of the entire cryogen container assembly. The optical assembly will be rigidly mounted to a solid reference point such as a marble table or cement slab which will provide a solid nonmoving reference point for the optical measurements. The optical assembly will be thermally connected to the nitrogen and helium cryogens by means of a copper (OFHC) rod which will contain a thermal switch or removable thermal joint for thermal coupling and decoupling. The thermal switch will allow the measurement of the cyrogen boiloff with and without the optical assembly coupled to the cryogens so that the heatleak to the detector and relay lens assembly can be determined. Temperature measurements will be made at critical locations as shown in Figure 143. Accurate temperature measurement of the detector assembly will require the use of a platinum resistance thermometer. Other locations will incorporate thermocouple measurements.

Two wet test meters will be required to measure boiloff rates from the two cryogens. A large variation in the control of the detector and relay lens assembly temperature range will be available. The temperature of the liquid nitrogen is nominally 77°K at 1 atmosphere, but this temperature can be reduced to 63.1°K by pumping on the vent line and reducing the pressure above the LN_2 to 92 torr, or the temperature can be reduced further to approximately 45°K by further pressure reduction and formation of solid nitrogen. The helium at 4.2°K will be used to cool the detector assembly to the nominal 15 to 20°K required for the detector. This will be accomplished by providing a heater on the thermal link and providing a suitable thermal resistance in the thermal link. In this manner, the detector temperature can be adjusted to various temperatures with the heater as required.

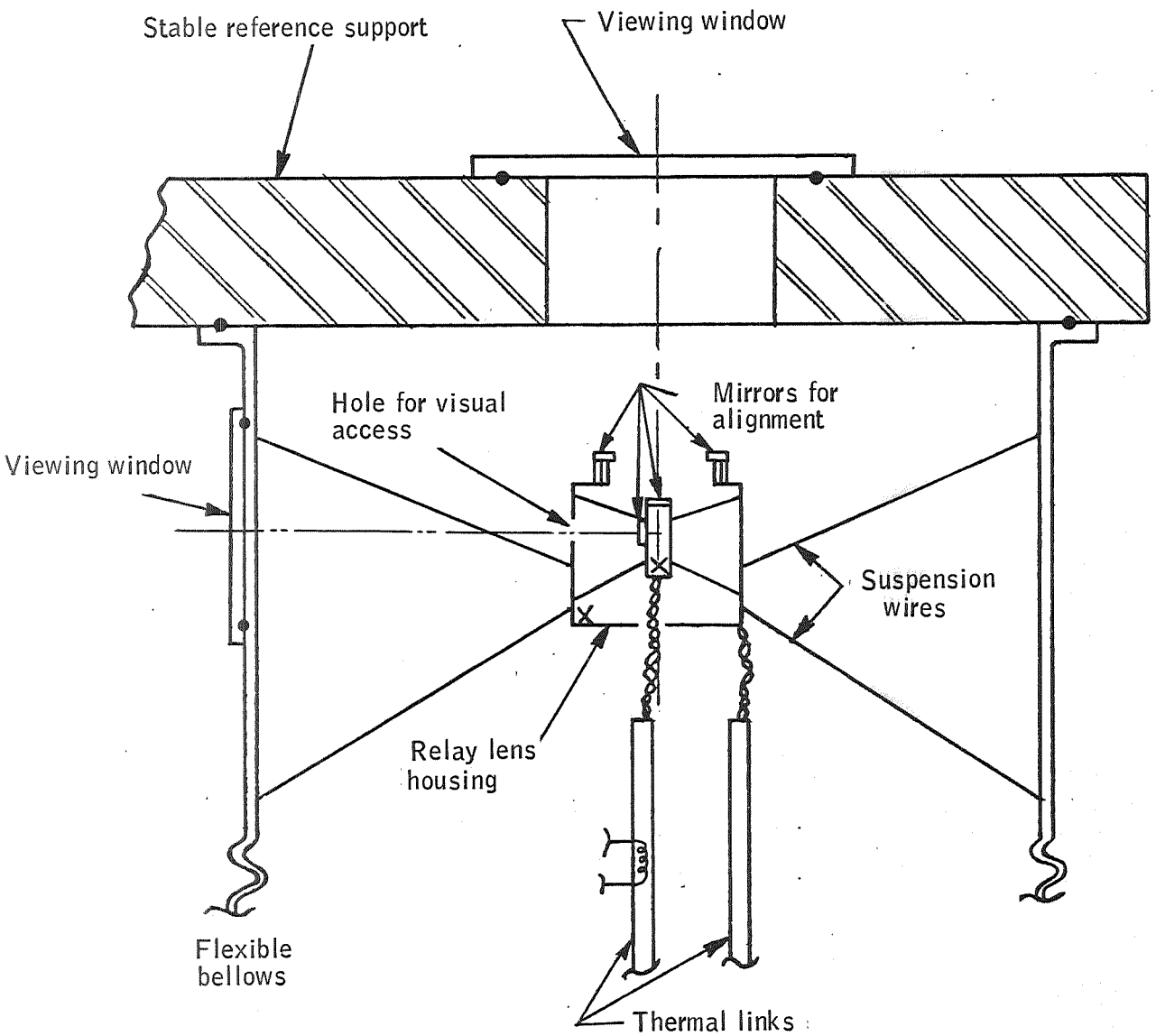

Figure 143. Typical Detector/Secondary Lens Support System

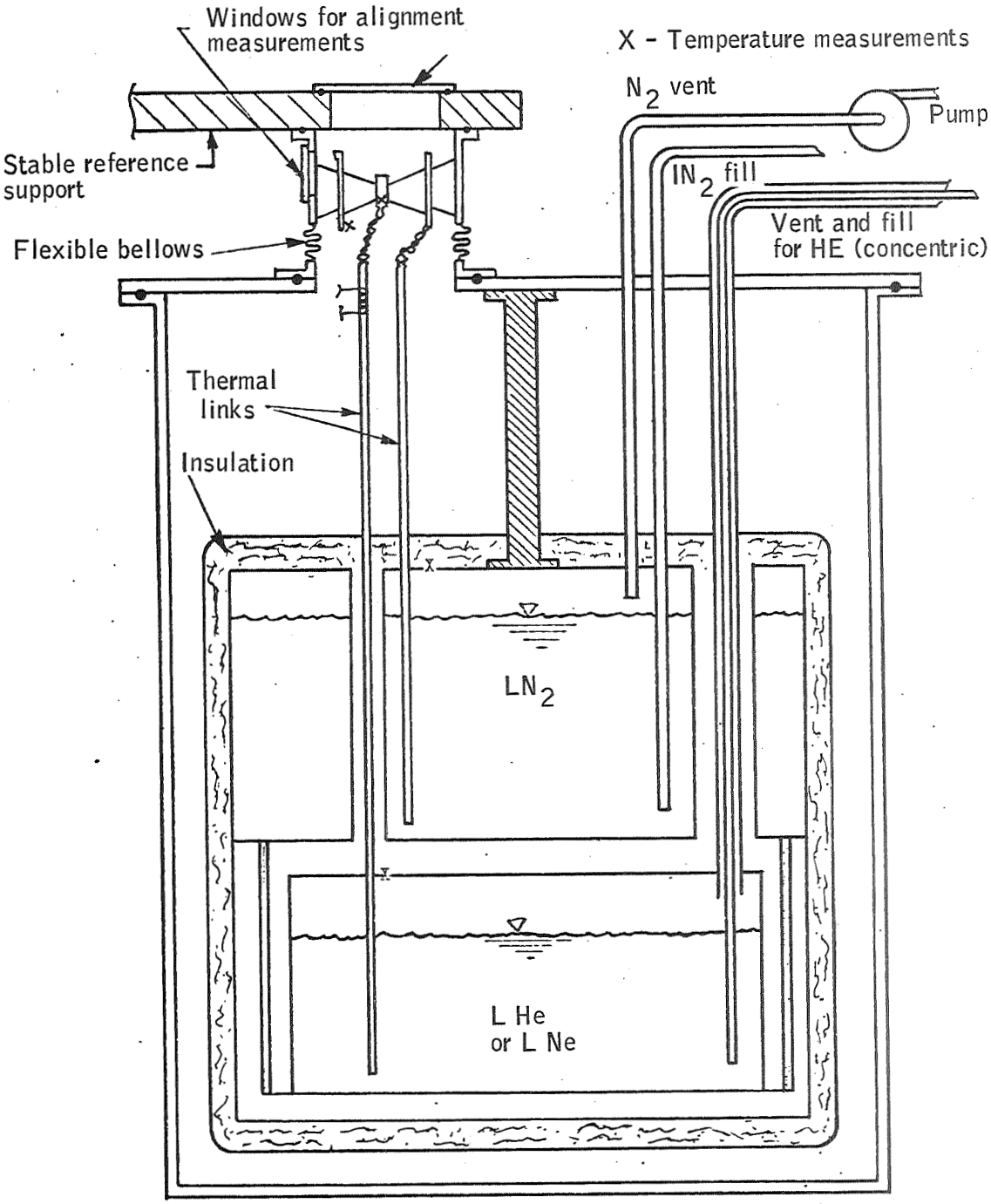

Figure 144. Detector and Lens Cooling Concept for Testing

One relay optics and detector mount assembly, which is being considered for testing, is shown in Figure 143. Mirror elements will contain crosshairs for precise optical measurements. The relay optics housing will contain a hole for optical measurements of detector housing shifts. The complete relay lens and housing assembly will be attached to the vacuum chamber by means of a bellows to structurally decouple the assembly from the vacuum chamber so that dimensional changes in the chamber during cooldown or vibrations from the pumps, etc., will not disturb the optical assembly. The optical assembly will be rigidly mounted to a solid marble or cement slab which has sufficient mass to provide a stable optical reference system. Precise optical alignment measurements will thus be made using the slab as a base. Precise measurements can be made of the dimensional changes in the optical elements resulting from cooldown. Visual access to the mirrors and optical assembly will be provided by glass viewing ports. The optical assembly will interface with the vacuum chamber and rigid support for ready removal with the vacuum chamber and rigid support so that the assembly can be readily removed and a modified or alternative assembly can be put in place for testing.

After the otpical assembly is fabricated, location of the mirror flats must be precisely determined with respect to some fixed point on the assembly. This optical calibration will be done at room temperature and before installation into the vacuum chamber. Dimensional measurements will be checked after installation into the vacuum chamber and prior to cooldown. The optical measurements will require six separate measurements to determine the position of the six mirror flats. Autocollimator accuracy is approximately 1 arc second. Measurements made with the autocollimator will give the rotational movement of the assembly but not the displacement. A theodolite will be used to determine displacement.

Cryogen containers will be installed in the vacuum chamber together with the thermal links but without the optical assembly mounting. The heatleak into the insulated cryogen containers will be determined by measuring the boiloff rate. This heatleak measurement will provide the required calibration of the containers so that the additional heatleak from the optical assembly can be measured.

After the thermal calibration of the containers has been completed, the optical assembly will be installed and attached to the thermal links and the optical alignment will be checked prior to cooldown. The cryogen containers will then be filled and the system will be allowed to reach thermal equilibrium. After equilibrium is established, the boiloff rate from the two cryogens will be measured to determine the heatleak to the detector holder and the lens holder. During the period when the boiloff is being measured with the wet test meters, the necessary optical alignment measurements will be made to determine the movement of the six mirror elements.

If time permits, the optical alignment can be checked again at a new set of temperatures for the detector holder and lens housing. These new temperatures can be obtained by adjusting the pressure above the LN_2 bath and

changing the power dissipation in the electrical heater mounted on the thermal link between the LHe and the detector holder. The measured thermal contraction of the otpical elements can then be compared with the analytical predictions at the various temperature settings required.

At the completion of this test phase, the results will be analyzed and a determination made as to what additional tests and/or modifications are required. The tests will culminate with the preparation of a test report.

Discussion

Initial studies of the detector mount led to the conclusion that the mount design is configuration dependent. A different design is required for an off-axis parabola configuration than for a cassegrainian configuration. Mechanical interference precludes use of a universal design. Therefore, detector mount tests do not appear justified for this program.

REFRACTIVE MATERIALS

The analytical models for the ARRS Study consider the use of refractive materials in three applications:

- Window support the the secondary mirror of a cassegrain primary
- All refractive relay system
- Bandpass Filter Substrate

The refractive materials considered for ARRS in the wavelength region 14.0 to 16.3μ are Germanium, Irtran-4 (ZnSe), Irtran-6 (Cd-Te), and Texas Instruments Glass 1173 (Ge Sb Se). Requirements of the refractive materials for ARRS are

- Low coefficient of expansion
- High transmittance
- Low absorption coefficient
- Low emittance

Material Characteristics

Germanium and Irtran-6 seemed to be the best choices of the candidate materials because they have the lowest emittance and the lowest thermal expansion over the ARRS temperature range of interest (60° to 300°K). See Figure 145 and Table 48. There has also been a substantial amount of quantitative evaluation of Irtran-6 performance in the temperature range of interest (refs. 24, 25 and 26). However, Irtran-6 has considerably higher chromatic aberrations than germanium and it is much easier to make aspheric surfaces on germanium than Irtran-6. Coating Irtran-6 is more difficult than germanium.

Measurements of the thermal expansion coefficient of some of the materials of interest were made by Dr. Ballard and Dr. Browden of the University of Florida. The results of their measurements are presented in Table 49 and Figures 145 and 146.

The absorption coefficients, α cm^{-1}, for germanium were measured and reported by John C. Alishouse (ref. 27) and are given in Table 50. The absorption coefficients for Irtran-4 (ZnSe) and Irtran-6 (Cd-Te) at cyrogenic temperatured were measured and reported by Dr. Stierwalt, (ref. 26). A comprehensive survey of Irtran-6 characteristics in the 14 to 16.3μ band is given in Table 50. Dr. Stierwalt has equipment to make measurements at cryogenic temperatures only, and since no data for the absorption coefficients at room temperature for Irtran-4 and Irtran-6 were found, the coefficients given in Table 50 for room temperature were calculated. The absorption coefficients for Irtran-4 at room temperature were calculated per J. C. Alishouse (ref. 27) based on the measured values at 200°K and 77°K from Dr. Stierwalt. The absorption coefficients for Irtran-6 at room temperature were calculated based on transmission values given by Kodak.

The transmittance curves for TI Glass No 1173 are shown in Figure 147, as a function of thickness uncoated, and in Figure 148 with an antireflection coating. These transmission curves indicate that this material is not feasible for ARRS. The emittance of germanium as a function of temperature as measured by Dr. Stierwalt is shown in Figure 149.

It would be of interest to know how nonuniform the absorption coefficient and refractive index are in refractive elements in the sizes and configuration applicable to ARRS and how this nonuniformity varies with temperature. Data from Texas Instruments, Inc., indicate that a particular Texas Instrument glass 1173 refractive index varies over the lens 6×10^{-5} $\Delta n/cm$. It is not known how this would change with temperature. A possible source of error in the ARRS conceptual design occurs because the inflight calibration beam passes through only a portion of the refractive element of interest. If the characteristics of this portion do not change uniformly with the rest of the refractive element, then an error of unknown magnitude is introduced. While these data would be of interest, there are no laboratories that are known to be presently engaged in this kind of investigation and the costs would exceed that deemed suitable for this study.

The major data required to analyze systems using Irtran-6 are already available with sufficient confidence to make further tests unnecessary.

The most promising material for use as both lens elements and for the filter substrate is germanium. The Irtran materials have a high degree of chromatic aberrations and difficulties in coating. The TI Glass No. 1173 has its cut-off edge partially within the region of interest.

More qualitative data on the index of refraction of germanium at the low ARRS temperatures and the uniformity of the index of refraction at low temperature would be desirable, but there are no known laboratories that are presently engaged in this kind of investigation, and the costs would exceed that deemed suitable for this study.

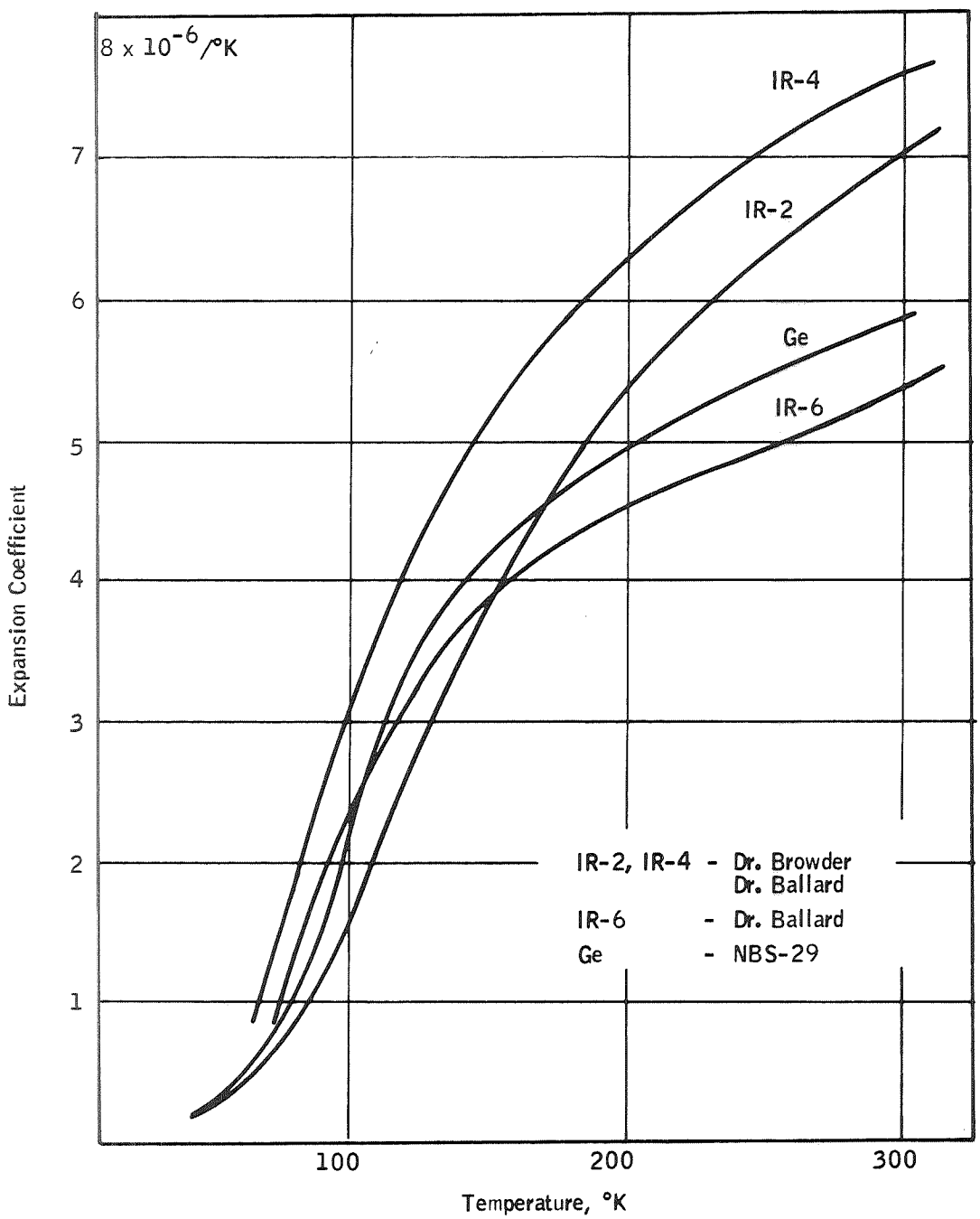

Figure 145. Coefficient of Linear Thermal Expansion

TABLE 49. - COEFFICIENT OF LINEAR THERMAL EXPANSION, $10^{-6}/°K$

T °K	NBS-29 Ge	Irtran-2	Zn-Se IR-4	Cd-Te IR-6
0				
10				
20				
30				
40	0.07			
50	0.20			
60	0.39	0.34	0.81	
70	0.67	0.53	1.17	0.77
80	1.05	0.75	1.81	1.24
90	1.54	1.07	2.46	1.72
100	2.20	1.52	3.07	2.28
110		2.08	3.58	2.65
120	3.25	2.57	4.04	3.04
130		3.01	4.46	3.33
140	3.91	3.40	4.77	3.60
150		3.78	5.08	3.80
160	4.29	4.14	5.37	3.97
170		4.48	5.58	4.11
180	4.58	4.76	5.79	4.23
190		5.03	5.99	4.33
200	4.82	5.26	6.17	4.45
210		5.47	6.32	4.53
220	5.03	5.67		4.61
230		5.86		4.70
240	5.23	6.02		4.77
250		6.18		
260	5.42	6.35		
270		6.51		
273	5.53			
280		6.65		
290		6.79		
293	5.67			
300	5.75	6.91		
310		7.02	7.5	5.38
320				5.7

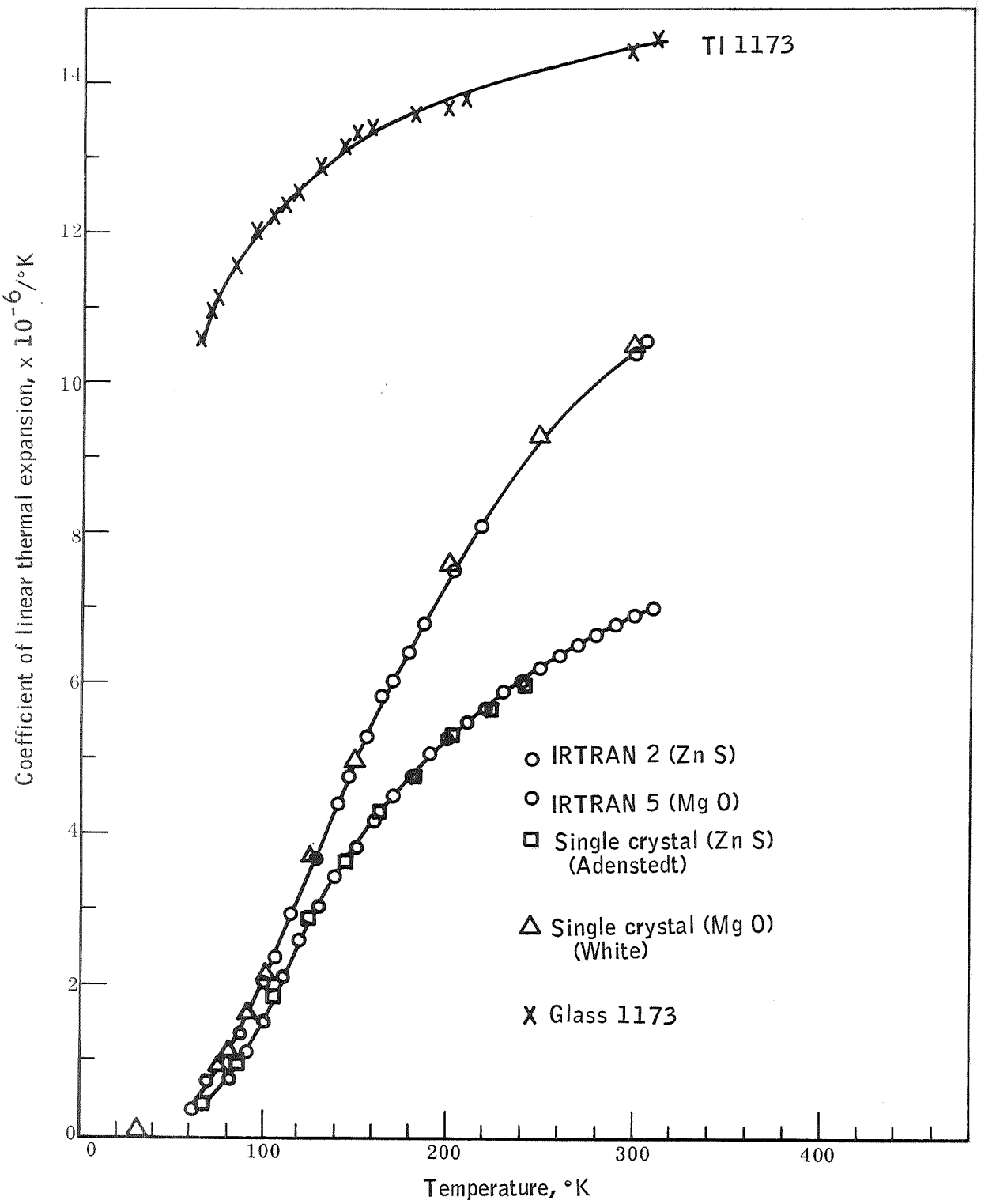

Figure 146. Coefficient of Linear Thermal Expansion ($x10^{-6}$/°K)

TABLE 50.—ABSORPTION COEFFICIENT α cm^{-1}

λ, μ	Germanium[a]	Irtran-4 (Zn Se)			Irtran-6 (Cd Te)		TI Glass 1173 (Ge Sb Se) from Ti-Graph
		Calculated[a]	Measured[b]		Calculated[c]	Measured[d]	
	293K	298K	200K	77K	298K	77K	298K
14	0.15	(a)	0.14	0.073	0.081	0.04	0.38
15	0.46	0.193	0.222	0.133	0.105	0.045	0.44
16.3	0.37	0.293	0.5	0.229	0.086	0.048	0.8
		0.716					

[a]As measured and reported by Alishouse, reference 27

[b]As reported by Dr. Stierwalt, 4 Oct 1968

[c]Per MIL-HDBK-141, par. 17, reference 24

[d]By Dr. Stierwalt, reference 26

TABLE 51. – CALCULATED VALUES, IRTRAN-6

λ, μ	Ref. Index n	Temp °K	Total measured ransmittance (Kodak)	Thickness of sample, cm	Calculated			
					Reflectance, ρ	Transmission, T	Absorption coefficient, α	Extinction coefficient, °K
14.0	2.660	298	0.64	0.3275	0.205709	0.973727	0.081297	3.40×10^{-6}
15.0	2.657		0.635	0.3275	0.205303	0.965932	0.105839	4.75×10^{-6}
15.2	2.657		0.637	0.3275	0.205303	0.968742	0.096966	4.41×10^{-6}
16.0	2.655		0.64	0.3275	0.205032	0.972441	0.085330	4.09×10^{-6}
16.3	2.654		0.64	0.3275	0.204896	0.972184	0.086138	4.21×10^{-6}
14.0	2.643	77	0.64	0.3275	0.203403	0.969353	0.095043	4.00×10^{-6}
15.0	2.640		0.64	0.3275	0.202995	0.968580	0.097479	4.40×10^{-6}
15.2	2.640		0.64	0.3275	0.202995	0.968580	0.097479	4.78×10^{-6}
16.0	2.638		0.64	0.3275	0.202723	0.968065	0.099104	4.91×10^{-6}
16.3	2.637		0.64	0.3275	0.202587	0.967807	0.099917	4.91×10^{-6}

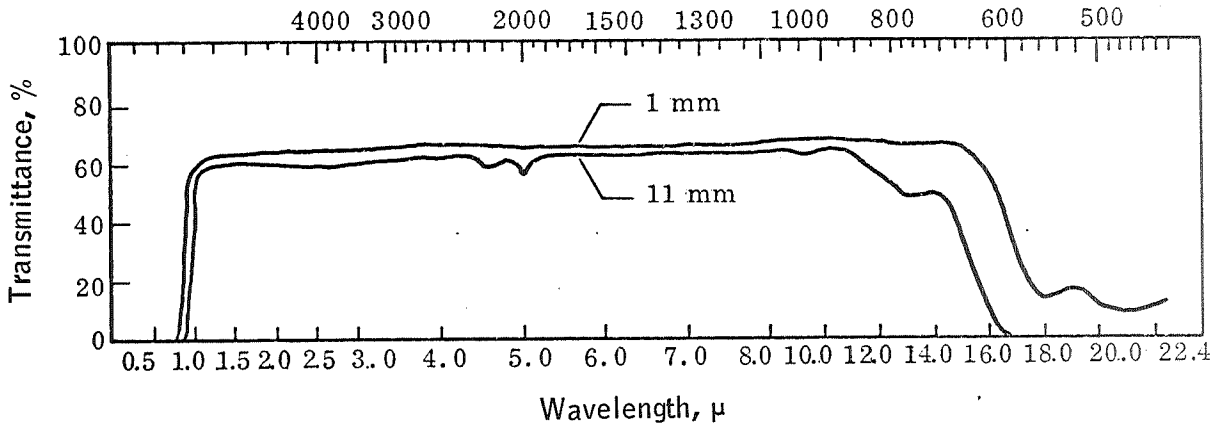

Figure 147. Curves for Uncoated 1173 Glass at 1 and 11 Millimeters

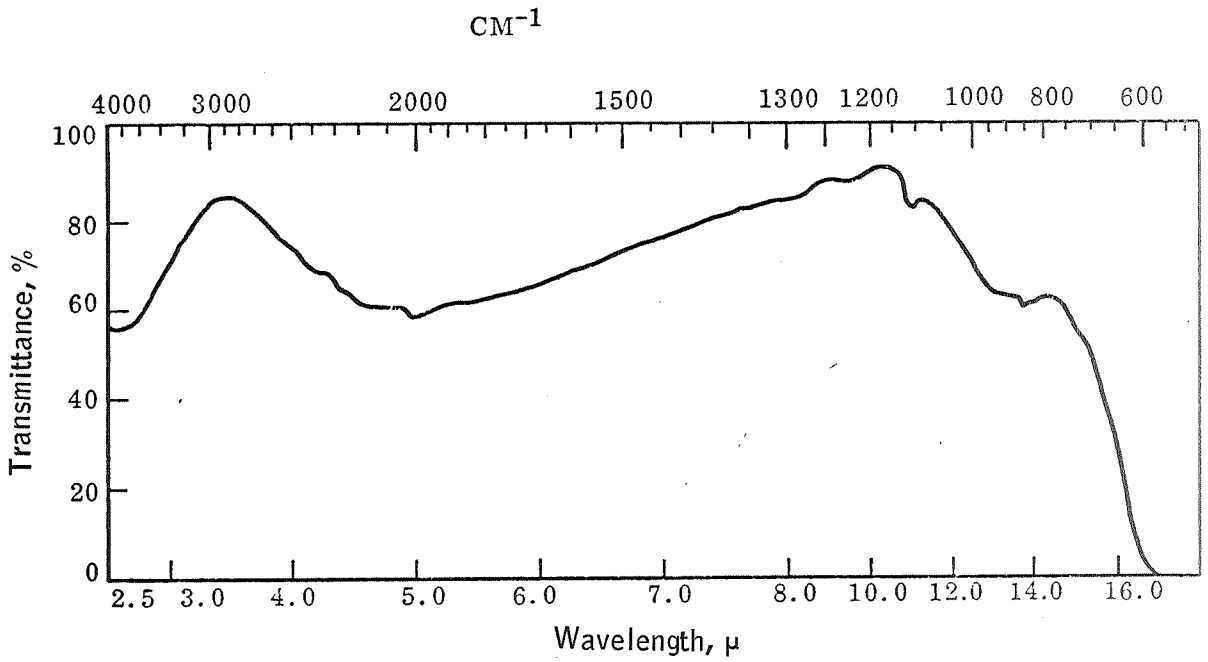

Figure 148. Curve for PbF_2 Coated 1173

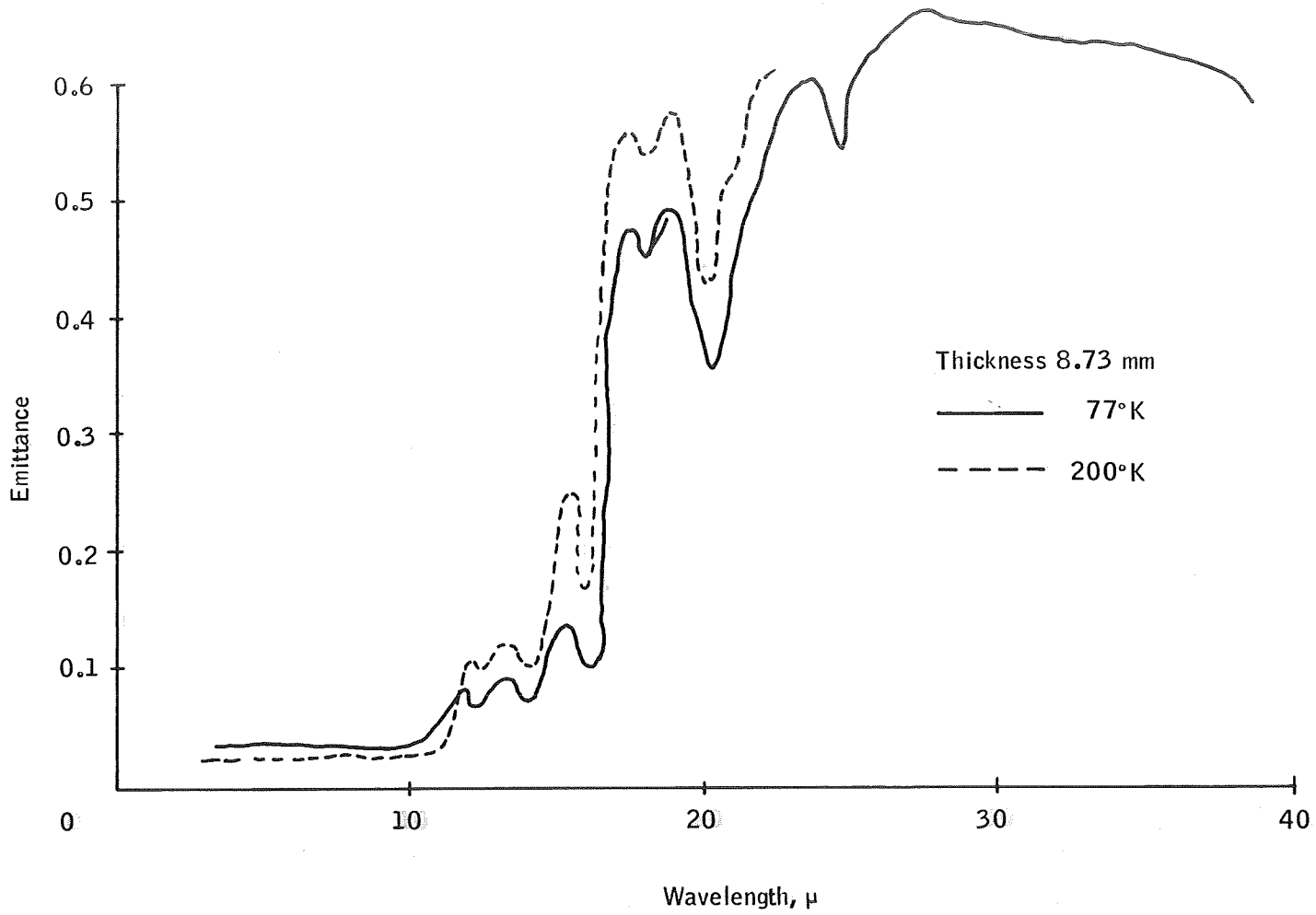

Figure 149. Emittance of Germanium

APPENDIX A
PARAMETER VARIATION CHECKLIST

APPENDIX A
PARAMETER VARIATION CHECKLIST

The parameter variation checklist (PVCL) summarizes the relationships between subsystems parameters and the system element that neither constrains or is constrained by each of the parameters (Table A1). This device is to account for, without freezing, the effects of parameter variations on each other and on the type of system and mission involved. Circled numbers refer to explanatory notes regarding the relationship between the affected parameter and the constraining element. These notes are summarized in this appendix.

RADIOMETER (RM)

RM-1 Spectral Band

① Range is defined by the basic ARRS requirement.

② Errors due to spectral filter require, for computation, some model of measured spectrum. Figures A1 and A2 depict estimates of the limiting in-band and out-of-band spectra, respectively. Figure A1 is based on extreme in-band absorptance spectra and a 230°K emitting temperature. Figure A2 is primarily aimed at defining the unknown out-of-band variables as well as absolute levels. An investigation of earth resources applications indicates that spectral signature information is expressable only in terms of apparent temperature and emittance and that neither is particularly wavelength dependent. Therefore, for these applications the product of the 300°K blackbody spectrum the atmospheric transmission may be assumed.

③ Effect of freeze (①) on applicability to other intervals. Two factors are evident, width and location of the spectral response curve. Width is typical of all but spectrometric application; ruling these out rules out nadir viewing inversion applications.

The location represents a worst-case for the 5 to 25μ region, requiring vacuum operating, lying near the performance cross-over of the relevant detectors, and including a Germanium absorption band. Applications in the 3 to 5 and 25 to 40μ bands will not be usefully served, particularly with respect to detectors and optical materials.

④ Limits number of intervals usable simultaneously.

TABLE A1.– PARAMETER VARIATION CHECK MATRIX

Constraining element Parameter	Mission	Spacecraft	Attitude determination	Radiometer	Data handling	Alignment monitor	Other
Radiometer							
1. Spectral band	1 2 3				4	5 6	
2. Scan rate	1	2	3		4		
3. Weight		1					
4. Volume and envelope		1 2	3 4				
5. Operating temperature	1 2	3 5	4				
6. Redundancy	1	2	3			4	
7. Power dissipation		1					
8. Cooling system	1	2 3	4				
9. Detector type	1				2		
10. Transfer function	1				2		3
11. Field of view	1	2				3	
12. Optics configuration		1	2			3	4
a) Aperture		1					
b) f/-number		1					3
13. Chopper type	1		2		4		
14. Chopper frequency					1		
15. Dynamic range	1				2		
16. Structural materials		1	2			3	
17. Internal alignment						1	
18. Stray radiation	1	2				3	
19. Inflight calibration system (number of levels)					1		
Attitude determination							
1. Torque models	1	2		3			
2. Scan rate		1			2		
3. Operating temperature				1			
4. Sensor type	1	2		3		4	
5. Volume		1		2			
6. Stray light baffling	1	2 4				3	
7. Viewing geometry	1	2		3			
8. Transfer function					1		2
9. Internal alignment						1	
10. Output bit rate					1		2
11. Redundancy	1	2		3			
12. Power dissipation		1		2			
13. Structural materials		1		2		3	
14. Field of view	1	2		3			
15. Scan type	1	2					

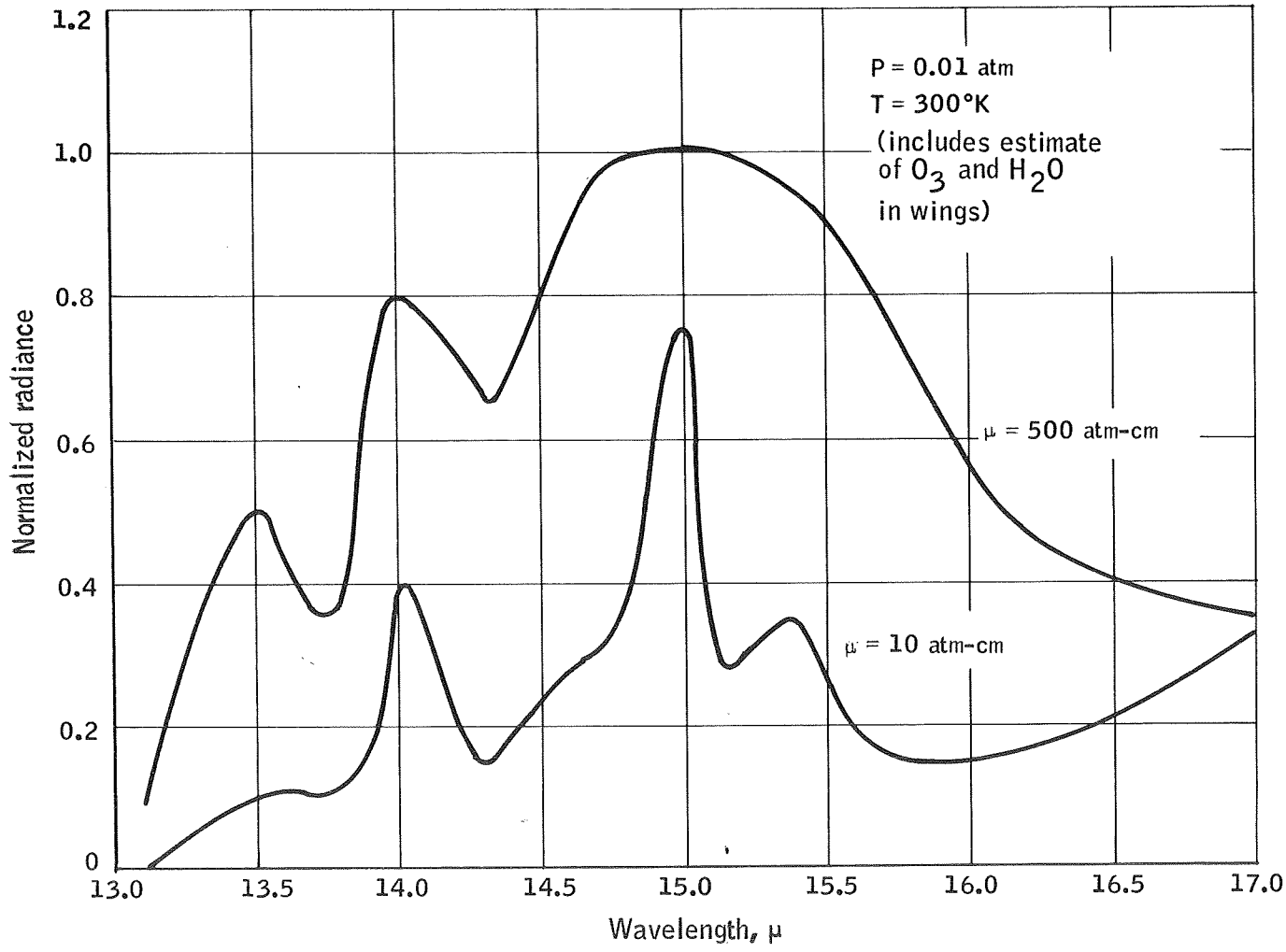

Figure A1. In-Band Limiting Spectra

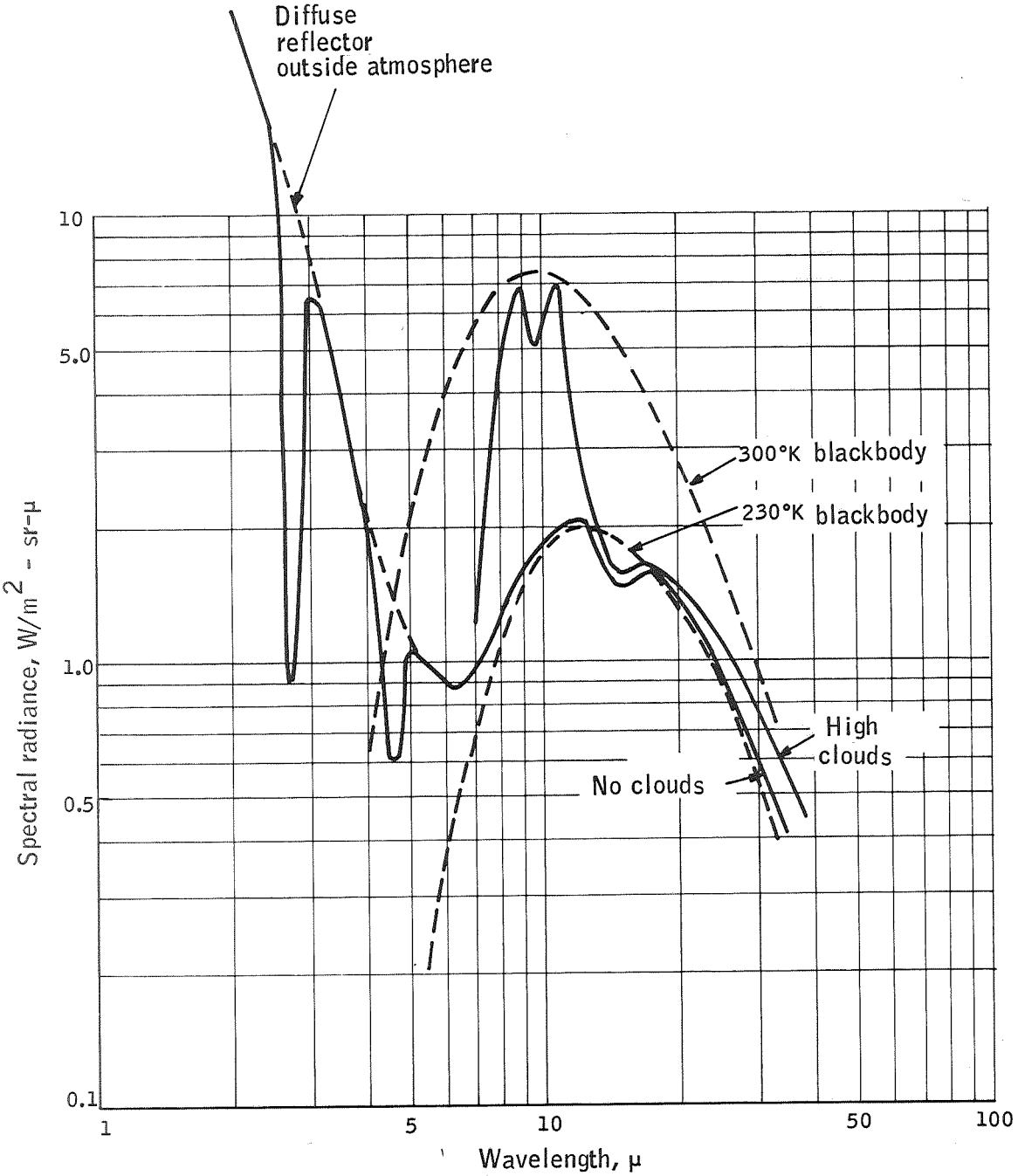

Figure A2. Out-of-Band Limiting Spectra

(5) Spectral interval definition point within system may constrain alignment monitor. If the field-defining stop is the detector, it will be inaccessible to an alignment monitor. The seriousness of this problem will be determined by the ratio of size between the first field stop and the detector.

(6) Emission of alignment monitor

RM-2 Scan Rate

(1) 1 rpm minimum for the Horizon Definition Study data re-requirements

(2) ≈1 rpm minimum for Attitude Control System (ACS)

(3) Update frequency/out-of-plane drift increase with decreasing scan rate; the frequency influencing the torque model, and the drift influencing the torque model and allowable cant angle for the starmapper

(4) Bit rate

RM-3 Weight

(1) Booster capacity

RM-4 Volume and Envelope

(1) Versus nose cone diameter

(2) Shape factor versus stability (ACS)

(3) Stability versus star frequency required

(4) Volume available for star sensors

RM-5 Operating Temperature

(1) Sensitivity required to satisfy mission requirements as determined or influenced by self-emission level

(2) Orbit will constrain lowest possible temperature obtainable passively

(3) Passive thermal control, as determined by insulations and coatings; ACS to maintain a constant sun angle; and the power subsystem relative to the allowable location of solar cells

④ The temperature range where both function was determined to be at least as broad as 150 - 300°K; alignment without specifications of similar materials is dependent on active alignment monitoring.

⑤ Cold secondary optics will involve vacuum requirements for the telescope interior. A mechanism must be provided for the removing of cap and seal. Prelaunch pumping probably will be required.

RM-6 Redundancy

① Mission life determines need

② Volume/weight limits

③ Volume/fit

④ Number of combinations that have to be monitored

RM-7 Power Dissipation

① Power dissipation and the spacecraft configuration determine feasibility of attaining desired operating temperature. Two watts dissipation is consistent with the baseline spacecraft base plate size and orbit.

RM-8 Cooling System

① Type-size determined by life

② L/D constrained for solid cryogen

③ Rolling wheel and low temperature (less than 20°K) rules out passive radiator

④ Changing moment model resulting from cryogen depletion

RM-9 Detector Type

① D*, cut-off wavelength, and frequency response determined by mission purpose

② Linearity determines the number of calibration levels and influences the quantizer curves.

RM-10 Transfer Function

(1) Determined by mission purpose

(2) Maximum output bit rate constrains

(3) PCS aperture diameter and the radiometer transfer function together will determine accuracy limit for a given instantaneous fov.

RM-11 Field-of-view

(1) Mission purpose

(2) Spacecraft -- stray radiation constrains (e.g., paddles)

(3) Stop location is monitored.

RM-12 Optics Configuration

(1) Shape, weight

(2) Fit

(3) Access to field stop and interference by the alignment monitors

12a (1) Volume, opening in skin

12b (1) Volume

RM-13 Chopper Type

(1) One-year life leads to vibrational or torsional

(2) Torque and impulses generated

(3) Redundancy required

(4) Instability effects with and without special electronics compensating features, e.g. with a gate wave

RM-14 Chopper Frequency

(1) Bit rate maximum

RM-15 Dynamic Range

(1) Mission purpose

(2) Bit rate, stability

RM-16 Structural Materials

(1) Thermal, EMC, etc.

(2) Compatability for alignment

(3) Dynamic range of monitors

RM-17 Internal Alignment

(1) Dynamic range of monitors

RM-18 Stray Radiation Protection

(1) Orbit

(2) Protrusions into fov

(3) Constrains location and type

ATTITUDE DETERMINATION SYSTEM (AD)

AD-1 Torque Models

(1) Orbit

(2) Coverage of effects of moving parts and assymmetry require extension of model.

(3) Change of cooler mass, chopper, and IFC (inflight calibrator) moments

AD-2 Scan Rate

(1) ACS interface varies with scan rate; results less applicable outside range

(2) Data rate

AD-3 Operating Temperature

(1) Range is determined by radiometer design.

AD-4 Sensor Type

1. Orbit determines starmapper stray-light problem, need/utility of other sensors
2. Spacecraft volume, passive scan
3. Fit with radiometer
4. Accessibility of focal surface constrains monitor, not vice-versa.

AD-5 Volume

1. Cant angle constraint
2. Fit with radiometer

AD-6 Stray Light Baffling

1. Requirement determined by orbit; noon orbit leads to totally different configuration.
2. No protruberance permissible near fov, stability
3. Monitor interaction
4. Paddle shadowing

AD-7 Viewing Geometry

1. Constrained by orbit, stray-light baffling, and determines available star field
2. Paddles, antennae, etc., determine available field.
3. Fit with radiometer

AD-8 Transfer Function

1. Basic constraint on resolution, number of words/star, etc.
2. Extent of on-board processing

AD-9 Internal Alignment

1. Determines monitor dynamic range

AD-10 Output Bit Rate

(1) Orbit ⇔ threshold setting

(2) Type of memory design (coupled to spacecraft torque model, if tape deck required)

(3) Extent of on-board processing

AD-11 Redundancy

(1) Life determines requirement

(2) Volume, weight constrain degree

(3) Fit with radiometer

AD-12 Power Dissipation

(1) Thermal control

(2) Gradient production

AD-13 Structural Materials

(1) Thermal, EMC, etc.

(2) Alignment, stress

(3) Monitor dynamic range

AD-14 Field-of-view

(1) Orbit constrains free area versus threshold setting

(2) Spacecraft limits free area -- paddles, antennae, etc.

(3) Radiometer may be in the way

AD-15 Scan Type

(1) Constrains mission to functions that do not perturb spacecraft

(2) Requires rolling wheel, both for "passive" stabilization and scan generation

APPENDIX B

GENERAL ANALYTIC RADIOMETER MODEL ALTERNATE APPROACH

APPENDIX B

GENERAL ANALYTIC RADIOMETER MODEL ALTERNATE APPROACH

The objective of the general analytic modeling is to get an arbitrarily accurate expression for the radiant power absorbed by the detector in a radiometer system. Increasing accuracy is achieved by making each radiometer element, which the radiometer is broken down to, smaller and at the same time increasing the number of elements so that all parts of the radiometer system are covered. A first natural selection of elements would be primary optics, field aperture, filter and so on; that is, the elements being optical components. For N elements the model requires knowledge of N x (N-1) nonzero (by definition) parameters for each element or totally N^2 x (N-1) parameters for the entire system. These parameters are not true component parameters but depend on the radiometer geometry, and they have to be computed one by one before the model is applied.

ELEMENT PARAMETERS

The radiometer is divided into a number (N) of elements. Element m, where m = 1, 2, ..., N is described by an N x N matrix $\overline{\overline{R}}_m$, and an N-dimensional vector $\overline{E}_m$. To each radiometer element there is an N-dimensional vector $\overline{X}^r_m$, where r denotes the r^{th} order term of the input. The output of element m is given by $\overline{X}^r_m$, $\overline{\overline{R}}_m$, and $\overline{E}_m$. These vectors are in turn inputs to the other elements. The model is recursive in the sense that the outputs from the r^{th} order inputs generates the $(r+1)^{th}$ order inputs.

Figure B1 illustrates the element parameters with input and output. In addition to $\overline{\overline{R}}_m$ and $\overline{E}_m$, another parameter τ_m is included. This is introduced only to show the desired performance of the radiometer system and $\tau_m \neq 0$ for r = 1 only. With the element $X_{i,m}$ of the vector $\overline{X}_m$ one understands the radiant power input to the radiometer element m for radiation coming from element i (not necessarily emitted from i). Element $\rho_{i,m,j}$ of $\overline{\overline{R}}_m$ is a reflection, transmission, or scattering factor for the radiant power coming from element i, $X_{i,m}$, and being reflected, transmitted or scattered into element j by element m. $E_{m,j}$ of $\overline{E}_m$ denotes the radiant power emitted from element m into element

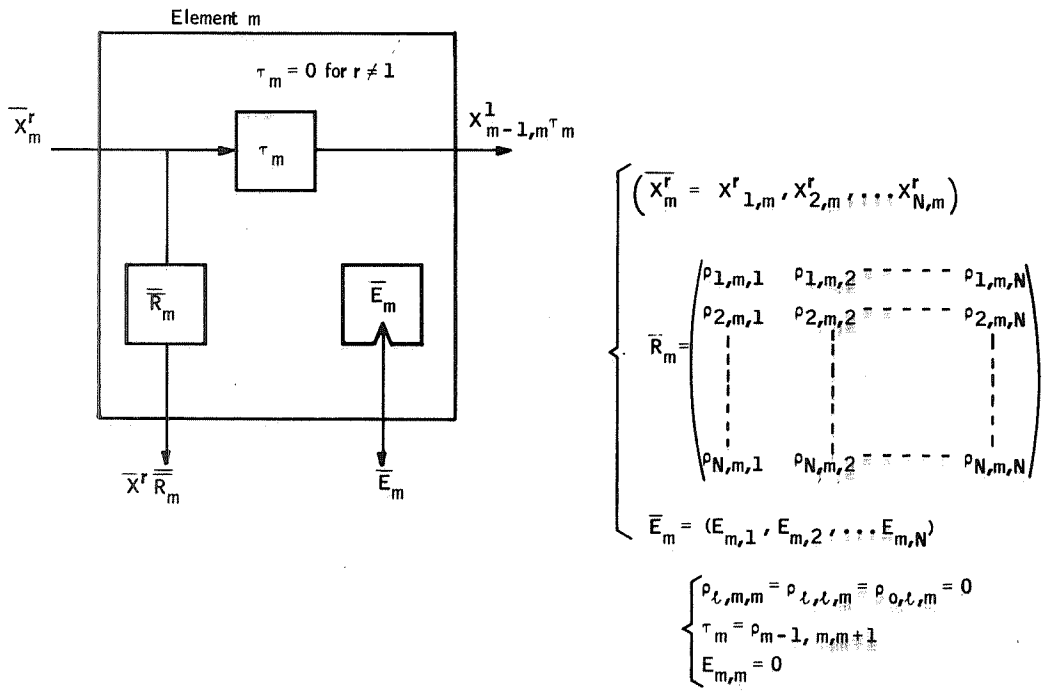

Figure B1. Radiometer Element Parameters

j. The scalar τ_m is by definition equal to $\rho_{m-1,m,m+1}$ and denotes the desired property of element m. For r = 1 set $\rho_{m-1,m,m+1} = 0$ and for $r \neq 1$ $\tau_m = 0$. The reason for introducing τ_m is to clearly show the functional performance of the radiometer system by considering r = 1. The model will work equally well when replacing τ_m by $\rho_{m-1,m,m+1}$ below.

ABSORBED POWER BY DETECTOR

Let P be the total absorbed power by the detector (element N). Then write P_D as

$$P_D = \sum_{r=1}^{\infty} P_D^r \tag{B1}$$

where P_D^r is the r^{th} order term of the absorbed power on the detector. Consider the r^{th} order radiant power from element k onto the detector, $X_{k,N}^r$. A fraction of this radiation is absorbed by the detector, namely $1 - \sum_{q=1}^{N-1} \rho_{k,N,q}$. Summing over all k, one gets the r^{th} order power absorbed by the detector

$$P_D^r = \sum_{k=1}^{N-1} X_{k,N}^r \left(1 - \sum_{q=1}^{N-1} \rho_{k,N,q}\right) \tag{B2}$$

And the total absorbed power

$$P_D = \sum_{r=1}^{\infty} \sum_{k=1}^{N-1} X_{k,N}^r \left(1 - \sum_{q=1}^{N-1} \rho_{k,N,q}\right) \tag{B3}$$

One now has to express $X_{k,N}^r$ in known system parameters; start with r = 1 and then r = 2, r = 3, ... recursively. Consider Figure B2 which shows the first-order terms. Take only $E_{m-1,m}$ (m = 2,3,...N) into account for the first-order terms. For $X_{p,m}^1$ there exists from Figure B2:

$$X^{i}_{p,m} = 0, \text{ if } p \neq m-1 \tag{B4}$$

$$X^{i}_{m-1,m} = E_{1,2}\,\tau_2\,\tau_3 \cdots \tau_{m-1} + E_{2,3}\,\tau_3\,\tau_4 \cdots \tau_{m-1} + \cdots + E_{m-2,\,m-1}\,\tau_{m-1} + E_{m-1,\,m} =$$

$$= E_{1,2} \prod_{i=2}^{m-1} \tau_i + E_{2,3} \prod_{i=3}^{m-1} \tau_i + \cdots + E_{m-2,\,m-1}\,\tau_{m-1} + E_{m-1,\,m} \tag{B5}$$

$$= \sum_{j=1}^{m-2} \left(E_{j,j+1} \prod_{i=j+1}^{m-1} \tau_i \right) + E_{m-1,m}$$

The first-order terms now generate the second-order terms according to Figure B3:

$$X^{2}_{m,n} = \begin{cases} X^{1}_{m-1,m}\,\rho_{m-1,m,n} + E_{m,n}, & \text{if } m \neq n-1 \\ 0, & \text{if } m = n-1 \end{cases} \tag{B6}$$

If $X^{2}_{m,n}$ were equal to $X^{1}_{m-1,m}\,\rho_{m-1,\,m,n} + E_{m,n}$ even for $m=n-1$ then $X^{2}_{m,m+1}$ would be identical to $X^{1}_{m,m+1}$ and would be accounted for twice in Equation (B3) for the total absorbed power by the detector. Figure B4 shows how the second-order terms generate the third-order terms:

$$X^{3}_{m,n} = \sum_{\ell=1}^{N} X^{2}_{\ell,m}\,\rho_{\ell,m,n} \tag{B7}$$

And for the r^{th} order terms we have:

$$X^{r}_{m,n} = \sum_{\ell=1}^{N} X^{r-1}_{\ell,m}\,\rho_{\ell,m,n} \tag{B8}$$

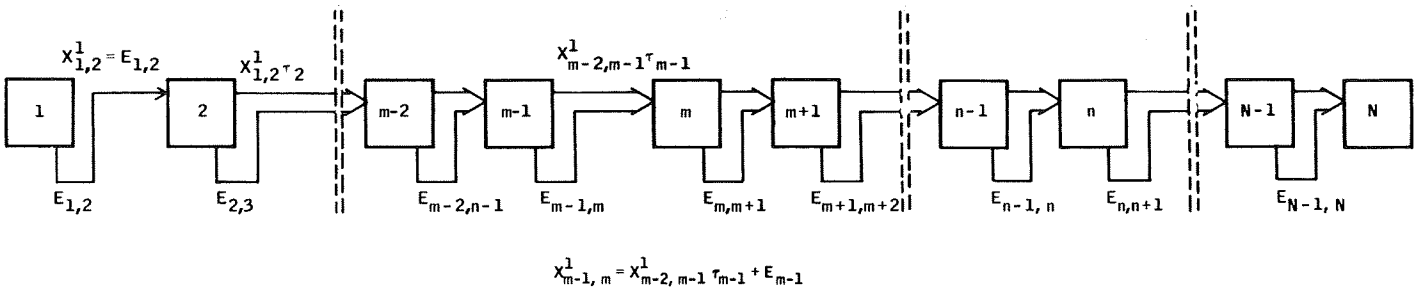

Figure B2. First-Order Terms for Radiation Transmitted (directly) from Element m to Element n

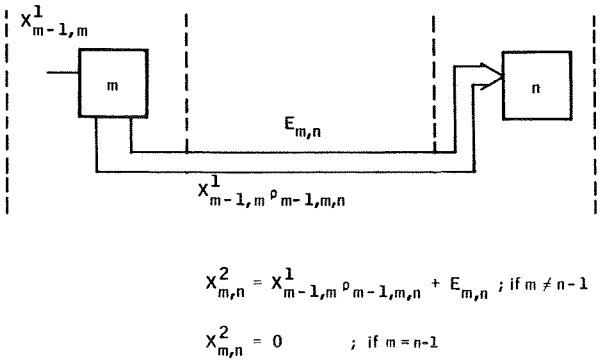

Figure B3. Second-Order Terms for Radiation Transmitted (directly) from Element m to Element n

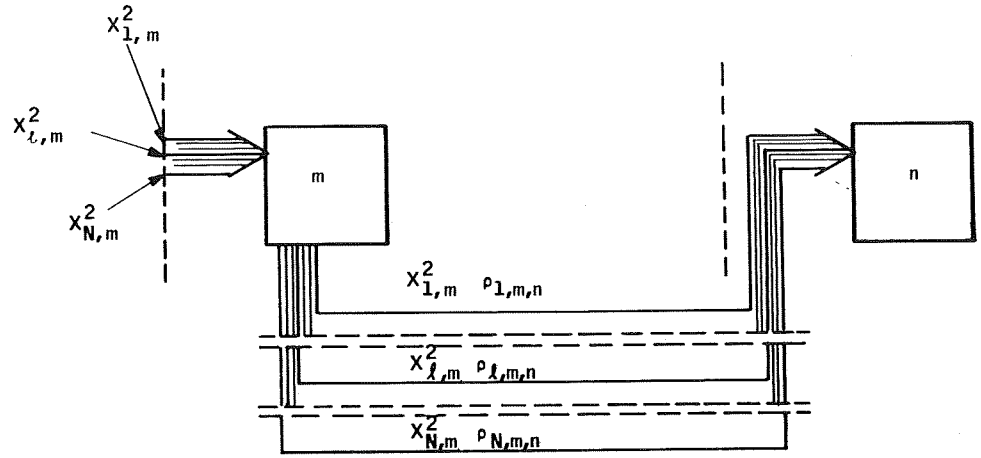

$$X^2_{m,n} = \sum_{\ell=1}^{N} X^2_{\ell,m}\,\rho_{\ell,m,n}$$

Figure B4. Third-Order Terms for Radiation Transmitted (directly) from Element m to Element n

By definition,

$$E_{m,m} = 0 \tag{B9}$$

$$\rho_{\ell,m,m} = \rho_{\ell,\ell,\ell} = \rho_{0,\ell,m} = 0 \tag{B10}$$

$$\tau_m = \rho_{m-1,m,m+1} \tag{B11}$$

SUMMARY OF EQUATIONS

The total power in the detector can now be summarized as follows:

$$P_D = \sum_{r=1}^{\infty} P_D^r \tag{B12}$$

where

$$P_D^r = \sum_{k=1}^{N-1} X_{k,N}^r \left(1 - \sum_{q=1}^{N-1} \rho_{k,N,q}\right) \tag{B13}$$

where

$$X_{m,n}^r = \sum_{\ell=1}^{N} X_{\ell,m}^{r-1} \rho_{\ell,m,n} \quad , \text{ for } r = 3.4.5, \ldots \tag{B14}$$

$$X_{m,n}^2 = \begin{cases} X_{m-1,m}^1 \rho_{m-1,m,n} + E_{m,n} & , \text{ if } m \neq n-1 \\ 0 & , \text{ if } m = n-1 \end{cases} \tag{B15}$$

$$X_{p,m}^1 = \begin{cases} \sum_{j=1}^{m-2} \left(E_{j,j+1} \prod_{i=j+1}^{m-1} \tau_i \right) + E_{m-1,m} & , \text{ if } p = m-1 \\ 0 & , \text{ if } p \neq m-1 \end{cases} \tag{B16}$$

$$E_{m,m} = 0 \tag{B17}$$

$$\tau_m = \rho_{m-1, m, m+1} \tag{B18}$$

$$\rho_{\ell, m, m,} = \rho_{\ell, \ell, m} = \rho_{0, \ell, m} = 0 \tag{B19}$$

GENERAL ANALYTICAL MODEL APPLIED TO NEWTONIAN OPTICS

Now apply the model to a Newtonian optical system. The radiometer system is divided into 11 elements according to Figure B5. The power absorbed by the detector is, then, given by Equation (B12):

$$P_D = \sum_{r=1}^{\infty} P_D^r \tag{B20}$$

where

$$P_D^r = \sum_{k=1}^{10} X_{k,11}^r \left(1 - \sum_{q=1}^{10} \rho_{k,11,q}\right) \tag{B21}$$

and

$$X_{m,n}^r = \sum_{\ell=1}^{11} X_{\ell,m}^{r-1} \rho_{\ell,m,n}, \quad \text{for } r = 3, 4, 5, \ldots \tag{B22}$$

$$X_{m,n}^2 = \begin{cases} X_{m-1,m}^1 \rho_{m-1,m,n} + E_{m,n}, & \text{if } m \neq n-1 \\ 0, & \text{if } m = n-1 \end{cases} \tag{B23}$$

$$X_{p,m}^1 = \begin{cases} \sum_{j=1}^{m-2} \left(E_{j,j+1} \prod_{i=j+1}^{m-1} \tau_i \right) + E_{m-1,m}, & \text{if } p = m-1 \\ 0, & \text{if } p \neq m-1 \end{cases} \tag{B24}$$

Computing the power on the detector for the two cases of chopper open (P_D) and chopper closed ($\overline{P}_D$) is of interest. The difference $\Delta P_D = P_D - \overline{P}_D$ will be compared with the difference ΔP computed in Appendix C. To make the comparison meaningful, make the same basic assumptions and use the same notations. Therefore, designate

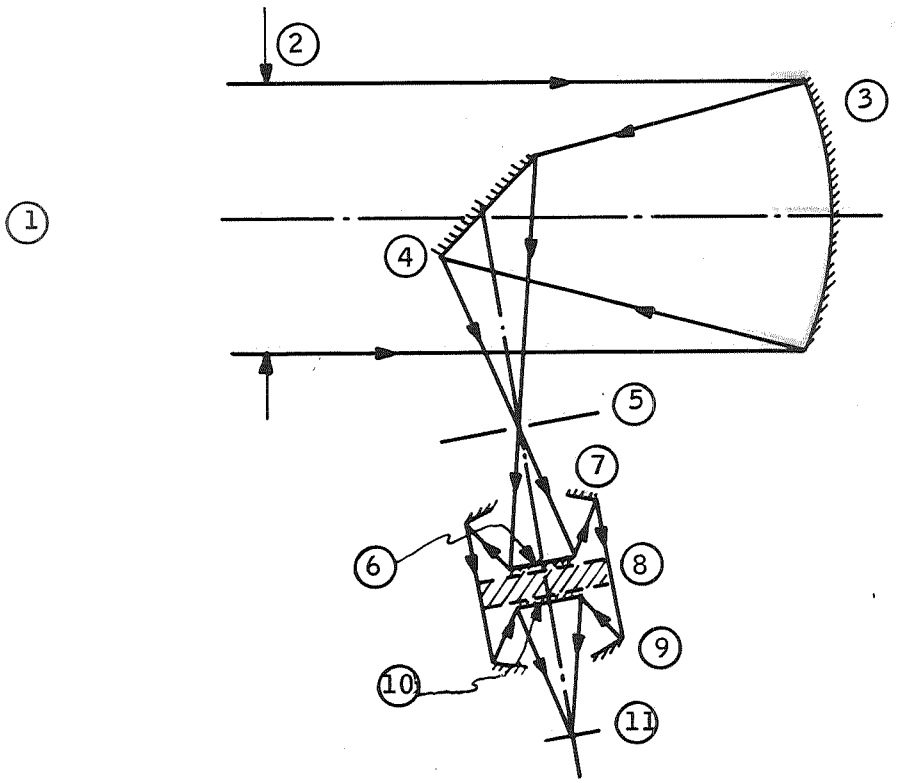

1. Object (B)
2. Aperture (p)
3. Primary collecting mirror (p1)
4. Primary folding mirror (p2)
5. Chopper (c)
6. Secondary optics mirror 1 (s1)
7. Secondary optics mirror 2 (s2)
8. Filter (f)
9. Secondary optics mirror 3 (s3)
10. Secondary optics mirror 4 (s4)
11. Detector (D)

Figure B5. Newtonian Optics

$$\tau_2 = \tau_p$$

$$\tau_3 = \eta_{p1}$$

$$\tau_4 = \eta_{p2}$$

$$\tau_5 = \begin{cases} 0, & \text{chopper closed} \\ 1, & \text{chopper open} \end{cases}$$

$$\rho_{5,6,7} = \tau_6 = \rho_{7,6,5} = \eta_{s1}$$

$$\rho_{6,7,8} = \tau_7 = \rho_{8,7,6} = \eta_{s2}$$

$$\rho_{7,8,9} = \tau_8 = \rho_{9,8,7} = \tau_f$$

$$\rho_{8,9,10} = \tau_9 = \rho_{10,9,8} = \eta_{s3}$$

$$\rho_{9,10,11} = \tau_{10} = \eta_{s4}$$

$$\rho_{6,5,6} = \begin{cases} 0, & \text{chopper open} \\ \eta_c, & \text{chopper closed} \end{cases}$$

$$\rho_{i,j,k} = 0 \text{ for all other } i, j, k$$

(B25)

For radiant power from one element to another, the same values prevail as used previously.

$$E_{1,2} = \frac{A_o A_d}{f^2} N_{B,\Delta\lambda}$$

$$E_{2,3} = 0$$

$$E_{3,4} = \frac{A_o A_d}{f^2} \tau_{p1} (1-\eta_{p1}) N_{p1,\Delta\lambda}$$

$$E_{4,5} = \frac{A_o A_d}{f^2} (1-\eta_{p2}) N_{p2,\Delta\lambda}$$

(B26)

$$E_{5,6} = \begin{cases} 0, \text{ chopper open} \\ \dfrac{A_o A_d}{f^2} (1 - \eta_c) N_{c, \Delta\lambda}, \text{ chopper closed} \end{cases}$$

$$E_{6,5} = E_{6,7} = \frac{A_o A_d}{f^2} (1-\eta_{s1}) N_{s1, \Delta\lambda}$$

$$E_{7,6} = E_{7,8} = \frac{A_o A_d}{f^2} (1-\eta_{s2}) N_{s2, \Delta\lambda} \qquad \text{(B26) continued}$$

$$E_{8,9} = \frac{A_o A_d}{f^2} \tau_{s3} (N_{f, tot} - \tau_f N_{f, \Delta\lambda})$$

$$E_{9,10} = \frac{A_o A_d}{f^2} \tau_{s3} (1-\eta_{s3}) N_{s3, tot}$$

$$E_{10,11} = \frac{A_o A_d}{f^2} (1 - \eta_{s4}) N_{s4, tot}$$

$$E_{8,7} = \frac{A_o A_d}{f^2} \tau_{s2} (1 - \tau_f) N_{f, \Delta\lambda}$$

$$E_{9,8} = \frac{A_o A_d}{f^2} \tau_{s3} (1 - \eta_{s3}) N_{s3, \Delta\lambda}$$

$$E_{10,9} = \frac{A_o A_d}{f^2} (1-\eta_{s4}) N_{s4, \Delta\lambda}$$

CHOPPER OPEN

Consider first the case when the chopper is open. Then, from Equation (B21) for r = 1,

$$P_D^1 = \sum_{k=1}^{10} X_{k,11}^1 \left(1 - \sum_{q=1}^{10} \rho_{k,11,q}\right) \tag{B27}$$

Then $\rho_{k,11,q} = 0$ for all k and q from (B25) and from (B24) $X_{k,11}^1 = 0$ for $k \neq 10$. Equation (B27) then reduces to

$$P_D^1 = X_{10,11}^1 =$$

$$= \sum_{j=1}^{9} \left(E_{j,j+1} \prod_{i=j+1}^{10} \tau_i\right) + E_{10,11} =$$

$$= \frac{A_o A_d}{f^2} \left[N_{B,\Delta\lambda} \tau_p \eta_{p1} \eta_{p2} \eta_{s1} \eta_{s2} \tau_f \eta_{s3} \eta_{s4} + \right.$$

$$+ \tau_{p1} (1 - \eta_{p1}) N_{p1,\Delta\lambda} \eta_{p2} \eta_{s1} \eta_{s2} \tau_f \eta_{s3} \eta_{s4} + \tag{B28}$$

$$+ (1 - \eta_{p2}) N_{p2,\Delta\lambda} \eta_{s1} \eta_{s2} \tau_f \eta_{s3} \eta_{s4} +$$

$$+ (1 - \eta_{s1}) N_{s1,\Delta\lambda} \eta_{s2} \tau_f \eta_{s3} \eta_{s4} + \tau_{s2} (1 - \eta_{s2}) N_{s2,\Delta\lambda} \tau_f \eta_{s3} \eta_{s4} +$$

$$+ \tau_{s3} (N_{f,tot} - \tau_f N_{f,\Delta\lambda}) \eta_{s3} \eta_{s4} + \tau_{s3} (1 - \eta_{s3}) N_{s3,tot} \eta_{s4} +$$

$$\left. + (1 - \eta_{s4}) N_{s4,tot}\right]$$

For r = 2, from (B19) and (B23)

$$P_D^2 = \sum_{k=1}^{10} X_{k,11}^2 \left(1 - \sum_{q=1}^{10} \rho_{k,11,q}\right) = \sum_{k=1}^{10} X_{k,11}^2 = \sum_{k=1}^{9} X_{k,11}^2$$

$$= \sum_{k=1}^{9} (X_{k-1,k}^1 \rho_{k-1,k,11} + E_{k,11}) = 0 \qquad \text{(B29)}$$

as $\rho_{k-1,k,11} = 0$ and $E_{k,11} = 0$ for $k \neq 10$.

r = 3 gives

$$P_D^3 = \sum_{k=1}^{10} X_{k,11}^3 \left(1 - \sum_{q=1}^{10} \rho_{k,11,q}\right) = \sum_{k=1}^{10} X_{k,11}^3 =$$

$$= \sum_{k=1}^{10} \sum_{m=1}^{11} X_{m,k}^2 \rho_{m,k,11} = X_{9,10}^2 \rho_{9,10,11} = 0 \qquad \text{(B30)}$$

as $\rho_{m,k,11} \neq 0$ only when m = 9, k = 10, and $X_{9,10}^2 = 0$

Similarly,

$$P_D^r = 0 \quad \text{for } r = 4, 5, 6, \ldots \qquad \text{(B31)}$$

CHOPPER CLOSED

As in Equation (B28), for r = 1

$$\overline{P_D^1} = \sum_{j=1}^{9} \left(E_{j,j+1} \prod_{i=j+1}^{10} \tau_i\right) + E_{10,11} \qquad \text{(B32)}$$

But now $\tau_5 = 0$; therefore,

$$\overline{P_D^1} = \sum_{j=5}^{9} \left(E_{j,j+1} \prod_{i=j+1}^{10} \tau_i \right) + E_{10,11} =$$

$$= \frac{A_o A_d}{f^2} \left[(1 - \eta_c) N_{c,\Delta\lambda} \eta_{s1} \eta_{s2} \tau_f \eta_{s3} \eta_{s4} + \right.$$

$$+ (1 - \eta_{s1}) N_{s1,\Delta\lambda} \eta_{s2} \tau_f \eta_{s3} \eta_{s4} +$$

$$+ \tau_{s2} (1 - \eta_{s2}) N_{s2,\Delta\lambda} \tau_f \eta_{s3} \eta_{s4} +$$

$$+ \tau_{s3} (N_{f,tot} - \tau_f N_{f,\Delta\lambda}) \eta_{s3} \eta_{s4} +$$

$$\left. + \tau_{s3} (1 - \eta_{s3}) N_{s3,tot} \eta_{s4} + (1 - \eta_{s4}) N_{s4,tot} \right] \qquad \text{(B33)}$$

As in Equation (B29), for $r = 2$

$$\overline{P_D^2} = \sum_{k=1}^{10} X_{k,11}^2 \left(1 - \sum_{q=1}^{10} \rho_{k,11,q} \right) =$$

$$= \sum_{k=1}^{9} (X_{k-1,k}^1 \rho_{k-1,k,11} + E_{k,11}) = 0 \qquad \text{(B34)}$$

and

$$\overline{P_D^3} = 0$$

$$\vdots \qquad \text{(B35)}$$

$$\overline{P_D^7} = 0$$

$$\overline{P_D^8} = \sum_{k=1}^{10} X^8_{k,11}\left(1 - \sum_{q=1}^{10} \rho_{k,11,q}\right) = \sum_{k=1}^{10} X^8_{k,11} =$$

$$= \sum_{k=1}^{10}\sum_{\ell=1}^{11} X^7_{\ell,k}\,\rho_{\ell,k,11} = X^7_{9,10}\rho_{9,10,11} =$$

$$= \sum_{\ell=1}^{11} X^6_{\ell,9}\,\rho_{\ell,9,10}\rho_{9,10,11} = X^6_{8,9}\rho_{8,9,10}\rho_{9,10,11} =$$

$$= \ldots = X^3_{5,6}\rho_{5,6,7}\rho_{6,7,8}\rho_{7,8,9}\rho_{8,9,10}\rho_{9,10,11} =$$

$$= X^3_{5,6}\prod_{i=6}^{10}\tau_i = \sum_{\ell=1}^{11} X^2_{\ell,5}\,\rho_{\ell,5,6}\prod_{i=6}^{10}\tau_i = \qquad \text{(B36)}$$

$$= X^2_{6,5}\rho_{6,5,6}\prod_{i=6}^{10}\tau_i =$$

$$= (X^1_{5,5}\rho_{5,6,5} + E_{6,5})\rho_{6,5,6}\prod_{i=6}^{10}\tau_i =$$

$$= E_{6,5}\rho_{6,5,6}\prod_{i=6}^{10}\tau_i =$$

$$= \frac{A_o A_d}{f^2}(1 - \eta_{s1})\,N_{s1,\Delta\lambda}\,\eta_c\,\eta_{s1}\,\eta_{s2}\,\tau_f\,\eta_{s2}\,\eta_{s3}$$

as $\rho_{\ell,5,6} = 0$ for $\ell \neq 6$ and $\rho_{5,6,5} = 0$

For r = 9, 10, 11, 12, one gets in a similar fashion

$$\overline{P_D^9} = E_{7,6}\rho_{7,6,5}\rho_{6,5,6}\prod_{i=6}^{10}\tau_i =$$

$$= \frac{A_o A_d}{f^2}\tau_{s2}(1-\eta_{s2})N_{s2,\Delta\lambda}\eta_{s1}\eta_c\eta_{s1}\eta_{s2}\tau_f\eta_{s3}\eta_{s4} \tag{B37}$$

$$\overline{P_D^{10}} = E_{8,7}\rho_{8,7,6}\rho_{7,6,5}\rho_{6,5,6}\prod_{i=6}^{10}\tau_i =$$

$$= \frac{A_o A_d}{f^2}\tau_{s2}(1-\tau_f)N_{f,\Delta\lambda}\eta_{s2}\eta_{s1}\eta_c\eta_{s1}\eta_{s2}\tau_f\eta_{s3}\eta_{s4} \tag{B38}$$

$$\overline{P_C^{11}} = E_{9,8}\rho_{9,8,7}\rho_{8,7,6}\rho_{7,6,5}\rho_{6,5,6}\prod_{i=6}^{10}\tau_i =$$

$$= \frac{A_o A_d}{f^2}\tau_{s3}(1-\eta_{s3})N_{s3,\Delta\lambda}\tau_f\eta_{s2}\eta_{s1}\eta_c\eta_{s1}\eta_{s2}\tau_f\eta_{s3}\eta_{s4} \tag{B39}$$

$$\overline{P_D^{12}} = E_{10,9}\rho_{10,9,8}\rho_{9,8,7}\rho_{8,7,6}\rho_{7,6,5}\rho_{6,5,6}\prod_{i=6}^{10}\tau_i =$$

$$= \frac{A_o A_d}{f^2}(1-\eta_{s4})N_{s4,\Delta\lambda}\eta_{s3}\tau_f\eta_{s2}\eta_{s1}\eta_c\eta_{s1}\eta_{s2}\tau_f\eta_{s3}\eta_{s4} \tag{B40}$$

And

$$\overline{P_D^r} = 0 \text{ for } r = 13, 14, 15, \ldots \tag{B41}$$

DIFFERENCE, CHOPPER OPEN AND CHOPPER CLOSED

The difference ΔP_D between signal and the detector for chopper open and chopper closed is thus

$$\Delta P_D = P_D - \overline{P}_D = \sum_{r=1}^{\infty} (P_D^r - \overline{P_D^r}) = P_D^1 - \overline{P_D^1} - \overline{P_D^8} - \overline{P_D^9} - \overline{P_D^{10}} - \overline{P_D^{11}} - \overline{P_D^{12}} =$$

$$= \frac{A_o A_d}{f^2} [N_{B,\Delta\lambda} \tau_p \eta_{p1} \eta_{p2} \eta_{s1} \eta_{s2} \tau_f \eta_{s3} \eta_{s4} +$$

$$+ (1-\eta_{p1}) N_{p1,\Delta\lambda} \tau_{p1} \eta_{p2} \eta_{s1} \eta_{s2} \tau_f \eta_{s3} \eta_{s4} +$$

$$+ (1-\eta_{p2}) N_{p2,\Delta\lambda} \eta_{s1} \eta_{s2} \tau_f \eta_{s3} \eta_{s4} -$$

$$- (1-\eta_c) N_{c,\Delta\lambda} \eta_{s1} \eta_{s2} \tau_f \eta_{s3} \eta_{s4} - \qquad \text{(B42)}$$

$$- (1 - \eta_{s1}) N_{s1,\Delta\lambda} \eta_c \eta_{s1} \eta_{s2} \tau_f \eta_{s3} \eta_{s4} -$$

$$- \tau_{s2} (1 - \eta_{s2}) N_{s2,\Delta\lambda} \eta_{s1} \eta_c \eta_{s1} \eta_{s2} \tau_f \eta_{s3} \eta_{s4} -$$

$$- \tau_{s2} (1 - \tau_f) N_{f,\Delta\lambda} \eta_{s2} \eta_{s1} \eta_c \eta_{s1} \eta_{s2} \tau_f \eta_{s3} \eta_{s4} -$$

$$- \tau_{s3} (1 - \eta_{s3}) N_{s3,\Delta\lambda} \tau_f \eta_{s2} \eta_{s1} \eta_c \eta_{s1} \eta_{s2} \tau_f \eta_{s3} \eta_{s4} -$$

$$- (1 - \eta_{s4}) N_{s4,\Delta\lambda} \eta_{s3} \tau_f \eta_{s2} \eta_{s1} \eta_c \eta_{s1} \eta_{s2} \tau_f \eta_{s3} \eta_{s4}$$

Equation (B42) is the same as shown in Appendix C for the same configuration.

COMMENTS ON GENERAL ANALYTIC MODEL

As seen from Equations (B36) through (B41), the terms in Equation (B20) are not converging very fast; in fact $\overline{P_D^r} = 0$ for r = 2, 3, ..., 7, but for r =8, 9, ...12 $\overline{P_D^r} \neq 0$. This makes the model somewhat inconvenient to use, since the term r + 1 is not necessarily smaller than the preceding r:th term (for instance r = 7 in this example). However, the model may be useful for computer application if some rule is used for how many terms P_D^r to use. For computerization, Equations (B20) through (B24) are programmed and the parameters (B25) and (B26) are the input parameters. Thus, it is not necessary to write down the long expressions for P_D, $\overline{P}_D$, or ΔP_D to get P_D, $\overline{P}_D$, or ΔP_D once the input parameters are given.

It may be possible to derive a general model that is converging faster than the present one. The method would probably be to build into the model more of the "serial" structure similar to the expression for $X^1_{p,m}$ in Equation (B24), but at the same time include the parallel structure of Equations (B22) and (B23). As seen from Equation (B22), each reflection (or scattering or transmission) generates a higher order X^r_{mn} and, therefore, radiation emitted from for instance the first secondary mirror onto the closed chopper, where it is reflected into the functional path, hits the detector as a eighth order term.

A model that may be correct, and if so certainly is converging faster, is the following:

$$P_D = \sum_{r=1}^{\infty} P_D^r$$

$$P_D^r = \sum_{k=1}^{N-1} X^r_{k,N} \left(1 - \sum_{q=1}^{N-1} \rho_{k,N,q}\right)$$

$$X^{2r}_{m,n} = \begin{cases} X^{2r-1}_{m+1,m}\ \rho_{m+1,m,m+1} & ;\ n = m+1 \\ X^{2r-1}_{m-1,m}\ \rho_{m-1,m,m-1} & ;\ n = m-1 \\ X^{2r-1}_{m-1,m}\ \rho_{m-1,m,n} + X^{2r-1}_{m+1,m}\ \rho_{m+1,m,n} & ;\ \begin{cases} n \neq m+1 \\ n \neq m-1 \end{cases} \end{cases}$$

$$X^{2r-1}_{n,\ell} = \begin{cases} \sum_{m=1}^{\ell-2} \left(X^{2r-2}_{m,m+1} \prod_{i=m+1}^{\ell-1} \tau_i \right) + \sum_{\substack{m=1 \\ m\neq\ell-2}}^{N} X^{2r-2}_{m,\ell-1}\, \rho_{m,\ell-1,\ell}; & n = \ell-1 \\ \sum_{m=\ell+2}^{N} \left(X^{2r-2}_{m,m+1} \prod_{i=\ell+1}^{m-1} \tau_i^1 \right) + \sum_{\substack{m=1 \\ m\neq\ell+2}}^{N} X^{2r-2}_{m,\ell+1}\, \rho_{m,\ell+1,\ell} & ; n = \ell+1 \\ \sum_{m=1}^{N} X^{2r-2}_{m,n}\, \rho_{m,n,\ell} & ; \begin{cases} n \neq \ell-1 \\ n \neq \ell+1 \end{cases} \end{cases}$$

$$X^{2}_{m,n} = \begin{cases} X^{1}_{n,n-1}\, \rho_{n,n-1,n} & ; \ m = n-1 \\ X^{1}_{n,n+1}\, \rho_{n,n+1,n} & ; \ m = n+1 \\ X^{1}_{m-1,m}\, \rho_{m-1,m,n} + X^{1}_{m+1,m}\, \rho_{m+1,m,n} + E_{m,n} & ; \begin{cases} m \neq n-1 \\ m \neq n+1 \end{cases} \end{cases}$$

$$X^{1}_{p,m} = \begin{cases} \sum_{j=1}^{m-2} \left(E_{j,j+1} \prod_{i=j+1}^{m-1} \tau_i \right) + E_{m-1,m} & ; \ p = m-1 \\ E_{m+1,m} + \sum_{j=m+2}^{N} \left(E_{j,j-1} \prod_{i=m+1}^{j-1} \tau_i \right) & ; \ p = m+1 \\ 0 & ; \begin{cases} p = m+1 \\ p \neq m-1 \end{cases} \end{cases}$$

The main feature of this modified model is that the serial structure is built into the odd terms and "reversals" are built into the even terms (a reversal occurs for instance at the chopper when the radiation from elements behind the chopper is reflected back into the functional path and finally hits the detector).

This modified model has not been checked out very carefully (e. g., so terms are not accounted for several times or are not accounted for at all).

APPENDIX C
SPECIFIC CONFIGURATION ANALYTICAL MODELS

APPENDIX C

SPECIFIC CONFIGURATION ANALYTICAL MODELS

In the early stage of ARRS, analytical modeling of specific configurations was performed only for radiance propagation; error propagation was to be defined later. This appendix presents the equations describing radiance propagation for each of the specific configurations analyzed. These configurations encompass

- All-refractive systems
- All-reflective systems
- Refracto-reflective systems
- Reflecto-refractive systems.

In conducting this portion of the overall study, it was found that every system could be represented in a generalized form that expressed the signal difference ΔF at the detector input; that is, the flux difference experienced by the chopper-open and the chopper-closed operation modes in terms of the input flux, originating from the target scene, and the flux contributions from the various optical elements in the direct- and indirect-radiation propagation chains.

This generalization approach revealed that the signal difference ΔF at the detector surface can be expressed as an aggregate of terms depending on the temperature and on the optical constants of the particular design elements to be taken into consideration. In a general form, this aggregate is given by

$$\Delta F = F_i + \sum_j \text{(direct components of primary optics)} - \sum_k \text{(direct chopper component + indirect components of secondary optics)}$$

In every component, F_j and F_k, the temperature dependence is primarily expressed by the surface radiances N_j and N_k, respectively, although some of the optical constants appearing as multiplicative factors also may show a temperature dependence. Beside an overall design constant, some of the multiplicative factors encountered are common to all flux contributors and therefore may be expressed by a single efficiency factor η_o. The remaining multiplicative factors belong to particular radiating surfaces and may be lumped together into efficiencies η_j and η_k, respectively. In this manner, one obtains

$$\Delta F = K \eta_o \left[\eta_i N_i + \sum_j \eta_j N_j - \sum_k \eta_k N_k \right]$$

where

$$K = \frac{A_o A_d}{f^2}$$

A_o = radiometer aperture area

A_d = detector surface area

f = effective radiometer focal length

The goal of the radiometric measurements is the determination of the horizon's radiance; that is, the input radiance N_i, which, however, must be corrected certainly for atmospheric attenuation, is to be expressed by measured and calculated quantities

$$N_i = \frac{1}{\eta_i}\left(\frac{\Delta F}{K\eta_o} - \sum_j \eta_j N_j + \sum_k \eta_k N_k\right)$$

The measured quantity, ΔF is subject to measurement and data processing errors. Values N_j, N_k are calculated, temperature-dependent quantities and are subject to computational errors and to uncertainties in determining the temperatures involved. The symbol K is for an overall design parameter that can be considered independent of specific configurations. The expression η_o, η_j on one hand and η_i, η_k on the other are products of optical constants pertaining to the primary and secondary optics, respectively. The number of terms in these products corresponds to the number of optical elements involved; for this reason, the efficiencies are configuration dependent.

Configuration dependence of N_i does not allow drawing general conclusions on the significance of the particular flux contributors. However, it certainly is possible to obtain numberically upper and lower limits for the flux contributions if reasonable values for the optical constants are assumed.

The schematic representation of any radiometer design indicates the presence of a number of curved and flat surfaces which supposedly radiate according to Lambert's law. If replacement of these surfaces by their projections into the planes through their apices is allowed, one encounters a situation similar to that shown in Figure C1. In this figure, the detector, A_d, is located at the effective focal distance, $d_1 = f$, of the total system from the apex of the first optical element. For simplification, restricting the consideration to three surfaces of equal efficiency (reflectivity or transmissivity), one obtains

$$F = (1-\eta)\eta^2 A_1 N_1 A_d/f^2 + (1-\eta)\,\eta A_2 N_2 A_d/d_2^2 + (1-\eta)\,A_3 N_3 A_d/d_3^2$$

However,

$$A_1/f^2 = A_2/d_2^2 = A_3/d_3^2$$

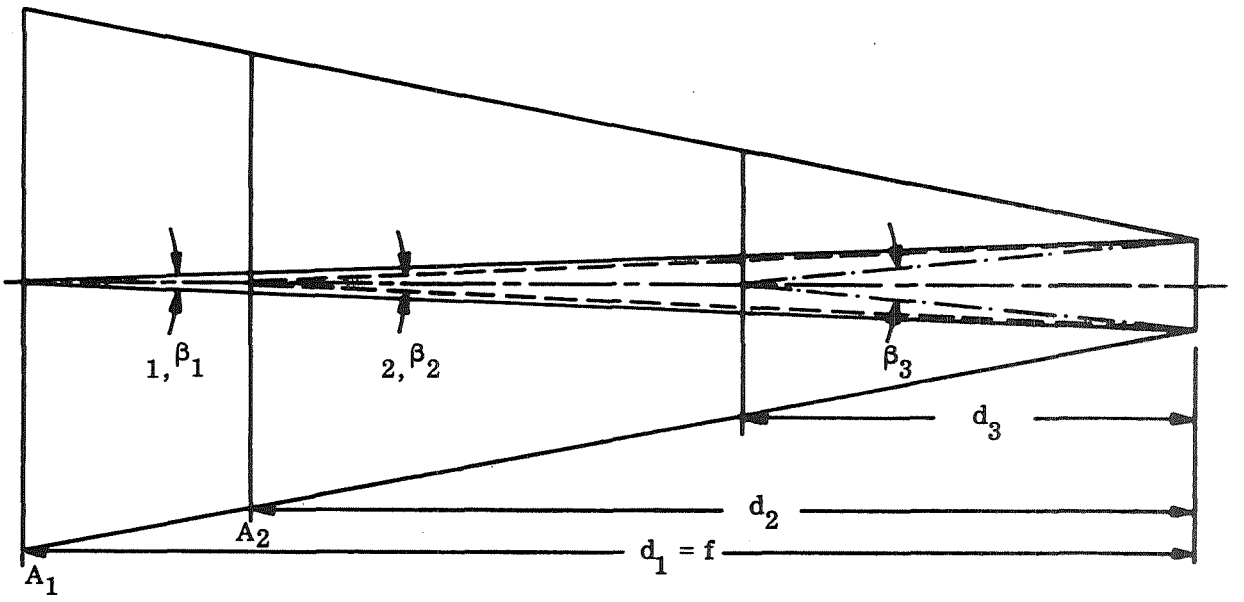

Figure C1. Simplified Situation Encountered in Deriving the Flux Falling on the Detector

Hence

$$F = \frac{A_1 A_d}{f^2} \left[(1 - \eta)\, \eta^2 N_1 + (1 - \eta) N_2 + (1 - \eta)\, N_3 \right]$$

However, it is to be noticed that the factor A_1/f^2, representing a solid angle, is only an approximation that holds for small view angles; it must be replaced by the true solid angle subtended at the detector by the cold stop as described in the next subsection. Nevertheless, the following derivations make use of the approximation

$$\Omega = A_o/f^2$$

where

A_o = entrance aperture area of the radiometer

f = effective focal length of the radiometer

ALL-REFRACTIVE SYSTEM

Without restricting the generality, an all-refractive radiometer concept, including a lowpass filter in front of the collector optics, is shown in Figure C2 where only a single-element optical component for the collector and the relay optics' collimator and concentrator are employed.

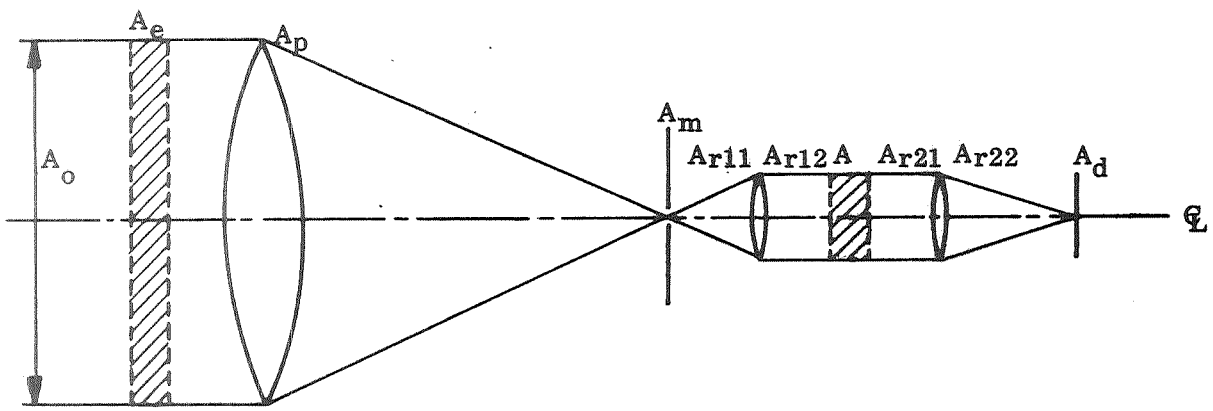

A_o = radiometer aperture area

A_e = low-pass filter area

A_p = collector optics' last surface area

Figure C2. Schematic of an All-Dioptric Radiometer Design

A_m, A_b = radiating surfaces of chopper and bandpass filter, respectively

A_{r11}, A_{r21} = relay optics' collimator and concentrator first surface areas, respectively

A_{r12}, A_{r22} = relay optics' collimator and concentrator last surface areas, respectively

A_d = detector area

℄ = optical axis

One obtains easily

$$F_i = \frac{A_o A_d}{f^2} \tau_1 \tau_p \tau_{r_1} \tau_f \tau_{r_2} N_{i,\Delta\lambda} = \text{input signal from absolute apparent radiance}$$

where

τ_1 = lowpass-filter transmission factor, obtained from both surface reflective ρ_1 and absorptivity α_1; ρ_1 may be very close to unity and, therefore, negligible in defining the emissivity $\epsilon_1 = 1-\tau_1$

τ_p = primary-optics transmission factor, reflecting surface reflectivity ρ_p and absorptivity α_p; ρ_p may be not close to unity such that the emissivity becomes $\epsilon_p = 1 - \tau_p - \rho_p = \alpha_p = 1 - \beta_p$

τ_{r1}, τ_{r2} = secondary optics transmission factors from (ρ_{r1}, α_{r1}); (ρ_{r2}, α_{r2})i for reasons as in τ_p, the emissivity must be defined by $\epsilon_{r1} = (1-\tau_{r1}-\rho_{r1}) = 1-\beta_{r1}$ and $\epsilon_{r2} = (1-\tau_{r2}-\rho_{r2}) = 1-\beta_{r2}$

τ_b = bandpass-filter transmission factor, as referred to ρ_b and α_b; arguing as in τ_1, one may define $\epsilon_b = (1-\tau_b)$

$$F_1 = \frac{A_o A_d}{f^2} (1-\tau_1) \tau_p \tau_{r1} \tau_f \tau_{r2} N_{1,\Delta\lambda} = \text{lowpass-filter flux contribution}$$

$$F_p = \frac{A_o A_d}{f^2} (1-\beta_p) \tau_{r1} \tau_f \tau_{r2} N_{p,\Delta\lambda} = \text{primary-optics flux contribution}$$

Direct radiation components (chopper-open and chopper-closed operation)

$$F_{r1} = \frac{A_o A_d}{f^2} (1-\beta_{r1}) \tau_b \tau_{r2} N_{r1,\Delta\lambda} = \text{secondary optics collimator contribution}$$

$$F_b = \frac{A_o A_d}{f^2} (1-\tau_b) \tau_{r2} N_{b,\Delta\lambda} = \text{bandpass-filter contribution}$$

$$F_{r2} = \frac{A_o A_d}{f^2} (1-\beta_{r2}) N_{r2,\Delta\lambda} = \text{secondary-optics-concentrator contribution}$$

Indirect-radiation components (chopper-closed operation only)

$$F_m' = \frac{A_o A_d}{f^2} (1 - \eta_m) \tau_{r1} \tau_b \tau_{r2} N_{m, \Delta\lambda} = \text{chopper flux contribution}$$

where

η_m = chopper reflectivity

$$F_{r1}' = \frac{A_o A_d}{f^2} (1 - \beta_{r1}) \eta_m \tau_{r1} \tau_b \tau_{r2} N_{r1, \Delta\lambda}$$

$$F_b' = \frac{A_o A_d}{f^2} (1 - \tau_b) \tau_{r1} \eta_m \tau_{r1} \tau_b \tau_{r2} N_{b, \Delta\lambda}$$

$$F_{r2}' = \frac{A_o A_d}{f^2} (1 - \beta_{r2}) \tau_b \tau_{r1} \tau_m \tau_{r1} \tau_b \tau_{r2} N_{r2, \Delta\lambda}$$

Chopper-open operation

$$F = F_i + F_l + F_p + F_{r1} + F_b + F_{r2}$$

Chopper-closed operation

$$\overline{F} = \left(F_m' + F_{r1}' + F_b' + F_{r2}'\right) + \left(F_{r1} + F_b + F_{r2}\right)$$

Signal difference

$$\Delta F = F - \overline{F} = F_i + F_l + F_p - F_m' - F_{r1}' - F_b' - F_{r2}'$$

In explicit form, this yields

$$\Delta F = \frac{A_o A_d}{f^2} \tau_{r1} \tau_b \tau_{r2} \left\{ \tau_l \tau_p N_{i, \Delta\lambda} + \left[(1 - \tau_l) \tau_p N_{l, \Delta\lambda} + (1 - \beta_p) N_{p, \Delta\lambda} - (1 - \eta_m) N_{m, \Delta\lambda} \right] - \eta_m \left[(1 - \beta_{r1}) N_{r1, \Delta\lambda} + (1 - \tau_b) \tau_{r1} N_{b, \Delta\lambda} + (1 - \beta_{r2}) \tau_b \tau_{r1} N_{r2, \Delta\lambda} \right] \right\}$$

Now, it is supposed that lowpass-filter, collector optics and chopper are at the same temperature level, and that simultaneously relay optics and bandpass filter are operated at another common temperature. For simplification, it may be assumed also that $\alpha_{r1} \approx \alpha_{r2} = \alpha_r$, and $\tau_{r1} \approx \tau_{r2} = \tau_r$. Then, one obtains specifically

$$\Delta F = \frac{A_o A_d}{f^2} \tau_b \tau_r^2 \left\{ \tau_l \tau_p N_{i,\Delta\lambda} + \left[\tau_p (1 - \tau_l) + (\eta_m - \beta_p) \right] N_{p,\Delta\lambda} - \eta_m \left[(1 - \beta_r) + \tau_r (1 - \tau_b \beta_r) \right] N_{r,\Delta\lambda} \right\}$$

ALL-REFLECTIVE SYSTEMS

The first catoptric (all Cassegraninian) system considered is shown schematically in Figure C3 which does not account for mounting structures of the collector optics second element and the chopper, nor for the radiometer-calibration unit. Although these design components will more or less affect the receivable signal, they are not considered essential at this moment.

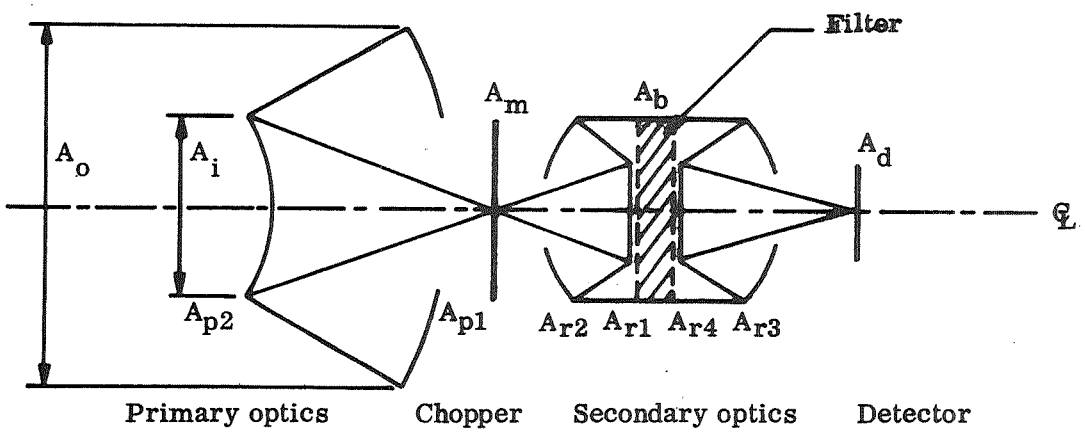

Figure C3. Schematic of a Catoptric Radiometer Design

NOTATIONS

A_o, A_i = outer and inner diameter areas of annular aperture

A_{p1}, A_{p2} = radiating areas of primary optics' first and second elements, respectively

$A_{r1}, \ldots\ldots A_{r4}$ = radiating areas of secondary optics' first through fourth elements

A_m, A_b = radiating areas of chopper and filter, respectively

A_d = detector area

$\mathcal{L}$ = optical axis

One obtains for both operation conditions, chopper open and chopper closed.

Chopper Open

Input signal from absolute apparent radiance is

where

$\tau_a = 1 - A_i/A_o$ = annular correction factor

τ_b = bandpass-filter transmission factor

ρ = reflectivities of primary and secondary elements

Signals from mirror and filter radiances are

$$F_{p1} = \frac{A_o A_d}{f^2} \tau_a (1 - \rho_{p1}) \rho_{p2} \rho_{r1} \rho_{r2} \tau_b \rho_{r3} \rho_{r4} N_{p1, \Delta\lambda}$$

A_{p1} = projected area of $A_{p1} \approx \tau_a A_o$

$$F_{p2} = \frac{A_o A_d}{f^2} (1 - \rho_{p2}) \rho_{r1} \rho_{r2} \tau_b \rho_{r3} \rho_{r4} N_{p2, \Delta\lambda}$$

$$F_{r1} = \frac{A_o A_d}{f^2} (1 - \rho_{r1}) \rho_{r2} \tau_p \rho_{r3} \rho_{r4} N_{r1, \Delta\lambda}$$

$$F_{r2} = \frac{A_o A_d}{f^2} \tau_{r2} (1 - \rho_{r2}) \tau_p \rho_{r3} \rho_{r4} N_{r2, \Delta\lambda}$$

where

$\tau_{r2} = 1 - A_{r1}'/A_{r2}'$

A_{r1}', A_{r2}' = projected areas of A_{r1} and A_{r2}, respectively

To determine the flux contribution of the filter, it is assumed that the filter absorbs completely outside the transmission region $\Delta\lambda$. It must be noted that the filter surface is obscured by the mirror surface A_{r4}. One gets

$$F_b = \frac{A_o A_d}{f^2}\Big[\tau_{r3}(1-\tau_b)\rho_{r3}\rho_{r4}N_{b,\Delta\lambda} + \tau_{r3}\rho_{r3}\rho_{r4}N_{b,\ 0\ \text{to}\ \lambda_1} + \tau_{r3}\rho_{r3}\rho_{r4}N_{b,\ \lambda_1\ \text{to}\ \lambda_2} + \tau_{r3}\rho_{r3}\rho_{r4}N_{b,\ \lambda_2\ \text{to}\ \lambda_c} - \tau_{r3}\rho_{r3}\rho_{r4}N_{b,\ \lambda_1\ \text{to}\ \lambda_2}\Big]$$

$$= \frac{A_o A_d}{f^2}\tau_{r3}\rho_{r3}\rho_{r4}\Big[N_{b,\Delta\lambda}' - \tau_b N_{b,\Delta\lambda}\Big]$$

where

$$\tau_{r3} = 1 - A_{r4}'/A_{r3}'$$

$$F_{r3} = \frac{A_o A_d}{f^2}(1-\rho_{r3})\rho_{r4}N_{r3,\Delta\lambda}'$$

$$F_{r4} = \frac{A_o A_d}{f^2}(1-\rho_{r4})N_{r4,\Delta\lambda}'$$

Hence

$$F = (F_i + F_{p1} + F_{p2}) + (F_{r1} + F_{r2} + F_b + F_{r3} + F_{r4})$$

Chopper Closed

Signal from chopper with reflectivity ρ_m is

$$\overline{F}_m = \frac{A_o A_d}{f^2}(1-\rho_m)\rho_{r1}\rho_{r2}\tau_b\rho_{r3}\rho_{r4}N_{m,\Delta\lambda}$$

The signals from all other surfaces consist always of two components:

- The "direct" component of the radiation passes through all elements behind the surface under consideration
- The "indirect" component passes first through all elements in front of the surface considered, is reflected at the chopper, and then passes through the total relay optics

Thus, one obtains

$$\bar{F}_{r1} = \frac{A_o A_d}{f^2}\Big[(1-\rho_{r1})\,\rho_{r2}\,\tau_b\,\rho_{r3}\,\rho_{r4}\,N_{r1,\Delta\lambda} + (1-\rho_{r1})\,\rho_m\rho_{r1}\,\rho_{r2}\,\tau_b\,\rho_{r3}\,\rho_{r4}\,N_{r1,\Delta\lambda}\Big]$$

$$\bar{F}_{r2} = \frac{A_o A_d}{f^2}\Big[\tau_{r2}\,(1-\rho_{r2})\,\tau_b\,\rho_{r3}\,\rho_{r4}\,N_{r2,\Delta\lambda} + \tau_{r2}\,(1-\rho_{r2})\,\rho_{r1}\,\rho_m\rho_{r1}\,\rho_{r2}\,\tau_b\,\rho_{r3}\,\rho_{r4}\,N_{r2,\Delta\lambda}\Big]$$

$$\bar{F}_b = \frac{A_o A_d}{f^2}\Big[\tau_{r3}\,\rho_{r3}\,\rho_{r4}\,(N_{b,\Delta\lambda'} - \tau_b N_{b,\Delta\lambda}) + \tau_{r2}\,(1-\tau_b)\,\rho_{r2}\,\rho_{r1}\,\rho_m\rho_{r1}\,\rho_{r2}\,\tau_b\,\rho_{r3}\,\rho_{r4}\,N_{b,\Delta\lambda}\Big]$$

$$\bar{F}_{r3} = \frac{A_o A_d}{f^2}\Big[\tau_{r3}\,(1-\rho_{r3})\,\rho_{r4}\,N_{r3,\Delta\lambda'} + \tau_{r3}\,(1-\rho_{r3})\,\tau_b\,\rho_{r2}\,\rho_{r1}\,\rho_m\rho_{r1}\,\rho_{r2}\,\tau_b\,\rho_{r3}\,\rho_{r4}\,N_{r3,\Delta\lambda}\Big]$$

$$\bar{F}_{r4} = \frac{A_o A_d}{f^2}\Big[(1-\rho_{r4})\,N_{r4,\Delta\lambda'} + (1-\rho_{r4})\,\rho_{r3}\,\tau_b\,\rho_{r2}\,\rho_{r1}\,\rho_m\rho_{r1}\,\rho_{r2}\,\tau_b\,\rho_{r3}\,\rho_{r4}\,N_{r4,\Delta\lambda}\Big]$$

Hence

$$\bar{F} = \bar{F}_m + (F_{r1} + F_{r2} + F_b + F_{r3} + F_{r4}) + \Sigma \text{ indirect components}$$

Signal Difference

Defining the signal difference by

$$\Delta F = F - \bar{F} = F_i + F_{p1} + F_{p2} - \bar{F}_m - \Sigma \text{ indirect components}$$

one obtains generally

$$\begin{aligned} F = \frac{A_o A_d}{f^2} \Big[& \tau_p \rho_{p1} \rho_{p2} \rho_{r1} \rho_{r2} \tau_b \rho_{r3} \rho_{r4} N_{i,\Delta\lambda} \\ & + \tau_a (1 - \rho_{p1}) \rho_{p2} \rho_{r1} \rho_{r2} \tau_b \rho_{r3} \rho_{r4} N_{p1,\Delta\lambda} \\ & + (1 - \rho_{p2}) \rho_{r1} \rho_{r2} \tau_b \rho_{r3} \rho_{r4} N_{p2,\Delta\lambda} \\ & - (1 - \rho_m) \rho_{r1} \rho_{r2} \tau_b \rho_{r3} \rho_{r4} N_{m,\Delta\lambda} \\ & - (1 - \rho_{r1}) \rho_m \rho_{r1} \rho_{r2} \tau_b \rho_{r3} \rho_{r4} N_{r1,\Delta\lambda} \\ & - \tau_{r2} (1 - \rho_{r2}) \rho_{r1} \rho_m \rho_{r1} \rho_{r2} \tau_b \rho_{r3} \rho_{r4} N_{r2,\Delta\lambda} \\ & - \tau_{r2} (1 - \tau_b) \rho_{r2} \rho_{r1} \rho_m \rho_{r1} \rho_{r2} \tau_b \rho_{r3} \rho_{r4} N_{b,\Delta\lambda} \\ & - \tau_{r3} (1 - \rho_{r3}) \tau_b \rho_{r2} \rho_{r1} \rho_m \rho_{r1} \rho_{r2} \tau_b \rho_{r3} \rho_{r4} N_{r3,\Delta\lambda} \\ & - (1 - \rho_{r4}) \rho_{r3} \tau_b \rho_{r2} \rho_{r1} \rho_m \rho_{r1} \rho_{r2} \tau_b \rho_{r3} \rho_{r4} N_{r4,\Delta\lambda} \Big] \end{aligned}$$

Assuming now

$$\rho_{p1} = \rho_{p2} = \rho_p$$

$$\rho_{r1} = \rho_{r2} = \rho_{r3} = \rho_{r4} = \rho_r$$

$$\tau_{r2} = \tau_{r3} = \tau_r$$

$$N_{p1,\Delta\lambda} = N_{p2,\Delta\lambda} = N_{m,\Delta\lambda} = N_{p,\Delta\lambda}$$

$$N_{r1,\Delta\lambda} = N_{r2,\Delta\lambda} = N_{b,\Delta\lambda} = N_{r3,\Delta\lambda} = N_{r4,\Delta\lambda} = N_{r,\Delta\lambda}$$

One has specifically

$$\Delta F = \frac{A_o A_d}{f^2} \left\{ \tau_a \tau_b \rho_p^2 \rho_r^4 N_{i,\Delta\lambda} + \tau_b \rho_r^4 \left[(1 - \rho_p)(1 + \tau_a \rho_p) - (1 - \rho_m) \right] N_{p,\Delta\lambda} - \tau_b \rho_r^4 \rho_m \left[(1 - \rho_r)(1 + \tau_r \rho_r + \tau_b \tau_r \rho_r^2 + \tau_b \rho_r^3) + (1 - \tau_b) \tau_r \rho_r^2 \right] N_{r,\Delta\lambda} \right\}$$

$$= \frac{A_o A_d}{f^2} \tau_b \rho_r^4 \left\{ \tau_a \rho_p^2 N_{i,\Delta\lambda} + \left[(1 - \rho_p) \tau_a \rho_p - (\rho_p - \rho_m) \right] N_{p,\Delta\lambda} - \rho_m \left[(1 - \rho_r)(1 + \tau_r \rho_r + \tau_b \tau_r \rho_r^2 + \tau_b \rho_r^3) + (1 - \tau_b) \tau_r \rho_r^2 \right] N_{r,\Delta\lambda} \right\}$$

Another type of a catoptric radiometer design is the common Newtonian system illustrated schematically in Figure C4. This system is quite similar to the Cassegrainian system insofar as the Cassegrainian's second element, a curved surface, is replaced by a folding, flat mirror. This special feature permits the determination of this second elements "form factor": If the beam folding angle is denoted by 2ϕ, one has a form factor of $\sec\phi$; that is, one obtains

$$A_{p2} = A_{p2'} \sec\phi = A_i \sec\phi$$

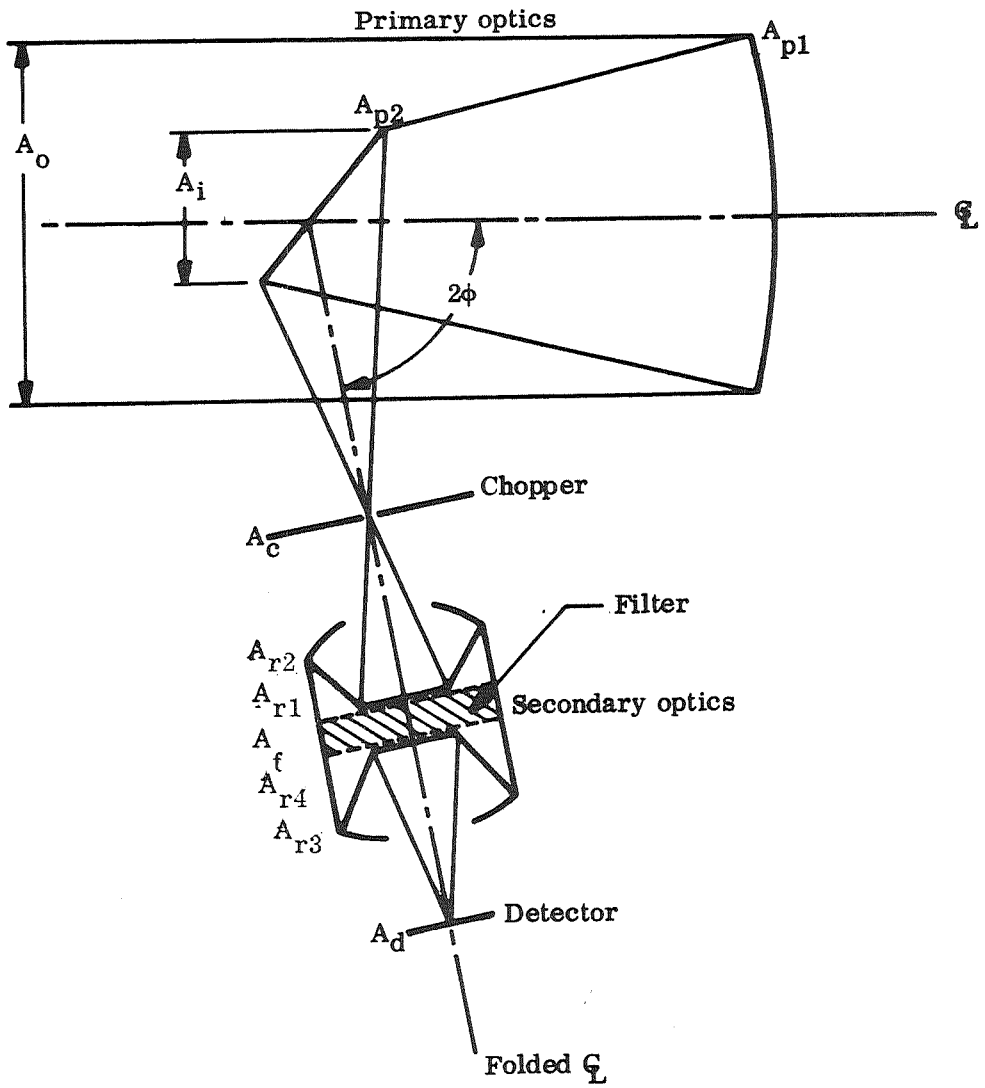

Notations as in Figure C3.

Figure C4. Schematic of a Newtonian Radiometer Design

The primary-optics first element must not necessarily have a hole in its center portion; therefore, one may define a transmission factor τ_{p1} within the range of $\tau_a \leq \tau_{p1} \leq 1$ where $\tau_a = 1 - A_i/A_o$. Since nothing else was changed in the design, the general result becomes

$$\Delta F = \frac{A_o A_d}{f^2} \Big[\tau_a \rho_{p1} \rho_{p2} \rho_{r1} \rho_{r2} \tau_b \rho_{r3} \rho_{r4} N_{i,\Delta\lambda}$$

$$+ \tau_{p1} (1 - \rho_{p1}) \rho_{p2} \rho_{r1} \rho_{r2} \tau_b \rho_{r3} \rho_{r4} N_{p1,\Delta\lambda}$$

$$+ \sec\phi\, (1 - \rho_{p2}) \rho_{r1} \rho_{r2} \tau_b \rho_{r3} \rho_{r4} N_{p2,\Delta\lambda}$$

$$- (1 - \rho_m) \rho_{r1} \rho_{r2} \tau_b \rho_{r3} \rho_{r4} N_{m,\Delta\lambda}$$

$$- (1 - \rho_{r1}) \rho_m \rho_{r1} \rho_{r2} \tau_b \rho_{r3} \rho_{r4} N_{r1,\Delta\lambda}$$

$$- \tau_{r2} (1 - \rho_{r2}) \rho_{r1} \rho_m \rho_{r1} \rho_{r2} \tau_b \rho_{r3} \rho_{r4} N_{r2,\Delta\lambda}$$

$$- \tau_{r2} (1 - \tau_b) \rho_{r2} \rho_r \rho_m \rho_{r1} \rho_{r2} \tau_b \rho_{r3} \rho_{r4} N_{b,\Delta\lambda}$$

$$- \tau_{r3} (1 - \rho_{r3}) \tau_b \rho_{r2} \rho_{r1} \rho_m \rho_{r1} \rho_{r2} \tau_b \rho_{r3} \rho_{r4} N_{r3,\Delta\lambda}$$

$$- (1 - \rho_{r4}) \rho_{r3} \tau_b \rho_{r2} \rho_{r1} \rho_m \rho_{r1} \rho_{r2} \tau_b \rho_{r3} \rho_{r4} N_{r4,\Delta\lambda} \Big]$$

Specifically, with $\phi = \pi/4$ and the assumptions of $\rho_p, \rho_r, \tau_r, N_{p,\Delta\lambda}, N_{r,\Delta\lambda}$ mentioned above, one obtains

$$\Delta F = \frac{A_o A_d}{f^2} \tau_b \rho_r^4 \Big\{ \tau_a \rho_p^2 N_{i,\Delta\lambda}$$

$$+ \Big[(1 - \rho_p) (\tau_{p1} \rho_p + \sqrt{2}) - (1 - \rho_m) \Big] N_{p,\Delta\lambda}$$

$$- \rho_m \Big[(1 - \rho_r) (1 + \tau_r \rho_r + \tau_b \tau_r \rho_r^2 + \tau_b \rho_r^3) + (1 - \tau_b) \tau_r \rho_r^2 \Big] N_{r,\Delta\lambda} \Big\}$$

The last catoptric radiometer design considered concerns an off-axis paraboloidal collector optics and a two-element, off-axis paraboloidal configuration for the relay optics. This design is shown schematically in Figure C5 with the paraboloids approximated by spheres for simplification.

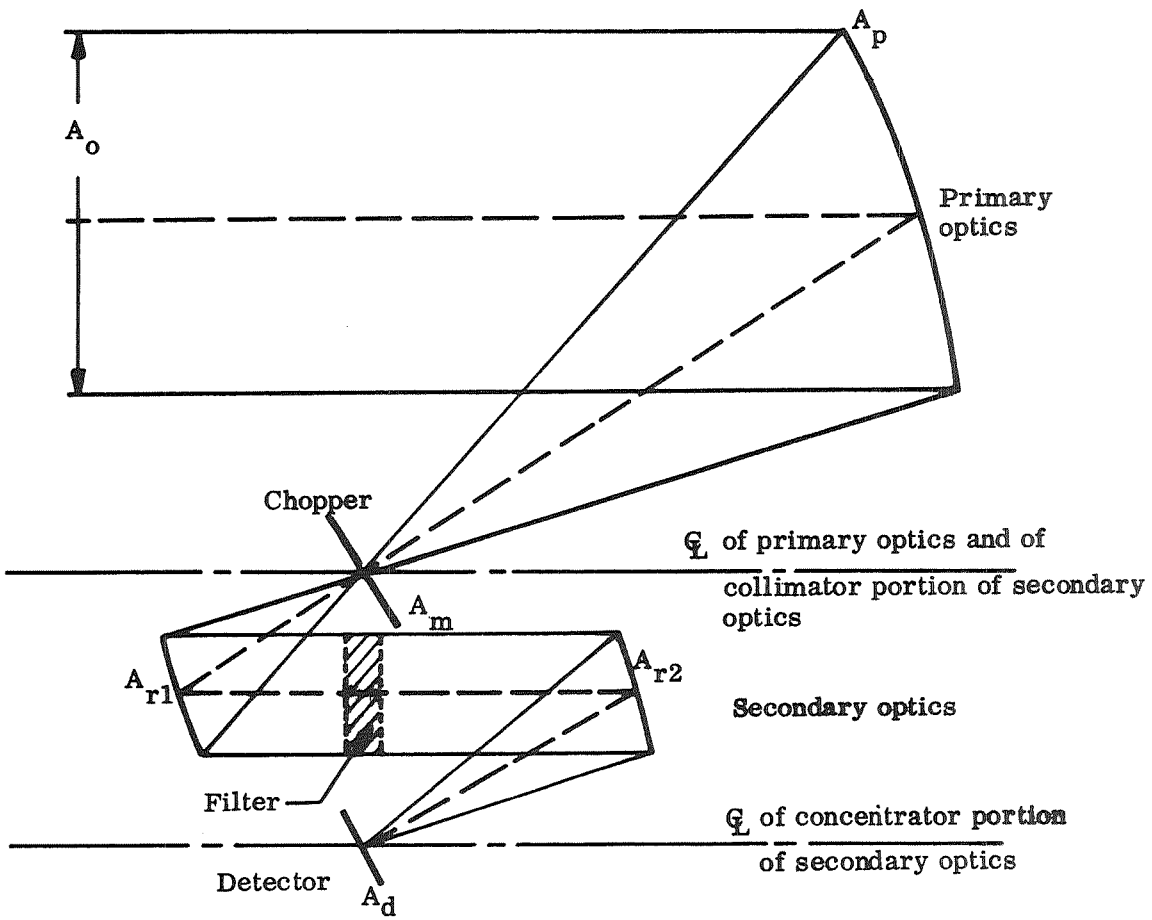

Notations as in Figure C3.

Figure C5. Schematic of an Off-Axis Paraboloidal Radiometer Design

The signal difference components are:

$$F_i = \frac{A_o A_d}{f^2} \rho_p \rho_{r1} \tau_b \rho_{r2} N_{i,\Delta\lambda}$$

$$F_p = \frac{A_o A_d}{f^2} (1 - \rho_p) \rho_{r1} \tau_b \rho_{r2} N_{p,\Delta\lambda}$$

$$F_m = \frac{A_o A_d}{f^2} (1 - \rho_m) \rho_{r1} \tau_b \rho_{r2} N_{m,\Delta\lambda}$$

$$\bar{F}_{r1} = \frac{A_o A_d}{f^2} (1 - \rho_{r1} \rho_m \rho_{r1} \tau_b \rho_{r2} N_{r1,\Delta\lambda}$$

$$\bar{F}_b = \frac{A_o A_d}{f^2} (1 - \tau_b) \rho_{r1} \rho_m \rho_n \tau_b \rho_{r2} N_{b,\Delta\lambda}$$

$$\bar{F}_{r2} = \frac{A_o A_d}{f^2} (1 - \rho_{r2}) \tau_b \rho_{r1} \rho_m \rho_{r1} \tau_b \rho_{r2} N_{r2,\Delta\lambda}$$

Hence, in general

$$\Delta F = \frac{A_o A_d}{f^2} \rho_{r1} \tau_b \rho_{r2} \left[\rho_p N_{i,\Delta\lambda} + (1 - \rho_p) N_{p,\Delta\lambda} - (1 - \rho_m) N_{m,\Delta\lambda} \right.$$
$$- (1 - \rho_{r1}) \rho_m N_{r1,\Delta\lambda} - (1 - \tau_b) \rho_{r1} \rho_m N_{b,\Delta\lambda}$$
$$\left. - (1 - \rho_{r2}) \tau_b \rho_{r1} \rho_m N_{r2,\Delta\lambda} \right]$$

Specifically, therefore, with the assumptions of ρ_p, ρ_r, $N_{p,\Delta\lambda}$, $N_{r,\Delta\lambda}$ used earlier, one has

$$F = \frac{A_o A_f}{f^2} \tau_b \rho_r^2 \left\{ \rho_p N_{i,\Delta\lambda} - (\rho_p - \rho_m) N_{p,\Delta\lambda} \right.$$
$$\left. - \rho_m \left[(1 - \rho_r)(1 + \tau_b \rho_r) + (1 - \tau_b) \rho_r \right] N_{r,\Delta\lambda} \right\}$$

A lowpass filter inserted into the light path of the primary optics and traversed only once constitutes an additional radiation source which may contribute an appreciable amount to the receivable flux difference. If τ_ℓ is the transmissivity of this lowpass filter and A_ℓ is its effective area, then one obtains generally

- Cassegrainian and Newtonian radiometer design

$$F_\ell = \frac{A_o A_\ell}{f^2} \tau_a (1 - \tau_\ell) \rho_{p1} \rho_{p2} \rho_{r1} \rho_{r2} \tau_b \rho_{r3} \rho_{r4} N_{e,\Delta\lambda}$$

- Paraboloidal radiometer design

$$F_\ell = \frac{A_o A_\ell}{f^2} (1 - \tau_\ell) \rho_p \rho_{r1} \tau_b \rho_{r2} N_{e,\Delta\lambda}$$

Further, the expression for the input signal, F_i, must be multiplied by the factor τ_ℓ in every case.

This yields for the above specified values of ρ_p ρ_r τ_r $N_{p,\Delta\lambda} N_{r,\Delta\lambda}$

- Cassegrainian radiometer design

$$\Delta F = \frac{A_o A_d}{f^2} \tau_b \rho_r^4 \left\{ \tau_a \tau_\ell \rho_p^2 N_{i,\Delta\lambda} + \left[(1 - \tau_\ell \rho_p) \tau_a \rho_p - (\rho_p - \rho_m) \right] N_{p,\Delta\lambda} \right.$$

$$- \rho_m \left[(1 - \rho_r) (1 + \tau_r \rho_r + \tau_b \tau_r \rho_r^2 + \tau_b \rho_r^3) \right.$$

$$\left. \left. + (1 - \tau_b) \tau_r \rho_r^2 \right] N_{r,\Delta\lambda} \right\}$$

- Newtonian radiometer design

$$\Delta F = \frac{A_o A_d}{f^2} \tau_b \rho_r^4 \left\{ \tau_a \tau_\ell \rho_p^2 N_{i,\Delta\lambda} \right.$$

$$+ \left[(1 - \tau_\ell \rho_p) \tau_a \rho_p + (1 - \rho_p) \sqrt{2} - (1 - \rho_m) \right] N_{p,\Delta\lambda}$$

$$- \rho_m \left[(1 - \rho_r) (1 + \tau_r \rho_r + \tau_b \tau_r \rho_r^2 + \tau_b \rho_r^3) \right.$$

$$\left. \left. + (1 - \tau_b) \tau_r \rho_r^2 \right] N_{r,\Delta\lambda} \right\}$$

- Paraboloidal radiometer design

$$F = \frac{A_o A_d}{f^2} \tau_b \rho_r^2 \left\{ \tau_\ell \rho_p N_{i,\Delta\lambda} - (\tau_\ell \rho_p - \rho_m) N_{p,\Delta\lambda} - \rho_m \left[(1 - \rho_r)(1 + \tau_b \rho_r) + (1 - \tau_b) \rho_r \right] N_{r,\Delta\lambda} \right\}$$

Spoke-Supported Secondary-Collector Element

Radiant-flux contributions of particular elements of all-catoptric radiometer-system concepts already were evaluated. However, the primary evaluation did not account for the mounting structures of the collector optics secondary mirror except briefly for a lowpass filter mount. To fill this gap in radiometer description, essentially three types of support structures were taken into consideration:

- The secondary mirror is mounted directly on a plane-parallel window (low or highpass filter) in the path of the incident, nearly parallel beam of radiation. Thus, optical performance of the collector system is not affected substantially. However, with respect to the radiometric performance, the window contributes with its transmissivity as a transfer function and a radiance term in the direct-radiation propagation chain to the total flux receivable by the detector. A more careful consideration must be directed toward the indirect-radiation propagation chain, for, in this case, the data flow starts with the detector-face radiance as input. This input propagates through the cavity, the relay optics concentrator, the bandpass filter, and the collimator. In the chain, these elements are characterized by a multiplicative transfer function and an additive radiance term. The subsequent field stop contributes only with a transfer function (form factor). Then, the radiation splits up into two separate directions since it is partially reflected by, partially passed through the modulator. The branch reflected by the chopper propagates through the relay optics, including field stop, bandpass filter, cavity, and cold stop, without involving additional radiance terms, and finally meets the detector. The branch passed through the modulator propagates through the collector which contributes two additional radiance terms and multiplicative transfer functions. The chopper itself is also characterized by its transfer function and a radiance term. If there are no reflective elements in front of the window, the radiation is reflected by the window and propagates through the entire chain from the collector optics to the detector without encountering other radiance terms.

- By means of an axial spike, the secondary mirror is mounted on a window in the opening of the collector's primary mirror. Since this window is located in the converging portion of the incident beam, the optical performance of the collector is more affected than in the first case. In view of the data flow, one encounters practically no changes if compared to the propagation chains described above. However, the branch of the indirect radiation propagation chain that is transmitted through the modulator is much shorter because it does not pass through the collector optics.

- This study specifically concerns the third type of mounting structures consisting of a number of equally sized radial spokes. The optical performance of the collector is affected insofar as the

diffraction pattern changes appreciably; in addition, light scattering from the edges of the spokes may occur, resulting in a variation of the image blur. With respect to the radiometric performance, the direct and indirect radiation propagation chains are quite similar to those experienced in the first case.

Applying appropriate definitions and denotations, the Cassegrainian and the Newtonian collector optics can be treated simultaneously, since the two systems differ from each other only by the form factor for the collector's secondary mirror, if one assumes the relay optics to be identical in both cases. One may, however, encounter another variation when the bandpass filter is placed in one case into the collimated, and in another case into the converging beam of the relay optics. It is anticipated that the relay optics consists of Cassegrainian collimator and concentrator components; therefore, positioning the bandpass filter behind the concentrator necessitates considerations in behalf of the secondary mirror supports similar to those encountered in the folded collector optics. At this moment, however, it is only intended to analyze the case of mounting the two secondary mirrors directly on the bandpass filter faces.

The radiometer configurations involved in this analysis are schematically shown in Figure C6. In these sketches, the following notations are used:

A_o, A_i = outer and inner diameter areas of annular aperture

A_{c1}, A_{c2} = radiating areas of collectors optics' primary and secondary mirrors

A_s = beam-obscuring and radiating area of spoke arrangement

A_m, A_b = radiating areas of modulator and bandpass filter

A_f = field stop area

A_c = cavity area

A_d = detector area

$\mathbb{C}$ = center line (optical axis)

2ϕ = folding angle of $\mathbb{C}$ in Newtonian radiometer design

The conceptual Cassegrainian radiometer design is now considered specifically for both operation modes, chopper open and chopper closed.

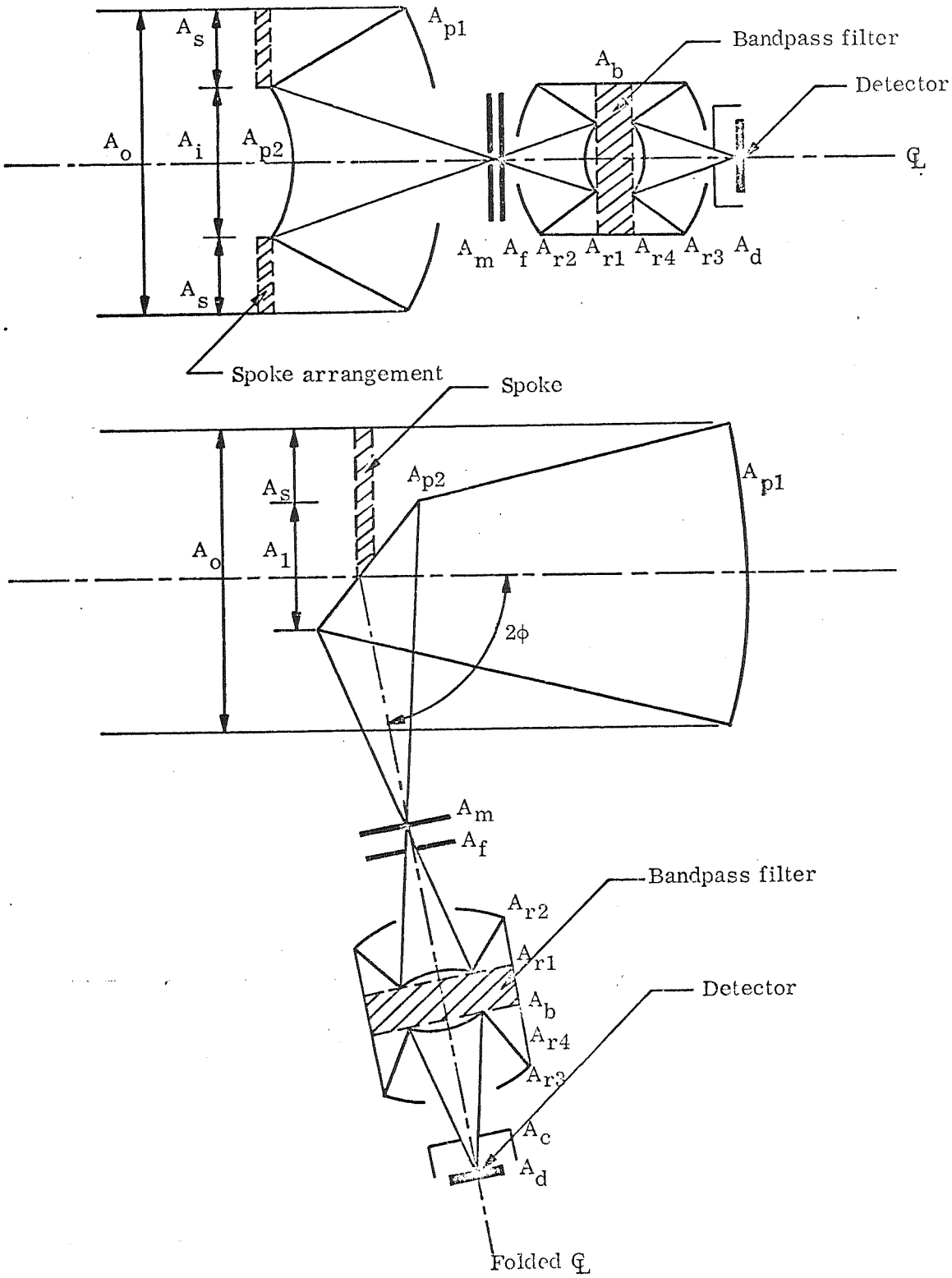

Figure C6. Schematic of Cassegrainian and Newtonian Radiometer Designs

Chopper open. -- Input signal from absolute apparent radiance $N_{i,\Delta\lambda}$

$$F_i = N_{i,\Delta\lambda} \tau_a \tau_s \rho_{p1} \rho_{p2} \xi_f \rho_{r1} \rho_{r2} \tau_b \rho_{r3} \rho_{r4} \xi_c A_d$$

where

$\Delta\lambda = \lambda_2 - \lambda_1$ = wavelength interval of bandpass filter

$\tau_a = 1 - A_i/A_o$ = annular correction factor

$\tau_s = 1 - A_s/(A_0 - A_i)$ = correction factor due to beam obscuration by spoke arrangement

ρ_{p1}, ρ_{p2} = reflectivities of collector optics' primary and secondary mirrors

$\xi_f = A_f/A_o'$ = ratio of field stop area to that of the image blur

ρ_{r1}, ρ_{r2} = reflectivities of relay collimator's primary and secondary mirrors

τ_b = bandpass filter transmissivity

ρ_{r3}, ρ_{r4} = reflectivities of relay concentrator primary and secondary mirrors

$\xi_{cs} \approx A_o/f^2$ = conversion factor derived from solid angle subtended at detector by the cold stop, and expressing the transition from radiance N ($W\ cm^{-2}\ sr^{-1}$) into irradiance H ($W\ cm^{-2}$).

The last term A_d converts finally H into incident flux P (W).

One must now first derive the contributions of the different elements in the direct radiation propagation chain to the total radiant flux receivable by the detector. These contributions are subsequently given by

- Signal from spoke arrangement

$$F_s = N_{s,\Delta\lambda} \tau_a (1 - \tau_s) \varepsilon_s \rho_{p1} \rho_{p2} \xi_f \rho_{r1} \rho_{r2} \tau_b \rho_{r3} \rho_{r4} \xi_c A_d$$

where

$\varepsilon_s = 1 - \rho_s$ = emissivity of spoke arrangement

ρ_s = reflectivity

This definition is based on the assumption of the spokes not being subject to absorption of radiation.

- Signals from the collector's primary and secondary mirrors

$$F_{p1} = N_{p1,\Delta\lambda}\, \tau_a\, \zeta_{p1}\, \epsilon_{p1}\, \rho_{p2}\, \zeta_f\, \rho_{r1}\, \rho_{r2}\, \tau_b\, \rho_{r3}\, \rho_{r4}\, \zeta_{cs} A_d$$

$$F_{p2} = N_{p2,\Delta\lambda} \zeta_{p2}\, \epsilon_{p2} \zeta_f\, \rho_{r1}\, \rho_{r2}\, \tau_b\, \rho_{r3}\, \rho_{r4}\, \zeta_{cs} A_d$$

where

$$\xi_{p1} = A_{p1}/(A_o - A_i)$$

$$\xi_{p2} = A_{p2}/A_i$$

$$\epsilon_{p1} = 1-\rho_{p1}$$

$$\epsilon_{p2} = 1-\rho_{p2}$$

- Signals from the relay collimator's secondary and primary mirrors

$$F_{r1} = N_{r1,\Delta\lambda}\, \zeta_{r1}\, \epsilon_{r1}\, \rho_{r2}\, \tau_b\, \rho_{r3}\, \rho_{r4}\, \zeta_c\, A_d$$

$$F_{r2} = N_{r2,\Delta\lambda}\, \tau_{r2}\, \zeta_{r2}\, \epsilon_{r2}\, \tau_b\, \rho_{r3}\, \rho_{r4}\, \zeta_c\, A_d$$

where

$\zeta_{r1} = A_{r1}/A'_{r1}$; A'_{r1} = projected area of A_{r1}

$\zeta_{r2} = A_{r2}/(A'_{r2} - A'_{r1})$; $(A'_{r2} - A'_{r1})$ = projected area of annulus

$\epsilon_{r1} = 1 - \rho_{r1}$

$\epsilon_{r2} = 1 - \rho_{r2}$

$$\tau_{r2} = \frac{A'_{r2} - A'_{r1}}{A'_{r2}}$$; A'_{r2} = outer diameter area of projected primary mirror

- Signal from bandpass filter

The filter characterized by a transmissivity $\tau_b = 1-a_b - \rho_b$ in the interval $\Delta\lambda$ is assumed to absorb completely outside $\Delta\lambda$; that is, outside $\Delta\lambda$ the

emissivity is given by $\epsilon_b = 1 - \rho_b$, where α_b and ρ_b denote the filter's absorptivity and surface reflectivity, respectively. This outside emissivity applies to the wavelenght intervals zero to λ_1 and λ_2 to λ_c,

where λ_c is the cut-off wavelength of the detector sensitivity. One obtains for the in-band component

$$N_{b,\Delta\lambda}\ \tau_{r3}\ \epsilon_b\ \rho_{r3}\ \rho_{r4}\ \zeta_{cs} A_d$$

where

$\tau_{r3} = (A'_{r3} - A'_{r4})/A'_{r3}$; $A'_{r3} - A'_{r4}$ = **projected area of annulus** = A_b

A'_{r3} = **outer diameter area of projected primary mirror**

$\epsilon_b = 1 - \tau_b - \rho_b$

outside $\Delta\lambda$

$$N_{b,0/\lambda_1}\ \tau_{r3}\ \epsilon'_b\ \rho_{r3}\ \rho_{r4}\ \zeta_c\ A_d + N_{b,\lambda_2/\lambda_c}\ \tau_{r3}\ \epsilon'_b\ \rho_{r3}\ \rho_{r4}\ \zeta_c\ A_d$$

$$= N_{b,\Delta\lambda'}\tau_{r3}\ \epsilon'_b\ \zeta_c\ A_d - N_{b,\Delta\lambda}\ \tau_{r3}\ \epsilon'_b\ \rho_{r3}\ \rho_{r4}\ \zeta_c\ A_d$$

where

$\Delta\lambda' = \lambda_c - 0$

$\epsilon'_b = 1 - \rho_b$

Hence

$$F_b = N_{b,\Delta\lambda'}\ \tau_{r3}\ (1 - \rho_b)\ \rho_{r3}\ \rho_{r4}\ \zeta_{cs} A_d - N_{b,\Delta\lambda}\ \tau_{r3}\ \tau_b\ \rho_{r3}\ \rho_{r4}\ \zeta_{cs} A_d$$

- **Signals from the relay concentrator's primary and secondary mirrors**

$$F_{r3} = N_{r3,\Delta\lambda}\, \zeta_{r3}\, \tau_{r3}\, \epsilon_{r3}\, \rho_{r4}\, \zeta_{cs} A_d$$

$$F_{r4} = N_{r4,\Delta\lambda}\, \zeta_{r4}\, \epsilon_{r4}\, \zeta_{cs} A_d$$

where

$$\zeta_{r3} = A_{r3}/(A'_{r3} - A'_{r4})$$

$$\zeta_{r4} = A_{r4}/A'_{r4}$$

A'_{r4} = projected area of secondary mirror

$$\epsilon_{r3} = 1 - \rho_{r3}$$

$$\epsilon_{r4} = 1 - \rho_{r4}$$

The contributions of the different elements in the indirect radiation propagation chain to the total radiant flux receivable by the detector are subsequently given by

- **Signal from the detector with radiance** $N_{d,\Delta\lambda}$

$$\bar{F}_i = N_{d,\Delta\lambda}\, \epsilon_d\, \rho_{r4}\, \rho_{r3}\, \tau_b\, \rho_{r2}\, \rho_{r1}\, \zeta'_f\, \rho_{p2}\, \rho_{p1}\, \tau_a\, \zeta_s\, \rho_s\, \rho_{p1}\, \rho_{p2}\, \rho_{r1}\, \rho_{r2}\, \tau_b\, \rho_{r3}\, \rho_{r4}\, \zeta_{cs} A_d$$

where

$$\zeta'_f = A_f/A'_d$$

A'_d = image of A_d in primary focal plane

$$\zeta_s = 1 - \tau_s$$

- Signals from relay concentrator's secondary and primary mirrors

$$\bar{F}_{r4} = N_{r4,\Delta\lambda}\,\zeta_{r4}\,\epsilon_{r4}\,\rho_{r3}\,\tau_b\,\rho_{r2}\,\rho_{r1}\,\zeta_f'\,\rho_{p2}\,\rho_{p1} \quad \tau_a\,\zeta_s\,\rho_s\,\rho_{c1}\,\rho_{c2}\,\rho_{r1}\,\rho_{r2}\,\tau_b\,\rho_{r3}\,\rho_{r4}\,\zeta_{cs}A_d$$

$$\bar{F}_{r3} = N_{r3,\Delta\lambda}\,\zeta_{r3}\,\tau_b\,\rho_{r2}\,\rho_{r1}\,\zeta_f'\,\rho_{p2}\,\rho_{p1} \quad \tau_a\,\zeta_s\,\rho_s\,\rho_{p1}\,\rho_{p2}\,\rho_{r1}\,\rho_{r2}\,\tau_b\,\rho_{r3}\,\rho_{r4}\,\zeta_{cs}A_d$$

- Signal from bandpass filter

$$\bar{F}_b = N_{b,\Delta\lambda}\,\tau_{r2}\,\epsilon_b\,\rho_{r2}\,\rho_{r1}\,\zeta_f'\,\rho_{p2}\,\rho_{p1} \quad \tau_a\,\zeta_s\,\rho_s\,\rho_{p1}\,\rho_{p2}\,\rho_{r1}\,\rho_{r2}\,\tau_b\,\rho_{r3}\,\rho_{r4}\,\zeta_{cs}A_d$$

- Signals from relay collimator's primary and secondary mirrors

$$\bar{F}_{r2} = N_{r2,\Delta\lambda}\,\tau_{r2}\,\zeta_{r2}\,\epsilon_{r2}\,\rho_{r1}\,\zeta_f'\,\rho_{p2}\,\rho_{p1} \quad \tau_a\,\zeta_s\,\rho_s\,\rho_{p1}\,\rho_{p2}\,\rho_{r1}\,\rho_{r2}\,\tau_b\,\rho_{r3}\,\rho_{r4}\,\zeta_{cs}A_d$$

$$\bar{F}_{r1} = N_{r1,\Delta\lambda}\,\zeta_{r1}\,\epsilon_{r1} \quad \zeta_f'\,\rho_{p2}\,\rho_{p1} \quad \tau_a\,\zeta_s\,\rho_s\,\rho_{p1}\,\rho_{p2}\,\rho_{r1}\,\rho_{r2}\,\tau_b\,\rho_{r3}\,\rho_{r4}\,\zeta_{cs}A_d$$

- Signals from collector's secondary and primary mirrors

$$\bar{F}_{p2} = N_{p2,\Delta\lambda}\,\zeta_{p2}\,\epsilon_{p2}\,\rho_{p1} \quad \tau_a\,\zeta_s\,\rho_s\,\rho_{p1}\,\rho_{p2}\,\rho_{r1}\,\rho_{r2}\,\tau_b\,\rho_{r3}\,\rho_{r4}\,\zeta_{cs}A_d$$

$$\bar{F}_{p1} = N_{p1,\Delta\lambda}\,\tau_a\,\zeta_{p1}\,\epsilon_{p1} \quad \tau_a\,\zeta_s\,\rho_s\,\rho_{p1}\,\rho_{p2}\,\rho_{r1}\,\rho_{r2}\,\tau_b\,\rho_{r3}\,\rho_{r4}\,\zeta_{cs}A_d$$

B. Chopper Closed

In the chopper-closed operation mode, there are no contributions from elements in front of the modulator. Thus, the direct radiation propagation chain consists of:

- Signal from the modulator with radiance $N_{m,\Delta\lambda}$

$$F_i' = N_{m,\Delta\lambda}\,\epsilon_m\,\zeta_f'\,\rho_{r1}\,\rho_{r2}\,\tau_b\,\rho_{r3}\,\rho_{r4}\,\zeta_c\,A_d$$

where

$\epsilon_m = 1 - \rho_m$

ρ_m = modulator reflectivity

- Signals from the relay collimator's secondary and primary mirrors

$$F'_{r1} = P_{r1} = N_{r1,\Delta\lambda}\, \zeta_{r1}\, \epsilon_{r1}\, \rho_{r2}\, \tau_b\, \rho_{r3}\, \rho_{r4}\, \zeta_c\, A_d$$

$$F'_{r2} = P_{r2} = N_{r2,\Delta\lambda}\, \tau_{r2}\, \zeta_{r2}\, \epsilon_{r2}\, \tau_b\, \rho_{r3}\, \rho_{r4}\, \zeta_c\, A_d$$

- Signal from bandpass filter

$$F'_b = P_b = [N_{b,\Delta\lambda'}\, (1 - \rho_b) - N_{b,\Delta\lambda}\, \tau_b]\, \tau_{r3}\, \rho_{r3}\, \rho_{r4}\, \zeta_c\, A_d$$

- Signals from the relay concentrator's primary and secondary mirrors

$$F'_{r3} = P_{r3} = N_{r3,\Delta\lambda'}\, \zeta_{r3}\, \tau_{r3}\, \epsilon_{r3}\, \rho_{r4}\, \zeta_c\, A_d$$

$$F'_{r4} = P_{r4} = N_{r4,\Delta\lambda'}\, \zeta_{r4}\, \epsilon_{r4}\, \zeta_c\, A_d$$

The subsequent flux contribution from the elements in the indirect radiation propagation chain are

- Signal from the detector

$$\bar{F}'_i = N_{d,\Delta\lambda}\, \epsilon_d\, \rho_{r4}\, \rho_{r3}\, \tau_b\, \rho_{r2}\, \rho_{r1} \quad \zeta'_f\, \rho_m\, \rho_{r1}\, \rho_{r2}\, \tau_b\, \rho_{r3}\, \rho_{r4}\, \zeta_c\, A_d$$

- Signals from relay concentrator's secondary and primary mirrors

$$\bar{F}'_{r4} = N_{r4,\Delta\lambda}\, \zeta_{r4}\, \epsilon_{r4}\, \rho_{r3}\, \tau_b\, \rho_{r2}\, \rho_{r1} \quad \zeta'_f\, \rho_m\, \rho_{r1}\, \rho_{r2}\, \tau_b\, \rho_{r3}\, \rho_{r4}\, \zeta_c\, A_d$$

$$\bar{F}'_{r3} = N_{r3,\Delta\lambda}\, \zeta_{r3}\, \tau_{r3}\, \epsilon_{r3}\, \tau_b\, \rho_{r2}\, \rho_{r1} \quad \zeta'_f\, \rho_m\, \rho_{r1}\, \rho_{r2}\, \tau_b\, \rho_{r3}\, \rho_{r4}\, \zeta_c\, A_d$$

- Signal from band-pass filter

$$\bar{F}'_b = N_{b,\Delta\lambda}\, \tau_{r2}\, \epsilon_b\, \rho_{r2}\, \rho_{r1} \quad \zeta'_f\, \rho_m\, \rho_{r1}\, \rho_{r2}\, \tau_b\, \rho_{r3}\, \rho_{r4}\, \zeta_{cs} A_d$$

- Signals from relay collimator's primary and secondary mirrors

$$\bar{F}'_{r2} = N_{r2,\Delta\lambda}\, \tau_{r2}\, \zeta_{r2}\, \epsilon_{r2}\, \rho_{r1} \quad \zeta'_f\, \rho_m\, \rho_{r1}\, \rho_{r2}\, \tau_b\, \rho_{r3}\, \rho_{r4}\, \zeta_{cs} A_d$$

$$\bar{F}'_{r1} = N_{r1,\Delta\lambda}\, \zeta_{r1}\, \epsilon_{r1} \quad \zeta'_f\, \rho_m\, \rho_{r1}\, \rho_{r2}\, \tau_b\, \rho_{r3}\, \rho_{r4}\, \zeta_{cs} A_d$$

The formulae derived for the Cassegrainian system apply also to the conceptual Newtonian radiometer design with only one minor difference. Whereas in both systems the transmisstion factors τ and the form factors ζ are generally design dependent parameters, the Newtonian system's form factor ζ_{p2} is easily expressible by the half folding angle ϕ; that is, one obtains

$$\zeta_{p2} = \sec\phi$$

For this reason, the total radiant flux incident on the detector face may be expressed as the sum of the particular flux contributions derived, in general form, for the Cassegrainian system.

$$\begin{aligned} F_{open} &= F_d + \bar{F}_d \\ &= F_i + F_s + F_{p1} + F_{p2} + F_{r1} + F_{r2} + F_b + F_{r3} + F_{r4} \\ &\quad + \bar{F}_i + \bar{F}_{r4} + \bar{F}_{r3} + \bar{F}_b + \bar{F}_{r2} + \bar{F}_{r1} + \bar{F}_{p2} + \bar{F}_{p1} \end{aligned}$$

$$\begin{aligned} F_{closed} &= F'_d + \bar{F}'_d \\ &= F'_i + F'_{r1} + F'_{r2} + F'_b + F'_{r3} + F'_{r4} \\ &\quad + \bar{F}'_i + \bar{F}'_{r4} + \bar{F}'_{r3} + \bar{F}'_b + \bar{F}'_{r2} + \bar{F}'_{r1} \end{aligned}$$

It must be noticed that handling the data flow in an on-off type fashion constitutes only an approximation. Actually, one encounters transition times during which the modulator is partially transmitting and partially reflecting; that is, one would experience both modes, P_{open} and P_{closed}, after modification by adequate, multiplicative, time-dependent form-factors, $\zeta(t)$, simultaneously. However, these transition periods are supposedly short enough as to be considered negligible.

The receivable power in both radiation propagation modes may be compared with the radiant flux in a straight Cassegrainian system without any structural support elements. Expanding the expressions of the earlier paper to comply with the deviations of the present study by considering multiplicative form factor, one obtains

$$F_{open} = F_i/\tau_s + F_{p1} + F_{p2} + F_{r1} + F_{r2} + F_b + F_{r3} + F_{r4}$$

$$F_{closed} = F_{closed}$$

As compared with F_{open}, it is seen that in F_{open} essentially the flux contributions from the elements of the indirect radiation propagation chain are missing. However, this can never happen in an actual system, as pointed out in the descriptions of the alternative support structures. In these alternatives, one will also always encounter a power term F_s. Specifically in the first alternative, this power term may be much greater than that obtained from the spoke support because of the larger area involved; on the other hand, the transmission coefficient of the support window may be smaller than that of the support spokes. Since, additionally, the amount of power F_d of the indirect radiation propagation chain is substantially dependent on the area and the reflectivity of the support structure, this amount of power will certainly be larger for the support window than for the support spokes.

The signal difference, $\Delta F = F_{open} - F_{closed}$, believed to be an important quantity in data processing, is now explicitly derived for completeness of the study.

$$\Delta F = \frac{A_o A_d}{f^2} \Big\{ N_{i,\Delta\lambda}\, \tau_a\, \tau_s\, \rho_{p1}\, \rho_{p2}\, \zeta_f\, \rho_{r1}\, \rho_{r2}\, \tau_b\, \rho_{r3}\, \rho_{r4}$$

$$+ N_{s,\Delta\lambda}\, \tau_a\, (1 - \tau_s)\, (1 - \rho_s)\, \rho_{p1}\, \rho_{p2}\, \zeta_f\, \rho_{r1}\, \rho_{r2}\, \tau_b\, \rho_{r3}\, \rho_{r4}$$

$$+ N_{p1,\Delta\lambda}\, \tau_a\, \zeta_1\, (1 - \rho_{p1})\, \rho_{p2}\, \zeta_f\, \rho_{r1}\, \rho_{r2}\, \tau_b\, \rho_{r3}\, \rho_{r4}$$

$$+ N_{p2,\Delta\lambda}\, \zeta_{p2}\, (1 - \rho_{p2})\, \zeta_f\, \rho_{r1}\, \rho_{r2}\, \tau_b\, \rho_{r3}\, \rho_{r4}$$

$$+ (\zeta_c\, \tau_c\, \rho_{p2}\, \rho_{p1} - \rho_m)\, \zeta_f'\, \rho_{r1}\, \rho_{r2}\, \tau_b\, \rho_{r3}\, \rho_{r4}$$

$$\times \Big[N_{d,\Delta\lambda}\, \epsilon_d\, \rho_{r4}\, \rho_{r3}\, \tau_b\, \rho_{r2}\, \rho_{r1}$$

$$+ N_{r4,\Delta\lambda}\, \zeta_{r4}\, (1 - \rho_{r4})\, \rho_{r3}\, \tau_b\, \rho_{r2}\, \rho_{r1}$$

$$+ N_{r3,\Delta\lambda}\, \zeta_{r3}\, \tau_{r3}\, (1 - \rho_{r3})\, \tau_b\, \rho_{r2}\, \rho_{r1}$$

$$+ N_{b,\Delta\lambda}\, (1 - \tau_b - \rho_b)\, \tau_{r2}\, \rho_{r2}\, \rho_{r1}$$

$$+ N_{r2,\Delta\lambda}\, \zeta_{r2}\, \tau_{r2}\, (1 - \rho_{r2})\, \rho_{r1}$$

$$+ N_{r1,\Delta\lambda}\, \zeta_{r1}\, (1 - \rho_{r1})\Big]$$

$$+ \zeta_s\, \tau_a \rho_s \rho_{p2}\, \rho_{p1}\, \zeta_f'\, \rho_{r1}\, \rho_{r2}\, \tau_b\, \rho_{r3}\, \rho_{r4}$$

$$\times \Big[N_{p2}\, \zeta_{p2}\, (1 - \rho_{p2})\, \rho_{p1}$$

$$+ N_{p1}\, \tau_a\, \zeta_{p1}\, (1 - \rho_{p1})\Big]$$

$$- N_m\, (1 - \rho_m)\, \zeta_f'\, \rho_{r1}\, \rho_{r2}\, \tau_b\, \rho_{r3}\, \rho_{r4}\Big\}$$

Assuming now that

$$\rho_{p1} = \rho_{p2} = \rho_p$$

$$\rho_{r1} = \rho_{r2} = \rho_{r3} = \rho_{r4} = \rho_r$$

$$\tau_{r2} = \tau_{r3} = \tau_r$$

$$\zeta_{r1} = \zeta_{r4}$$

$$\zeta_{r2} = \zeta_{r3}$$

$$N_{s,\Delta\lambda} = N_{p1,\Delta\lambda} = N_{p2,\Delta\lambda} = N_{m,\Delta\lambda} = N_{p,\Delta\lambda}$$

$$N_{r1,\Delta\lambda} = N_{r2,\Delta\lambda} = N_{b,\Delta\lambda} = N_{r3,\Delta\lambda} = N_{r4,\Delta\lambda} = N_{r,\Delta\lambda}$$

one obtains specifically

$$\Delta F = \frac{A_o A_d}{f^2} \rho_r^4 \tau_b \Big[\tau_a \tau_s \rho_p^2 \zeta_f N_{i,\Delta\lambda}$$

$$+ \Big\{ \Big[\tau_a (1 - \tau_s)(1 - \rho_s) \rho_p^2 + (1 - \rho_p)(\tau_a \zeta_{p1} \rho_p + \zeta_{p2}) \Big] \zeta_f$$

$$+ \Big[\zeta_s \rho_s \tau_a \rho_p^2 (1 - \rho_p)(\zeta_{p2} \rho_p + \tau_a \zeta_{p1}) - (1 - \rho_m) \Big] \zeta_f' \Big\} N_{p,\Delta\lambda}$$

$$+ (\zeta_s \rho_s \tau_a \rho_p^2 - \rho_m) \zeta_f' \Big\{ (1 - \rho_r) \Big[\zeta_{r1} (\rho_r^3 \tau_b + 1)$$

$$+ \zeta_{r2} \tau_r \rho_r (\rho_r \tau_b + 1) \Big] + (1 - \tau_b - \rho_b) \tau_r \rho_r^2 \Big\} N_{r,\Delta\lambda}$$

$$+ (\zeta_c \tau_c \rho_p^2 - \rho_m) \zeta_f' \epsilon_d \rho_r^4 \tau_b N_{d,\Delta\lambda} \Big]$$

REFRACTO-REFLECTIVE SYSTEMS

The radiant-flux contributions to the signal receivable by the detector from the elements in all-refractive and all-reflective radiometer designs have been determined previously. Results of these studies now are applied to other element combinations. In this application it is assumed that refractive collector optics intended to concentrate the incoming radiation from the target scene in its focal plane can be represented by one single component even if it is actually composed of a number of elements to correct for chromatic and geometric-optical aberrations. It was shown previously that this assumption is permitted.

The term "refracto-reflective" system is applied to a configuration that is composed of refractive collector optics and all-reflective relay optics. Two types of an all-reflective relay system are specifically taken into consideration.

- Cassegrainian system pair
- Off-axis paraboloidal reflector pair

Appropriately combining the results of the previous derivations, one obtains:

- Refractive collector and Cassegrainian collimator and concentrator optics:

$$\Delta F = \frac{A_o A_d}{f^2} \tau_b \rho_r^4 \left\{ \tau_\ell \tau_a N_{i,\Delta\lambda} + \left[(1 - \tau_\ell) \tau_a + (\rho_m - \tau_p - \rho_p)\right] N_{p,\Delta\lambda} \right.$$

$$\left. - \rho_m \left[(1 - \rho_r)(1 + \tau_b \rho_r + \tau_b \tau_r \rho_r^2 + \tau_b \rho_r^3) + (1 - \tau_b) \tau_r \rho_r^2\right] N_{r,\Delta\lambda} \right\}$$

where τ_ℓ = transmissivity of a lowpass filter in front of the collector optics

- Refractive collector and off-axis paraboloidal collimator and concentrator:

$$\Delta F = \frac{A_o A_d}{f^2} \tau_b \rho_r^2 \left\{ \tau_\ell \tau_a N_{i,\Delta\lambda} + \left[(1 - \tau_\ell) \tau_a + (\rho_m - \tau_p - \rho_p)\right] N_{p,\Delta\lambda} \right.$$

$$\left. - \rho_m \left[(1 - \rho_r)(1 + \tau_b \rho_r) + (1 - \tau_b) \rho_r\right] N_{r,\Delta\lambda} \right\}$$

where τ_ℓ has the same meaning as above.

REFLECTO-REFRACTIVE SYSTEMS

The term "reflecto-refractive" system denotes a combination of an all-reflective collector and all-refractive relay optics. These relay optics are assumed to consist of a collimator and a concentrator component both of which, though possibly composed of several elements, can be handled as single elements. Three collector configurations were taken into specific consideration:

- Cassegrainian collector
- Newtonian collector
- Off-axis paraboloidal collector

Again, appropriate combination of the earlier results yields:

- Cassegrainian collector and refractive collimator and concentrator:

$$\Delta F = \frac{A_o A_f}{f^2} \tau_b \tau_r^2 \left\{ \tau_a \tau_\ell \rho_p^2 N_{i,\Delta\lambda} + \left[(1 - \tau_\ell \rho_p) \tau_a \rho_p + (\rho_m - \rho_p) \right] N_{p,\Delta\lambda} - \rho_m \left[(1 - \tau_r - \rho_r) + \tau_r (1 - \tau_b \tau_r - \tau_b \rho_r) \right] N_{r,\Delta\lambda} \right\}$$

- Newtonian collector and refractive collimator and concentrator:

$$\Delta F = \frac{A_o A_d}{f^2} \tau_b \tau_r^2 \left\{ \tau_a \tau_\ell \rho_p^2 N_{i,\Delta\lambda} + \left[(1 - \tau_\ell \rho_p) \tau_a \rho_p + (1 - \rho_p)\sqrt{2} - (1 - \rho_m) \right] N_{p,\Delta\lambda} - \rho_m \left[(1 - \tau_r - \rho_r) + \tau_r (1 - \tau_b \tau_r - \tau_b \rho_r) \right] N_{r,\Delta\lambda} \right\}$$

- Off-axis paraboloidal collector and refractive collimator and concentrator:

$$\Delta F = \frac{A_o A_d}{f^2} \tau_b \tau_r^2 \left\{ \tau_\ell \rho_p N_{i,\Delta\lambda} + (\rho_m - \tau_\ell \rho_p) N_{p,\Delta\lambda} - \rho_m \left[(1 - \tau_r - \rho_r) + \tau_r (1 - \tau_b \tau_r - \tau_b \rho_r) \right] N_{r,\Delta\lambda} \right\}$$

In these expressions τ_ℓ denotes generally the transmissivity of a lowpass filter in front of the collector optics. This lowpass filter can be used to support the secondary optical element in Cassegrainian and Newtonian collectors. It is to be noted that, with respect to these two specific configurations, τ_ℓ can also define the transmissivity of a spoke-supported structure for the secondary element; that is, it denotes transmissivity of an annulus that is obscured by the spokes.

APPENDIX D
SPECIFIC ERROR MODEL

APPENDIX D
SPECIFIC ERROR MODEL

This appendix describes the method used for predicting radiometer-measurement-accuracy capability. Errors associated with attitude knowledge, typical energy variations at the source (horizon or loud noise), and transfer to earth of radiometric data are considered elsewhere as systems errors since they are basically error sources which can be treated only at the radiometer level.

In a conventional error analysis, the method used is to write a comprehensive analytical expression and to determine sensitivity to a given parameter either by differentiations or by evaluating the expression numerically and varying each parameter about the nominal. This method can be used successfully on relatively simple models with specific characteristics, but becomes considerably less useful for analyzing the general uses of a complex radiometer system.

The form of the error analysis used in this case permits a systematic means of evaluation of radiometric performance without the necessity for end-to-end equations for each configuration. All major elements of the radiometer are considered in modular form to simplify evaluation and comparison of alternatives in design.

It was found that the elements could be represented by two types of modifying factors, the first factor describing the characteristics of the element which modify preceding elements and the second factor describing the intrinsic characteristics (usually additive).

Figure D1 shows the element used for this particular analysis. For alternate cases, similar models could be used as appropriate to given configurations. For each alternative for a modular element, an appropriate transfer function can be written and evaluated for expected nominal and extreme values. The transfer functions within an element also can be basically in modular form whenever possible. That is, the technique used for the overall analysis also is useful in analyzing characteristics of an individual element.

Figure D1 illustrates the manner in which the serial analysis is performed. Each element to the left in the figure constitutes a source of energy which can reach the collection system of the radiometer. A table of possible sources is given in Table D1. The value Z in the equations of Figure D1 represents any of these signals. The designator 1a, 3a, 4a, . . ., 16a can be applied equally to the signal or to the resultant output for the appropriate Z. Associated with each signal is an appropriate output 1b, 3b, 4b, . . . , 16b corresponding to the same conditions for the chopper closed. Obviously, for many situations 1b = 3b = 4b, . . . , etc.

As illustrated in Table D1, for each description A, B, C there is an uncertainty or bias, appropriate to that value which can be represented as a percentage; that is, $A(1 \pm a)$. In propagating values through the radiometer, relations for the uncertainties were accumulated as shown in Table D2.

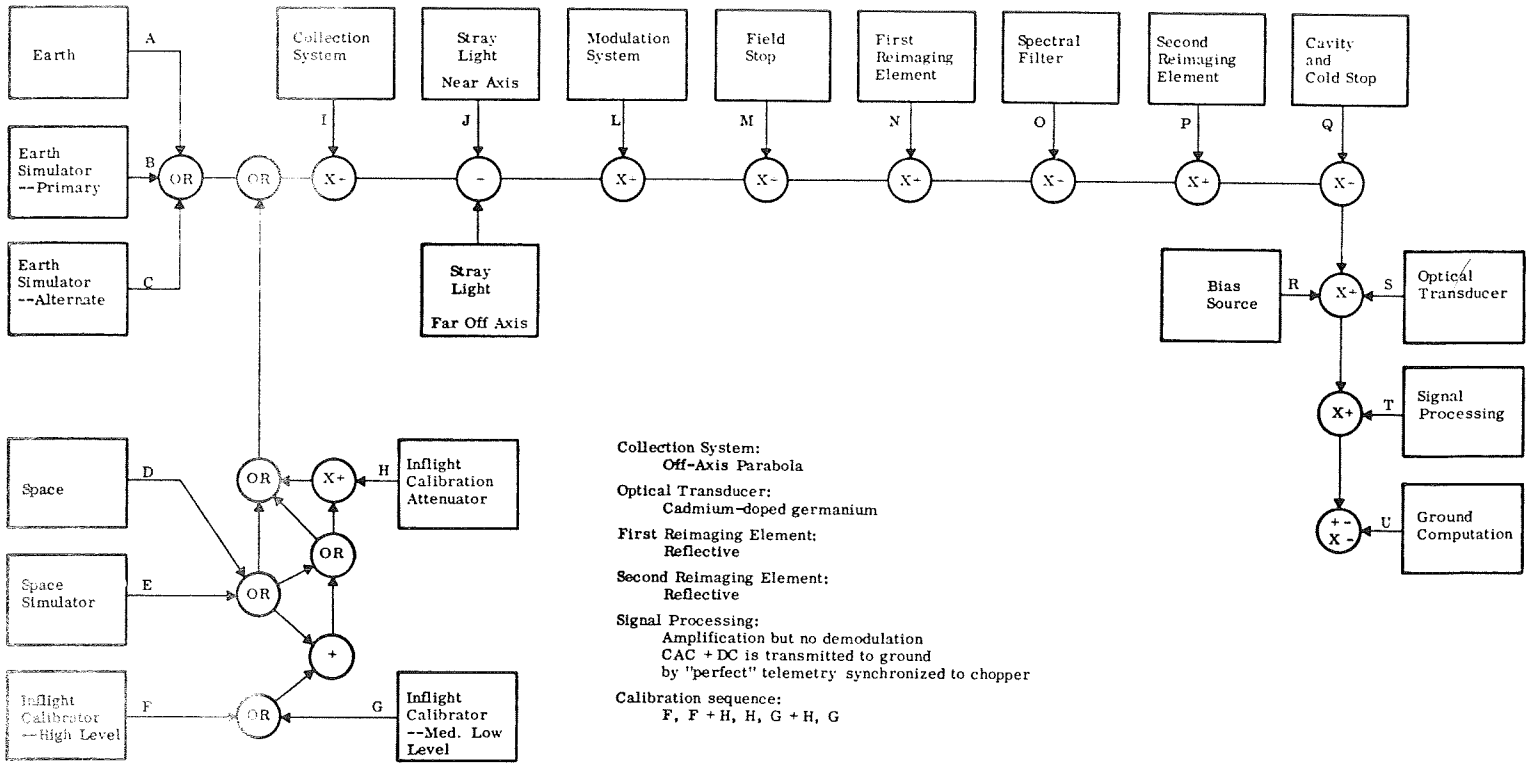

Figure D1. Model for Specific Error Analysis

TABLE D1. - INPUT-SIGNAL EQUATIONS FOR SPECIFIC ERROR ANALYSIS

Designation	Description	Form
1a	Space-zero reference	$D(1 \pm d)$
3a	High inflight calibration level	$D(1 \pm d) + F(1 \pm f)\, H_{HIGH}(1 \pm h_{HIGH}) + H_2\,(1 \pm h_2)$
4a	Medium high inflight calibration level	$D(1 \pm d) + F(1 \pm f)\, H_{MED\ HI}(1 \pm h_{MED\ HI}) + H_2\,(1 \pm h_2)$
5a	Medium low inflight calibration level	$D(1 \pm d) + F(1 \pm f)\, H_{MED\ LO}(1 \pm h_{MED\ LO}) + H_2(1 \pm h_2)$
6a	Low inflight calibration level	$D(1 \pm d) + F(1 \pm f)\, H_{LOW})\ (1 \pm h_{LOW}) + H_2\,(1 \pm h_2)$
7a	High earth radiance level	$A_{High}\ (1 \pm a_{High})$
8a	Medium high earth-radiance level	$A_{Med.\ High}\ (1 \pm a_{Med.\ High})$
9a	Medium low earth radiance level	$A_{Med.\ Low}\ (1 \pm a_{Med.\ Low})$
10a	Low earth radiance level	$A_{Low}\ (1 \pm a_{Low})$
11a	Space simulator	$E\ (1 \pm e)$
13a	High primary calibration level	$B_{High}\ (1 \pm b_{High})$
14a	Medium high primary calibration level	$B_{Med.\ High}\ (1 \pm b_{Med.\ High})$
15a	Medium low primary calibration level	$B_{Med.\ Low}\ (1 \pm b_{Med.\ Low})$
16a	Low primary calibration level	$B_{Low}\ (1 \pm b_{Low})$

TABLE D2. - COMPUTATIONAL-ERROR MODEL

Deviations are assumed to propagate as follows:

Addition and Subtraction

$$A(1 \pm a) + B(1 \pm b) + C(1 \pm c) + \ldots \approx (A + B + C + \ldots)\left(1 \pm \frac{Aa + Bb + Cc + \ldots}{A + B + C + \ldots}\right)$$

For multiplication and division a, b, c, etc., are assumed much smaller than one so that:

Multiplication

$$A(1 \pm a) \cdot B(1 \pm b) \cdot C(1 \pm c) \ldots \approx ABC \ldots \left[1 \pm (a + b + c + \ldots)\right]$$

Division

$$\frac{1}{A(1 \pm a)} \approx \frac{1}{A}(1 \mp a); \quad \frac{1}{B(1 \pm b)} \approx \frac{1}{B}(1 \mp b); \quad \text{etc.}$$

and $$\frac{A(1 \pm a)C(1 \pm c)\ldots}{B(1 \pm b)D(1 \pm d)\ldots} \approx \frac{AC\ldots}{BD\ldots} \left[1 \pm (a - b + c - d + \ldots)\right]$$

Modules are structured in what can be considered to be a serial form. Each element was made to stand as an individual block. When it is necessary to include one block consideration outside the element, the configuration dependency can be identified and alternative modes can be used as appropriate. Factors such as component aging, particle bombardment, or temperature changes caused by variations in the cooling system are treated as parallel functions modifying each of the other transfer functions individually.

A detailed specific error analysis was performed using parameters shown in Table D3. Each of the boxes of Figure D1 is described below. The uncertainties are summarized in Table D5.

TABLE D3. - SPECIFIC SYSTEM PARAMETERS

Collector optics (off-axis parabola)

Aperture diameter: D_p = 20 cm

f/number = 2

nominal reflectivity: $0.990 \leq \rho_{po} \leq 0.994$; long-term change: ±0.001;

emissivity: $\epsilon_p = 1 - \rho_p$

form factor: ζ_p = essentially constant and not considered to be an error source = 1.2000 (assumed value)

Relay optics (off-axis parabola pair)

f/number = 2

nominal reflectivity: $0.990 \leq \rho_{ro} \leq 0.994$ (±0.001)

emissivity: $\epsilon_r = 1 - \rho_r$

form factor: ζ_p = 1.2000 (assumed value)

Bandpass filter between relay parabolas

transmissivity: τ_b = 0.60 from 14.0 to 16.3 μ
= 0.0 from 0 to 14.0 μ
= 0.0 from 16.3 to 23 μ

emissivity: ϵ_b = 0.02 from 2 to 23 μ
= 1.0 for $\lambda < 2\mu$ and $\lambda > 23\mu$

Temperatures for boxes	F, G, I, L, M	150°K	low
		200°K	nominal
		300°K	high
	N, O, P, Q	60°K	low
		80°K	nominal
		200°K	high
		300°K	very high

Detector (on-axis): Ge:Cd at 15°K

angular size: 0.2 mr x 1.0 mr

area: $(2 \times D_p)^2 \times 0.2 \times 10^{-6} = 3.2 \times 10^{-4}$ cm^2

Field stop 20% larger than detector.
Cold stop defines acceptance angle of system.

TABLE D3. - SPECIFIC SYSTEM PARAMETERS (Continued)

For the form factor ξ_p, a value of 1.2000 was assumed. Form factor is essentially a constant and is not considered to be an error source. Since emissivity is derived from 1 − reflectivity, small uncertainties in reflectivity cause large uncertainties in emissivity. The nominal value for E_{po} is 0.00800 ±0.00200. The long-term change is ±0.00100.

Bias	Long-term drift	Short-term drift
E = 0.00800 (1 ±0.25)	(1 ±0.125)	(1. ±0.0000)

Temperature is the determining factor for N_{po} since the spectral region is chosen. For the primary, temperatures were chosen as

Nominal	Bias	Long-term drift	Short-term drift
300°K	±20°	±5°	±0.1°
200°K	±20°	±5°	±0.1°
150°K	±20°	±5°	±0.1°
$N_{\Delta\lambda 300}$ = 0.150245 x 10^2	(1 ±0.221474)	(1 ±0.055368)	(1 ±0.001727) W/m^{-2}-sr
$N_{\Delta\lambda 300}$ = 2.96170 x	(1 ±0.480404)	(1 ±0.120098)	(1 ±0.002402) W/m^{-2}-sr
$N_{\Delta\lambda 300}$ = 0.602688 x	(1 ±0.853702)	(1 ±0.211425)	(1 ±0.004229) W/m^{-2}-sr

Using the value for form factor ξ_p and the values for emissivity and radiance, one obtains for I_2

$I2_{300}$ = 0.144235 x	(1. ±0.471474)	(1 ±0.180368)	(1 ±0.001727) W/m^{-2}-sr
$I2_{200}$ = 284323 x 10^{-1}	(1 ±0.25) (1 ±0.480404)	(1 ± 0.125) (1 ± 0.120098)	(1 ±0.002402) W/m^{-2}-sr
$I2_{150}$ = 0.578580 x 10^{-2}	(1 ±1.104)	(1. ±0.3364)	(1 ±0.004229) W/m^{-2}-sr

Using the value for the form factor ζ_p and the values for emissivity and radiance we obtain for I_2

	Nominal	Bias	Long-term drift	Short-term drift
$I_{2_{300}}$	= 0.144235	(1 ±0.471474)	(1 ±0.180368)	(1 ±0.001727) W/m^2-sr
$I_{2_{200}}$	= 0.284323 x 10^{-1}	(1 ±0.25) (1 ±0.480404)	(1 ±0.125) (1 ±0.120098)	(1 ±0.002402) W/m^2-sr
$I_{2_{150}}$	= 0.578580 x 10^{-2}	(1 ±1.104)	(1 ±0.3364)	(1 ±0.004229) W/m^2-sr

This factor is the additive term due to the primary optical system. In its simplest form, as used in the specific analysis, this term is due to the radiance from a single surface.

STRAY LIGHT -- NEAR AXIS J, FAR OFF AXIS K

No values are assigned for J and K in specific error analysis. Since the only radiometer transfer term preceding stray light is the primary mirror reflectivity of 0.992, these terms would add their radiance values almost directly. A stray-light value of 0.001 times the maximum radiance thus would produce an accuracy error of 0.001 times the maximum radiance. To indicate that these terms may vary from zero up to the maximum level, one can write

$$J = 0.0005\ N_{max}\ (1 \pm 1)$$

$$K = 0.0005\ N_{max}\ (1 \pm 1)$$

The most difficult term to assess is J, since this term deals with energy from near-axis objects. Obviously, image quality is important in determining stray-light effects attributable to this module. Although extended targets should tend to mask image effects, consideration must be given at the systems level to effects of targets with uniform appearance over large angles.

*Short-term drift is drift between collection cycles.

MODULATION SYSTEM

L_1 dimensionless multiplier

$L_1 = 1$ (open)

$L_1 = 0$ (closed)

The frequency characteristics of L are considered in the detector and signal-processing elements.

$$L_2 = \epsilon_{mo}\, N_{mo,\,\Delta\lambda} \left(1 \pm \frac{\Delta\rho_m}{\epsilon_{mo}}\right) \left(1 \pm \frac{\Delta N_{m,\,\Delta\lambda}}{N_{mo,\,\Delta\lambda}}\right)$$

$$L_2' = ((((S_2' Q_1 + Q_2') P_1 + P_2') O_1 + O_2') N_1 + N_2') M_1 + M_2'$$

for the model of 26 March.

The chopper is assumed to be painted black and to have an emissivity of 0.975 ± 0.015. The long-term drift is ± 0.01.

	Bias	Long-term drift	Short-term drift
$\epsilon_m = 0.975$	(1 ± 0.015385)	(1 ± 0.010256)	(1 ± 0.000000)

	Bias	Long-term drift	Short-term drift
$L_{2_{300}} = 0.146489 \times 10^{+2}$	(1 ± 0.236859)	(1 ± 0.065624)	(1 ± 0.001727) W/m^2-sr
$L_{2_{200}} = 0.288766 \times 10^{+1}$	(1 ± 0.015385) (1 ± 0.480404)	(1 ± 0.010256) (1 ± 0.120098)	(1 ± 0.002402) W/m^2-sr
$L_{2_{150}} = 0.587621$	(1 ± 0.868087)	(± 0.221681)	(1 ± 0.004229) W/m^2-sr

FIELD STOP

$M_1 = \zeta_f = A_{f_s/A_D}$ = a ratio

$M_1 = 0.92$ for point target at infinity but,

$= 1.00$ for extended sources when convoluted with off-axis images.

M_2 = 0 for field stop larger than detector area

= a radiance for other cases: W/m^2-sr

M_2' = 0. This assumption says that no radiance from the front of the field stop is reflected from the chopper at an angle which will allow radiation to reach the detector

FIRST REIMAGING ELEMENT

N_1 = ratio of reflected to transmitted flux

For the reflective system, N_1 is determined by the reflectivity of the mirror surface.

$$N_1 = I_1$$

For the refractive system, N_1 is determined both by the surface reflection from the lens and from the absorption within the lens. Assuming after anti-reflection coating an efficiency of 0.95 (1 ± 0.020) bias (1 ± 0.001) long-term drift, for the surface and for absorption considerations an efficiency of 0.975 (1 ± 0.002) bias (1 ± 0.001) long-germ drift, one finds an efficiency of

		Bias	Long-term drift
N_{1A} = 0.92625	(1 ±0.020)	(1 ±0.002)	(1 ±0.001)(1 ±0.001)

N_2 = radiance, $(W/m^2\text{-sr})$

For the reflective system

$$N_2 = \zeta_{r1}\, \epsilon_{r10}\, N_{r10,\Delta\lambda} \left(1 \pm \frac{\Delta\rho_{r1}}{\epsilon_{r10}}\right)\left(1 \pm \frac{\Delta N_{r1,\Delta\lambda}}{N_{r10,\Delta\lambda}}\right)$$

Temperatures considered are

Nominal	Bias	Long-term drift	Short-term drift
300°K	±20°	±5°	±0.1°
200°K	±20°	±5°	±0.1°
80°K	±5°	±1°	±0.01°
60°K	±5°	±1°	±0.01°

The form factor ζ_{r1} is assumed to be 1.2 and to have no error and the variation in emissivity is assumed as that used for I_2.

Then,

$$N_{2_{300}} = I_{2_{300}}$$

$$N_{2_{200}} = I_{2_{200}}$$

		Bias	Long-term drift	Short-term drift
$N_{r1,\,\Delta\lambda\,80^{\circ}K}$	$= 0.243033 \times 10^{-2}$	(1 ± 0.073445)	(1 ± 0.146890)	(1 ± 0.001469) $W/m^2\text{-sr}$
$N_{r1,\,\Delta\lambda\,60^{\circ}K}$	$= 0.490111 \times 10^{-4}$	(1 ± 0.129693)	(1 ± 0.259387)	(1 ± 0.002594) $W/m^2\text{-sr}$
$N_{2_{80}}$	$= 0.233312 \times 10^{-4}$	(1 ± 0.25) (1 ± 0.073445)	(1 ± 0.125) (1 ± 0.146890)	(1 ± 0.001469) $W/m^2\text{-sr}$
$N_{2_{60}}$	$= 0.470507 \times 10^{-6}$	(1 ± 0.380)	(1 ± 0.3844)	(1 ± 0.002594) $W/m^2\text{-sr}$

For the refractive element, one has

$$N_2A = \zeta_{r1}\ \epsilon_{r10}\ N_{r10,\,\Delta\lambda} \left(1 \pm \frac{\Delta\epsilon_{r1}}{\epsilon_{r10}}\right) \left(1 \pm \frac{\Delta N_{r1,\,\Delta\lambda}}{N_{r10,\,\Delta\lambda}}\right)$$

ζ_{r1} = form factor, assumed to be unity

Emissivity is assumed to be $\epsilon_{r1} = 1 - \rho_{r1} - \tau_{r1} = 0.07385$

		Bias	Long-term drift	Short-term drift
$N_{2A_{300}}$	$= 0.110806 \times 10^{+1}$	(1 ± 0.287051) (1 ± 0.508525)	(1 ± 0.026102) (1 ± 0.081470)	(1 ± 0.001727) $W/m^2\text{-sr}$
$N_{2A_{200}}$	$= 0.218425$	(1 ± 0.287051) (1 ± 0.480404)	(1 ± 0.026102) (1 ± 0.120098)	(1 ± 0.002402) $W/m^2\text{-sr}$
$N_{2A_{80}}$	$= 0.179237 \times 10^{-3}$	(1 ± 0.287051) (1 ± 0.146890)	(1 ± 0.073445) (1 ± 0.001469)	(1 ± 0.026102) $W/m^2\text{-sr}$
$N_{2A_{60}}$	$= 0.361457 \times 10^{-5}$	(1 ± 0.287051) (1 ± 0.259387)	(1 ± 0.129693) (1 ± 0.002594)	(1 ± 0.026102) $W/m^2\text{-sr}$

SPECTRAL FILTER

O_1 = ratio of transmitted to incident flux

The spectral filter is assumed to have a square bandpass for purposes of this analysis. Actual filter characteristics should be used when available. The assumed substrate is Irtran 6. Detailed parameters of filter behavior vary significantly from sample to sample.

$$O_1 = {}_{bo}\left(1 \pm \frac{\Delta\tau_b}{\tau_{bo}}\right)$$

$$\tau_b = 1 - \alpha_b(\lambda) - \rho_b(\lambda) = 0.600 \text{ in band}$$
$$= 0.0 \quad \text{out of band}$$

$$\alpha_b(\lambda) = 0.02 \quad \text{in band}$$
$$= 0.20 \quad \text{out of band}$$

$$\rho_b(\lambda) = 0.38 \quad \text{in band}$$
$$= 0.80 \quad \text{out of band}$$

The spectral filter is assumed to have the values of temperature and tolerances also associated with the first reimaging element.

The tolerances associated with α_b and ρ_b are estimated as

	Bias	Long-term drift	Short-term drift	
$\alpha_b(\lambda) = 0.02$	(1 ±1.0)	(1 ±0.00100)	(1 ±0.00010)	in band
$= 0.20$	(1 ±0.50)	(1 ±0.00500)	(1 ±0.00010)	out of band
$\rho_b(\lambda) = 0.38$	(1 ±0.06)	(1 ±0.00200)	(1 ±0.00010)	in band
$= 0.80$	(1 ±0.125)	(1 ±0.00500)	(1 ±0.00010)	out of band

For the multiplication term, only in-band characteristics are required. The filter is assumed at an angle which reflects radiation to a blackened part of the radiometer so that multiple reflections also are not important.

	Bias	Long-term drift	Short-term drift
$O_1 = 0.600$	(1 ±0.067667)	(1 ±0.001300)	(1 ±0.000067)

O_2 – a radiance in W/m^2-sr

$$O_2 = \epsilon_{bo}(\lambda)\, N_{bo,\,\Delta\lambda'} \left(1 \pm \frac{\Delta\alpha_b(\lambda)}{\epsilon_{bo}(\lambda)}\right)\left(1 \pm \frac{\Delta N_{b,\,\Delta\lambda'}}{N_{bo,\,\Delta\lambda'}}\right)$$

The expression $\Delta\lambda'$ refers to radiance from 0 to 22 microns, that is, the radiance from the filter reaches the detector broadband.

The expression $N_{\Delta\lambda}$ for in-band radiance is defined as N_2. N_{OB} for out-of-band radiance is defined by $N_{\Delta\lambda'} - N_{\Delta\lambda}$. (The assumption is made for the analysis that the detector and filter both have flat responses.)

	Bias	Long-term drift	Short-term drift
$N_{b,\Delta\lambda' 300^{o}K} = 1.148 \times 10^{-2}$ W/m^2-sr	(1 ±0.304)	(1 ±0.076)	(1 ±0.001520)
$N_{b,\Delta\lambda' 200^{o}K} = 15.84$ W/m^2-sr	(1 ±0.627)	(1 ±0.157)	(1 ±0.003135)
$N_{b,\Delta\lambda' 800^{o}K} = 25.48$ W/m^2-sr	(1 ±0.761)	(1 ±0.1525)	(1 ±0.01525)
$N_{b,\Delta\lambda' 60^{o}K} = 1.115 \times 10^{-3}$ W/m^2-sr	(1 ±1.80)	(1 ±0.3600)	(1 ±0.0360)
$N_{OB_{300^{o}K}} = 0.99775 \times 10^{+2}$	(1 ±0.383)	(1 ±0.0958)	(1 ±0.0016) W/m^2-sr
$N_{OB_{200^{o}K}} = 12.88$	(1 ±0.8816)	(1 ±0.2207)	(1 ±0.004408) W/m^2-sr
$N_{OB_{80^{o}K}} = 2.306 \times 10^{-2}$	(1 ±0.8486)	(1 ±0.18399)	(1 ±0.01701) W/m^2-sr
$N_{OB_{60^{o}K}} = 1.046 \times 10^{-3}$	(1 ±1.93)	(1 ±0.396)	(1 ±0.0385) W/m^2-sr

Radiance in band is presented in Table D4.

TABLE D4. - IN-BAND RADIANCE VALUES

Filter radiance	Bias	Long-term drift	Short-term drift
$O_{2IB_{300}} = 0.300490$	(1 ±1.221)	(1 ±0.056)	(1 ±0.0018) W/m^2-sr
$O_{2IB_{200}} = 0.592340 \times 10^{-1}$	(1 ±1.480)	(1 ±0.121)	(1 ±0.0025) W/m^2-sr
$O_{2IB_{80}} = 0.486066 \times 10^{-4}$	(1 ±1.073)	(1 ±0.148)	(1 ±0.0015) W/m^2-sr
$O_{2IB_{60}} = 0.980220 \times 10^{-6}$	(1 ±1.130)	(1 ±0.260)	(1 ±0.0027) W/m^2-sr
$O_{20B_{300}} = 22.96$	(1 ±0.804)	(1 ±0.081)	(1 ±0.0016) W/m^2-sr
$O_{20B_{200}} = 3.168$	(1 ±1.127)	(1 ±0.162)	(1 ±0.0032) W/m^2-sr
$O_{20B_{80}} = 5.096 \times 10^{-3}$	(1 ±1.261)	(1 ±0.157)	(1 ±0.0153) W/m^2-sr
$O_{20B_{60}} = 2.230 \times 10^{-4}$	(1 ±2.30)	(1 ±0.365)	(1 ±0.0361) W/m^2-sr
$O_2 = O_{2IB} + O_{20B}$	$O_2^1 = O_{21B}$		W/m^2-sr
$O_{2_{300}} = 23.26$	(1 ±0.793)	(1 ±0.086)	(1 ±0.00160) W/m^2-sr
$O_{2_{200}} = 3.227$	(1 ±1.134)	(1 ±0.1582)	(1 ±0.00319) W/m^2-sr
$O_{2_{80}} = 5.048 \times 10^{-3}$	(1 ±1.283)	(1 ±0.1599)	(1 ±0.01546) W/m^2-sr
$O_{2_{60}} = 2.239 \times 10^{-4}$	(1 ±2.295)	(1 ±0.3648)	(1 ±0.03595) W/m^2-sr

One obtains immediately the relations

$$P_1 = N_1$$

$$P_{1A} = N_{1A}$$

$$P_2 = \zeta_{r2}\ \epsilon_{r20}\ N_{r20,\,\Delta\lambda}'\left(1 \pm \frac{\Delta\rho_{r2}}{\epsilon_{r20}}\right)\left(1 \pm \frac{\Delta N_{r2,\,\Delta\lambda}'}{N_{r20,\,\Delta\lambda}'}\right)$$

ζ_{r2} = form factor assumed to be 1.2

$$P_{2A} = \zeta_{r2}\ \epsilon_{r20}\ N_{r20,\,\Delta\lambda}'\left(1 \pm \frac{\Delta\epsilon_{r2}}{\epsilon_{r20}}\right)\left(1 \pm \frac{\Delta N_{r2,\,\Delta\lambda}'}{N_{r20,\,\Delta\lambda}'}\right)$$

ζ_{r2} = form factor assumed to be unity

$$P_2^1 = N_2$$

$$P_{2A}^1 = N_{2A}$$

In-band radiance is presented in Table D5.

TABLE D5. - SECOND-REIMAGING-ELEMENT IN-BAND RADIANCE VALUES

Element radiance	Bias	Long-term drift	Short-term drift
$P_{2_{300}} = 9.184 \times 10^{-1}$	(1 ±0.554)	(1 ±0.201)	(1 ±0.001520) W/m^2-sr
$P_{2_{200}} = 1.2672 \times 10^{-1}$	(1 ±0.877)	(1 ±0.282)	(1 ±0.003135) W/m^2-sr
$P_{2_{80}} = 2.0384 \times 10^{-4}$	(1 ±1.011)	(1 ±0.278)	(1 ±0.01525) W/m^2-sr
$P_{2_{60}} = 8.920 \times 10^{-5}$	(1 ±2.05)	(1 ±0.485)	(1 ±0.0360) W/m^2-sr
$P_{2A_{300}} = 8.466$	(1 ±0.591)	(1 ±0.092)	(1 ±0.001520) W/m^2-sr
$P_{2A_{200}} = 1.168$	(1 ±0.914)	(1 ±0.183)	(1 ±0.003135) W/m^2-sr
$P_{2A_{80}} = 1.879 \times 10^{-3}$	(1 ±1.05)	(1 ±0.179)	(1 ±0.01525) W/m^2-sr
$P_{2A_{60}} = 8.223 \times 10^{-5}$	(1 ±2.09)	(1 ±0.386)	(1 ±0.0360) W/m^2-sr
$P_2^1 = N_2$ $P_{2A}^1 = N_{2A}$			

Cold Stop

$$Q_1 = \text{a solid angle} = \pi \sin^2 \theta$$

Assuming an f/2 system, defined by an accurately made cold stop, Q_1 = 0.184726 bias (1 ±0.002) $Q_1^1 = Q_1$ by assumption

Cavity

$$Q_2 = \epsilon_{cy0}\, N_{cy0,\Delta\lambda}' \left(1 \pm \frac{\Delta\epsilon_{cy}}{\epsilon_{cy0}}\right) \left(1 \pm \frac{\Delta N_{cy,\Delta\lambda}'}{N_{cy0,\Delta\lambda}'}\right) \pi \cos^2\theta \left(1 \pm \frac{\Delta \cos^2\theta}{\cos^2\theta}\right);\ W/m^2$$

ϵ_{cy} = 0.975 (1 ±0.015385) (1 ±0.010256) (1 ±0.000)

$\cos^2\theta$ = 2.957 (1 ±0.002) for an f/2 system

$Q_{2_{300}}$	= $3.3097 \times 10^{+2}$	(1 ±0.321)	(1 ±0.086)	(1 ±0.001520) W/m^2
$Q_{2_{200}}$	= 45.667	(1 ±0.644)	(1 ±0.167)	(1 ±0.003135) W/m^2
$Q_{2_{80}}$	= 7.3459×10^{-2}	(1 ±0.778)	(1 ±0.163)	(1 ±0.01525) W/m^2
$Q_{2_{60}}$	= 3.2145×10^{-3}	(1 ±1.817)	(1 ±0.370)	(1 ±0.0360) W/m^2

The expression Q_2^1 is neglected in this analysis since this value eventually will be 0.0031 Q_2 due to reflectance from the detector, blackened chopper, and spectral limiting by the filter.

OPTICAL TRANSDUCER

Total irradiance of the detector is measured in W/m^2. However, it must be realized that the actual detector resistance is inversely proportional to the photon flux (photons sec^{-1}), if a constant-bias current is supplied. According to Planck's radiation law, radiance and photon flux are given by

$$F_{\Delta\lambda} = K A_d \Omega\, 2c^2 h \int_{\lambda 1}^{\lambda 2} \lambda^{-5} \left[\exp\left(\frac{hc}{\lambda kT}\right) - 1\right]^{-1} d\lambda \text{ (watts), and}$$

$$Q_{\Delta\lambda} = \frac{\lambda}{hc} F_{\Delta\lambda}$$

$$= K A_d \Omega\, 2c \int_{\lambda 1}^{\lambda 2} \lambda^{-4} \left[\exp\left(\frac{hc}{\lambda kT}\right) - 1\right]^{-1} d\lambda \text{ (photons sec}^{-1}\text{), respectively,}$$

where K = constant expressing the fact that the flux is not generated by a blackbody.

A_d = detector area exposed to the radiation

Ω = solid angle subtended at the cold stop

h = Planck's constant

c = light velocity

k = Boltzmann's constant

λ = wavelength

T = temperature

Unfortunately, therefore, a unique constant that converts radiant into photon flux cannot be determined readily; that is, the conversion factor is generally a function of λ. However, in the wavelength intervals of interest, one may define

$$C_{FQ} = F_{\Delta\lambda}/Q_{\Delta\lambda}$$

$$= ch \int_{\lambda 1}^{\lambda 2} \lambda^{-5} \left[\exp\left(\frac{hc}{\lambda kT}\right) - 1\right]^{-1} d\lambda \Big/ \int_{\lambda 1}^{\lambda 2} \lambda^{-4} \left[\exp\left(\frac{hc}{\lambda kT}\right) - 1\right]^{-1} d\lambda \left(\frac{\text{watt sec}}{\text{photons}}\right)$$

In general, since the sum of the irradiance terms ΣH is not completely known, the actual detector resistance R_d must be referred to a value R_m that is measured under well-defined experimental conditions:

$$R_d = \frac{R_m \Sigma Q_{cal} C_{FQ}}{A_d \Sigma H}$$

where ΣQ_{cal} 4 sum of calculated photon flux that defines the experimental conditions. In this manner, one obtains the detector output voltage

$$E_d = R_d i_b$$

where i_b = constant-bias current. This derivation reveals that the multiplying factor of the optical transducer is defined by

$$S_1 = \frac{R_m \Sigma Q_{cal} i_b C_{FQ}}{A_d} \text{ volt-watt m}^{-2}$$

Numerically, one has

$$S_1 = 7.03379 \times 10^{-4} \text{ volt-watt m}^{-2} \quad \underline{\text{Bias}} \quad (1 \pm 0.100) \quad \underline{\text{Long-term drift}} \quad (1 \pm 0.001) \quad \underline{\text{Short-term drift}} \quad (1 \pm 0.0001)$$

where drift characteristics are determined from the current-bias-source characteristics and the bias value is dctermined by measurement and manufacturing tolerances. In actuality, the value for bias might be larger than the assumed value; however, it is anticipated that once the basic model has been verified, values of the order indicated would be practical. The nominal value of S_1 is derived in the error-analysis working notes.

The additive term, S_2, of the optical transducer is a noise voltage. If only shot and photon noise are considered to contribute to this voltage, and if one defines

$$\Sigma Q = \frac{A_d}{C_{FQ}} \Sigma H \text{ (photons sec}^{-1}) = 2.5179 \times 10^{20} \Sigma H$$

one obtains

$$S_2 = \frac{\sqrt{2 i_b \Delta\lambda R_m^2 \left(\Sigma Q_{cal}\right)^2 \left(9 + \frac{i_b}{C_{FQ} \Sigma Q}\right)}}{\Sigma Q} \text{ (volts)}$$

where 9 = charge of an electron. Numerically, one has

$$S_2 = \frac{7.229 \times 10^{20}}{\Sigma Q} \sqrt{1.6021 \times 10^{-19} + \frac{5 \times 10^{-4}}{C_{FQ} \Sigma Q}} \text{ (volts)}$$

SIGNAL PROCESSING

The multiplying factor of the preamplifier is generally the product of the gain, C_a and a frequency-response function, $G_o(\omega)$. Defining specifically

$$G_o(\omega) = \left[\left(1 + R_d/R_i\right) + j\omega C_i R_d\right]^{-1}$$

where R_i, C_i = amplifier input resistance and capacitance, respectively.

$$G_o(\omega) = \left\{1 + \frac{1}{\Sigma Q}\left[R_m \Sigma Q_{cal}\left(\frac{1}{R_i} + j\omega C_i\right)\right]\right\}^{-1}$$

$$T_1 = \frac{C_a}{1 + \frac{1}{\Sigma Q}\left[R_m \Sigma Q_{cal}\left(\frac{1}{R_i} + j\omega C_i\right)\right]}$$

With

$$C_a = 1$$

$$R_i = 50 \times 10^6 \text{ ohms}$$

$$\omega = 2\pi \ 5500 \text{ cps}$$

$$C_i = 5 \times 10^{-12} \text{ farads}$$

$$j = \sqrt{-1}$$

one obtains

$$T_1 = \frac{1}{1 - \frac{5.412 \times 10^{+13}}{\Sigma Q}} \qquad \underline{\text{Bias}} \quad (1 \pm 0.050) \qquad \underline{\text{Long-term drift}} \quad (1 \pm 0.0001) \qquad \underline{\text{Short-term drift}} \quad (1 \pm 0.00001)$$

The preamplifier is characterized by two additive terms

T_{21} = an offset in volts

T_{22} = a noise in volts

$$T_{21}' = \frac{C_a \ E_{off}}{1 + \frac{R_i}{R_d} + j\omega \ C_i \ R_i}$$

$$T_{22} = \frac{C_a \ E_{am}}{1 + \frac{R_i}{R_d} + j\omega \ C_i \ R_i}$$

E_{off} = 0.005 volts, bias: (1 ± 0.01), long-term drift: (1 ± 0.001)

$E_{am} = 1.2145 \times 10^{-2}$ volts

$\frac{R_i}{R_d} = 1.412 \times 10^{-3} \Sigma Q$, $j\omega \ C_i \ R_i = -8.58$

SPECIFIC ERROR ANALYSIS, UNIVERSAL MULTIPLIERS, AND REFRACTIVE REIMAGING ELEMENTS

The specific error analysis is summarized in Table D6.

$$Q_1 = 0.184\,726\ (1\pm0.002)\ (1\pm0.0000)\ (1\pm0.000\,000)$$

$$Q_1P_{1A} = 0.171\,102\ (1\pm0.024)\ (1\pm0.0020)\ (1\pm0.000\,000)$$

$$Q_1P_{1A}O_1 = 0.102\,661\ (1\pm0.092)\ (1\pm0.0033)\ (1\pm0.000\,067)$$

$$Q_1P_{1A}O_1N_{1A}M_1L_1 = 0.095\,090\ )1\pm0.114)\ (1\pm0.0053)\ (1\pm0.000\,067)$$

$$Q_1P_{1A}O_1N_{1A}M_1L_1I_1 = 0.094\,329\ (1\pm0.117)\ (1\pm0.0063)\ (1\pm0.000\,067)$$

$$L_1 = 1 \qquad M_1 = 1 \qquad M_2 = 0 \qquad P_{1A} = N_{1A}$$

The signal multiplier is reduced to 0.872 of the value for the reflective reimaging system, but this change would not appear to affect significantly signal measurement. Uncertainty in the nominal value and bias is increased by 50%, as is the long-term-drift characteristic. Short-term drift still is determined primarily by changes in the optical filter. From a multiplier point of view, it would appear that there is little real difference between the specific system using the reflective or refractive reimaging elements.

SPECIFIC ERROR ANALYSIS, UNIVERSAL MULTIPLIER, AND REFLECTIVE REIMAGING ELEMENTS

$$Q_1 = 0.184726(1\pm.002)(1\pm.0000)(1\pm.000\,000)$$

$$Q_1P_1 = 0.183248(1\pm.005)(1\pm.0010)(1\pm.000\,000)$$

$$Q_1P_1O_1 = 0.109949(1\pm.072)(1\pm.0023)(1\pm.000\,067)$$

$$Q_1P_1O_1N_1M_1L_1 = 0.109069(1\pm.075)(1\pm.0033)(1\pm.000\,067)$$

$$Q_1P_1O_1N_1M_1L_1I_1 = 0.108197(1\pm.078)(1\pm.0043)(1\pm.000\,067)$$

$$L_1 = 1 \qquad M_1 = 1 \qquad M_2 = 0 \qquad P_1 = N_1 = I_2$$

Since for purposes of specific error analysis no terms of this form are considered to be temperature dependent except as indicated by the short-term drift characteristics, the above terms are applied to all systems regardless of temperatures of individual elements of the radiometer.

TABLE D6. - SPECIFIC ERROR ANALYSIS
(Plus units are W/m^2-sr)

Module	Factor	Description	Bias	Long-term drift	Short-term drift
Collection system	I_1 (x) I_2 (+) (300) (200) (150)	Transfer function of primary emission of primary optics	0.003 700 200 60	0.001 300 70 20	0.0000 2 0.7 0.2
Stray light	J (+) K (+)	Near axis Far-off axis	0.0005 N_{max} 0.0005 N_{max}		
Modulation system	L_1 (x) (open) (closed) L_2 (+) (300) (200) (150)	Transfer function of chopper (chop wave) Chopper radiances (= 0.975 ±0.015)	1 0 4000 5100	 9500 3800 1300	 300 70 20
Field stop	M_1 (x) (point) (extended) M_2 (+) (fs at det) (fs at fs)	A_{fs}: Ap Field-stop radiance	0.92 1.00 0.00 N_{FS}		
First reimaging element	N_1 (x) (refl) (refr) N_2 (+) (refl-300) -200) - 80) - 60) (refr-300) -200) - 80) - 60)	Transfer function of secondary Mirror radiances Lens radiance	0.003 0.02 700 200 8×10^{-2} 1.6×10^{-3} 5500 1700 0.63 x 1.5×10^{-2}	0.001 0.002 300 70 6×10^{-2} 1.6×10^{-7} 900 300 0.31 1.1×10^{-2}	0.000 2 0.7 3×10^{-4} 7.5×10^{-6} 20 5 2.5×10^{-3} 9.3×10^{-5}

TABLE D6. - SPECIFIC ERROR ANALYSIS (Continued)

Module	Factor	Description	Bias	Long-term drift	Short-term drift
Spectral	O_1 (x)	Filter transfer function	0.04	0.008	0.00004
	O_2 (+) (300)	Filter radiance	8500	20000	400.
	(200)		3600	4800	100.
	(80)		65	8	0.8
	(60)		4.9	.8	0.08
Second reimaging element	P_1 (x) (refl)	Element transfer function	0.003	0.001	0.000
	(refr)		0.02	0.002	
	P_2 (+) (refl-300)	Mirror radiances	5100	1900.	14.
	-200)		1100	400	4.
	- 80)		2	0.6	.03
	- 60)		1.8	0.4	.03
	(refr-300)	Lens radiances	50000.	0.8×10^4	.00100
	-200)		11000.	0.2×10^4	40
	- 80)		20	3.4	0.3
	- 60)		1.7	.31	0.03
Cold stop	Q_1 (x)	Transfer function	0.0004		
	Q_2 (+) (300)	Cavity radiance	103×10^4	28×10^4	0.51×10^4
	(200)		29×10^4	7.8×10^4	0.14×10^4
	(80)		600.	100.	10.
	(60)		58	12	1.1

$$Z_{max} = 1.0000 \times 10^{+1} \text{ w/m}^2\text{-sr}$$

$$Z_{accuracy} = 3.000 \times 10^{-2} \text{ w/m}^2\text{-sr}$$

$$Z_{min} = 5.00 \times 10^{-3} \text{ w/m}^2\text{-sr}$$

$$Z_{max.}\ Q_1P_1O_1N_1M_1L_1I_1 = 1.08197(1\pm.078)(1\pm.0043)(1\pm.000\ 067) \text{ w/m}^2\text{-sr}$$

$$Z_{acc.}\ Q_1P_1O_1N_1M_1L_1I_1 = 3.24591\text{x}10^{-3}(1\pm.078)(1\pm.0043)(1\pm.000\ 067) \text{ w/m}^2\text{-sr}$$

$$Z_{min.}\ Q_1P_1O_1N_1M_1L_1I_1 = 5.40985\text{x}10^{-4}(1\pm.078)(1\pm.0043)(1\pm.000\ 067) \text{ w/m}^2\text{-sr}$$

SUMMARY

To bound the performance which could be obtained from the type of system documented in the specific error analysis, an analysis was made of the extremes. That is, detailed data were computed for the system producing the least internal radiance and for the system producing the most internal radiance. Tables below document the radiance levels associated with the various radiance sources to be considered. Total power for each appropriate condition is summarized in both W/m^2 and photon $m^{-2}sec^{-1}$.

The bandwidth will be between 615.5 Hz and 4931.8 Hz. Observation time used to evaluate photon noise is $T = 1/20b.811\ \mu sec \geq t \geq 101\ \mu sec$. Photons associated with the noise equivalent signals and with the photon noise are tabulated below.

Photons

	Minimum radiance system		Maximum radiance system	
	$811_{\mu sec}$	$101_{\mu sec}$	$811_{\mu sec}$	$101_{\mu sec}$
$\sqrt{Q_{Amin}}$ Equivalent	$1.10\text{x}10^6$	$1.38\text{x}10^5$	$9.63\text{x}10^5$	$1.20\text{x}10^5$
$\sqrt{Q_{dark}}$	$2.82\text{x}10^3$	$9.96\text{x}10^2$	$8.29\text{x}10^5$	$2.93\text{x}10^5$
$\sqrt{Q_{Amax}}$	$4.71\text{x}10^4$	$1.67\text{x}10^4$	$8.30\text{x}10^5$	$2.93\text{x}10^5$
$\sqrt{Q_{Aacc}}$	$3.82\text{x}10^3$	$1.31\text{x}10^3$	$8.29\text{x}10^5$	$2.93\text{x}10^5$
$\sqrt{Q_{Amin}}$	$3.01\text{x}10^3$	$1.07\text{x}10^3$	$8.29\text{x}10^5$	$2.93\text{x}10^5$
$\sqrt{Q_{closed}}$	$1.17\text{x}10^4$	$4.14\text{x}10^3$	$8.31\text{x}10^5$	$2.93\text{x}10^5$

Minimum Radiance System*

Components are at 150° and 60°; all optical elements are reflective except for filter.

F, I, L, M at 150°K — N, O, P, Q at 60°K

Description	Bias	Long-term drift, w/m^2	Short-term drift, w/m^2
$Q_2 = 3.214500 \times 10^{-3}$	(1±1.817)	(1±0.3700)	(1±0.036000)
$Q_1P_2 = 0.016477 \times 10^{-3}$	(1±2.025)	(1±0.4850)	(1±0.036000)
$Q_1P_1O_2 = 0.041029 \times 10^{-3}$	(1±2.300)	(1±0.3658)	(1±0.035950)
$Q_1P_1O_1N_2 = 0.000052 \times 10^{-3}$	(1±0.452)	(1±0.3867)	(1±0.002661)
$Q_1P_1O_1N_1M_1L_1I_2 = 0.631050 \times 10^{-3}$	(1±1.179)	(1±0.3397)	(1±0.004296)
$Q_1P_1O_1N_1M_1L_1I_1\ A_{max} = 1081.970000 \times 10^{-3}$	(1±0.078)	(1±0.0043)	(1±0.000067)
$Q_1P_1O_1N_1M_1L_1I_1\ A_{acc} = 3.245910 \times 10^{-3}$	(1±0.078)	(1±0.0043)	(1±0.000067)
$Q_1P_1O_1N_1M_1L_1I_1\ A_{min} = 0.540985 \times 10^{-3}$	(1±0.078)	(1±0.0043)	(1±0.000067)
$Q_1P_1O_1N_1M_1L_2 = 64.091200 \times 10^{-3}$	(1±0.943)	(1±0.2250)	(1±0.004296)
ΣH: $\Sigma P_{dark} = 3.903200 \times 10^{-3}$	(1±1.7198)	(1±0.3655)	(1±0.030874)
$\Sigma P_{amax} = 1085.810000 \times 10^{-3}$	(1±0.0839)	(1±0.0056)	(1±0.000178)
$\Sigma P_{aacc} = 7.148910 \times 10^{-3}$	(1±0.9744)	(1±0.2015)	(1±0.016886)
$\Sigma P_{amin} = 4.443990 \times 10^{-3}$	(1±1.5200)	(1±0.3216)	(1±0.027123)
$\Sigma P_{closed} = 67.363200 \times 10^{-3}$	(1±0.9858)	(1±0.2321)	(1±0.005836)
		$\frac{\text{proton m}^{-2}\ \text{sec}^{-1}}{}$	
$\Sigma Q'$: $\Sigma Q'_{dark} = 2.975214 \times 10^{+17}$	(1±1.7198)	(1±0.3655)	(1±0.030874)
$\Sigma Q'_{amax} = 827.704000 \times 10^{+17}$	(1±0.0839)	(1±0.0056)	(1±0.000178)
$\Sigma Q'_{aacc} = 5.449256 \times 10^{+17}$	(1±0.9744)	(1±0.2015)	(1±0.016886)
$\Sigma Q'_{amin} = 3.387431 \times 10^{+17}$	(1±1.5200)	(1±0.3216)	(1±0.027123)
$\Sigma Q'_{closed} = 51.347599 \times 10^{+17}$	(1±0.9858)	(1±0.2321)	(1±0.005836)

*No consideration was given to the actual spectral response. All W-to-photon sec^{-1} conversions are based on 0.762255×10^{20} photon W sec^{-1}.

Maximum Radiance System

All components at 300°K except for the detector; this system uses refractive reimaging optics.

Description	Bias	Long-term drift, w/m^2	Short-term drift, w/m^2
$Q_2 = 330.9700000$	(1±0.321)	(1±0.0860)	(1±0.001520)
$Q_1P_{2A} = 1.5638900$	(1±0.593)	(1±0.0920)	(1±0.001520)
$Q_1P_{1A}O_2 = 3.9798399$	(1±0.736)	(1±0.0880)	(1±0.001600)
$Q_1P_{1A}O_1N_{2A} = .1137540$	(1±0.601)	(1±0.0848)	(1±0.001794)
$Q_1P_{1A}O_1N_{1A}M_1L_1I_2 = .0137540$	(1±0.585)	(1±0.1857)	(1±0.001794)
$Q_1P_{1A}O_1N_{1A}M_1L_1I_1A_{max} = .9433000$	(1±0.117)	(1±0.0063)	(1±0.000067)
$A_{acc} = .0028000$	(1±0.117)	(1±0.0063)	(1±0.000067)
$A_{min} = .0005000$	(1±0.117)	(1±0.0063)	(1±0.000067)
$Q_1P_{1A}O_1N_{2A}M_1L_2 = 1.3929600$	(1±0.351)	(1±0.0709)	(1±0.001794)
ΣH: $\Sigma P_{dark} = 336.6411000$	(1±0.329)	(1±0.0863)	(1±0.001527)
$\Sigma P_{amax} = 337.5844000$	(1±0.354)	(1±0.0863)	(1±0.001527)
$\Sigma P_{aacc} = 336.6439000$	(1±0.329)	(1±0.0863)	(1±0.001527)
$\Sigma P_{min} = 336.6416000$	(1±0.329)	(1±0.0863)	(1±0.001527)
$\Sigma P_{closed} = 338.0204000$	(1±0.329)	(1±0.0863)	(1±0.001527)
			Photons m^{-2} sec^{-1}
$\Sigma Q'$: $\Sigma Q'_{dark} = 2.566047 \times 10^{+22}$	(1±0.329)	(1±0.0863)	(1±0.001527)
$\Sigma Q'_{amax} = 2.573237 \times 10^{+22}$	(1±0.354)	(1±0.0863)	(1±0.001527)
$\Sigma Q'_{aacc} = 2.566068 \times 10^{+22}$	(1±0.329)	(1±0.0863)	(1±0.001527)
$\Sigma Q'_{amin} = 2.556051 \times 10^{+22}$	(1±0.329)	(1±0.0863)	(1±0.001527)
$\Sigma Q'_{closed} = 2.576560 \times 10^{+22}$	(1±0.329)	(1±0.0863)	(1±0.001527)

For the minimum radiance system, the number of photons associated with the minimum signal input is $4.123\ 658 \times 10^{16}$ photons m^{-2} sec^{-1} and for the maximum radiance system $3.595\ 114 \times 10^{16}$ photons m^{-2} sec^{-1}. The detector is 0.2 mrad x 1.0 mrad, so the area is 3.30322 m^2 for the 16-inch focal length used.

These tables indicate that all of the system-design requirements can be met with the system corresponding to the minimum radiance components and temperatures. Major parameters to be considered are (1) noise - well below the desired level; that is, the $\sqrt{Q_{dark}}$, $\sqrt{Q_{Amax}}$, $\sqrt{Q_{Amin}}$, or $\sqrt{Q_{closed}}$ compared to Q_{Amin}-equivalent: (2) long-term drift in transfer characteristics - removed by virtue of the inflight calibrator; that is, the drift factor associated with the product $Q_1P_1O_1N_1M_1L_1I_1$: (3) short-term drift of the dark radiance level and of the chopper-closed radiance value is small in comparison to the required a absolute accuracy; that is, short-term drifts of ΣQ_{dark} and ΣQ_{closed} are small with regard to the accuracy required. Note that, because the short-term drift of ΣQ_{dark} and of universal multipliers is small, a d-c system could be employed. In other words, no chopper is required actually to provide sufficient accuracy, presuming drift is minimized in the amplifiers.

The maximum radiance system (300° components except detector, refractive imaging elements) can be seen to provide many problem areas. For example: (1) the noise is within acceptable limits only for the slower systems; when the dwell time is equivalent to only 101 μsec, the photon noise will exceed the required maximum level: (2) the long-term drift in transfer characteristic still can be removed by virtue of the inflight calibrator; however, the relatively large noise level will limit accuracy of the inflight calibration: (3) the short-term drift of the dark level is much larger than the acceptable accuracy - due mostly to the filter second reimaging element, and cavity. Short-term drift of the chopper also is important relative to the allowable accuracy for this system.

Thus, one can see readily that an acceptable system is bounded by the chosen limits. A system using reflective reimaging elements with most components cooled to 60°K will provide sufficient accuracy, and a system with all elements except the detector at 300°K will not be satisfactory. However, it is not possible at this time to say where the limiting conditions will occur so that each component can be run at the maximum temperature to minimize cooling. The trade between temperatures of components cannot be handled readily because of the many variables which must be modified for each example. If the analysis can be computerized in this format, a more thorough analysis can be made. In fact, this specific analysis actually has not been done to the optimum level (i.e., incorporation of detector, amplifier, and detailed comparison of the various signal combinations) because of the limited time and scope of the effort.

A description of radiance terms is shown in Table D7.

TABLE D7. - RADIANCE TERM DESCRIPTION

Radiance term	Description
Q_2	Cavity
$Q_1 P_2$	Second reimaging mirror
$Q_1 P_1 O_2$	Spectral filter
$Q_1 P_1 Q_1 N_2$	First reimaging mirror
$Q_1 P_1 O_1 N_1 M_1 L_1 I_2$	Primary mirror
$Q_1 P_1 O_1 N_1 M_1 L_1 I_1 A_{max}$	Maximum earth signal
$Q_1 P_1 O_1 N_1 M_1 L_1 I_1 A_{acc}$	Required accuracy
$Q_1 P_1 O_1 N_1 M_1 L_1 I_1 A_{min}$	Required maximum noise
$Q_1 P_1 O_1 N_1 M_1 L_2$	Chopper

APPENDIX E
CORRECTION FOR SIGNAL DISTORTION

APPENDIX E
CORRECTION FOR SIGNAL DISTORTION

TIME-INVARIANT LINEAR SYSTEM

Recovering the input signal $s_{in}(t)$ (Figure E1) from the output signal $s_{out}(t)$ for a linear and time-invariant system is possible if the systems transfer function, H(f), has a wider bandwidth than the input signal spectrum, $S_{in}(f)$, and if the system is noise free. The inputs are then given by

$$s_{in}(t) = \int_{-\infty}^{\infty} \frac{s_{out}(f)}{H(f)} \; e^{j2\pi ft} \; df \qquad \text{(E1)}$$

or

$$s_{in}(t) = \int_{-\infty}^{\infty} g(\tau) \; s_{out}(t-\tau) \; d\tau \qquad \text{(E2)}$$

where

$$g(t) = \int_{-\infty}^{\infty} \frac{1}{H(f)} \; e^{j2\pi ft} \; df \qquad \text{(E3)}$$

In the discrete case, that is, s_{in}, h, and s_{out} are sequences of numbers - this inverse convolution can be done without introducing the Fourier integrals (refs. 28 and 29).

In the practical case when the system is not noise-free, the result from the operation in Equations (E1) or (E3) may be an incorrect estimate of the true input signal; this cannot be recovered with any operation on the output signal because of the random noise. Similarly, if the system is noise free, but the systems transfer function has a narrower width than the input spectrum, the true input signal cannot be recovered, since part of the input spectrum is filtered out by the system.

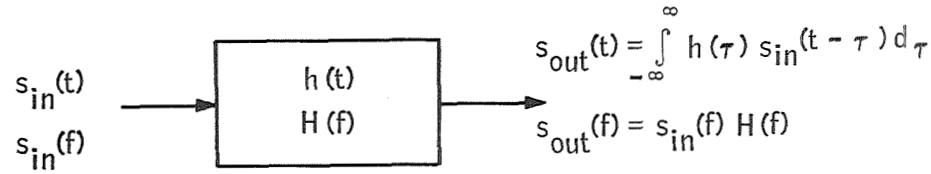

Figure E1. Input/Output Signal

Different operations can be performed on the output signal to give corrected or modified outputs that in different senses approximate the input signal.

If the systems transfer function H(f) is zero beyond f_1 and the system is noise-free, one gets for the operation in Equation (B1)

$$\bar{S}(f) = \frac{S_{out}(f)}{H(f)} = \frac{S_{in}(f)\ H(f)}{H(f)} = \begin{cases} S_{in}(f) & , \text{ if } |f| < f_1 \\ 0 & , \text{ if } |f| \geq f_1 \end{cases} \qquad \text{(E4)}$$

and the corrected time-domain output

$$\bar{s}(t) = \int_{-\infty}^{\infty} \bar{S}(f)\ e^{j2\pi ft}\ df = \int_{-f_1}^{f_1} S(f)\ e^{j2\pi ft}\ df \qquad \text{(E5)}$$

That is, the input spectrum is completely recovered for frequencies $|f| < f_1$, or in other words the input signal was filtered by a square filter

$$\bar{S}(f) = S(f)\ G(f) \qquad \text{(E6)}$$

where

$$G(f) = \begin{cases} 1 & , \text{ if } |f| < f_1 \\ 0 & , \text{ if } |f| > f_1 \end{cases}$$

However, the corrected output $\bar{s}(t)$ may be wild [due to sharp cutoff of G(f)] compared to the true input $s_{in}(t)$. Instead of filtering the output by $1/H(f)$ only, in reference 30 the output signal is also filtered by a smoothing function to reduce overshoot. In reference 30, cases using different parameters on a particular smoothing function are shown with and without noise. Reference 29 describes a way of reducing systems distortion, in the presence of noise, by a deconvolution scheme in the time domain (without going via Fourier domain) suitable for digital computer application.

The methods in references 29 and 30 for correction of systems output do not require any a priori knowledge of the input signal and noise. For known input signal auto-correlation and noise auto-correlation functions, a correction scheme based on Wiener filtering can be used to get a corrected output signal that approximates the input in the least mean square sense (reference 21).

PERIODICALLY TIME-VARYING LINEAR SYSTEM

For a chopped radiometer system, the input/output relationship cannot generally be described by a time-invariant impulse response. For an input spectrum band-limited to less than half chop frequency and a noise-free system, the input signal can be recovered from the output signal by replacing H(f) in Equation (E3) by the fundamental transfer function. In addition to the effect discussed in relation to Equations (E4), (E5), and (E6), there will be aliasing errors for nonbandlimited input signals. The aliasing errors can be considered as colored noise (which can be predicted for known inputs). The periodically time-varying system can thus be considered as time-invariant with the fundamental transfer function being the equivalent of the transfer function for a time-invariant system and with the addition of an extra signal-dependent noise source, aliasing noise, for nonbandlimited inputs. When correcting the output from a time-varying system, more care should, therefore, be taken than in the time-invariant case.

FIDELITY

In the ARRS program, a figure of 0.1% was quoted as the goal for fidelity of the signal processing system. This has different meanings, depending on the application. If the true input signal is designated $s(t)$ and the estimate $\bar{s}(t)$, a few interpretations are [$\bar{s}(t)$ is bandlimited to $|f| < f_1$]

$$\frac{s(t) - \bar{s}(t)}{s(t)} < 0.001, \text{ for all } t \qquad \text{(E7)}$$

$$\frac{s(t) - \bar{s}(t)}{s_{max}} < 0.001, \text{ for all } t \qquad \text{(E8)}$$

$$\frac{s_1(t) - \bar{s}(t)}{s_1(t)} < 0.001, \text{ for all } t \qquad \text{(E9)}$$

where

$$s_1(t) = \int_{-\infty}^{\infty} S(f) H_1(f) e^{j2\pi ft}\, df = \int_{-f_2}^{f_2} S(f)\, e^{j2\pi ft}\, df$$

$$S(f) = \int_{-\infty}^{\infty} s(t)\, e^{-j2\pi ft}\, dt$$

$$H_1(f) = \begin{cases} 1, & \text{if } |f| < f_2 \\ 0, & \text{if } |f| > f_2 \end{cases}$$

$$\frac{s_1(t) - \bar{s}(t)}{s_{1_{max}}} < 0.001, \text{ for all } t \qquad \text{(E10)}$$

$$\frac{s_2(t) - \bar{s}(t)}{s_2(t)} < 0.001, \text{ for all } t \qquad \text{(E11)}$$

where

$$s_2(t) = \frac{1}{T_1} \int_{t - \frac{T_1}{2}}^{t + \frac{T_1}{2}} \bar{s}(\tau)\, d\tau = \int_{-\infty}^{\infty} s(\tau)\, h_2(t - \tau)\, d\tau$$

$$h_2(t) = \begin{cases} 1/T_1, \text{ if } |t| < T_1/2 \\ 0 \text{ , if } |t| > T_1/2 \end{cases}$$

$$\frac{s_2(t) - \bar{s}(t)}{s_{2_{max}}} < 0.001, \text{ for all } t \qquad \text{(E12)}$$

$$\frac{\left\{ \int_{-\infty}^{\infty} [s_2(t) - \bar{s}(t)]^2\, dt \right\}^{1/2}}{s_{2_{max}}} < 0.001 \qquad \text{(E13)}$$

The rms expression in Equation (E13) is analytically computable, but to find the error $s_2(t) - s(t)$ for any particular time t requires computer assistance.

NOISE EQUIVALENT BANDWIDTH

A detector with uniform response and width (dwell time) $= \frac{1}{\pi}$ has a spectral representation of $\frac{\sin f}{f}$. If this is to be included in $H(f)$ in Equation (E1) and if the output noise is assumed white before correction (Figure E2), the rms noise will increase by a factor of

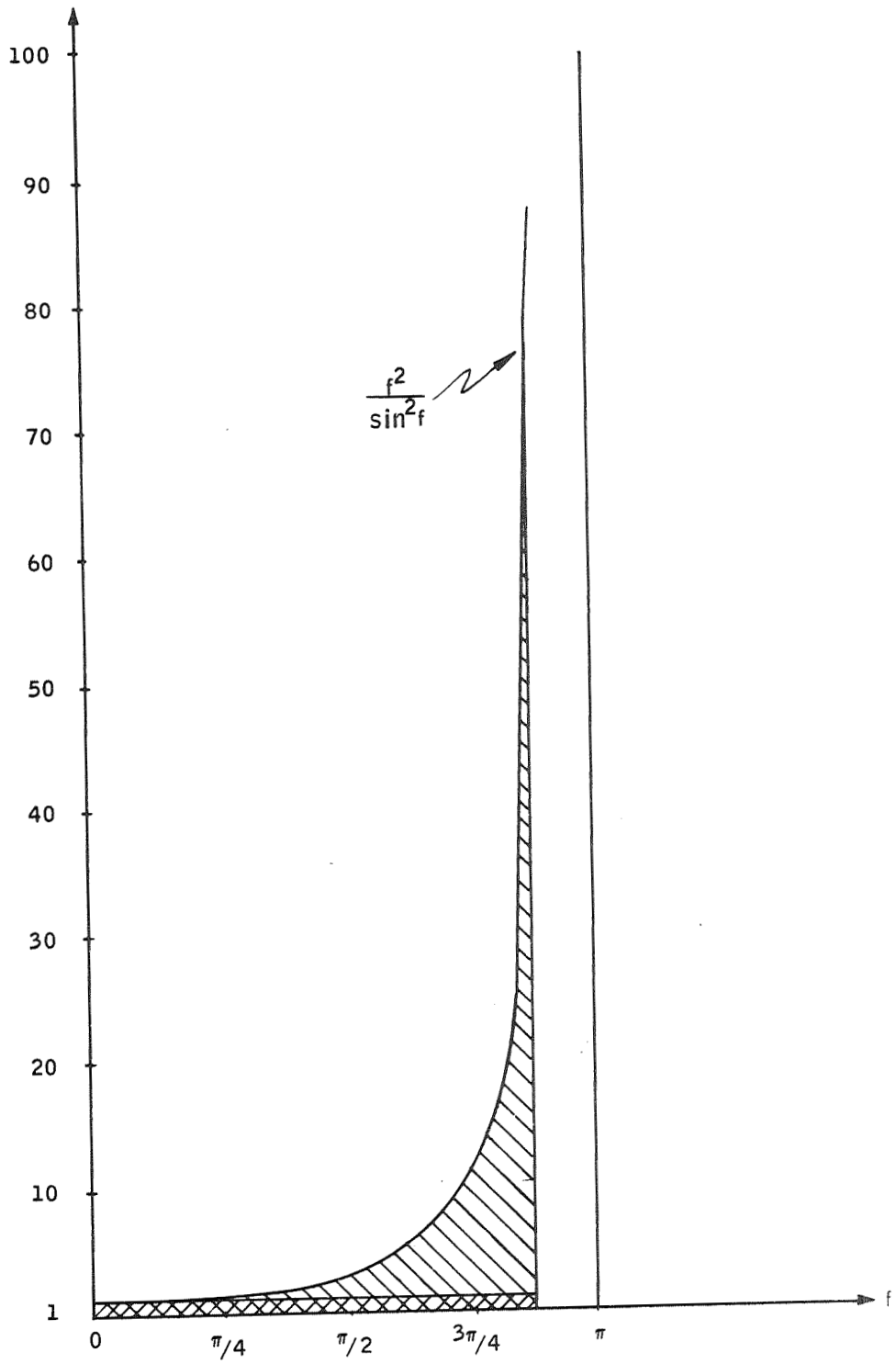

Figure E2. Detector Output Noise

$$\gamma = \left[\frac{1}{f_3} \int_0^{f_3} \frac{f^2}{\sin^2 f} \, df \right]^{1/2}$$

For $f_3 = \frac{3\pi}{8}$, one gets from Figure E2.

$$\gamma \approx 2.5$$

As seen from Figure E2, γ increases rapidly for increasing f_3, and correction up to $f = \pi$ for the detector seems highly undesirable. Incidentally, the operation to get $s_2(t)$ from $s(t)$ in Equation (E11) is equivalent to scanning with a detector with uniform spatial response. Equation (E11) is, therefore, a scheme that does not correct for the detector smoothing.

APPENDIX F
BOUNDS ON OUTPUT MEAN SQUARE NOISE $\sigma^2_{t_o}$ FOR ALL TIMES t_o

APPENDIX F
BOUNDS ON OUTPUT MEAN SQUARE NOISE $\sigma^2_{t_o}$ FOR ALL TIMES t_o

As the output mean square noise $\sigma^2_{t_o}$ is periodically varying with time, one wants to find its bounds. Therefore, one has to find the bounds of the squared infinite sum:

$$H_{\Sigma}(f) = \left|\sum_{m=-\infty}^{\infty} g_m e^{j2\pi m f_o t_o} H_2(f+mf_o)\right|^2 \tag{F1}$$

If

$$A_i = |A_i| e^{j\alpha i} \text{ for } i = \ldots, -1, 0, 1, \ldots \tag{F2}$$

one has

$$\left|\sum_{i=-\infty}^{\infty} |A_i| e^{j\alpha i}\right|^2 = \left(\sum_{i=-\infty}^{\infty} |A_i| e^{j\alpha i}\right)\left(\sum_{k=-\infty}^{\infty} |A_k| e^{-j\alpha k}\right)$$

$$= \sum_{i=-\infty}^{\infty} \sum_{k=-\infty}^{\infty} |A_i| |A_k| e^{j(\alpha_i - \alpha_k)}$$

$$= \sum_{i=-\infty}^{\infty} |A_i|^2 + \sum_{i=-\infty}^{\infty} \sum_{k=1}^{\infty} \left[|A_i| |A_{i+k}| e^{j(\alpha_i - \alpha_{i+k})} + |A_i| |A_{i-k}| e^{j(\alpha_i - \alpha_{i-k})}\right] \tag{F3}$$

$$= \sum_{i=-\infty}^{\infty} |A_i|^2 + \sum_{i=-\infty}^{\infty} \sum_{k=1}^{\infty} |A_i| |A_{i-k}| e^{j(\alpha_i - \alpha_{i+k})}$$

$$+ \sum_{m=-\infty}^{\infty} \sum_{k=1}^{\infty} |A_{m+k}| |A_m| e^{j(\alpha_{m+k} - \alpha_m)}$$

$$= \sum_{i=-\infty}^{\infty} |A_i|^2 + 2 \sum_{i=-\infty}^{\infty} \sum_{k=1}^{\infty} |A_i| |A_{i+k}| \cos(\alpha_i - \alpha_{i+k})$$

Define θ_m such that

$$g_m H_2(f \pm mf_o) = |g_m| \, |H_2(f \pm mf_o)| \, e^{j\theta_m} \tag{F4}$$

Then Equation (F1) becomes

$$H_{\sum}(f) = \Big| \sum_{m=-\infty}^{\infty} g_m e^{j2\pi mf_o t_o} H_2(f+mf_o) \Big|^2$$

$$= \Big| \sum_{m=-\infty}^{\infty} |g_m| \, |H_2(f+mf_o)| \, e^{j(2\pi mf_o t_o + \theta_m)} \Big|^2 = \sum_{m=-\infty}^{\infty} |g_m|^2 |H_2(f+mf_o)|^2$$

$$+ 2 \sum_{m=-\infty}^{\infty} \sum_{k=1}^{\infty} |g_m| |g_{m+k}| |H_2(f+mf_o)| \, |H_2(f+mf_o+kf_o)| \cos(\theta_m - \theta_{m+k} - 2\pi kf_o t_o) \tag{F5}$$

and the bounds of $H_{\sum}(f)$

$$\sum_{m=-\infty}^{\infty} |g_m|^2 |H_2(f+mf_o)|^2 - 2\Delta H_{\sum}(f) \le H_{\sum}(f) \le \sum_{m=-\infty}^{\infty} |g_m|^2 |H_2(f+mf_o)|^2$$

$$+ 2\Delta H_{\sum}(f) \tag{F6}$$

where

$$\Delta H_{\sum}(f) = \sum_{m=-\infty}^{\infty} \sum_{k=1}^{\infty} |g_m| \, g_{m+k} |H_2(f+mf_o)| |H_2(f+mf_o+kf_o)| \tag{F7}$$

Defining

$$\sigma^2 = \int_{-\infty}^{\infty} \Phi_{nn}(f) |H_1(f)|^2 \left[\sum_{m=-\infty}^{\infty} |g_m|^2 |H_2(f+mf_o)|^2 \, df \right] \tag{F8}$$

and

$$\Delta\sigma^2 = 2 \int_{-\infty}^{\infty} \Phi_{nn}(f) |H_1(f)|^2 \, \Delta H_{\sum}(f) \, df \tag{F9}$$

we can thus write

$$\sigma^2 - \Delta\sigma^2 \le \sigma_{t_o}^2 \le \sigma^2 + \Delta\sigma^2 \tag{F10}$$

EXAMPLE 1, IDEAL FILTERS

Consider the low pass filter in Figure F1b. For this filter $H_2(f + mf_o)H_2(f + mf_o + kf_o) = 0$ for $k \neq 0$ and, therefore,

$$\Delta H_{\sum}(f) = 0 \tag{F11}$$

That is,

$$\Delta\sigma^2 = 0 \tag{F12}$$

Equation (F8) then gives for white noise $(\Phi_{nn}(f) = N_o)$

$$\sigma_{t_o}^2 = \sigma^2 = N_o \int_{-\infty}^{\infty} |H_1(f)|^2 \sum |g_m|^2 |H_2(f+mf_o)|^2 \, df \tag{F13}$$

The output mean square noise is thus time-invariant for this case. Generally, σt_o^2 is time-invariant if there is no "crosstalk" between the terms $H_2(f + mf_o)$ and $H_2(f + mf_o + kf_o)$ for $k \neq 0$.

With the bandpass filter in Figure F1a and g(t), according to Figure F2, one gets

$$\sigma_{3f_o}^2 = N_o \int_{-3f_o}^{3f_o} |H_1'(f)|^2 [|g_1|^2 |H_2(f+f_o)|^2 + |g_{-1}|^2 |H_2\ f-f_o)|^2] \, df$$

$$= 2N_o |g_1|^2 \int_{f_o/2}^{3f_o/2} |H_1'(f)|^2 |H_2(f+f_o)|^2 \, df = 2N_o |g_1|^2 f_o \tag{F14}$$

$$= 4N_o |g_1|^2 (f_o/2) = 4N_o (0.552)^2 (f_o/2) = 1.22\, N_o (f_o/2)$$

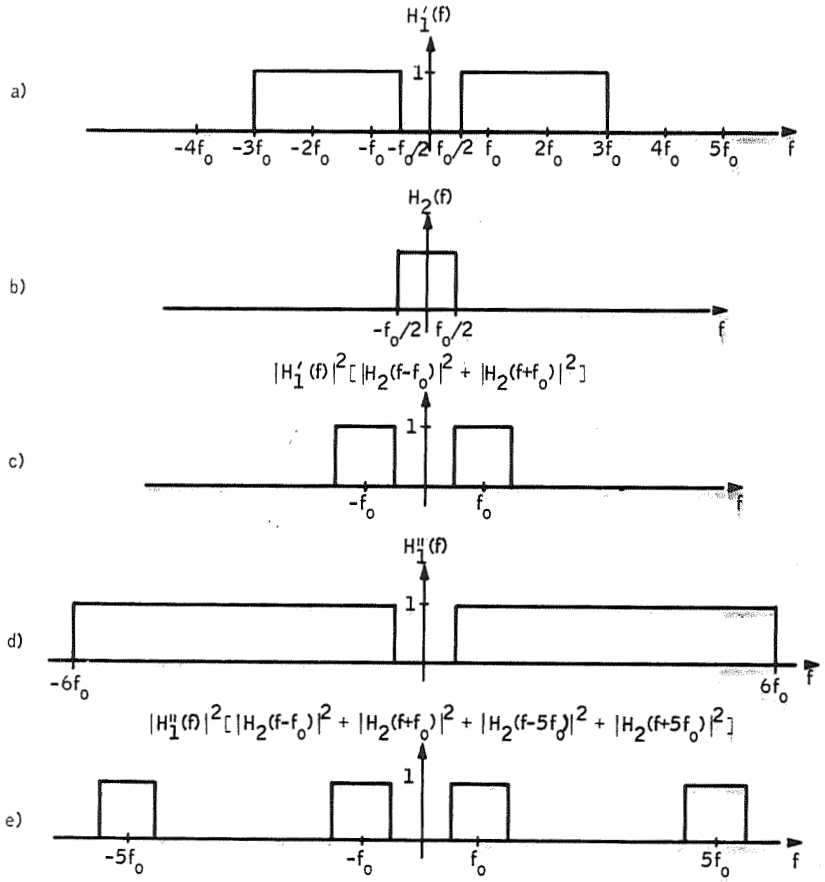

Figure F1. Idealized Electronic Filters

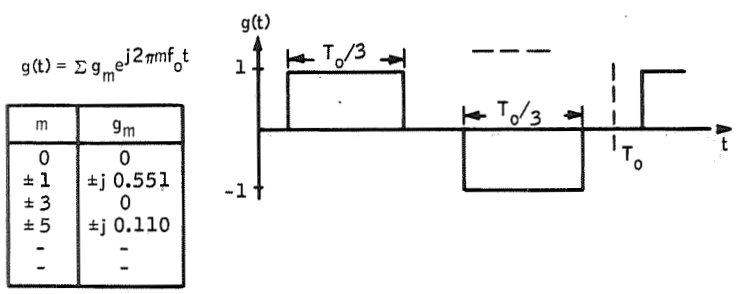

m	g_m
0	0
± 1	±j 0.551
± 3	0
± 5	±j 0.110
-	-
-	-

Figure F2. Gate Wave

For bandpass filters with upper cutoff at $6f_o$ (Figure F1), one gets

$$\sigma_{6f_o}^2 = N_o \int |H_1'(f)|^2 \left[|g_1|^2 |H_2(f+f_o)|^2 + |g_{-1}|^2 |H_2(f-f_o)|^2 \right.$$

$$\left. + |g_5|^2 |H_2(f+5f_o)|^2 + |g_{-5}|^2 |H_2(f-5f_o)|^2 \right] = 2N|g_1|^2 \left[1 + \left|\frac{g_5}{g_1}\right|^2 \right] \quad \text{(F15)}$$

$$= \sigma_{3f_o}^2 \left(1 + \left|\frac{g_5}{g_1}\right|^2 \right) = \sigma_{3f_o}^2 \left[1 + \left(\frac{0.110}{0.552} \right)^2 \right] = \sigma_{3f_o}^2 \, 1.04 = 1.27 \, N_o (f_o/2)$$

Increasing the upper cutoff frequency of the bandpass filter from $3f_o$ to $6f_o$ increases the effective noise bandwidth only 4%. A further increase in cutoff frequency would cause an even smaller increase in effective noise bandwidth. When g(t) has no d-c component ($g_o = 0$) as in Figure F2, the passband of the bandpass filter can be extended to include dc without affecting the noise output for this ideal lowpass filter.

EXAMPLE 2, REAL FILTERS

Next, estimate the output mean square noise when using realizable filters. The bandpass filter shown in Figure F3 is assumed. Its amplitude square characteristic, $|H_1(f)|^2$, is shown in Figure F4. The lowpass filter used is the same as in Figure F5.

For the gate wave in Figure F2,

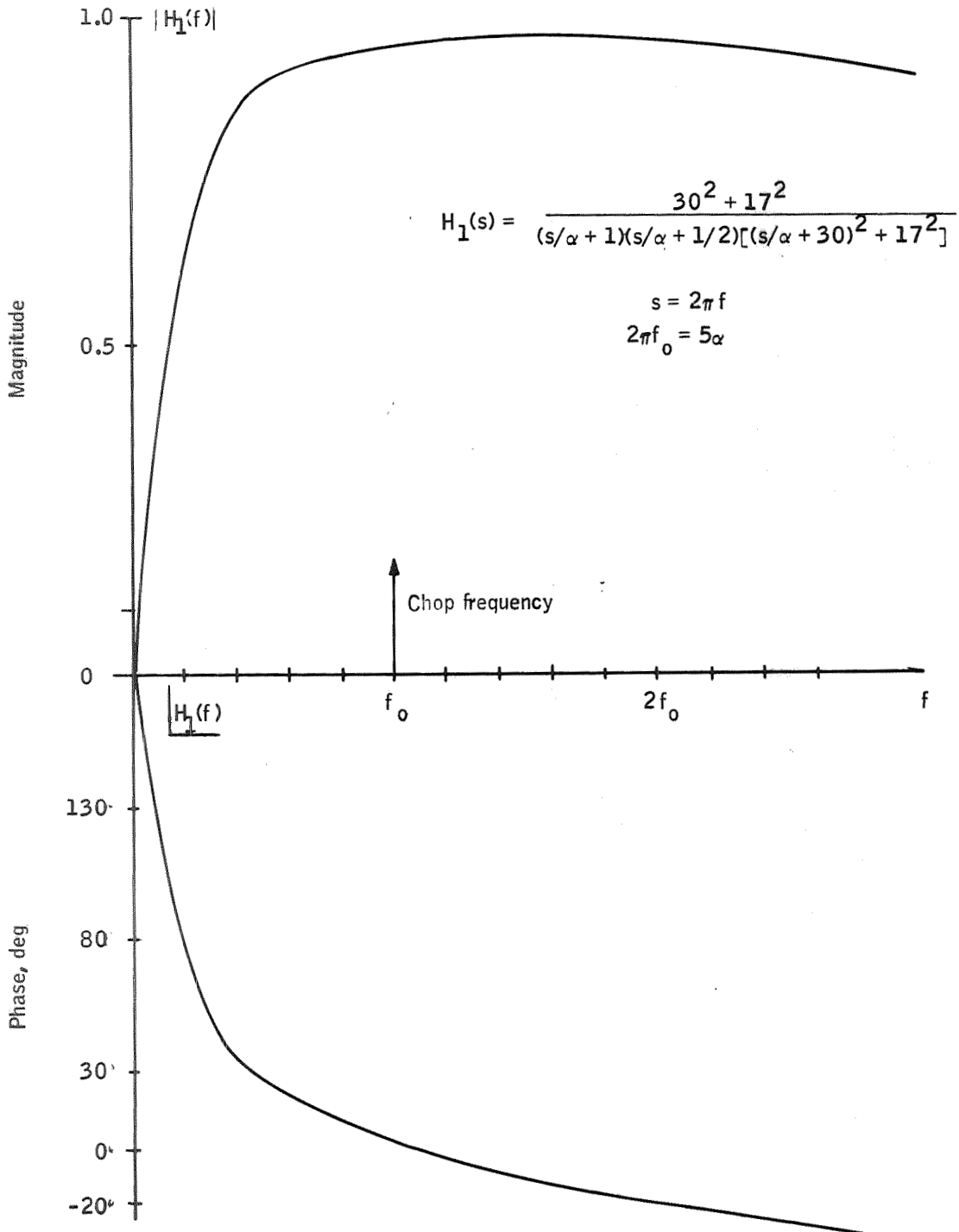

Figure F3. Filter Amplitude Characteristics

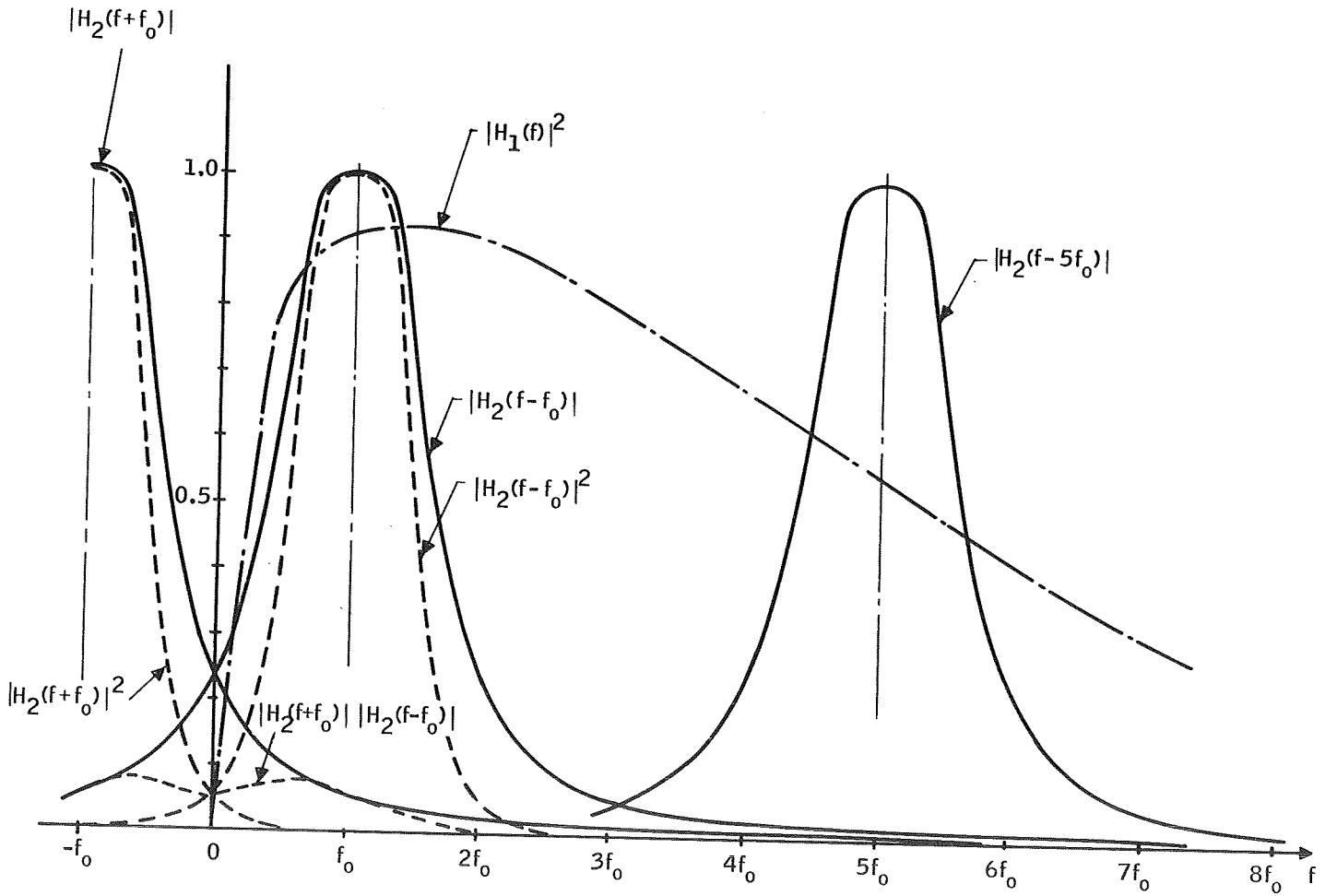

Figure F4. Filter Amplitude Characteristics

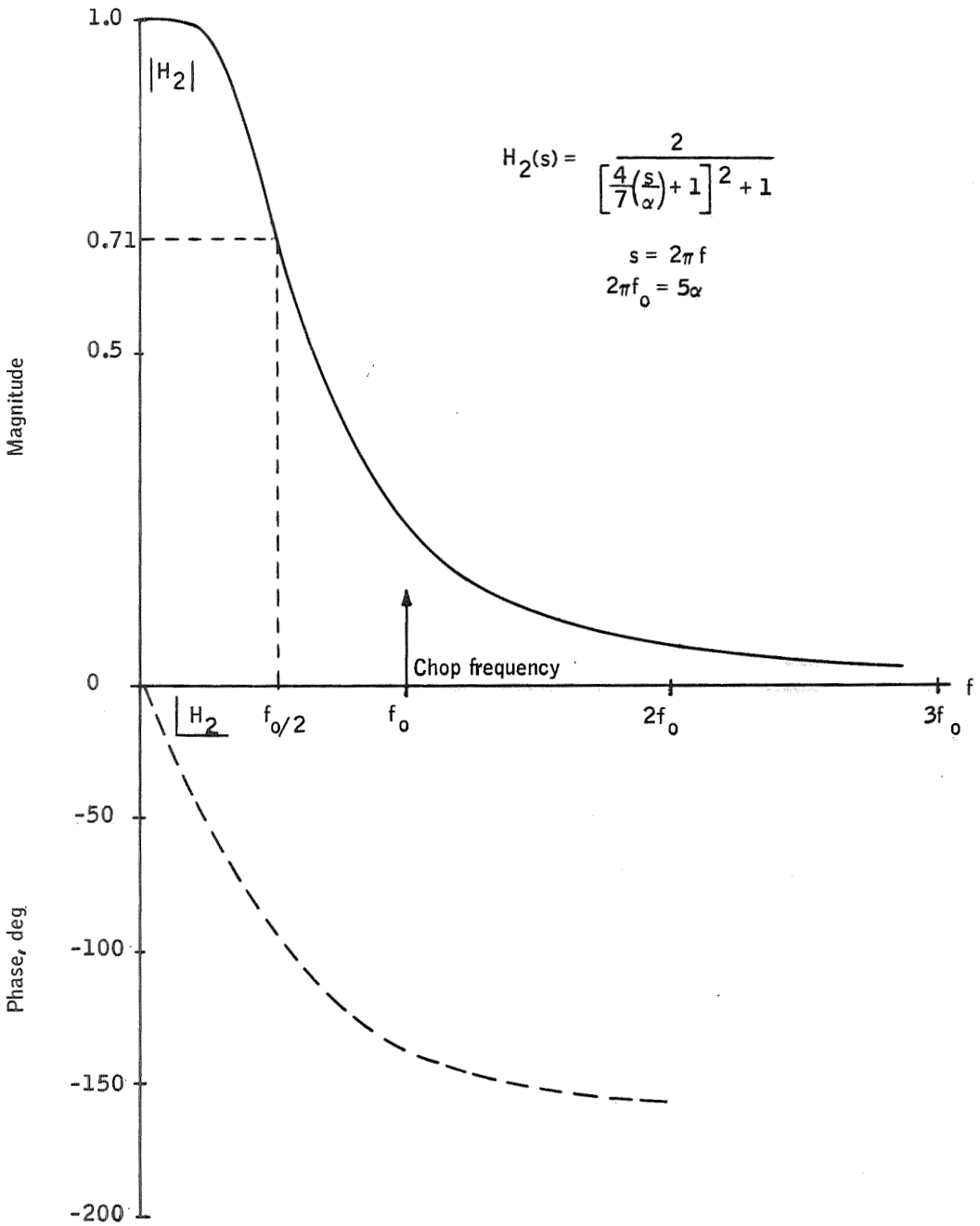

Figure F5. Second-Order Butterworth Lowpass Filter

$$\sum_{m=-\infty}^{\infty} |g_m|^2 |H_2(f+mf_o)|^2 = |g_1|^2 \Big\{ |H_2(f+f_o)|^2 + |H_2(f-f_o)|^2$$

$$|\frac{g_5}{g_1}|^2 [\,|H_2(f+5f_o)|^2 + |H_2(f-5f_o)|^2] + |\frac{g_7}{g_1}|^2 [\,|H_2(f+7f_o)|^2 + |H_2(f-7f_o)|^2] \quad \text{(F16)}$$

$$+ \ldots \Big\} = 0.305 \Big\{ |H_2(f+f_o)|^2 + |H_2(f-f_o)|^2 + 0.040 [\,|H_2(f+5f_o)|^2$$

$$+ |H_2(f-5f_o)|^2] + 0.021 [\,|H_2(f+7f_o)|^2 + |H_2(f-7f_o)|^2] + \ldots$$

$$\Delta H_{\sum}(f) = \sum_{m=-\infty}^{\infty} \sum_{k=1}^{\infty} |g_m|\, |g_{m+k}|\, |H_2(f+mf_o)|\, |H_2(f+mf_o+kf_o)|$$

$$= |g_1|^2 \; |H_2(f-f_o)|\; |H_2(f+f_o)| + \frac{g_5}{g_1} [\,|H_2(f-5f_o)| + |H_2(f+5f_o)|] [\,|H_2(f-f_o)|$$

$$+ |H_2(f+f_o)|] + |\frac{g_5 g_7}{g_1^2}| [\,|H_2(f-5f_o)| + |H_2(f+5f_o)|] [\,|H_2(f-7f_o)|$$

$$+ |H_2(f+7f_o)|] + \ldots \Big\}$$

Assume white noise, $\Phi_{nn}(f) = N_o$. One then has from Equation (F8)

$$\sigma^2 \approx N_o \int_{-\infty}^{\infty} |H_1(f)|^2 \, 0.305 \, [\,|H_2(f+f_o)|^2 + |H_2(f-f_o)|^2] \, df$$

$$= N_o \, 0.61 \int_{-\infty}^{\infty} |H_1(f)|^2 \, |H_2(f-f_o)|^2 \, df \quad \text{(F18)}$$

The approximation in Equation (F18) is good to about 3% since $|H_1(f)|^2$ is dropping off at higher frequencies, as seen from Figure F4.

From Equation (F9)

$$\Delta\sigma^2 = 2N_o \int_{-\infty}^{\infty} |H_1(f)|^2 \, \Delta H_{\sum}(f) \, df \approx N_o \, 0.61 \int_{-\infty}^{\infty} |H_1(f)|^2 \, [\,|H_2(f-f_o)|\, |H_2(f+f_o|df \quad \text{(F19)}$$

This approximation is good to approximately 3%, as the terms that contribute most are those adjacent to each other (m = -1, m = +1; m = -5, m = -7; etc.) and as

$$2\left|\frac{g_5 g_7}{g_1^2}\right| |H_1(6f_o)|^2 = 0.025 \qquad \text{(F20)}$$

Integrating Equations (F18) and (F19) graphically in Figure F6 gives

$$\sigma^2 = N_o\, 0.61 \int_{-\infty}^{\infty} |H_1(f)|^2 |H_2(f-f_o)^2\, df \approx N_o\, 0.61 \times 0.98\, f_o = 1.20\, N_o(f_o/2) \qquad \text{(F21)}$$

$$\Delta\sigma^2 = N_o\, 0.61 \int_{-\infty}^{\infty} |H_1(f)|^2 |H_2(f-f_o)|\, |H_2(f+f_o)| = 0.20\, N_o(f_o/2) \qquad \text{(F22)}$$

Thus,

$$1.0\, N_o\, (f_o/2) \lesssim \sigma_{t_o}^2 \lesssim 1.4\, N_o\, (f_o/2) \qquad \text{(F23)}$$

and using σ according to Equation (F8) as an estimate for the output mean-square noise for any t_o would here yield an accuracy of the order of 17%.

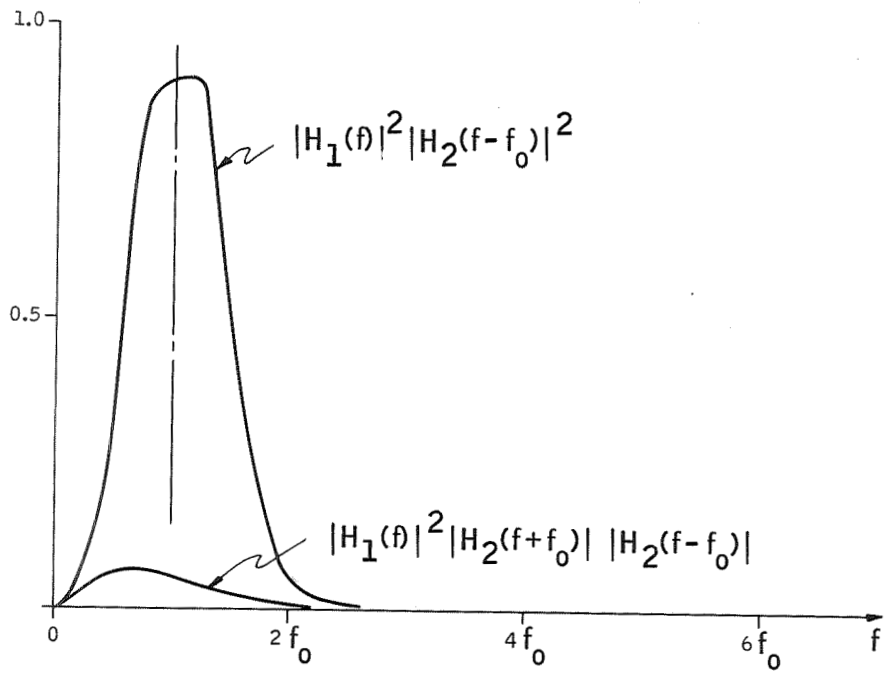

Figure F6. Practical Filter Example

APPENDIX G
RELATED TRANSFER FUNCTION MODEL ANALYSES

APPENDIX G

RELATED TRANSFER FUNCTION MODEL ANALYSES

The following computations and analyses were performed using the FDM and related considerations and are presented in this appendix:

- Choice of sampling frequency for a given aliasing error
- Evaluation of idealized chopping approximation in the RMS
- Chopper instability analyses
- Aliasing errors

SAMPLING FREQUENCY ANALYSIS

Consider the time function f(t). If f(t) is sampled with a sampling frequency ω_s and then reconstructed by the interpolation filter

$$h(t) = \frac{\sin \frac{\omega_s t}{2}}{\frac{\omega_s t}{2}} \tag{G1}$$

One has the output

$$f_a(t) = \sum_{n=-\infty}^{\infty} f(nT) \frac{\sin \frac{\omega_s (t-nT)}{2}}{\frac{\omega_s (t-nT)}{2}} \tag{G2}$$

where

$$T = \frac{2\pi}{\omega_s}$$

If f(t) is bandlimited to $\omega_s/2$, then

$$f_a(t) = f(t)$$

If, however, f(t) is not bandlimited, denote by

$$e_a(t) = f_a(t) - f(t) \tag{G3}$$

the aliasing error and by $E_a(\omega)$ its Fourier transform.

A bound on the aliasing error is then (see ref. 6)

$$|e_a(t)| \leq \frac{\int_{-\infty}^{\infty} |E_a(\omega)|\, d\omega}{2\pi} \left|\sin \frac{\omega_s t}{2}\right| \tag{G4}$$

Example 1 Gaussian Pulse

The signal

$$f(t) = e^{-t^2\sigma^2/2} \tag{G5}$$

has the Fourier transform

$$F(\omega) = \frac{1}{\sqrt{2\pi}\,\sigma} e^{-\omega^2/2\sigma^2} \tag{G6}$$

Choose $\omega_s = 2 \times 3.09\,\sigma$. One then gets (see Figure G1)

$$\begin{aligned}
\int_{-\infty}^{\infty} E_a(\omega)\, d\omega &= \frac{1}{\sqrt{2\pi}\,\sigma}\left\{2\int_{\omega_s/2}^{\infty} e^{-\omega^2/2\sigma^2}\, d\omega + 2\int_{-\omega_s/2}^{\omega_s/2} e^{-(\omega-\omega_s)^2/2\sigma^2}\, d\omega \right.\\
&\left. + 2\int_{-\omega_s/2}^{\omega_s/2} e^{-(\omega-2\omega_s)^2/2\sigma^2}\, d\omega + 2\int_{-\omega_s/2}^{\omega_s/2} e^{-(\omega-3\omega_s)^2/2\sigma^2}\, d\omega + \ldots\right\}\\
&= \frac{2}{\sqrt{2\pi}}\left\{\int_{\omega_s/2\sigma}^{\infty} e^{-x^2/2}\, dx + \int_{\omega_s/2\sigma}^{3\omega_s/2\sigma} e^{-x^2/2}\, dx + \int_{3\omega_s/2\sigma}^{5\omega_s/2\sigma} e^{-x^2/2}\, dx + \ldots\right\}\\
&= 4\frac{1}{\sqrt{2\pi}}\int_{\omega_s/2\sigma}^{\infty} e^{-x^2/2}\, dx = 4\frac{1}{\sqrt{2\pi}}\int_{3.09}^{\infty} e^{-x^2/2}\, dx = 0.004
\end{aligned} \tag{G7}$$

And thus

$$|e_a(t)| \leq \frac{0.004}{2\pi}\left|\sin(\omega_s t/2)\right| = 0.00064\left|\sin\frac{\omega_s t}{2}\right|$$

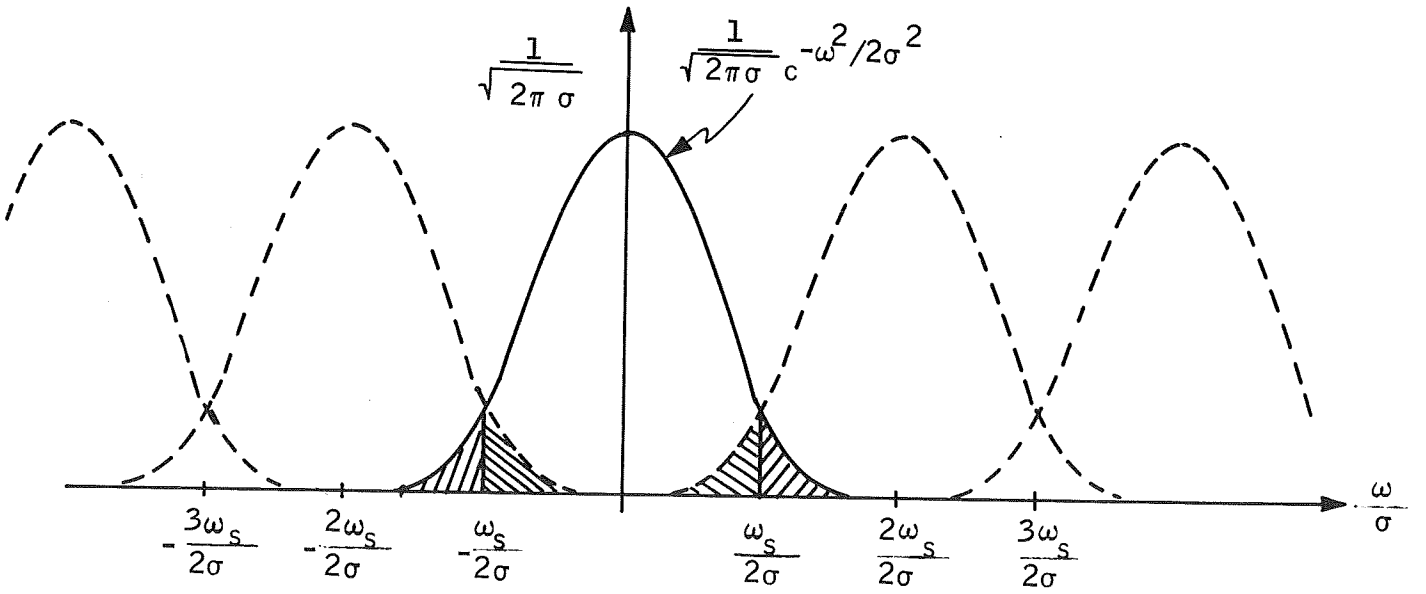

Figure G1. Spectrum of Sampled Gaussian Pulse ($e^{-t^2d^2/2}$)

Assume that one needs $2n + 1$ samples to reconstruct $f(t)$ for $10^{-4} < f(t) < 1$ with an error

$$|e_a(t)| \leq 0.00064 \left| \sin \frac{\omega_s t}{2} \right| \tag{G9}$$

Then as

$$\frac{2\pi}{T_s} = \omega_s = 2 \times 3.09\, \sigma \tag{G10}$$

one has

$$10^{-4} = e^{-t^2\sigma^2/2} = e^{-n^2T^2\sigma^2/2} = e^{-n^2\pi^2/2 \times 3.09^2} = e^{-0.52\, n^2} \tag{G11}$$

$$n = 4.2$$

Rounding off to $n = 5$, one thus sees that one needs 11 samples to reconstruct a Gaussian pulse to an accuracy of 0.00064 of the peak for time values corresponding to amplitude values larger than 10^{-4} of the peak value. The choice of σ in $e^{-t^2\sigma^2/2}$ determines the required sampling frequency

$$f_s = \frac{\omega_s}{2\pi} = \frac{2 \times 3.09\sigma}{2\pi} \tag{G12}$$

Example 2

$$f(t) = \frac{1}{1 + \frac{t^2}{a^2}} \tag{G13}$$

with Fourier transform

$$F(\omega) = \frac{a}{2} e^{-a|\omega|} \tag{G14}$$

Sampling with $\omega = \omega_s$, one gets (Figure G2)

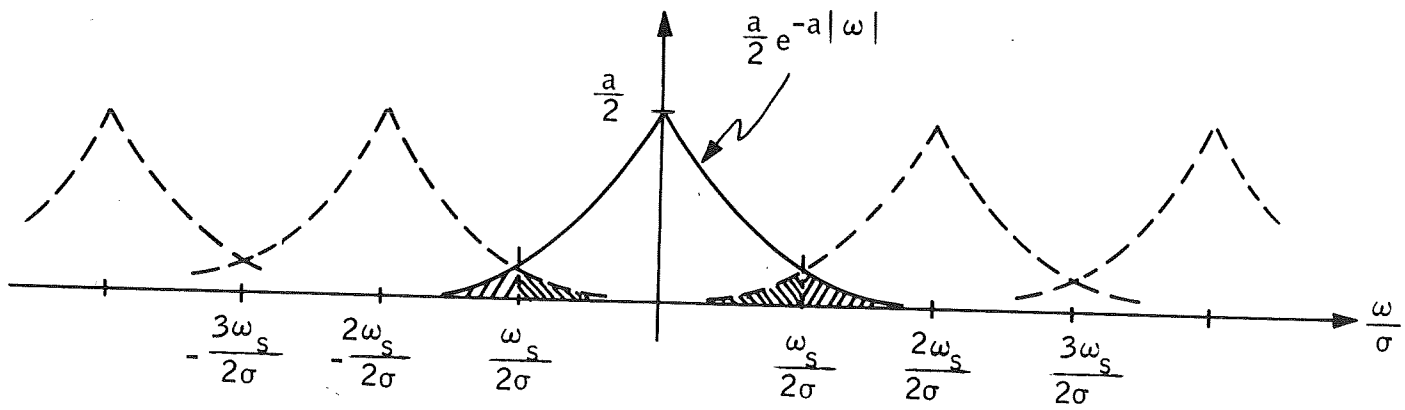

Figure G2. Spectrum of the Sampled $(1 + t^2/a^2)^{-1}$ Pulse

$$\int_{-\infty}^{\infty} |E_a(\omega)| d\omega = 2 \int_{\omega_s/2}^{\infty} \frac{a}{2} e^{-a\omega} d\omega + 2 \int_{-\omega_s/2}^{\omega_s/2} \frac{a}{2} e^{-a(\omega-\omega_s)} d\omega$$

$$+ 2 \int_{-\omega_s/2}^{\omega_s/2} \frac{a}{2} e^{-a(\omega-2\omega_s)} d\omega + \ldots = 2 \int_{a\omega_s/2}^{\infty} e^{-x} dx$$

$$= 2 e^{-a\omega_s/2} \qquad \text{(G15)}$$

Choose $\omega_s = \frac{2}{a} \times 6.21$; then

$$\int_{-\infty}^{\infty} |E_a(\omega)| d\omega = 0.004$$

as in Example 1

$$t = nT \Rightarrow \frac{1}{1 + t^2/a^2} = \frac{1}{1 + \frac{n^2 T^2}{a^2}} = \frac{1}{1 + \frac{n^2 (2\pi)^2}{\omega_s^2 a^2}} = \frac{1}{1 + \frac{n^2 \pi^2}{6.21^2}}$$

$$= \frac{1}{1 + 0.256\, n^2} \qquad \text{(G16)}$$

With

$$\frac{1}{1 + 0.256\, n^2} = 10^{-4} \qquad \text{(G17)}$$

one has

$$n = 198$$

One thus needs $2n + 1 \approx 400$ samples to reconstruct the time function $1/(1 + t^2/a^2)$ to an accuracy of 0.00064 of the peak for time values corresponding to amplitude values larger than 10^{-4} of the peak value. The choice of "a" in $(1 + t^2/a^2)^{-1}$ determines the required sampling frequency

$$f_s = \frac{\omega_s}{2\pi} = \frac{2 \times 6.21}{a 2\pi} \qquad \text{(G18)}$$

Example 3

Convolution of Gaussian pulse and square pulse (see Figure G3)

$$f(t) = \int_{-\infty}^{\infty} e^{-(t-\tau)^2\sigma^2/2}\, g(\tau)\, d\tau = \int_{-T/2}^{T/2} e^{-(t-\tau)^2\sigma^2/2}\, d\tau = \frac{1}{\sigma}\int_{\left(t-\frac{T}{2}\right)\sigma}^{\left(t+\frac{T}{2}\right)\sigma} e^{-x^2/2}\, dx \qquad \text{(G19)}$$

where

$$g(t) = \begin{cases} 1\ , & \text{if } (t) < T/2 \\ 0\ , & \text{if } (t) > T/2 \end{cases}$$

Fourier transform of $f(t)$

$$F(\omega) = \frac{T}{\sqrt{2\pi}\,\sigma}\, e^{-\omega^2/2\sigma^2}\, \frac{\sin\ \omega T/2}{\omega T/2} \qquad \text{G20)}$$

And thus

$$\int_{-\infty}^{\infty} |E_a(\omega)|\, d\omega = \frac{T}{\sqrt{2\pi}\,\sigma}\left\{ 2\int_{\omega_s/2}^{\infty} \frac{e^{-\omega^2/2\sigma^2}\,|\sin \omega T/2|}{\omega T/2}\, d\omega \right.$$

$$+ 2\int_{-\omega_s/2}^{\omega_s/2} \frac{e^{-(\omega-\omega_s)^2/2\sigma^2}\,|\sin(\omega-\omega_s)\ T/2|}{|(\omega-\omega_s)\ T/2|}\, d\omega$$

$$\left. + 2\int_{-\omega_s/2}^{\omega_s/2} \frac{e^{-(\omega-2\omega_s)^2/2\sigma^2}\,|\sin\ (\omega-2\omega_s)\ T/2|}{|(\omega-2\omega_s)\ T/2|}\, d\omega + \ldots \right.$$

$$= \frac{4T}{\sqrt{2\pi}\,\sigma} \int_{\omega_s/2}^{\infty} \frac{e^{-\omega^2/2\sigma^2}\,|\sin \omega\ T/2|}{\omega T/2}\, d\omega$$

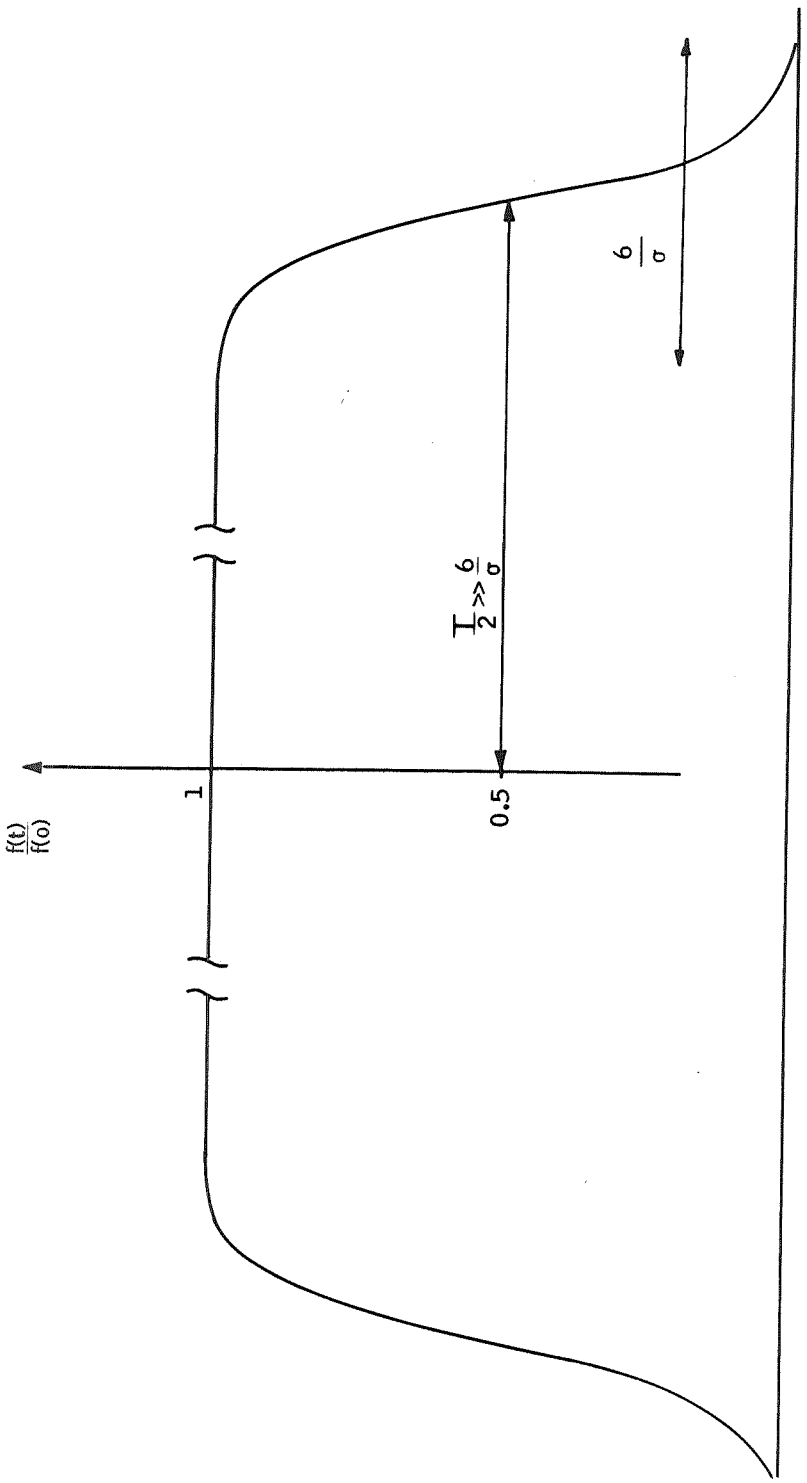

Figure G3. Convolution of Gaussian Pulse and Square Pulse

$$\leq \frac{4T}{\sqrt{2\pi}\,\sigma}\ \frac{1}{\omega_s T/4}\int_{\omega_s/2}^{\infty} e^{-\omega^2/2\sigma^2}\,d\omega$$

$$= \frac{16}{\omega_s}\frac{1}{\sqrt{2\pi}}\int_{\omega_s/2\sigma}^{\infty} e^{-x^2/2}\,dx \qquad \text{(G21)}$$

Therefore,

$$|e_a(t)| \leq \frac{1}{2\pi}\ \frac{16}{\omega_s}\frac{1}{\sqrt{2\pi}}\int_{\omega_s/2\sigma}^{\infty} e^{-x^2/2}\,dx \qquad \text{(G22)}$$

$$\text{Large } \frac{T\sigma}{2} \Rightarrow f(o) \approx \frac{2\pi}{\sigma}\frac{1}{\sqrt{2\pi}}\int_{-\infty}^{\infty} e^{-x^2/2}\,dx = \frac{\sqrt{2\pi}}{\sigma} \qquad \text{(G23)}$$

For large $\frac{T\sigma}{2}$, one then has

$$\frac{|e_a(t)|}{f(o)} \leq \frac{8}{2\pi\sqrt{2\pi}}\ \frac{1}{(\omega_s/2\sigma)}\frac{1}{\sqrt{2\pi}}\int_{\omega_s/2\sigma}^{\infty} e^{-x^2/2}\,dx \qquad \text{(G24)}$$

$$= 0.508\ \frac{1}{\omega_s/2\sigma}\frac{1}{\sqrt{2\pi}}\int_{\omega_s/2\sigma}^{\infty} e^{-x^2/2}\,dx$$

Pick $\omega_s/2\sigma = 2.75$; then,

$$\frac{e_a(t)}{f(o)} \leq \frac{0.508}{2.75}\ \frac{1}{\sqrt{2\pi}}\int_{2.75}^{\infty} e^{-x^2/2}\,dx = 0.00056 \qquad \text{(G25)}$$

The normalized function can be written

$$\frac{f(t)}{f(o)} = \frac{1}{\sqrt{2\pi}} \int_{(t-\frac{T}{2})\sigma}^{(t+\frac{T}{2})\sigma} e^{-x^2/2} = \frac{1}{\sqrt{2\pi}} \int_{o}^{(t+\frac{T}{2})\sigma} e^{-x^2/2}\, dx$$

$$- \frac{1}{\sqrt{2\pi}} \int_{o}^{(t-\frac{T}{2})\sigma} e^{-x^2/2}\, dx = 0.5 - \frac{1}{\sqrt{2\pi}} \int_{o}^{(t-\frac{T}{2})\sigma} e^{-x^2/2}\, dx \qquad \text{(G26)}$$

One wants to determine the number of samples between $t = t_1$ and $t = t_2$ where

$$\frac{f(t_1)}{f(o)} = 10^{-4}; \quad \frac{f(t_2)}{f(o)} = 1 - 10^{-4}$$

This is equivalent to

$$(t_1 - T/2)\,\sigma = 3.72$$

$$(t_2 - T/2)\,\sigma = -3.72$$

so

$$t_1 - t_2 = 7.44/\sigma$$

But as

$$\omega_s/2\sigma = 2.75$$

one gets for the time between samples

$$T_s = \frac{2\pi}{\omega_s} = \frac{2\pi}{5.5\sigma} \qquad \text{(G27)}$$

The number of samples necessary in the time interval (t_2, t_1) to get an error

$$\frac{e_a(t)}{f(o)} < 0.00056$$

that one needs is thus

$$\frac{t_1 - t_2}{T_s} = \frac{7.44 \times 5.5}{2\pi} = 6.5 < 7$$

Seven samples between time values corresponding to 10^{-4} and $1 - 10^{-4}$ will thus give an error smaller than 0.056 percent of the peak value for the function which is a convolution of a wide square pulse and a Gaussian pulse.

Results and Conclusions

As demonstrated by Example 1 and Example 3 on the one hand and Example 2 on the other, well-behaved smooth time functions require different sampling frequencies. For instance, if σ and a in Examples 1 and 2, respectively,

are picked so that $e^{-t_1^2 \sigma^2/2} = (1 + t^2/a^2)^{-1} = 10^{-4}$

then the first function requires five samples and the second function 198 samples from $t = t_1$ to $t = 0$ for reconstructing the sampled signal to an accuracy of 0.06 percent of the peak value. The reason is that the two functions have different spectra. When trying to estimate the aliasing error, care should therefore be taken when choosing a typical function.

ERROR ANALYSIS OF IDEALIZED CHOPPING APPROXIMATION

To estimate the error in the "ideal chopping" approximation for actual chopping in the detector plane, a simplified signal processing system according to Figure G4 is assumed. The filter h(t) passes the demodulated signal only and blocks the other components. The output is then given by

$$s_o(t) = [s_d(t)\, g(t)] * h(t) \tag{G28}$$

and as $g(t)$ is periodic, one has from Figure G44

$$s_o(t) = \sum_{m=-\infty}^{\infty} g_m \left[s_d(t)\, e^{jm2\pi t/T_o} * h(t) \right] \tag{G29}$$

The energy distribution in the detector plane will be assumed to vary in one direction and constant in the other. The coordinate unit used in the detector plane is detector dwell time (that is, the time that it takes to scan an angle corresponding to the detector width). Assuming the image energy distribution to be $s(\tau')$ in the coordinate system of the image (τ' in detector dwell time units), one gets in the detector coordinate system the distribution $s(\tau - t)$, where τ is the coordinate in the detector system and t is the position of the image coordinate system origin (see Figure G5). Designate the detector response by $b(\tau)$ and a chopper function $c(t, \tau)$, which is either 1 or 0 depending on t and τ. The exact detector output for chopping in the detector plane is then

$$s_d(t) = \int_{-\infty}^{\infty} s(\tau - t)\, c(t, \tau)\, b(\tau)\, d\tau \tag{G30}$$

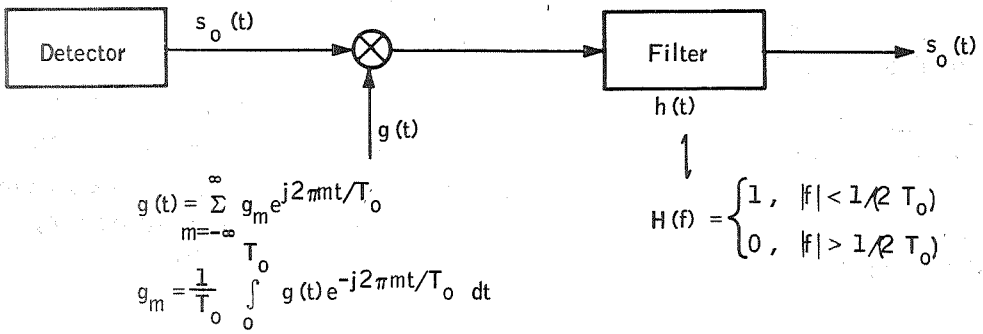

Figure G4. Simplified Signal Processing System

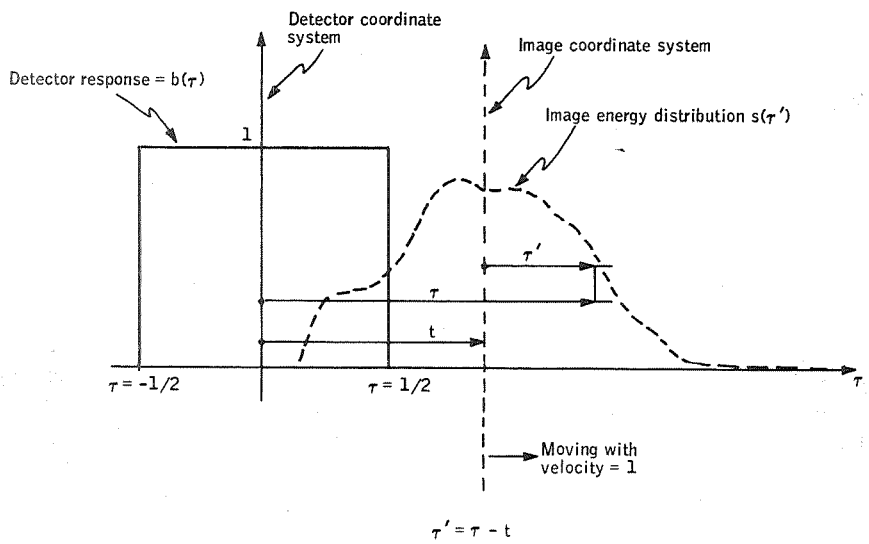

Figure G5. Coordinate Systems

But as $b(\tau)$ is in detector dwell time units and by assuming the detector response to be unity,

$$b(\tau) = \begin{cases} 1, & \text{if } |\tau| < 1/2 \\ 0, & \text{if } |\tau| > 1/2 \end{cases} \tag{G31}$$

Equation (G30) thus becomes

$$s_d(t) = \int_{-1/2}^{1/2} s(\tau - t)\, c(t, \tau)\, d\tau \tag{G32}$$

For the ideal chopping approximation, one writes the chopper function outside the integral

$$\bar{s}_d(t) = \bar{c}(t) \int_{-1/2}^{1/2} s(\tau - t)\, d\tau \tag{G33}$$

where the new chopper function $\bar{c}(t)$ (chop wave) is defined as the normalized detector output for a constant image energy distribution in the detector plane. Or as $s(\tau)$ = constant = A,

$$\bar{c}(t) = \frac{\int_{-1/2}^{1/2} A\, c(t, \tau)\, d\tau}{\int_{-1/2}^{1/2} A\, d\tau} = \int_{-1/2}^{1/2} c(t, \tau)\, d\tau \tag{G34}$$

The systems output for "ideal chop" is thus given by replacing $s_d(t)$ by $s_d(t)$

$$\bar{s}_o(t) = \sum_{m=-\infty}^{\infty} g_m \left[\bar{s}_d(t)\, e^{jm2\pi t/T_o} * h(t) \right] \tag{G35}$$

The error

$$\Delta s_o(t) = \frac{s_o(t) - \bar{s}_o(t)}{s_o(t)} \tag{G36}$$

in the approximation will be computed when the following is the image energy distribution in the detector plane:

$$s(\tau') = A + \sin(2\pi f \tau' + \phi) \tag{G37}$$

Actual Detector Plane Chopping

Assume the chopper motion as shown in Figure G6. This chopper motion is assumed because it approximates the transient portion of a sinusoidal chopper motion and has a well behaved Fourier series representation. The chopper motion can be represented by two infinite choppers, each moving with the same constant velocity but in different directions, (See Figure G7). With the phasing shown in Figure G7 (which is consistent with Figure G6) one has the following Fourier series representation of the two choppers:

$$c'(\tau) = \sum_{n=-\infty}^{\infty} c_n e^{j 2\pi n\tau / T} \tag{G38}$$

$$c''(\tau) = c'(\tau + T/2) = \sum_{n=-\infty}^{\infty} c_n e^{j 2\pi n\tau/T} e^{j\pi n} = \sum_{n=-\infty}^{\infty} (-1)\, n c_n e^{j2\pi n\tau / T} \tag{G39}$$

From Figure 47 one gets the chopper function

$$c(t,\tau) = c'(\tau - vt)\, c''(\tau + vt) \tag{G40}$$

$$c'(\tau - vt) = \sum_{n=-\infty}^{\infty} c_n e^{j2\pi n\tau / T} e^{-j2\pi nv\tau / T} \tag{G41}$$

$$c''(\tau+vt) = \sum_{k=-\infty}^{\infty} (-1)\, k c_k e^{j2\pi k\tau / T} e^{j2\pi kv\tau/ T} \tag{G42}$$

Inserting Equations (82), (83),into (81) then yields

$$c(t,\tau) = \sum_{k=-\infty}^{\infty} \sum_{n=-\infty}^{\infty} (-1)^k c_k c_n e^{j2\pi (k+n)\tau/ T} e^{j2\pi (k-n)v\tau/ T} \tag{G43}$$

The period of chopper motion is $2T$ (see FigureG6). During this time $c'(t)$ and $c''(t)$ have moved a distance T (see FigureG7), which is the period of the choppers in detector dwell time units. But the velocity was v; therefore,

$$T = 2T_o v \tag{G44}$$

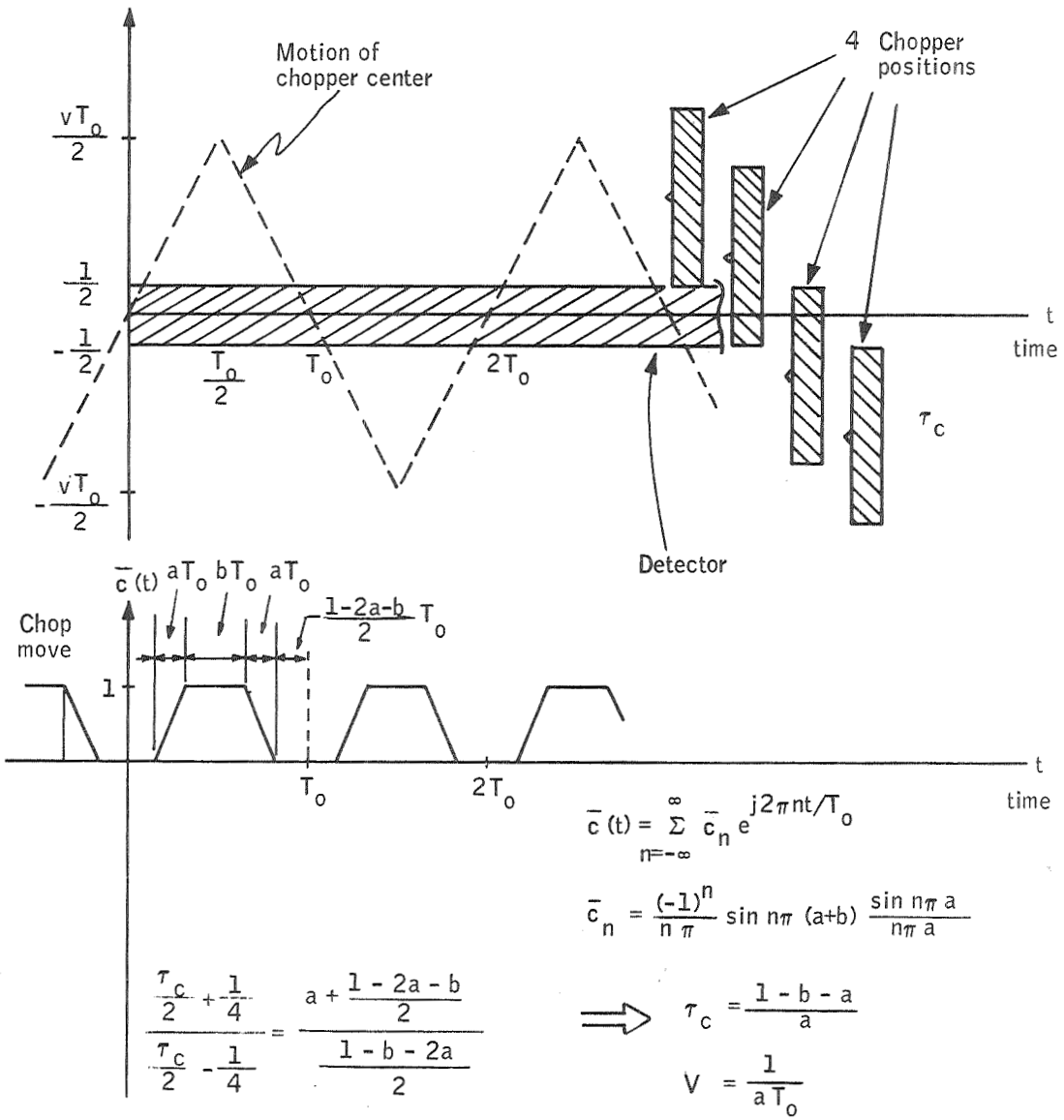

Figure G6. Chopper Motion and Chop Wave

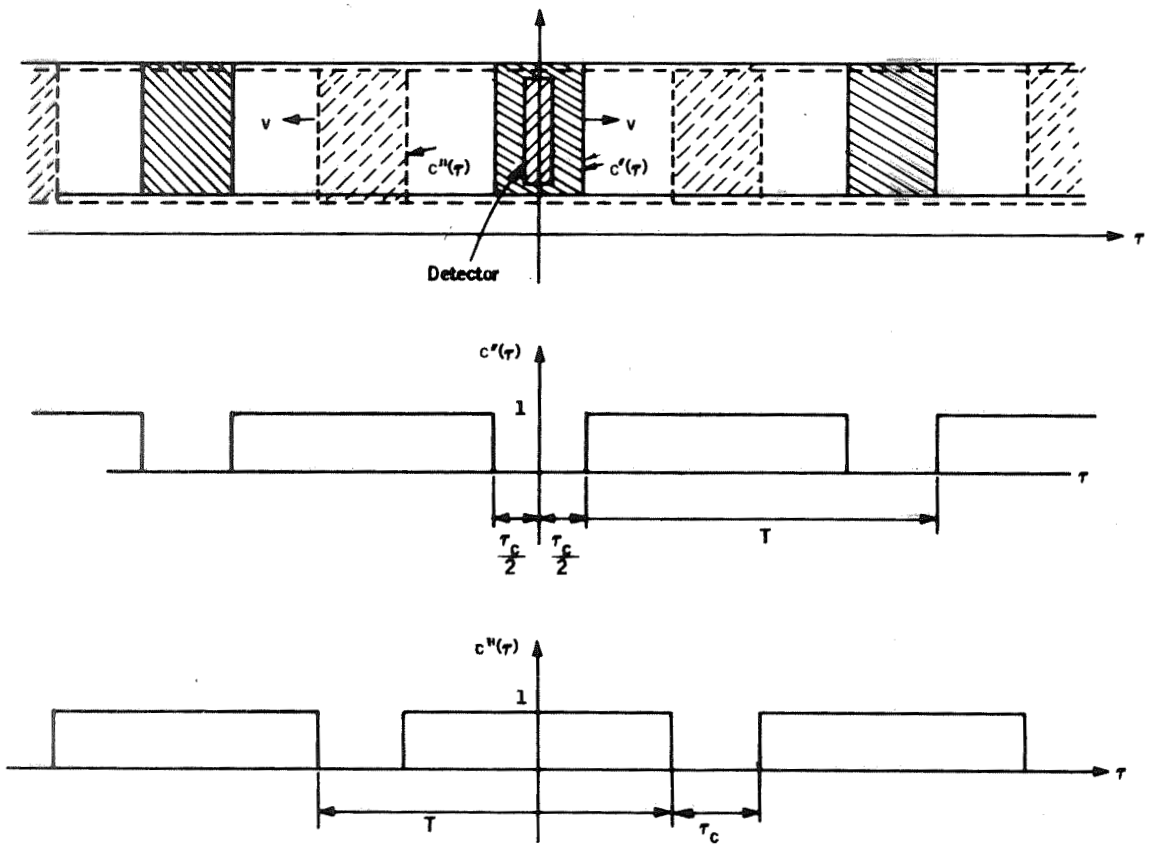

$$c'(\tau) = \sum_{n=-\infty}^{\infty} c_n e^{j2\pi n\tau/T}$$

$$c_n = \frac{1}{T}\int_0^T c'(\tau)\, e^{-j2\pi n\tau/T}\, d\tau = \frac{(-1)^n}{n\pi} \sin n\pi\left(1 - \frac{\tau_c}{T}\right)$$

Figure G7. Equivalent Chopper Representation of Figure G6 (Positions shown for t = 0)

Using this relation in Equation (G43)

$$c(t,\tau) = \sum_{k=-\infty}^{\infty} \sum_{n=-\infty}^{\infty} (-1)^k c_k c_n e^{j2\pi(k+n)\tau/T} e^{j\pi(k-n)\tau/T_o} \quad \text{(G45)}$$

Now insert (G45) into (G32); then

$$s_d(t) = \sum_{k=-\infty}^{\infty} \sum_{n=-\infty}^{\infty} (-1)^k c_k c_n e^{j\pi(k-n)t/T_o} \int_{-1/2}^{1/2} s(\tau-t)\, e^{j2\pi(km)\tau/T}\, d\tau \quad \text{(G46)}$$

Equation (G46) and (G29) now yield

$$s_o(t) = h(t) * \left[\sum_{k=-\infty}^{\infty} \sum_{n=-\infty}^{\infty} \sum_{m=-\infty}^{\infty} (-1)^k d_k c_n g_m e^{j2\pi(\frac{k-n}{2}+m)t/T_o} \int_{-1/2}^{1/2} s(\tau-t) e^{j2\pi(k+n)\tau/T} \right] dt \quad \text{(G47)}$$

Make the substitution $n = 2m + k - 2n'$ in Equation (G47).

Then (G38) becomes

$$s_o(t) = h(t) * \left[\sum_{k=-\infty}^{\infty} \sum_{n=-\infty}^{\infty} \sum_{m=-\infty}^{\infty} (-1)^k c_k c_{2m+k-2n'} g_m e^{j2\pi n' t/T_o} \int_{-1/2}^{1/2} s(\tau-t) e^{j2\pi 2(k+m-n')\tau/T} \right] dt \quad \text{(G48)}$$

$$s_o(t) = \left[\sum_{k=-\infty}^{\infty} \sum_{m=-\infty}^{\infty} (-1)^k c_k c_{2m+k} g_m \int_{-1/2}^{1/2} s(\tau - t)\, e^{j4\pi(k+m)\tau/T}\, dt \right.$$

$$= \sum_{k=-\infty}^{\infty} (-1)^k c_k \int_{-1/2}^{1/2} s(\tau - t) e^{j4\pi k\tau/T} \sum_{m=-\infty}^{\infty} c_{2m+k} g_m e^{j4\pi m\tau/T}\, d\tau$$

$$= \sum_{k=-\infty}^{\infty} (-1)^k c_k \int_{-1/2}^{1/2} s(\tau - t) e^{j4\pi k\tau/T} \; c_k g_o$$

$$\left. + \sum_{m=1}^{\infty} \left(c_{k+2m} g_m e^{j4\pi m\tau/T} + c_{k-2m} g_{-m} e^{-j4\pi m\tau/T} \right) \right] d\tau \qquad \text{(G49)}$$

From Figure G6 c(t) is an even function and, therefore, g(t) should also be even and $g_m = g_{-m}$; therefore

$$s_o(t) = \left[\sum_{k=-\infty}^{\infty} (-1)^k c_k \int_{-1/2}^{1/2} s(\tau - t) e^{j4\pi k\tau/T} \left(c_k g_o \right.\right.$$

$$\left.\left. + \sum_{m=1}^{\infty} g_m \left(c_{k+2m} e^{j4\pi m\tau/T} + c_{k-2m} e^{-j4\pi m\tau/T} \right) \right] d\tau \right.$$

$$= c_o \left\{ \int_{-1/2}^{1/2} s(\tau - t) \left[c_o g_o + \sum_{m=1}^{\infty} g_m \left(c_{2m} e^{j4\pi m\tau/T} + c_{-2m} d^{-j4\pi m\tau/T} \right) \right] d\tau \right.$$

$$+ \sum_{k=1}^{\infty} (-1)^k \int_{-1/2}^{1/2} s(\tau - t) \left[c_k c_k g_o + c_{-k} c_{-k} g_o + \sum_{m=1}^{\infty} c_k g_m c_{k+2m} e^{j4\pi(m+k)\tau/T} \right.$$

$$+ c_k g_m c_{k-2m} e^{-j4\pi(m-k)\tau/T} + c_{-k} g_m c_{-k+2m} e^{j4\pi(m-k)\tau/T}$$

$$\left.\left. + c_{-k} g_m c_{-k-2m} e^{-j4\pi(m+k)\tau/T} \right] d\tau \right\} \qquad \text{(G50)}$$

But as $c_k = c_{-k}$

$$s_o(t) = \int_{-1/2}^{1/2} s(\tau - t) \left\{ c_o^2 g_o + 2 c_o \sum_{m=1}^{\infty} g_m c_{2m} \cos 4\pi m \tau / T \right.$$

$$+ 2 \sum_{k=1}^{\infty} (-1)^k \left[c_k^2 g_o + c_k \sum_{m=1}^{\infty} g_m \left(c_{k+2m} \cos 4\pi (m+k) \tau / T \right.\right. \quad \text{(G51)}$$

$$\left.\left. \left. + c_{k-2m} \cos 4\pi (m-k) \tau / T \right) \right] \right\} d\tau$$

Assuming $g_o = 0$ means that the unmodulated portion of $s_d(t)$ (due to the d-c component of the chop wave) will be modulated by $g(t)$ so that the portion of $s_d(t)$ without carrier will eventually be filtered out by $h(t)$.

$$s_o(t) = 2 \sum_{m=1}^{\infty} g_m \int_{-1/2}^{1/2} s(\tau - t) \; c_o c_{2m} \cos 4\pi m \tau / T$$

$$+ \sum_{k=1}^{\infty} (-1)^k c_k \left(c_{k+2m} \cos 4\pi (k+m) \tau / T + c_{k-2m} \cos 4\pi (k-m) \tau / T \right) \Bigg] d\tau \quad \text{(G52)}$$

With (G37)

$$s(\tau') = \sin (2\pi f \tau' + \phi) \quad \text{(G53)}$$

one has

$$\int_{-1/2}^{1/2} s(\tau - t) \cos p\tau \, d\tau = \int_{-1/2}^{1/2} \sin [2\pi f(\tau - t) + \phi] \cos p\tau \, d\tau \quad (94) \quad \text{(G54)}$$

$$= \frac{1}{2} \sin (-2\pi f t + \phi) \left[\frac{\sin(\pi f + p/2}{\pi f + p/2} + \frac{\sin(\pi f - p/2)}{\pi f - p/2} \right]$$

Further, with $T = 2/a$ from Figure G6 and Equation (G44), (G52) reduces to

$$s_o(t) = \sin(-2\pi f t + \phi) \left\{ \sum_{m=1}^{\infty} g_m c_o c_{2m} \left[\frac{\sin \pi (f + ma)}{\pi (f + ma)} + \frac{\sin \pi (f - ma)}{\pi (f - ma)} \right] \right.$$

$$+ \sum_{m=1}^{\infty} \sum_{k=1}^{\infty} (-1)^k g_m c_k \left[c_{k+2m} \left(\frac{\sin \pi [f + (m+k) a]}{\pi [f + (m+k) a]} + \frac{\sin \pi [f - (m+k) a]}{\pi [f - (m+k) a]} \right) \right.$$

$$\left. \left. + c_{k-2m} \left(\frac{\sin \pi [f + (k-m) a]}{\pi [f + (k-m) a]} + \frac{\sin \pi [f - (k-m) a]}{\pi [f - (k-m) a]} \right) \right] \right\} \quad \text{(G55)}$$

which is the demodulated output when chopping in the detector plane.

Chopping Approximation

Equation (G33) gives the approximation for the detector output. Using (G37) in (G33),

$$\bar{s}_d(t) = \bar{c}(t) \int_{-1/2}^{1/2} \sin [\, 2\pi f(\tau - t) + \phi \,] d\tau \qquad \text{(G56)}$$

$$= \bar{c}(t) \frac{\sin \pi f}{\pi f} \sin (-2\pi f t + \phi)$$

But $\bar{c}(t)$ is periodic and one has from Figure G46

$$\bar{c}(t) = \sum_{n=-\infty}^{\infty} c_n e^{j 2\pi n t / T_o} \qquad \text{(G57)}$$

From Figure G7:

$$c_k = \frac{(-1)^k}{k\pi} \sin k\pi \left(1 - \frac{\tau_c}{T}\right) \qquad \text{(G58)}$$

but according to Equation (G44):

$$T = 2T_o v$$

and from Figure G6

$$v = \frac{1}{a\, T_o} \qquad \text{(G59)}$$

$$\tau_c = \frac{1 - b - a}{a} \quad \mu \qquad \text{(G60)}$$

Thus,

$$\frac{\tau_c}{T} = \frac{1 - b - a}{a\frac{2}{a}} = \frac{1 - a - b}{2} \qquad \text{(G61)}$$

And inserting (G61) in (G58)

$$c_k = \frac{(-1)^k}{k\pi} \sin \frac{k\pi}{2} (1 + a + b) \qquad \text{(G62)}$$

From Figure G6

$$\bar{c}_n = \frac{(-1)^n}{n\pi} \sin n\pi (a+b) \frac{\sin n\pi a}{n\pi a} \tag{G63}$$

Specializing to $a + b = 1/2$, $a = 1/6$:

$$c_k = \frac{(-1)^k}{k\pi} \sin \frac{3k\pi}{4} \tag{G64}$$

$$\bar{c}_n = \begin{cases} 0 & , \text{ if } n \text{ even} \\ \frac{(-1)^{(n+1)/2}}{n\pi} \frac{\sin n\pi/6}{n\pi/6}, & \text{if } n \text{ odd} \end{cases} \tag{G65}$$

Combining Equations (G56), (G57), and (G35),

$$\bar{s}_o(t) = \left[\sum_{m=-\infty}^{\infty} \sum_{n=-\infty}^{\infty} c_n g_m e^{j2\pi(m+n)t/T_o} \frac{\sin \pi f}{\pi f} \sin(-2\pi f t + \phi) \right] * h(t) \tag{G66}$$

but h(t) passes only the demodulated signal (that is, $m + n = 0$). Thus,

$$\bar{s}_o(t) = \sin(-2\pi f t + \phi) \frac{\sin \pi f}{\pi f} \sum_{m=-\infty}^{\infty} \bar{c}_{-m} g_m \tag{G67}$$

Approximation Error

The error $\Delta s_o(t)$ as given by Equation (G36) for a particular case will be estimated. Assume that $g(t)$ is a sinusoidal wave with frequency $1/T_o$. One thus has $g_{\pm 1} \neq 0$ and $g_m = 0$ for $m \neq \pm 1$. Assume also that $a = 1/6$ and $f = 1/2$ (f is cycles/dwell time unit).

Then,

$$\bar{s}_o(t) = \sin(-\pi f t + \phi) \frac{4}{\pi} \bar{c}_{-1} g_1 \tag{G68}$$

as $c_{-m} g_m = c_m g_{-m}$.

And

$$s_o(t) = \sin(-2\pi ft + \phi)\left[c_o g_1 c_2\left(\frac{\sin\frac{2\pi}{3}}{\frac{2\pi}{3}} + \frac{\sin\frac{\pi}{3}}{\frac{\pi}{3}}\right)\right.$$

$$+ \sum_{k=1}^{\infty}(-1)^k g_1 c_k\left\{c_{k+2}\left[\frac{\sin\pi\left(\frac{2}{3}+\frac{k}{6}\right)}{\pi\left(\frac{2}{3}+\frac{k}{6}\right)} + \frac{\sin\pi\left(\frac{1}{3}-\frac{k}{6}\right)}{\pi\left(\frac{1}{3}-\frac{k}{6}\right)}\right]\right.$$

$$\left.\left. + c_{k-2}\left[\frac{\sin\pi\left(\frac{1}{3}+\frac{k}{6}\right)}{\pi\left(\frac{1}{3}+\frac{k}{6}\right)} + \frac{\sin\pi\left(\frac{2}{3}-\frac{k}{6}\right)}{\pi\left(\frac{2}{3}-\frac{k}{6}\right)}\right]\right\}\right] \qquad \text{(G69)}$$

So

$$\frac{\bar{s}_o(t)}{s_o(t)} = \frac{4\bar{c}_{-1}}{\frac{c_o c_2}{4}\,9\sqrt{3} + \sum_{k=1}^{\infty}(-1)^k c_k\left[c_{k+2}\frac{\sin\pi\left(\frac{1}{3}-\frac{k}{6}\right)}{\left(\frac{2}{3}+\frac{k}{6}\right)\left(\frac{1}{3}-\frac{k}{6}\right)} + c_{k-2}\frac{\sin\pi\left(\frac{1}{3}+\frac{k}{6}\right)}{\left(\frac{2}{3}-\frac{k}{6}\right)\left(\frac{1}{3}+\frac{k}{6}\right)}\right]} \qquad \text{(G70)}$$

Inserting the values for c_{-1}, c_o, and c_2 in Equation (G70),

$$\frac{\bar{s}_o(t)}{s_o(t)} = \frac{-1/(3\pi^2)}{-\frac{3\sqrt{3}}{128\pi} + \sum_{k=1}^{\infty}(-1)^k c_k\left[c_{k+2}\frac{\sin\pi\left(\frac{1}{3}-\frac{k}{6}\right)}{(4+k)(2-k)} + c_{k-2}\frac{\sin\pi\left(\frac{1}{3}+\frac{k}{6}\right)}{(4-k)(2+k)}\right]} \qquad \text{(G71)}$$

$$= \frac{-0.03377}{-0.01274 - 0.00732 - 0.01274 - 0.00145 + 0.00028 - 0.00005 - 0.000001}$$

$$\approx 0.03377/0.03402$$

k	c_k	n	c_n
0	3/4		
±1	$-\frac{1}{\pi\sqrt{2}}$	±1	$-\frac{3}{\pi^2}$
±2	$-\frac{1}{2\pi}$		
±3	$-\frac{1}{3\pi\sqrt{2}}$		
±4	0		
±5	$\frac{1}{5\pi\sqrt{2}}$		
±6	$\frac{1}{6\pi}$		
±7	$\frac{1}{7\pi\sqrt{2}}$		
±8	0		
±9	$-\frac{1}{9\pi\sqrt{2}}$		
±10	$-\frac{1}{10\pi}$		

Inserting this in (G36),

$$\Delta S_o(t) \approx \frac{0.00025}{0.034} = 0.007 \qquad \text{(G72)}$$

Equation (G36) together with Equations (G55) and (G67) (where $\overline{c}_n$ and c_k are given by Figure G6 and G7, respectively) give the error for sine wave inputs with the simplified signal processing system when assuming ideal chopping as opposed to actual chopping in detector plane. For the particular case - a = 1/6, b = 1/3, and the demodulator wave g(t) a sine wave - the error was found to be approximately 1% for a sine wave input with a period equal to twice the detector dwell time.

CHOP-WAVE INSTABILITY EFFECTS

Because of chopper instability in null position and amplitude, there will be instability in the magnitude of the fundamental harmonic of the chop wave. There will also be a new harmonic at half-frequency of the fundamental harmonic due to the null shift. As chop wave harmonics are carriers, which modulate the radiometer (optical) signal input, the radiometer (electrical) signal output will vary with amplitude changes and null shifts.

The detector and the chopper blade sizes as functions of chopper motion amplitude and chop wave parameters are determined for a harmonic motion of the chopper. The errors in chop wave parameters as functions of amplitude and null errors are determined, and then the fundamental harmonic error and new harmonic are computed as functions of the chop wave parameter errors.

Chop Wave

Assume a harmonic motion of the chopper (see Figure G8). The positions of the chopper center as a function of time for nominal, amplitude changed, and null-shifted chop motions are shown in Figure G9 . The resulting chop waves are also shown. With chop wave one understands the detector output when the detector (aperture) is illuminated with a uniform, extended, time-constant illumination which is chopped in front of the detector (aperture).

The chop motion is described by

$$X(t) = A \sin \frac{\pi}{T_o} t \tag{G73}$$

For the detector width (X_d), the chopper width (X_c), chop amplitude (A), the parameters "a" describing waveform rise time, and "b" describing dwell time, one has the following relations:

$$\begin{cases} \dfrac{X_c - X_d}{2} = A \sin \dfrac{\pi}{2}(1-b-2a) & \text{(G74)} \\[2ex] \dfrac{X_c + X_d}{2} = A \sin \dfrac{\pi}{2}(1-b) & \text{(G75)} \end{cases}$$

$$X_c = A \left[\sin \frac{\pi}{2}(1-b-2a) + \sin \frac{\pi}{2}(1-b)\right] \tag{G76}$$

$$X_d = A \left[\frac{\pi}{2}(1-b) - \sin \frac{\pi}{2}(1-b-2a)\right] \tag{G77}$$

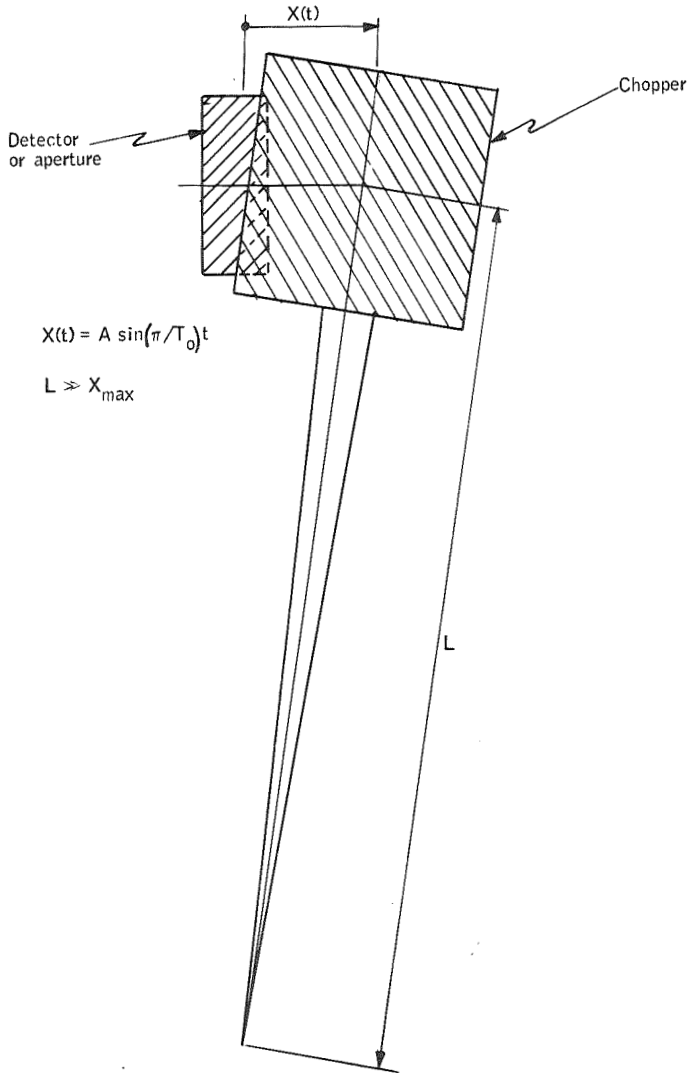

Figure G8. Chopper Motion

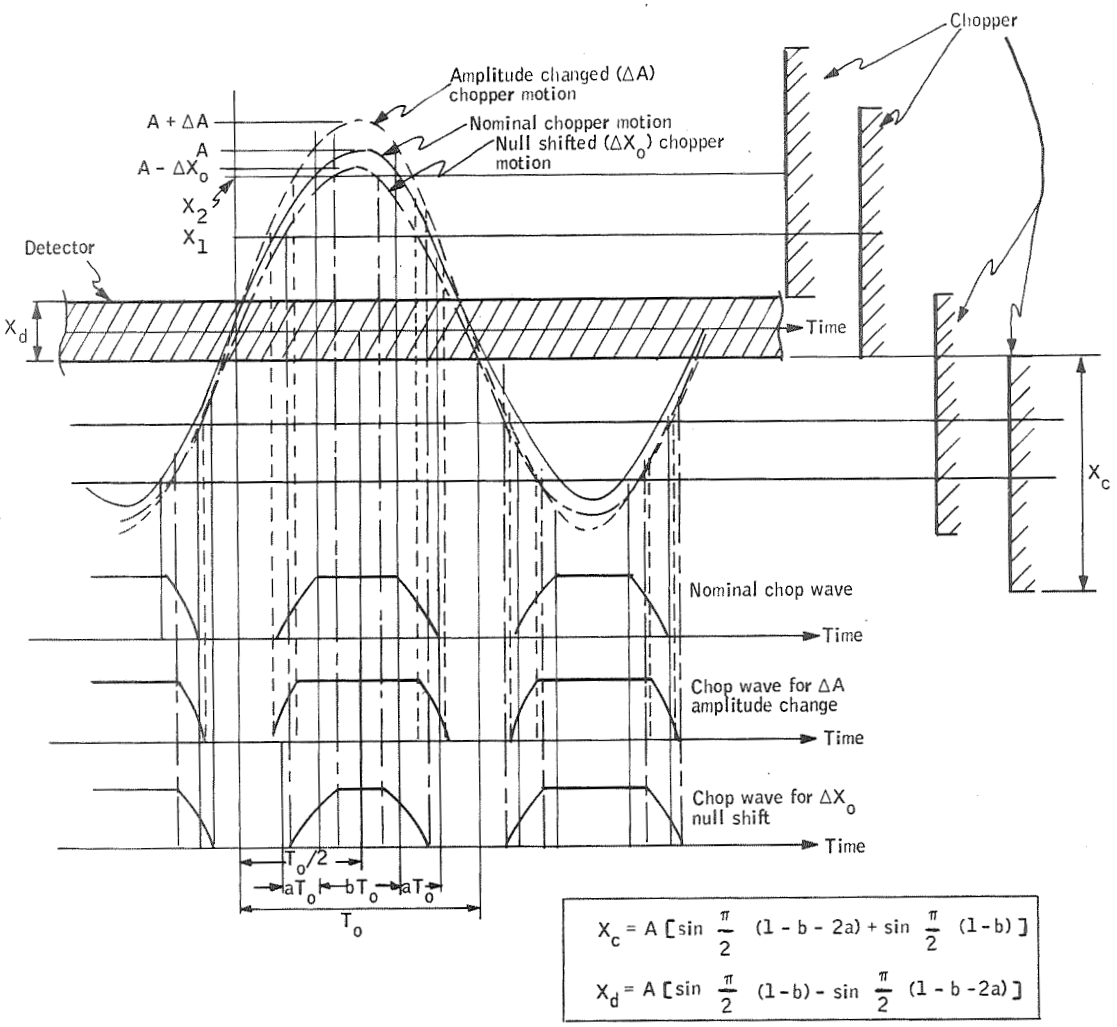

Figure G9. Chopper Motion and Chop Waves

Example:

$$a = 1/6$$

$$b = 1/3$$

$$\left.\begin{aligned} \frac{X_c}{A} &= \frac{\sqrt{3}+1}{2} \approx 1.38 \\ \frac{X_d}{A} &= \frac{\sqrt{3}-1}{2} \approx 0.36 \end{aligned}\right\} \rightarrow \frac{X_c}{X_d} \approx 3.8$$

From Figure G8,

$$\left\{\begin{aligned} \frac{X_c - X_d}{2} &= X_1 = A \sin \frac{\pi}{T_o} t_1 \qquad \text{(G78)} \\ \frac{X_c + X_d}{2} &= X_2 = A \sin \frac{\pi}{T_o} t_2 \qquad \text{(G79)} \\ \frac{X_c + X_d}{2} &= X_2 = A \sin \frac{\pi}{T_o} t_3 \qquad \text{(G80)} \end{aligned}\right.$$

$$\frac{t_1}{T_o} = \frac{1}{\pi} \arcsin \frac{X_1}{A} \qquad \text{(G81)}$$

$$\frac{t_2}{T_o} = \frac{1}{\pi} \arcsin \frac{X_2}{A} \qquad \text{(G82)}$$

$$\frac{t_3}{T_o} = 1 - \frac{1}{\pi} \arcsin \frac{X_2}{A} \qquad \text{(G83)}$$

Therefore,

$$a = \frac{t_2 - t_1}{T_o} = \frac{1}{\pi} \left(\arcsin \frac{X_2}{A} - \arcsin \frac{X_1}{A} \right) \qquad \text{(G84)}$$

$$b = \frac{t_3 - t_2}{T_o} = 1 - \frac{2}{\pi} \arcsin \frac{X_2}{A} \qquad \text{(G85)}$$

Amplitude Change and Null Shift

Introduce an amplitude change, ΔA, and a null shift, ΔX_o, in Equation (G1). Then,

$$X(t+\Delta t) + \Delta X_o = (A + \Delta A) \sin \frac{\pi}{T_o} (t + \Delta t_\theta) \tag{G86}$$

The effect on Equations (G84) and (G85) is

$$a + \Delta a = \frac{1}{\pi}\left[\arcsin \frac{X_2 + \Delta X_o}{A + \Delta A} - \arcsin \frac{X_1 + \Delta X_o}{A + \Delta A}\right] \tag{G87}$$

$$b + \Delta b = 1 - \frac{2}{\pi} \arcsin \frac{X_2 + \Delta X_o}{A + \Delta A} \tag{G88}$$

Subtracting Equation (G84) from Equation (G87) gives

$$\Delta a = \frac{1}{\pi}\left[\arcsin \frac{X_2 + \Delta X_o}{A + \Delta A} - \left(\arcsin \frac{X_2}{A} - \arcsin \frac{X_1 + \Delta X_o}{A + \Delta A} - \arcsin \frac{X_1}{A}\right)\right] \tag{G89}$$

And subtracting Equation (G85) from Equation (G88) gives

$$\Delta b = -\frac{2}{\pi} \arcsin \frac{X_2 + \Delta X_o}{A + \Delta A} - \arcsin \frac{X_2}{A} \tag{G90}$$

Equation (G89) reduces to

$$\Delta a = \frac{1}{\pi}\left[\frac{\Delta X_o - \Delta A \frac{X_2}{A}}{(A^2 - X_2^2)^{1/2}} - \frac{\Delta X_o - \Delta A \frac{X_1}{A}}{(A^2 - X_1^2)^{1/2}}\right] \tag{G91}$$

This is a good approximation when

$$X_2 - X_1 \gg \Delta X_o, \ \Delta A$$

Using Equations (G78) and (G79) in Equation (G85) with

$$t_1 = \frac{T_o}{2}(1-b-2a) \tag{G92}$$

$$t_2 = \frac{T_o}{2}(1-b) \tag{G93}$$

then

$$\Delta a = \frac{1}{\pi}\left[\frac{\Delta X_o - \Delta A \sin\frac{\pi}{2}(1-b)}{A\cos\frac{\pi}{2}(1-b)} - \frac{\Delta X_o - \Delta A \sin\frac{\pi}{2}(1-b-2a)}{A\cos\frac{\pi}{2}(1-b-2a)}\right]$$

$$= \frac{1}{\pi}\left\{\frac{\Delta X_o}{A}\left[\frac{1}{\cos\frac{\pi}{2}(1-b)} - \frac{1}{\cos\frac{\pi}{2}(1-b-2a)}\right] + \frac{\Delta A}{A}\left[\tan\frac{\pi}{2}(1-b-2a) - \tan\frac{\pi}{2}(1-b)\right]\right\} \tag{G94}$$

With the corresponding manipulations on Equation (G91),

$$\Delta b = -\frac{2}{\pi}\left[\frac{\Delta X_o}{A}\,\frac{1}{\cos\frac{\pi}{2}(1-b)} - \frac{\Delta A}{A}\tan\frac{\pi}{2}(1-b)\right] \tag{G95}$$

Effect on Chop Wave Harmonics

Approximate the chop wave by the trapezoidal form in Figure G10. For the first harmonic,

$$|c_1| = \frac{1}{\pi}\sin\pi(a+b)\,\frac{\sin\pi a}{\pi a} \tag{G96}$$

and thus

$$\frac{\Delta|c_1|}{|c_1|} = \frac{\pi(\Delta a + \Delta b)}{\tan\pi(a+b)} + \frac{\pi\Delta a}{\tan\pi a} - \frac{\Delta a}{a} \tag{G97}$$

Equation (G97) gives the change in the fundamental harmonic for an amplitude change. For the effect on the fundamental harmonic for a null shift, consider Figure G11. The chop wave in Figure G11 is equivalent to the one in Figure G10

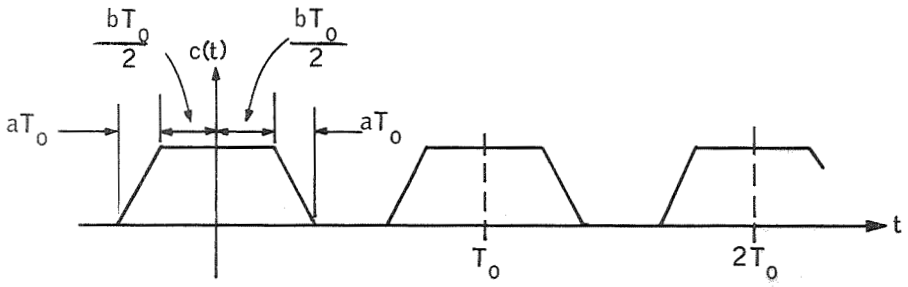

$$c(t) = \sum_{n=-\infty}^{\infty} c_n e^{jn2\pi t/T_o}$$

$$c_n = \frac{1}{n\pi} \sin n\pi(a+b) \frac{\sin n\pi a}{n\pi a}$$

Figure G10. Chop Wave Approximation

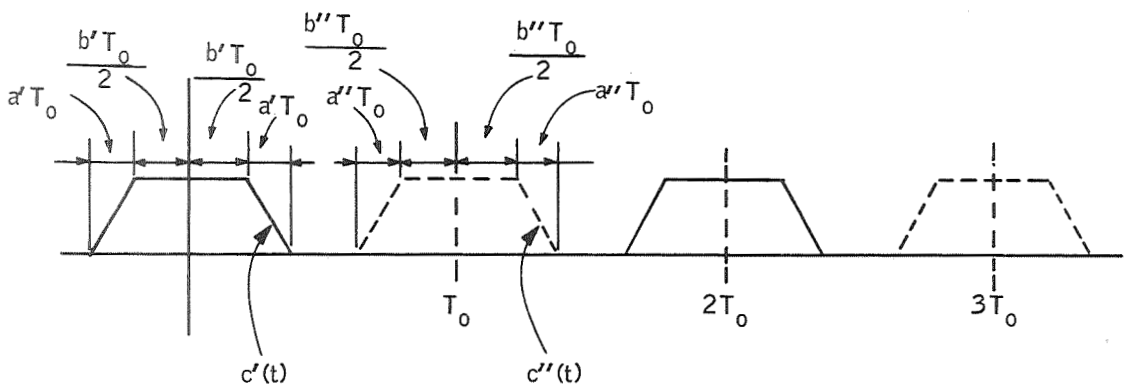

$$c'(t) = \sum_{k=-\infty}^{\infty} c'_k e^{jk2\pi t/2T_o}$$

$$c'_k = \frac{1}{k\pi} \sin k\frac{\pi}{2}(a'+b') \frac{\sin k\frac{\pi}{2}a}{k\frac{\pi}{2}a}$$

$$c''(t) = \Sigma\, c''_k\, e^{jk2\pi t/2T_o}$$

$$c''_k = \frac{1}{k\pi} e^{-jk\pi} \sin k\frac{\pi}{2}(a''+b'') \frac{\sin k\frac{\pi}{2}a}{k\frac{\pi}{2}a}$$

Figure G11. Chop Wave Approximation -- Effect of Null Shift on Fundamental Harmonic

when $a' = a'' = a$ and $b' = b'' = b$, because

$$c'''(t) = c'(t) + c''(t) = \sum_{k=-\infty}^{\infty} (c'_k + c''_k)\, e^{jk2\pi t/2T_o} \tag{G98}$$

$$c'''_k = c'_k + c''_k = \frac{1}{k\pi}\left[\sin\frac{k\pi}{2}(a'+b')\frac{\sin\frac{k\pi}{2}a'}{\frac{k\pi}{2}a'} + (-1)^k \sin\frac{k\pi}{2}(a''+b'')\right. \tag{G99}$$

$$\left.\frac{\sin\frac{k\pi}{2}a''}{\frac{k\pi}{2}a''}\right] = \frac{1}{k\pi}\left[1+(-1)^k\right]\sin\frac{k\pi}{2}(a+b)\,\frac{\sin\frac{k\pi}{2}a}{\frac{k\pi}{2}a} \tag{G100}$$

$$c'''_o = a+b \tag{G101}$$

$$c'''_{\pm 1} = 0 \tag{G102}$$

$$c'''_{\pm 2} = \frac{1}{\pi}\sin\pi(a+b)\,\frac{\sin\pi a}{\pi a} \tag{G103}$$

Thus,

$$c_i = c'''_{2i} \text{ for } i = 0, \pm 1, \pm 2, \ldots \tag{G104}$$

For a null shift with

$$\left.\begin{aligned} a' &= a'' = a \\ \Delta a' &= \Delta a'' \end{aligned}\right\} \tag{G105}$$

$$\left.\begin{aligned} b' &= b'' = b \\ \Delta b' &= -\Delta b'' \end{aligned}\right\} \tag{G106}$$

one has

$$c_k''' + \Delta c_k''' = \frac{1}{k\pi}\left[\sin\frac{k\pi}{2}(a+b+\Delta a'+\Delta b')\frac{\sin\frac{k\pi}{2}(a+\Delta a')}{\frac{k\pi}{2}(a+\Delta a')} + (-1)^k\sin\frac{k\pi}{2}(a+b-\Delta a'-\Delta b')\frac{\sin\frac{k\pi}{2}(a-\Delta a')}{\frac{k\pi}{2}(a-\Delta a')}\right] \tag{G107}$$

$$\approx \frac{1}{k\pi}\frac{\left[\sin\frac{k\pi}{2}(a+b)+\frac{k\pi}{2}(\Delta a'+\Delta b')\cos\frac{k\pi}{2}(a+b)\right]\left[\sin\frac{k\pi}{2}a+\frac{k\pi}{2}\Delta a'\cos\frac{k\pi}{2}a\right]\left[1-\frac{\Delta a'}{a}\right]}{\frac{k\pi}{2}a}$$

$$+\frac{(-1)^k}{k\pi}\frac{\left[\sin\frac{k\pi}{2}(a+b)-\frac{k\pi}{2}(\Delta a'+\Delta b')\cos\frac{k\pi}{2}(a+b)\right]\left[\sin\frac{k\pi}{2}a-\frac{k\pi}{2}\Delta a'\cos\frac{k\pi}{2}a\right]\left[1+\frac{\Delta a'}{a}\right]}{\frac{k\pi}{2}a}$$

and

$$\Delta c_k''' = \frac{1}{k\pi a}\left[1+(-1)^{k+1}\right]\left\{\Delta a'\left[\sin\frac{k\pi}{2}(2a+b)-\frac{1}{a}\sin\frac{k\pi}{2}a\sin\frac{k\pi}{2}(a+b)\right] + \Delta b'\left[\sin\frac{k\pi}{2}a\cos\frac{k\pi}{2}(a+b)\right]\right\} \tag{G108}$$

Thus,

$$\Delta c_1''' = \frac{2}{\pi a}\left\{\Delta a'\left[\sin\pi\left(a+\frac{b}{2}\right)-\frac{1}{a}\sin\frac{\pi a}{2}\sin\frac{\pi}{2}(a+b)\right] + \Delta b'\sin\frac{\pi a}{2}\cos\frac{\pi}{2}(a+b)\right\} \tag{G109}$$

and

$$\Delta c_2''' = 0 \tag{G110}$$

or

$$\Delta c_1 = 0$$

From Equation (G110) it thus follows that there is no first-order effect on the fundamental harmonic (c_1) from a null shift. There is, however, a first-order effect in the creation of a new harmonic ($c_1''' = c_{1/2}$) with a frequency half of the fundamental harmonic.

Summary of equations. -- Let subscript N denote null shift and subscript A amplitude change; then, one can summarize Equations (G94), (G95), (G97), (G109), and(G110):

$$\frac{\Delta|c_1|}{|c_1|} = \frac{\pi(\Delta a_A + \Delta b_A)}{\tan\pi(a+b)} + \frac{\pi\Delta a_A}{\tan\pi a} - \frac{\Delta a_A}{a} \tag{G111}$$

$$\frac{\Delta c_{1/2}}{|c_1|} = \frac{2\pi}{\sin\pi(a+b)\sin\pi a}\left\{\Delta a_N\left[\sin\pi\left(a+\frac{b}{2}\right) - \frac{1}{a}\sin\frac{\pi a}{2}\sin\frac{\pi(a+b)}{2}\right]\right.$$
$$\left. + \Delta b_N \sin\frac{\pi a}{2}\cos\frac{\pi(a+b)}{2}\right\} \tag{G112}$$

$$\Delta a_A = \frac{1}{\pi}\frac{\Delta A}{A}\left[\tan\frac{\pi}{2}(1-b-2a) - \tan\frac{\pi}{2}(1-b)\right] \tag{G113}$$

$$\Delta a_N = \frac{1}{\pi}\frac{\Delta X_o}{A}\left[\frac{1}{\cos\frac{\pi}{2}(1-b)} - \frac{1}{\cos\frac{\pi}{2}(1-b-2a)}\right] \tag{G114}$$

$$\Delta b_A = \frac{2}{\pi}\frac{\Delta A}{A}\tan\frac{\pi}{2}(1-b) \tag{G115}$$

$$\Delta b_N = \frac{-2}{\pi}\frac{\Delta X_o}{A}\frac{1}{\cos\frac{\pi}{2}(1-b)} \tag{G116}$$

Examples and discussion. -- In Figure G12 , the relative change in the fundamental chop wave harmonic is shown as a function of relative amplitude change for various a and b. As pointed out above, there is no first-order effect on the fundamental harmonic from a chopper null shift. The high slope for $a + b = 3/8$, $\frac{b}{a} = 2$. can be qualitatively understood by looking at Figure G9 . There it can be seen that if b is small, X_2 will be large and the slope of the sine wave will be small; therefore, an amplitude shift will cause $|\Delta a|$ and $|\Delta b|$ and consequently a large $\left|\frac{\Delta c_1}{c_1}\right|$.

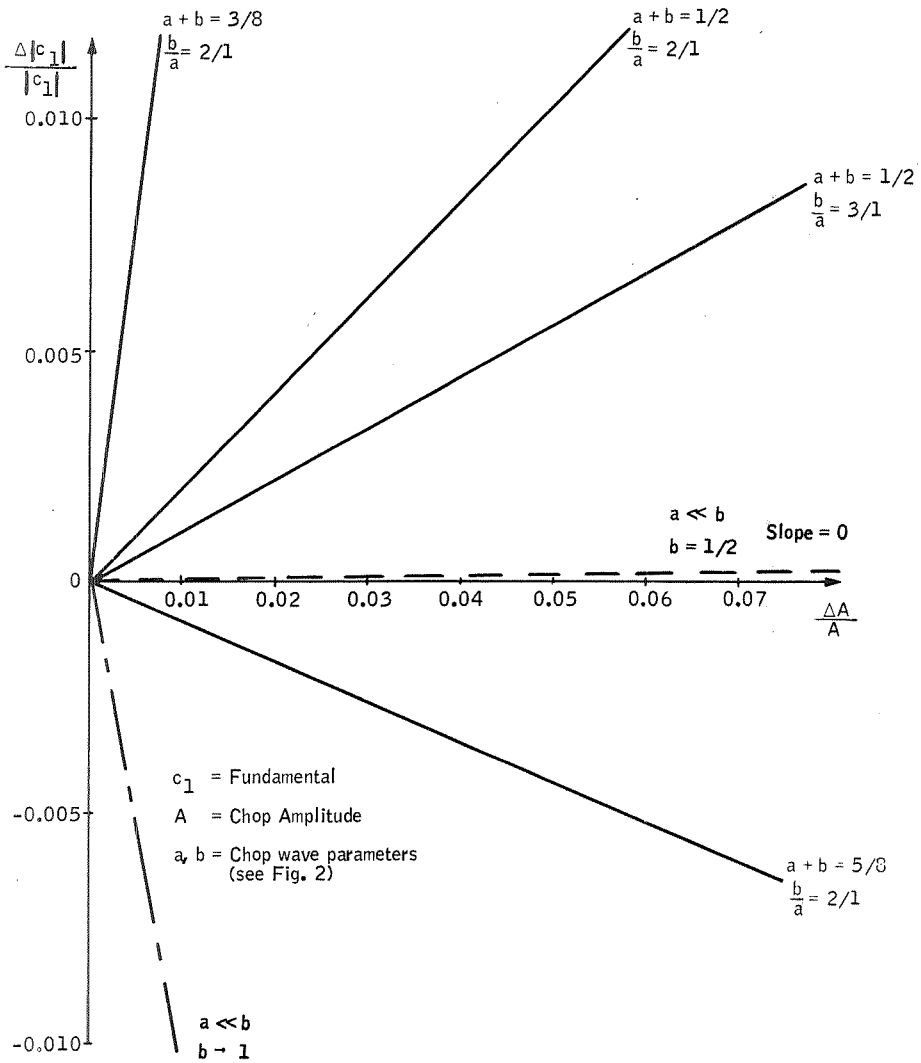

Figure G12. Relative Change in First Chop Harmonic as a Function of Relative Amplitude Change

Figure G13 shows the new harmonic relative to the fundamental harmonic as a function of the chop motion null shift relative to amplitude for various a and b. If one assumes $a + b = 1/2$, $\frac{b}{a} = 2$, one sees from Figure (G12) that a 0.5% amplitude change produces a 0.1% change in the fundamental harmonic. From Figure G13 , one sees that a 0.03% null shift creates a new harmonic at half fundamental harmonic frequency, which is 0.1% of the fundamental harmonic. This new harmonic will be an extra carrier at half-chop frequency for the optical input signal.

If amplitude change and null shift cannot be controlled to the desired magnitude, an obvious solution is to use a gate with an on time less than $(b-|\Delta b|)T_o$, and no amplitude and null instability effects will be seen after gating. However, when gating is used, synchronization between chopper and gate is important if the on time is close to bT_o. Furthermore, a wideband filter (amplifier) between detector and gate is necessary to accomplish the desired effect.

It should again be noted that the above instability analysis is a first-order approximation and that the chop wave was assumed to be trapezoidal (Figure G10). The first-order approximation should be good for at least small disturbances in amplitude and null position. Equation (G111) states that the change in the fundamental does not depend on b when $a + b = 1/2$, which is somewhat surprising. It is believed, however, that a second-order analysis will not give a significantly different result for small disturbances.

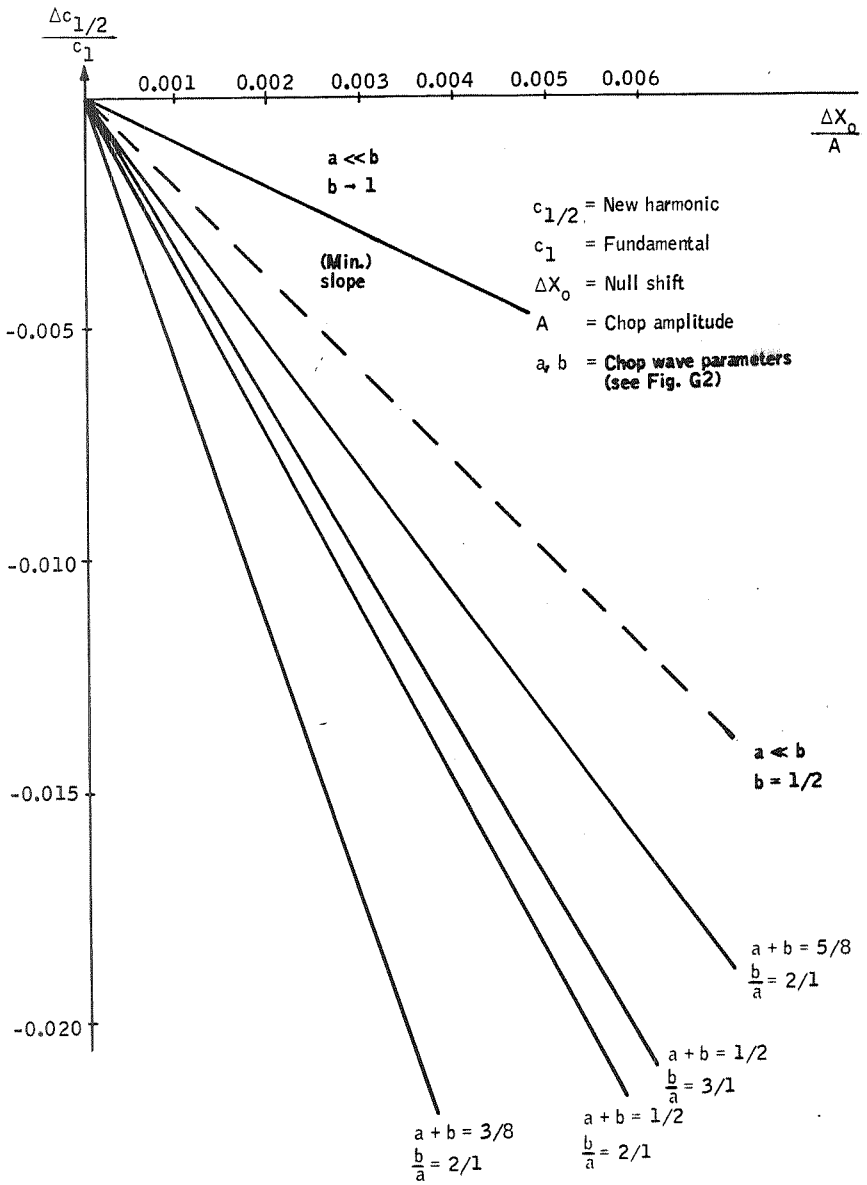

Figure G13. New Harmonic Due to Null Shift as a Function of Null Shift

Phase Instability

Phase relation stability between the modulating wave and the demodulating wave in a synchronous detection system is important since it affects the demodulated signal amplitude. An expression for output signal amplitude instability as a function of instability in phase between modulating wave and demodulating wave is derived in terms of the Fourier series coefficients of the two periodic waves. The demodulated signal instability as a function of phase instability is also computed for a special case of chop wave and gate wave not using the derived expression in Fourier series coefficients. The modulating wave is referred to as chop wave.

General derivation of phase instability effect. -- When no filter is at hand, one has for the synchronous detection system in Figure G14 :

$$s_{out}(t) = s_{in}(t)\, c(t)\, g(t)$$

$$= s_{in}(t) \left[\sum_{n=-\infty}^{\infty} c_n e^{j2\pi n f_o t} \right] \left[\sum_{m=-\infty}^{\infty} g_m e^{j2\pi m f_o t} \right]$$

$$= s_{in}(t) \sum_{n=-\infty}^{\infty} \sum_{m=-\infty}^{\infty} c_n g_m e^{j2\pi (n+m) f_o t}$$

$$= s_{in}(t) \sum_{k=-\infty}^{\infty} \sum_{m=-\infty}^{\infty} c_{k-m}\, g_m\, e^{j2\pi k f_o t}$$

$$= s_{in}(t) \sum_{m=-\infty}^{\infty} c_{-m}\, g_m + \sum_{m=-\infty}^{\infty} g_m \sum_{k=1}^{\infty} \left(c_{k-m} e^{j2\pi k f_o t} + c_{-k-m} e^{-j2\pi k f_o t} \right) \qquad \text{(G117)}$$

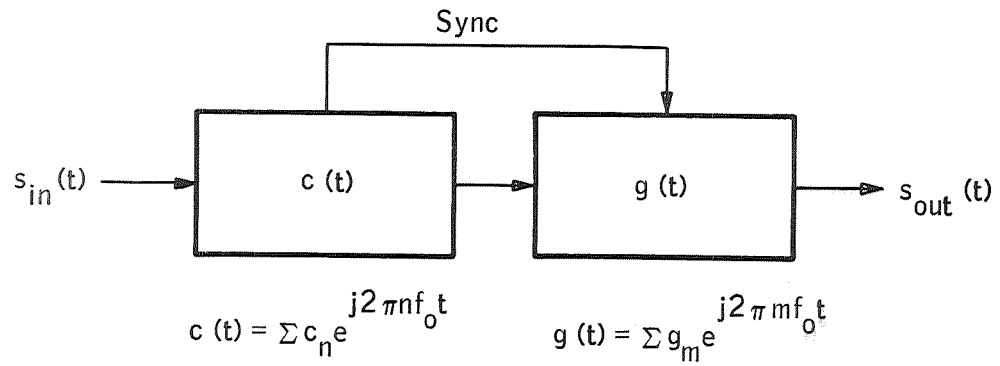

Figure G14. Synchronous Detection

Define a demodulating wave $g'(t) = \Sigma g'_m e^{j2\pi mf_o t}$ such that the i;th harmonic of g(t) is in phase with the i;th harmonic of c(t). Let

$$g(t) = g'(t-\tau) \tag{G118}$$

Then,

$$g'(t-\tau) = \sum_{m=-\infty}^{\infty} g'_m e^{j2\pi mf_o(t-\tau)} = \sum_{m=-\infty}^{\infty} g'_m e^{-j2\pi mf_o t} e^{j2\pi mf_o t} \tag{G119}$$

and thus,

$$g_m = g'_m e^{-j2\pi mf_o \tau} \tag{G120}$$

with

$$f_o = 1/T_o$$

and

$$\phi = 2\pi \frac{\tau}{T_o}$$

$$g_m = g'_m e^{-jm\phi} \tag{G121}$$

Interest centers in the demodulated (k=0) signal amplitude, or more specifically

$$\sum_{-\infty}^{\infty} c_{-m} g_m$$

in Equation (G117). Using (G121):

$$K \equiv \sum_{m=-\infty}^{\infty} c_{-m}\, g_m = \sum_{m=-\infty}^{\infty} c_{-m}\, g'_m\, e^{-jm\phi} \tag{G122}$$

Introducing a phase shift $\Delta\phi$ in (G122),

$$K + \Delta K = \sum_{m=-\infty}^{\infty} c_{-m}\, g'_m e^{-jm(\phi + \Delta\phi)} \tag{G123}$$

and thus,

$$\frac{\Delta K}{K} = \frac{\displaystyle\sum_{m=-\infty}^{\infty} c_{-m}\, g'_m\, e^{-jm\phi}\left(e^{-jmo\phi} - 1\right)}{\displaystyle\sum_{m=-\infty}^{\infty} c_{-m}\, g'_m\, e^{-jm\phi}} \tag{G124}$$

Assume that the chop wave $c(t)$ and the demodulating wave $g(t)$ are even functions; that is,

$$c(t) = c(-t) \tag{G125}$$

$$g'(t) = g'(-t) \tag{G126}$$

then

$$c_m = c_{-m} \tag{G127}$$

$$g'_m = g'_{-m} \tag{G128}$$

Inserting (G127) and (G128) into (G124),

$$\frac{\Delta K}{K} = \frac{\sum_{m=1}^{\infty} c_m g'_m \left[e^{-jm\phi} \left(e^{-jm\Delta\phi} - 1 \right) + e^{jm\phi} \left(e^{jm\Delta\phi} - 1 \right) \right]}{c_o g'_o + \sum_{m=1}^{\infty} c_m g'_m \left[e^{-jm\phi} + e^{jm\phi} \right]}$$

$$= \frac{\sum_{m=1}^{\infty} c_m g'_m 2 \left[\cos m(\phi+\Delta\phi) - \cos m\phi \right]}{c_o g'_o + \sum_{m=1}^{\infty} c_m g'_m 2 \cos m\phi} \qquad \text{(G129)}$$

$$= \frac{\sum_{m=1}^{\infty} c_m g'_m \left[\cos m\phi \, (\cos m\Delta\phi - 1) - \sin m\phi \, \sin m\Delta\phi \right]}{\frac{c_o g'_o}{2} + \sum_{m=1}^{\infty} c_m g'_m \cos m\phi}$$

For the special case $\phi = 0$,

$$\frac{\Delta K}{K} = - \frac{\sum_{m-1}^{\infty} c_m g'_m (1 - \cos m\Delta\phi)}{\frac{c_o g'_o}{2} + \sum_{m=1}^{\infty} c_m g'_m} \qquad \text{(G130)}$$

If the demodulating wave is a sine wave - that is, $g_m = 0$ for $m \neq 1$ - or if the chop wave is a sine wave (or all carriers c_n except $n = 1$ have been filtered out, then (G129) becomes

$$\frac{\Delta K}{K} = \frac{c_1 g'_1 \left[\cos\phi (\cos\Delta\phi - 1) - \sin\phi \sin\Delta\phi \right]}{c_1 g'_1 \cos\phi} \qquad \text{(G131)}$$

$$= \cos\Delta\phi - 1 - \tan\phi \sin\Delta\phi - \frac{(\Delta\phi)^2}{2} - \Delta\phi \tan\phi$$

In Figure G15 , $\frac{\Delta K}{K}$ (relative error in output signal) is a function of phase error $\Delta\phi$ for $\phi = 0, \pm 5°$ and for $c(t)$ and/or $g(t)$ being sine waves. However, for general (even) waveforms Equation (G129) has to be used. Note that approximations of $1 - \cos m\Delta\phi$ and $\sin m\Delta\phi$ by

$$\frac{(m\Delta\phi)^2}{2}$$

and $m\Delta\phi$, respectively, are generally not very good since $m\Delta\phi$ is increasing for increasing m and the sequence $c_m g_m'$ may not converge fast enough. Formula (129) is useful when a filter is used between chopper and demodulator in Figure G14 . (In reality the filter would be between detector and gate, since the chopper modulates the optical signal in front of the detector), because then the summation would be over those m whose carriers are transmitted by the filter.

Special case with trapezoidal chop wave and square demodulating wave. -- For a trapezoidal chop wave and a square demodulating wave the phase instability effect on the demodulated signal amplitude (or more accurate: the effect on the dc-component of the product of the chop and gate waves) is computed in a more direct way below. A chop wave without a dc-component is of course not physically realizable; however, for a highpass filter between the detector and the demodulator, the dc-component of the chop wave is filtered out. The component $s_{in}(t)\, c_o$ of

$$s_{in}(t) \sum_{-\infty}^{\infty} c_n e^{j2\pi n f_o t} \tag{G132}$$

is not necessarily filtered out entirely. If the highest frequency, f_i, of of $s_{in}(t)$ is greater than $f_o/2$, then $s_{in}(t)\, c_o$ cannot be filtered out without filtering out part of

$$s_{in}(t) \sum_{\substack{n=-\infty \\ n\neq 0}}^{\infty} c_n\, e^{j2\pi n f_o t} . \tag{G133}$$

The simplified model with no chop wave d-c component is therefore only entirely correct for $f_i < f_o/2$ and a highpass filter with an ideal cutoff frequency larger than f_i and smaller than $f_o - f_i$. If, however, the demodulator wave has no d-c component ($g_o = 0$), the component $s_{in}(t)\, c_o\, g_o$ of

$$s_{in}(t) \sum_{m=\infty}^{\infty} c_{-m}\, g_m \tag{G134}$$

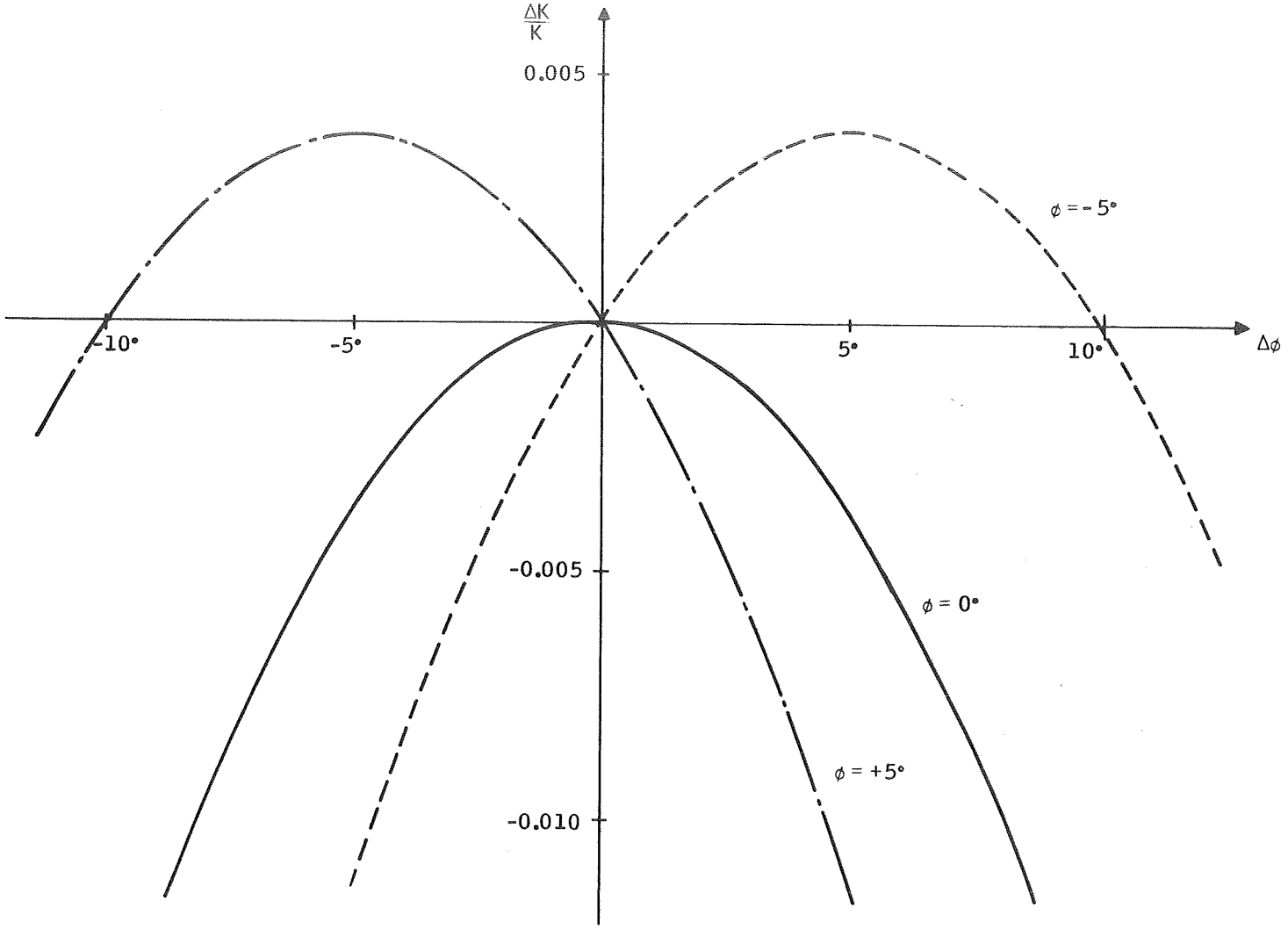

Figure G15. Relative Error in Demodulated Signal for Instability in Phase for Sine Waves

will equal zero. In fact, the d-c component of $c(t)\,g(t)$ is independent of g_o if $c_o = 0$ and independent of c_o if $g_o = 0$.

Now, assume that the chop wave $c(t)$ in Figure G16a is without d-c component. We are interested in the d-c component of $c(t)\,g(t)$ in Figure G16c. The demodulator wave $g(t)$ is shown in Figure G16b. As $c_o = 0$ the d-c component of $c(t)\,g(t)$ is equal to the one of $c(t)\,g_1(t)$, shown in Figure G16c.

No d-c component of $c(t)$ gives

$$X = -(a+b) \tag{G135}$$

$$d = a(1+X) = a(1-a-b) \tag{G136}$$

Thus, the d-c component of $f(t) = c(t)\,g(t)$:

$$K = 2(1-a-b)\left(b + \frac{2d}{2}\right) = 2(1-a-b)[b+a(1-a-b)] \tag{G137}$$

$$= 2(1-a-b)(a+b)(1-a)$$

For $f(t) = c(t)\,g(t-\delta)$ the d-c component is $K + \Delta K$, where

$$\Delta K = -\delta\,\frac{2(1-a-b)\delta}{d} = -\frac{2\delta^2}{a} \tag{G138}$$

$$\delta \le \min\,[a(1-a-b),\ a(a+b)] \tag{G139}$$

$$\frac{\Delta K}{K} = \frac{-\delta^2}{a(1-a)(1-a-b)(a+b)} \tag{G140}$$

With $\Delta\phi = 2\pi\delta$ ($\Delta\phi$ in radians),

$$\frac{\Delta K}{K} = -\frac{1}{4\pi^2\,a(1-a)(1-a-b)(a+b)}\,(\Delta\phi)^2 \tag{G141}$$

From (G141) the inequality

$$\frac{\Delta K}{K} \le -\frac{4}{\pi^2}\,(\Delta\phi)^2 \tag{G142}$$

follows [as for the expression $z = x(1-x)\,y(1-y)$, we have $0 < z \le \frac{1}{16}$ for $0 < x < 1$, $0 < y < 1$. In (G141) a corresponds to x and $a = b$ to y].

In Figure (G17), $\frac{\Delta K}{K}$ as a function of $\Delta\phi$ is plotted for various a and b; $a = 1/2$, $b = 0$ corresponds to the equal sign in the inequality (G142).

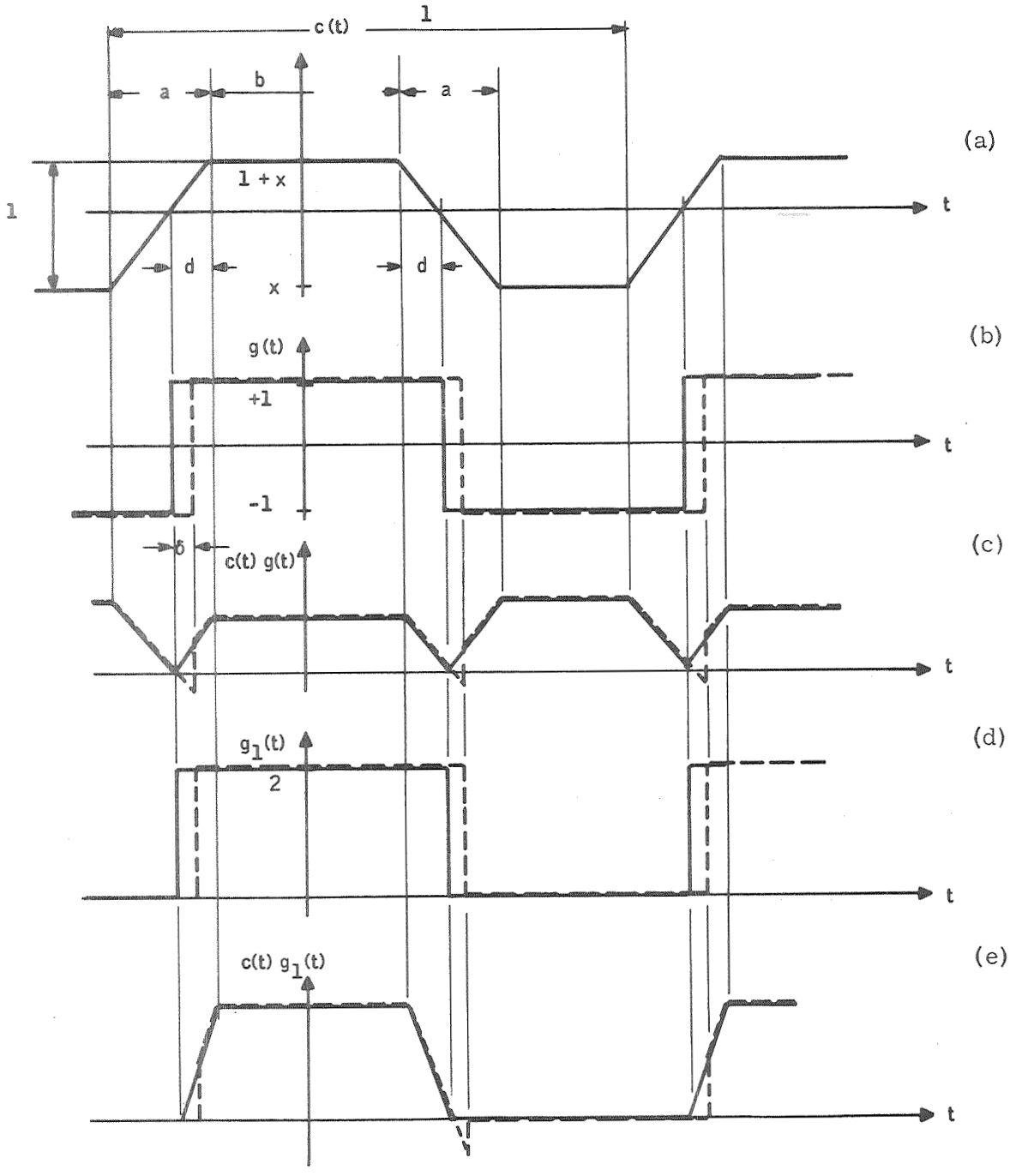

Figure G16. Chopper/GateWave Shifts

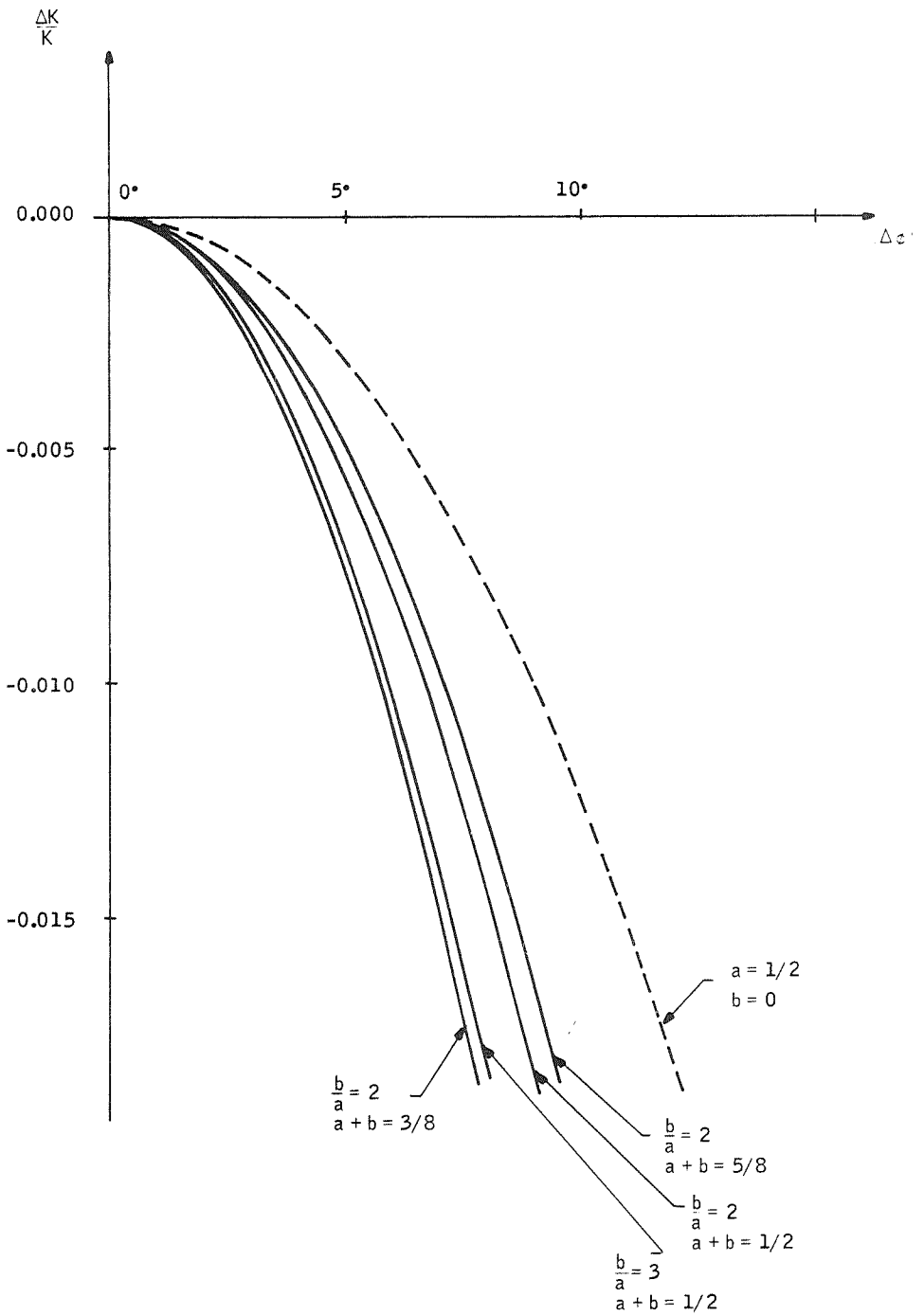

Figure G17. Relative Error in Demodulated Signal as a Function of Instability in Phase Relation Between or Trapezoidal Chop Wave (without d-c Component) and a Square Gate Wave

Conclusions. -- If the chop wave and the demodulator wave nominally are in phase with each other and at least one of them is a single harmonic sine wave and at least one of them has no d-c component, a phase shift of 2.5° yields a 0.1% error in demodulated signal. A chop wave with the ratio 1:2:1:2 for turn-on, on, turn-off, and off-time and a square demodulator wave that is positive for the time that the chop wave is above its d-c level and negative for the time the chop wave is below, causes a 0.1% error in demodulated signal for a phase shift of 2.2°, when at least one of the two waves has no d-c component.

Chop Frequency Shift

A shift f_o of the chopping frequency f_o, in the synchronous detection system in Figure G18, will cause a phase shift and an amplitude shift in the Fourier transform $S_{out}(f)$ of the output signal $s_{out}(t)$. If we only consider the chopper-modulated input signal with the carrier $\pm f_o$ (the fundamental harmonic of the chop wave), we can write the BP-filter output as

$$S'_{out}(f) = \left[c_1 S_{in}(f-f_o) + c_{-1} S_{in}(f+f_o)\right] H_1(f) \qquad \text{(G143)}$$

and the gate output

$$\begin{aligned} S''_{out}(f) = {} & H_1(f-f_o)\left[c_1 g_1 S_{in}(f-2f_o) + c_{-1} g_1 S_{in}(f)\right] \\ & + H_1(f+f_o)\left[c_1 g_{-1} S_{in}(f) + c_{-1} g_{-1} S_{in}(f+2f_o)\right] \end{aligned} \qquad \text{(G144)}$$

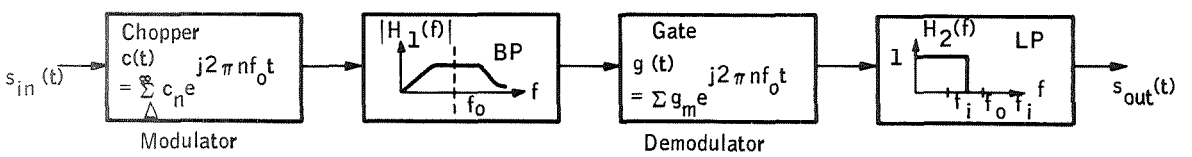

Figure G18. Synchronous Detection System Model

Assume $S_{in}(f)$ bandlimited to $f_i < f_o/2$ and $S''_{out}(f)$ is ideally LP-filtered with cutoff $f_o/2$. Consider $S_{out}(f)$ for positive f only.

Then,

$$S_{out}(f) = c_{-1}g_{-1}\, S_{in}(f)\, H_1(f - f_o) \tag{G145}$$

For the same shift in frequency, Δf_o, for chop wave and gate wave, we have

$$S_{out}(f) + \Delta S_{out}(f) = c_{-1}g_1 S_{in}(f)\, H_1(f - f_o - \Delta f_o) \tag{G146}$$

Combining (G145) and (G146)

$$\Delta S_{out}(f) = c_{-1}g_1 S_{in}(f)\left[H_1(f - f_o - \Delta f_o) - H_1(f - f_o)\right] \tag{G147}$$

We thus see that instability in frequency of the chop wave does not cause a frequency shift in the output signal $S_{out}(f)$ for fixed input frequency $f = f_1$ if the gate wave is synchronous in frequency. However, the bandpass-filter output S_{out} shifts in frequency for a frequency shift in chop wave, because for a fixed input frequency $f - f_o = f_1$ we get for positive frequencies from (G60):

$$S'_{out}(f_1 + f_o) = c_1 S_{in}(f_1)\, H_1(f_1 + f_o) \tag{G148}$$

and a frequency shift Δf_o gives

$$S'_{out}(f_1 + f_o + \Delta f_o) = c_1 S_{in}(f_1)\, H_1(f_1 + f_o + \Delta f_o) \tag{G149}$$

Frequency instability. --Rigorously, $S_{out}(f)$ is given by

$$S_{out}(f) = S_{in}(f) \sum_{m=-\infty}^{\infty} c_{-m}g_m H_1(f - mf_o) \tag{G150}$$

when $S_{in}(f)$ is bandlimited to $|f_i| < f_o/2$ and $H_2(f)$ is an ideal lowpass filter with cutoff between f_i and $f_o - f_i$. Splitting (G150) in two expressions, one for magnitude and one for phase,

$$\left|S_{out}(f)\right| = \left|S_{in}(f)\right| \left| \sum_{m=-\infty}^{\infty} c_{-m}g_m\, H_1(f - mf_o) \right| \tag{G151}$$

$$\underline{\left|S_{out}(f)\right.} = \underline{\left|S_{in}(f)\right.} + \underline{\left| \sum_{m=-\infty}^{\infty} c_{-m}g_m\, H_1(f - mf_o) \right.} \tag{G152}$$

Now, introduce a frequency shift Δf_o in chop and gate frequency f_o. Then,

$$\frac{\Delta|S_{out}(f)|}{|S_{out}(f)|} = \frac{\left|\sum_{m=-\infty}^{\infty} c_{-m} g_m H_1(f-mf_o-m\Delta f_o)\right| - \left|\sum_{m=-\infty}^{\infty} c_{-m} g_m H_1(f-mf_o)\right|}{\left|\sum_{m=-\infty}^{\infty} c_{-m} g_m H_1(f-mf_o)\right|} \qquad \text{(G153)}$$

$$\Delta\underline{|S_{out}(f)} = \underline{\left|\sum_{m=-\infty}^{\infty} c_{-m} g_m H_1(f-mf_o-m\Delta f_o)\right|} - \underline{\left|\sum_{m=-\infty}^{\infty} c_{-m} g_m H_1(f-mf_o)\right|} \qquad \text{(G154)}$$

If we can find upper bounds for all frequencies, f, of interest for the absolute magnitude error (G153) and the phase error (G154) as functions of f_o, we have upper bounds for the time domain errors, namely amplitude errors and timing error.

For given c_m, g_m, and H_1, the functions

$$\frac{\Delta|S_{out}(f)|}{|S_{out}(f)|}$$

and

$$\underline{|S_{out}(f)}$$

as functions of f_o, Δf_o are very complex to compute. The direct effect on the output time domain signal for a frequency shift is of course easily obtained by simulation runs of the RMS program for various inputs and system parameters. However, a rough estimate on the upper bounds of (G153) and (G154) for a two-pole Butterworth bandpass filter is computed as follows.

Assume that the chop wave and the gate wave contain only one signal frequency mf_o. Then (G153) and (G154) reduce to

$$\left.\frac{\Delta|S_{out}(f)|}{|S_{out}(f)|}\right|_m = \frac{|H_1(f-mf_o-m\Delta f_o)| - |H_1(f-mf_o)|}{|H_1(f-mf_o)|} \qquad \text{(G155)}$$

$$\Delta\underline{|S_{out}(f)}\Big|_m = \underline{|H_1(f-mf_o-m\Delta f_o)} - \underline{|H_1(f-mf_o)} \qquad \text{(G156)}$$

Consider the filter in Figure G19 and assume ω_b = 25 krad/sec. For frequencies $|\omega_i| < 12.5$ krad/sec we have for m = 1

$$\left|\frac{\Delta|S_{out}(f)|}{|S_{out}(f)|}\right|_{m=1} < \frac{0.05\text{ dB}}{12500}|\Delta\omega_o| = 0.012\left|\frac{\Delta f_o}{f_o}\right| \qquad \text{(G157)}$$

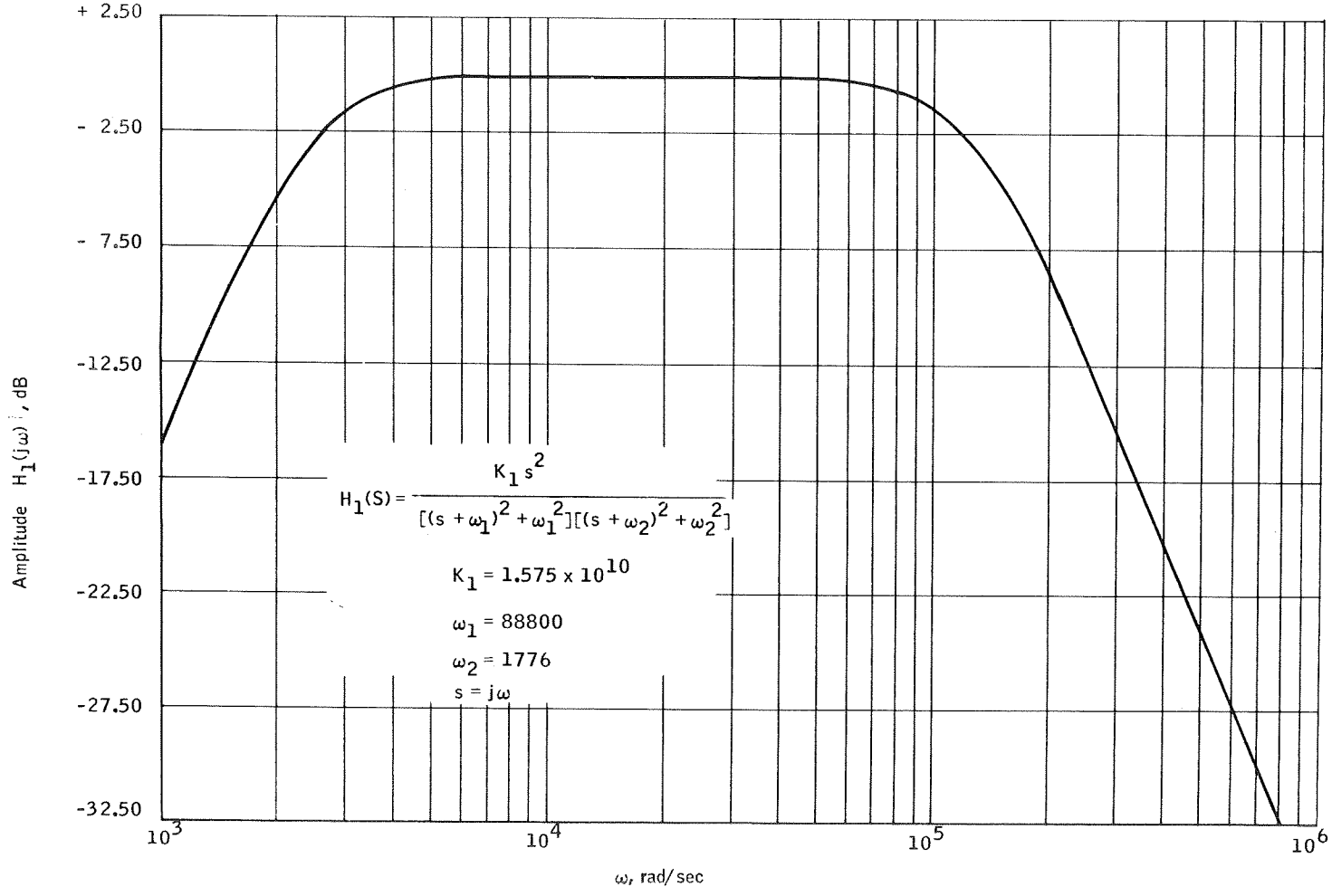

Figure G19a. Two-Pole Butterworth

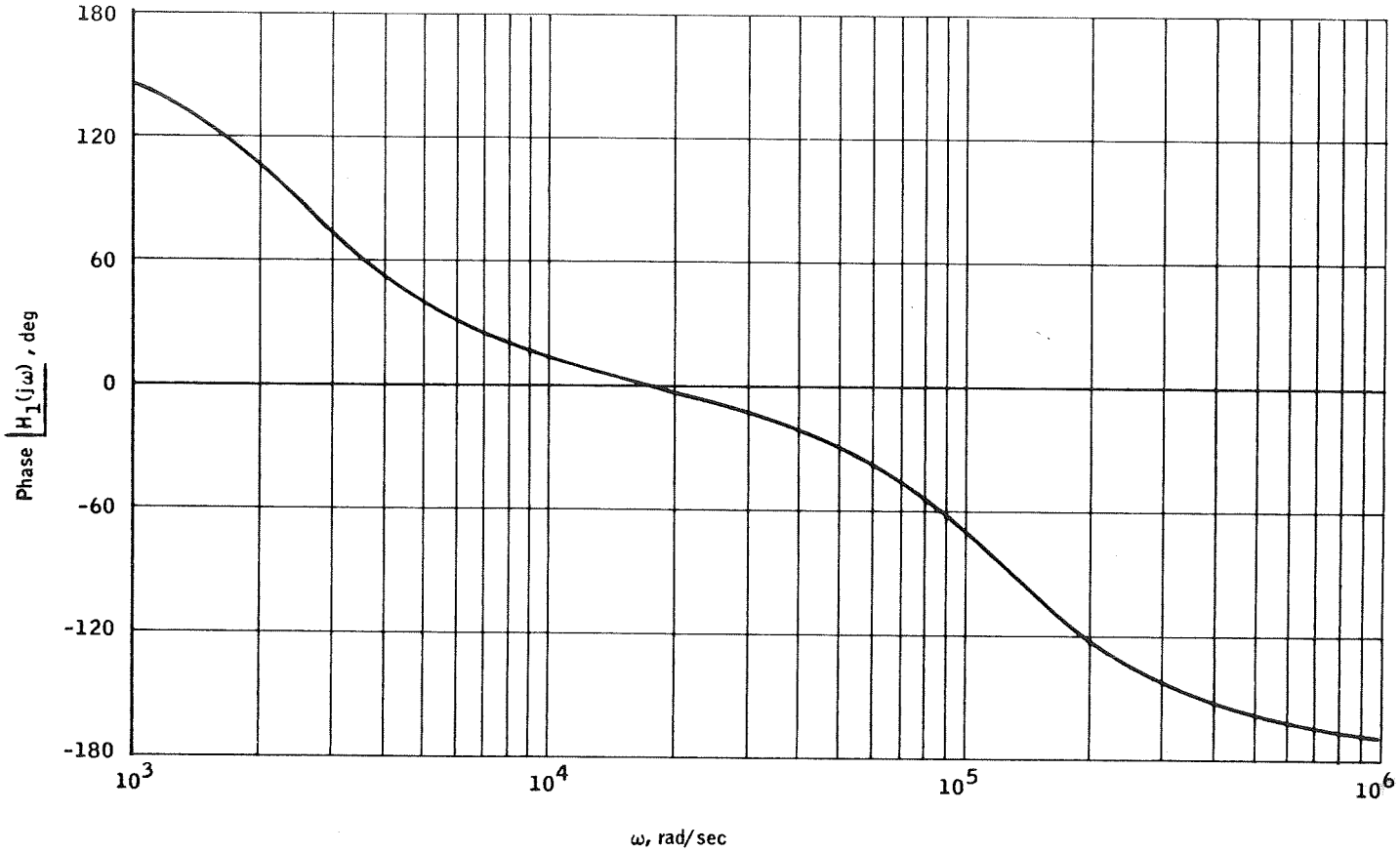

Figure G19b. Two-Pole Butterworth

Equation (G157) is the relative change in $H_1(f-f_o)$ for a change Δf_o in chop frequency f_o. The change in $H_1(f-f_o)$ for a certain change Δf_o and fixed $f-f_o$ is obtained from Figure G19a.

A chop angular frequency of $\omega_o = 2\pi f_o = 25,000$ rad and an information bandwidth of $|2\pi f| = |\omega| < \omega_i = 12,500$ rad were assumed for computation.

Thus, the argument of interest for $|H_1|$ is $12,500 < 2\pi(f-f_o) = \omega - \omega_o < 25,000$. The maximum of the slope for $|H_1|$ in this interval is estimated from Figure G19a to be 0.05 dB/25,500 rad; 0.05 dB corresponds to a ratio of 1.006, that is, a relative change of $(1.006 - 1,000)/1 = 0.006$ or a relative slope of 0.006/12,500 rad. With $\omega_o = 25,000$ rad, this relative shope can be written as $0.012/\omega_o$ rad^{-1}, and for an angular chop frequency shift of $\Delta\omega_o$ we have the bound in Equation (G157).

Thus a 10% shift in frequency causes less than 0.12% change in signal amplitude. For m = 3

$$\left| \frac{\Delta|S_{out}(f)|}{|S_{out}(f)|} \right|_{m=3} < \frac{0.6 \text{ dB}}{15000} 3|\Delta\omega_o| = 0.36 \left| \frac{\Delta f_o}{f_o} \right| \qquad \text{(G158)}$$

When computing (G158) it must be remembered that a change of $\Delta\omega_o$ causes a change of $3\Delta\omega_o$ for the third harmonic of the chop wave.

And for m = 5

$$\left| \frac{\Delta|S_{out}(f)|}{|S_{out}(f)|} \right|_{m=5} < \frac{2.0 \text{ dB}}{25000} 5|\Delta\omega_o| = 1.25 \left| \frac{\Delta f_o}{f_o} \right| \qquad \text{(G159)}$$

From (G156) and Figure G19b, we have for m = 1

$$\left| \Delta \underline{|S_{out}(f)|} \right|_{m=1} < \frac{12°}{15000} |\Delta\omega_o| = 20 \left| \frac{\Delta f_o}{f_o} \right| \text{[deg]} \qquad \text{(G160)}$$

For m = 3

$$\left| \Delta \underline{|S_{out}(f)|} \right|_{m=3} < \frac{12°}{15000} 3|\Delta\omega_o| = 60 \left| \frac{\Delta f_o}{f_o} \right| \text{[deg]} \qquad \text{(G161)}$$

and m = 5

$$\left| \Delta \underline{|S_{out}(f)|} \right|_{m=5} < \frac{9°}{15000} 5|\Delta\omega_o| = 75 \left| \frac{\Delta f_o}{f_o} \right| \text{[deg]} \qquad \text{(G162)}$$

For a chop wave c(t) with turn-on, on, turn-off, and on-time ratios of 1:2:1:2 and a gate wave g(t) that has the value +1 for the chopper on-time and the value -1 for the off-time and 0 for turn-on and turn-off, we have (see Figures G6 and G7)

TABLE G1

m	$\frac{c_{\mp m} g_{\pm m}}{c_{\mp 1} g_{\pm 1}}$
1	1
2	0
3	0
4	0
5	0.008
6	0

With the ratios 1:3:1:3 for the chop wave, we get

TABLE G2

m	$\frac{c_{\mp m} g_{\pm m}}{c_{\mp 1} g_{\pm 1}}$
1	1
2	0
3	0.037
4	0
5	0.008
6	0

From Tables G1 and G2 we see that $S_{out}(f)$, in the infinite sum (G150), is dominated by the term m = 1. We therefore conclude

$$\left| \frac{\Delta \, |S_{out}(f)|}{S_{out}(f)} \right| \lesssim 0.012 \left| \frac{\Delta f_o}{f_o} \right| \tag{G163}$$

$$\Delta \phi(f) = \left| \Delta \, \underline{|S_{out}(f)|} \right| \lesssim 20 \left| \frac{\Delta f_o}{f_o} \right| \tag{G164}$$

Thus, from (G163) we have that a 10% frequency causes less than 0.12% amplitude shift in the demodulated output signal for a bandlimited input signal.

The phase shift $\Delta\phi(f)$ causes a delay in time of

$$\tau = \frac{\Delta\phi(f)}{360}\frac{1}{f} < \frac{\Delta\phi(f)}{360}\frac{2}{f_o} \lesssim \frac{20}{360}\frac{2}{f_o}\left|\frac{\Delta f_o}{f_o}\right| = \frac{1}{9f_o}\left|\frac{\Delta f_o}{f_o}\right| = \frac{1}{36} \times 10^{-3}\left|\frac{\Delta f_o}{f_o}\right| \qquad \text{(G165)}$$

With a radiometer scan rate of ω_1 rpm we get a pointing error of $\Delta\psi$ for the time error τ, where

$$\Delta\psi_{deg} = \frac{360}{60}\omega_1\tau = 6\omega_1\tau \qquad \text{(G166)}$$

or in arc sec

$$\Delta\psi_{arc\ sec} = 3600 \times 6\omega_1\tau \lesssim 0.6\,\omega_1\left|\frac{\Delta f_o}{f_o}\right| \qquad \text{(G167)}$$

With a scan rate of $\omega_1 = 5$ rpm we have

$$\Delta\psi_{arc\ sec} \lesssim 3\left|\frac{\Delta f_o}{f_o}\right| \qquad \text{(G168)}$$

A chop and gate frequency shift of 10% thus causes a timing error equivalent to an angle of 0.3 arc sec for a 5 rpm scan rate.

Results

For a two-pole Butterworth bandpass filter with the 3 dB points at $0.1\,f_o$ and $5\,f_o$, where f_o is the chop and gate frequency, an approximate calculation shows that a 10% shift in f_o will cause am amplitude error less than 0.1% and a timing error equivalent to a spatial angle of less than 0.3 arc sec for a radiometer scan rate of 5 rpm. This is valid only for input signals bandlimited to $f_i < f_o/2$ and ideal cutoff of lowpass filter. For non-bandlimited signals the frequency instability effects is preferably evaluated in simulation runs. Results of the total chopper instability analysis are summarized in Table G3.

ALIASING ERRORS

Aliasing Error In Detector Output

Expanding the sum in Equation (27) of the main text, one has

$$S_d(f) = \sum_{n=-\infty}^{\infty} \bar{c}_n M(f-nf_c) S_i(f-nf_c) \tag{G169}$$

$$= \bar{c}_c M(f) S_i(f) + \bar{c}_1 M(f-f_c) S_i(f-f_c) +$$

$$+ \bar{c}_{-1} M(f+f_c) S_i(f+f_c) + \bar{c}_2 M(f-2f_c) S_i(f-2f_c)$$

$$+ \bar{c}_{-2} M(f+2f_c) S_i(f+2f_c) + \ldots$$

The amplitude of the terms $|\bar{c}_n M(f-nf_c) S_i(nf_c)|$ are shown in Figure G20b for $[M(f) S_i(f)]$ according to Figure G20a. Thus, one sees that it is impossible to recover $S_i(f)$ exactly by demodulating and filtering: for instance from the term $n = \pm 1$, if the information bandwidth $|f_i| > f_c/2$, $\bar{c}_o \neq 0$, and/or $\bar{c}_{\pm 2} \neq 0$. For the information bandwidth, f_i, shown in Figure G20, the terms $\bar{c}_n M(f-nf_c) S_i(f-nf_c)$ $n = 0, \pm 2$ will mix with $\bar{c}_{\pm 1} M(f \mp f_c) S_i(f \mp f_c)$ due to the foldover of the spectra. If the information bandwidth is greater than shown in Figure G20, this aliasing error will occur from even higher order n ($n = \pm 3, \pm 4, \ldots$). Note that if $f_c/2 < |f_i| < f_c$, $S_i(f)$ can be recovered exactly for frequencies $|f| < f_c - f_i$ after $S_i(f)$ has been chopped. To reduce the aliasing error, the optics-detector transfer function M(f) should have a low response beyond $|f| > f_c/2$ and if in particular $M(f) = 0$ for $|f| > f_c/2$ and $M(f) \neq 0$ for $|f| < f_c/2$ theoretically, $S_i(f)$ can be recovered for frequencies $|f| < f_c/2$ even if $S_i(f)$ has an information bandwidth wider than $f_c/2$. Making $\bar{c}_n$ small for $n = 0, \pm 2, \pm 3 \ldots$ (if demodulating the term $n = \pm 1$) will also reduce the aliasing error in detector output.

Aliasing In Systems Output

Equation (55) of the main text gave the system output. The infinite summation expanded over n is

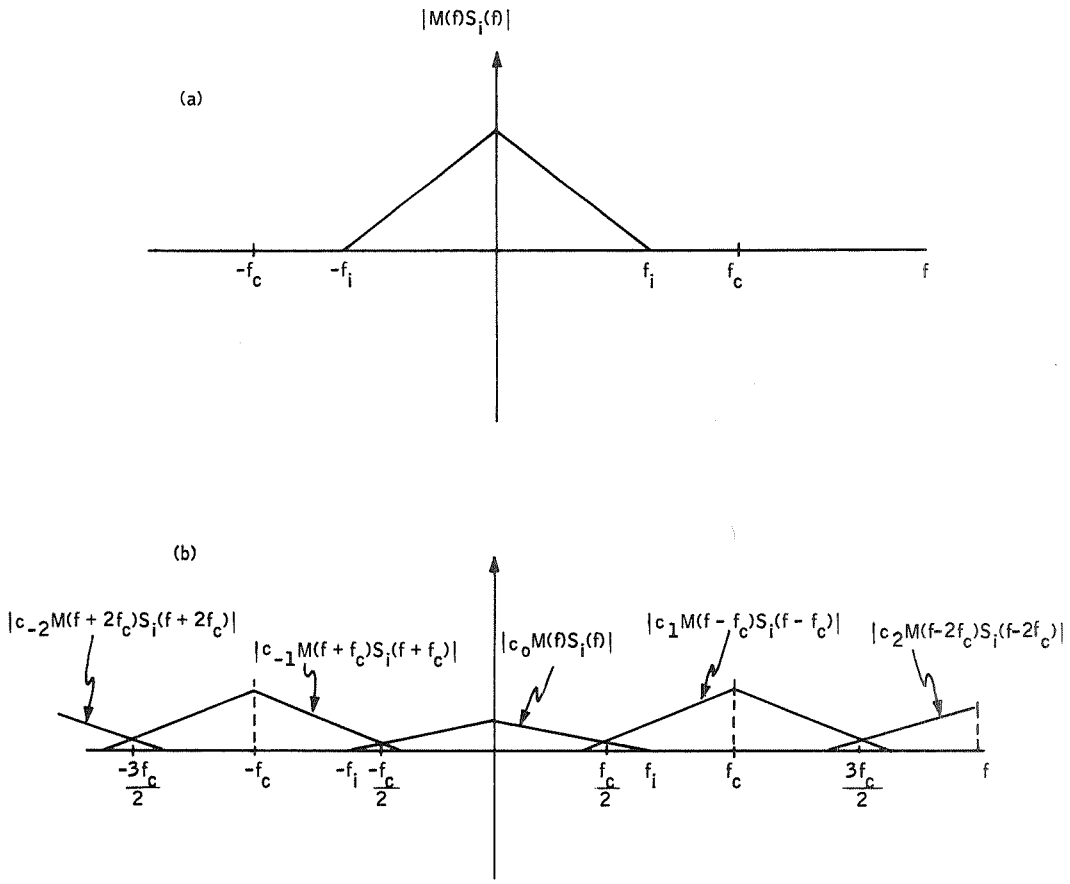

Figure G20. Aliasing Effects

TABLE G3. - CHOPPER INSTABILITY EFFECTS SUMMARY

Instability effect		Resultant error in output signal for constant input signal	Resultant Pointing error for 5 rpm scanning radiometer
Amplitude instability in chopper motion. a)	$\frac{\Delta A}{A} = 0.5\%$	0.1%	
Null point instability in chopper motion. a)	$\frac{\Delta X}{A} = 0.03\%$	0.1%	
Instability in phase relation between chop wave and demodulating wave. a)	= 2.2%	0.1%	
Frequency instability in chopper motion. b)	= 10%	0.1%	0.3 arc sec

a) Chop wave with the ratio 1:2:1:2 for turn-on, on, turn-off, and off time (a = 1/6, b = 1/3)

b) With two-pole Butterworth bandpass filter; 3 dB-points at $0.1 f_c$ and $5 f_c$

$$S_o(f) = H_3(f) \sum_n S_i(f-nf_o)\, M(f-nf_o) \sum_m \sum_k \bar{c}_{n-m}\, g_{m-k}\, d_k H_1(f-mf_o)\, H_2(f-kf_o)$$

$$= H_3(f) \Big[S_i(f)\, M(f) \sum_m \sum_k \bar{c}_{-m}\, g_{m-k}\, d_k\, H_1(f-mf_o)\, H_2(f-kf_o)$$

$$+ S_i(f-f_o)\, M(f-f_o) \sum_m \sum_k \bar{c}_{1-m}\, g_{m-k}\, d_k\, H_1(f-mf_o)\, H_2(f-kf_o)$$

$$+ S_i(f+f_o)\, M(f+f_o) \sum_m \sum_k \bar{c}_{-1-m}\, g_{m-k}\, d_k H_1(f-mf_o) H_2(f-kf_o) + \ldots \Big]$$

Eq. (G170)

The system output spectrum has the same character as the detector output spectrum. The difference is that $\bar{c}_n$ has not been replaced by the frequency-dependent factor

$$H_3(f) \sum_m \sum_k c_{n-m}\, g_{m-k}\, d_k\, H_1(f-mf_o)\, H_2(f-kf_o) \qquad \text{(G171)}$$

One still has the problem with aliasing errors for information bandwidths $|f_i| > f_o/2$ of $M(f)\, S_i(f)$. To illustrate the problem, set $d_k = 0$ for $k \neq 0$ and $d_o H_3(f) = 1$, which is equivalent to studying the output of H_2. Also designate

$$S(f) = M(f)\, S_i(f)$$

Then

$$S_o(f) = H_2(f) \sum_n S(f-nf_o) \sum_m \bar{c}_{n-m}\, g_m\, H_1(f-mf_o)$$

$$= S(f)\, H_2(f) \sum_m \bar{c}_{-m}\, g_m\, H_1(f-mf_o) \qquad \text{(G172)}$$

$$+ S(f-f_o)\, H_2(f) \sum_m \bar{c}_{1-m}\, g_m\, H_1(f-mf_o)$$

$$+ S(f+f_o)\, H_2(f) \sum_m \bar{c}_{-1-m}\, g_m\, H_1(f-mf_o) + \ldots .$$

Example 1 - Ideal Filters. -- Assume the trapezoidal chop wave in Figure G21a and the demodulator wave (gating and rectifying) in Figure G21b with $a = 1/3$, $b = 1/6$. Table G4 gives some of the Fourier series coefficients for the chop and demodulator waves. Assume furthermore the ideal filters in Figures G22(a) and G22(b). Figure G22(c) shows $H_1(f+f_o)\, H_2(f)$ and $H_1(f-f)\, H_2(f)$, which are identical. As for these filters $H_1(f-mf_o)\, H_2(f) = 0$ for $|m| \geq 4$ and $g_o = g_{\pm 3} = g_{\pm 2} = 0$, only $m = \pm 1$ contributes to $S_o(f)$ in Equation (G172).

TABLE G4. - FOURIER SERIES COEFFICIENTS FOR CHOP WAVE AND DEMODULATOR WAVE

n	c_n	m	g_m	
0	0.5	0	0	
±1	± j0.305	±1	± j0.552	a = 1/3, b = 1/6
±3	± j0.063	±3	0	
±5	± j0.012	±5	± j0.110	

Figure G23 shows the fundamental term and the lower-order aliasing terms for the triangular spectrum $S(f) = S_1(f)$ in Figure G22(d) and the impulse spectrum $S(f) = S_2(f)$ in Figure G22(e). Note here that for the impulse spectrum the first-order aliasing term is greater than the fundamental term and the second-order aliasing term is of the same order of magnitude as the fundamental term. If one has a spectrum S(f) bandlimited to $f_o/2$, there will be no aliasing errors, and for noisefree system S(f) can be recovered by dividing $S_o(f)$ by the fundamental transfer function

$$H_2(f) \sum_m \bar{c}_{-m}\, g_m\, H_1(f-mf_o) \qquad \text{(G173)}$$

for $|f| < f_o/2$ [see Equation (116)].

Example 2 - Practical Filters. -- Figure G24 shows a practical lowpass filter and Figure G25 shows a practical bandpass filter. Figure G26 gives

$$H_2(f)\,[H_1(f-f_o) - H_1(f+f_o)]$$

which is a good approximation of the fundamental transfer function divided by $\bar{c}_{-1}\, g_1\ (=\bar{c}_1 g_{-1})$.

a) Chopper

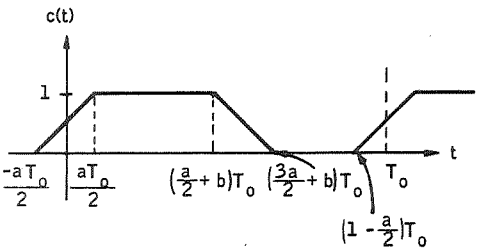

$$f_o = \frac{1}{T_o}$$

$$c(t) = \sum_{n=-\infty}^{\infty} c_n e^{jn2\pi f_o t}$$

$$c_n = \frac{1}{n\pi} e^{-jn\pi(a+b)} \sin n\pi(a+b) \frac{\sin n\pi a}{n\pi a}$$

For $a + b = 1/2$:

$$c_n = \begin{cases} \frac{-j\sin n\pi a}{n^2\pi^2 a} & \text{if n is odd} \\ 0 & \text{if n is even} \end{cases}$$

b) Gate and rectify

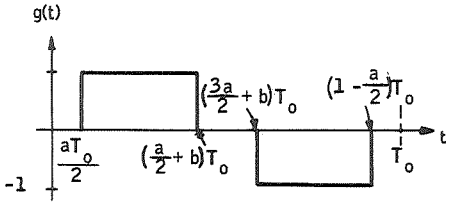

$$f_o = \frac{1}{T_o}$$

$a + b = 1/2$:

$$g(t) = \sum_{m=-\infty}^{\infty} g_m e^{jm2\pi f_o t}$$

$$g_m = \begin{cases} (-1)^{\frac{(m+1)}{2}} \frac{2j}{m\pi} \sin m\pi b, & \text{if m is odd} \\ 0, & \text{if m is even} \end{cases}$$

Figure G21. Examples of Chop Wave and Demodulator Wave

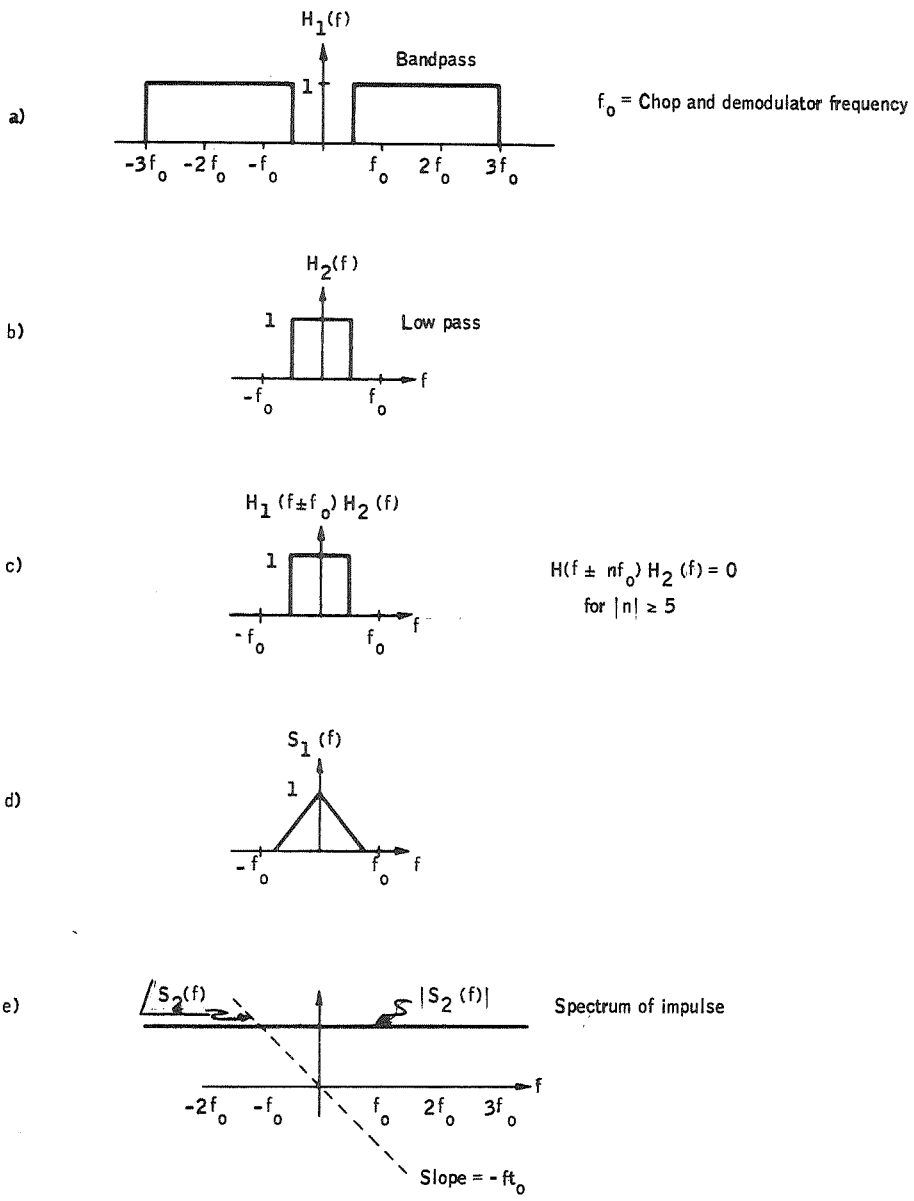

Figure G22. Idealized Signal and Filter Spectra

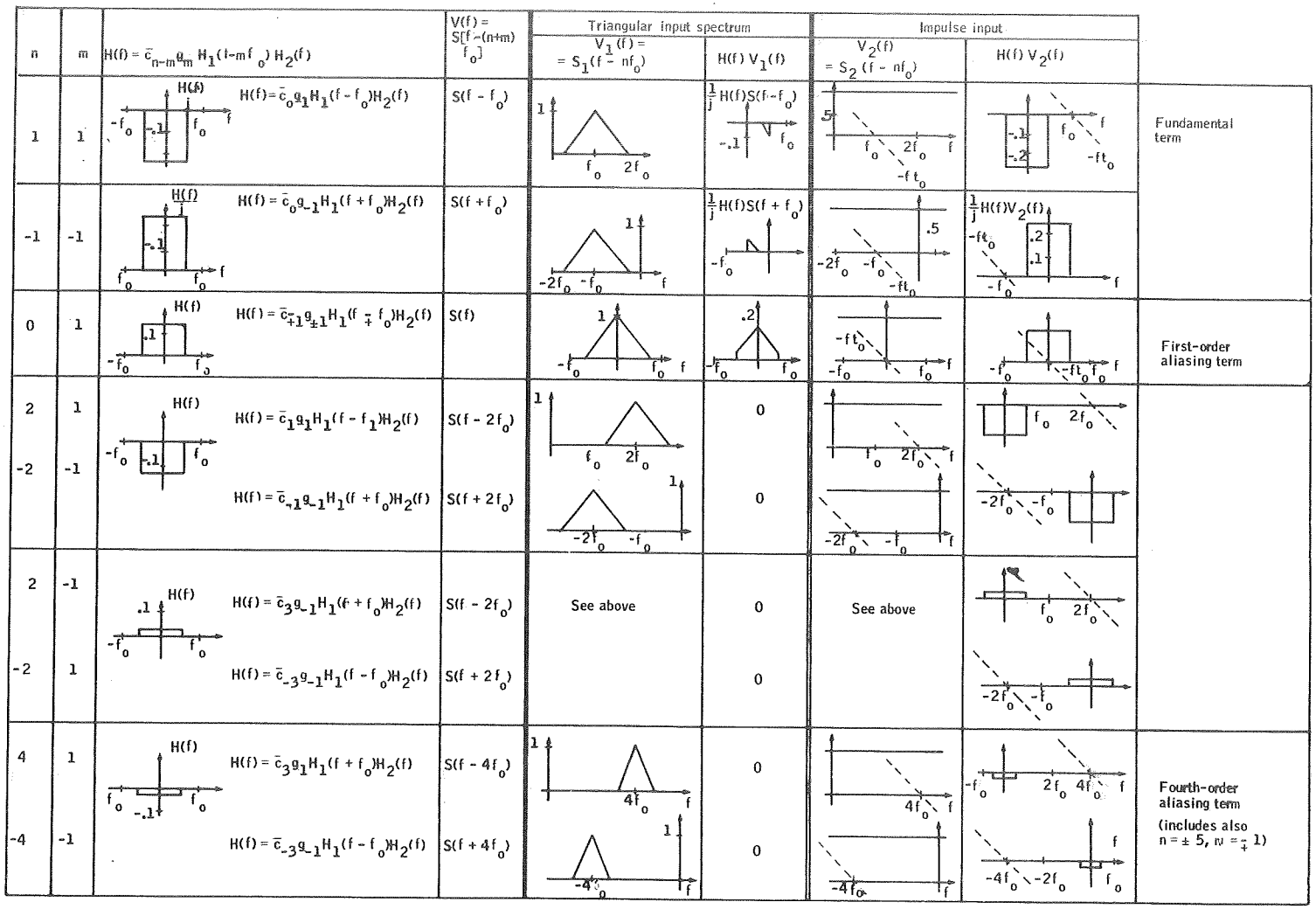

Figure G23. Idealized Representation of Fundamental and Aliasing Terms

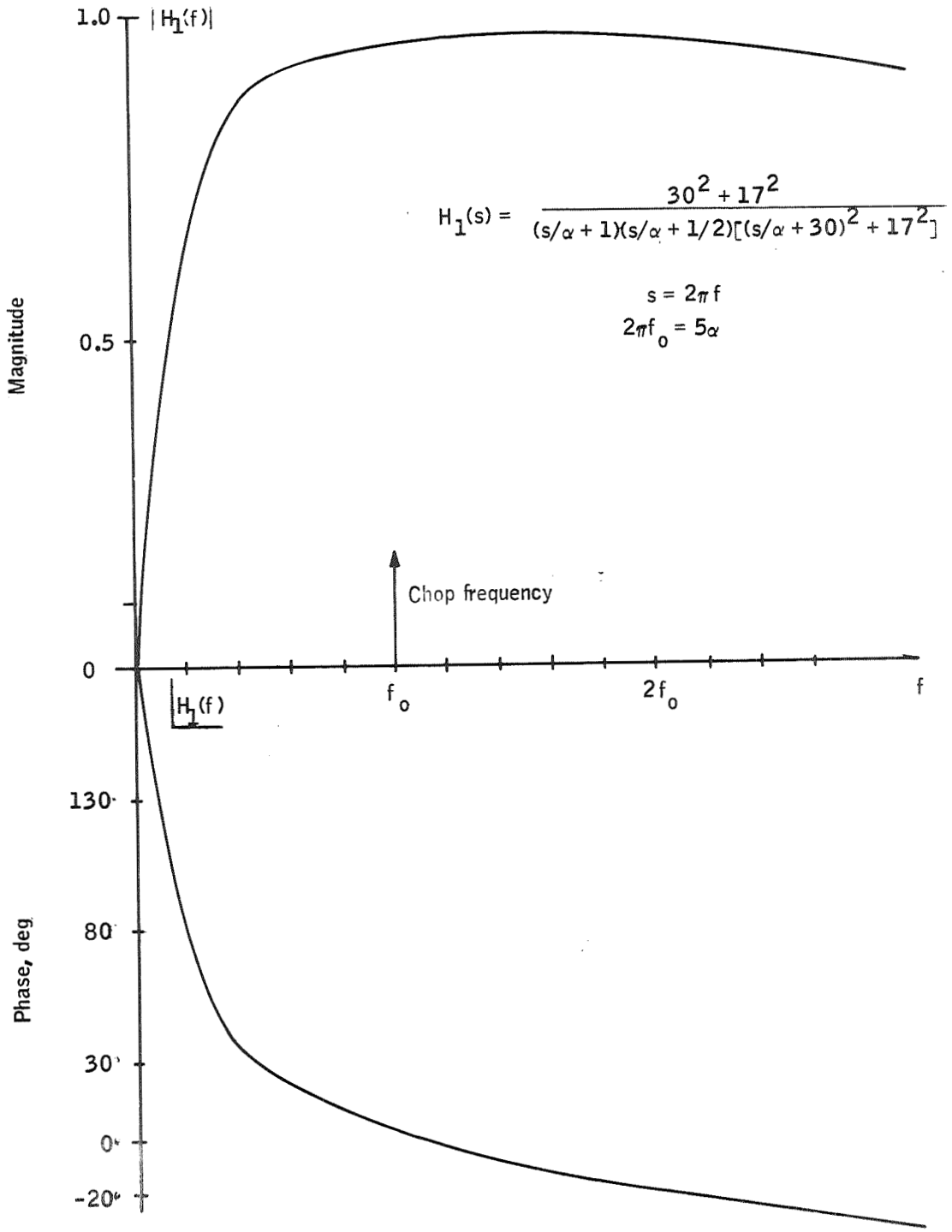

Figure G24. Butterworth-Bessel Bandpass Filter

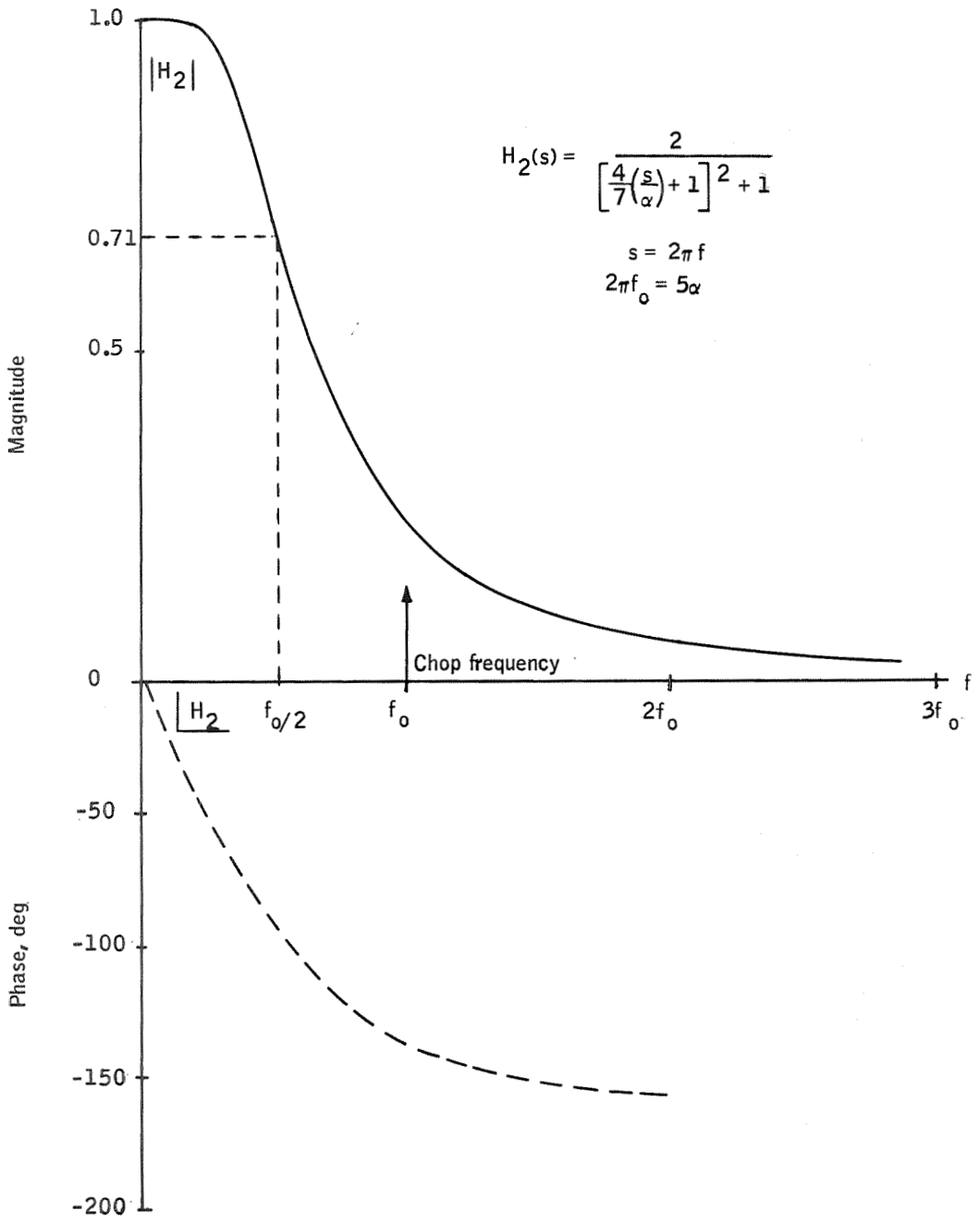

Figure G25. Second-Order Butterworth Lowpass Filter

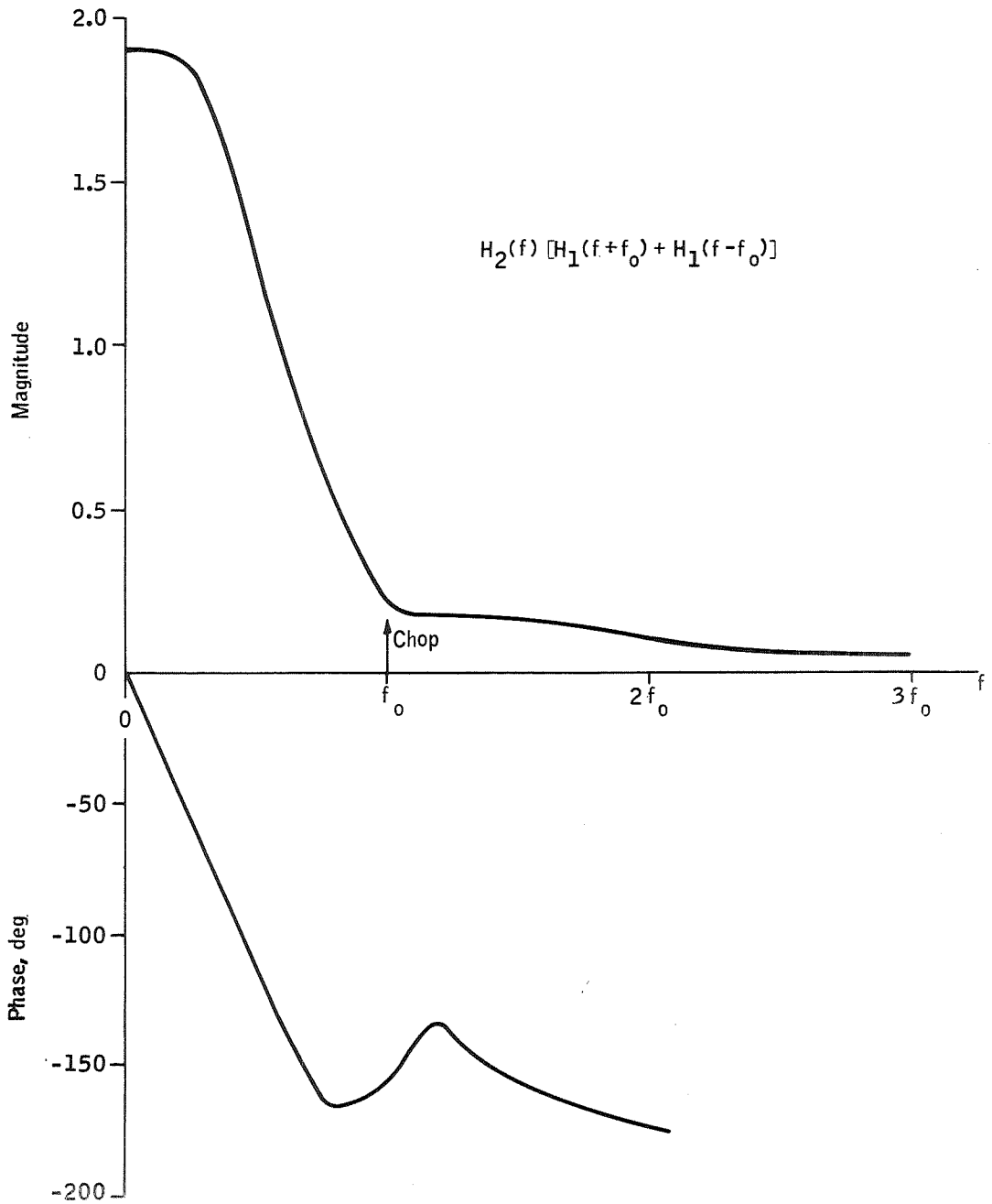

Figure G26. Resultant of Bandpass--Lowpass Filter

From Table G4

$$\bar{c}_{-1}\, g_1 = \bar{c}_1\, g_{-1} = 0.168,\quad \bar{c}_{-3}\, g_3 = \bar{c}_3\, g_{-3} = 0,\quad \bar{c}_{-5}\, g_5 = 0.001 \tag{G174}$$

and

$$\bar{c}_{-2n} g_{2n} = 0 \text{ for } n = 0,\ 1,\ 2,\ \ldots \tag{G175}$$

The approximation is good also because of the decreasing values of $H_2(f)$ and $H_1(f - mf_o)$ for increasing f.

If a spectrum S(f) is bandlimited to $f_o/2$, S(f) can be recovered by dividing $S_o(f)$ by the fundamental transfer function as in Example 1.

Systems transfer function: As discussed in Examples 1 and 2, the input to a sampled system can be recovered if the input is bandlimited to half sampling frequency and if the system is noise free. The Fourier transform of the input is then recovered by dividing the Fourier transform of the output by the fundamental transfer function. Applied to the idealized chopping approximation, the fundamental term is given by

$$S_{of}(f) = S_i(f)\, M(f)\, H_3(f) \sum_m \sum_k \bar{c}_{-m}\, g_{m-k}\, d_k\, H_1(f-mf_o)\, H_2(f-kf_o) \tag{G176}$$

where the index "of" stands for output fundamental term.

The fundamental transfer function

$$H(f) = M(f)\, H_3(f) \sum_m \sum_k \bar{c}_{-m}\, g_{m-k}\, d_k\, H_1(f-mf_o)\, H_2(f-kf_o) \tag{G177}$$

If

$$\left.\begin{aligned} H_3(f) &= 0 \quad \text{for } |f| > f_o/2 \\ H_3(f) &\neq 0 \quad \text{for } |f| < f_o/2 \end{aligned}\right\} \tag{G178}$$

and if $S_i(f)$ is bandlimited to $f_o/2$, then the output spectrum

$$S_o(f) = S_{of}(f) = S_i(f)\, H(f) \tag{G179}$$

The fundamental transfer function is then equivalent to the systems response of the input spectrum

$$V(f) = \begin{cases} 1, & \text{if } |f| < f_o/2 \\ 0, & \text{if } |f| > f_o/2 \end{cases} \tag{G180}$$

which corresponds to the time-domain function

$$v(t) = f_o \frac{\sin \pi f_o t}{\pi f_o t} \qquad \text{(G181)}$$

With Equation (G178) and the input spectrum bandlimited, the output spectrum is thus given as the product of the input spectrum and the fundamental transfer function as given by (G177). The fundamental transfer function is different from the impulse response spectrum of the system. In fact, there is no single impulse response function, but one for each phase relation between the impulse and the chop wave. This is due to aliasing terms that add differently, depending on the phase. Figure G27 shows the impulse response amplitude spectra for 10 different phasings between the input impulses and the time-varying system in Figure G21. Figure G28 shows the phase spectra for the same responses. The curves in Figures G27 and G28 were obtained by simulation runs using the RMS program.

When the input is not bandlimited to $f_o/2$, the output spectrum is not given by Equation (G179) only, but the aliasing terms have to be included also. Each aliasing term will then have its own n^{th} order aliasing transfer function.

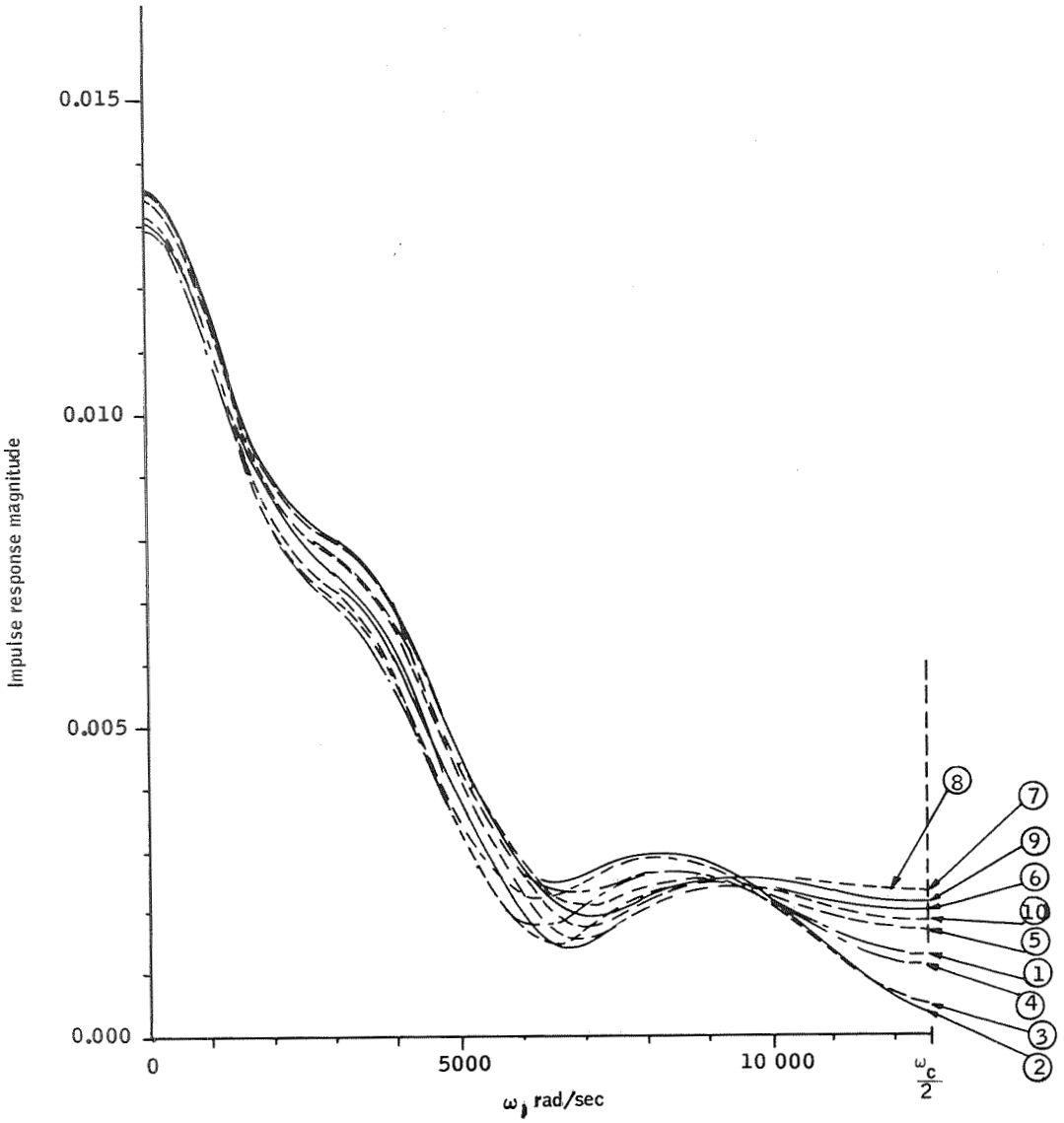

Figure G27. Impulse Response Magnitude

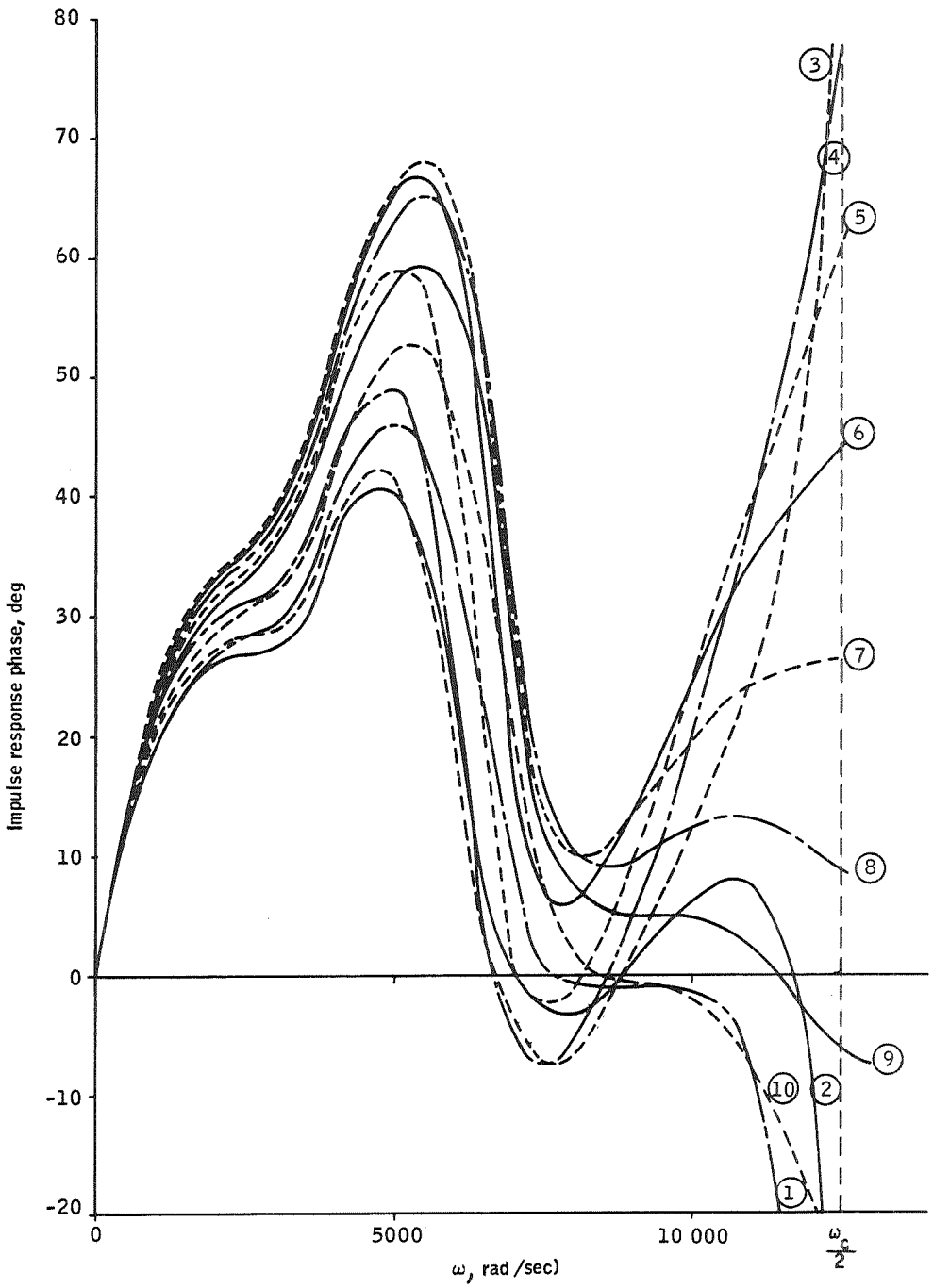

Figure G28. Impulse Response Phase

APPENDIX H
SOURCE-GUARD ASSEMBLY THERMAL ANALYSIS

APPENDIX H
SOURCE-GUARD ASSEMBLY THERMAL ANALYSIS

SOURCE THERMAL ANALYSIS

General Considerations

Before the new source and its control system could be sized, it was necessary to determine the following information:

1) Determine heat loads/losses between source, guard heater, and chamber.

2) Obtain analytical model of thermal control system response characteristics. Compare proportional thermal control versus on-off control. Determine control-loop requirements to stabilize source at all operating temperatures.

3) Determine operating characteristics of source when slewing its temperature and then stabilizing it at some desired point.

4) Investigate effects of increasing source aperture size $\left[\frac{1}{(L/D \text{ ratio})}\right]$ and enlarging entire source.

5) Quantify thermal gradients through source, guard heater, and to the chamber.

The blackbody calibration source at Langley Research Center (LRC) was briefly investigated with the following objectives in mind:

1) To determine what experimental information was available or could be obtained with further testing which would aid in designing a larger blackbody source and its temperature control system in the new calibration system.

2) To determine if the previous thermal analysis on the source (contained in NASA CR-66614) could be used to aid in the new source design

Previous test data on the system at LRC provided the following information:

- The source stabilizes at a lower temperature ($\sim$6°C) than the guard heater control temperature.

- The thermal data available on the present LRC calibration system are those given in Table H1 and Figure H1.

- A lack of required guard heater power was solved at LRC by going from a 110-V source to a 220-V source across the 440-Ω resistive guard heater.

The previous thermal analysis on the source and its control system was reported in NASA CR-66614. Here, a three-node thermal network was used to simulate the LRC calibration system (see Figure H2). This analysis indicates that the three-node thermal network does not adequately represent the present LRC system, and thus cannot be used with confidence in designing the new calibration system's source and control system. One of the shortcomings in the three-node analysis is that it does not account for a significant temperature drop between the source block and its heater surface and between the inner and outer surface of the guard heater. Engineering drawings of the source and guard show that their heater cylinders are merely slipped over the liquid-nitrogen cooling coils with a slide fit. This implies a significant thermal resistance between the source and guard heaters and their heating objective (especially in a vacuum environment) -- mainly the source block and guard inner radiating surface, respectively. This specific effect may indeed be the cause of the source stabilizing at a significantly lower temperature than the guard heater control temperature.

From the results of the initial investigation, it was concluded that

1) Both the LRC experimental data (given in Figure H1) and the previous thermal analyses were inadequate to describe in proper detail the thermal characteristics of the PCS and to aid in the design of the new system.

2) A new thermal model consisting of approximately 10 nodes would be required to simulate the PCS. This model then would be used to design the new control system parameters, size the source and guard heaters, and determine the overall thermal transient characteristics of the new calibration system.

EXPANDED THERMAL MODEL

The information required for the new system design could only be obtained by a more detailed thermal analysis. Figure H3 is a schematic representation of the LRC blackbody source and its temperature control system. It is believed that a 10- to 12-node thermal network, as shown in Figure H4, adequately represents the LRC system and provides the required information, except the local temperature gradients in the source block. These may be estimated by a hand analysis once the results of the 10-node computer solutions are known. A new 10-node thermal math model of the LRC calibration system was

TABLE H1. - THERMAL CONTROL SYSTEM STABILITY CHARACTERISTICS-- LANGLEY CHAMBER -- CONTROL SHROUD = 27°C

Source temperature		Guard heater (110 watts), % on time
°C	°K	
+20.3	+293.3	59.2
+ 8.5	281.5	53.4
-20	253	29.2
-26	247	27.6
-40	233	24.8
-50	223	25.2
-60	213	14.6
-74	199	12.4
-85	188	10.1
-100	173	8.0
-122	151	4.6

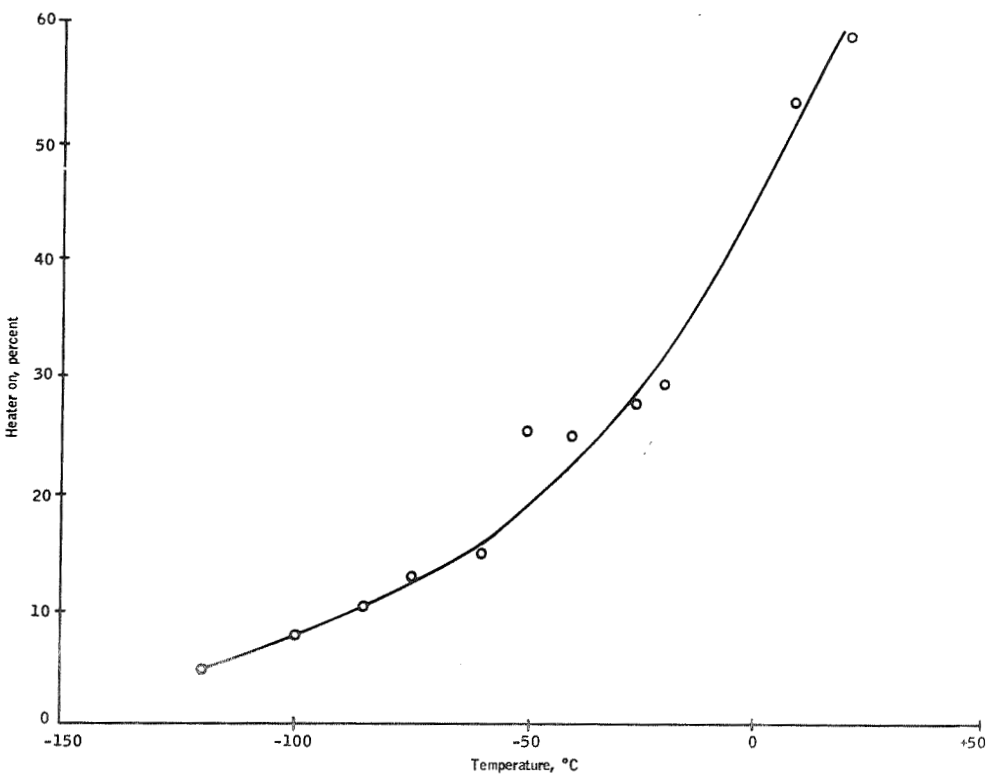

Figure H1. Percent Heater Power versus Source Temperature -- Langley Chamber

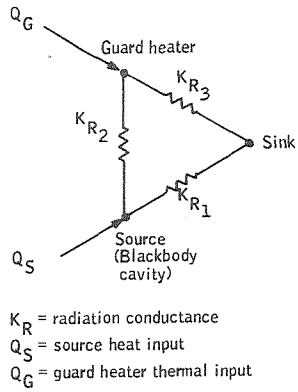

Figure H2. Three-Node Thermal Network Simulation of the LRC Calibration System

developed to serve as an aid in designing the new calibration system. The philosophy adopted was to model the LRC system and compare the computer results with LRC experimental data. Then, on obtaining confidence in the thermal math model, the model could be easily modified to represent the new PCS. This was done and the results are discussed in the following paragraphs.

LRC SOURCE THERMAL MODEL

In developing a math model to simulate any thermal device or system, several initial assumptions must be made. The assumptions made for the LRC system model were:

- The vacuum chamber is at room temperature and constant at 70°F.
- All shrouds are assumed to be held at liquid nitrogen temperatures.
- The source cavity emits blackbody radiation at the source temperature.
- All other surfaces are assumed to be gray and transmitting radiation between gray surfaces.
- The contact conductance on slide fits in vacuum are 2 BTU/ hr-in^2-°F (ref. 32)
- Most nodes in the thermal network represent volumes of revolution.

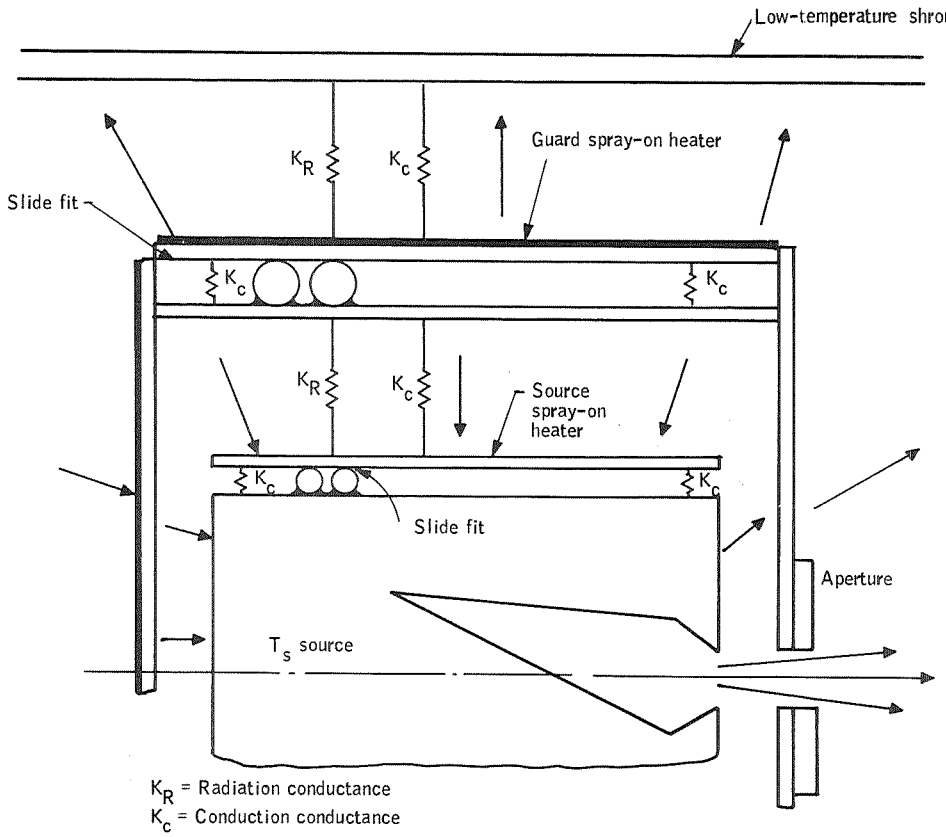

Figure H3. Schematic of LRC Source and Temperature Control System

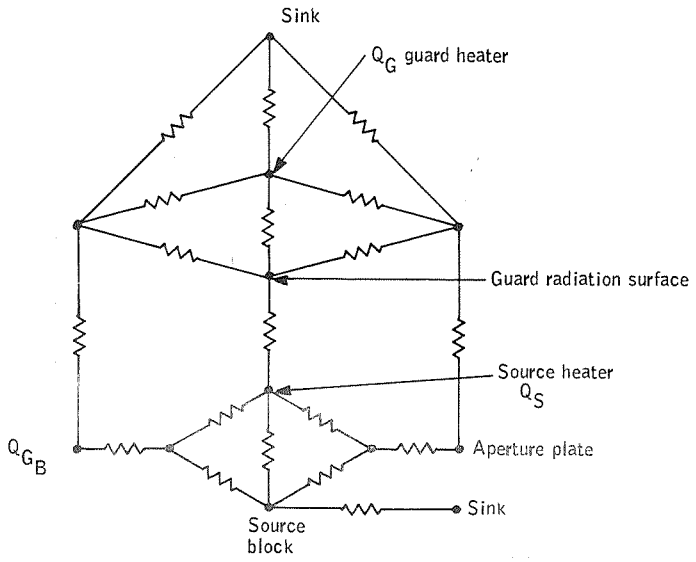

Figure H4. Twelve-Node Thermal Network Simulation of the LRC Calibration System

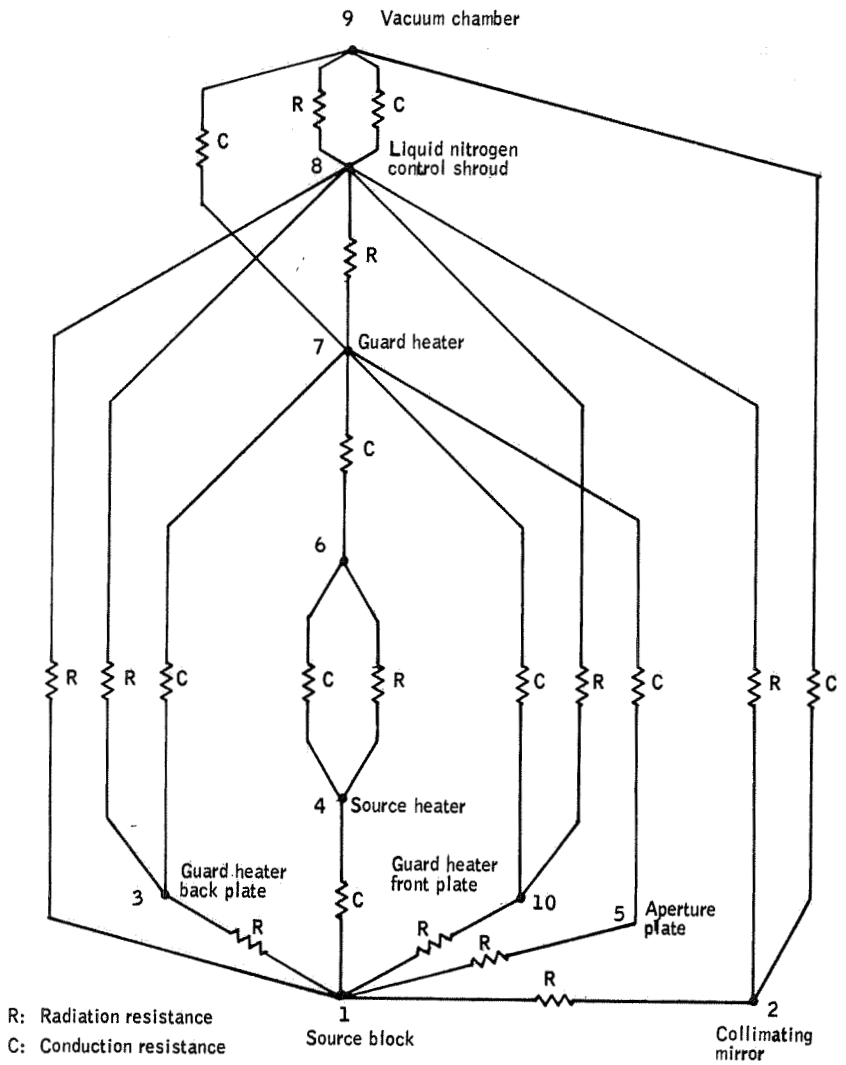

Figure H5. Thermal Resistance Network Representing both the LRC and New Primary Calibration Systems

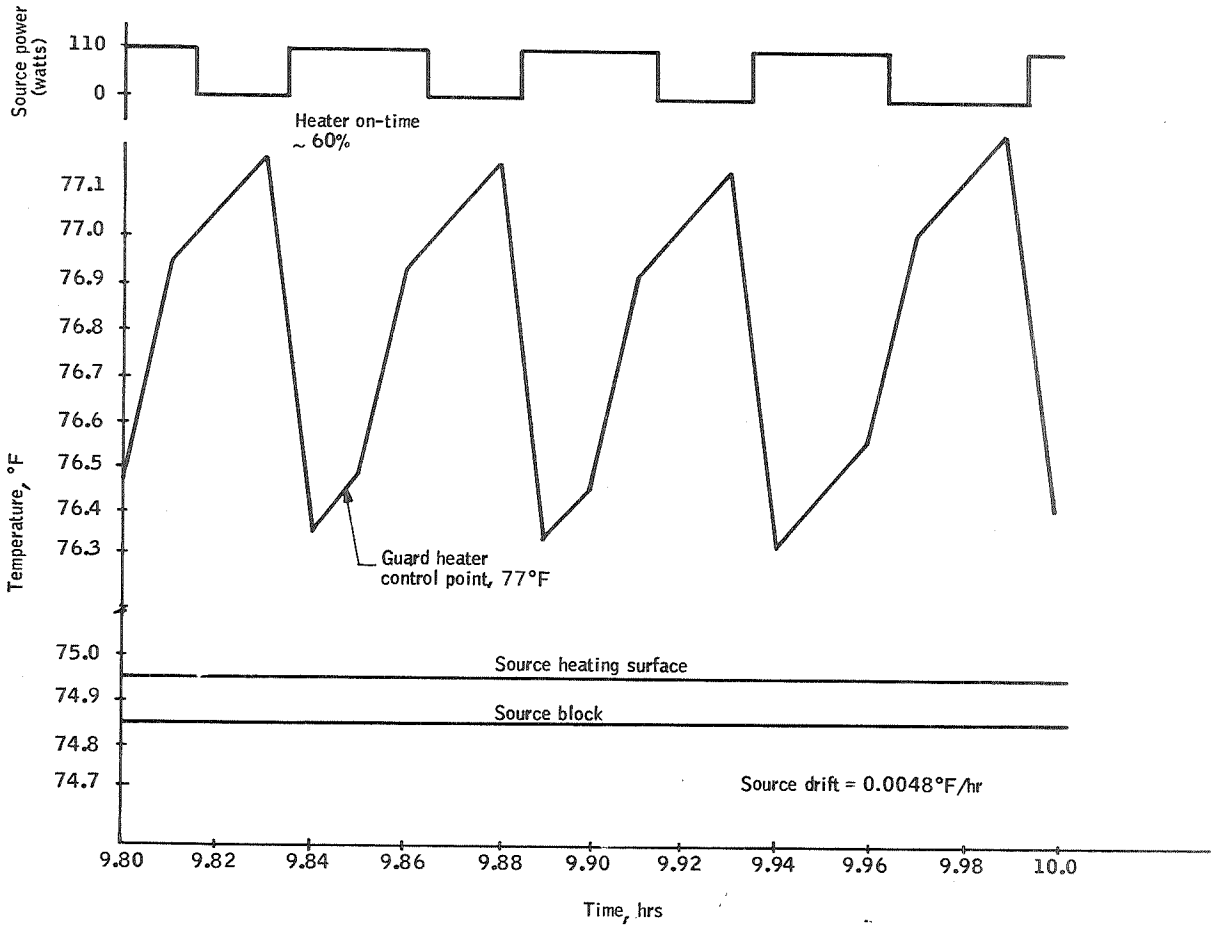

Figure H6. Math Model Simulation of the LRC Calibration System

Property values assumed for the materials in the LRC calibration system are given in Table H2. The thermal resistance network developed to represent both the LRC source and PCS is given in Figure H5.

TABLE H2.- MATERIAL PROPERTIES USED IN THE THERMAL ANALYSIS

Material	ρ (lb/in^3)	k (BTU/hr ft°F)	c_p (BTU/lb °F)	ϵ
Electrofilm spray on heater	*	*	*	0.9 - 0.97
Epoxy fiberglass (6473, 6892)	0.052	0.21	0.3	0.8
Allstate silver solder No. 430	0.264	41	0.0541	---
Copper (pure) (6534, 6532, 7197)	0.324	230	0.0915	0.03
Aluminum 6376 (6061-T6)	0.098	90	0.23	0.6 - 0.8
Aluminum 7596 (2014)	0.101	70	0.23	0.6 - 0.8
Aluminum 6055 (2024-0)	0.100	50	0.18	0.6 - 0.8
Aluminum 6504 (17S-T4)	0.101	78	0.23	0.6 - 0.8
Aluminum 6093 (5052-H32)	0.097	70	0.23	0.6 - 0.8
Liquid nitrogen	0.0289	0.081	0.5	---
Steel	0.282	26	0.113	---
Brass	0.308	64	0.092	---
Pyrex	0.0805	0.63	0.2	---

*Assumed negligible.

Experimental data from the LRC system given in Figure H1 indicate that at source temperature of 20°C (68°F) the guard heater was on 59% of the time. The thermal math model of the LRC system predicts a 60% on-time (for the on-off heater), as shown in Figure H6. This agreement between model and system was believed adequate to verify the math model and justify using it to size the new calibration system heaters.

PCS THERMAL MODEL

The following logic was used for calculating the PCS thermal network based on the LRC model:

1) Those resistive elements associated with the source support structure were increased by the ratio of the two source masses.

2) Those resistive elements associated with pure radiative or conductive heat transfer were increased by the ratio of the corresponding source areas.

3) The environment shroud was assumed to be stainless steel.

Significant changes in geometry between the two systems were accounted for and minor changes neglected.

Results of the computer analysis are shown in Figures H7 and H8. The worst-case transient rise-time condition is shown in Figure H7. The source and guard were assumed to start at -300°F (90°K), and the guard heater sized to provide optimum control characteristics and be powered from an off-the-shelf thermal control amplifier, with a 100-Watt capacity.

The source heater sizing cannot be optimized for a short warm-up time unless the guard heater is oversized. Analysis indicates that the guard heater, if optimized to a steady-state control value, lags the source block in warm-up transients.

Thus, it was decided to size the source heater so as to follow the guard closely, as shown in Figure H7. Note that this results in a source heater size of 260 W and a rise time of about 4 hours over the extreme -300°F to 77°F temperature ramp.

Details of the last few hours of Figure H7 are shown in Figure H8. These results indicate the dynamics of the source and guard heaters under the guard proportional control characteristics. The guard settles out at just over 78°F, while the source will reach equilibrium at about 77.7°F. Note that the new source design with its grooved liquid-nitrogen passages in the source and guard results in a much tighter thermal link between the source and guard (0.3°F temperature difference as compared to the several °F experienced in the present LRC chamber). The required steady-state, guard heater power calculates to be about 79 W, leaving about 20 W cushion for a design factor of safety and to cover effects not included in the thermal analysis such as line losses and manufacturing tolerances.

Note that settling out-times (after the temperature ramp) may be reduced significantly by adjusting the source cut-off temperature and knowing the guard control temperature accurately with a good temperature sensor.

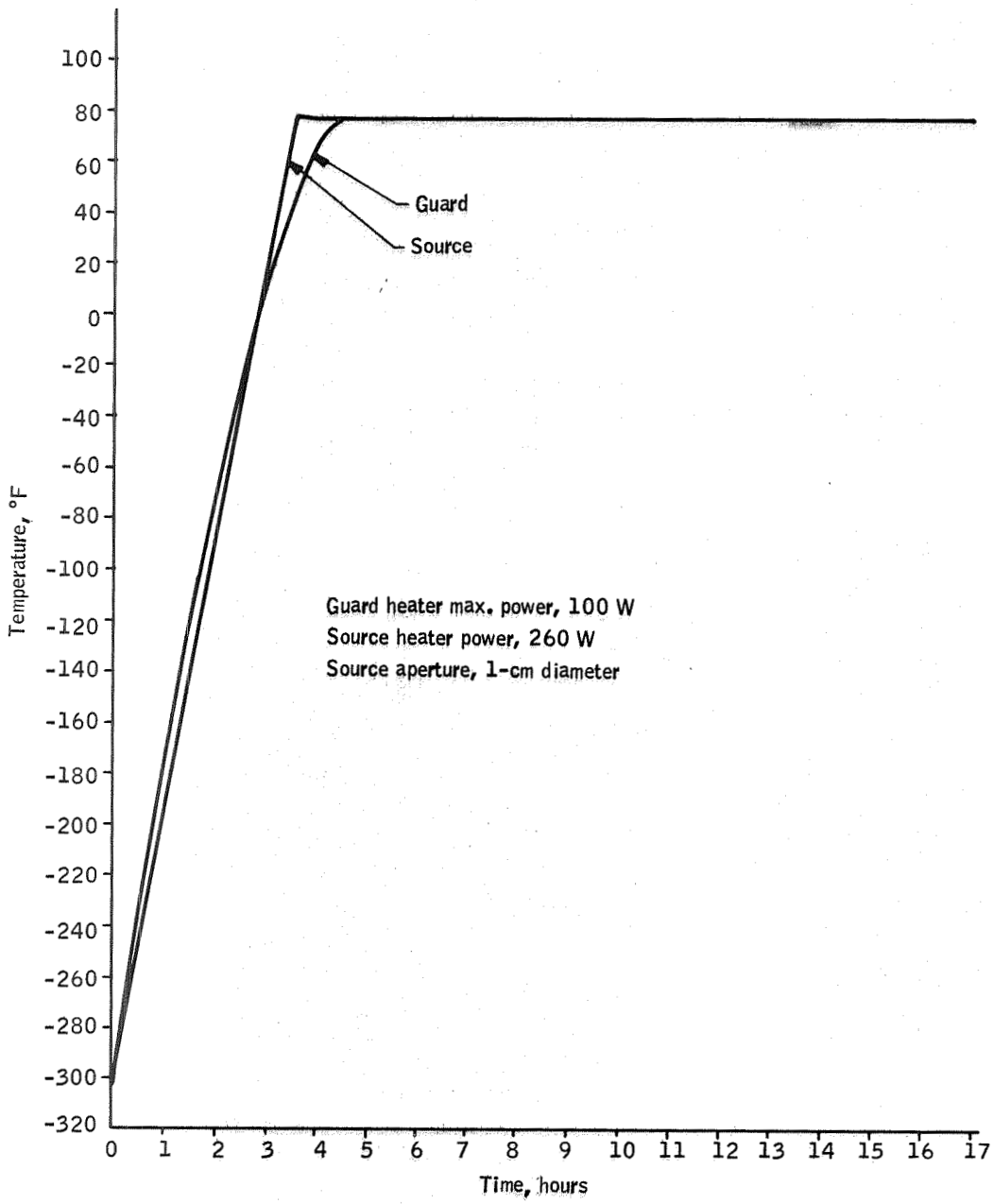

Figure H7. Proportional Control of PCS Guard Heater

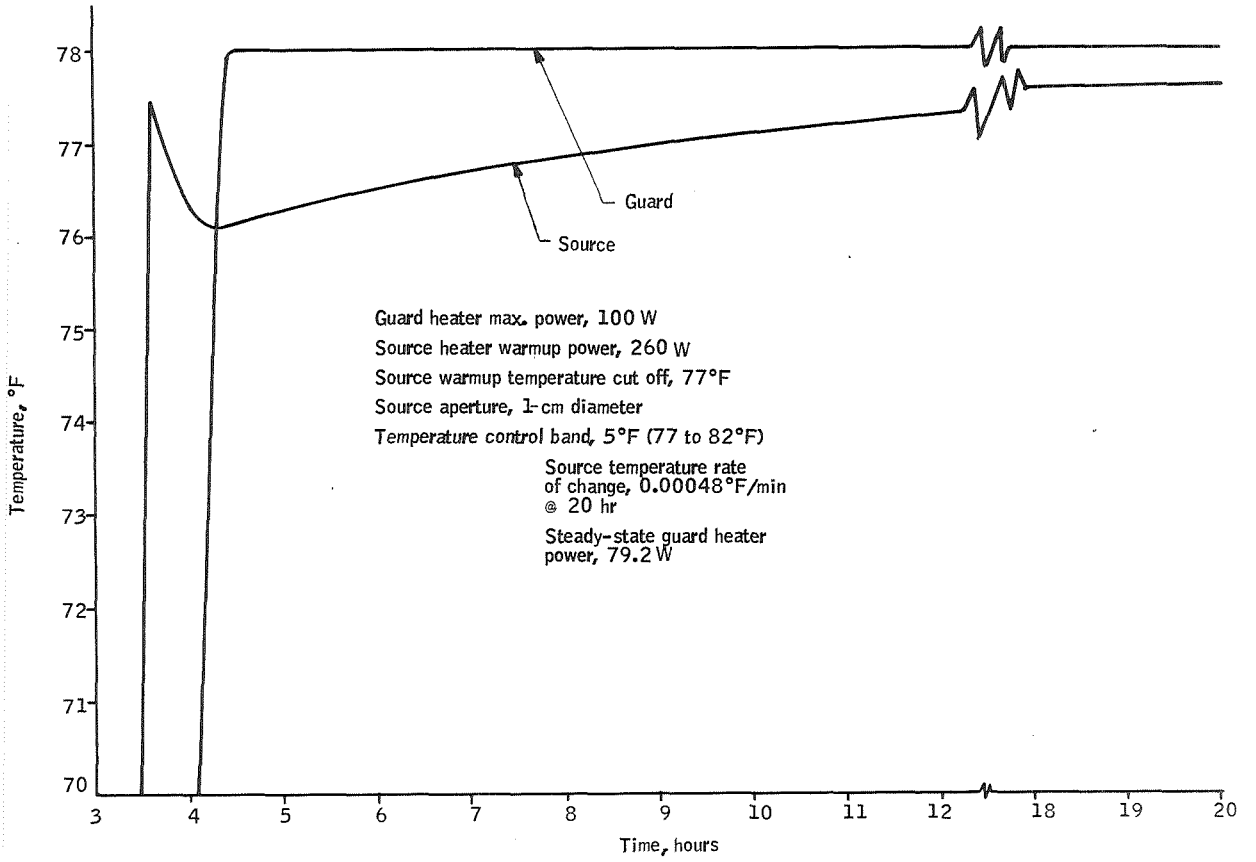

Figure H8. Proportional Control of PCS Guard Heater

In summary, a source heater of 260 W and a guard heater of 100 W with proportional control is adequate for the new PCS.

APPENDIX I
CHOPPER TRANSIENT THERMAL ANALYSIS

APPENDIX I

CHOPPER TRANSIENT THERMAL ANALYSIS

The chopper and its environment may be represented in a simplified manner by a three-node thermal network as shown in Figure I1. Here the chopper blade is linked to the vacuum chamber wall (70°F) through the fiberglass drive shaft. The blade is assumed to be completely surrounded by a liquid-nitrogen baffle system as shown in Figure I1. Chopper blade cooling is accomplished by pure radiative cooling between the baffles and the blade.

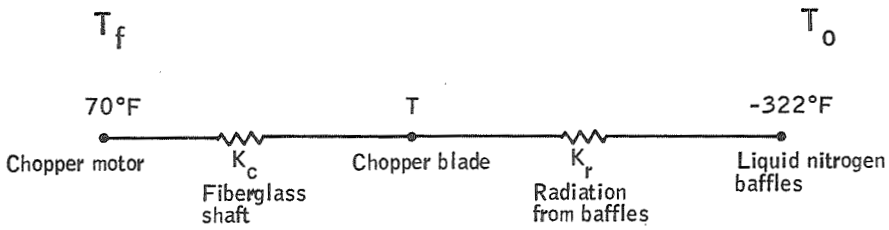

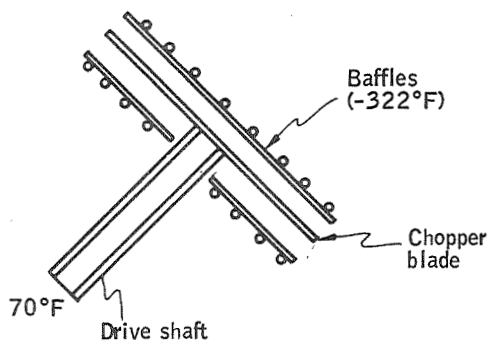

Figure I1. Three-Node Thermal Network

The chopper energy balance is given by the following equation:

$$C_{chopper} \frac{dT}{d\tau} = K_c (T_f - T) + K_r \sigma A \epsilon (T^4 - T_o^4)$$

T_f = environment temperature, 70°F

T_o = liquid-nitrogen temperature, -322°F, 138°R

T = chopper blade temperature, °F or °R

K_c = shaft conductance

K_r = radiation conductance

σ = Stephan-Boltzman constant

ε = blade emittance

The fiberglas shaft conductance may be calculated by

$$OD = 0.5 \text{ in.} \qquad ID = 0.38 \text{ in.}$$

$$L = 6 \text{ in.}$$

$$A = \frac{\pi}{4}(D_1^2 - D_2^2) = 7.1 \times 10^{-4} \text{ ft}^2$$

k thermal conductivity of fiberglas = 0.21 BTU/hr ft °F

$$\text{conductance: } K_c = \frac{kA}{L} = \frac{0.21\,(7.1 \times 10^{-4})}{0.5} = 3 \times 10^{-4} \text{ BTU/hr °F}$$

To perform this transient analysis by hand (instead of a computer), the radiation loss from the blade to the baffles must be linearized. The radiation heat transfer equation is given by

$$Q_{\text{blade - baffle}} = \varepsilon_{1-2}\,\sigma\,(T_1^4 - T_2^4)\,A_1$$

The radiation conductance is then

$$Q_{\text{blade-baffle}} = K\Delta T = \underbrace{\varepsilon_{1-2}\,\sigma\,A_1\,\frac{(T_1^4 - T_2^4)}{(T_1 - T_2)}}_{K_r}\,(T_1 - T_2)$$

Figure I2 gives a set of curves for the function h_r, the radiation heat transfer coefficient between two black surfaces.

$$h_r = \sigma\,\frac{(T_1^4 - T_2^4)}{T_1 - T_2}$$

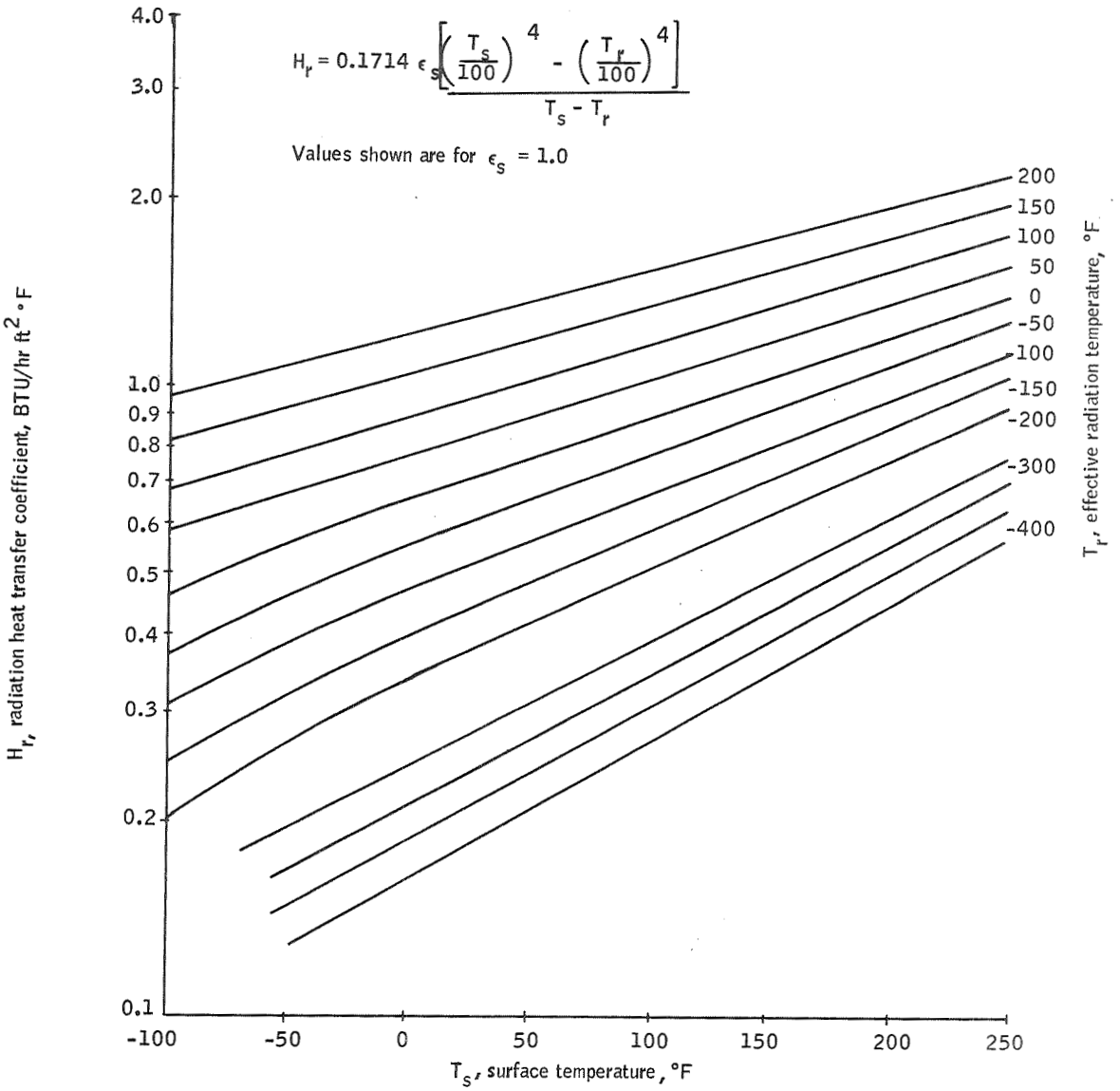

Figure I2. Radiation Heat Transfer Coefficient versus Surface Temp.

Using this function to linearize the radiation allows a closed-form solution for the transient cooling of the chopper blade; however, it requires guessing the chopper blade temperature. Thus, assume the following values:

h_r	Temperatures
0.3	70°F → 322°F
0.15	-100°F → 322°F
0.10	-180°F → 322°F
0.05	-320°F → 322°F

$$\epsilon_{1-2} = \frac{1}{\frac{1}{\epsilon_1} + \frac{1}{\epsilon_2} - 1}$$

configuration interchange factor between two gray plates.

for $\epsilon_1 = 0.9 \quad \epsilon_2 = 0.9$

$$\epsilon_{1-2} = 0.82$$

Thus, K_r the linearized radiation conductance is given by

$$K_r = \epsilon_{1-2} A_1 h_r$$

A_1 = area chopper blade = 1.14 ft^2 (total)

Chopper blade thermal capacitance is computed by

$$C_{chopper} = C_{blade} + C_{shaft}$$

$$= C_{P\rho} V_{(blade)} + C_{P\rho} V_{(shaft)}$$

where

$C_{P\ blade}$ = blade specific heat = 0.23

ρ_{blade} = blade density = 0.098

V_{blade} = blade volume = 82 x 0.062

$C_{P\ shaft}$ = shaft specific heat = 0.3

ρ_{shaft} = shaft density = 0.052

V_{shaft} = shaft volume = 6 x 0.102

$$C_{chopper} = (0.23)(0.098)(82 \times 0.062) + (0.3)(0.052)(6 \times 0.102)$$

$$C_{chopper} = 0.115 + 0.00955 = 0.12455 \text{ BTU/°F}$$

Rearranging the above equation yields

$$\frac{dT}{d\tau} + BT = A$$

where

$$B = \frac{K_c - K_r}{C}$$

$$A = \frac{K_c T_f - K_r T_o}{C}$$

An order of magnitude observation yields

$$B = \frac{K_c}{C} - \frac{K_r}{C} = \frac{0.0003}{0.1245} - \frac{0.05\,(1.14)\,(0.82}{0.1245} \text{ (minimum } h_r)$$

$$= 0.0024 - 0.376$$

or $B \approx \frac{-K_r}{C}$ for all h_r choices

$$A = \frac{K_c T_f}{C} \quad \frac{K_r T_o}{C} = 0.00255\,(70) - (0.398)\,(-322)$$
$$= 0.178 + 128$$

or $A \approx -\frac{K_r T_o}{C}$ for all h_r choices

Thus, realistically the heat balance equation is given by

$$\frac{dT}{d\tau} - \left(\frac{K_r}{C}\right) T = \left(\frac{K_r}{C}\right) T_o$$

The solution to the above equation is

$$T = T_o + (T_1 - T_o)\, e^{+H\tau}$$

$T_1 = 70°F$ $\qquad H = \frac{-K_r}{C}$ $\qquad \tau$ = time hrs

$T_o = -322°F$

Thus,

$$T = -322 + 392\, e^{\frac{-(K_r)_\tau}{C}}$$

at $\tau = 0$ $T = 70°F$

at $\tau = \infty$ $T = -322°F$

The solution of this equation for various choices of h_r is shown in Figure I3. In a practical sense, h_r changes with the temperature difference between the chopper and the baffles; thus, the actual transient behavior might look like the dotted curve in Figure I3.

CONDUCTION COOLING

Cooling the chopper blade by pure radiation will be a very slow process and the settling out to its equilibrium temperature may take many hours. Since this is undesirable, an analysis was made considering the effect of a mechanical thermal link between one baffle and the still chopper blade.

A brief look at the effectiveness of the cooling of the chopper blade by the preceding procedure can be made as follows.

Assume 1% of blade area in contact with the baffle conductor strip. A conservative contact conductance value between metal interfaces in vacuum is

$$2\ \text{BTU}/_{\text{hr-in}^2\text{-}°F} \quad \text{(see ref. 32)}$$

Thus, the conductance is given by

$$K_{\text{baffle conductor}} = 2\ (\text{BTU}/\text{in}^2\ h_r\ °F)\ 77\ \text{in}^2\ (0.01)$$
$$= 1.54\ \text{BTU/hr}\ °F$$

then

$$\frac{K_{\text{baffle conductor}}}{C_{\text{chopper}}} = \frac{1.54}{0.1176} = 13.1\ h_r^{-1}$$

This completely dominates $\frac{K_r}{C}$ and $\frac{K_c}{C}$; thus, the transient equation becomes

$$T = -322 + 392 e^{-(13.1)\tau}$$

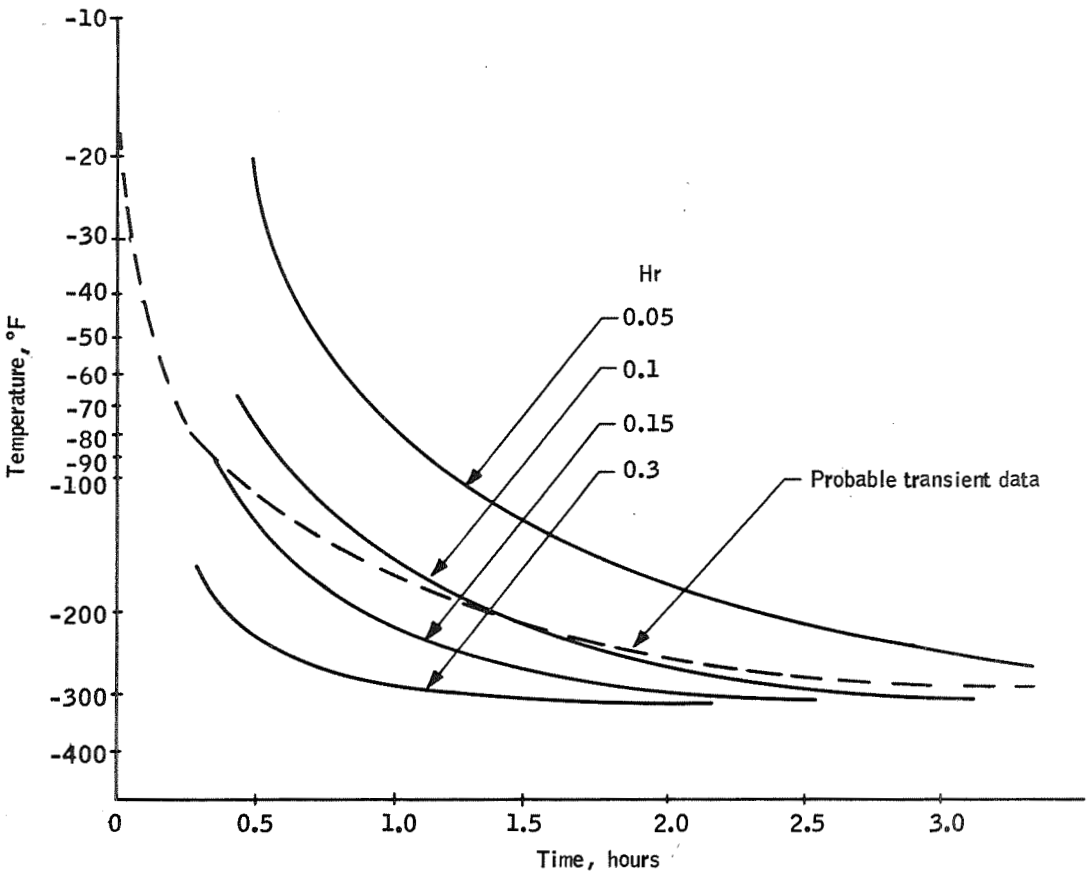

Figure 13. Transient Response of Chopper Blade with Radiation Cooling

This yields the fact that the chopper blade cools from room temperature to -320°F in just 24 minutes. This is a conservative calculation because of the following facts:

- Radiation cooling to the other baffle was neglected, and it was shown previously that this path dominates over the shaft conduction.
- Even under the above conditions, the baffle conductor dominates over the shaft conductance.

$$Q_{\substack{\text{shaft}\\\text{conductance}}} = K_c(\Delta T) = 3 \times 10^{-4} (70 - (-322))$$

$$= 0.118 \text{ BTU/hr}$$

$$Q_{\substack{\text{baffle}\\\text{conductance}}} = k_{\text{baffle c}} (\Delta T) = 1.54(2) = 3.08 \text{ BTU/hr}$$

This means that the baffle conductor will eventually bring the blade to within a few tenths of a degree of the liquid-nitrogen temperature, -322°F (77°K).

BLADE EQUILIBRIUM TEMPERATURE DETERMINATION

The conductive heat flow P_C from the PCS chamber to the chopper blade is calculated as follows:

$$P_C = \frac{K_c \Delta T A_s}{\ell}$$

where

K_c = thermal conductivity of fiberglas

= 30 mW/ft

ΔT = thermal gradient through the shaft; assume this is 220°K (300°K-80°K)

ℓ = shaft length = 0.5 ft

A_s = shaft cross sectional area

= $\pi/4 (D_1^2 - D_2^2)$ D_1 = shaft OD = 0.50 in.

D_2 = shaft ID = 0.38 in.

= 7.1×10^{-4} ft^2

$$P_C = \frac{3 \times 10^{-2} \times 220 \times 7.1 \times 10^{-4}}{0.5} = 9.35 \times 10^{-3} \text{ W}$$

The radiative heat flow P_R from the chopper blade and shaft to the cooled baffles must equal the conductive heating through the shaft for equilibrium to occur.

$$P_R = A_{CH} \varepsilon \sigma (T_1^4 - T_2^4)$$

where

A_{CH} = chopper radiative area

chopper blade total area = 154 in^2

chopper shaft outside area = 10 in^2

total chopper radiative area = 164 in^2

= 1.14 ft^2

ε = emissivity of blade and shaft being cooled = 0.9

Assume T_1, chopper equilibrium temperature = 80°K

T_2, baffle temperature = 77°K

σ = Stefen-Boltzmann constant = 5.67×10^{-4}

$$P_R = 1.14 \times 0.9 \times 5.67 \times 10^{-4} \left[\left(\frac{80}{100}\right)^4 - \left(\frac{77}{100}\right)^4\right] = 3.24 \times 10^{-2} \text{W}$$

$$P_R > P_C$$

therefore, the chopper equilibrium temperature will be less than 80°K. After the chopper has been cooled down to liquid nitrogen temperature by the conduction mechanism, it will slowly rise to 80°K, the radiation equilibrium temperature.

CHOPPER RADIATIVE ABSORPTANCE DETERMINATION

The radiative power, P_a of the blackbody source absorbed by the chopper blade, may be calculated by

$$P_a = \frac{N \times A_s \times A_{ec} \times \alpha \times \eta}{d^2}$$

where

N = source radiance = 145 W/m^2-sr at 300°K

A_s = source area = 0.785×10^{-4} m^2

A_{ec} = exposed chopper area = 1.3×10^{-4} m^2

α = chopper absorptivity = 0.1

η = duty cycle = 0.5

d = chopper/source distance = 5×10^{-2} in

$$P_a = \frac{145 \times 0.785 \times 10^{-4} \times 1.3 \times 10^{-4} \times 0.1 \times 0.5}{(5 \times 10^{-2})^2} = 3 \times 10^{-3} W$$

$$P_a \ll Q_R;$$

therefore, the heating effect of the source power absorbed by the chopper blade can be considered negligible.

APPENDIX J
PCS COOLING ANALYSIS

APPENDIX J
PCS COOLING ANALYSIS

Cooling requirements for the PCS are of a two fold nature: (1) the requirements must be determined for maintaining each element at a steady-state cold temperature; (2) the transient cooling load necessary to cool the elements down to their steady-state temperature levels in a reasonable time period. The elements in the PCS required to be cooled are listed below.

1) Main shroud - fabricated in one section
   - three parallel-feed sections
2) C-shaped shroud
3) C-shroud bottom plate
4) Mirror cooling coil
5) Mirror front baffle
6) Rear ion pump baffle
7) Folding mirror cooling coil
8) Chopper baffles
9) Source aperture
10) Source cooling coil
11) Guard cooling coil
12) Front baffle - behind source
13) Output beam baffle between source and collimated beam
14) Triple-point cell aperture

STEADY-STATE COOLING ANALYSIS

Steady-State cooling loads are calculated below.

Main Cooling Shroud

The main cooling shroud consists of three parallel stainless steel sections, each having dimensions of 36 inches long by 40 inches in diameter. Steady-state heat loss from all three (this includes the two C-shaped shrouds) is made up of radiation and conduction losses.

- Radiation loss from outer shroud surface to chamber

  $\varepsilon_1 = 0.1$ outer shroud surface

  $\varepsilon_2 = 0.1$ inner chamber surface

  $$\varepsilon_{1-2} = \frac{1}{\frac{1}{\varepsilon_1} + \frac{D_2}{D_1}\left(\frac{1}{\varepsilon_2} - 1\right)} = 0.054 \quad \text{gray body interchange factor}$$

  $$\text{Area}_{\text{outer shroud}} = \frac{\pi D_1 L}{12} = \pi \frac{(40)}{12} (13.5) = 142 \text{ ft}^2$$

  $T_1 = -322°F = 138°R$ $\qquad$ $T_2 = 77°F = 537°R$

  $$Q_{\text{radiation from shroud}} = \frac{\sigma \varepsilon_{1-2} A \left(T_1^4 - T_2^4\right)}{3.41} = 320 \text{ watts}$$

- Conduction losses from shroud to chamber

  Conduction losses occur through six bearings and epoxy fiberglas tracks. Considering only major resistances:

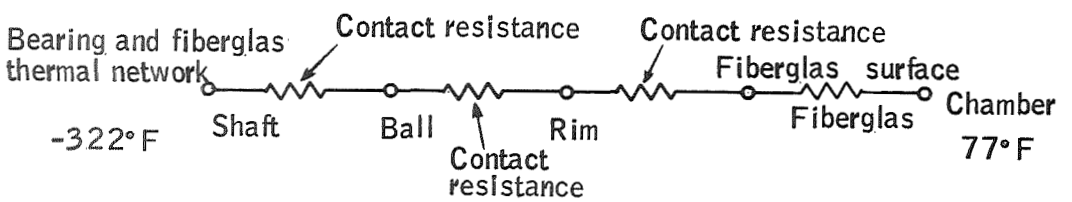

Bearing contact area dimension assumed to be 1/16 inch. Vacuum contact conductance used is 2 BTU/hr-in^2°-F.

Point contact $\frac{\pi (0.0625)^2}{4} (2) = 0.0066$

Line contact $(0.0625)\ (0.25)\ (2) = 0.03125$ Length of line contact equivalent to bearing width

Fiberglass $\frac{KA}{\Delta x} = 0.0175\ \frac{(0.125)\ (0.25)}{0.125} = 0.00437$

Total shaft-to-chamber conductance

$K_{total} = 0.0107$ BTU/hr°F Total of six paths

Total conductor loss

$$Q_{cond} = \frac{K_{total}\ (392)°F}{3.41} = 1.229 \text{ w}$$

3.41 is the conversion factor from BTU/hr to w

Thus, total main shroud losses are approximately 322 w

Collimating Mirror

Mirror heat losses are also made up of radiation and conduction.

- Radiation

$$\text{Area}_{\text{backplate}} = \frac{\pi}{4}\frac{(26)^2}{144} = 3.68 \text{ ft}^2$$

$$\epsilon_{1-2} = 0.054 = \frac{1}{\frac{1}{\epsilon_1} + \frac{1}{\epsilon_2} - 1} \qquad \epsilon_1 = 0.1 \qquad \epsilon_2 = 0.1$$

$$Q_{\text{radiation mirror}} = \frac{\sigma A\ \epsilon_{1-2}}{3.41}\left(T_1^4 - T_2^4\right) = 8.3 \text{ w}$$

radiation to chamber end

- Conduction losses are estimated by only calculating the major resistance paths out the mirror support structure.

  1) major support bracket (two in parallel)

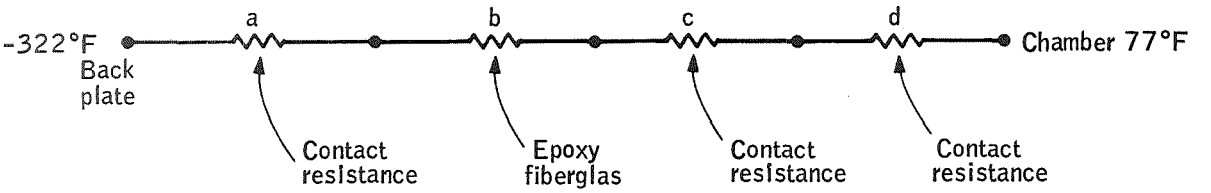

$k_a = \pi (3)(4)(2) = 24\pi \ BTU/hr°F$

$k_b = \frac{2\pi KL}{\ell n \ r_1/r_2} = \frac{2\pi (0.21)}{\ell n \ 1.5/1} \frac{(2)}{12} = 0.5 \ BTU/hr°F$

$k_c = \pi (2)(4)(2) = 16\pi \ BTU/hr°F$

$k_d = \pi (1.5)(4)(2) = 12\pi BTU/hr°F$

$k_1 \ (a, b, c, d) \approx 0.5$ each path

$k_{1\,[1]} = 1.0 \ BTU/hr°f$ Two in parallel

  2) Adjustment bracket

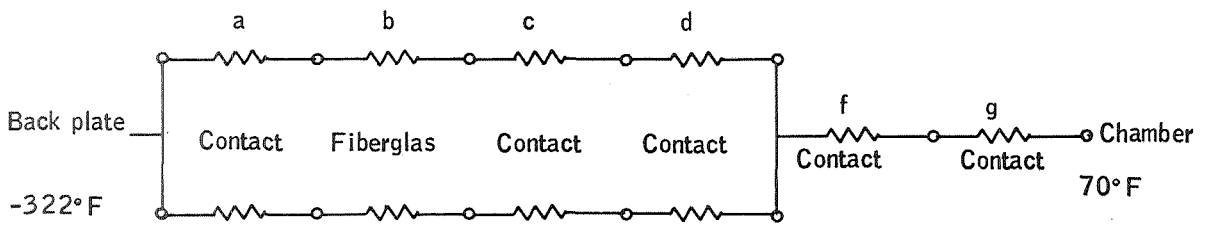

$$k_a = \pi (0.625)\ (0.75)\ (2) = 5.88$$

$$k_b = \frac{2\pi k\ \ell}{\ell n\, r_1/r_2} = \frac{2\pi(0.21)}{\ell n\, 0.625/0.25}\ \frac{(0.75)}{12\ (2)} = 0.044$$

$$k_c = \pi\ (0.25)\ (0.75)\ (2) = 2.35$$

$$k_d = \pi (0.25)\ (0.75)\ (2) = 2.35$$

$$k_{\text{adjustment bracket}} \approx 2\ (0.0425) \approx 0.085$$

Steady-State Conduction Loss

$$Q_{cond} = K_t\ (\Delta T) = \frac{(1.0 + 1.0 + 0.085)}{3.41}\ (392)$$

$$\approx 270\,W$$

Thus, the total mirror heat loss is

$$Q_{rad} + Q_{cond} = 279\,W$$

Other Elements

The main shroud and the mirror represent the major heat loss elements in the PCS. The other elements were analyzed by estimating view factors and ratioing areas, and using the above analyses as a guide to determine the steady-state heat losses from the following system elements.

- Front baffle

  $A = 5\ ft^2$ $\qquad Q_{loss} = 11.5\,W$

- Rear ion pump $\qquad Q_{loss} = 20\,W$

- Folding mirror and mirror front baffle $\qquad Q_{loss} = 0.5\,W$

- Output beam baffle $\qquad Q_{loss} = 30\,W$

- Source aperture and chopper baffles $\qquad Q_{loss} = 2.3\,W$

TRANSIENT COOLING ANALYSIS

Listed below are some of the assumptions used in the transient analysis:

- At time zero the cooling lines drop to liquid nitrogen temperature and are held there.
- The collimating mirror and the main shrouds determine the maximum cooling times.
- When components achieve within 10°F of their steady-state values, cooldown is considered complete.
- The initial condition determines a maximum cooling load while the steady-state condition yields a final cooling load. The average of these loads represents the proper cooldown flow.

Again this is a simplified approach which should yield practical values. During Part II, a more sophisticated cooling evaluation with some basic experimental tests will be performed.

Collimating Mirror

Figure J1 gives a schematic representation of the mirror, its wave plate, and aluminum cooling plate. Also shown are the resistance network and temperature time chart for the mirror. The mirror is the limiting cooldown element in the chamber because of its large mass and low conductivity.

The cooling analysis considered two cases:

1) Infinitely conducting wave plate

2) Wave plate contacting over 25% of the mirror's surface

The first condition can be analyzed by assuming that the collimating mirror is a plate whose temperature throughout is initially 77°F. Then suddenly the back surface temperature is dropped to -322°F by liquid nitrogen cooling. Figure J2 gives the temperature-time chart for such a condition. Cooling of the mirror may be analyzed as follows:

$$F_o = \frac{\alpha\theta}{\delta^2} \qquad \alpha = \frac{K}{\rho c}$$

Cervit

$K = 0.965$ BTU/hr ft °F

$c = 0.2$ BTU/lb m °F

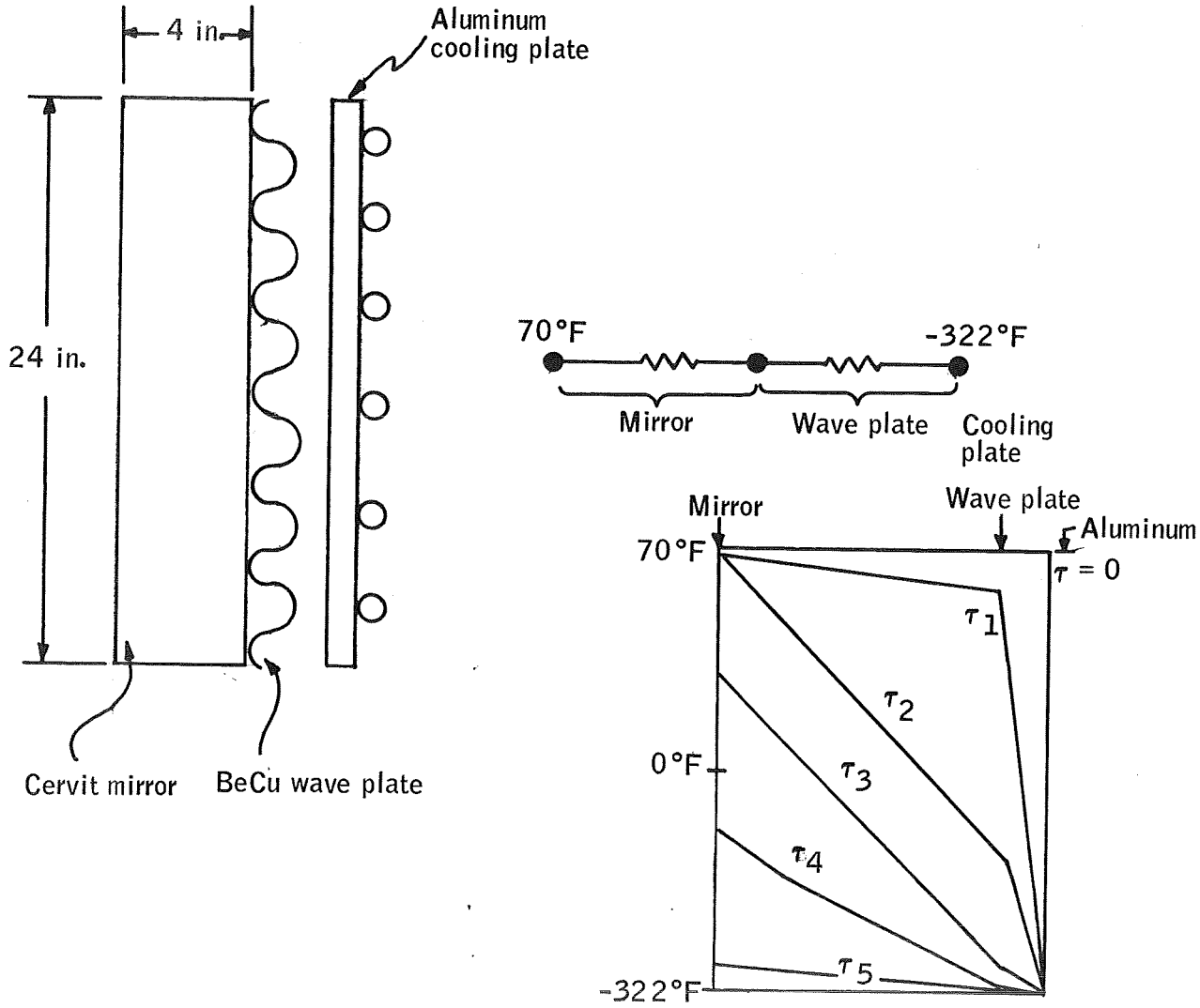

Figure J1. Collimating Mirror Thermal Characteristics

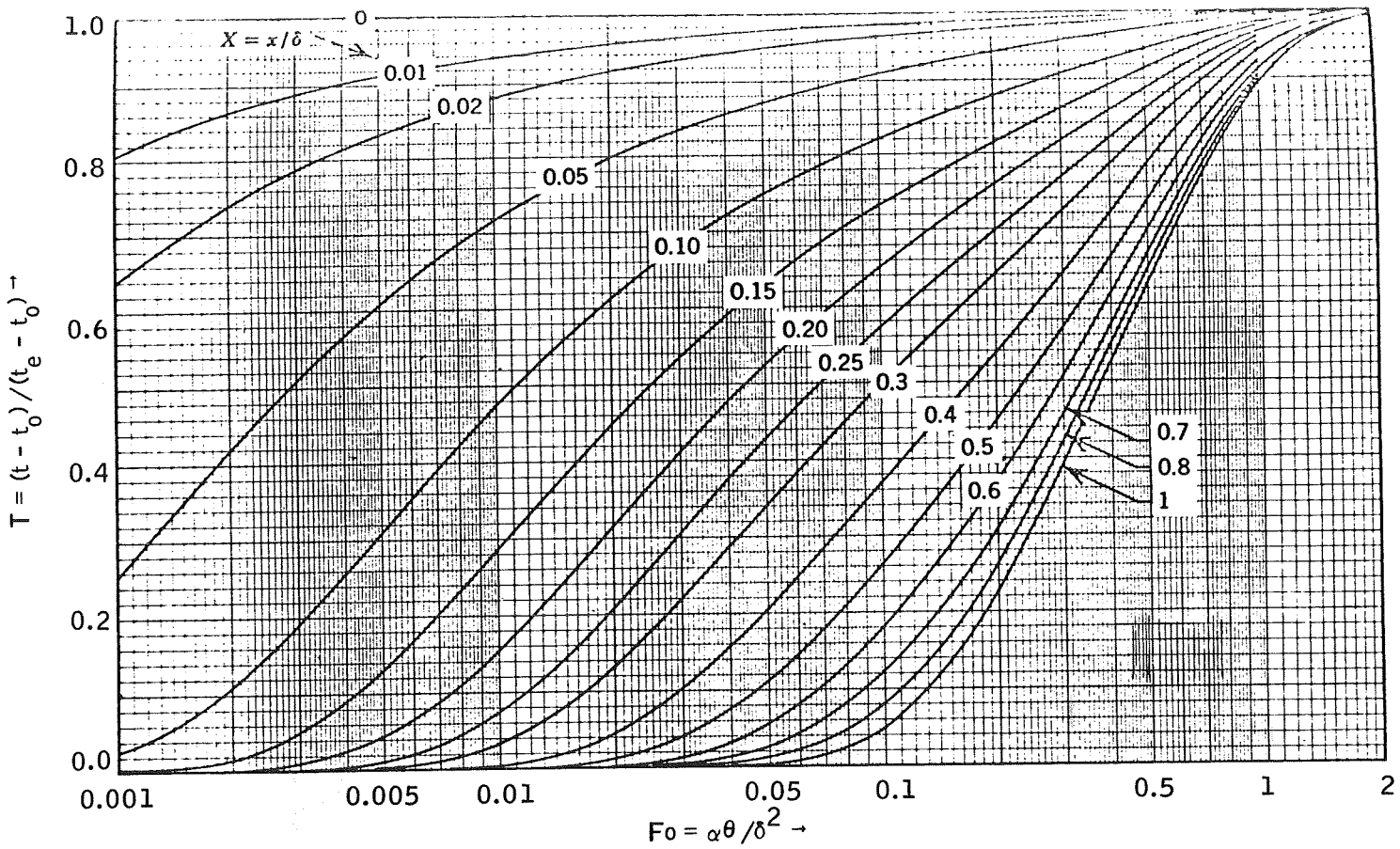

Figure J2. Temperature Response of a Plate, $0 \leq x \leq \delta$, with Insulated Back Face $x = \delta$ After Sudden Change in External Surface Temperature at $x = 0$ from t_o when $\theta < 0$ to t_o for $\theta \geq 0$, (E)

ρ = 139 lb/ft^3

θ = time, hr

δ = position, ft

A cooldown time is defined as complete when the mirror surface temperature is within 10°F of liquid nitrogen temperature.

Then,

$$\frac{t - to}{te - to} = \frac{382}{392} \approx 0.975$$

The mirror cooling time for this condition is 5.2 hours. This analysis has neglected the waveplate conductance.

An attempt was made to estimate the effect of the wave plate conductance. The mirror's and wave plate's total conductances were calculated and combined to give the total conductance between the mirror reflecting surface and the cooling plate.

$$K_{total} = K_{mirror} + K_{wave\ plate}$$

$$= \left(\frac{KA}{\Delta X}\right)_{mirror} + \frac{K'A}{2}$$

where

K' = thermal vacuum contact conductance between two surfaces, 2 BTU/hr-in.^{2}-°F

The ratio of mirror conductance to total conductance was then used to modify the Cervit thermal conductivity to yield an "effective mirror thermal conductivity".

$$K_{Cervit} \times \frac{K_{mirror}}{K_{total}} = K'_{Cervit}$$

The new "effective thermal conductivity" was then factored into the temperature-time curve analysis to yield new cooling times, including the influence of the wave plate resistance. The results indicate that for a 25% wave plate contact area:

$$T_{cooling} = 5.6 \text{ hr}$$

It is believed that this approach to factoring in the effect of the wave plate is conservative.

The analysis assumed that at time t = 0 the aluminum plate was cooled instantly to -322°F, liquid nitrogen temperature. Liquid nitrogen flow was maintained at a rate to hold the aluminum plate at this temperature throughout the cooldown time. Radial conduction and radiation losses were neglected. This assumption is probably good since, as will be shown later, the shrouds cool rapidly and neglecting radiation is thus reasonable from a cooldown-time point of view.

Cooling flow requirements are estimated by determining the initial flow rate required to hold the aluminum cooling plate at -322°F and then averaging this flow rate with the steady-state flow requirements (270W). The initial cooling load is given by:

$$Q = \frac{K_{\substack{\text{mirror-cooling} \\ \text{plate}}} (\Delta T)}{3.41}$$

$$= \frac{9.1\,(392)}{341} = 1040 \text{ W}$$

$$\text{Average cooling load } \frac{270 + 1040}{2} = \frac{1310}{2} = 655 \text{ W}$$

This is equivalent to 14.5 liters/hr.

Main Shrouds

Figure J3 gives a schematic representation of the shroud, its fiberglas standoffs, and the vacuum chamber. The main stainless steel shroud is composed of three 36-inch-wide by 125-inch-long (40-inch diameter) parallel sections. Each section weighs 48 pounds.

The analysis assumed that the inner surfaces of the flow channels were instantly cooled to liquid nitrogen temperature and radiation losses were neglected. The results are shown in Figure J4. Main shroud cooling will take place in less than five hours. Also, a perfectly insulated shroud would not cool in much shorter time. Initial cooling load for three shrouds was 1000 W. The steady-state cooling load was 347 W. This leads to an average cooling load of 673W or 15 liters/hr.

Source

The source, insulated from the chamber, will cool with an adiabatic boundary condition and will require 1200W or 27 liters/hr cooling load.

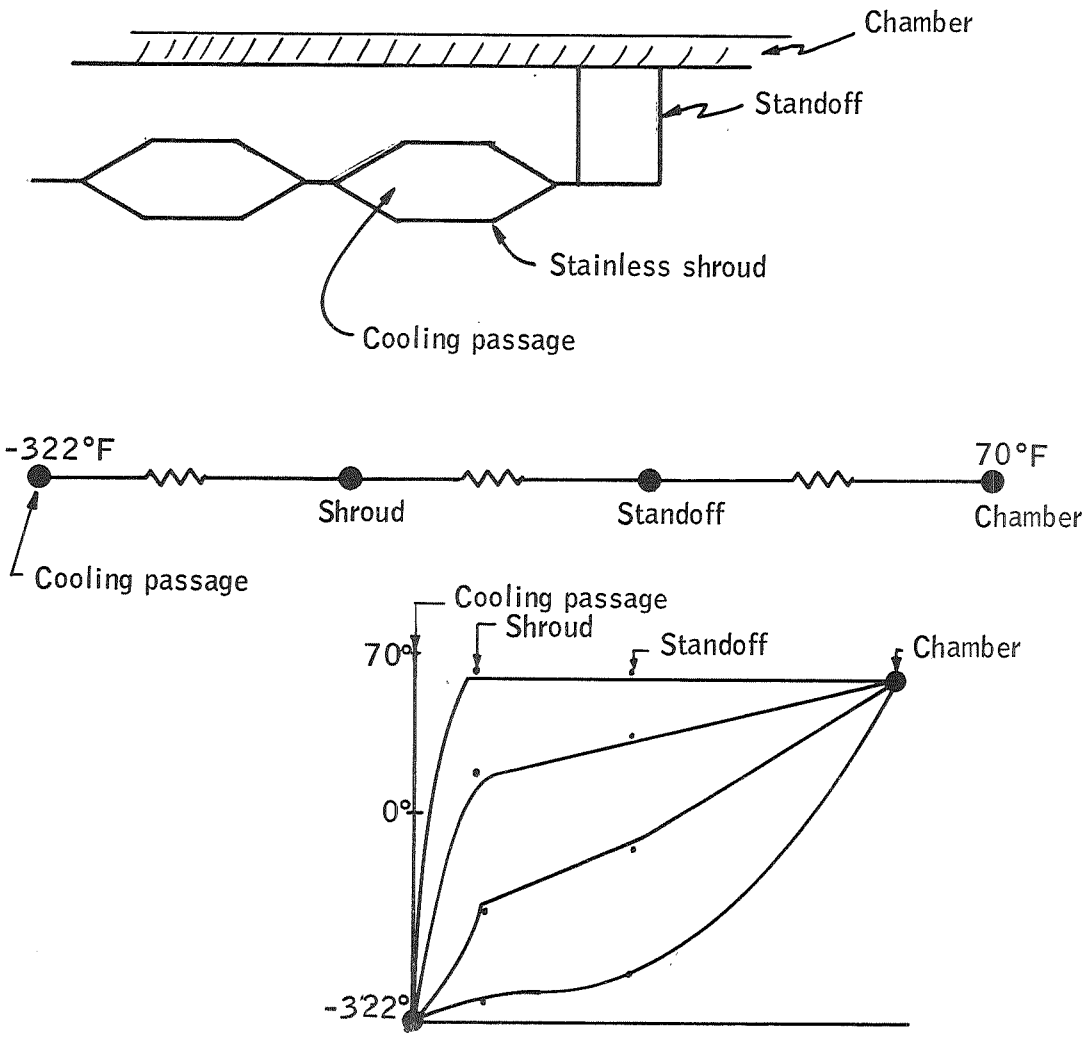

Figure J3. Shroud Conduction Characteristics

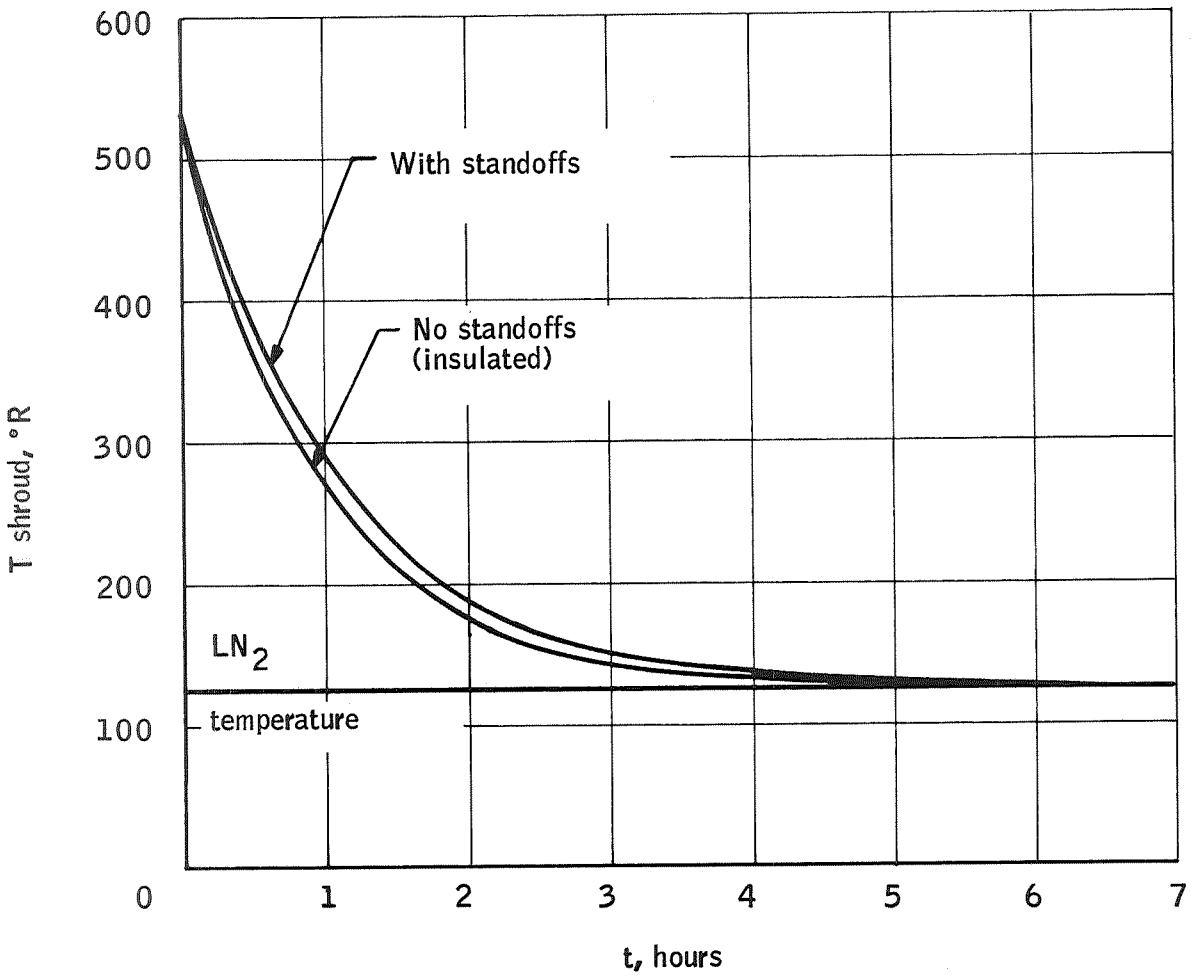

Figure J4. Cooldown of Shrouds

Other System Components

It is assumed that all the remaining system components will be cooled to their steady-state temperature levels in five hours with their steady-state cooling loads. Thus, the system cooling time will take approximately five hours and will require a total transient cooling load of

Item	Transient Cooling Load, Liters/hr
Mirror	14.5
Main shrouds	15.0
Source and guard	27
Others (steady-state load)	54
	110.5 liters/hr

APPENDIX K

DESIGN CONSIDERATIONS
FOLDED LENS SUPPORT TUBE

APPENDIX K

DESIGN CONSIDERATIONS FOLDED LENS SUPPORT TUBE

Two factors must be considered in choosing the lens support tube materials: (1) the material must be highly resistant to heat flow (a low K value) to limit the heat flux to the secondary; (2) the material must possess a low expansion coefficient so that misalignment problems between the lens and the secondary mirror are minimized. A thermal analysis of the system has shown that fiberglas/epoxy tubes mounted as shown in Figure K1 will minimize the heat flux to the secondary, while still maintaining structural integrity.

This appendix analyzes the misalignment that occurs in cooling the refrigerator and lens system from room temperature to operating temperature and, also, the effects of skin temperature change on lens alignment.

Two proposed lens aligning systems will be analyzed for misalignment.

1) Align lens, detector, and mirror at room temperature. Check for misalignment upon cooling to the nominal operating temperature of 200°K.

2) Align lens, detector, and mirror at the nominal operating temperature of 200°K

   a) Check for misalignment due to ±20°K change in skin temperature, using the same material for both sections of the support tube.

   b) Check for misalignment due to ±20°K change in skin temperature, using materials with different coefficients of thermal expansion for the inner and outer support tube.

Misalignment of the lens in relation to the secondary mirror reduces to the problem of analyzing the expansion of any element dx, at a temperature T, along the support tube configuration shown below. Note that temperature may be written as a function of x.

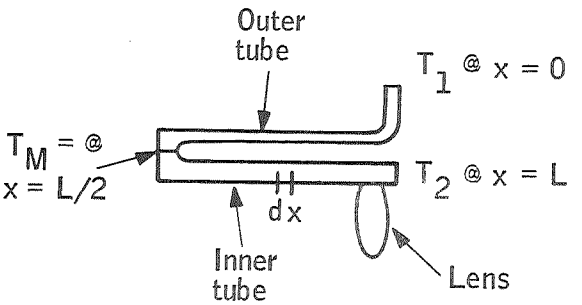

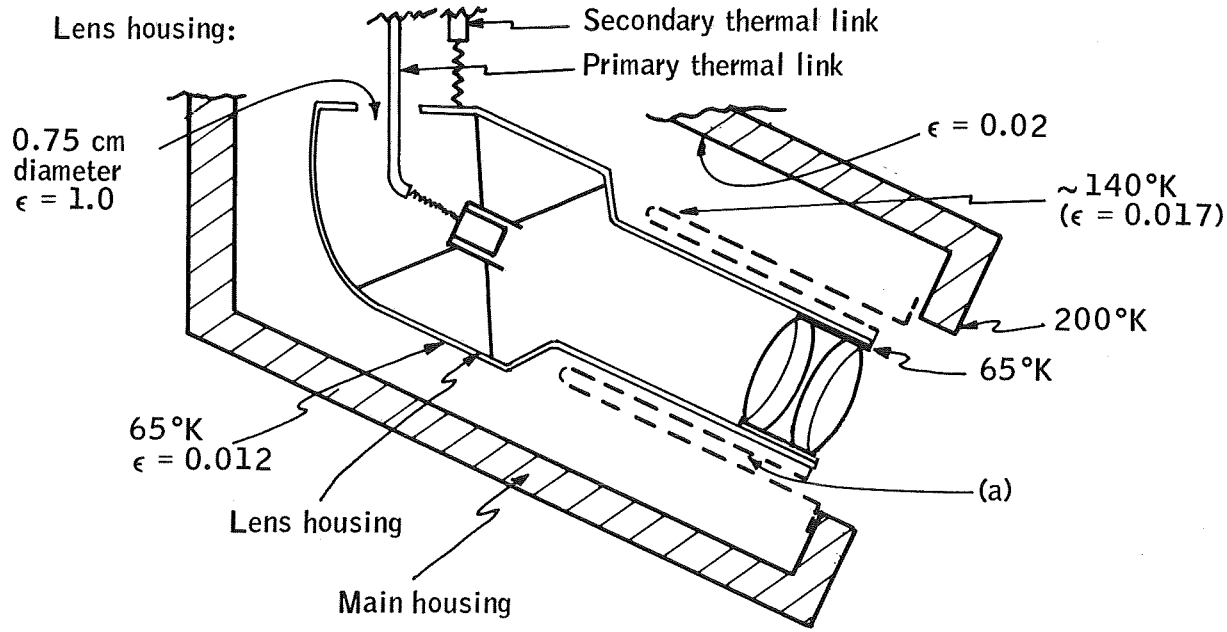

Figure K1. Detector and Relay Optics Mount

so that,

$$\Delta L = \int_0^L \mathcal{L}(T)\, dx \qquad (K1)$$

where

$$\mathcal{L}(T) = \frac{L_{297} - L(T)}{L_{297}} \qquad (K2)$$

This integral may be handled more easily by changing its limits to values of T. This can be done by writing dx in terms of dT.

So,

$$q = \frac{A}{X} \int_{T_1}^{T_2} k(T)\, dT$$

where

q = heat flow from T_1 to T_2 - W

A = cross sectional area of support tubes - cm^2

X = distance along tube - cm

T = temperature - °K

k(T) = fiberglas-epoxy thermal conductivity as a function of T

Using data from reference 33, K(T) may be written

$$k(T) = \frac{T^2}{(1.42)\,(10^4)} + 1.15$$

so that letting $\frac{q}{A} = C$, using the above expression for k(T), and integrating

$$Cx = \left(\frac{T_1^{\,3}}{(4.26)\,(10^4)} + 1.15\, T_1\right) - \left(\frac{T^3}{(4.26)\,(10^4)} + 1.15\, T\right) \qquad (K3)$$

At any given skin temperature T_1 = constant. Thus, differentiating Equation (K3) w.r.t. T and substituting into Equation (K1), we have

$$\Delta L = \int_{T_1}^{T_2} \left[\mathcal{L}(T)\right] \left[\frac{-3T^2}{(C)\,(4.26)\,(10^4)} - \frac{1.15}{C}\right] dT \qquad (K4)$$

MISALIGNMENT CALCULATIONS

Proposed System (1)

Align lens, detector, and mirror at room temperature. Use S glass/E787 resin (UFW roving) in the parallel direction for both inner and outer tubes. This material has one of the lower expansion coefficients of the available fiberglas/epoxies. The misalignment of the lens with respect to the secondary mirror on cooling this system from room temperature to operating temperature can be calculated as follows:

$$\Delta L = \int_{T_1}^{T_M} [\mathcal{L}(T)] \left[\frac{-3T^2}{(C)(4.26)(10^4)} - \frac{1.15}{C}\right] dt - \int_{T_M}^{T_2} [\mathcal{L}(T)] \left[\frac{-3T^2}{(C)(4.26)(10^4)} - \frac{1.15}{C}\right] dt$$

Where

T_1 = skin temperature = 200°K

T_M = temperature at inner-outer tube junction = 148°K [solved for using (3)]

T_2 = solid methane temperature = 65°K

C = 33.4 (solved for using Equation (K3) with x = 10 cm)

$\mathcal{L}(T)$ = $(-2.35)(10^{-6})(T) + 8.2 \times 10^{-4}$ (written using data from reference 1)

so that

ΔL = 0.66×10^{-3} cm or 0.26 mils

Proposed System (2)

The misalignment of 0.26 mils is greater than the allowable misalignment of 0.20 mils which can be tolerated and still have the system behave optically as designed. Therefore, the second of the two proposed lens aligning systems appears to be in order, that is the detector, lens, and secondary mirror are aligned at operating temperature. Any misalignments occurring in this system would be caused by variations in vehicle skin temperature. Once again, using S glass E/787 resin for both inner and outer support tubes and assuming a ±20°K variation in skin temperature, the movement of the lens with respect to the secondary mirror can be calculated as follows:

$$\Delta L = \int_{T_1^1}^{T_M^1} \mathcal{L}(T)\left[\frac{-3T^2}{(C^1)(4.26)(10^4)} - \frac{1.15}{C^1}\right]dt - \int_{T_1}^{T_M} \mathcal{L}(T)\left[\frac{-3T^2}{(C)(4.26)(10^4)} - \frac{1.15}{C}\right]dt$$

$$-\int_{T_M^1}^{T_2^1} \mathcal{L}(T)\left[\frac{-3T^2}{(C^1)(4.26)(10^4)} - \frac{1.15}{C^1}\right]dt + \int_{T_M}^{T_2} \mathcal{L}(T)\left[\frac{-3T^2}{(C)(4.26)(10^4)} - \frac{1.15}{C}\right]dt$$

where

$T_2^1 = T_2$ (constant lens temperature)

T_1^1 = skin temperature = 220°K

T_M^1 = temperature at inner-outer tube junction computed to be 164°K

$C^1 = 42.4$

$\Delta L = \left[1.74 \times 10^{-3} - 2.09 \times 10^{-3}\right] - \left[2.65 \times 10^{-3} - 2.75 \times 10^{-3}\right]$

$\Delta L = -0.35 \times 10^{-3} + 0.10 \times 10^{-3}$

$\Delta L = 0.25 \times 10^{-3}$ cm or ≈ 0.1 mil

Even though 0.1 mil misalignment is within the tolerable limit (0.2 mil), misalignments caused by variations in vehicle skin temperature can be minimized by selecting a different fiberglas-epoxy for the inner tube of the support (see Figure K2). If the material is selected so that the expansion of the outer tube will effectively cancel the inner tube's expansion, the material selected must have an expansion coefficient approximately three times greater than the expansion coefficient of the outer tube. This is necessary, since a 20°K change in skin temperature does not increase the average temperature of the inner tube as much as it does the average temperature of the outer tube. Using S glass E/787 resin for the support's outer tube, then, from data given in reference 33, S glass/E 787 resin (1581 cloth laminate, parallel) appears to be the logical selection for the inne tube. The misalignment due to a 20°K change in skin temperature can now be calculated for this proposed system. Therefore,

$$\Delta L = \int_{T_1^1}^{T_M^1} \mathcal{L}(T)\left[\frac{-3T^2}{(C^1)(4.26)(10^4)} - \frac{1.15}{C^1}\right]dt - \int_{T_1}^{T_M} \mathcal{L}(T)\left[\frac{-3T^2}{(C)(4.26)(10^4)} - \frac{1.15}{C}\right]dt$$

$$-\int_{T_M^1}^{T_2^1} \mathcal{L}^1(T)\left[\frac{-3T^2}{(C^1)(4.26)(10^4)} - \frac{1.15}{C^1}\right]dt + \int_{T_M}^{T_2} \mathcal{L}^1(T)\left[\frac{-3T^2}{(C)(4.26)(10^4)} - \frac{1.15}{C}\right]dt$$

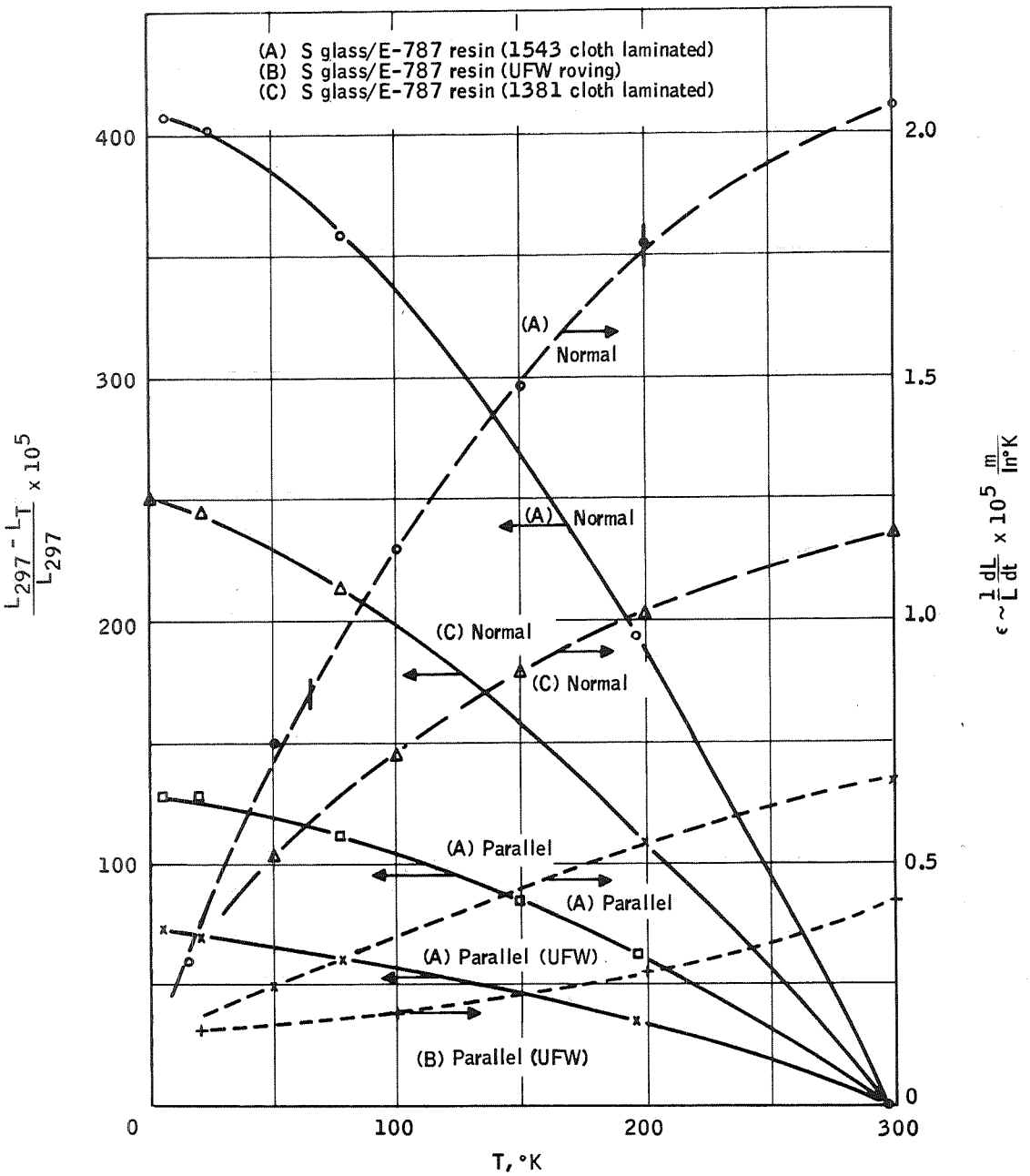

Figure K2. Thermal Expansion Coefficients and Integrals for Fiberglas Epoxies (ref. 1)

where,

$$\mathcal{L}'(T) = (-7.17)(10^{-6})(T) + 2.66 \times 10^{-3}$$

and

$$\Delta L = \left[1.74 \times 10^{-3} - 2.09 \times 10^{-3}\right] - \left[8.89 - 10^{-3} - 9.24 \times 10^{-3}\right]$$

$$\Delta L \lesssim 2.0 \times 10^{-5} \text{ cm} \quad \text{or} \quad \Delta L \lesssim 10^{-2} \text{ mils}$$

which is well within the acceptable displacement limits.

In all previous misalignment calculations the movement of the lens in relation to secondary mirror was considered. However, there will also be misalignment of the lens in relation to the detector, if alignment of lens, detector, and mirror is done at room temperature. Using aluminum as the lens housing material and data from reference 34, the ΔL of the housing in cooling from room temperature to 65°K was found to be $\approx 8.0 \times 10^{-3}$ inches, which is intolerable; thus alignment at the normal operating condition is impossible using aluminum as housing material. However, the use of other materials will be considered.

Since the variation in ΔT of the solid methane will be < 1°K, housing misalignments due to a change in vehicle skin temperature are negligible.

In conclusion, it appears that in order to minimize misalignment problems provision must be made for aligning the lens, detector, and secondary mirror at operating temperature. In addition, the effects of skin temperature variation can be minimized by using different fiberglas-epoxies for the inner and outer section of the support tube.

APPENDIX L

SPECTRAL SHIFT EFFECTS

APPENDIX L
SPECTRAL SHIFT EFFECTS

OBJECTIVES

This study had two objectives: to determine, quantitatively, the effects of spectral filter variations caused by temperature shifts and angular misalignments on measurement precision; and to obtain, qualitatively, insight into the effects of spectral filter shape on measurement accuracy.

RESULTS SUMMARY

For the source and filter spectral models used, a filter shape can be specified that will result in negligible measurement instability (precision well within requirement) over the ARRS temperature and alignment stability environment. For a standard filter with a center wavelength of 15.15μ, and 2.8μ wide between the 5% points, the radiometer output sensitivity to temperature shift is $\leq 0.0011\%/°K$ and the angular alignment shift is $\leq 0.008\%/°$.

APPROACH

The approach was to first obtain practical models of filter spectral transmission and source spectral distribution, then to vary those filter characteristics which are known to be sensitive to environment and determine the resultant variation in the integrated spectral radiance through the perturbed filter. Output variations were expressed as a variation in average transmission of the filter to the source spectral distribution used. Note that the definition of average filter transmission used here differs from the definition sometimes applied in which average transmission is defined by

$$\overline{T} = \frac{\int_{\lambda_1}^{\lambda_2} T(\lambda)\, d\lambda}{\lambda_2 - \lambda_1}$$

Average transmission used here includes the effect of source radiance spectral distribution, $N(\lambda)$, and is given by

$$\overline{T} = \frac{\int_0^{\infty} T(\lambda)\, N(\lambda)\, d\lambda}{\int_0^{\infty} N(\lambda)\, d\lambda}$$

Filter parameters to be varied were, initially, in band shape, leading edge slope, trailing edge slope, leading edge location, trailing edge location, and out-of-band rejection. Results of varying each of the above parameters were to be combined and used to predict effects on accuracy and precision. Results were obtained for each of the variations given above, but further investigation showed that varying only one parameter at a time was unrealistic since parameter cross-coupling effects were not obtained. Further investigation of actual filter variations showed that only spectral shift and neither in-band shape nor leading and trailing edge slopes were sensitive to angle and temperature variations. A second approach was then taken in which filters with various spectral widths were shifted in wavelength, and average transmission variation was determined as described above. Results of this latter approach are reported here.

SPECTRAL MODELS

Source Model

Determination of a source spectral model proved to be a somewhat perplexing task because of the variety of definitions which could be applied to ARRS measurement accuracy, each of which is affected differently by the source. Accuracy here refers to the difference between a measurement of some quantity and the actual value of that quantity, the difference expressed as an error (i.e., in an oversimplified statement)

$$\Delta X = \bar{X}_m - X_a$$

where

ΔX = error

$\bar{X}_m$ = average of a set of measured values of X_a

X_a = actual value

Precision here refers to the spread in the set of measured values, often expressed in terms of the variance or standard deviation of the measured value distribution.

In the ARRS application, accuracy is specified to be ± 0.03 W/m^2-sr. The question of relating that accuracy requirement to a measurement can be answered in a variety of ways, depending on the measurement objectives. It could, in a horizon definition experiment, refer to the measurement of limb radiance in an exclusive spectral interfal - e.g., 14.0 to 16.28μ. In that case the error would be the difference between limb radiance in the 14.0 to 16.28μ interval and the measured radiance passed through a practical spectral filter which, because of its nonrectangular spectral shape, rejects some in-band (14.0 to 16.28μ) radiance and transmits some out-of-band radiance.

A second definition is related to the method of primary and inflight calibration, both of which use blackbody radiance spectral distribution. Measurement accuracy relates back to calibration and is an accuracy of determining the equivalent blackbody radiance of the source regardless of the source spectral distribution. Spectral interval considerations are important here, as well, because of the nonrectangular spectral shape of the filter.

A third definition of accuracy, which might be applicable, relates to integrated radiance in the instrument spectral response without regard to source spectral content or specific spectral interval. In this case the result of a measurement would be a statement that the source emits N W/m^2-sr in the spectral region (not interval) defined by the instrument response. This is the definition customarily applied to measurement programs of the ARRS type, but which seems to be lacking in terms of measuring a real physical quantity.

Other accuracy definitions could probably be applied as well. The intent here, however, is only to open the discussion of accuracy as related to defined spectral region or interval and source spectral distribution. For this analysis the first definition - i.e., accuracy of measuring limb radiance in the exclusive 14.0 to 16.28μ spectral interval - was used as being the most stringent of those discussed.

The source spectral models used were obtained from data generated under contract NAS1-6010. Limb radiance spectral distributions are dependent on both atmospheric characteristics and tangent height altitude. Because of time constraints, a comprehensive set of atmospheres and tangent heights could not be analyzed. Rather, in attempts to bound the problem distributions at the NAS 1-6010 tangent height extremes were used, corresponding to atmospheric path lengths of 500 atmosphere-cm and 10 atmosphere-cm, each at a temperature of 230°K. The distributions are shown in Figure L1. Out-of-band spectra, including solar radiance and effects of clouds, are shown in Figure L2. While it had been planned to perform out-of-band analyses using the spectra of Figure L2, time did not permit completion of this part of the analysis. The spectra are included here for future use.

Filter Model

A filter model was derived based on characteristics of filter parameters obtained from OCLI, a leading filter supplier. Parameter definition and characteristics are described as follows:

Out-of-band rejection. -- This is an independent variable, specified in terms of a maximum value on absolute transmission, In-band average transmission to a spectrally flat source is dependent on the value used as shown in Table L1 for out-of-band rejection between 2μ and 22μ.

Leading edge cut-on. -- Location of the wavelength at which transmission = 5% is a specified quantity. Wavelength region from λ_o, where transmission begins to rise above the out-of-band rejection value, to λ_1, the wavelength of the 5% point is roughly $\lambda_1 - \lambda_o \leq 0.05\,\lambda_1$.

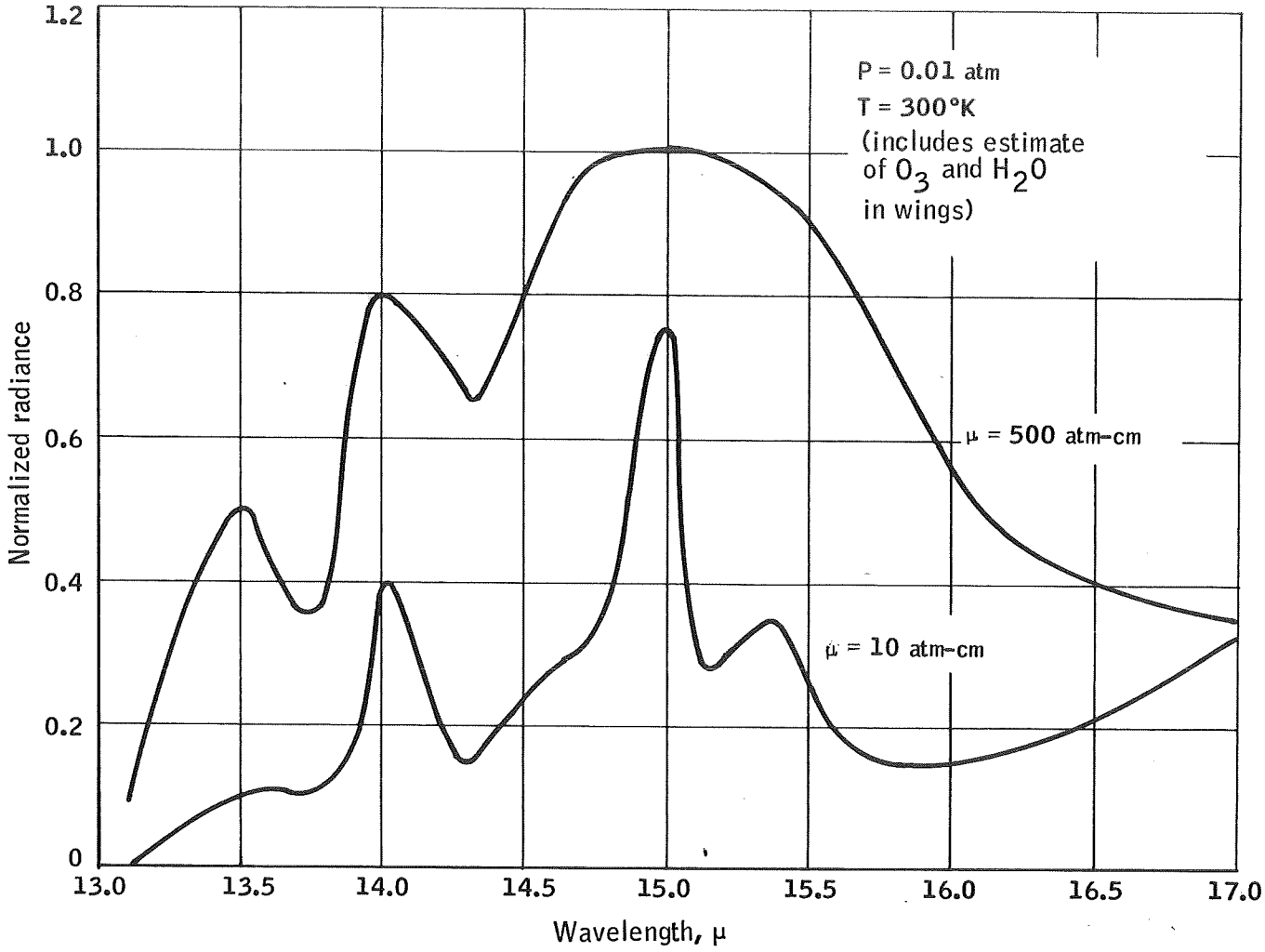

Figure L1. In-Band Limiting Spectra

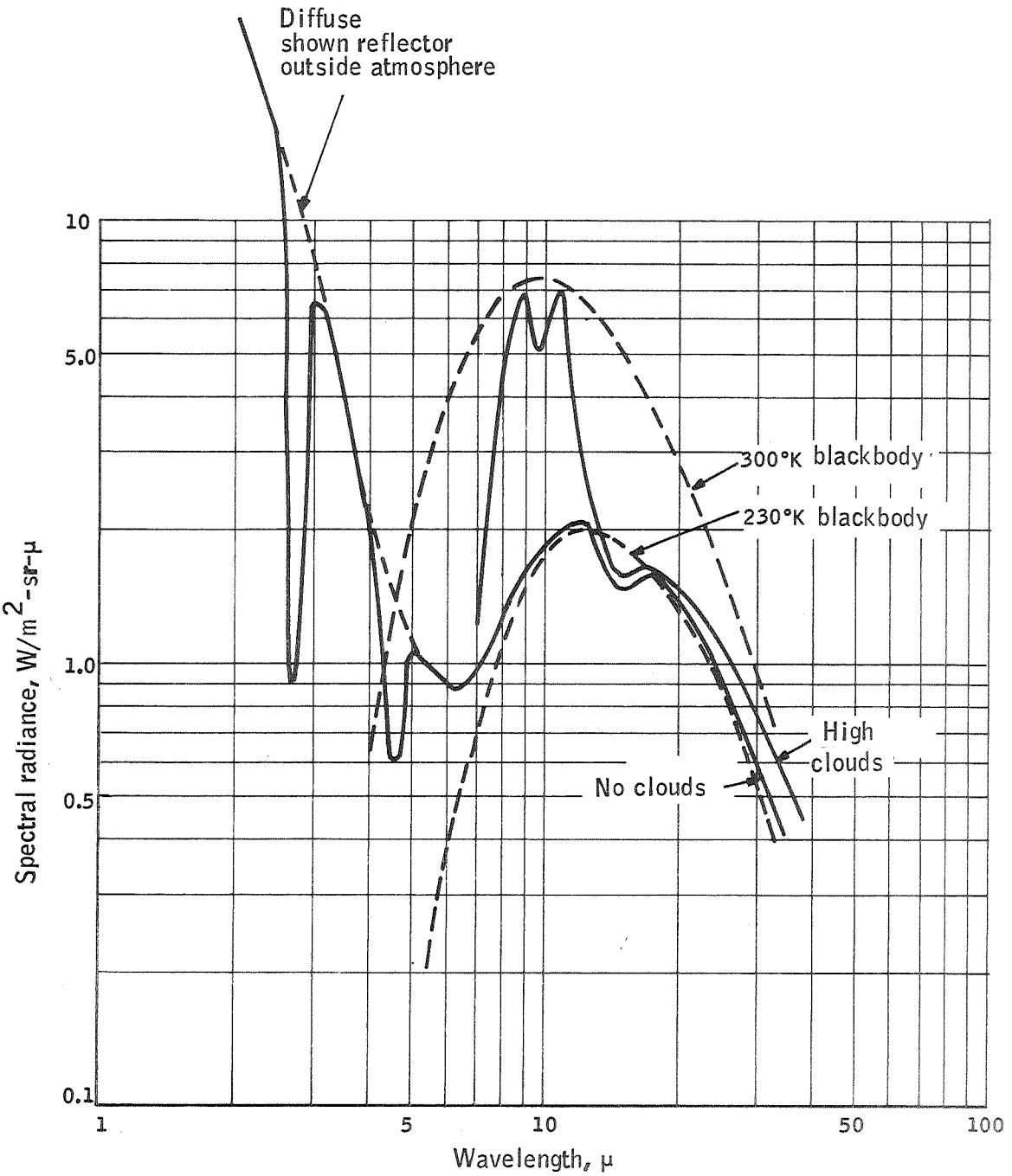

Figure L2. Out-of-Band Limiting Spectra

TABLE L1. - FILTER PARAMETERS

Out-of-band maximum transmission	In-band average transmission
0.01%	45%
0.1%	50%
1%	52.5%

Leading edge slope. -- From 5% transmission at λ_1 at 80% of peak transmission at λ_2,

$$\text{slope} \simeq \frac{\lambda_2 - \lambda_1}{\lambda_1} \approx 0.05$$

In-band structure. -- Typical in-band structure is shown in Figure L3.

Trailing edge cutoff. -- Wavelength at 5% transmission is a specified quantity. Wavelength at which transmission is equal to out-of-band rejection value is ≈ 1.05 times 5% wavelength.

Trailing edge slope. -- From 80% of peak transmission at λ_3 to 5% transmission at λ_4,

$$\text{slope} = \frac{\lambda_4 - \lambda_3}{\lambda_4} \cong 0.05$$

Based on the above characteristics and the filter spectral transmission curve of Figure L3, a linearized nominal filter model was derived and is shown in Figure L4.

COMPUTATIONS

The parameter of interest in terms of accuracy and precision is the average filter transmission including the source spectral distribution; i.e.,

$$\overline{T} = \frac{\int_0^{\infty} T(\lambda)\, N(\lambda)\, d\lambda}{\int_{14.0}^{16.3} N(\lambda)\, d\lambda}$$

The source models were linearized to facilitate computation as shown in Figure L5.

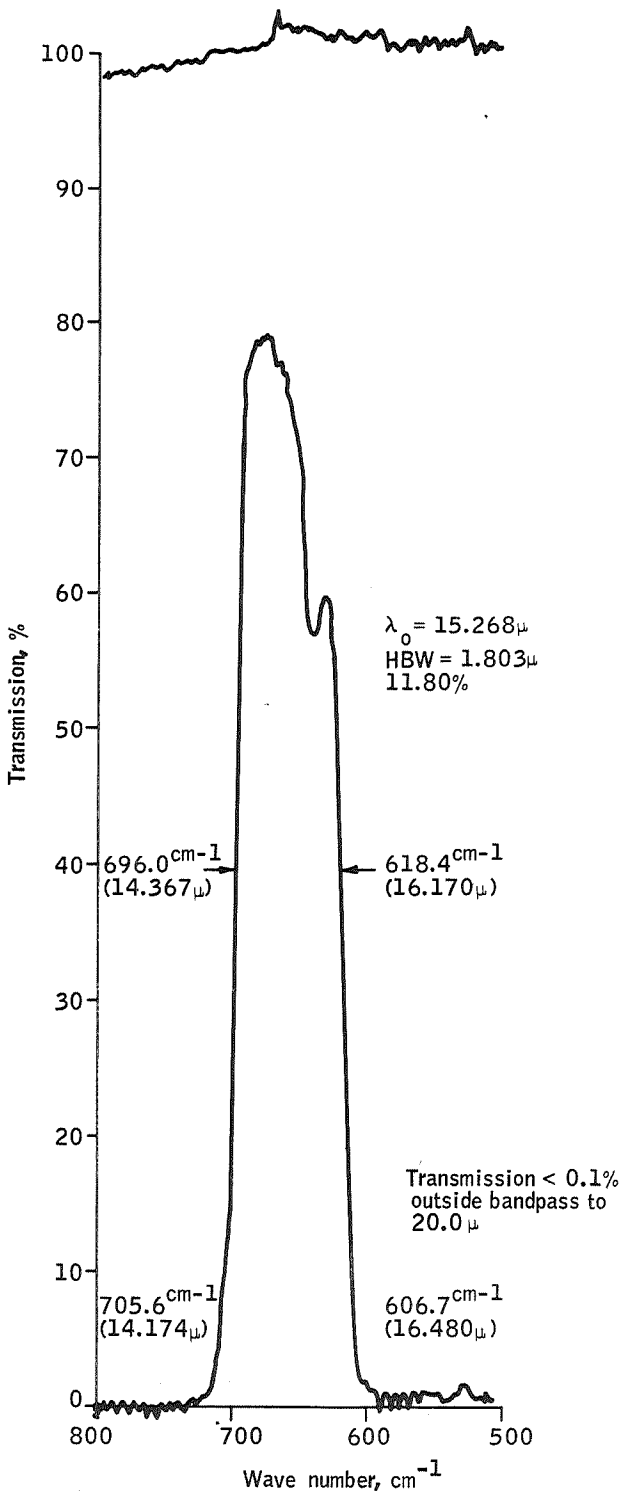

Figure L3. Typical Filter Transmission

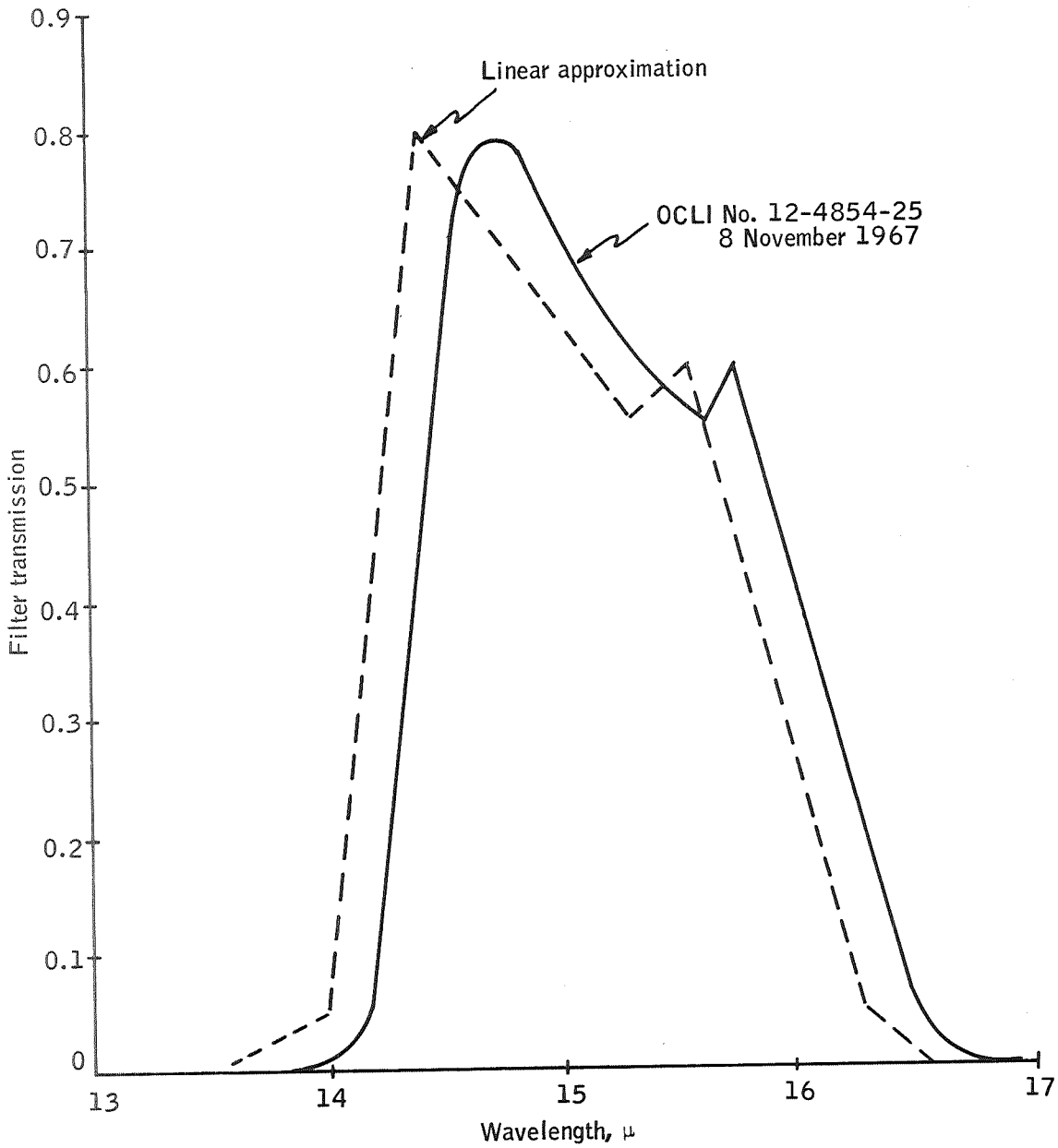

Figure L4. Nominal Linearized Filter Model

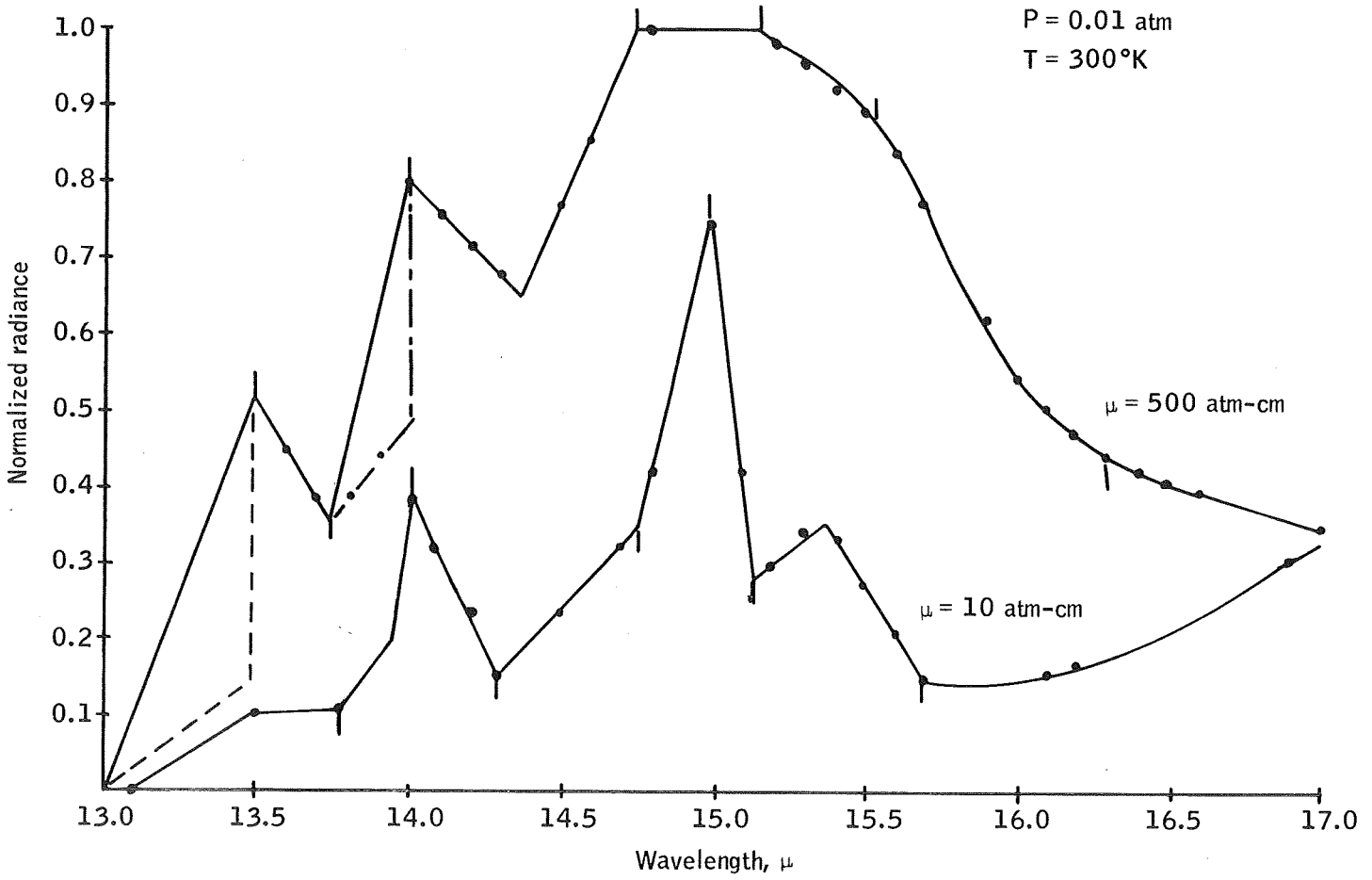

Figure L5. In-Band Limiting Spectra, L_∞ Near Approximation

Integrations were carried out on a digital computer using the rectangular rule which approximates the integrals as follows:

$$\int_{\lambda_1}^{\lambda_2} T(\lambda)\, N(\lambda)\, d\lambda \cong \Delta\lambda \sum_{\lambda_1}^{\lambda_2} T(\lambda_i)\, N(\lambda_i)$$

Sensitivity of the integral approximation to interval size was investigated and the results are shown in Figure L6. Results show that numerical approximation error is less than 0.05%. An interval of 0.04μ was subsequently used in all computer runs.

Results

Sensitivity of average transmission, $\overline{T}$, to spectral filter width between its 5% points for a center wavelength of 15.15μ is shown in Figure L7. The result shown is for a 10 atm cm path length. The difference in average transmission between the 10 atm cm and 500 atm cm paths is shown in Figure L8.

Note that the parameter $\Delta\overline{T}$ of Figure L9 could be construed to be a measure of error since it is a measure of the variability of the radiometer output caused by spectral variations of the source. Note also that the curve of Figure L8 suggests that a filter bandwidth does exist which will minimize this error source; for the models used, the optimum spectral bandwidth is 3.2μ, for which the error is only ≈ 0.01%.

Effects of spectral shift are shown in Figure L9. This figure shows that for small spectral shifts the output sensitivity is 0.27%/μ for 10 atm cm, and 1.1%/μ for 500 atm cm with a 2.8μ wide filter, the smallest sensitivity values of those spectral widths considered.

Translation into environmental effects is done using vendor-supplied data on temperature and angle shifts. OCLI supplied temperature shift is 0.125%/20°K, expressed in terms of percent shift of center wavelength per °K. At 15.15μ, in the shift is 0.001μ/°K. From Figure L9, the error in average transmission becomes 0.0011%/°K. Angle shift data published by OCLI are shown in Figure L10, which shows a family of curves applicable to different filter operating modes. Using the greatest shift and conservatively approximating it linearly to facilitate computation over small angles, the shift toward shorter wavelengths is always less than 1% in 20° angle shift, or 0.05%/°. For a 15.15μ center wavelength, shift becomes ≈0.0075μ/°. Using the sensitivity coefficients of Figure L9 for a 2.8μ wide filter, the error in average transmission will be smaller than ≈0.008%/°.

These results cannot be applied to determine actual error values since the temperature range over which the "ARRS flight radiometer" filter will operate is not presently known and the angular alignment integrity of the filter is not known. However, considering that the filter will be cooled as part of a temperature-controlled relay optics assembly, a temperature variation of ±10°K could be considered a severe worst case. Similarly, it is inconceivable that

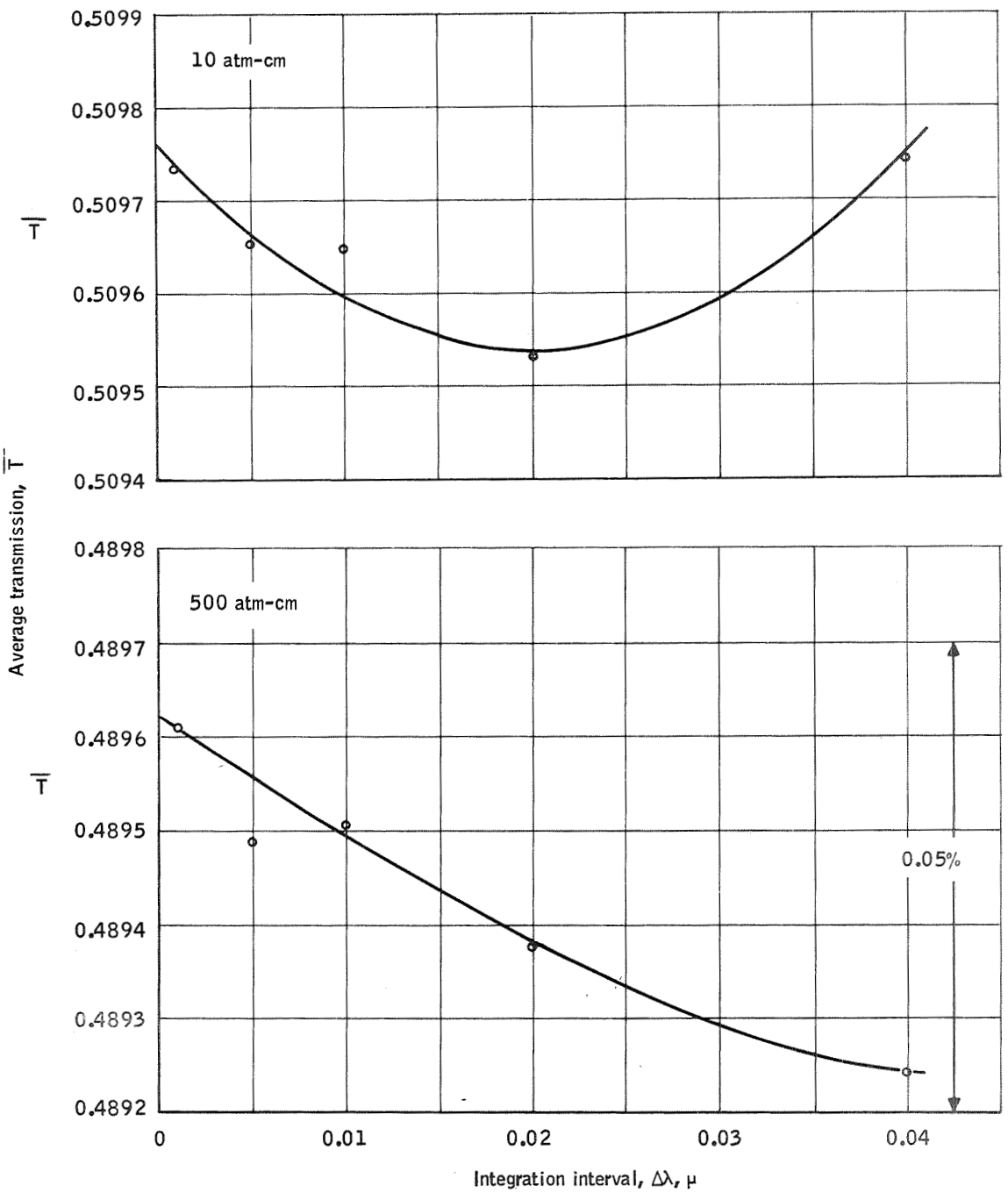

Figure L6. Computed Average Transmission Sensitivity to Integrated Interval

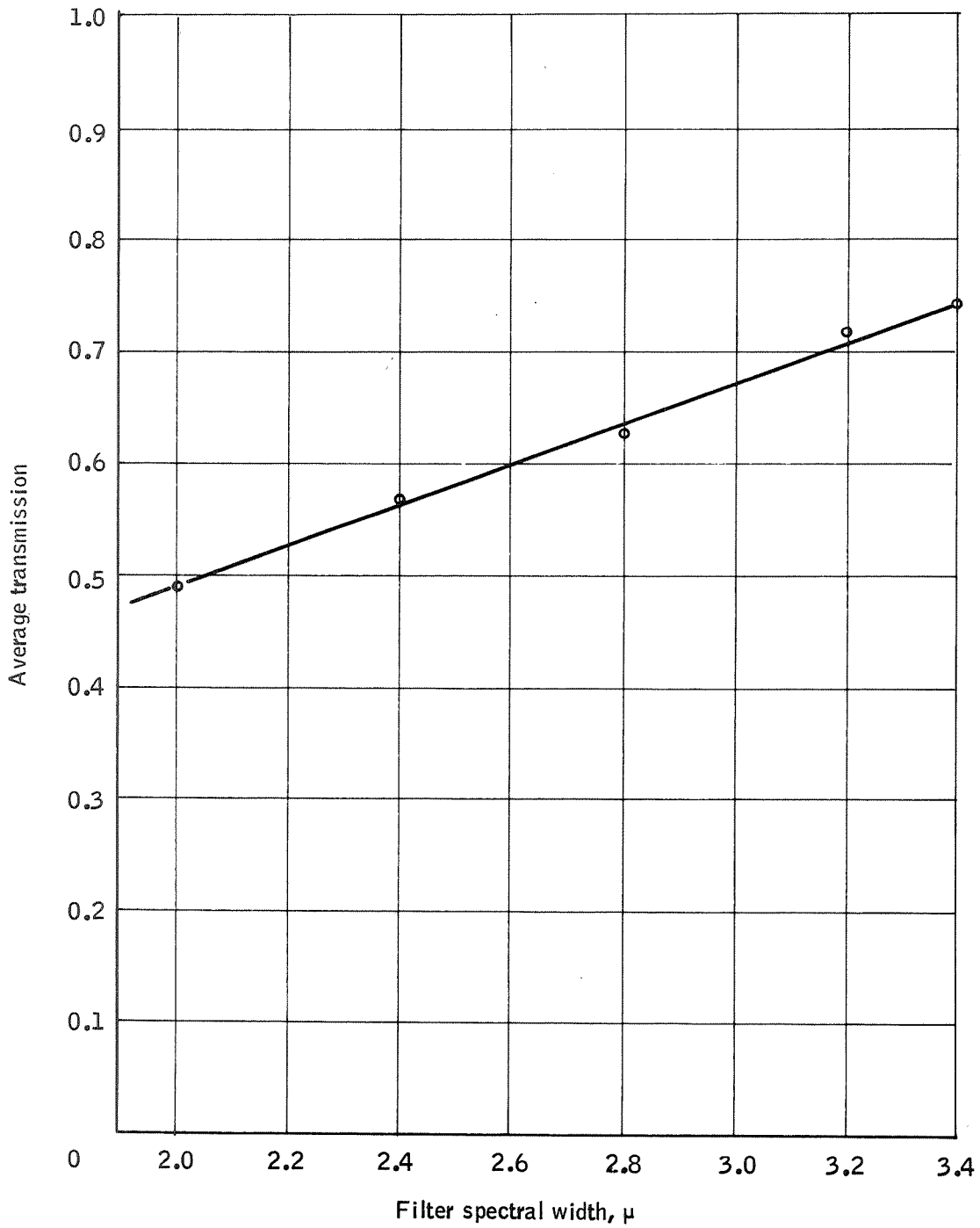

Figure L7. Average Transmission versus Filter Spectral Bandwidth

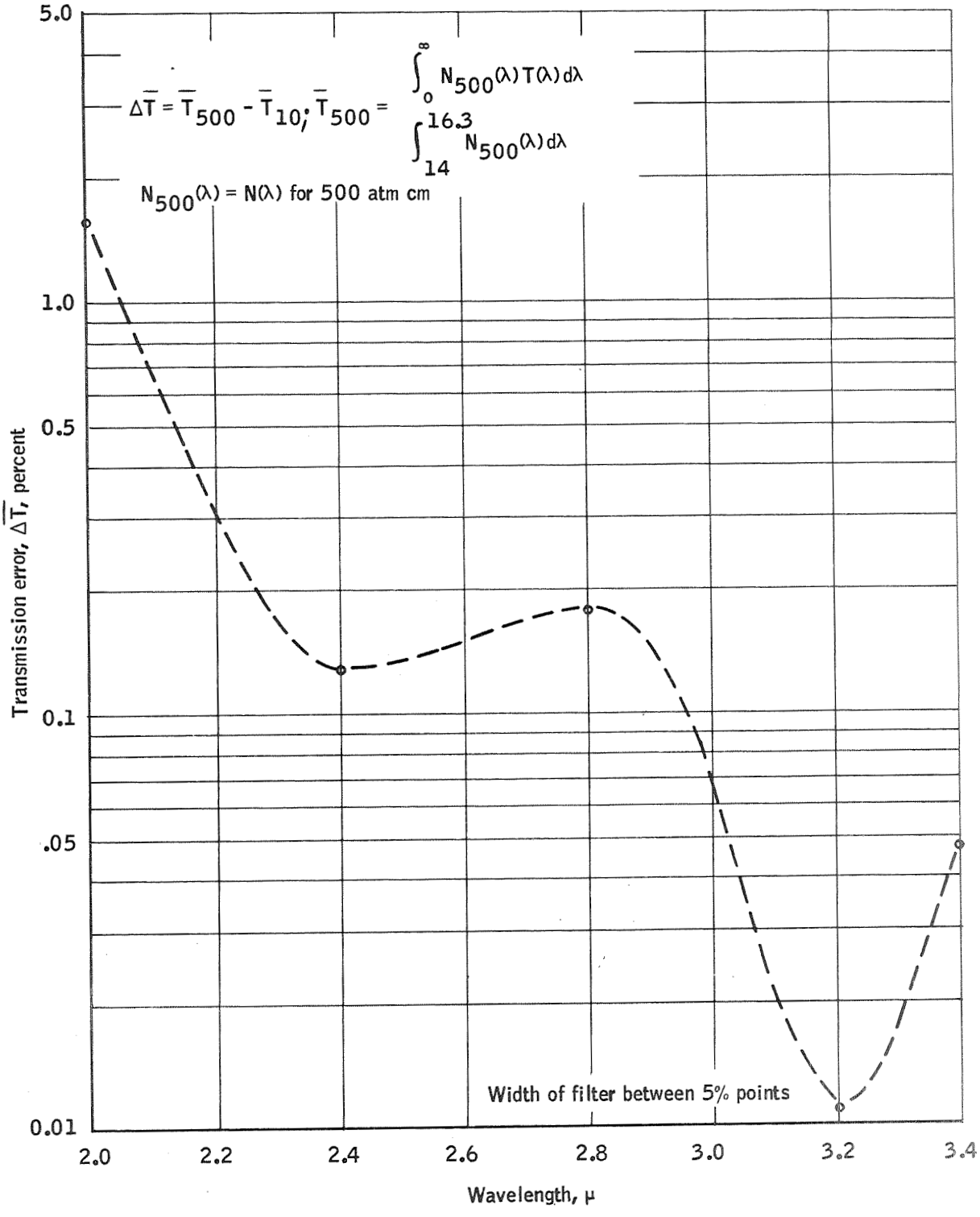

Figure L8. Average Transmission Error versus Width of Spectral Filter (between 5% points); Center at 15.15μ

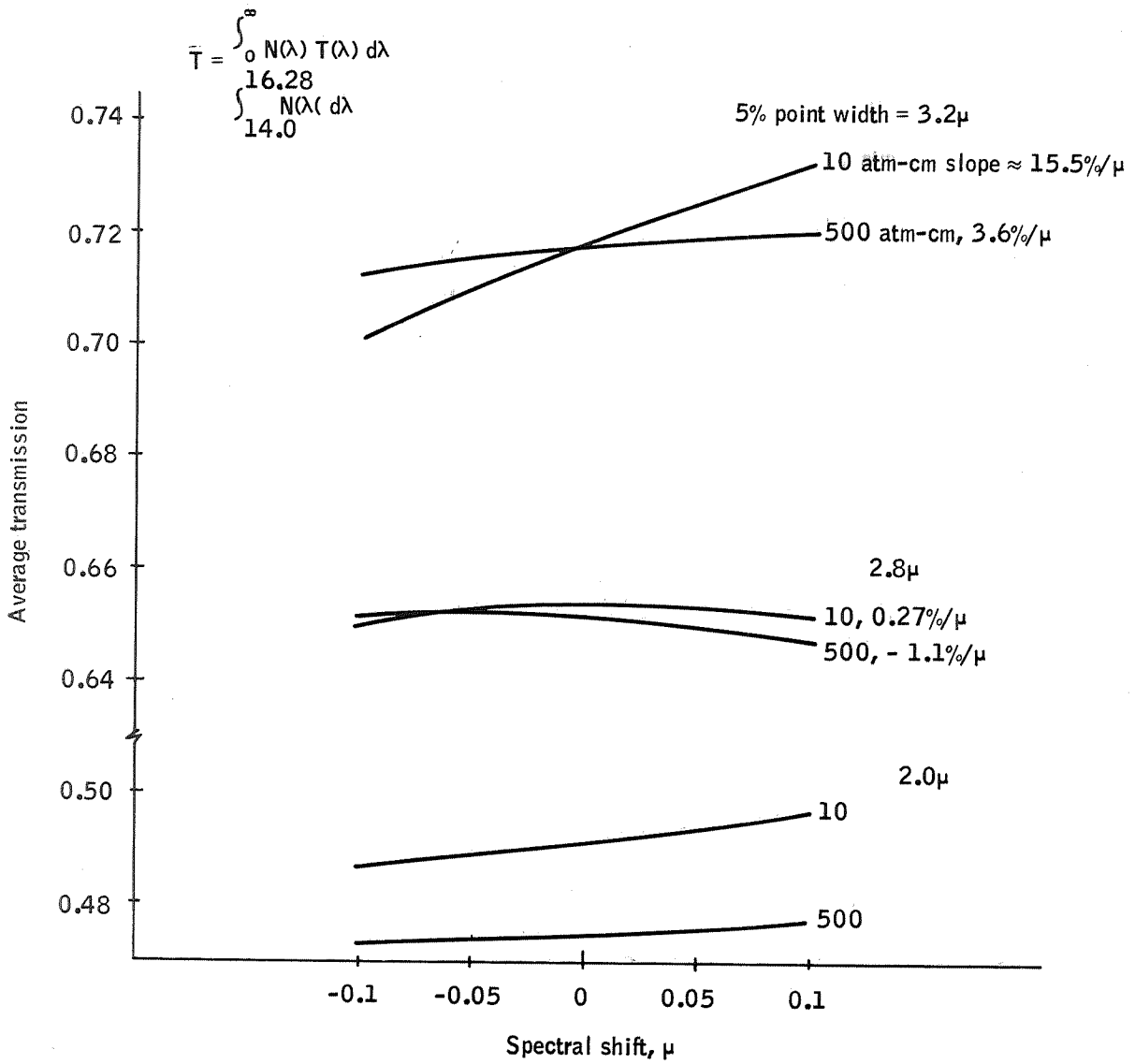

Figure L9. Spectral Shift Effects on Average Transmission

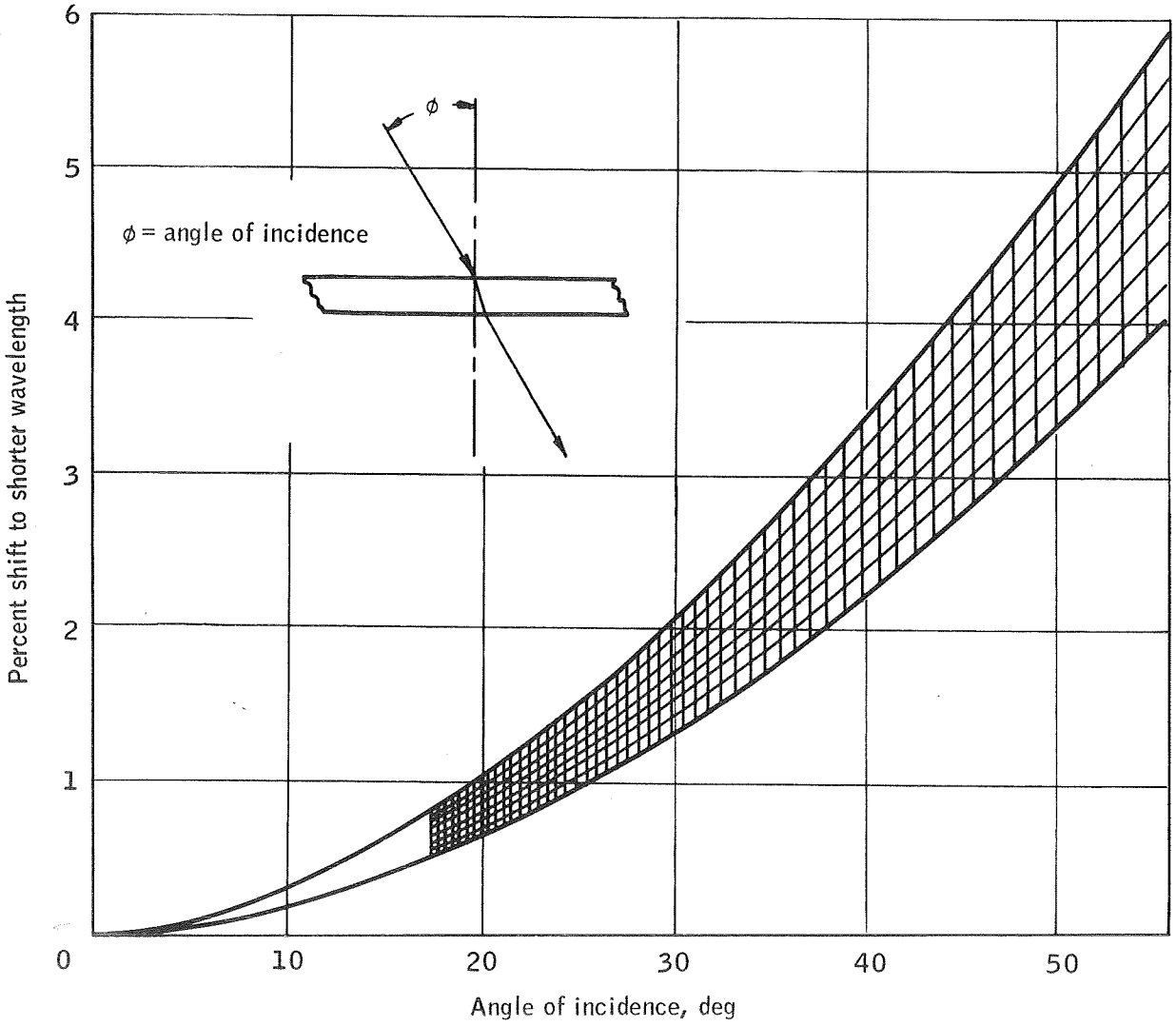

Figure L10. Wavelength Shift as a Function of Angle

angular misalignments as high as several degrees could occur except in the case of structural failure which is outside the scope of this type of analysis. The maximum error that could be expected, then, from temperature shifts is $\approx 0.01\%$ and from angle shifts $\approx 0.025\%$, both negligible.

CONCLUSIONS AND RECOMMENDATIONS

It was shown that the effects of temperature shift and angular misalignments on the spectral characteristics of an ARRS-type filter produce negligible errors in repeatability or precision. Accuracy was also shown to be relatively independent of these effects within the constraints of the definition of accuracy assumed.

Recommendations for upgrading and expanding the study started here are to

1) Obtain better definition of ARRS accuracy

2) Expand the study to include spectral response (and response stability) of the complete radiometer, primarily including detector and any refractive materials.

3) Upgrade source and response spectral models

4) Expand study to include effects of spectral response stability on inflight calibration stability

5) Include effects of other environments such as aging and nuclear bombardment

6) Widen spectral range studied to obtain better definition of out-of-band effects

REFERENCES

1. Zanoni, C. A.; and Hill, H. A.: Reduction of Diffracted Light for Astrometry Near the Sun. JOSA 55, Dec. 1965, pp. 1608-11.

2. Zanoni, C. A.; and Hill, H. A.: Reduction of Diffracted Light for Astrometry Near the Sun. JOSA 55, Dec. 1965, pp. 1608-11.

3. Born, M.; and Wolfe, E.: Principles of Optics. Pergamon Press N.Y., 1959.

4. Born, M.; and Wolfe, E.: Principles of Optics. Pergamon Press N.Y., 1959.

5. Wolfe, W. L., ed.: Handbook of Military Infrared Technology. Office of Naval Research, 1965.

6. Papoulis, A.: Error Analysis in Sampling Theory. Proc. IEEE, 54 p. 947, 1966.

7. Born, M.; and Wolfe, E.: Principles of Optics. Pergamon Press, N.Y., p. 397, 1959.

8. Smith, Warren J.: Modern Optical Engineering. McGraw-Hill, N.Y., p. 400, 1966.

9. Redden, R. C.; Clow, R. G.; Greinel, H.P.; and Day, R. P.: Infrared Diffraction Pattern Scanning Study - Semiannual Report. LMSC-2-03-61-1, Oct. 1961.

10. Nagaoka, H.: Diffraction of a Telescopic Objective in the Case of a Circular Source of Light. Astrophys. J. 51, pp. 73-101, 1920.

11. Milne-Thomson, L. M.: Jakobian Elliptic Function Tables. Dover Publications, Inc., N.Y., 1950.

12. Bennett, H.E.; and Koehler, W. F.: Precision Measurement of Absolute Specular Reflectance with Minimized Systematic Errors. JOSA, vol. 50, no. 1, Jan. 1960, pp. 1-6.

13. Bennett, J. M.; and Ashley, E. J.: Infrared Reflectance and Emittance of Silver and Gold Evaporated in Ultrahigh Vacuum. Applied Optics, vol. 4, no. 2, Feb. 1965, pp. 221-224.

14. Brownlee, D. E.; Hodge, P. W., Univ. of Washington, Seattle; and Wright, F. W., Smithonian Astrophysics Observatory, Cambridge, Massachusetts.: Upper Limits to the Micron and Submicron Particle Flux at Satellite Altitudes. Journal of Geophysical Research, Space Physics, vol. 74, no. 3, Feb. 1, 1969, 876-883.

15. Poehlmann, H. C.; and Austin, J. D.: Materials Contamination of Optical Systems in a Space Environment. Ball Brothers Research Corporation, Boulder, Colo., 80302, JOSA 57, 1430A, Nov. 1967.

16. Becker, R. A.: Optical Material Problems of Interplanetary Space. Jet Propulsion Lab., Pasadena, Calif., 91103, Applied Optics, 6, 955, May, 1967.

17. King, J. H.: Models of the Trapped Radiation Environment. Low Energy Protons, NASA-SP-3024, Vol. IV, Aerospace Corporation, Washington, D.C., 1967.

18. Anon.: Number of Micro Meteoroids. Space Physics, John Wiley and Sons, Inc., 1964, p. 289.

19. Anon: EGG-Electronic Product Division Photodiode Application Notes for SGD-100A and SGD-444 Photodiodes, Jan. 1969.

20. Anon: Effects of Variation of Angle of Incidence and Transmission on Infrared Filter Characteristics. Tech. Rept. Optical Coatings Laboratory, Inc., May 1967.

21. Carson, J. C.; et al: Feasibility Design of an Instrument System for Measurement of the Horizon Radiance in the CO_2 Absorption Band, Horizon Definition Study. NASA CR-66429, May 1967.

22. Eisenman, W. L.; Baten, R. L.; and Merriam, J. D.: Black Radiation Detector, JOSA, vol. 53, no. 6, June 1964, p. 729.

23. Eisenman, W. L.; and Bates, R. L.: Improved Black Radiation Detector, JOSA, vol. 54, no. 10, Oct. 1964, p. 1280.

24. Ladd, L. S.: IRTRAN-6 Material, Eastman-Kodak Company, 1966.

25. Funai, A. I.: Optical Properties of Seven Far-Infrared Window and Lens Materials. A Literature Review, TP-2706 LMSC/6-78-68-34.

26. Stierwalt, D. L.: I.R. Spectral Emittance Measurement of Optical Materials. Applied Optics 5, I.R. Division Research Laboratory, U.S. Naval Weapons Center, Corona, Calif. 91720, 1966, p. 1911.

27. Alishouse, J. C.: Temperature Variation of the Absorption Coefficient of Germanium. JOSA, Vol. 56, April 1966, pp. 525 and 526.

28. Healy, T. J.: Convolution Revisited. IEEE Spectrum, vol. 6, no. 4, April 1969, p. 87.

29. Rhoads, R. L.; and Ekstrom, M.P.: Removal of Intervening System Distortion by Deconvolution. IEEE Trans. Inst. Meas., vol. 17, Dec. 1968, p. 333.

30. George, C. F.; Smith, H. W.; and Bostick Jr., F. X.: The Application of Inverse Convolution Techniques to Improve Signal Response of Recorded Geophysical Data. Proc. IRE, vol. 50, Nov. 1962, p. 2313.

31. Lee, Y. W.: Statistical Theory of Communication.

32. Anon.: Thermal Contact Conductance in a Vacuum Environment. Missile and Space System Division, Douglas Aircraft Co., Inc. SM-47700, 13 Dec. 1964.

33. Anon.: Program for the Evaluation of Structural Reinforced Plastic Materials at Cryogenic Temperatures. Final Report of Goodyear Aerospace Corp. to NASA, July 1963 through July 1966.

34. Johnson, V. J.; ed.: A Compendium of the Properties of Material at Low Temperature Phase I. WADD Technical Report 60-56, Oct. 1960.